

AFRL-AFOSR-VA-TR-2022-0135

Surface Irregularity Effects on Laminar-Turbulent Transition - understanding the surface quality requirements for laminar flow on wings

Faraco de Medeiros, Marcello
Fundacao de Apoio a Universidade de Sao Paulo
Av. Afranio Peixoto 14
Sao Paulo, SP, , 05507-000
BR

04/24/2022
Final Technical Report

DISTRIBUTION A: Distribution approved for public release.

Air Force Research Laboratory
Air Force Office of Scientific Research
Arlington, Virginia 22203
Air Force Materiel Command

REPORT DOCUMENTATION PAGE

PLEASE DO NOT RETURN YOUR FORM TO THE ABOVE ORGANIZATION.

1. REPORT DATE	2. REPORT TYPE	3. DATES COVERED	
		START DATE	END DATE
20220424	Final	20171221	20211220

4. TITLE AND SUBTITLE
Surface Irregularity Effects on Laminar-Turbulent Transition - understanding the surface quality requirements for laminar flow on wings

5a. CONTRACT NUMBER	5b. GRANT NUMBER	5c. PROGRAM ELEMENT NUMBER
	FA9550-18-1-0112	
5d. PROJECT NUMBER	**5e. TASK NUMBER**	**5f. WORK UNIT NUMBER**

6. AUTHOR(S)
Marcello Faraco de Medeiros

7. PERFORMING ORGANIZATION NAME(S) AND ADDRESS(ES)	8. PERFORMING ORGANIZATION REPORT NUMBER
Fundacao de Apoio a Universidade de Sao Paulo Av. Afranio Peixoto 14 Sao Paulo, SP 05507-000 BR	

9. SPONSORING/MONITORING AGENCY NAME(S) AND ADDRESS(ES)	10. SPONSOR/MONITOR'S ACRONYM(S)	11. SPONSOR/MONITOR'S REPORT NUMBER(S)
Air Force Office of Scientific Research 875 N. Randolph St. Room 3112 Arlington, VA 22203	AFRL/AFOSR IOS	AFRL-AFOSR-VA-TR-2022-0135

12. DISTRIBUTION/AVAILABILITY STATEMENT
A Distribution Unlimited: PB Public Release

13. SUPPLEMENTARY NOTES

14. ABSTRACT
The effect of gaps and bumps on transition to turbulence in boundary layers was investigated. Linear stability theory and direct numerical simulations revealed that gaps can behave like large cavities and induce transition. Results explained experiments recently developed and published by Boeing. The effect of Re, Ma, ratio between boundary layer thickness and gap dimensional and gap aspect ratio was investigated and explained physically. Transition is caused by the interaction of Rossiter and centrifugal modes. Centrifugal modes nonlinearly affect the Rossiter instability, but the linear instability provides a lower safe bound for laminar flow. The interaction of TS waves and bumps were studied via very accurate direct numerical simulations. A boundary for a linear effect of the bump height on TS waves was found to be about 10% boundary layer displacement thickness. The effect of Mach and frequency was also investigated. A very precise and efficient model based on a Taylor expansion combined with a Stokes layer was developed to be used in numerical simulations. Theoretical equations were deduced for the optimal choice of computational parameters for use of matrix-free methods of
global instability analysis.

15. SUBJECT TERMS

16. SECURITY CLASSIFICATION OF:			17. LIMITATION OF ABSTRACT	18. NUMBER OF PAGES
a. REPORT	b. ABSTRACT	c. THIS PAGE		
U	U	U	SAR	356

19a. NAME OF RESPONSIBLE PERSON	19b. PHONE NUMBER *(Include area code)*
DANIEL MONTES	000-0000

FINAL REPORT

Surface Irregularity Effects on Laminar-Turbulent Transition - understanding the surface quality requirements for laminar flow on wings

Grant FA9550-18-1-0112

Principal Investigator
Mar ello Augusto Faraco de Medeiros
Department of Aeronautical Engineering
University of São Paulo
Av. Trabalhador São Carlense, 400 - São Carlos - 13566-590 - SP - Brazil
Fone: +55 16 3373 8285
E-mail: marcello@sc.usp.br

Collaborating investigators
Marlon Sproesser Mathias
Fernando Henrique Tadashi Himeno
Matheus Maia Beraldo
Christian Bresci Salaro
Victor Barcelos Victorino
Ana Elisa Basilio
Felipe Oliveira Aguirre

DISTRIBUTION A: Distribution approved for public release. Distribution unlimited

Summary and introduction to report

This document constitutes the final report of the project FA9550-18-1-0112.

Initially the project comprised three Principal Investigators, Prof. Dan Henningson and Prof. Ardeshir Hanifi, both from KTH Sweden, and Prof. Marcello Augusto Faraco de Medeiros, from USP – Brazil, and was submitted to be co-sponsored by EOARD and SOARD. It comprised 4 workpackages:

- WP1: Effects of TS-waves on roughness elements
- WP2: Effects of roughness elements
- WP3: Effects of step/gaps
- WP4: Effects of suction holes

It turns out that the EOARD part of the project was not approved while that of SOARD was. In view of that it was decided to execute the parts which were initially intended to be developed at USP, which fell on WP1 and WP3. To better develop these parts of the project after this set back, it was organized in 2 workpackages:

- WP1 – effect of gaps on transition;
- WP2 – effect of bumps and isolated roughness on TS wave evolution.

All 4 packages, and consequently the two remaining packages involved only numerical and theoretical studies. Eventually, what amounted to a third package was included at no cost

- WP3 wind tunnel experiments on gap and bump effects on transition,

which constituted an attempt on a wind tunnel experiment on this topic to help future experimental developments.

The document is organized along these three workpackages, and contains 4 appendices, 2 corresponding to WP1, and one for each of the other worpackages. In this introduction we explain the content of each document, present their most important contributions and challenges faced and provide guidelines on how to best read the material. These documents were essentially PhD dissertation or Msc. (complete or parts of). This introduction is written in the spirit of an executive summary. In the introduction, reference is made to the appendices.

WP1 - Effect of gaps on transition.

The flow within open cavities is very complex and involves at least four parameters. Under some conditions this flow spontaneously gives rise to several kinds of velocity fluctuations normally referred to as modes. The first identified was the Rossiter mode, which is essentially two-dimensional. It involves the formation of Kelvin-Helmholtz vortices in the mixing layer at the cavity opening. They impinge on the cavity trailing edge and generate upstream propagating acoustic waves that interact with the cavity leading edge, triggering new vortices. This loop becomes unstable under some circumstances and promotes the selection of specific frequencies. Each frequency corresponds to one Rossiter mode order which is defined by the number of vortice that fit into the cavity opening at the same time. Three dimensional steady and unsteady modes caused by centrifugal effects are also present in the cavity, and are driven by the shear layer at the cavity opening. In the project we were able to advance several aspects of the behavior of these modes and their effect on boundary layer transition. These developments constitute appendices 1 and 2.

1- Effect of boundary layer thickness on Rossiter modes. The literature on open cavity flow is vast. The gap is a small cavity, but it was unclear what would constitute a boundary between gaps and cavities, or even if there really was one. In any case, the parameter defining a boundary would have to considered the size of the cavity relative to the thickness of the upstream boundary layer. Hence our first initiative was to investigate the effect of the ratio between cavity depth and boundary layer thickness on Rossiter instability, a parameter that was severely overlooked in the previous literature. It was concluded that boundary layer thickness is the parameter that selects the order of the Rossiter mode that will dominate the cavity flow (Appendix 1) .

2- Gaps are really only small cavities. It turns out that there is no qualitative differences between gaps and cavities. Both display Rossiter and centrifugal modes, albeit with quantitative differences that smoothly change as the ratio cavity depth to boundary layer thickness varies. Except for Mach number, there is no consensus in the literature about the four parameters used to characterize this flow. Reynolds number based on either cavity depth, cavity length or different measures of boundary layer thickness are used. The cavity aspect ratio is also often considered, and the last is either cavity depth or length over some measure of boundary layer thickness. If however the literature data is reduced to the same set of of 4 parameters, it is found that some nominally cavity

DISTRIBUTION A: Distribution approved for public release. Distribution unlimited

studies fall in the parameter space of interest to cavity induced boundary layer transition, even though they were only investigated from the point of view of open cavity flow (Appendix 1).

3- Mach is destabilizing. The effect of Mach on cavity instability was also investigate in the scenarios of large and small cavities (gaps). The literature assigned the effect of Mach to competition between the stabilizing effect of compressibility on the mixing layer and the destabilizing effect of resonance with acoustic cavity modes. In the project we established that Mach number has a dominant destabilizing effect associated with the acoustic emission at the cavity trailing edge, which increases with a large power of Ma (in general 3rd). Because of its power nature, a Ma increase from 0.1 to 0.2 has a much larger impact than from 0.6 to 0.7. It was found that the destabilizing effect of Ma saturates at about Ma=0.5. This is due the nature of the acoustic emission and the stabilizing effect of Ma on the mixing layer instability, which is stronger as we approach transonic speeds.

4- Acoustic resonances. It was also demonstrated that, in this saturated regime of the higher Ma the effect of resonance with acoustic modes is active and accounts for an irregular effect of Ma (Appendix 1).

5- Centrifugal modes are also present and affect Rossiter modes. Next we addressed the linear stability of the centrifugal modes and their nonlinear interaction with the Rossiter modes. The centrifugal modes have frequency an order of magnitude lower than Rossiter ones, and may also be steady. It could be thought that with such a disparity in frequency any interaction would be weak. However, it was demonstrated that even marginally unstable centrifugal modes have a very strong impact on highly unstable Rossiter modes. The effect is associated with a substantial modification of the base flow promoted by the centrifugal mode and can lead to Rossiter modes of orders different from the linear predictions (Appendix 1).

6- A convenient set of parameters. The work eventually led to the conclusion that the often used cavity aspect ratio is a misleading parameter. With a fixed aspect ratio it may arise that Re_θ is stabilizing, a somewhat disturbing conclusion. This is however the effect of variations of other parameters that may overshadowed the Re destabilizing effect. It appeared that the most compelling set of parameters would include the ratios cavity depth to boundary layer thickness (displacement, momentum or any other measure of boundary layer thickness) and cavity length to boundary layer thickness. With these parameters fixed, Re can be based on any dimension (cavity depth, cavity length or any measure of boundary layer thickness), in which case it will always be destabilizing. It was also found that, for both Rossiter and centrifugal modes, the main effect of Reynolds number is in controlling the rate of increase of the mixing layer thickness at the cavity opening and thereby altering the effective values of the ratios above introduced. This is a mild effect at higher Re. Interestingly, these ratios are used in the very few studies of gap induced transition, in which Re was not considered to be very relevant. (Appendix 1).

7- Gap instability boundary. At this stage the 2D and 3D linear instability of the gap flow was performed for a range of ratios boundary layer thickness – cavity depth and cavity length, for Re_δ =600 and Ma=0.5. At these conditions, the boundaries of instability for both Rossiter and centrifugal modes are similar, and point to asymptotic limits of lowest ratios cavity depth over boundary layer thickness for long cavities and of lower ratio cavity length over boundary layer thickness for deep cavities. The shape of this boundary was remarkably similar to the boundary of by-pass transition obtained in recent experiments by Boeing at low Mach numbers. The boundaries were slightly shifted because of differences in Mach and Reynolds numbers between our theoretical results and those of Boeing (Appendix 1 and 2).

8- Prediction of by-pass transition. It was found that both Rossiter and centrifugal modes are needed to promote transition. It is conjecture that the Rossiter mode contributes the necessary high frequencies and the centrifugal modes gives the essential three-dimensionality. However, predictions based on linear stability alone are hindered by the fact that the centrifugal mode alter the base flow and affects the Rossiter instability. Nevertheless, the linear stability provides a lower boundary of by-pass transition, which does not seem to be far from the experimental observations of Boeing and DNS simulations we performed. (Appendix 2).

9- The process of by-pass transition. The by-pass transition process is however not so simple. For marginally unstable conditions the flow does not undergo by-pass transition. Increasing the instability, there is a regime of intermittence. Then, progressively more unstable flow lead to transition increasingly closer to the cavity. This is similar to what would be expected in a process where the gap affected the evolution of a TS wave, which could be modeled by a variation of the N-factor in the e^N method. However this is an entirely different phenomenon which, for example, would not be affected by the free-stream turbulence. The intermittence is likely to give rise to hysteresis. The boundary of gap instability displays different regions where different Rossiter and centrifugal modes first become unstable. This may lead to different transition regimes, a possibility that deserves investigation (Appendix 2).

10- Interaction of TS waves with a cavity. We have also investigated the effect of a stable cavity on the evolution of a TS wave. In the parameter space of short cavities the effect was negligible. However, the recent experiments by Boeing show that for long cavities there is an effect. We were not able to investigate this scenario in the project time frame. (Appendix 1)

DISTRIBUTION A: Distribution approved for public release. Distribution unlimited

11- Optimization of numerical solution of global instability. In the course of the project it was necessary to perform a very large number of global instability analysis. The standard technique for it uses an algorithm that needs the selection of at least 4 computational parameters. We developed theoretical equations that lead to the optimal choice of parameters in terms of accuracy and computational cost. This can lead to orders of magnitude improvement in relation to sub-optimal, commonly used choices. This contribution is likely to have a wide range of applications.

Note that this introduction discusses two appendices in combination and relates them in aspects that are not specifically addressed in either of them. This results from the fact that, in isolation, each document could not present this systemic view and also from the fact that recent results led to a deeper and wider understanding of previous ones. Note also that the appendices exhibit some overlap in literature review and methodology. This was needed because the documents were used partially or completely as a report of a graduate student project. In reading the full report, the reader may like to skip some parts previously covered.

WP2 – effect of bumps and isolated roughness on evolution of TS waves.

The initial focus here was on the interaction of TS waves with a two dimensional bump. In this workpackage this was intended both as a model for the effect of steps on transition and as a way towards the isolated roughness. Previous experiments developed in the group on the interaction between isolated roughness and TS waves showed that under some circumstances even the nominally smooth surface case (meaning the roughness completely retracted, height less than $0.01\delta^*$ - displacement thickness), the roughness had a strong effect. In that work this was associated with a critical amplitude of TS waves which triggered secondary instability at the roughness. In that work, it was further observed that the effect on the TS wave scaled linearly with the isolated roughness height only up to heights of $0.05\delta^*$. Hence on the two dimensional scenario we also focused on small roughness. The small two dimensional bump has an also small effect on the evolution of a TS wave. A $0.05\delta^*$ high bump increases the amplitude of the TS wave by only 2,5%, which would be negligible for practical purposes. However, this is also a primary model for distributed roughness, which can have a large integrated effect. Hence, understanding this scenario is relevant. The developments in this front constitutes Appendix 3.

1- Accuracy requirements. The simulation of the interaction between a small bump and a TS wave has proven to be more difficult and more computational demanding than anticipated. Accurately capturing the 2.5% increase in amplitude of a TS wave caused by a roughness required a 10 fold increase in resolution in the wall normal direction and 100 fold in the streamwise direction, in comparison to smooth surfaces. These results improved upon previous less accurate numerical results pf bump effect on TS wave and provided almost perfect agreement with carefully controlled experiments.
2- Linear regime. The more accurate results indicated that the regime within which the bump height has a linear effect on the TS wave evolution in limited to about 0.1 δ^*, whereas previous works suggested 0.4 δ^*. Above 0.1 δ^* the effect of the bump increases massively and at 0.4 δ^* it causes an increase of 170% in the TS wave amplitude.
3-The two effects of the bump on the TS evolution. First there is an effect at the roughness, but there is also an effect at the bump wake. To establish the downstream region over which the roughness had a effect, the growth rates were extracted from the DNS results with and without a bump, and compared. It was found that the waves require a substantial extent to return to what would be effectively its growth on a smooth surface. Somewhat unexpected, it was found that, within the roughness height range covered, the region affected by the roughness was almost independent on the bump height. Nevertheless, the effect within that region was very dependent on the bump height. The good accuracy of the simulations was fundamental for these conclusions.
4- Downstream region of influence of the bump. It would be interesting to establish a region of influence based on the baseflow parameters and hence avoid the need to simulate the TS waves. Several parameters were considered, such as, the pressure gradient, the displacement and momentum thicknesses, the shape factor and the Falkner-Skan parameter. It seems that the shape factor is a good indicator of the extent of region whose growth rates is affected by the bump.
5- Compressibility effects. The influence of Ma number on the effect of a bump on the TS wave evolution has not been addressed systematically in the literature. Here it was found that Mach had a small effect up to Ma=0.6 and a large effect to transonic speeds. For example, for a bump height 40% at Mach M = 0.1, the TS wave amplitude increases by 160% whereas at M = 0.9, it increases by 250%. However the effect at the roughness is relatively small. The Mach effect is mostly a consequence of the downstream region affected by the bump, which increases substantially when approaching the transonic speeds. For example, from M = 0.1 to M = 0.9 the extent of this region increases two-fold.

DISTRIBUTION A: Distribution approved for public release. Distribution unlimited

6- Influence of frequency. The influence of frequency on the effect of a bump on the TS wave evolution has been overlooked in the literature. We are left with the impression that it is assumed that this effect is negligible. We addressed this issue by investigating the interaction of pulse generated wavepackets with a bump. Theoretically, the pulse contains all frequencies. In practice it contains a large number of frequencies which in the linear regime behave independently. The packet can be made very small so as to behave linearly and, if the code is sufficiently accurate, the modes can be extracted from the packet to provide the influence of frequency. It was found that for bump heights below 0.1δ*, the effect was independent on frequency. Above it, the effect of the bump increased with the frequency. The frequency influence is larger at higher Mach numbers and higher bump heights. The difference within the range of unstable TS waves can amount to 100% increase in bump effect.
7- Underlying physics. It is conjectured that the underlying physics is as follows. The effect of the bump has two origins, one at the bump itself, here referred to as bump effect, and the other associated with the wake, the wake effect. The bump effect is linear with respect to bump height, independent on the frequency and dominates at small heights. The roughness wake is thought to have an effect of the same nature as that of an adverse pressure gradient, albeit smaller. Indeed the profile in the wake leans towards that of an adverse pressure gradient. As the bump height increases the region affected by the roughness does not extend, but within this region the profile is substantially more distorted and produce much larger effects on the TS waves. As Ma increases, the wake region extends, intensifying the bump effect. The adverse pressure gradient has a small effect on the first branch of the boundary layer instability loop, but substantially increases the frequencies at the second branch. One effect of the adverse pressure gradient is then to increase the frequency of the dominant modes. The argument is consistent with a negligible influence of frequency for small bump heights and enhancement of higher frequencies in the nonlinear regime of the high bumps.
8- New method for the simulation of small surface imperfections. The high demand on computational grid for the correct simulation of the effect of bump on the TS waves would pose even higher demands for the isolated roughness case, not only because a third dimension would be added, but also because strong refinement would also be needed in this direction. However, it should be possible to develop less demanding but sufficiently accurate methods to represent a 0.05 δ* high roughness. The idea was to apply a condition at the wall that would enforce a no-slip and no penetration condition at the roughness top. This can be done using a Taylor expansion, and has been applied in some analytical approaches in fluid mechanics, among them, receptivity to acoustic waves. The approach can be viewed as an application of perturbation methods. The problem here was that in 2D the effect was very small and so required very high accuracy. This situation demanded several improvements on this technique. For instances the time lag (and amplitude decay) between the application of boundary condition at the wall and its effect at the roughness top position was important. To compensate for it a Stokes layer flow correction was implemented which precisely time advanced (and magnified) the boundary condition. These however was not sufficient and a second order approximation had to be used, in an approach that can be viewed as an application of iterative perturbation methods. For the 0.05δ*, the target for the 3D simulations, the approach was very accurate, but degraded rapidly above it and was inadequate for 0.1δ*. It must also be considered that the isolated 3D case will be less demanding in accuracy for the reason that follows. For the 2D case the effect is an increase of about 2% in TS wave amplitude. Hence 2% error in amplitude may lead to 100% error in the estimation of this effect. The isolated roughness problem is one of receptivity of 3D waves from the 2D ones. Just in any receptivity problem, the aim is to estimate accurately the amplitude of the resulting initial wave, here the oblique TS wave. In this problem, a 2% error in TS wave amplitude imparts a similar level of inaccuracy to the problem.
9- Isolated roughness problem. With the difficulties faced we were not yet able to simulate the interaction between a TS wave and an isolated roughness. We have support from another agency for the PhD student that was responsible for this workpackage. The simulations are under way and we intend to report to AFOSR within a year.

Note that the methodology used in the direct numerical simulations is largely identical to that reported in appendices 1 and 2. Because here the accuracy was paramount, more attention was given to this aspect.

WP3 - wind tunnel experiments on gap and bump effects on transition

The objective here was an attempt at a first experiment on these problems in our group. This workpackage was added at no cost half way through the project, shortly before the pandemic. Because of its experimental nature, the need of work by third parties and conflict with other commitments, this initiative was more severely affected. For it also contributed its late introduction. In any case, we are now in a position to advance this workpackage and intend to report to AFOSR within a year. The developments in this front constitute Appendix 4.

DISTRIBUTION A: Distribution approved for public release. Distribution unlimited

1- Model design. The initial task was to design the experimental model. This is composed of a 2m chord airfoil whose pressure side is used to produced the zero pressure gradient boundary layer. A flap and a tab are used to adjust the pressure gradient. The model is instrumented with a 100 microphones that can be placed at about 500 different positions to capture the surface pressure. High precision microphones were used, which are housed inside the model. The cavity is housed in a model insert. Its depth or height can be modified with the wind tunnel running via computer controlled stepper motors.
2- Instrumentation. Besides the microphones, which is an innovative technique in this scenario, the instrumentation to be used involves PIV and, in particular, hot-wire anemometry. A new, more accurate, hot-wire system was specified and acquired for the study.
3- Parameter space. The parameter space of cavity depth over boundary layer thickness and cavity length over boundary layer thickness was carefully studied and discussed with Boeing to cover a region where, from their experience, different regimes of transition could be observed.
4- Model construction. The model construction was ordered outside the university and suffered severe delay owing to the pandemic.
5- Effect of the pandemic. We had obtained from another agent (FAPESP- Sao Paulo - Brazil) support for the design and construction of a new fan to improved flow quality and speed, which was planned to be installed after the first experimental campaign. In view of the delay in model construction and the deadlines placed by FAPESP, we were forced to anticipate the fan replacement, which in turn was even more affected by the pandemic. The new fan and the model were finally installed in March 2022, and experiments are due to start in April. We intend to report to AFOSR within a year.

The corresponding appendix reports on the model design and selection of the parameter space.

Final remarks

It is noted that the workpackages had different levels of achievement. In WP1 it is our impression that the development went beyond the initial plan. A substantially wider and deeper understanding of cavity and gap flow instability was obtained and its relation to by pass transition was demonstrated. A lower bound for by-pass transition based on linear stability theory was established. Theoretical improvements on the methods for the solution of global instability problems were also developed. With regard to WP2, there were difficulties associated with severe grid refinement demands. In any case, we were able to performed very accurate simulations which led to correction of concepts presented in the established literature. It also led to a deeper understanding of several aspects that influence the effect of bump on the evolution of TS waves. An efficient and accurate technique for the simulation of small bumps was developed that will allow the simulation of the interaction of TS waves with small isolated roughness. WP3 was severely affect by the pandemic, but was not in the original proposal. We nevertheless were able to complete the model construction and installation, and are ready to perform the experimental campaign in an improved version of the wind tunnel.

It is felt that overall the achievements were substantial and can be said to correspond to a third of the original proposal, which is consistent with the fact that only one PI remained from the three PI’s originally involved.

DISTRIBUTION A: Distribution approved for public release. Distribution unlimited

Appendix 1

DISTRIBUTION A: Distribution approved for public release. Distribution unlimited

UNIVERSIDADE DE SÃO PAULO
ESCOLA DE ENGENHARIA DE SÃO CARLOS

Marlon Sproesser Mathias

Computational study of the hydrodynamic stability of gaps and cavities in a subsonic compressible boundary layer

São Carlos

2021

DISTRIBUTION A: Distribution approved for public release. Distribution unlimited

DISTRIBUTION A: Distribution approved for public release. Distribution unlimited

Marlon Sproesser Mathias

Estudo computacional da estabilidade hidrodinâmica de cavidades em uma camada limite compressível subsônica

Tese apresentada à Escola de Engenharia de São Carlos da Universidade de São Paulo, para obtenção do título de Doutor em Ciências - Programa de Pós-Graduação em Engenharia Mecânica.

Área de concentração: Aeronáutica

Supervisor: Prof. Dr. Marcello Augusto Faraco de Medeiros

VERSÃO CORRIGIDA

São Carlos

2021

DISTRIBUTION A: Distribution approved for public release. Distribution unlimited

AUTORIZO A REPRODUÇÃO TOTAL OU PARCIAL DESTE TRABALHO, POR QUALQUER MEIO CONVENCIONAL OU ELETRÔNICO, PARA FINS DE ESTUDO E PESQUISA, DESDE QUE CITADA A FONTE.

Ficha catalográfica elaborada pela Biblioteca Prof. Dr. Sérgio Rodrigues Fontes da EESC/USP com os dados inseridos pelo(a) autor(a).

Mathias, Marlon Sproesser
M431c Computational study of the hydrodynamic stability of gaps and cavities in a subsonic compressible boundary layer / Marlon Sproesser Mathias; orientador Marcello Augusto Faraco de Medeiros. São Carlos, 2021.

Tese (Doutorado) - Programa de Pós-Graduação em Engenharia Mecânica e Área de Concentração em Aeronáutica -- Escola de Engenharia de São Carlos da Universidade de São Paulo, 2021.

1. Gap. 2. Open Cavity. 3. Compressible flow. 4. Global stability. 5. Direct Numerical Simulation. 6. Wave packets. I. Título.

Eduardo Graziosi Silva - CRB - 8/8907

DISTRIBUTION A: Distribution approved for public release. Distribution unlimited

FOLHA DE JULGAMENTO

Candidato: Engenheiro **MARLON SPROESSER MATHIAS.**

Título da tese: "Estudo computacional da estabilidade hidrodinâmica de cavidades em uma camada limite compressível subsônica".

Data da defesa: 07/12/2021.

Comissão Julgadora	**Resultado**
Prof. Associado **Marcello Augusto Faraco de Medeiros** **(Orientador)** (Escola de Engenharia de São Carlos – EESC/USP)	**Approved**
Prof. Dr. **Vassilis Theofilis** (Aerospace Engineering/University of Liverpool)	**Approved**
Prof. Dr. **Ardeshir Hanifi** (KTH Royal Institute of Technology)	**Approved**
Prof. Titular **Gherhardt Ribatski** (Escola de Engenharia de São Carlos – EESC/USP)	**Approved**
Prof. Dr. **André Valdetaro Gomes Cavalieri** (Instituto Tecnológico de Aeronáutica/ITA)	**Approved**

Coordenador do Programa de Pós-Graduação em Engenharia Mecânica:
Prof. Associado **Adriano Almeida Gonçalves Siqueira**

Presidente da Comissão de Pós-Graduação:
Prof. Titular **Murilo Araujo Romero**

DISTRIBUTION A: Distribution approved for public release. Distribution unlimited

DISTRIBUTION A: Distribution approved for public release. Distribution unlimited

Acknowledgements

Gostaria de agradecer a todos que tornaram este trabalho possível e contribuíram em seu desenvolvimento, direta ou indiretamente.

À minha namorada e melhor amiga, Ana Carolina, que sempre me apoiou e esteve ao meu lado. À minha família, João Carlos, Sônia e Marcel, que me apoiaram nesta etapa e nas que a precederam.

Ao meu orientador, Marcello, pelas produtivas conversas e pela orientação que se iniciou com minha IC e continuou até este momento. Aos colegas de laboratório, Ana Elisa, Andrés, Christian, Daniel, Elmer, Fernando, Felipe, Filipe, Giovanni, Juan, Matheus, Pedro e Victor, pela companhia no desenvolvimento do trabalho e pelas conversas relacionadas, ou não, à pesquisa. Aos amigos da pós-graduação no Departamento de Engenharia Aeronáutica.

Ao professores Poti, Sávio e Vassilis, que deram valiosas dicas para a continuação da pesquisa.

À Fundação de Amparo à Pesquisa do Estado de São Paulo (FAPESP), pelo apoio financeiro por meio do projeto número 2018/04584-0. Além do Air Force Office of Scientific Research (AFOSR), projeto FA9550-18-1-0112; da University of Liverpool, pelo acesso ao Cluster Barkla; ao Centro de Ciências Matemáticas Aplicadas a Industria (CeMEAI-USP), pelo acesso ao Cluster Euler (FAPESP 2013/07375-0); e ao Laboratório Nacional de Computação Científica (LNCC), pelo acesso ao Supercomputador Santos Dumont.

E a todos os demais que, de alguma forma, contribuíram para este trabalho.

DISTRIBUTION A: Distribution approved for public release. Distribution unlimited

DISTRIBUTION A: Distribution approved for public release. Distribution unlimited

"Apesar de [redacted]
amanhã há de ser outro dia"
Chico Buarque

DISTRIBUTION A: Distribution approved for public release. Distribution unlimited

DISTRIBUTION A: Distribution approved for public release. Distribution unlimited

ABSTRACT

MATHIAS, M. S. **Computational study of the hydrodynamic stability of gaps and cavities in a subsonic compressible boundary layer**. 2021. 160p. Tese (Doutorado) - Escola de Engenharia de São Carlos, Universidade de São Paulo, São Carlos, 2021.

We study the effect of small cavities, or other discontinuities, on the laminar to turbulent flow transition over a flat plate. Understanding the transition mechanism is of significant importance for the reduction of drag in an aerodynamic project, which impacts the fuel consumption of aircrafts, for example. Predicting the correct region in which the transition to turbulence occurs is still a challenge, especially when accounting for parameters such as surface imperfections or manufacturing tolerances. Ideally, aircraft designers would balance the costs of manufacturing smoother surfaces with their aerodynamic benefits. We use two different computational tools in this work. First, a Direct Numerical Simulation (DNS) code is used to simulate the flow, either just by itself or in conjunction with controlled disturbances designed to model a natural transition. The second tool is a Linear Stability Theory (LST) code which can compute the linear stability modes of a given base flow, this algorithm is of the time-stepping type, for which we analyze the sources of errors and develop guidelines for obtaining optimum results. Both tools were designed to capture a wide spectrum of oscillations, even at very low amplitudes, which is essential for such modeling, as the natural transition is triggered by the interaction of multiple modes of different frequencies that are several orders of magnitude smaller than the base flow. There are many previous works that study either the natural transition on a flat plate or the flow disturbances caused by discontinuities on the surface, but the interaction between those two phenomena is still open for investigation. We study two different scenarios: when the cavity is much larger than the incoming boundary layer; and when they are of comparable magnitudes. Similar conclusions are reached in both cases. Increasing the Mach number has a mostly destabilizing effect on the 2D modes of the cavity. Greater ratios between cavity size and the incoming boundary layer thickness also increase the instability. We then compare the linear stability results to non-linear simulations. We also conclude that, even though 2D modes are usually more linearly unstable, the presence of 3D modes is essential for an accurate simulation of the flow. Moreover, we compare our results to experimental works and conclude that when both 2D and 3D modes are unstable in a small open cavity, it may cause a bypass transition in the boundary layer.

Keywords: Gap. Open Cavity. Compressible flow. Global stability. Direct Numerical Simulation. Wave packets.

DISTRIBUTION A: Distribution approved for public release. Distribution unlimited

DISTRIBUTION A: Distribution approved for public release. Distribution unlimited

RESUMO

MATHIAS, M. S. **Estudo computacional da estabilidade hidrodinâmica de cavidades em uma camada limite compressível subsônica**. 2021. 160p. Tese (Doutorado) - Escola de Engenharia de São Carlos, Universidade de São Paulo, São Carlos, 2021.

Estudamos o efeito de pequenas cavidades, ou outras descontinuidades, na transição de um escoamento do regime laminar para o turbulento sobre uma placa plana. Entender o mecanismo de transição para turbulência é de grande importância para a redução de arrasto em um projeto aerodinâmico, o que impacta, por exemplo, o consumo de combustível de um avião. Prever corretamente a região da transição para turbulência ainda é um desafio, especialmente ao considerar parâmetros como imperfeições da superfície ou tolerâncias de manufatura. Idealmente, os projetistas de um avião devem balancear os custos de fabricar superfícies mais lisas com seus benefícios. Duas ferramentas computacionais são usadas. Primeiro, um código de Simulação Numérica Direta (DNS) é usado para simular e escoamento, tanto sozinho quanto somado de perturbações criadas para simular a transição natural. A segunda ferramenta é um código de estabilidade linear (LST) que calcula os modos do escoamento, este algoritmo é do tipo time-stepping e analisamos suas fontes de erros e desenvolvemos diretrizes para obtenção resultados ótimos. Ambas as ferramentas foram projetadas para capturar um amplo espectro de oscilações, mesmo com amplitudes baixas, o que é essencial para tal modelagem pois a transição natural depende da interação de múltiplos modos com diferentes frequências e de amplitudes muitas ordens de grandeza menores que o escoamento. Existem muitos trabalhos anteriores que estudam a transição natural em uma placa plana ou os distúrbios causados por descontinuidades na superfície, mas a interação entre esses dois fenômenos ainda está aberta para investigação. Estudamos dois cenários diferentes: quando a cavidade é muito maior do que a camada limite; e quando são de magnitudes comparáveis, chegando a conclusões semelhantes. O aumento do número de Mach tem um efeito geralmente desestabilizador nos modos 2D da cavidade. Razões maiores entre o tamanho da cavidade e a espessura da camada limite também aumentam a instabilidade. Em seguida, comparamos os resultados de estabilidade linear com simulações não lineares. Também concluímos que, embora os modos 2D sejam geralmente mais linearmente instáveis, a presença de modos 3D é essencial para uma simulação precisa do escoamento. Por fim, comparamos nossos resultados com trabalhos experimentais e concluímos que quando modos 2D e 3D são instáveis em uma pequena cavidade aberta, ela pode causar uma transição de by-pass na camada limite.

Palavras-chave: Cavidade pequena. Cavidade aberta. Escoamento compressível. Estabilidade global. Direct Numerical Simulation. Pacotes de onda.

DISTRIBUTION A: Distribution approved for public release. Distribution unlimited

DISTRIBUTION A: Distribution approved for public release. Distribution unlimited

LIST OF FIGURES

Figure 1.1 – Illustration of the open cavity flow. 28

Figure 1.2 – Neutral stability curves for a $L/D = 2$ and $D/\delta^*_{LE} = 10.2$ open cavity as a function of Mach and Reynolds. 29

Figure 2.1 – The various regions of a boundary layer transition. 34

Figure 2.2 – Illustration of TS waves evolution before transition to turbulence. . . 35

Figure 2.3 – Typical routes from receptivity to turbulent breakdown. 36

Figure 2.4 – Schlieren image of the cavity flow showing its acoustic output. 37

Figure 2.5 – Cavity acoustic directivity at Mach 0.05 and Mach 0.1. 39

Figure 2.6 – Cavity acoustic directivity at Mach 0.1 for various frequencies. 39

Figure 2.7 – Effect of the gap on the transition location. 42

Figure 3.1 – Example of mesh generated using two attractor points at both ends of a cavity. 46

Figure 3.2 – Domain, mesh and boundary conditions of the flow simulation. The useful domain is marked in gray, while the buffer zone is green. One in every 10 nodes of the mesh is shown in black. The blue line represents wall boundaries, while the red line is a free-slip wall condition. 47

Figure 3.3 – Modified wave number for various numerical differentiation schemes. . 49

Figure 3.4 – Close-up of the corner nodes in the domain and the regions considered for derivatives. 51

Figure 3.5 – Spectral function for the tenth order low-pass filter. 55

Figure 3.6 – Scheme of a three-dimensional domain decomposed for a grid of 3x4 processes. 58

Figure 3.7 – Flowchart to obtain derivatives of the decomposed domain. 59

Figure 3.8 – Flowchart of the DNS. The top line of each frame identifies the task, while the bottom line shows which file contains it. 61

Figure 3.9 – Flowchart of the simulation routine of the DNS. The top line of each frame identifies the task, while the bottom line shows which file contains it. 62

Figure 3.10 – Speed-up obtained for different numbers of processors for our 2D and 3D test cases. 64

Figure 3.11 – Mesh spacing (top) and relative spacing change (bottom) for X (left) and Y (right) in a gap case. Buffer zones are represented by the dashed lines and are not fully shown for clarity. 66

DISTRIBUTION A: Distribution approved for public release. Distribution unlimited

Figure 3.12 – Time series of stream-wise velocity (U) at three probes as the domain evolves from the initial condition towards a base flow for three different SFD strategies: only at the buffer zones (blue), at the buffer zones and at the gap trailing edge (red) and at the whole domain (yellow). Note that the time scale is changed after $t = 2000$ for better visualization of the initial transient phase. 68
Figure 3.13 – Maximum residual of each variable towards a base flow. 69
Figure 4.1 – (Top) Number of Arnoldi iterations (M) and total integration time (τM) as a function of integration time τ for two values of C. (Bottom) Fraction of time spent in each part of the procedure. 79
Figure 4.2 – (Top) Streamwise velocity of the base flow (contours every 10% of the free-flow, from -30% to 90%) and velocity field inside the cavity. (Bottom) Maximum residue of each variable as the flow evolves to the steady state. 81
Figure 4.3 – (Left) Eigenspectrum of the base flow, with the unstable Rossiter modes (Rn) and the least stable stationary mode (S1) indicated, (Right) Density contours for the Rossiter modes 1 to 3 and the Stationary mode 1. 82
Figure 4.4 – Real part of the R2 eigenvalue as a function of ε for different values of τ. Dashed lines represent first-order accurate Fréchet derivative, and full lines, second-order accurate. (Left) Absolute value. (Right) Difference to the reference case. 83
Figure 4.5 – Real part of the S1 eigenvalue as a function of ε for different values of τ. Dashed lines represent first-order accurate Fréchet derivative, and full lines, second-order accurate. (Left) Absolute value. (Right) Difference to the reference case. 84
Figure 4.6 – Values of ε_{opt} and the corresponding E_B as a function of ε_S and N for 1^{st}, 2^{nd} and 4^{th} order accuracy Fréchet approximations. 86
Figure 4.7 – (Left) Lower limit for τ according to equation 4.21. The dashed line represents the product $\tau M = 2500$, which was used in this work. (Right) Upper limit for τ according to equation 4.22. 88
Figure 4.8 – Real part of the R2 eigenvalue as a function of τ for selected values of ε. Dashed lines represent the first-order accurate Fréchet derivative, while full lines represent the second-order accurate derivative. (Left) Absolute value. (Right) Difference to the reference case. 89
Figure 4.9 – Real part of the S1 eigenvalue as a function of τ for selected values of ε. Dashed lines represent the first-order accurate Fréchet derivative, while full lines represent the second-order accurate derivative. (Left) Absolute value. (Right) Difference to the reference case. 89

DISTRIBUTION A: Distribution approved for public release. Distribution unlimited

Figure 4.10 – (Left) Evolution of each mode in the flow as it is simulated starting from the base flow without the introduction of any disturbance other than the discretization error. Modes R1 to R3 and S1 are highlighted. Solution projections on the 100^{th} least stable are shown as thin gray lines. (Right) Snapshots of the density fluctuation at $\tau = 5$, 10, and 20. 90

Figure 4.11 – Evolution of each mode in the flow as it is simulated from different starting conditions. Modes R1 to R3 and S1 are highlighted. Modes up to the 100^{th} least stable are shown as thin gray lines. Vertical lines depict the upper limits of τ, as given by equation 4.24. 91

Figure 4.12 – Estimate of the error in $A\zeta$ as a function of τ for select values of ε, (Left) using equation 4.29 and (Right) using equation 4.30 with values corresponding to mode S1. The solid lines represent second order accurate Fréchet derivative approximation and the dashed lines, first order approximation. 93

Figure 4.13 – (Left) Values of E_A for mode R2 when the real part of its eigenvalue is changed. (Center) Values of E_A for mode S1 when the real part of the leading eigenvalue is changed. (Right) Values of E_A for mode S1 when the real part of its eigenvalue is changed. 94

Figure 4.14 – Estimate of the error in $A\zeta$ as a function of τ for select values of ε, using equation 4.30 for modes R2 (Left) and S1 (Right). The solid lines represent the case with renormalization and dashed lines, without. 95

Figure 4.15 – Difference in the real part of the eigenvalue corresponding to modes R2 (Left) and S1 (Right) as a function of τ for $\varepsilon = 10^{-7}$ and second order accurate Fréchet derivative. The black line is the reference case, with no renormalization and the colored lines represent different intervals of renormalization. 96

Figure 4.16 – Estimate of the error in $A\zeta$ as a function of τ for select values of ε, using equation 4.30 for a hypothetical flow with the least stable eigenvalues given by $\sigma_1 = -0.1$, $\sigma_2 = -0.12$, $\sigma_1 = -0.2$. The solid lines represent the case with renormalization and dashed lines, without. 96

Figure 4.17 – Isocontours of $\log_{10}$(Error) of the real part of the R2 mode, using $\varepsilon = 10^{-6}$. The full gray lines represent a constant computational cost of 5 minutes, 10 minutes, 30 minutes and 1 hour from left to right. The dashed gray lines indicate constant $t = \tau M$. (Left) First order accurate Fréchet derivative. (Right) Second order accurate Fréchet derivative. 98

DISTRIBUTION A: Distribution approved for public release. Distribution unlimited

Figure 4.18 – Isocontours of $\log_{10}$(Error) of the real part of the S1 mode, using $\varepsilon = 10^{-6}$. The full gray lines represent a constant computational cost of 5 minutes, 10 minutes, 30 minutes and 1 hour from left to right. The dashed gray lines indicate constant $t = \tau M$. (Left) First order accurate Fréchet derivative. (Right) Second order accurate Fréchet derivative. 98
Figure 4.19 – Error of the first four eigenvalues as computational time is increased. $\tau = 0.1, 1, 10$, $\varepsilon = 10^{-6}$. Note that the time scale for mode S1 is different than that of modes R1 to R3. 100
Figure 4.20 – Isocontours of $\log_{10}$(Error) of the eigenfunction of R2 for (Left) first-order accurate Fréchet derivative and (Right) second-order derivative. 101
Figure 4.21 – Isocontours of $\log_{10}$(Error) of the eigenfunction of S1 for (Left) first-order accurate Fréchet derivative and (Right) second-order derivative. 101
Figure 4.22 – Weight of each disturbance ζ_i in the eigenfunctions of modes R1, R2, R3 and S1. 102
Figure 5.1 – Eigenfunctions of Rossiter mode linear approximations at $Re_D = 1000$, $D/\theta = 100$ and $Ma = 0.5$, at an arbitrary phase. (Left) Contours of pressure for mode 2. Black lines indicated level zero. (Right) Contours of wall-normal velocity for modes 1 to 5. 107
Figure 5.2 – Eigenvalues from the D/θ ratio sweep ($Re_D = 1000$, $Ma = 0.5$). (Left) Eigenspectrum. (Right) Real and imaginary parts of Rossiter mode eigenvalues. 107
Figure 5.3 – Mixing layer integrated spatial amplification factor compared to the global instability results. The asterisks indicate the global modes eigenvalues of Rossiter modes and the dots are other eigenvalues, they refer to the scale on the right-hand side of the frame. 108
Figure 5.4 – Eigenvalues from the first Mach number sweep ($Re_D = 1149$, $D/\theta = 29.7$). (Left) Eigenspectrum. (Right) Real and imaginary parts of Rossiter mode eigenvalues. 110
Figure 5.5 – Eigenvalues from the second Mach number sweep ($Re_D = 1000$, $D/\theta = 100$). (Left) Eigenspectrum. (Right) Real and imaginary parts of Rossiter mode eigenvalues. 110
Figure 5.6 – Location of probes for the analysis of sound emission. Gray contours indicate dilatation fluctuations of the second Rossiter mode at $Ma = 0.6$, full line for positive contours and dashed line for negative ones. Colored contours indicate vorticity fluctuations. The black line indicates region of evaluation of sound source magnitude. Red and green lines indicate regions of evaluation of the magnitude of the pressure fluctuations. 111

DISTRIBUTION A: Distribution approved for public release. Distribution unlimited

Figure 5.7 – Acoustic energy transfer (ET_{AC}) as a function of Mach number for the linear approximation of Rossiter modes 1 (blue) and 2 (red). The dashed and dashed-dotted lines represent Ma^3 and Ma^2 respectively. 112

Figure 5.8 – Frequency predictions of Rossiter modes (blue) and standing wave modes (orange) compared to the global mode results (circles). The circle radius is proportional to the distance from neutral stability, the solid circles represent instability while hollow circles represent stability. 113

Figure 5.9 – Eigenvalues from the span-wise wave number sweep ($Re_D = 1000$, $D/\theta = 100$, $L/D = 2$, $Ma = 0.5$). (Left) Spectra in the complex plane. (Right) Real and imaginary parts of the eigenvalues of the Rossiter and centrifugal modes. 114

Figure 5.10 – Most unstable eigenmodes from the 3D LST analysis. (Left) $\beta = \pi/4$, isosurfaces of density. (Right) $\beta = 2\pi$, isosurfaces of span-wise velocity. 115

Figure 5.11 – Comparison between 2D and 3D simulations of the $Re_D = 1000$, $D/\theta = 100$, $L/D = 2$, $Ma = 0.5$ case. (Left) Time series of pressure at the trailing edge. (Right) Spectrum. The vertical lines mark angular velocities predicted by the linear stability analysis for each Rossiter mode (R1 through R3) and centrifugal mode (C2 and C3). 116

Figure 5.12 – Most unstable mode at each β for the first three cases defined in table 5.1. Each colored region represents a different type of mode. . . 117

Figure 5.13 – Time series of pressure fluctuation for the cases defined in table 5.1. Blue and orange curves represent different span-wise positions. 118

Figure 5.14 – Spectra of cases `R`, `C` and `R+C 1`. The linear predictions of angular velocities of each mode are also marked. 118

Figure 5.15 – Most unstable linear mode for cases `R+C 1`, `R+C 2` and `R+C 3` for various values of β. 119

Figure 5.16 – Comparison between 2D and 3D simulations of case `R+C 3` ($Re_D = 1500$, $D/\theta = 100$, $L/D = 2$, $Ma = 0.5$). (Left) Time series of pressure at the trailing edge. The dashed lines were measured at another span-wise position. (Right) Spectrum. The vertical lines mark angular velocities predicted by the linear stability analysis for each Rossiter mode (R1 through R3). 119

Figure 5.17 – Snapshots of wall-normal velocity for the 2D simulation of cases `R+C 2` and `R+C 3` and the 3D simulation of case `R+C 3`. The snapshots of the 3D simulation were taken at an arbitrary span-wise position. . . . 120

Figure 5.18 – (Top) Velocity profiles of the mean flow. (Middle) Mixing layer thickness for different situations of case `R+C 3` (Bottom) Total spatial amplification of each mixing layer as a function of ω. 121

DISTRIBUTION A: Distribution approved for public release. Distribution unlimited

Figure 5.19 – Spectrum of pressure at the trailing edge as a function of time for case `R+C 3` ($Re_D = 1500$, $D/\theta = 100$, $L/D = 2$, $Ma = 0.5$) for (Left) the 2D simulation, (Center) the 3D simulation and (Right) the filtered 3D simulation. LST-predicted frequencies for Rossiter modes are also shown. 122

Figure 5.20 – Spectrum of wall-normal velocity inside the cavity as a function of time for case `R+C 3` ($Re_D = 1500$, $D/\theta = 100$, $L/D = 2$, $Ma = 0.5$) for (Left) the 2D simulation, (Center) the 3D simulation and (Right) the filtered 3D simulation. LST-predicted frequencies for Rossiter modes are also shown. 122

Figure 5.21 – Comparison between 2D and 3D simulations of case `R+C 3` ($Re_D = 1500$, $D/\theta = 100$, $L/D = 2$, $Ma = 0.5$). (Left) Time series of wall-normal velocity in the cavity. The dashed lines were measured at another span-wise position. (Right) Spectrum. The vertical lines mark angular velocities predicted by the linear stability analysis for each Rossiter mode (R1 through R3). 123

Figure 5.22 – Temporal and span-wise spectrum for the limit cycle of `R+C 3` ($Re_D = 1500$, $D/\theta = 100$, $L/D = 2$, $Ma = 0.5$). (Left) Pressure at the cavity trailing edge (Right) Wall-normal velocity inside the cavity. 124

Figure 5.23 – Spectrum of (Left) pressure and (Right) velocity of case `R+C 3` ($Re_D = 1500$, $D/\theta = 100$, $L/D = 2$, $Ma = 0.5$), beginning with the 2D limit cycle, then with 3D effects turned on and off at $t = 0$ and $t = 250$, respectively. Expected frequencies for Rossiter modes are also shown. 124

Figure 5.24 – Spectrum of (Top) pressure at the trailing edge and (Bottom) wall-normal velocity inside the cavity as a function of time for case `R+C 3` ($Re_D = 1500$, $D/\theta = 100$, $L/D = 2$, $Ma = 0.5$) for various span-wise domain lengths. Expected frequencies for Rossiter modes are also shown. 125

Figure 5.25 – Comparison between 2D and 3D simulations of case `R+C 2` ($Re_D = 1000$, $D/\theta = 100$, $L/D = 2$, $Ma = 0.5$). (Left) Time series of wall-normal velocity inside the cavity. The dashed lines were measured at another span-wise position. (Right) Spectrum. The vertical lines mark angular velocities predicted by the linear stability analysis for each Rossiter mode (R1 through R3) and centrifugal mode (C2 and C3). 126

Figure 5.26 – Spectrum of wall-normal velocity inside the cavity as a function of time for case `R+C 2` ($Re_D = 1000$, $D/\theta = 100$, $L/D = 2$, $Ma = 0.5$) for (Left) the 2D simulation, (Center) the 3D simulation and (Right) the filtered 3D simulation. Expected frequencies for Rossiter modes are also shown. 126

DISTRIBUTION A: Distribution approved for public release. Distribution unlimited

Figure 5.27 – Temporal and span-wise spectrum for the limit cycle of R+C 2 ($Re_D = 1000$, $D/\theta = 100$, $L/D = 2$, $Ma = 0.5$). (Left) Pressure at the cavity trailing edge (Right) Wall-normal velocity inside the cavity. 127
Figure 6.1 – Mesh for the gap simulation with $Re_{\delta_0^*} = 600$, $L/\delta_0^* = 10$, $D/\delta_0^* = 5$, $Ma = 0.5$. 132
Figure 6.2 – Baseflow at the gap for $Re_{\delta_0^*} = 600$, $L/\delta_0^* = 10$, $D/\delta_0^* = 5$, $Ma = 0.5$. Each contour represents 20% of the free-flow velocity. 132
Figure 6.3 – Global stability results for $Re_{\delta_0^*} = 600$, $L/\delta_0^* = 10$, $D/\delta_0^* = 5$, $Ma = 0.5$. (Left) Eigenvalues map with the first Rossiter mode highlighted. (Right) Real part of the eigenfunctions of the first Rossiter mode: (Top) Stream-wise velocity and (Bottom) Density. 133
Figure 6.4 – Eigenvalues obtained with the regular mesh compared to those obtained with the refined mesh. 133
Figure 6.5 – Eigenfunction of stream-wise velocity of the mode at $\sigma = -0.0175 \pm 0.155i$. 134
Figure 6.6 – Eigenvalues obtained with various values of χ in the SFD filter. . . . 135
Figure 6.7 – Boundary layer displacement and momentum thickness with and without the gap for the following parameters: $Re_{\delta_0^*} = 600$, $L = 10$, $D = 5$, $Ma = 0.5$ 136
Figure 6.8 – (Left) Temporal evolution of the wave packet with and without the gap. (Right) Spectrum of the wave packet at each probe. 136
Figure 6.9 – Density (Top) and stream-wise velocity (Bottom) fluctuations at times $t = 250$ (Left) and $t = 500$ (Right). Red and blue areas represent positive and negative oscillations of the flow, respectively. Black and white lines represent the positive and negative oscillations predicted by the global stability analysis, note that the phase and levels were shifted to match the flow's. 137
Figure 6.10 – (Left) Effect of the Mach number on the eigenmodes. (Right) Effect of gap length on the eigenmodes. 139
Figure 6.11 – Amplification rate of the leading mode for the parameters $L = 10$, $D = 5$, $Ma = 0.5$ and $Re_{\delta_0^*} = 400$, 600, 1000 at various span-wise wave numbers 139
Figure 6.12 – Centrifugal modes I, II and III for $Re_{\delta_0^*} = 1000$, $L = 10$, $D = 5$ and $Ma = 0.5$. $\beta = 3/4\pi$, $\pi/2$ and $\pi/4$, respectively. (Left) Stream-wise velocity. (Right) Span-wise velocity. 140
Figure 6.13 – Types of instabilities found for various combinations of gap length and depth, at $Re_{\delta_0^*} = 600$ and $Ma = 0.5$. The numbers beside the markers indicate which types of unstable centrifugal modes were found, in decreasing order of amplification rate. 141

DISTRIBUTION A: Distribution approved for public release. Distribution unlimited

Figure 6.14 – Isosurfaces of (Left) stream-wise and (Right) span-wise velocity fluctuations at two different times (Top and Bottom) for the $Re_{\delta_0^*}$, $L = 10$, $D = 5$ and $Ma = 0.5$ case. Only a quarter of the span-wise domain is shown for clarity. 142
Figure 6.15 – (Top) Temporal series of pressure at the trailing edge of the gap at two different span-wise positions, at opposite phases for the $Re_{\delta_0^*}$, $L = 10$, $D = 5$ and $Ma = 0.5$ case. (Bottom) Spectrum of the limit cycle. . . 143
Figure 6.16 – Temporal and span-wise spectrum for the limit cycle of the $Re_{\delta_0^*}$, $L = 10$, $D = 5$ and $Ma = 0.5$ case. 143
Figure 6.17 – Boundary layer displacement and momentum thickness of the base flow and of the limit cycle $Re_{\delta_0^*} = 600$, $L = 10$, $D = 5$, $Ma = 0.5$ . . . 144

DISTRIBUTION A: Distribution approved for public release. Distribution unlimited

LIST OF TABLES

Table 3.1 – DNS execution time for different numbers of parallel processes, two-dimensional case. 63
Table 3.2 – DNS execution time for different numbers of parallel processes, three-dimensional case. 64
Table 4.1 – Estimated coefficients of computational cost, in seconds 78
Table 5.1 – Cases defined to investigate the interaction of Rossiter and centrifugal modes 117

DISTRIBUTION A: Distribution approved for public release. Distribution unlimited

DISTRIBUTION A: Distribution approved for public release. Distribution unlimited

LIST OF SYMBOLS

L	Cavity length
D	Cavity depth
Re	Reynolds number
Ma	Mach number
δ^*	Boundary layer displacement thickness
θ	Boundary layer momentum thickness
t	Time
x	Stream-wise direction
y	Wall-normal direction
z	Span-wise direction
u	Stream-wise velocity component
v	Wall-normal velocity component
w	Span-wise velocity component
ρ	Fluid density
e	Fluid internal energy
p	Fluid pressure
$\boldsymbol{U_0}$	Base flow
$\boldsymbol{u}$	Flow disturbance
σ	Eigenvalue of a flow mode ($\sigma = \sigma_r + i\sigma_i$)
σ_r	Temporal growth of a flow mode
σ_i	Angular velocity a flow mode
ω	Angular velocity
β	Span-wise wavenumber

DISTRIBUTION A: Distribution approved for public release. Distribution unlimited

DISTRIBUTION A: Distribution approved for public release. Distribution unlimited

CONTENTS

1 INTRODUCTION 27

1.1 Motivation 27

1.2 Problem description 28

1.3 Objectives 30

1.4 Summary of this work 30

2 REVIEW 33

2.1 Flow instability 33

2.2 Cavity instability 36

2.2.1 Motivation 36

2.2.2 Cavity instability and acoustic modes 37

2.2.3 Gaps 40

3 DIRECT NUMERICAL SIMULATION 43

3.1 Numerical methods 44

3.1.1 Governing equations 44

3.1.2 Meshing and domain 45

3.1.3 Boundary and initial conditions 46

3.1.4 Spatial derivatives 47

3.1.5 Time integration 52

3.1.6 Anti-aliasing filtering 53

3.1.7 Artificial damping 54

3.2 Implementation 57

3.2.1 Domain decomposition and parallel execution 58

3.2.2 Linear system solver 59

3.2.3 Flowchart 60

3.3 Performance 63

3.4 Strategies for mesh generation 65

3.5 Obtaining a base flow 66

4 LINEAR STABILITY THEORY 71

4.1 Introduction 71

4.2 Methods 73

4.2.1 Linear stability computations 73

4.2.2 Initial disturbance 77

4.2.3 Computational cost 77

DISTRIBUTION A: Distribution approved for public release. Distribution unlimited

4.3 Baseline results of the studied case . . . 80
4.4 Order of accuracy of the Fréchet derivative and disturbance magnitude . . . 82
4.5 Effect of integration time length . . . 87
4.6 Krylov span dimension and optimization of the total computational time . . . 96
4.7 Rate of convergence of eigenfunctions and eigenvalues . . . 100
4.8 Conclusion . . . 102

5 LARGE OPEN CAVITIES . . . 105
5.1 Introduction . . . 105
5.2 Two-dimensional results . . . 106
5.2.1 Influence of the boundary layer thickness . . . 106
5.2.2 Influence of the Mach number . . . 109
5.3 Three-dimensional global stability . . . 114
5.4 Non-linear effects . . . 115
5.5 Conclusion . . . 128

6 EFFECTS OF GAPS ON BOUNDARY LAYER TRANSITION . . . 131
6.1 Introduction . . . 131
6.2 Mesh and domain independence . . . 131
6.2.1 Mesh independence . . . 133
6.2.2 Domain independence . . . 134
6.3 Effects of the gap on the boundary layer thickness and spatial stability . . . 135
6.4 Two-dimensional global stability . . . 138
6.5 Three-dimensional global stability . . . 139
6.6 Direct Numerical Simulation of three-dimensional modes . . . 142
6.7 Conclusion . . . 144

7 DISCUSSION AND FINAL REMARKS . . . 147
7.1 Direct Numerical Simulation . . . 147
7.2 Linear Stability Analysis . . . 147
7.3 Cavities . . . 148
7.4 Gaps . . . 149
7.5 Suggestion for future works . . . 149

BIBLIOGRAPHY . . . 151

DISTRIBUTION A: Distribution approved for public release. Distribution unlimited

Chapter 1

Introduction

1.1 Motivation

In the aeronautical industry, a good prediction of the turbulent transition location is of significant importance as it affects the aircraft drag and therefore, its fuel consumption. This effect is both direct, due to the increased surface friction of turbulent flows, and indirect, due to changes in the pressure field.

Reneaux (2004) estimates that fuel corresponds to about 22% of the operational cost of an airline and that a 1% reduction in drag would correspond to increasing the payload of an Airbus A320-sized aircraft in about 1.6 ton or 10 passengers. However, current drag prediction methods may err with margins higher than 1%. For instance, Tinoco et al. (2018) summarize the data from the Sixth AIAA CFD Drag Prediction Workshop, in which eighteen participant groups used state-of-the-art CFD codes to predict drag for a standard transonic aircraft model, their results fall within a 10 Drag Counts margin, corresponding to about 4% of the total drag of the reference model.

Taking an Airbus A320 as reference, Marec (2001) concludes that the friction drag is around 50% of the total drag, of which 25% comes from the wings. If the laminar flow region can be increased, it will directly reduce those numbers, especially in longer routes.

The flow on a real surface is subject to its imperfections, which may affect its stability and change the location of the transition from laminar to turbulent. A robust model of the turbulent transition - including the effects of small surface imperfections such as rivets, panel junctions, dents or even dust - may aid designers in creating new and more efficient aerodynamic solutions.

These figures show that improvement in this area would be greatly beneficial for the industry and that better transition predictions would positively impact both fuel

DISTRIBUTION A: Distribution approved for public release. Distribution unlimited

consumption and operational costs.

The use of Natural Laminar Flow designs, or NLF, requires lower tolerances in manufacturing in both surfaces' shapes and junctions. The lack of better models for the effect of such imperfections leads designer to overshoot tolerances, which impacts costs of manufacturing and maintenance. Improving turbulent transition models would allow designers to reduce this kind of overhead.

1.2 Problem description

Figure 1.1 illustrates a flat plate with a cavity. There is a uniform flow coming from the left-hand side, a boundary layer is formed on the flat plate and there is a rectangular cavity in this plate after a certain distance. The geometry is considered uniform and infinite in the span-wise direction, as is the downstream to the cavity.

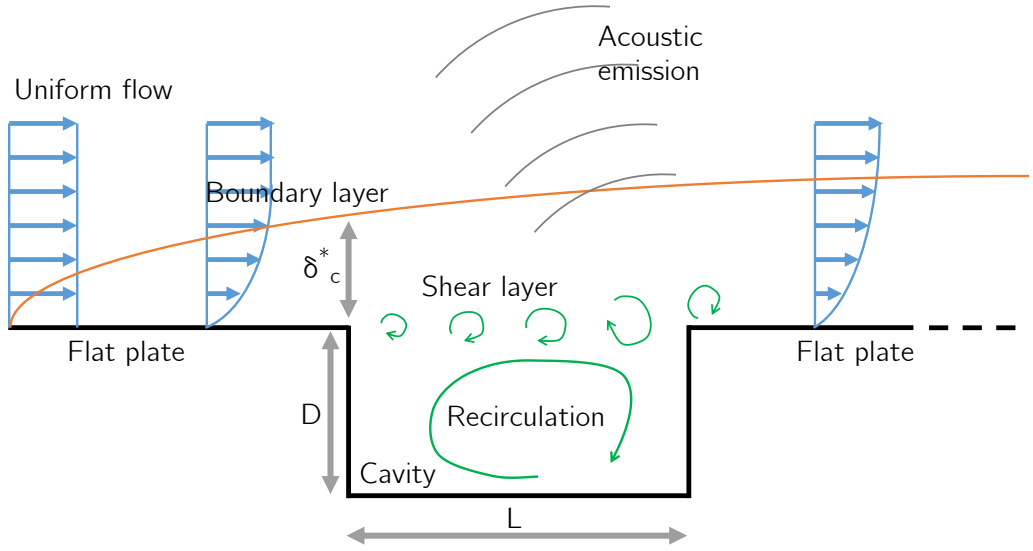


Figure 1.1 – Illustration of the open cavity flow.

All values in this study are non-dimensional and the parameters to be chosen are:

- L/D - Cavity aspect ratio (length by depth)
- δ^*_{LE} - Boundary layer displacement thickness at the cavity leading edge
- Re - Reynolds number
- Ma - Mach number

Depending on these parameters, the flow might be either stable or unstable. A stable flow will develop into a permanent regime, while an unstable flow will develop into an oscillating regime.

DISTRIBUTION A: Distribution approved for public release. Distribution unlimited

Figure 1.2 brings a diagram with neutral stability curves by Brès and Colonius (2008) for a fixed cavity aspect ratio of $L/D = 2$ and a boundary layer thickness given by $D/\delta^*_{LE} = 10.2$. At low Mach numbers, increasing the Reynolds number triggers three-dimensional instabilities, while two-dimensional instabilities tend to appear first if the Mach number is higher. For this length to depth ratio, flows above a Re_D of roughly 1300 are 3D unstable. The minimum Re for a 2D unstable flow is reduced as the Mach number increases, becoming lower than the 3D instability threshold above around Mach 0.4. These disturbances eventually saturate to become large oscillations in the flow. Some of their runs are indicated in this diagram. Two types of unstable modes may be present in an open cavity: Rossiter modes, which are essentially two-dimensional and centrifugal modes, which are three-dimensional.

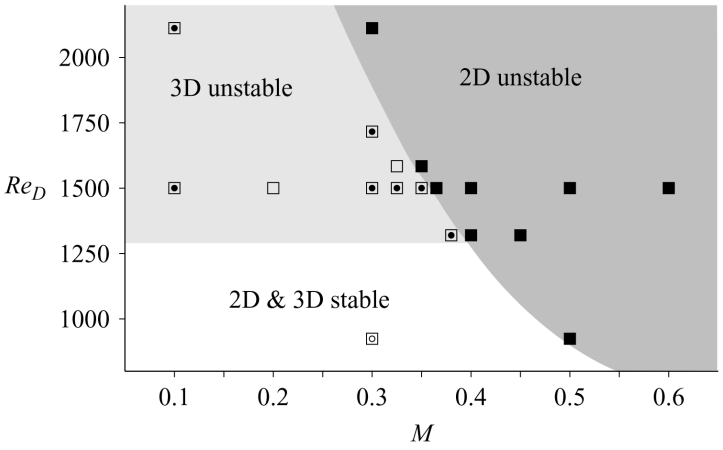


Figure 1.2 – Neutral stability curves for a $L/D = 2$ and $D/\delta^*_{LE} = 10.2$ open cavity as a function of Mach and Reynolds. The symbols indicate results by Brès and Colonius (2008), filled markers indicated unstable cases, squares for two-dimensional and circles for three-dimensional. (BRÈS; COLONIUS, 2008)

In stable scenarios, a steady flow is reached. In these cases, a known disturbance may be added upstream of the cavity so that we can measure its influence on the spatial instability of the boundary layer.

A computational model of this geometry is created and used to study the flow stability. Both two and three-dimensional cases are considered. The simulation is always compressible, even at low Mach numbers. In a three-dimensional case, the flow is periodic in the span-wise direction.

Two types of cavities are investigated in this work. First, we simulate larger cavities so that the types of modes present can be better understood. The instability modes of large cavities are mostly independent on those of the boundary layer. Nonetheless, the thickness of the incoming boundary layer plays a key role in determining the instability of the cavity.

DISTRIBUTION A: Distribution approved for public release. Distribution unlimited

Later, we studied small cavities, also called gaps, with depths no more than one order of magnitude larger than the boundary layer displacement thickness. In the case of gaps, their instability modes may interact with those of the boundary layer. In some cases, incoming TS waves may be amplified by the gap, even if the gap itself is globally stable, which would cause the transition to happen earlier. Unstable gaps may function as a source of disturbances for the downstream boundary layer or even cause a by-pass transition, depending on the type of oscillations.

It was found that both large cavities and gaps are subject to the same types of instability modes, which justifies them being studied together.

1.3 Objectives

The general objective of this work is to investigate the instability of open cavities and gaps in a boundary layer. More specifically, we wish to clarify the following points:

- How does each parameter affect the linear stability of an open cavity?
- What is the underlying physics of the effect of each parameter on the instability?
- To which extent can the linear analysis predict the non-linear regime?
- What are the effects of a gap on the instability of the boundary layer?

Moreover, due to the extensive use of a Linear Stability Theory calculation procedure to obtain the global modes of the flow, we also worked on optimizing the use of this technique so that it can be used more quickly and reliably.

1.4 Summary of this work

After this introduction and the bibliographic review in Chapter 2, we present the flow solver used in this work in Chapter 3, which is of the Direct Numerical Solver (DNS) kind. It brings details on its underlying numerical methods and their implementation, as well as code performance data and strategies for the generation of efficient meshes and techniques for accelerating the convergence towards a base flow. An entirely new DNS code was developed for this study, albeit based on previous experience in the group.

The Linear Stability Theory (LST) algorithm used in this work is shown in Chapter 4, which also brings a detailed study on the accuracy of such implementation and on the optimization of computational parameters used in the method. This development constitutes a contribution of this work.

DISTRIBUTION A: Distribution approved for public release. Distribution unlimited

Chapter 5 explores the physics of open cavity flows, using both DNS and LST codes. These flows are defined by a large ratio between the cavity dimensions and the thickness of the incoming boundary layer. Similarly, Chapter 6 explores the physics of boundary layers over gaps, which are small cavities, close in size to the boundary layer thickness, and that can impact the transition to turbulence either by amplifying TS waves or by causing a by-pass transition.

Chapter 7 summarizes the conclusions and suggests further research topics in this theme.

DISTRIBUTION A: Distribution approved for public release. Distribution unlimited

DISTRIBUTION A: Distribution approved for public release. Distribution unlimited

Chapter 2

Review

2.1 Flow instability

Flow transition from laminar to turbulent regimes has been largely studied for the past century. Despite great advances in these last decades, it remains an open problem.

Among the first studies for this phenomenon, Osbourne Reynolds' work stands out. His first publication in this matter (REYNOLDS, 1883) classifies two types of flow: "Direct" and "Sinuous", referring to both the flow surface and the shape of a colored marker he would add to the water. His following publication (REYNOLDS, 1894) brought a new, non-dimensional parameter that relates to the transition location, accounting for the flow velocity, the fluid's viscosity and a characteristic length, taken as the tube diameter. This would later be known as the Reynolds number.

Prandtl (1904) brought the concept of the boundary layer above a flat plate, already mentioning the phenomenon of transition from laminar to turbulent flow and boundary layer separation. His students continued his work, Walter Tollmien and Hermann Schlichting were among them. (SCHLICHTING; GERSTEN, 2000)

Earlier, Rayleigh (1879) studied the stability of a parallel, inviscid flow, concluding that a necessary condition for instability was the existence of an inflection point in the velocity profile. Orr (1909) and Sommerfeld (1908) derived the equation used to determine the stability modes of a parallel, viscous flow. It would, later, be known as the Orr-Sommerfeld equation. Tietjens (1925) has investigated the transition in a boundary layer, concluding the viscosity would play a destabilizing role.

Tollmien (1929) (translated in (TOLLMIEN, 1932)) and Schlichting (1933) have studied the effects of a small perturbation in a Blasius profile by modeling them as waves that are attenuated or amplified, depending on the flow stability, known today as the

DISTRIBUTION A: Distribution approved for public release. Distribution unlimited

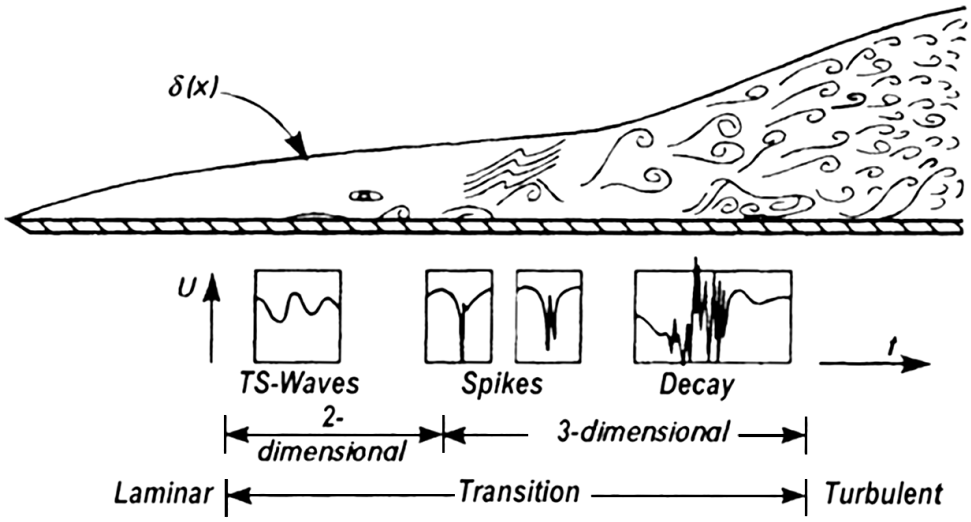


Figure 2.1 – The various regions of a boundary layer transition. (SCHLICHTING; GERSTEN, 2000)

Tollmien-Schlichting (TS) waves. In summary, Tollmien has drawn the critical stability curve in the Reynolds number versus wave number plane; and Schlichting has computed the amplification levels in this plane.

For the next decade, this theory could not be reproduced due to the high turbulence in the wind tunnels of the time. Finally, Schubauer and Skramstad (1947) were able to use a low turbulence wind tunnel and successfully observe the amplification of periodic waves just upwind of the transitional region in a boundary layer, soon followed by Liepmann (1943). These observations matched Tollmien and Schlichting's theory.

Schubauer and Skramstad (1947) used a vibrating ribbon in the boundary layer to generate controlled TS waves and observed the spatial evolution of their amplitude, as illustrated in Fig. 2.2. This image also shows the stability diagram from the Orr-Sommerfeld equation.

Gaster (1962) has connected the effects of temporal disturbance growth, which could be predicted theoretically, to the spatial growth, observed experimentally, later proposing the solution of the Orr-Sommerfeld equations for spatial modes (GASTER, 1965).

Ingen (1956) has proposed a method to predict the transition location from the disturbance amplification rates, known as the e^n method. Its idea is to integrate the amplification rate through the boundary layer and to assume transition happens when this integral reaches a certain threshold, represented by the constant e^n. Usually, $e = 9$ is taken as an average value, in flight, greater values may be used.

In either simulations or experiments, an initial disturbance is needed to trigger the transition process. It is either given by ambient noise, which cannot be controlled,

DISTRIBUTION A: Distribution approved for public release. Distribution unlimited

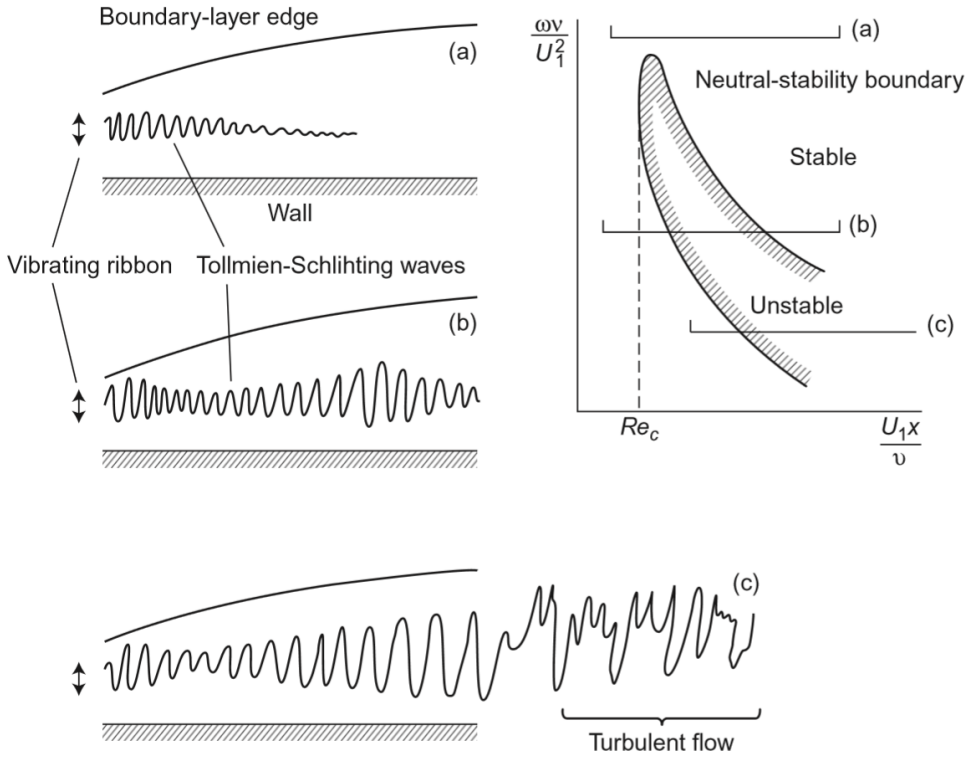


Figure 2.2 – Illustration of TS waves evolution before transition to turbulence. (HOUGHTON et al., 2012)

or by artificially introducing waves to the flow. In those studies that introduce a known wave, usually only a small number of distinct frequencies are present in the signal. In a natural transition, a broad range of frequencies are present in the spectrum. One way of replication this phenomenon is to use wave packets, which have a temporally short wave form with a broad spectrum (MARTINEZ; MEDEIROS, 2016; MARTINEZ, 2016).

Figure 2.3 (MORKOVIN; RESHOTKO; HERBERT, 1994) brings the typical routes of a natural transition, from the receptivity to the turbulent breakdown.

Typically, in a flat plate, routes "a" or "b" are taken, such as what is shown in Fig. 2.1. If large enough disturbances are given, a bypass transition might happen. A cavity with temporally unstable modes may lead to a bypass transition.

DISTRIBUTION A: Distribution approved for public release. Distribution unlimited

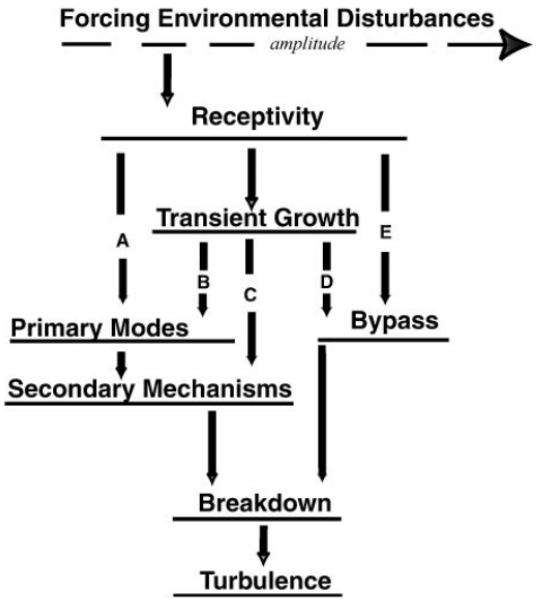


Figure 2.3 – Typical routes from receptivity to turbulent breakdown. (MORKOVIN; RESHOTKO; HERBERT, 1994)

2.2 Cavity instability

2.2.1 Motivation

Initially, open cavity research was motivated by their vibration modes, with special attention given to the frequencies. The concern was whether or not there would be oscillatory modes and what would their frequencies be, as these oscillations could excite modes in the structure, speeding up fatigue. To a smaller extent, there was also some concern on the increased drag caused by the oscillations and in their acoustic emissions. (OWEN, 1958).

Krishnamurty (1956), motivated by the buffeting observed in aircraft cavities such as open cockpits or landing gear doors, performed an experimental campaign and concluded that the minimum cavity size that generates sound is reduced as the Mach number increases and that this size is inversely proportional to the sound frequency observed. He has also reported that sound intensity grows quickly with the Mach number, roughly at its eighth power, as predicted by the existing theories. Acoustic waves were also visualized by Schlieren photography, qualitatively showing the sound directivity, as shown in Fig. 2.4.

At the same time, Roshko (1955) performed experiments to generate more data on open cavity flow and to observe its structures, also looking to understand the relevance of the cavity aspect ratio. His work is focused on the mean flow over the cavity, not on the

DISTRIBUTION A: Distribution approved for public release. Distribution unlimited

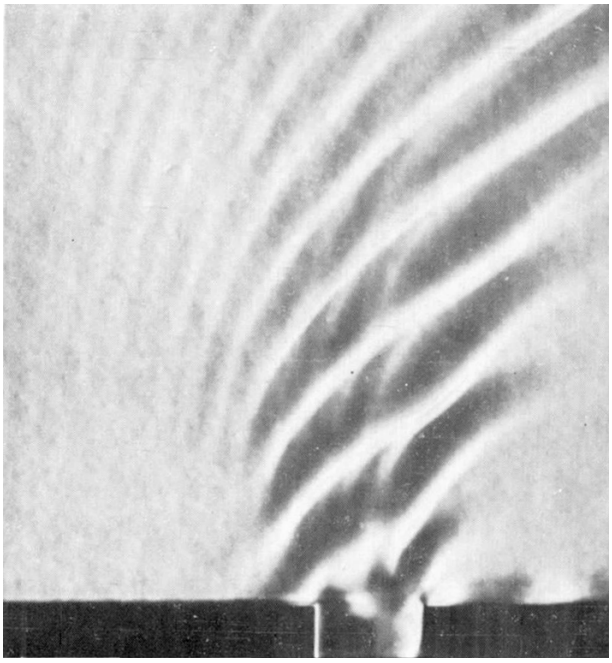


Figure 2.4 – Schlieren image of the cavity flow showing its acoustic output. (KRISHNAMURTY, 1956)

oscillations that, eventually, become sound waves.

McGregor and White (1970) justified research on cavity instability by concluding that, in transonic and supersonic flows, aerodynamic drag in surfaces with cavities is greatly increased if there is an acoustic resonance. Dix and Bauer (2000) point out that pressure fluctuations due to cavities may reach great amplitudes that, besides the acoustic emission, might cause structural fatigue as they are specially correlated waves, causing repetitive stress on some structural points. Outside of the aeronautical scope, other justifications may be found. Kook and Mongeau (2002), for example, were motivated by automotive sunroofs.

More recently, cavity flow control came into the scope of researchers (HOWE, 1997; COLONIUS, 2001; ROWLEY; WILLIAMS, 2006). Control can be either passive, done by features such as grills, spoilers and ramps, or active, by using suction, jets, oscillators and piezoelectric components (CATTAFESTA et al., 2003; WILLIAMS; ROWLEY, 2006; THEOFILIS, 2011).

2.2.2 Cavity instability and acoustic modes

Rossiter (1964) has performed an experimental campaign at subsonic and transonic velocities, resulting in his famous semi-empirical equation, which connects flow parameters, such as Mach number and cavity length to the observed sound frequencies. It is still largely used to this date (COLONIUS, 2001; GLOERFELT, 2009). His equation has some

DISTRIBUTION A: Distribution approved for public release. Distribution unlimited

empirical constants, obtained experimentally.

This equation assumes that the unstable mode that generates sound is triggered by acoustic feedback. In short, when a vortex reaches the cavity's downstream edge, it generates acoustic waves that travel back to the upstream edge, triggering the shear layer modes that generate another vortex.

Rossiter's equation matches well with experimental results, despite a considerable dispersion, especially at lower Mach numbers. The saturation amplitudes of the modes present a much higher dispersion that the frequencies, due to the high sensitivity to disturbances in the shear layer. (COLONIUS, 2001)

Through the years, various corrections and adjustments of empirical values have been suggested to Rossiter's equation. (HELLER; HOLMES; COVERT, 1971; ROCKWELL; NAUDASHER, 1979)

Plumblee, Gibson and Lassiter (1962) have proposed another mode for sound generation in an open cubic cavity, later extended to other geometries by Tam (1976). In this mode, stationary waves normal to the flow receive energy from the shear layer over the cavity, modes are selected depending on their frequencies and this energy is sent back to the flow in acoustic form. In this work, the Navier-Stokes equations were simplified by several hypotheses. After the boundary conditions were applied, the resulting equation predicts the frequencies and modes and depends on no empirical constants, just on two integers, related to the mode number.

East (1966) linked aeroacoustic feedback mechanisms (Rossiter) to acoustic resonance mechanisms (Plumblee), concluding that they may interact with each other, amplifying the sound output if their frequencies match.

Comparing his results to experiments, Tam concluded that they are valid only for cavities with a depth greater than their length and above a certain Mach number, around 0.25. He arguments that in shallow cavities or at lower Machs, the energy absorbed by the standing waves is much less than what is needed to generate sound, damping these waves until they are practically non-existent. This complements East's conclusions.

Block (1976) has also compared both mechanisms experimentally, reaching a similar conclusion. Deeper cavities tend to have stronger acoustic resonance modes while longer ones have stronger aeroacoustic feedback modes. Peaks in sound intensity were also observed when the modes matched in frequency. She has also noted that at higher velocities, only the feedback modes are seen, other modes appear at lower velocities, widening the spectrum. This mode interaction was also discussed by Rockwell and Naudasher (1979), Yamouni, Sipp and Jacquin (2013).

Sarohia (1977), motivated by issues such as the changes in drag caused by cavities, has experimentally swept a range of cavity dimensions and Reynold numbers. In these

DISTRIBUTION A: Distribution approved for public release. Distribution unlimited

experiments, he has found that there is a minimum cavity length that causes it to oscillate, given as a function of incoming boundary layer thickness and Reynolds number. He also notes that when Rossiter modes appear in the cavity, only a single Rossiter mode is present at any given time and that the order of this mode is highly dependent on the length of the cavity.

Howe (2004) identifies the sound generation mechanisms at low Mach numbers, roughly from 0.01 to 0.2. He uses a Green's function for this geometry and analytical models of the sources, treating them as monopoles and dipoles. The monopole source is associated with the net flux of mass entering or leaving the cavity, while the dipole is associated with an unsteady drag force caused by the interaction of the vorticity and the cavity trailing edge, which happens due to the shear layer instability.

Howe concludes that at very low Mach numbers the sound radiation is dominated by the dipole source caused by the unsteady drag force, while at slightly higher Mach numbers, the monopole source takes over. This is illustrated in Fig. 2.5, which compares the directivity at Mach 0.05 and at Mach 0.1.

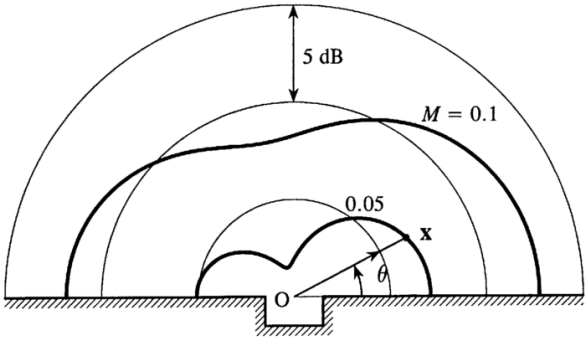


Figure 2.5 – Cavity acoustic directivity at Mach 0.05 and Mach 0.1. (HOWE, 2004)

He also concludes that, at lower frequencies, the emission is dominated by the dipole and, at higher frequencies, by the monopole, as can be seen in Fig. 2.6.

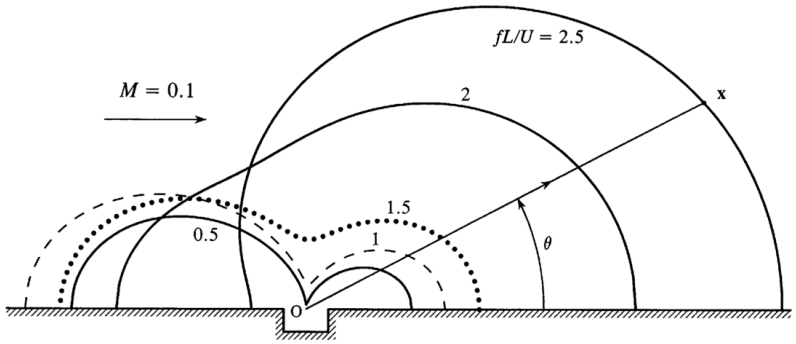


Figure 2.6 – Cavity acoustic directivity at Mach 0.1 for various frequencies. (HOWE, 2004)

DISTRIBUTION A: Distribution approved for public release. Distribution unlimited

Brès and Colonius (2008) performed open cavity simulations with high order finite difference schemes (LELE, 1992) to investigate the interaction between two and three-dimensional modes. Mack and Schmid (2010) have studied the instability in a swept cavity in supersonic flows by using a combination of a DNS and Krylov subspace algorithms.

The acoustic emission of a cavity is strongly linked to its oscillation modes and depends on the existence of unstable eigenvalues. Great advances were achieved in this direction by bi-global instability analysis (THEOFILIS, 2003; BRÈS; COLONIUS, 2008; VICENTE et al., 2014). Eigenvalues in the complex plane can be mapped for the cavity flow, indicating the existence of unstable modes and their respective frequencies. These modes grow until non-linear effects cause them to reach a saturation point.

Yamouni, Sipp and Jacquin (2013) related modes from bi-global stability analysis to Rossiter and standing wave modes in a square cavity. They conclude that interactions between these two phenomena may affect the global mode, causing it to be more unstable when their frequencies match.

Many recent investigations on open cavities focus on the flow stability. Meseguer-Garrido et al. (2014) perform a parametric study of the flow and its instability modes. Liu, Gómez and Theofilis (2016) compare two-dimensional cavities, with an infinite span, to three-dimensional ones, with a finite span, concluding that most effects are shared by both geometries. These last results were obtained for incompressible flows and acoustic analogies might be done from them. A compressible flow would be needed if direct observation of the acoustic field is desired.

A limited number of papers were found in the literature about mid to high subsonic flows over a cavity, such as Brès and Colonius (2008), Yamouni, Sipp and Jacquin (2013), Sun et al. (2016), Sun et al. (2017), which mostly focus on how the Mach number affects the stability. This range of Mach numbers is certainly important for practical reasons as this is where most modern aircraft fly. This work is in the direction of expanding the current knowledge of open cavity flows in this sense, a focus will be given to the effect of the boundary layer thickness over the cavity, about which not much was found.

2.2.3 Gaps

Small geometry elements in a flat plate have also been studied recently, they differ from larger geometries because their effect is strongly related to the boundary layer mechanics. We define a gap as a subset of open cavities in which its dimensions are of the same order of the boundary layer thickness. The flow over a gap may be divided into two different scenarios. One is when the gap is globally unstable, which means that its oscillations are self-sustained. In this case, it acts as a source of disturbances to the flow, and might even cause bypass transition, regardless of incoming disturbances. This

DISTRIBUTION A: Distribution approved for public release. Distribution unlimited

behavior resembles that of larger open cavities, as external disturbances have little effect on the modes inside the gap.

The second scenario is when the gap is globally stable. In this case, the flow upstream to the gap already has some kind of disturbance, which will then interact with the gap. Therefore, the surface imperfection is not the cause of disturbances as is the case with larger cavities, instead it modifies the existing flow instabilities. (CROUCH; NG, 2000; PLOGMANN; WÜRZ; KRÄMER, 2014; PAULA et al., 2017)

Klebanoff and Tidstrom (1972) concludes that the effect of a small two-dimensional imperfection is mostly related to the change in the mean flow and in the boundary layer thickness. A similar conclusion is reached by (WORNER; RIST; WAGNER, 2003), who simulate monochromatic TS waves passing over a small bump in the surface.

Experiments by Wang and Gaster (2005), Crouch, Kosorygin and Ng (2006) lead to empirical relations on how much a step in the flat plate affects the incoming Tollmien-Schlichting waves (TS waves). In terms of the transition n-factor, backward-facing steps have a stronger destabilizing effect on the boundary layer than forward-facing steps, caused by both the increase in its thickness and the laminar recirculation bubble that is created. Crouch mentions that these results are valid up to a step height of 1.5 times the boundary layer displacement thickness.

Paula et al. (2017) has experimentally measured 2D TS waves interacting with a small, localized roughness element. Part of his conclusion is that the roughness may cause the scattering of these waves, which may trigger non-linear interaction between different modes.

Qadri and Schmid (2017) have studied the mechanisms present in small cavities that select and amplify certain frequencies of the disturbances, even if the cavity itself is globally stable.

Gaster (2016) models a series of very sinusoidal bumps, which form a rough region, he concludes that this region amplifies the growth of unstable waves, causing the transition to move upstream. He also concludes that a good model for such flow is separating it in two regions, one governed by the Orr-Sommerfeld equations, above the bumps and one governed by the Stokes equation, in between the bumps.

Crouch, Kosorygin and Sutanto (2020) experimentally measure the change in the transition location of when a gap is present. They note that a bypass transition takes place when either the gaps length or depth are above certain threshold values. Figure 2.7, by Crouch, Kosorygin and Sutanto (2020), shows the movement of the transition to turbulence for gaps of various lengths (w) and depths (d), the value ξ represents the distance from the gap to the transition in comparison to the case without the gap. The dashed lines in the figure correspond to bypass transition data by Beguet et al. (2017). These experiments

DISTRIBUTION A: Distribution approved for public release. Distribution unlimited

were performed at Reynolds numbers similar to those used in Chapter 6 of this work, but at lower Mach numbers.

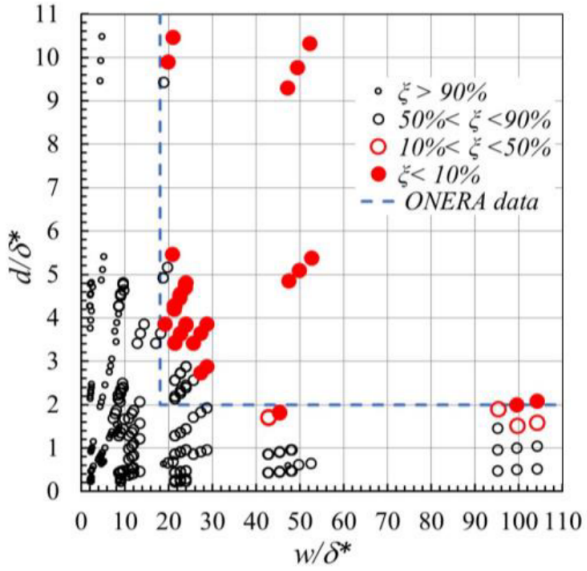


Figure 2.7 – Effect of the gap on the transition location. (CROUCH; KOSORYGIN; SUTANTO, 2020)

DISTRIBUTION A: Distribution approved for public release. Distribution unlimited

Chapter 3

Direct Numerical Simulation

The Direct Numerical Simulation code used in this work was developed as part of this project and is specifically tailored for our needs, in the form of the following requirements:

1. High order of precision both spatially and temporally wise and low rounding error.
2. Ability of accepting any Cartesian geometry, such as cavities and roughness elements or any combination of both.
3. Modularity for the implementation of new features needed for future research topics by the group.
4. Scalability to run in computers ranging from workstations to clusters.
5. Ease of use, including pre- and post-processing phases.

This code is based on previous works by the research group and inherits many of their algorithms but was completely rewritten. (SOUZA; MENDONÇA; MEDEIROS, 2005; SILVA; SOUZA; MEDEIROS, 2010; BERGAMO et al., 2015; MARTINEZ, 2016; MATHIAS; MEDEIROS, 2018)

Besides the studies presented in this thesis, the code is also in use by other members of the research group, such as for the simulation of TS waves passing over a small roughness element (HIMENO; MATHIAS; MEDEIROS, 2019; CARVALHO; MATHIAS; MEDEIROS, 2020; HIMENO; MATHIAS; MEDEIROS, 2020), the acoustic receptivity of roughness elements (SANTOS et al., 2020) and ongoing research on the influence of a small gap on the turbulent transition.

The code is published online on the Github platform at <https://github.com/marlonsmathias/GATT_DNS>. It is licensed under the GPLv3, meaning everyone can

DISTRIBUTION A: Distribution approved for public release. Distribution unlimited

use and modify the code, as long as credits are given and eventual modifications are also under the same license and, therefore, remain open-source.

3.1 Numerical methods

3.1.1 Governing equations

The compressible Navier-Stokes equations are used to model the flow, along with mass and energy conservation equations. A compressible flow can be entirely defined by five variables: density (ρ), internal energy (e) and the three velocity components (u,v,w), in this case. Each variable depends on location (x,y,z) and time (t).

Equations are written in the non-conservative form, which solves for each individual variable mentioned above, simplifying the boundary conditions.

$$\frac{\partial \rho}{\partial t} = -\rho \frac{\partial u_i}{\partial x_i} - \frac{\partial \rho}{\partial x_i} u_i \tag{3.1}$$

$$\frac{\partial u_j}{\partial t} = \frac{\partial u_j}{\partial x_i} u_i - \frac{1}{\rho} \frac{\partial p}{\partial x_j} + \frac{1}{\rho} \frac{\partial \tau_{ij}}{\partial x_i} \tag{3.2}$$

$$\frac{\partial e}{\partial t} = \frac{\partial e}{\partial x_i} u_i - \frac{p}{\rho} \frac{\partial u_i}{\partial x_i} + \frac{1}{\rho} \tau_{ij} \frac{\partial u_j}{\partial x_i} - \frac{1}{\rho} \frac{\partial q_i}{\partial x_i} \tag{3.3}$$

Where the viscous tensor and the heat flux term are:

$$\tau_{ij} = \frac{\mu(T)}{Re} \left(\frac{\partial u_i}{\partial x_j} + \frac{\partial u_j}{\partial x_i} - \frac{2}{3} \delta_{ij} \frac{\partial u_k}{\partial x_k} \right) \tag{3.4}$$

$$q_i = -\frac{\mu}{(\gamma - 1)\, Re\ Pr\ M_\infty^2} \frac{\partial T}{\partial x_i} \tag{3.5}$$

Temperature and pressure, assuming an ideal gas, are given by:

$$T = e\gamma\,(\gamma - 1)\, M_\infty^2, \quad p = (\gamma - 1)\,\rho\ e \tag{3.6}$$

Viscosity is modeled by Sutherland's law:

$$\frac{\mu^*}{\mu_\infty} = \mu(T) = \frac{1 + C}{T + C} T^{\frac{3}{2}} \tag{3.7}$$

Defining $C = \frac{110K}{T_\infty^*}$ and $T_\infty^* = 300K$.

DISTRIBUTION A: Distribution approved for public release. Distribution unlimited

All values are non-dimensional, being normalized by the free flow speed, cavity depth and initial density. Reynolds, Prandtl and Mach numbers are given by:

$$Re = \frac{\rho^*_\infty \, U^*_\infty \, L_0}{\mu^*_\infty}, \quad Pr = \frac{\mu^*_\infty c^*_p}{k^*}, \quad M_\infty = \frac{U^*_\infty}{\sqrt{\gamma \frac{p^*_\infty}{\rho^*_\infty}}} \tag{3.8}$$

Dimensional (denoted with a *) and non-dimensional values are related by the following equations.

$$\rho = \frac{\rho^*}{\rho^*_\infty}, \quad p = \frac{p^*}{p^*_\infty U^{*2}_\infty}, \quad x_i = \frac{x^*_i}{L_0}, \quad T = \frac{T^*}{T^*_\infty}, \quad u_i = \frac{u^*_i}{U^*_\infty}, \quad t = \frac{t^* U^*_\infty}{L_0}, \quad e = \frac{e^*}{U^{*2}_\infty} \tag{3.9}$$

3.1.2 Meshing and domain

The mesh is structured and Cartesian, meaning it can be stored is array format, which simplifies programming and speeds up the execution.

The grid can be stretched so that specific regions of the flow can have a higher density of nodes, such as the leading edge of the flat plate or the corners of the cavity. A stretching function was developed so that grid spacing always changes smoothly.

As a default, the mesh is uniformly spaced. Points and regions we call "attractors" can be added to the domain, those will cause nearby nodes to move towards the attractor, creating a region with greater refinement. Each attractor point has two parameters: strength and size; the former defines the ratio between the most refined nodes and the base spacing of the mesh, and the latter defines the size of the region the attractor affects. Attractor regions are defined by five parameters: region start, start of maximum refinement, end of maximum refinement, region end and refinement strength.

Figure 3.1 illustrates a mesh generated by this scheme. There are 100 nodes in the domain $0 \leq X \leq 10$. Two attractors were used at $X = 3$ and $X = 4$, which in this example could be both corners of a cavity. The strengths are set to 2 and 3; therefore, node concentrations are tripled and quadrupled, respectively. Both attractors are of size 0.5.

After the mesh is generated, a second routine is called to make sure there are mesh nodes right on top of certain geometric features, such as the leading edge or the cavity nodes. This routine finds which node is closest to each feature and slightly and smoothly distorts the mesh to make sure they match.

DISTRIBUTION A: Distribution approved for public release. Distribution unlimited

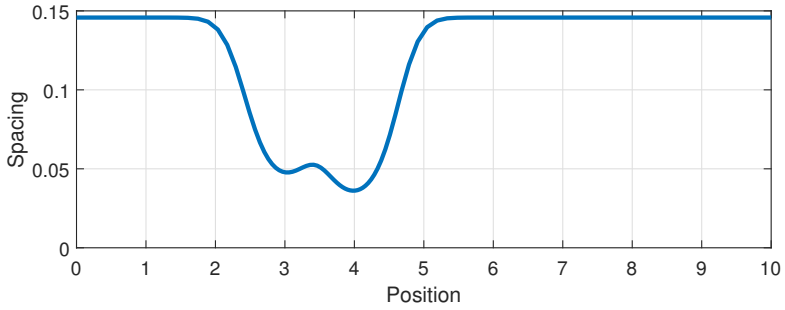


Figure 3.1 – Example of mesh generated using two attractor points at both ends of a cavity.

3.1.3 Boundary and initial conditions

The inflow boundary is defined as a uniform flow at constant temperature and a Neumann condition is placed for the pressure so that its derivative is null in the flow direction. In the outflow, pressure is kept constant, and the second derivative is null for the other variables. The outer flow condition sets the second derivative of all variables to zero.

Walls have no-slip and no-penetration conditions for velocity, the pressure gradient is set to zero in the normal direction and the temperature is fixed. Just downstream of the inflow, there is a free-slip region in the wall, it is necessary to accommodate the flow before the boundary layer starts forming.

Pressure and temperature are not directly available as variables in the code and are computed from the density and energy values. The temperature depends solely on the energy and pressure depends on both density and energy. This way, the boundary conditions routine first changes the energy to observe the temperature conditions and, later, the density to keep the pressure conditions.

Wall corners are points of particular attention for the boundary conditions. The Neumann homogeneous condition for pressure in other points is observed by computing the density at each point of the boundary so that the pressure's derivative is null in the normal direction on the wall. Corner nodes present a problem as walls in distinct directions meet and the density that observes the Neumann condition in one direction might violate it for the other. The pressure in set to the mean of the pressures that meet the boundary condition for each direction.

Open boundaries have the second derivative of all variables set to zero. We also add buffer (or sponge) zones near these boundaries. In these regions, three different techniques are combined to damp oscillations and prevent them from reflecting to the physical domain: The mesh spacing is greatly increased; the spatial derivative accuracy

DISTRIBUTION A: Distribution approved for public release. Distribution unlimited

order is reduced; Selective Frequency Damping is used (see Section 3.1.7). The transition between the physical domain and the buffer zones happens smoothly.

The inlet boundary has the stream-wise velocity set to unity. The energy is set to its free-stream value and the pressure stream-wise derivative is set to zero. The outlet has the pressure fixed at its free-stream value. Figure 3.2 illustrates these conditions and shows the mesh used for the cases of Chapter 4.

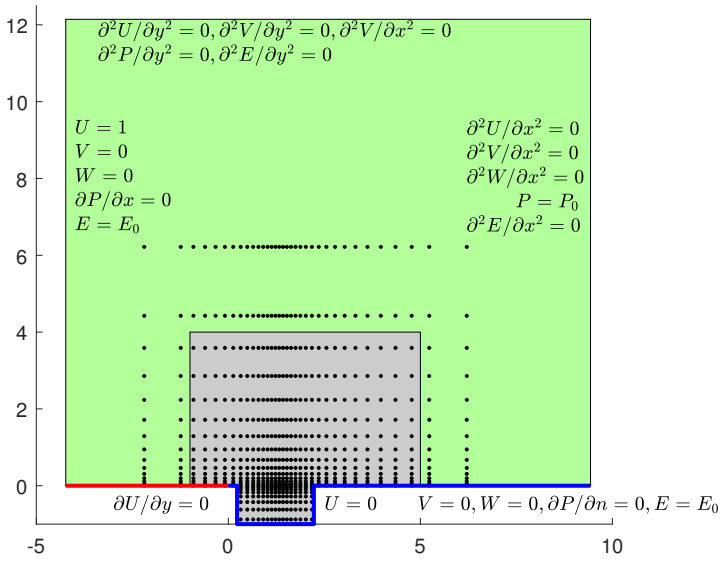


Figure 3.2 – Domain, mesh and boundary conditions of the flow simulation. The useful domain is marked in gray, while the buffer zone is green. One in every 10 nodes of the mesh is shown in black. The blue line represents wall boundaries, while the red line is a free-slip wall condition.

The initial condition is a Blasius boundary layer at constant pressure and temperature. Results from previous runs can also be used as initial condition; Reynolds and Mach numbers and the numerical methods may be changed; the code is also capable of interpolating the flow filed in case a different mesh was used to generate the initial flow. The boundary layer thickness at the cavity is controlled by changing its position with respect to the flat plate leading edge.

3.1.4 Spatial derivatives

Spatial derivatives are computed by a finite differences method chosen before runtime. Explicit second and fourth order methods are implemented, as well as compact fourth order spectral-like and sixth order schemes described by Lele (1992). It is possible to use a distinct differentiation method for the buffer zone, usually of a lower order, the transition from one method to the next happens smoothly.

DISTRIBUTION A: Distribution approved for public release. Distribution unlimited

The following equation must be solved when the derivative is needed:

$$\beta u'_{i-2} + \alpha u'_{i-1} + u'_i + \alpha u'_{i+1} + \beta u'_{i+2} = a\frac{u_{i+1} - u_{i-1}}{2h} + b\frac{u_{i+2} - u_{i-2}}{4h} + c\frac{u_{i+3} - u_{i-3}}{6h} \quad (3.10)$$

α, β, a, b and c are adjustable coefficients, h is the mesh spacing, f_i is the function value at node i and f'_i, its approximated derivative.

If both α and β are null, there is no need to solve a linear system as the derivative is given explicitly. The simplest scheme is the explicit second order, in which $a = 1$ and all other parameters are null. An explicit fourth order scheme has a=4/3 and b=-1/3.

The order of accuracy of a scheme is given by which of the following equations hold true for its coefficients.

$$\text{2nd order:} \quad a + b + c = 1 + 2(\alpha + \beta) \quad (3.11)$$

$$\text{4th order:} \quad a + 2^2 b + 3^2 c = 6\left(\alpha + 2^2\beta\right) \quad (3.12)$$

$$\text{6th order:} \quad a + 2^4 b + 3^4 c = 10\left(\alpha + 2^4\beta\right) \quad (3.13)$$

$$\text{8th order:} \quad a + 2^6 b + 3^6 c = 14\left(\alpha + 2^6\beta\right) \quad (3.14)$$

Despite being able to achieve high orders of formal accuracy, explicit schemes quickly lose precision at higher wave numbers, due to the increased high-order derivatives.

The modified wave number after the derivative is given by:

$$\omega'(\omega) = \frac{a\sin(\omega) + b\sin(2\omega)/2 + c\sin(3\omega)/3}{1 + 2\alpha\cos(\omega) + 2\beta\cos(2\omega)} \quad (3.15)$$

Lele (1992) uses this relation to derive some spectral-like derivative schemes. Ideally, the modified wave number would always match the original wave number.

Besides both explicit schemes, spectral-like derivative routines were implemented for fourth and sixth order accuracies. As an example, for the fourth order scheme, the restrictions are as follow:

1. Fourth order accuracy

2. Tridiagonal system

DISTRIBUTION A: Distribution approved for public release. Distribution unlimited

3. 5-point stencil

4. $\omega'(1.8) = 1.8$

For the first item, equations 3.11 and 3.12 must hold true. For the second and third items, chosen to reduce the computational cost, β=0 and c=0. For the fourth item, equation 3.15 must hold true for ω'=ω=1.8.

Therefore, there are five equations for the five variables, fully defining the system and resulting in α=0.364957272268410, β=0, a=1.57663818151227, b=0.153276363024547 and c=0.

The sixth order spectral-like scheme is done in a similar manner and results in a seven-point stencil in the right-hand side.

Figure 3.3 shows the modified wave number for some numerical schemes. Note how the spectral-like method stays closer to the exact value even at higher wave numbers.

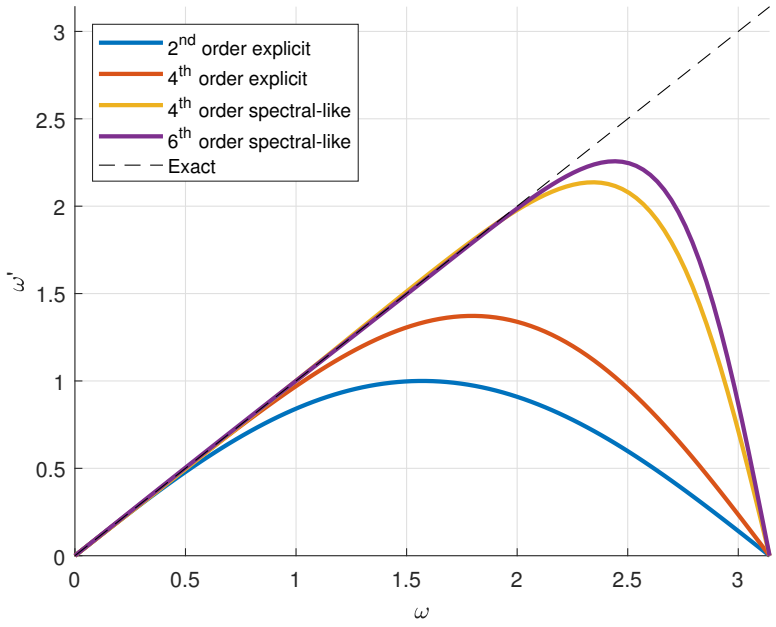


Figure 3.3 – Modified wave number for various numerical differentiation schemes.

Close to the boundaries, the stencil is shifted, and coefficients are adjusted accordingly. In order to avoid using large, decentered stencils, which has caused numeric stability problems, the derivative accuracy order may be decreased. For example, the sixth-order spectral-like scheme uses a seven-point stencil, accounting for the center point and three additional nodes on each side. Therefore, the node at the boundary and the two nodes next to it must have their stencil modified. In this work, we use the fourth-order spectral-like scheme two points removed from the boundary, the fourth-order Padé scheme one point remove from the boundary and a decentered third-order scheme at the wall with

DISTRIBUTION A: Distribution approved for public release. Distribution unlimited

coefficients so that the dissipation error at $\omega = \pi$ is $\pi/2$. In our experience, this scheme has a good stability and does not affect the accuracy of the solution.

It is important to note that these finite difference methods only work for equally spaced meshes. Therefore, the well know chain rule for derivatives must be used, as shown in the following equation.

$$\frac{\partial u}{\partial x} = \frac{\partial u}{\partial \phi}\frac{\partial \phi}{\partial x} \tag{3.16}$$

u is the function value and x is the actual mesh dimension. ϕ is the dimension in an intermediate mesh which corresponds node to node with the actual mesh. This intermediate mesh is equally spaced with $h = 1$. Therefore, both terms on the right-hand side of equation 3.16 can be obtained by standard finite difference methods. Note that the second term only needs to be computed once as it depends only on the mesh.

Once more, both corner nodes presented a challenge for these methods when computing the derivative. Figure 3.4 illustrates the Regions considered. In an inner node, i.e., away from the boundaries, finite differences method uses the nodes around it to approximate the derivative. If no other changes were made to the code, corners nodes 1 and 2 would be considered as inner nodes and, thus, derivatives computed for them would account for both points on the wall and points immersed in the flow, which would not be correct and cause the solution to fail. Because of this, both these nodes only consider values in Region 2 of figure 3.4.

This has solved the problem for both corner nodes and for the region between them. But nodes in Regions 1 and 3 of the figure would still have its derivatives miscalculated, causing discontinuities in the domain close to the corner, which would later cause the simulation to fail. This was solved by considering both the last node in Region 1 and the first node in Region 3 as inner nodes for the finite differences method, which makes the derivative a continuous function again.

In sum, derivatives in Region 2 depend only on values in it. Derivatives in Regions 1 and 3 depend on values both in their respective regions and on values in Region 2. The approach for wall-normal derivatives is analogous.

Equation 3.17 illustrates how the derivatives would be computed close to corner node 1, with index c_1. α, a, b and c are the finite differences coefficients, note that they are different for the corner nodes and more coefficients may be added depending on the derivative scheme chosen. D and f are vectors containing the derivatives and the function

DISTRIBUTION A: Distribution approved for public release. Distribution unlimited

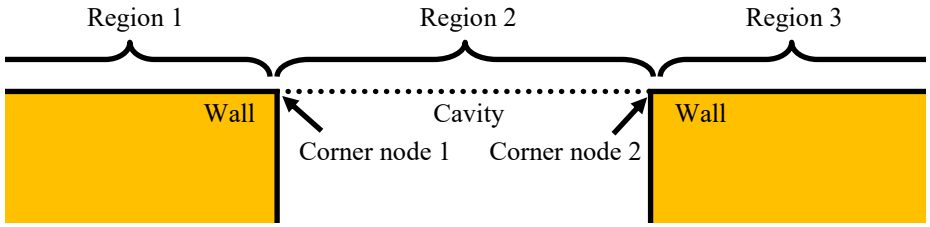


Figure 3.4 – Close-up of the corner nodes in the domain and the regions considered for derivatives.

values for each node, respectively.

$$\begin{bmatrix} 1 & \alpha & & & & \dots & 0 \\ \alpha & 1 & \alpha & & & & \vdots \\ & \ddots & \ddots & \ddots & & & \\ & & \alpha & 1 & \alpha & & \\ & & & & 1 & \alpha & \\ \vdots & & & & \alpha & 1 & \alpha \\ 0 & \dots & & & & \ddots & \ddots & \ddots \end{bmatrix} \begin{bmatrix} D_1 \\ D_2 \\ \vdots \\ D_{c_1-1} \\ D_{c_1} \\ D_{c_1+1} \\ \vdots \end{bmatrix} = \tag{3.17}$$

$$= \begin{bmatrix} a & b & c & & & & \dots & 0 \\ -a & 0 & a & & & & & \vdots \\ & \ddots & \ddots & \ddots & & & & \\ & & -a & 0 & a & & & \\ & & & & a & b & c & \\ \vdots & & & & -a & 0 & a & \\ 0 & \dots & & & & \ddots & \ddots & \ddots \end{bmatrix} \begin{bmatrix} f_1 \\ f_2 \\ \vdots \\ f_{c_1-1} \\ f_{c_1} \\ f_{c_1+1} \\ \vdots \end{bmatrix}$$

These matrices are analogous at to the second corner index, c_2.

As seen above, the linear system for nodes c_1 to c_2 can be decoupled from the others, while nodes from 1 to $c_1 - 1$ and from $c_2 + 1$ to n still depend on the central region. An analogous approach is taken in the wall-normal direction.

The code allows the buffer zones to use different schemes for spatial derivatives, usually lower orders are desired. A smooth cosine-shaped transition happens from the main scheme to the lower order one in this region.

For three-dimensional cases in which a single span-wise wave number is required, the code has a special routine that allows spectral derivatives to be computed in this direction. This is done by using four equally spaced nodes and setting $\alpha = 0$ and $a = \pi/2$ in the matrices of equation 3.17. These coefficients were obtained by setting $\omega' = \omega = \pi/2$ in

DISTRIBUTION A: Distribution approved for public release. Distribution unlimited

equation 3.15. When using this routine, one must make sure that all span-wise oscillations in the domain have the correct wave number, or else the derivatives will be miscalculated. This is especially useful for the global stability analysis, which will be explained in further detail in Chapter 4.

3.1.5 Time integration

Time integration is performed at a fixed time step by either an explicit Euler, a third order or a fourth order Runge-Kutta scheme.

The simplest method is the explicit Euler, shown in the following equation. $\boldsymbol{U}^n$ is the flow state at time step n and $\boldsymbol{f}$ is the time derivative of this flow.

$$\boldsymbol{U}^{n+1} = \boldsymbol{U}^n + \Delta t \boldsymbol{f}\left(\boldsymbol{U}^n\right) \tag{3.18}$$

The fourth order Runge-Kutta method is given by the equations below. Despite its higher computational cost at each step, it pays off by being able to take much larger steps without losing stability or precision.

$$\boldsymbol{U}^{n+1} = \boldsymbol{U}^n + \frac{\Delta t}{6}\left(\boldsymbol{K}_1 + 2\boldsymbol{K}_2 + 2\boldsymbol{K}_3 + \boldsymbol{K}_4\right) \tag{3.19}$$

$$\boldsymbol{K}_1 = \boldsymbol{f}\left(\boldsymbol{U}^n\right) \tag{3.20}$$

$$\boldsymbol{K}_2 = \boldsymbol{f}\left(\boldsymbol{U}^n + \frac{\Delta t}{2}\boldsymbol{K}_1\right) \tag{3.21}$$

$$\boldsymbol{K}_3 = \boldsymbol{f}\left(\boldsymbol{U}^n + \frac{\Delta t}{2}\boldsymbol{K}_2\right) \tag{3.22}$$

$$\boldsymbol{K}_4 = \boldsymbol{f}\left(\boldsymbol{U}^n + \Delta t \boldsymbol{K}_3\right) \tag{3.23}$$

The boundary conditions routine is called after each sub-step of the method.

The largest time step possible is defined by the method's numerical stability. For the flow's diffusive characteristics, equation 3.24 must be observed, and for the flow's convective characteristics, equation 3.25 must be observed. The maximum CFL value depends on the time integration method chosen. For the fourth order Runge Kutta, a CFL under around 1.3 is stable.

$$\Delta t \leq \frac{Re}{\left(\frac{1}{\Delta x_{min}^2} + \frac{1}{\Delta y_{min}^2} + \frac{1}{\Delta z_{min}^2}\right)} \tag{3.24}$$

DISTRIBUTION A: Distribution approved for public release. Distribution unlimited

$$\Delta t \leq \frac{CFL_{max}}{\left(\frac{1/Ma+u_{max}}{\Delta x_{min}} + \frac{1/Ma+v_{max}}{\Delta y_{min}} + \frac{1/Ma+w_{max}}{\Delta z_{min}}\right)} \tag{3.25}$$

The diffusive stability does not depend on the flow state, only on the mesh and on the Reynolds number, so it is only computed once. The convective stability depends on the flow velocity field and is computed at every step. Equation 3.25 also shows that for very low Mach numbers, closer to an incompressible flow, the time step would have to be significantly reduced due to the increased speed of sound waves compared to the flow velocity, considerably increasing the computational cost.

At very low Mach numbers, the incompressible Navier-Stokes equations would yield a much faster solution at the cost of not being able to identify any acoustic phenomena or the instability modes related to it. In the research group, there is an ongoing work evaluating the viability of the SIMEX method, which combines implicit and explicit time marching methods for distinct parts of the governing equations as a way of allowing larger time steps to be taken without the large computational penalty of solving all the governing equations implicitly. (RODRIGUES, 2017)

3.1.6 Anti-aliasing filtering

In this type of simulation, high-frequency numerical noise may quickly build up, causing the simulation to diverge from the physical solution.

In a real flow, some mechanisms transport energy from long wavelengths to shorter ones, until the molecular viscosity becomes strong enough to dissipate this energy. In a fully turbulent flow, this is known as the Kolmogorov scale (KOLMOGOROV, 1991). Simulations down to this scale would require extremely fine meshes and are outside the scope of this work and have a huge computational cost, outside the reach of modern computers for most geometries, even one as simple as an open rectangular cavity.

Eriksson and Rizzi (1985) state that, due to aliasing effects, the motion in the shortest wavelength resolved by the mesh is numerically transferred to long wavelengths, which causes the solution to diverge from the physical system.

A numerical low-pass filter attenuates this noise (GAITONDE; VISBAL, 1998). The filter strength can be adjusted before runtime and, ideally, should be as low as possible, minimizing its effect on results.

This filtering should be enough to dissipate the motion in short wavelengths before they reach the Nyquist frequency limit, which states that a mesh can only resolve wave lengths of, at least, twice the node spacing and that shorter oscillations would cause aliasing issues.

DISTRIBUTION A: Distribution approved for public release. Distribution unlimited

At both ends of the stencil and at discontinuities in the domain, a special treatment must be done as the stencil spans five points to each side. Three options are available in this implementation. Filtering can be turned off at those five last points; or decentered stencils can be used to keep the 10^{th} order filtering; or the filtering order is progressively decreased in order to reduce the stencil and to keep it inside the useful domain.

Filtering is done at the end of each time step and requires solving a tridiagonal linear system for each direction.

It is implemented in a very similar manner to the spatial derivatives. The matrices for the linear system are formed and solved at the end of each time step. The treatment for border and corner nodes is the same as described in figure 3.4 and equation 3.17.

The system to be solved is the following:

$$\alpha_f \bar{u}_{i-1} + \bar{u}_i + \alpha_f \bar{u}_{i+1} = \sum_{n=0}^{N} \frac{a_n}{2} \left(u_{i-n} + u_{i+n}\right) \tag{3.26}$$

For this tenth order scheme, the coefficients are:

$$\begin{gathered} a_0 = \frac{193 + 126\alpha_f}{256}, \quad a_1 = \frac{105 + 302\alpha_f}{256}, \quad a_2 = \frac{-15 + 30\alpha_f}{64} \\ a_3 = \frac{45 - 2\alpha_f}{512}, \quad a_4 = \frac{-5 + 10\alpha_f}{256}, \quad a_5 = \frac{1 + -2\alpha_f}{512} \end{gathered} \tag{3.27}$$

α_f is an adjustable parameter from -0.5, which is maximum filtering, to 0.5, which is no filtering. u_i is the function value at node i and $\bar{u}_i$ denotes this value after filtering.

The spectral function of the filter shows the attenuation for each wavenumber. It is given by:

$$SF(\omega) = \frac{\sum_{n=0}^{N} a_n \cos\left(n\omega\right)}{1 + 2\alpha \cos\left(\omega\right)} \tag{3.28}$$

Figure 3.5 is a plot of this spectral function for various values of α for this tenth order scheme.

3.1.7 Artificial damping

This DNS is used in two distinct parts of this work. Besides being called during the instability analysis, it is also used to generate the base flow.

A fundamental requirement for this base flow to be used for instability analysis is to be steady, i.e., its derivatives with respect to time are null. Given that $\boldsymbol{f}(\boldsymbol{U})$ describes

DISTRIBUTION A: Distribution approved for public release. Distribution unlimited

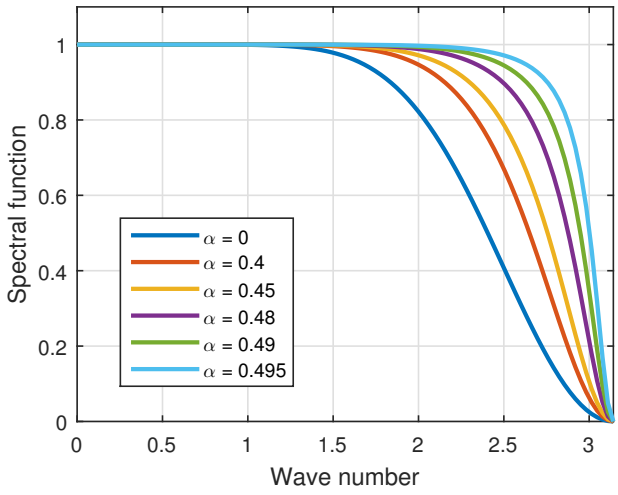


Figure 3.5 – Spectral function for the tenth order low-pass filter.

the time derivative of the flow $\boldsymbol{U}$, a steady state solution $\boldsymbol{U}_0$ suitable to be a base flow would yield

$$\boldsymbol{f}(\boldsymbol{U}_0) = \boldsymbol{0} \tag{3.29}$$

Two of the most straightforward methods to obtain $\boldsymbol{U}_0$ are:

1. Run the time evolution for a sufficient time to reach a steady flow within a certain tolerance.

2. Use a Newton iteration method to solve the non-linear system.

The first solution works only if all the base flow modes are stable and requires long simulations when close to critical stability conditions. An open cavity flow may not always meet this criterion, as it may be two dimensionally unstable, which would cause the simulation to reach a periodical solution.

At the critical stability condition, the time average of this periodical solution coincides with the base flow, but this is not true for unstable conditions. (SIPP; LEBEDEV, 2007)

The second solution has a very large computational cost for this type of system, with many variables. It would also require a considerable amount of recoding of the DNS.

Åkervik et al. (2006) propose a solution based on the first method, called the Selective Frequency Damping (SFD). It works as a low pass filter in the time domain, which damps the unstable modes present in the flow so that a physical steady state is reached by the simulation, even if it is physically unstable.

DISTRIBUTION A: Distribution approved for public release. Distribution unlimited

It is based on a proportional feedback control and works by adding a forcing term to the governing equations.

$$\frac{\partial \boldsymbol{U}}{\partial t} = \boldsymbol{f}(\boldsymbol{U}) - \chi(\boldsymbol{U} - \boldsymbol{w}) \tag{3.30}$$

Where $\boldsymbol{w}$, ideally, would be the target steady flow, but as it is not available at run time, it is substituted by a time filtered flow obtained by the convolution of $\boldsymbol{U}$ with a time filtering kernel T.

$$\boldsymbol{w} = \bar{\boldsymbol{U}}(t) = \int_{-\infty}^{t} T(\tau - t, \Delta)\boldsymbol{U}(\tau)d\tau \tag{3.31}$$

The filtering kernel can be defined as:

$$T(\tau - t, \Delta) = \frac{1}{\Delta} \exp\left(\frac{\tau - t}{\Delta}\right) \tag{3.32}$$

The cutoff frequency is given by:

$$\omega_c = \frac{1}{\Delta} \tag{3.33}$$

For the implementation, equations 3.31 and 3.32 as rewritten in the equivalent differential form:

$$\frac{\partial \bar{\boldsymbol{U}}}{\partial t} = \frac{\boldsymbol{U} - \bar{\boldsymbol{U}}}{\Delta} \tag{3.34}$$

This equation can be solved along with the actual flow, with few changes to the code and a small increase in the computational cost. Both χ from equation 3.30 and Δ from equation 3.34 are adjustable parameters.

χ controls the strength of the artificial damping. Low values may cause the system to remain unstable or very close to the critical condition. High values add too much damping, causing the system to take a very long time to converge.

Δ controls the cutoff frequency, which should be lower than the unstable mode's frequency. On the other hand, high values of Δ, therefore low cutoff frequencies, cause a similar effect to a strong damping, increasing the time needed for the solution to reach the steady state.

In summary, the following system of equations is solved through time:

$$\frac{\partial \boldsymbol{U}}{\partial t} = \boldsymbol{f}(\boldsymbol{U}) - \chi(\boldsymbol{U} - \bar{\boldsymbol{U}}) \tag{3.35}$$

DISTRIBUTION A: Distribution approved for public release. Distribution unlimited

$$\frac{\partial \bar{\boldsymbol{U}}}{\partial t} = \frac{\boldsymbol{U} - \bar{\boldsymbol{U}}}{\Delta} \tag{3.36}$$

When this system reaches a steady state, $\boldsymbol{U}$ and $\bar{\boldsymbol{U}}$ will be equal and the second term of the first equation will vanish. Therefore, $\boldsymbol{U}$ will represent the physical flow $\boldsymbol{U}_0$, which is steady.

To reduce the computational cost, a fourth order Runge-Kutta scheme may be used to solve for the physical part of the flow, which is only the first term of the right-hand side of equation 3.35, for its increased stability. While the other parts are solved by the simpler explicit Euler method. Hence, equation 3.19 is replaced by:

$$\boldsymbol{U}^{n+1} = \boldsymbol{U}^n + \frac{\Delta t}{6}\left(\boldsymbol{K}_1 + 2\boldsymbol{K}_2 + 2\boldsymbol{K}_3 + \boldsymbol{K}_4\right) - \Delta t\ \chi(\boldsymbol{U} - \bar{\boldsymbol{U}}) \tag{3.37}$$

With equations 3.20 to 3.23 still used for the sub steps $\boldsymbol{K}_1$ to $\boldsymbol{K}_4$. Equation 3.36 is solved through time by:

$$\bar{\boldsymbol{U}}^{n+1} = \bar{\boldsymbol{U}}^n + \Delta t \frac{\boldsymbol{U}^n - \bar{\boldsymbol{U}}^n}{\Delta} \tag{3.38}$$

It is worth noting that the goal of using this Selective Frequency Damping method is simply obtaining a steady state flow as quickly as possible. Therefore, there is no need for high precision algorithms for the time stepping. The Runge-Kutta algorithm is used because of its excellent stability properties, allowing larger time steps.

It is also possible to use this method only in the buffer zone to mitigate problems at the boundary conditions such as reflections. In this case, χ is multiplied by a parameter η that depends on the position, which varies smoothly from zero at the beginning of the buffer zone to one at the domain boundary.

3.2 Implementation

The DNS code used in this work is developed in-house and is a revision of the code used previously by our group. The preprocessing is done in Matlab® and includes the following steps:

- Receive the input parameters
- Create a directory for the results and initialize log files
- Generate the mesh
- Identify walls immersed in the domain

DISTRIBUTION A: Distribution approved for public release. Distribution unlimited

- Organize the domain partition for parallelization
- Set up the boundary conditions
- Set up matrices with coefficients for the spatial derivatives and filters
- Create the initial flow

The processing itself is written in FORTRAN, compiled by gfortran[1]. The Matlab® part of the code automatically writes some of the FORTRAN files and calls the compiler, this is done to minimize overheads as the DNS is executed.

Flow files are saved in .mat format, which is a compressed lossless format that takes roughly half the disk space of an equivalent binary file in our usage.

3.2.1 Domain decomposition and parallel execution

For the parallel execution, the domain is decomposed in slices and each one is sent to a different process. Figure 3.6 illustrates this decomposition, as done by the 2DECOMP&FFT library, which uses the MPI protocol (LI; LAIZET, 2010).

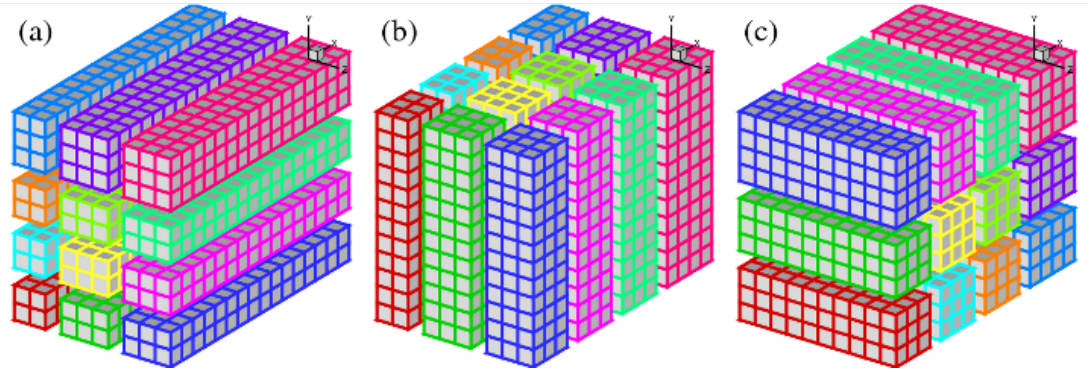


Figure 3.6 – Scheme of a three-dimensional domain decomposed for a grid of 3x4 processes (LI; LAIZET, 2010).

Each MPI process holds all points of the domain in one direction, but not in the others. For most operations, the decomposition in x is used, i.e., each process can access all points in x for their values of y and z. Which means that for the derivatives and filters in all directions to be computed, the domain must be transposed once for each direction. This process is illustrated in figure 3.7. An analogous routine is used for the noise filtering in each direction.

The flow geometry must be taken in account when choosing the number of nodes to be used. The subroutine for the boundary conditions is called when the domain in

[1] <https://gcc.gnu.org/fortran/>

DISTRIBUTION A: Distribution approved for public release. Distribution unlimited

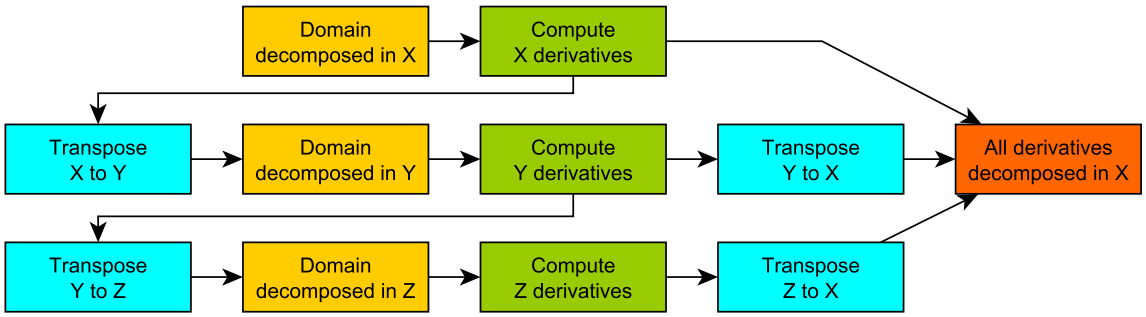


Figure 3.7 – Flowchart to obtain derivatives of the decomposed domain.

decomposed in the stream-wise x direction, i.e., no program instance has access to all values of y and z in the domain. This becomes an issue when computing wall-normal Neumann boundary conditions, as a number of points in the y direction are needed at this step and all these nodes should be contained in the same instance, to avoid communication overhead. Therefore, all points needed for the Neumann conditions must be contained in a single instance.

3.2.2 Linear system solver

Both the spatial derivatives and the spatial filter are implicit. Using either of them involves solving a tridiagonal matrix, which is done with the Thomas algorithm. A sample system is shown below, where y_i are known values and the solver must compute d_i.

$$\begin{bmatrix} b_1 & c_1 & & \cdots & a_1 \\ a_2 & b_2 & c_2 & & \vdots \\ & a_3 & b_3 & \ddots & \\ \vdots & & \ddots & \ddots & c_{n-1} \\ c_n & \cdots & & a_n & b_n \end{bmatrix} \begin{bmatrix} d_1 \\ d_2 \\ \vdots \\ d_n \end{bmatrix} = \begin{bmatrix} y_1 \\ y_2 \\ \vdots \\ y_n \end{bmatrix} \tag{3.39}$$

When $a_1 = c_n = 0$, the system is non-cyclical and therefore can be solved by the Thomas algorithm:

1: **for** $i = 2 \cdots n$ **do**
2: $\quad a_i = a_i / b_{i-1}$
3: $\quad b_i = b_i - a_i c_{i-1}$
4: $\quad y_i = y_i - a_i y_{i-1}$
5: **end for**
6: $d_n = y_n / b_n$
7: **for** $i = n - 1 \cdots 1$ **do**
8: $\quad d_i = (y_i - c_i d_i) / b_i$
9: **end for**

DISTRIBUTION A: Distribution approved for public release. Distribution unlimited

If the system is cyclical, the algorithm proposed by Temperton (1975) is used. The first line of the inverse of the tridiagonal matrix is computed during the preprocessing and stored. This line is used to obtain the value of d_1 from the vector y. The system is then modified to:

$$\begin{bmatrix} b_2 & c_2 & & \cdots & 0 \\ a_3 & b_3 & c_3 & & \vdots \\ & a_4 & b_4 & \ddots & \\ \vdots & & \ddots & \ddots & c_{n-1} \\ 0 & \cdots & & a_n & b_n \end{bmatrix} \begin{bmatrix} d_2 \\ d_3 \\ \vdots \\ d_n \end{bmatrix} = \begin{bmatrix} y_2 - a_1 d_1 \\ y_3 \\ \vdots \\ y_n - c_n d_1 \end{bmatrix} \tag{3.40}$$

which can be solved by the Thomas algorithm.

3.2.3 Flowchart

Two flowcharts were prepared to illustrate how the distinct parts of the code interact. The first one, in figure 3.8, focuses on the preprocessing stage. The top line of each frame identifies the task, while the bottom line shows which file contains it. The second flowchart, in figure 3.9, shows the interaction between the routines in the FORTRAN part of the code, where the simulation is performed.

DISTRIBUTION A: Distribution approved for public release. Distribution unlimited

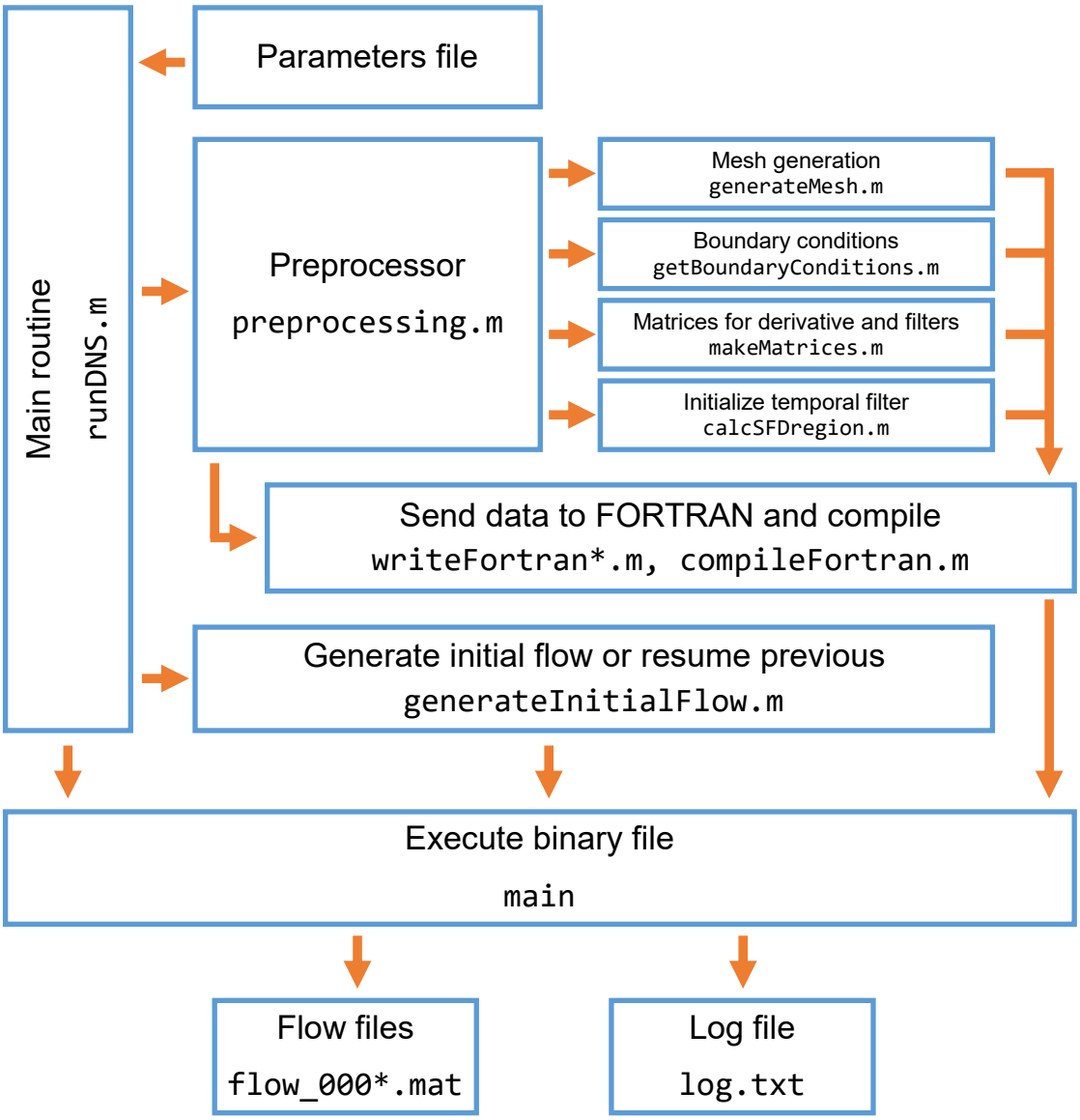


Figure 3.8 – Flowchart of the DNS. The top line of each frame identifies the task, while the bottom line shows which file contains it.

DISTRIBUTION A: Distribution approved for public release. Distribution unlimited

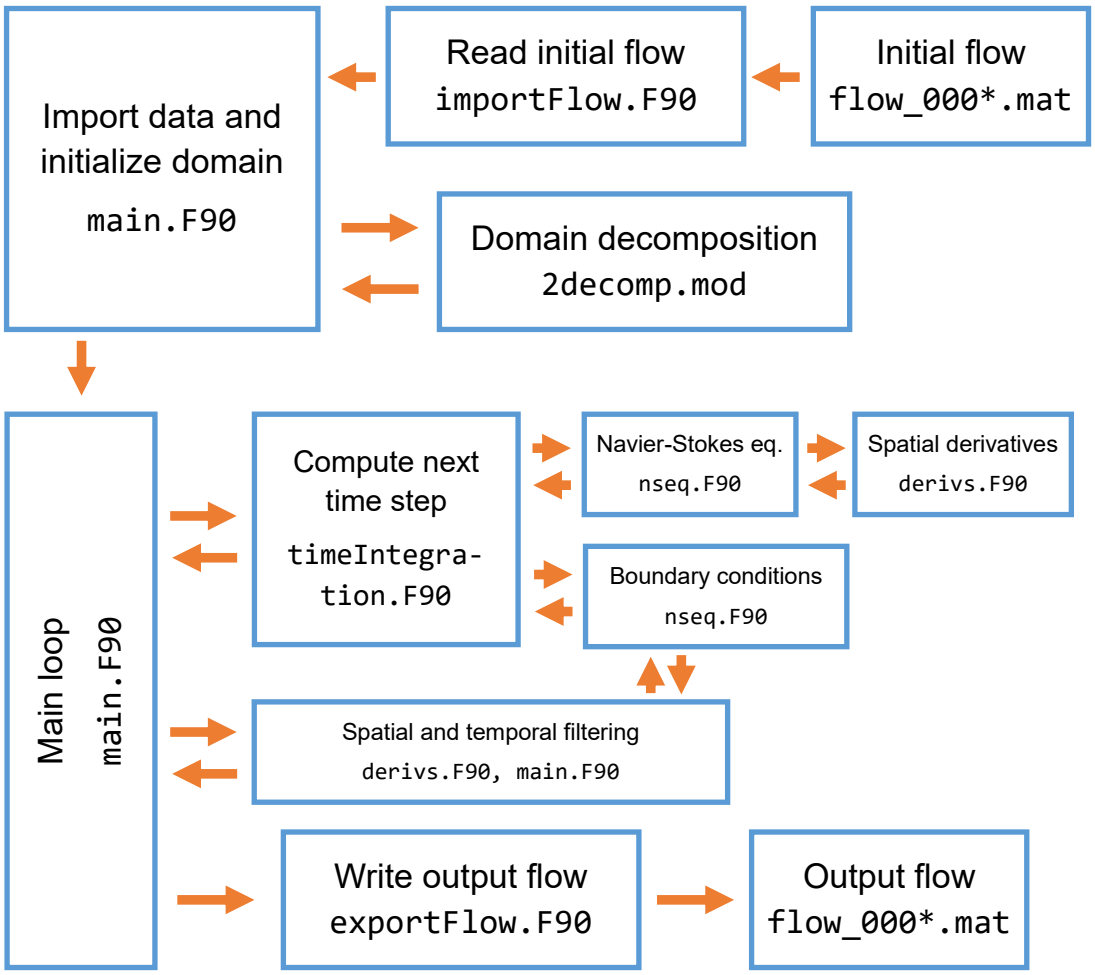


Figure 3.9 – Flowchart of the simulation routine of the DNS. The top line of each frame identifies the task, while the bottom line shows which file contains it.

DISTRIBUTION A: Distribution approved for public release. Distribution unlimited

3.3 Performance

To test the code performance, two test scenarios were defined. The code was executed in a server with 72 CPU cores at a nominal clock of 3.1 GHz.

The first scenario is a 2D domain, with 640×260 mesh nodes, run for 1000 time steps (each with 4 sub-steps due to the fourth order Runge Kutta method plus a filtering step). Table 3.1 brings the total execution times and the respective parallelization efficiency. Some of the cases were run multiple times with no significant change in results.

The normalized time is the total run time divided by the number of nodes in the mesh and amount of time steps. The efficiency is calculated by dividing the total speed-up by the number of processors used.

The parallelization strategy was highly efficient with up to 12 processors. Above that number, the MPI overhead started significantly affecting the performance gains. With 8 and 10 processors, an efficiency greater than 100% was achieved, this is a phenomenon known as super-linear speed-up, which may be caused by several factors, most likely the increased cache memory available to the code as more processors were allocated, reducing the data transfer to and from the RAM.

The second scenario is a 3D case with $640 \times 260 \times 16$ mesh nodes, run for a total of 100 time steps. This time, there was no super-linear scaling of performance, likely due to the increased total domain size. The array column in table 3.2 indicates how many domain partitions were used in the y and z directions, respectively.

Figure 3.10 summarizes the results from tables 3.1 and 3.2. In cases where multiple array configurations were used for the same number of processors, only the best result is

Table 3.1 – DNS execution time for different numbers of parallel processes, two-dimensional case.

Processors	Total time (s)	Normalized time (ns)	Speed-up	Efficiency
1	240	1445	1.00	100%
2	122	734	1.97	98%
3	81.4	489	2.95	98%
4	63.1	379	3.81	95%
6	42.2	254	5.69	95%
8	27.7	167	8.66	108%
10	23.4	141	10.3	103%
12	22.1	133	10.9	91%
15	20.7	124	11.6	77%
20	14.1	85	17.0	85%
30	10.4	63	23.0	77%
35	10.5	63	22.9	65%
40	10.0	60	24.0	60%

DISTRIBUTION A: Distribution approved for public release. Distribution unlimited

Table 3.2 – DNS execution time for different numbers of parallel processes, three-dimensional case.

Processors	Array	Total time (s)	Normalized time (ns)	Speed-up	Efficiency
1	1 × 1	913	3432	1.00	100%
2	1 × 2	469	1762	1.95	97%
2	2 × 1	472	1773	1.94	97%
4	1 × 4	234	880	3.90	97%
4	2 × 2	234	879	3.90	98%
4	4 × 1	247	928	3.70	92%
8	1 × 8	118	444	7.72	97%
8	2 × 4	119	448	7.66	96%
8	4 × 2	122	459	7.47	93%
8	8 × 1	123	465	7.38	92%
10	10 × 1	104	394	8.71	87%
16	2 × 8	70.0	263	13.1	82%
16	4 × 4	70.3	264	13.0	81%
16	8 × 2	71.6	269	12.8	80%
20	10 × 2	62.3	234	14.7	73%
32	4 × 8	47.6	179	19.2	60%
32	8 × 4	47.4	178	19.3	60%
40	10 × 4	43.8	165	20.8	52%
64	8 × 8	38.8	146	23.5	37%

shown in the figure. Note that these values are only valid for this case in this computer and may vary drastically for larger or smaller meshes and for different computational environments. Larger meshes tend to be more scalable.

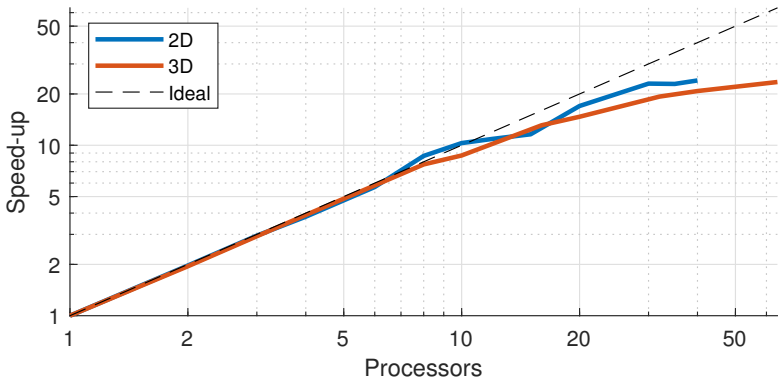


Figure 3.10 – Speed-up obtained for different numbers of processors for our 2D and 3D test cases.

When compared to the previous code developed by our group, the performance was considerably improved. In 2D cases, for the same number of processors, the run time was reduced to about one third, while in 3D cases it was roughly halved.

DISTRIBUTION A: Distribution approved for public release. Distribution unlimited

3.4 Strategies for mesh generation

When setting up a case to be solved by this DNS, a new mesh must be defined. By combining an analysis of the numerical methods with the experience of the research group, we have created a small set of rules that one could follow when generating a new mesh. Naturally, following these rules does not guarantee that the simulation is mesh-independent; however, they provide a good starting point.

- At least 13 points per period are necessary to accurately resolve a spatial wave.
- The minimum wall-normal mesh spacing must be, at most, 10% of δ^* at the region of interest.
- The cavity corners are usually the most critical region for mesh spacing, due to the large gradients.
- Node spacing should not change more than 10% from one node to the next in regions the flow if expected to oscillate.
- The wall-normal physical domain must be, at least twice as large as δ_{99} at the outflow.

To follow these rules, one must first estimate which frequencies are to be expected in each part of the domain. For a flat plate, spatially unstable TS waves have an angular velocity below $\omega = 0.15$, when normalized by the local δ^*. By approximating the convection velocity of TS wave to a third of the free flow velocity, the minimum length of an unstable TS wave is around $15\delta^*$, therefore the stream-wise spacing of the flow should be, at most, $1.15\delta^*$.

Phenomena inside the cavity may happen at higher frequencies. A cavity of length $L = 10\delta^*$ in a flow of Mach number $Ma = 0.5$ is expected to have its third Rossiter mode (R3) at an angular velocity of $\omega = 0.7$. Therefore, the maximum spacing should be $0.25\delta^*$, if R3 is assumed to be the phenomenon of interest that happens at the highest frequency.

Figure 3.11 illustrates the mesh for a gap case with the following parameters: $Re_{\delta_0^*} = 600$, $L = 10$, $D = 5$, $Ma = 0.5$. All lengths are normalized by δ^* at the gap leading edge. The spacing in the flow direction (X) is 1 at most of the domain. There is a region with spacing 4 upstream from the cavity, as TS waves are not expected there. The spacing at the flat plate leading edge is locally reduced to 2 as means to correctly resolve the larger gradients there. A region with spacing 0.2 spans from the gap leading edge to $30\delta^*$ downstream from its trailing edge. This is necessary due to the higher frequency phenomena in the gap and their resulting TS waves, which dissipate downstream due to

DISTRIBUTION A: Distribution approved for public release. Distribution unlimited

being spatially stable. Both gap corners are further refined due to the large gradients, the leading edge has a minimum spacing of 0.065 and the trailing edge, of 0.05.

In the flow-normal direction (Y), the minimum spacing is 0.065 and occurs at the flat plate. The spacing is smoothly increased to 0.5 at the gap bottom and to 1 at the free flow, away from the flat plate. Including the buffer zones, this mesh has 766 nodes in X and 214 in Y.

The physical domain goes from 0 to 413 in X and from -5 to 20.7 in Y. The origin is placed at the flat plate leading edge. Including the buffer zones, the domain spans $-517 \leq X \leq 1006$ and $-5 \leq Y \leq 274$. The gap is between $X = 202.8$ and $X = 212.8$.

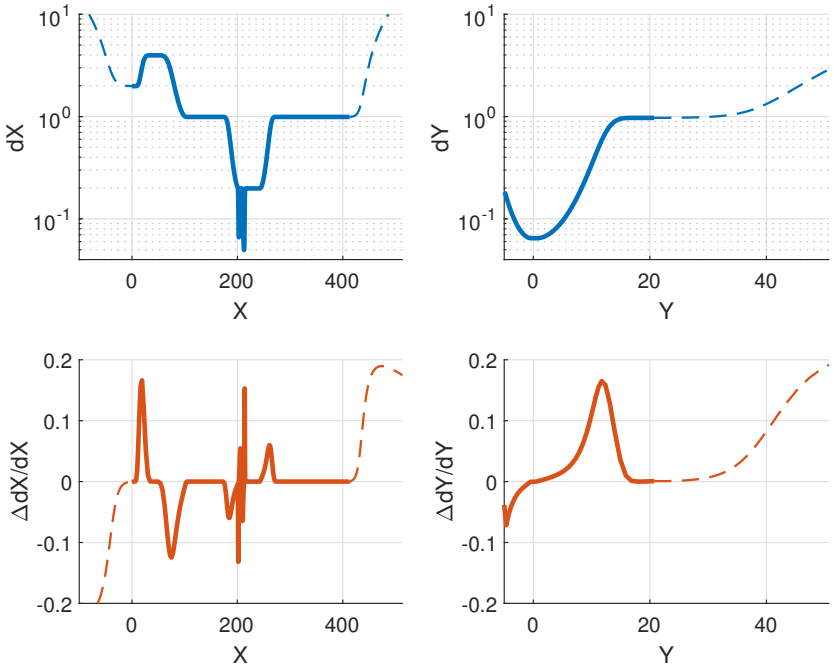


Figure 3.11 – Mesh spacing (top) and relative spacing change (bottom) for X (left) and Y (right) in a gap case. Buffer zones are represented by the dashed lines and are not fully shown for clarity.

3.5 Obtaining a base flow

A base flow is defined as an equilibrium point of the Navier-Stokes equation, it is, when the time derivatives of all variables are null. Such flow is often required as initial state for distinct types of instability analysis and, therefore, must be obtained with great accuracy.

In the case of stable flows, by simply starting the DNS with an arbitrary flow (such as a Blasius boundary layer) and letting it evolve will cause it to eventually reach the

DISTRIBUTION A: Distribution approved for public release. Distribution unlimited

base flow, as all modes will be damped out. This strategy, however, is often very time consuming, especially at the near-critical scenarios we wish to address in this study. On the other hand, if the flow is unstable, it would not reach the base flow naturally, as it is an unstable equilibrium point.

Two techniques are combined to reach a base flow quickly and reliably for both stable and unstable scenarios. The Selective Frequency Damping (SFD) method is used to stabilize any unstable mode present (ÅKERVIK et al., 2006) and a time-averaging process is done in a manner that whole periods of the least stable modes are contained within the window, damping them by roughly an order of magnitude every cycle.

In this code, it is possible to turn on the SFD filter only at selected parts of the domain, where we can maximize its benefits while reducing the possibility it would cause new near-critical modes or slow down the convergence of other modes. For example, by activating the SFD only at the cavity's trailing edge, it is possible to stabilize Rossiter modes by breaking their acoustic feedback mechanism. A similar concept is employed at the buffer zones to damp out any oscillations that might reach the open boundaries and reflect.

We have found the SFD to be most effective when dealing with modes that have high frequencies. Using it to damp low frequency modes requires its Δ parameter to be set too high, which would cause the flow to converge much slower due to the modes relative to the $\bar{\boldsymbol{U}}$ term of equations 3.35 and 3.36. Therefore, for these modes, a time-averaging process is used. We either estimate or measure the period of the least stable low frequency modes and compute the mean flow at the end of every cycle.

A test scenario was established with the following parameters: $Re_{\delta_0^*} = 600$, $L = 15$, $D = 5$, $Ma = 0.5$. Once more, all lengths are normalized by δ^* at the gap leading edge. This is a slightly unstable flow and, therefore, the SFD filter must be used to stabilize it. The initial condition is a Blasius profile on the flat plate and a stationary flow in the gap. Figure 3.12 shows the temporal evolution of stream-wise velocity (U) at three probes, one upstream from the gap ($X = 100$), one just before the gap ($X = 200$) and one downstream from it ($X = 300$). All probes are 1 length unit away from the flat plate. Three types of SFD filter were used: only at the buffer zones, at the buffer zones and at the gap trailing edge and at the whole domain. In all cases, the SFD parameters were $\Delta = 10$ and $\chi = 0.05$.

When SFD was used only at the buffer zones, which represents the physically accurate case, the unstable Rossiter mode was able to grow and reach a limit cycle, while both other cases successfully damped these oscillations. By analyzing the first probe, which is upstream from the gap, when the SFD filter was applied only around the trailing edge, the overall trend of the flow was not affected when compared to the first case, apart from the absence of the Rossiter mode. When the filter was applied to the whole domain,

DISTRIBUTION A: Distribution approved for public release. Distribution unlimited

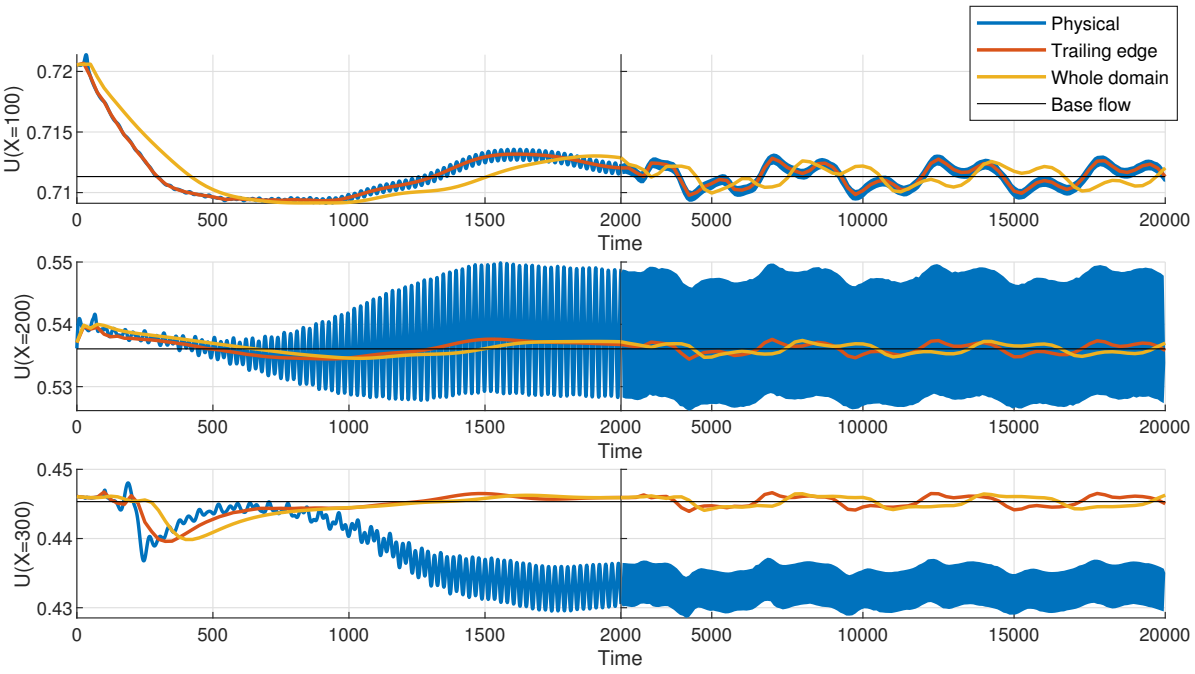


Figure 3.12 – Time series of stream-wise velocity (U) at three probes as the domain evolves from the initial condition towards a base flow for three different SFD strategies: only at the buffer zones (blue), at the buffer zones and at the gap trailing edge (red) and at the whole domain (yellow). Note that the time scale is changed after $t = 2000$ for better visualization of the initial transient phase.

the whole time series was slowed down, and the remaining modes took a longer time to complete a cycle.

The second and third probes present yet another effect, which is the shift of the mean flow due to the limit cycle in the physical case. Once more, turning on the SFD only at the leading edge did not affect the low frequency oscillations in the domain, while using the SFD in the whole domain did.

We have identified this low frequency oscillation as a standing acoustic wave that spans the whole domain in the stream-wise direction. Due to the Dirichlet boundary conditions in one side of the domain and the Neumann boundary conditions in the other, the length of this wave can be estimated as four times that of the domain.

After the flow finishes its initial transient, and assuming all the unstable modes are correctly damped, the remaining oscillations in the domain are caused by this acoustic mode. Due to the very long wave lengths, the buffer zones are not very effective at damping it, which would cause it to oscillate for a long time before dissipating. Damping it with the SFD is also impractical, as the cut-off frequency required would be very low, causing the whole solution to move at a slow pace towards the base flow. Therefore, we use time averaging techniques to damp these modes. When the solution completes a whole cycle of

DISTRIBUTION A: Distribution approved for public release. Distribution unlimited

this mode, the mean flow is computed and the simulation resumes from this new state. Every time the mean flow is computed, the oscillations reduce by about one order of magnitude.

Figure 3.13 shows the residual of the simulation as the baseflow is reached. This residual shows the maximum change for each variable between two consecutive time steps. The SFD filter was turned on at the trailing edge of the cavity. The solution was simulated until $t = 10000$, which is enough for the transient flow to dissipate and for the first acoustic wave cycle to finish. The mean flow is computed, and the simulation resumes until a new acoustic wave cycle is finished, which takes another 6200 time units. This process is repeated until all residuals are in the order of 10^{-13}, which is considered the numerical noise floor for this solver.

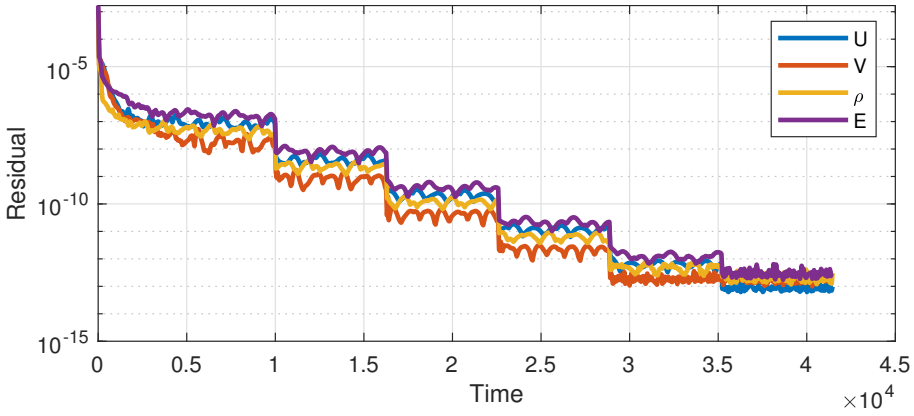


Figure 3.13 – Maximum residual of each variable towards a base flow.

DISTRIBUTION A: Distribution approved for public release. Distribution unlimited

DISTRIBUTION A: Distribution approved for public release. Distribution unlimited

Chapter 4

Linear Stability Theory

4.1 Introduction

Methods for computing the global stability of flows have been used on several applications in the past decades (THEOFILIS, 2011). Many implementations involve building the Jacobian matrix of the flow and solving its eigenproblem. However, starting with Eriksson and Rizzi (1985), who worked with the Euler equations, the alternative, time-stepping method was developed and became popular. Edwards et al. (1994) and Chiba (1998) used this method for the Navier-Stokes equations and Tezuka and Suzuki (2006), to solve a 3D global stability case for the first time. These methods do not require the Jacobian matrix explicitly, but, instead, require a flow solver. An overview of the global stability analysis and other types of modal analysis can be found in (TAIRA et al., 2017).

One reason for the popularity of time-stepping methods is that the flow solver can be treated as a black box, which is simply incorporated into the algorithm, greatly reducing code implementation and verification efforts. Gómez, Gómez and Theofilis (2014) and Liu, Gómez and Theofilis (2016) demonstrated the great flexibility of this method by coupling it to the well-known OpenFOAM CFD software. Time-stepping methods have also been successfully used to solve the adjoint eigenproblem for flow sensitivity analysis (BRYNJELL-RAHKOLA et al., 2017) and for transient growth analysis (BARKLEY; BLACKBURN; SHERWIN, 2008). Mack and Schmid (2010) implement a time-stepping solver and use Cayley transformations to accelerate the convergence of the algorithm in specific parts of the spectrum. More recently, Negi, Hanifi and Henningson (2020) have employed this method for fluid-structure interaction problems. A review of similar methods and its applications can be found in Loiseau et al. (2019). However, if a very large number of eigenvalues is required, the matrix-forming methods are usually more

DISTRIBUTION A: Distribution approved for public release. Distribution unlimited

efficient (THEOFILIS, 2011).

The widely used time-stepping approach discussed in this work is based on the Arnoldi method (ARNOLDI, 1951) for solving eigenproblems. Instead of needing the flow's Jacobian matrix, this method only requires the ability to obtain the product of such matrix by an arbitrary vector. The governing equations are rearranged in a way that the result of this product can be obtained from a run of a flow solver.

In this chapter we investigate parameters that influence the accuracy and cost of this method and develop equations that provide optimal parameter values for its efficient use. We will use the classical open cavity flow as an example. Even though the specific optimal parameters will vary according to, for example, the flow studied, flow solver used and the computational resources available, the trend and sensitivity of the method's performance with respect to each parameter, the guidelines, the equations for estimating optimal values and the conclusions are general.

The chapter focuses on four choices that need to be made when setting up this algorithm: the disturbance magnitude; the Fréchet derivative accuracy order; flow simulation time for each Arnoldi iteration; and the size of the Krylov span. Section 4.2 covers the methods employed in our global stability analysis and explains these parameters and where each of them is needed. As will be explained, even though all these parameters affect accuracy in complicated ways, the optimal value of disturbance magnitude is mostly independent on the integration time and on the size of the Krylov span. In turn, the optimal integration time is also independent on the Krylov span dimension and is only weakly dependent on the disturbance magnitude.

The first two choices are discussed in section 4.4 and are associated to the trade-off between Fréchet truncation errors and flow solver discretization errors. Section 4.5 discusses the effect of the integration time. Section 4.6 analyses the trade-off between the Krylov span size and the integration time of each Arnoldi iteration. Section 4.7 covers the convergence of eigenmodes as well as the contribution of each Arnoldi iteration to the overall result. The last section summarizes the findings.

Goldhirsch, Orszag and Maulik (1987) developed a similar method for obtaining the leading eigenvalues of a large matrix by converting it into a time-dependent differential equation and using this new system to select only the leading modes. They analyzed some sources of errors and part of the current study extends their work. We are concerned with the accuracy in retrieving flow modes. The important topic of the emergence of spurious modes owing to ill-posed boundary conditions is outside our scope; this is discussed by Ohmichi and Suzuki (2016). Our results do not apply to matrix forming methods, whose accuracy and efficiency are analyzed by Gennaro et al. (2013).

Local instability analysis is also used in this work. Since it is nowadays considered

DISTRIBUTION A: Distribution approved for public release. Distribution unlimited

a relatively well-known technique, we refrain from reviewing this topic and describing our implementation. Juniper, Hanifi and Theofilis (2014) describe this technique in detail and present simple codes that can be used to develop research codes.

4.2 Methods

4.2.1 Linear stability computations

A flow evolution can be expressed as

$$\frac{dU}{dt} = f(U) \ , \tag{4.1}$$

where U is a vector that contains all flow variables for each node of a mesh. The flow U is given by the base flow plus a disturbance: $U = U_0 + \tilde{u}$. The known base flow satisfies the steady Navier-Stokes equations, and the disturbance is small. A is the Jacobian matrix

$$A = \frac{\partial f(U_0)}{\partial U} \ , \tag{4.2}$$

hence, after linearizing equation 4.1 around U_0, we obtain

$$\frac{d\tilde{u}}{dt} = A\tilde{u} \ . \tag{4.3}$$

For an initial disturbance $\tilde{u}_0$, the solution $\tilde{u}$ is, formally,

$$\tilde{u} = e^{tA}\tilde{u}_0 \ . \tag{4.4}$$

By computing the eigenvalues S and eigenvectors V of A, equation 4.4 can be rewritten as

$$\tilde{u} = Ve^{tS}V^{-1}\tilde{u}_0 \ . \tag{4.5}$$

Each column ϕ_A of V corresponds to a flow mode and is associated to a value σ_A in S the diagonal matrix of eigenvalues, which gives the mode's amplification rate and oscillation frequency as its real and imaginary parts, respectively. Positive amplification rates indicate instability.

The Jacobian matrix is $N \times N$, where N is the number of nodes in the domain multiplied by the number of dependent variables, namely, 4 for 2D flows and 5 for 3D ones, when using the compressible Navier-Stokes equations; hence the interest in methods that

DISTRIBUTION A: Distribution approved for public release. Distribution unlimited

avoid the solution of the full Jacobian matrix. In the approach used here (ERIKSSON; RIZZI, 1985; CHIBA, 1998; TEZUKA; SUZUKI, 2006; GÓMEZ; GÓMEZ; THEOFILIS, 2014), it is convenient to define a matrix

$$B = e^{\tau A} \ . \tag{4.6}$$

The concept behind the eigenvalue solver method used here is that by recursively multiplying a matrix B by a vector, the eigenvector corresponding to the eigenvalue with the greatest absolute value is selected. Using this idea, it is possible to construct a set of n linearly independent vectors that approximate the eigenvectors of the n largest eigenvalues of B, which correspond to the leading eigenvalues of A. If care is taken, the approximation can be excellent. The method is implemented via the Arnoldi algorithm (ARNOLDI, 1951) and belongs to the class of orthogonal projection techniques for approximate solutions of linear systems (SAAD, 2003).

The Arnoldi algorithm starts with a ℓ^2 normalized vector ζ_1, which will be discussed in the next section. At each iteration k, the Arnoldi algorithm takes a normalized vector ζ_k, and calculates the product $B\zeta_k$. Next, the dot products of ζ_j $(j = 1 \dots k)$ with $B\zeta_k$ are stored in positions $h_{j,k}$ of matrix H. A vector $\tilde{u}_{k+1}$ is given by the Gram-Schmidt orthonormalization of $B\zeta_k$ with respect to all previous ζ_j $(j = 1 \dots k)$. The norm of this vector is stored in $h_{k+1,k}$. The disturbance distribution vector for the following iteration, ζ_{k+1}, is obtained by normalizing $\tilde{u}_{k+1}$. The matrix H is of the Hessemberg form, and is constructed so that (TEZUKA; SUZUKI, 2006)

$$B\left[\zeta_1, \zeta_2, \dots, \zeta_M\right] = \left[\zeta_1, \zeta_2, \dots, \zeta_M\right] \begin{bmatrix} h_{1,1} & \dots & & \dots & h_{1,M} \\ h_{2,1} & \dots & & & \vdots \\ 0 & \ddots & & & \\ \vdots & \ddots & \ddots & \vdots & \vdots \\ 0 & \dots & 0 & h_{M,M-1} & h_{M,M} \end{bmatrix} . \tag{4.7}$$

After enough Arnoldi iterations, the eigenvalues of B, σ_B, with the largest modulus are approximated by the eigenvalues of H. In turn, the eigenvalues of A are $\sigma_A = \log(\sigma_B)/t \approx \log(\sigma_H)/t$, therefore, the eigenvalues of B with the largest modulus correspond to the eigenvalues of A with the largest real part, which are the most unstable and, therefore, usually most of interest in a global stability analysis. The respective eigenvectors are given by $\phi_A = \phi_B \approx [\zeta_1 \dots \zeta_M]\phi_H$. The H matrix is orders of magnitude smaller than the original Jacobian matrix of the flow problem, which massively reduces the computational resources needed. In calculating the eigenvalues of A from those of B, the procedure is ambiguous because the complex logarithm function is multivalued. The imaginary part,

DISTRIBUTION A: Distribution approved for public release. Distribution unlimited

which relates to the frequency, has an undetermined contribution of $2\pi n/\tau$, with n integer. Its value must be verified by, for example, observing the mode oscillation in the flow simulation. This ambiguity of the imaginary part does not affect the accuracy, and often it is the real part that is most vulnerable to discretization errors.

Finally, to multiply B by ζ_k, define F as

$$F(U) = U(0) + \int_0^\tau f(U)dt \ , \tag{4.8}$$

where τ is hereinafter referred to as integration time. The flow $U(t)$ is given by the sum $U_0 + \tilde{u}(t)$, in which $\tilde{u}(0) = \tilde{u}_0$ and $\tilde{u}(\tau)$ is given by equation 4.4. Substituting these in equation 4.8 and $e^{\tau A}$ by B shows that F can provide an approximation for the linear model as:

$$F(U) \approx U_0 + B\tilde{u}_0 \ . \tag{4.9}$$

Hence, B is the Jacobian of F:

$$\frac{\partial F(U)}{\partial \tilde{u_0}} = B \ . \tag{4.10}$$

Using a Taylor series expansion, we can write

$$F(U_0 + \varepsilon_0\zeta) = F(U_0) + \varepsilon_0 B\zeta + \overrightarrow{\mathcal{O}}(||\varepsilon_0\zeta||^2) \ , \tag{4.11}$$

where ε_0 is a small scalar. Keeping in mind that ζ has unitary norm, this leads to

$$B\zeta = \frac{1}{\varepsilon_0}\left[F\left(U_0 + \varepsilon_0\zeta\right) - F\left(U_0\right)\right] + \overrightarrow{\mathcal{O}}(\varepsilon_0) \ . \tag{4.12}$$

$B\zeta$ is the directional derivative of F in the ζ direction, known as Fréchet derivative. Equation 4.12 provides a first-order accurate approximation for $B\zeta$.

A second-order approximation is given by:

$$B\zeta = \frac{1}{2\varepsilon_0}\left[F\left(U_0 + \varepsilon_0\zeta\right) - F\left(U_0 - \varepsilon_0\zeta\right)\right] + \overrightarrow{\mathcal{O}}(\varepsilon_0^2) \ ; \tag{4.13}$$

and a fourth-order:

$$B\zeta = \frac{1}{12\varepsilon_0}\left[-F\left(U_0 + 2\varepsilon_0\zeta\right) + 8F\left(U_0 + \varepsilon_0\zeta\right) - 8F\left(U_0 - \varepsilon_0\zeta\right) + F\left(U_0 - 2\varepsilon_0\zeta\right)\right] + \overrightarrow{\mathcal{O}}(\varepsilon_0^4) \ . \tag{4.14}$$

DISTRIBUTION A: Distribution approved for public release. Distribution unlimited

Most of the literature chooses the second-order approximation (CHIBA, 1998; TEZUKA; SUZUKI, 2006; GÓMEZ et al., 2015), while, for example, Eriksson and Rizzi (1985) used the fourth-order variant. In this chapter this choice is analyzed. The values F to be used in equations 4.12 to 4.14 are obtained by integrating equation 4.1 numerically for a given disturbance $\tilde{u}_0$. This is carried out by the flow solver. The initial disturbance is discussed in the next section and the flow solver used is described later.

Algorithm 1 summarizes the full process.

Algorithm 1

Steady state flow U_0 from flow solver
Initial disturbance ζ_1 of norm 1
for k = 1 ... M **do**
    Compute $B\zeta_k$ using equation 4.12, 4.13, or 4.14
    $h_{j,k} \leftarrow \zeta_j^T \cdot B\zeta_k \qquad j = 1 \dots k$
    $\tilde{\zeta}_{k+1} \leftarrow B\zeta_k - \sum_{j=1}^{k} h_{j,k}\zeta_j$
    $h_{k+1,k} \leftarrow ||\tilde{\zeta}_{k+1}||$
    $\zeta_{k+1} \leftarrow \tilde{\zeta}_{k+1}/h_{k+1,k}$
end for
Compute eigenvalues σ_H and eigenvectors ϕ_H of H
$\sigma_A \leftarrow \log(\sigma_H)/\tau$
$\phi_A \leftarrow \{\zeta_1 \dots \zeta_k\}\phi_H$

Two different sources cause most of the errors. One is the Arnoldi algorithm, which uses the reduced order matrix H to approximate the large matrix B. Increasing the number of Arnoldi iterations (M) creates a larger Krylov span which can more accurately reproduce the true modes of the flow. However, τ also affects this approximation, and the product τM is what governs this accuracy (GOLDHIRSCH; ORSZAG; MAULIK, 1987). In sections 4.6 and 4.7, we present results for various values of M and τ and analyze the convergence of different modes.

The other error is the inaccuracy in approximating $B\zeta_k$ in equations 4.12 to 4.14 and can be further divided into two parts: the errors in the Fréchet derivative approximation and errors associated with the evaluation of F via the flow solver. They are affected by the choices of truncation order in the Fréchet derivative, ε_0 and τ. The error in evaluating F is associated with discretization error and nonlinear terms. Naturally, linearized flow solvers are not subject to nonlinear error, such as the one used by Loiseau et al. (2014), however, often the flow solver is not linearized. Sections 4.4 and 4.5 explore these issues and make it clear that some parameters affect more than one source of error.

DISTRIBUTION A: Distribution approved for public release. Distribution unlimited

4.2.2 Initial disturbance

The Arnoldi method efficiency also depends on the initial vector (ζ_1), as modes with a larger contribution to the initial disturbance tend to converge faster. In principle, the initial disturbance should contain all desired modes. However, Goldhirsch, Orszag and Maulik (1987) argue that even if a certain mode is not contained in the initial disturbance, it is likely to appear in the result due to numerical errors.

Random distributions, such as white noise, which have a flat spectrum may be seen as an advantage. However, they excite high-frequency modes, which are soon damped out, resulting in a quick loss of disturbance energy. We used as the initial disturbance a Gaussian distribution centered close to the cavity, where most of the activity takes place. The characteristic lengths in each direction are chosen so that the disturbance approaches zero well before the boundaries of the domain.

Equations 4.12 to 4.14 require the selection of a small scalar ε_0, which is the norm of the disturbance $\tilde{u_0}$ that is added to the flow. It is convenient to also define a parameter ε, such that $\varepsilon = \varepsilon_0/\sqrt{N}$, where N is the total number of variables in the flow solver and remains constant in our study. ε is the RMS of the disturbance $\tilde{u_0}$.

The error when computing $B\zeta$ has two major contributors: the truncation error in the Fréchet derivative and the accuracy of the F approximations. The former is directly linked to the norm of the disturbance (ε_0), while the latter is related to its RMS (ε).

4.2.3 Computational cost

One objective of this chapter is to provide guidelines for accessing efficiency in computing the modes with a desired accuracy. There are several measures of computational cost. CPU time is often used; however, this can be difficult to establish if parallel processing is used. In our case, while most parts of the computational procedures are parallelized, in some of them, notably the eigenvalue solution, the algorithms are closed, and we have limited access to the parallelization level achieved. Moreover, CPU cost is especially important with large clusters shared by many users. In our case, the code was allowed full access to 10 CPU cores of a workstation. Under these circumstances the time to a solution is an interesting measure of cost. This measure was used here and referred to as wall-time; however, as discussed at the end of the chapter, the conclusions can be extrapolated to other measures of cost.

Often a large part of the computational demand comes from the flow solver runs which provides the product $B\zeta$. In our framework, this cost is proportional to the number of Arnoldi iterations M, yielding a computational complexity of $\mathcal{O}(M)$. Some steps involve computational complexities above $\mathcal{O}(M)$; for instance, the Gram-Schmidt

DISTRIBUTION A: Distribution approved for public release. Distribution unlimited

orthonormalization in the Arnoldi algorithm has a complexity of $\mathcal{O}(M^2)$ and the eigenvalue solution of H, despite optimizations that can be used in some cases, tends to $\mathcal{O}(M^3)$ complex. There is also an overhead for transferring data between the flow solver and the global stability solver, as well as an overhead for starting up the flow solver at each Arnoldi iteration. Hence a total cost estimate of the method is given by:

$$C = (C_\tau \, \tau + C_{It}) \, N_{call} \, M + C_{GS} \, M^2 + C_{Eig} \, M^3 + C_0 \ , \tag{4.15}$$

where τ is the integration time; $C_\tau \tau$ is the wall-time the flow solver takes to integrate until τ; C_{It} is the wall-time of calling the flow solver once, which includes the IO operations between the flow solver and the eigenvalue problem solver, and the flow solver startup overhead; N_{call} is the number of flow solver calls to form one column in the Krylov span and depends on the order of accuracy of the Fréchet derivative; C_{GS} is the wall-time of the Gram-Schmidt operation, normalized by M^2. C_{Eig} is the wall-time of computing the eigenvalues of H, normalized by M^3; C_0 includes all other overheads, such as start-up and compilation time, and is fixed and negligible in the scope of this study.

Our Arnoldi algorithm implementation is in MATLAB and uses its built-in parallelization capabilities; the flow solver is written in FORTRAN and is parallelized by MPI. The cost coefficients were estimated with the aid of MATLAB's profiling tool and averaged across many executions with different parameters, in the ranges $100 \leq M \leq 4000$ and $0.01 \leq \tau \leq 10$. Table 4.1 shows these values in seconds. They are highly dependent on the implementation, on the computer and on the specific details of each flow case. Nevertheless, they provide an idea of the order of magnitude of the overall cost and how it scales with the Krylov span dimension, M. In our investigation, the discretization time interval of the flow solver was fixed at 10^{-3}. Moreover, the wall-time is associated to the number of time steps, while, as seen below, the accuracy is mostly related with the integration time τ, that is, the number of time steps multiplied by the discretization time interval. Fixing the discretization time interval makes them proportional. In our flow solver, the time step is upper bounded by the numerical stability of the solution, in the form of the Courant–Friedrichs–Lewy (CFL) condition, and the time integration truncation error at largest stable time step possible is negligible in comparison with the space integration error.

Table 4.1 – Estimated coefficients of computational cost, in seconds

	Value (s)	Complexity
C_τ	10	τM
C_{It}	0.6	M
C_{GS}	$1.5 \cdot 10^{-4}$	M^2
C_{Eig}	$4 \cdot 10^{-10}$	M^3

DISTRIBUTION A: Distribution approved for public release. Distribution unlimited

To illustrate these concepts, figure 4.1 (Top) shows the dimension M of the problem that was possible to construct and solve for $C = 1$ hour and 1 day as a function of τ. For a fixed C, M increases as τ reduces. Also, as a function of τ, the figure displays τM, here called total integration time, which increases with τ. Figure 4.1 (Bottom) gives the fraction of C spent on each part of the procedure. For $C = 1$ hour or for larger values of τ with $C = 1$ day, M is small, and C is dominated by the flow solver. As the Krylov space grows larger, the Gram-Schmidt normalization takes a greater portion of C, as it scales with M^2. Despite having a cost that scales with up to M^3, the time spent computing the eigenvalues of H is still comparatively small in the parameter space searched. For smaller values of τ (thus larger M), the overhead of starting the flow solver also becomes more relevant. This plot considers a first-order accurate Fréchet derivative, but results are qualitatively similar for 2$^{\text{nd}}$ and 4$^{\text{th}}$orders.

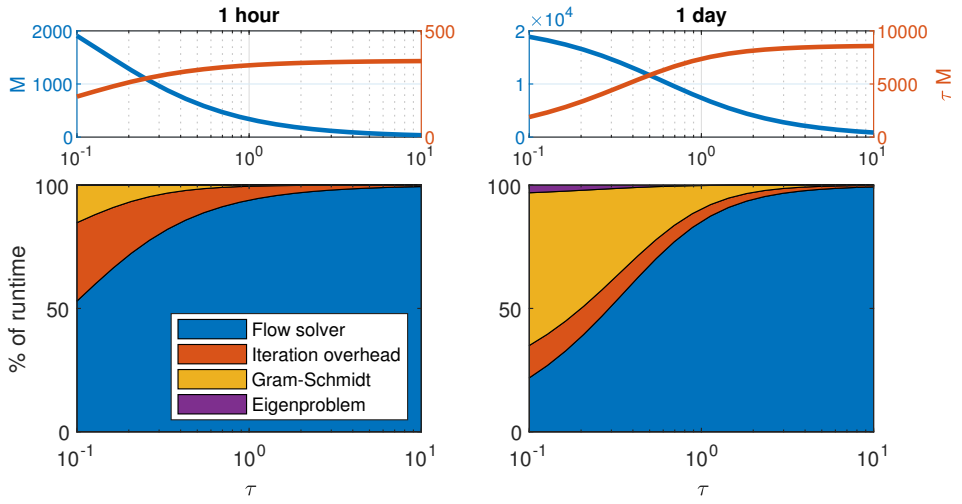


Figure 4.1 – (Top) Number of Arnoldi iterations (M) and total integration time (τM) as a function of integration time τ for two values of C. (Bottom) Fraction of time spent in each part of the procedure.

Restarted Arnoldi techniques (EDWARDS et al., 1994; LEHOUCQ; SORENSEN, 1996; KNOLL; KEYES, 2004; BAGHERI et al., 2009), allow the use of multiple smaller Krylov spans instead of a single larger one, which reduces the total memory usage of the algorithm as well as the cost components that scale super-linearly with M, such as the Gram-Schmidt orthonormalization. As will be seen, with optimal computational parameters these techniques have a limited impact, and, hence, are not investigated here.

Another aspect that may be considered when analyzing the trade-off between τ and M is memory usage. This algorithm requires storing all previous disturbances in memory in the $[\zeta_1 \dots \zeta_k]$ matrix, in our case up to around 2.4 MB per disturbance. However, memory optimization is of greater concern for the matrix-forming strategy (GENNARO et al., 2013), and is outside the scope of this work.

DISTRIBUTION A: Distribution approved for public release. Distribution unlimited

4.3 Baseline results of the studied case

Our test scenario is a flow over a two-dimensional open rectangular cavity. The Mach number is $Ma = 0.5$, Reynolds number based on the cavity depth (Re_D) is 1000 and the boundary layer momentum thickness at the cavity leading edge is given by $D/\theta_0 = 100$. The cavity's aspect ratio is $L/D = 2$. We chose this case as it is well documented and representative of typical cavity instability problems currently under study (BRÈS; COLONIUS, 2008; YAMOUNI; SIPP; JACQUIN, 2013; MATHIAS; MEDEIROS, 2021b). Under these conditions, this flow is unstable. In this work the simulations are two-dimensional as this is enough for our purpose and limits the computational cost. Nevertheless, the conclusion is general and applicable to three-dimensional flows, as discussed in the last section.

The mesh has 340×220 nodes in the stream-wise and wall-normal directions, respectively. The coordinate system origin is at the beginning of the boundary layer, while the cavity leading edge is at (0.23,0). All lengths are normalized by the cavity depth and the density and velocities, by the free-stream values. The useful domain spans from $x = -1$ to 5 in the stream-wise direction and from $y = -1$ to 4 in the wall-normal direction. At the open boundaries of the domain, there is a buffer zone, which progressively increases node spacing and lowers differentiation accuracy order, designed to prevent boundary effects from contaminating the solution. Upstream of the origin, a free-slip condition on the wall was used, which better negotiates the stagnation point at the origin (MARTINEZ; MEDEIROS, 2016). Figure 3.2 shows the domain, the mesh and the boundary conditions. Both base flow and stability results were independent on the computational mesh and domain.

The base flow was obtained using the flow solver with the aid of a Selective Frequency Damping (SFD) filter, which damps modes below a certain frequency threshold (ÅKERVIK et al., 2006). Without such filter, the unstable modes of the flow would prevent reaching a steady state. The SFD filter was turned off during the stability analysis. Figure 4.2 (Top) depicts the base flow in the cavity region, while figure 4.2 (Bottom) shows the base flow convergence history. All residuals are in the order of 10^{-13} relative to free-flow values.

Using the techniques described, the global stability analysis of this flow was performed. Figure 4.3 (Left) shows the eigenvalue spectrum. A positive real part indicates an unstable mode. There are six unstable modes, known as Rossiter modes ($\sigma_{R1} = 0.1344 \pm 1.5276i$, $\sigma_{R2} = 0.3230 \pm 2.7762i$ and $\sigma_{R3} = 0.2672 \pm 3.9143i$) (ROSSITER, 1964; MATHIAS; MEDEIROS, 2021b), and their respective complex conjugates. Also indicated is mode S1 ($\sigma_{S1} = -0.0215 \pm 0i$) the least stable stationary mode, i.e., with a null imaginary part. It relates to the transport of internal energy in the cavity (BERGAMO et al., 2015).

DISTRIBUTION A: Distribution approved for public release. Distribution unlimited

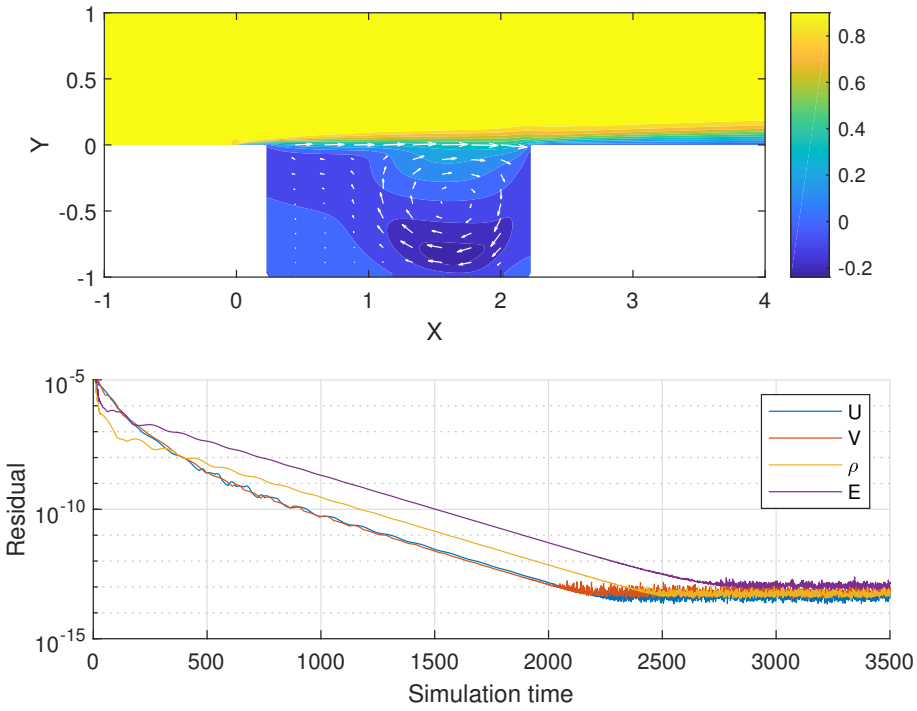


Figure 4.2 – (Top) Streamwise velocity of the base flow (contours every 10% of the free-flow, from -30% to 90%) and velocity field inside the cavity. (Bottom) Maximum residue of each variable as the flow evolves to the steady state.

The right-hand side of the figure shows density contours of these modes, the Rossiter modes at an arbitrary phase. In the following sections, we will use as examples mode R2, the most unstable for this set of parameters and mode S1, which is slightly stable. Their stability results will illustrate the sensitivity analysis and optimal value estimates presented in the following sections.

DISTRIBUTION A: Distribution approved for public release. Distribution unlimited

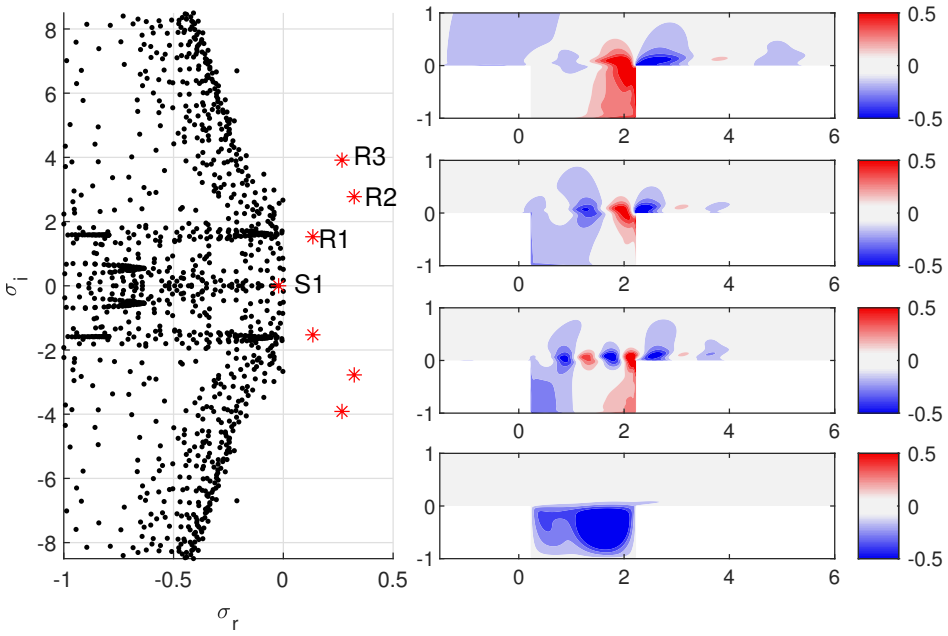


Figure 4.3 – (Left) Eigenspectrum of the base flow, with the unstable Rossiter modes (Rn) and the least stable stationary mode (S1) indicated, (Right) Density contours for the Rossiter modes 1 to 3 and the Stationary mode 1.

4.4 Order of accuracy of the Fréchet derivative and disturbance magnitude

The Fréchet derivative approximates the product $B\zeta$ for the Arnoldi algorithm. In this section we focus on two choices that must be made: the truncation order of the derivative approximation and the magnitude of the disturbance, ε. On the one hand, reducing the disturbance magnitude reduces the truncation error in the Fréchet derivative. On the other hand, owing to the discretization error in the flow solver, reducing the disturbance may deteriorate the approximations of F, as it involves the evolution of disturbances that are several orders of magnitude smaller than the base flow. Moreover, stable modes may attenuate to orders of magnitude smaller than their original amplitude. These aspects advocate the use of high accuracy order methods (LELE, 1992; GAITONDE; VISBAL, 1998; SOUZA; MENDONÇA; MEDEIROS, 2005; SILVA; SOUZA; MEDEIROS, 2010). Often, the flow equations include the nonlinear terms. This may pose another upper bound for ε, but this is strongly dependent on τ and hence is postponed to the next section.

If the truncation error of the Fréchet derivative becomes a limiting factor for the disturbance magnitude, a higher order approximation must be used. This brings the extra computational cost of increasing the number of calls to the flow solver. As an

DISTRIBUTION A: Distribution approved for public release. Distribution unlimited

example, Tezuka and Suzuki (2006) used the second-order method and noted that the effect of changing ε within two orders of magnitude was negligible. This indicates that the discretization error of the flow solver, the nonlinear terms, and the truncation error of the Fréchet derivative were negligible within the range of parameters of that study.

In our study, we tested disturbance magnitudes in the range $10^{-11} \leq \varepsilon \leq 10^{-3}$, combined with different values of τ. Both first and second-order accurate Fréchet derivatives were evaluated. The Krylov span M was so large that, within machine accuracy, the results for the eigenvalues tracked did not change for larger spans.

Figure 4.4 (Left) shows the values of the real part of the R2 eigenvalue obtained with different combinations of parameters. The results are in better agreement with each other in the range $10^{-9} \leq \varepsilon \leq 10^{-6}$. For reference, we performed calculations with $\tau = 1$, $\varepsilon = 10^{-6}$, $M = 2500$ and a fourth-order accurate Fréchet derivative. This Fréchet derivative is more expensive but provides more accurate results. Throughout this study, this case will be called reference case. Figure 4.4 (Right) shows the difference between each case and this reference.

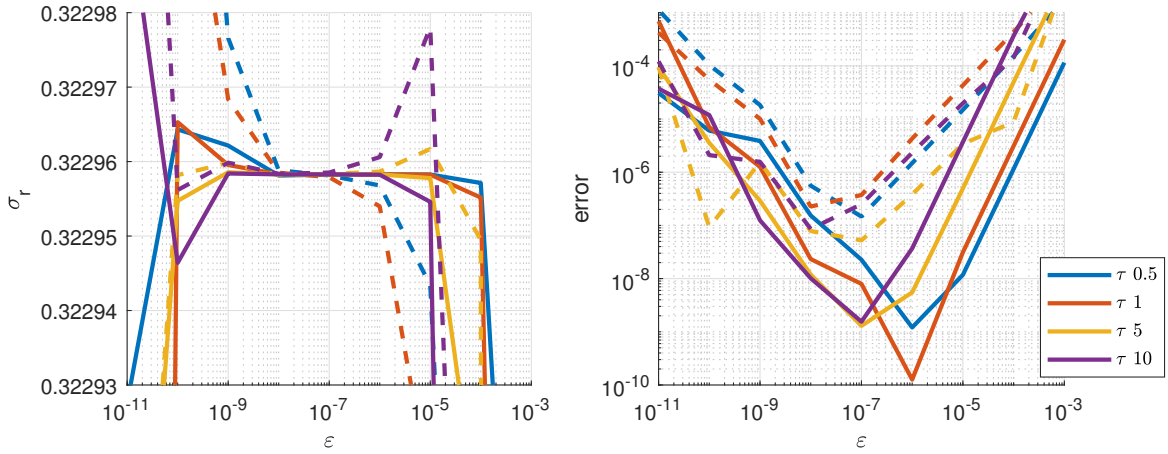


Figure 4.4 – Real part of the R2 eigenvalue as a function of ε for different values of τ. Dashed lines represent first-order accurate Fréchet derivative, and full lines, second-order accurate. (Left) Absolute value. (Right) Difference to the reference case.

From figure 4.4 (Right), in comparison with first-order accurate Fréchet, the second-order one considerably improved the accuracy. For large ε the truncation error dominates and the error decreases as ε diminishes. Accordingly, this is the region most affected by the Fréchet derivative truncation order. Close inspection reveals that, in this region, the error for σ_r decays approximately with either first or second-order, depending on the Fréchet derivative approximation used. This lends support to the approach here used and demonstrates the reference case represents an effective exact solution for the problem.

Also from figure 4.4 (Right), for small ε, the error grows as ε decreases. This

DISTRIBUTION A: Distribution approved for public release. Distribution unlimited

is associated with inaccuracy in the F approximations and originates in the flow solver discretization error. Accordingly, in this region the error is less affected by the Fréchet derivative truncation order. There, the error scales roughly linearly with $1/\varepsilon$, which is the expected scale for this type of error in the estimates of a first derivative like the Fréchet one. For first-order accurate Fréchet derivative the error scaling produces the characteristic "V" shape of the error curve in figure 4.4 (Right).

The maximum accuracy is better than 10^{-8}, but the optimum for $\tau = 1$ is likely to be fortuitous owing to the greater similarity of parameters with the reference case. The minimum error for 2nd order accuracy is about two orders of magnitude lower than for first-order accuracy; however, if an accuracy of 10^{-6} were acceptable, first-order would have produced sufficiently accurate results at about half the cost. For first-order accurate, the optimum ε is between 10^{-8} and 10^{-7}. Consistent with the error scaling discussed above, the optimum ε for second-order accuracy is larger than that of first-order accuracy. The optimum value of ε is lower for larger values of τ due to the nonlinear effects to be discussed in section 4.5.

Figure 4.5 shows the result for mode S1. In general, the same conclusions are reached. Being a stable mode, S1 is more vulnerable to discretization errors in the flow solver. Hence the effect of the discretization error is felt earlier for this mode, slightly raising the minimum error.

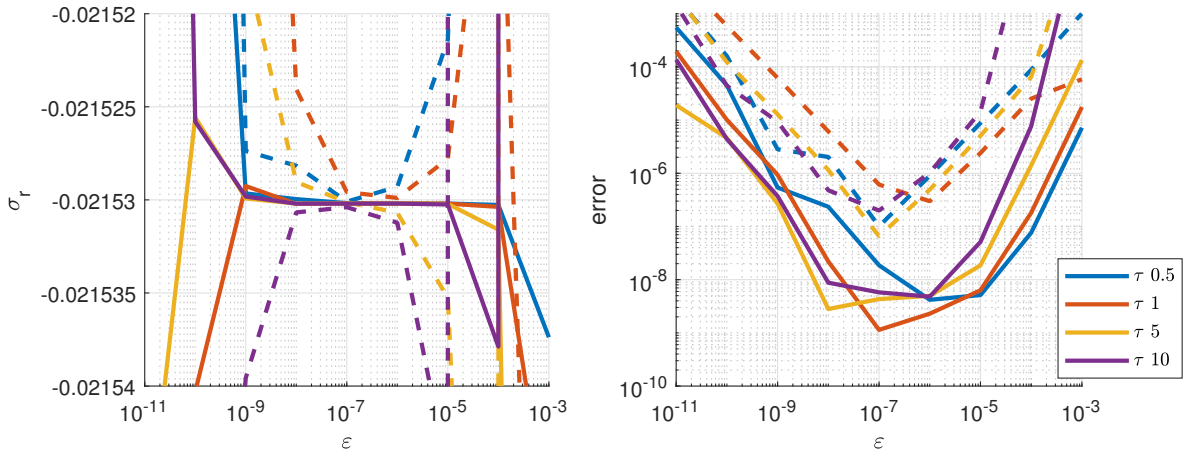


Figure 4.5 – Real part of the S1 eigenvalue as a function of ε for different values of τ. Dashed lines represent first-order accurate Fréchet derivative, and full lines, second-order accurate. (Left) Absolute value. (Right) Difference to the reference case.

Despite the complexity, the error behavior closely follows the theoretical error scaling in the asymptotic range of discretization (SILVA; SOUZA; MEDEIROS, 2010). It is possible to predict the order of magnitude of the optimal ε for a first order accurate Fréchet derivative approximation by replacing the exact solution F by the numerical

DISTRIBUTION A: Distribution approved for public release. Distribution unlimited

solution of the solver in equation 4.11. This introduces all the errors intrinsic to the flow solver. Using $\tilde{F}$ to indicate the numerical solution,

$$\tilde{F}(U_0 + \varepsilon_0\zeta) = \tilde{F}(U_0) + \varepsilon_0 B\zeta + \overrightarrow{\mathcal{O}}\left(\|\varepsilon_0^2\zeta\|\right) + \overrightarrow{E_F} \,, \tag{4.16}$$

where $\overrightarrow{E_F}$ is the error of the numerical approximation of F. Isolating $B\zeta$ (remember that $||\zeta|| = 1$),

$$B\zeta = \frac{1}{\varepsilon_0}\left[\tilde{F}\left(U_0 + \varepsilon_0\zeta\right) - \tilde{F}\left(U_0\right)\right] + \overrightarrow{\mathcal{O}}(\varepsilon_0) + \frac{\overrightarrow{E_F}}{\varepsilon_0} \,. \tag{4.17}$$

It is possible to derive similar expressions for Fréchet derivatives of arbitrary accuracy order n, which we can write in general form as:

$$B\zeta = \delta_n\tilde{F} + \overrightarrow{\mathcal{O}}(\varepsilon_0^n) + \frac{\overrightarrow{E_F}}{\varepsilon_0} \,, \tag{4.18}$$

where $\delta_n\tilde{F}$ is the n^{th} order accurate finite differences approximation for the Fréchet derivative.

The numerical error of F, $\overrightarrow{E_F}$, has two main components: the discretization errors of the flow solver, and the errors caused by nonlinear effects in the flow solution. However, as anticipated, the nonlinear error is neglected in the analysis here and considered in the next section. Each scalar component in the vector $\overrightarrow{E_F}$ has a discretization error of the order of ε_S, which is a measure of the flow solver's error. Therefore, the norm of $\overrightarrow{E_F}$ is $\varepsilon_S\sqrt{N}$, where N is the total number of variables in the system. Replacing ε_0 by $\varepsilon\sqrt{N}$, the total error of $B\zeta$ in equation 4.18 is estimated as

$$E_B = \left\| \overrightarrow{\mathcal{O}}(\varepsilon_0^n) + \frac{\overrightarrow{E_F}}{\varepsilon_0} \right\| = \mathcal{O}\left((\varepsilon\sqrt{N})^n\right) + \mathcal{O}\left(\varepsilon_S/\varepsilon\right) \,. \tag{4.19}$$

The optimum E_B is where $\partial E_B/\partial\varepsilon$ is null, leading to

$$\varepsilon_{opt} = \mathcal{O}\left(\left(\frac{\varepsilon_S}{N^{n/2}}\right)^{\frac{1}{n+1}}\right) \,. \tag{4.20}$$

With $\varepsilon_S = 10^{-13}$, from figure 4.2, we can estimate the minimum error for first-order accurate Fréchet derivative as $\varepsilon_{opt} = \mathcal{O}(10^{-8})$ and for the second-order accuracy as $\varepsilon_{opt} = \mathcal{O}(10^{-6})$. The error scaling involves coefficients which were disregarded, yet the estimates are close to what was observed in figures 4.4 and 4.5.

It is important to note that the theoretical analysis estimates the error in $B\zeta$ while figures 4.4 and 4.5 show the error for selected eigenvalues. Moreover, this equation does

DISTRIBUTION A: Distribution approved for public release. Distribution unlimited

not account for non-linear errors, which occur if both ε and τ are large enough. These issues are best discussed in connection with τ and are, hence, left to the next section. In any case, as will be seen, following the guidelines for use of optimal integration time, the nonlinear error becomes negligible and equation 4.20 is enough to determine the optimal value of ε.

According to equations 4.19 and 4.20, the size of the grid, the discretization error of the flow solver, and the truncation order of the Fréchet derivative approximation affect the optimal disturbance amplitude and the minimal error E_B in different ways. These dependencies are explored in figure 4.6. Regarding the error E_B, higher order Fréchet derivative approximations provide better results, which deteriorate faster with an increase in N or ε_S. For example, if $\varepsilon_S = 10^{-16}$ and $N = 10^3$, going from first order accurate to fourth order accurate Fréchet derivative reduces E_B by 10^6. For a less accurate code and larger grids, say $\varepsilon_S = 10^{-8}$ and $N = 10^7$, the same change reduces E_B by only a factor of 10, even at optimal conditions. This warns that numerical errors associated with less accurate codes in large grids cannot be compensated by higher order accurate Fréchet derivative. About ε_{opt}, high-order accurate Fréchet derivative approximations require a substantially larger ε for optimal performance. Moreover, for low-order accurate Fréchet derivatives, ε_S has a much larger impact on ε_{opt}. This indicates that, for a given grid, the use of low order accurate Fréchet derivatives requires a finer tuning to achieve optimal conditions. On the other hand, for low order accurate Fréchet derivative approximation, the optimal conditions are less sensitive to the grid size N.

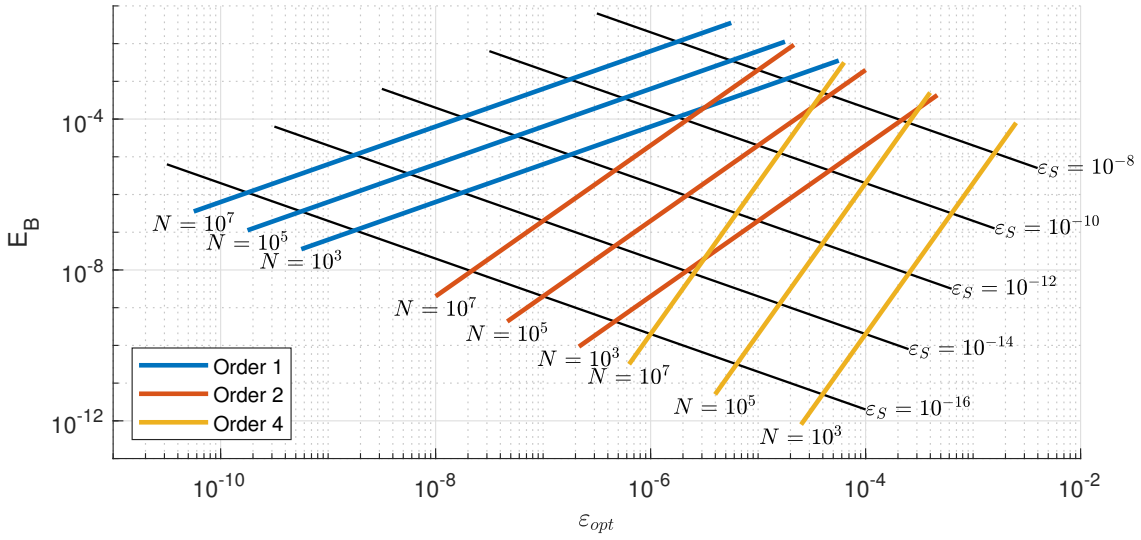


Figure 4.6 – Values of ε_{opt} and the corresponding E_B as a function of ε_S and N for 1st, 2nd and 4th order accuracy Fréchet approximations.

DISTRIBUTION A: Distribution approved for public release. Distribution unlimited

4.5 Effect of integration time length

Another parameter to be chosen when solving the Fréchet derivative to approximate $B\zeta$ is the integration time τ. A larger τ can better isolate one mode from the others within the Arnoldi algorithm; on the other hand, if the integration time is too long, unstable modes may grow sufficiently to develop nonlinear effects, and stable modes may be attenuated enough as to be contaminated by the discretization error of the solver. Small τ also reduces the accuracy of the Fréchet derivative approximations. In this section, we compute the overall error for various values of τ and develop equations for optimal τ. According to Goldhirsch, Orszag and Maulik (1987), every time the flow solver is called, it acts in the direction of filtering the most unstable (or least stable) modes present in the flow; they introduced the concept of filtering time, τM, which we refer to as total integration time. They defined a lower limit for τM as

$$\tau M \gg \frac{1}{\left|\sigma_i^R - \sigma_{M+1}^R\right|} , \tag{4.21}$$

where σ_{M+1} is the eigenvalue to be retrieved in the next iteration and σ_i^R is the real part of the sought eigenvalue, $M + 1 > i$. For a fixed M, equation 4.21 is a lower bound for τ. According to Gómez, Gómez and Theofilis (2014), there is also an upper bound of τ for a stable mode as:

$$\tau \ll \frac{\ln\left(\frac{\varepsilon_S}{\varepsilon}\right)}{\sigma_i^R} , \tag{4.22}$$

where ε is the magnitude of the disturbance added to the base flow and ε_S is the flow solver's discretization error. This limit is associated with the amplitude of the stable mode becoming too small and hence vulnerable to the flow solver's discretization errors.

Figure 4.7 gives both (Left) lower and (Right) upper bounds for τ according to equations 4.21 and 4.22. Lower limits for modes R1, R2, R3 and S1 are presented, but only S1 has its upper limit shown, as equation 4.22 is only valid for stable modes. In our tests, $\tau M = 2500$ (dashed line), which places our simulations well above the lower bounds for all modes considered. The upper bound equation requires ε_S, which is estimated as 10^{-13}, from figure 4.2. The maximum τ used in our study was 50, which places our simulations well below this bound for the range $10^{-11} < \varepsilon < 10^{-3}$ tested.

In practice, however, more restrictive bounds often apply. Moreover, the bounds do not indicate optimum values. To investigate this, we used results similar to those of the previous session but presented in a way to better explore the sensitivity of the performance to the integration time.

DISTRIBUTION A: Distribution approved for public release. Distribution unlimited

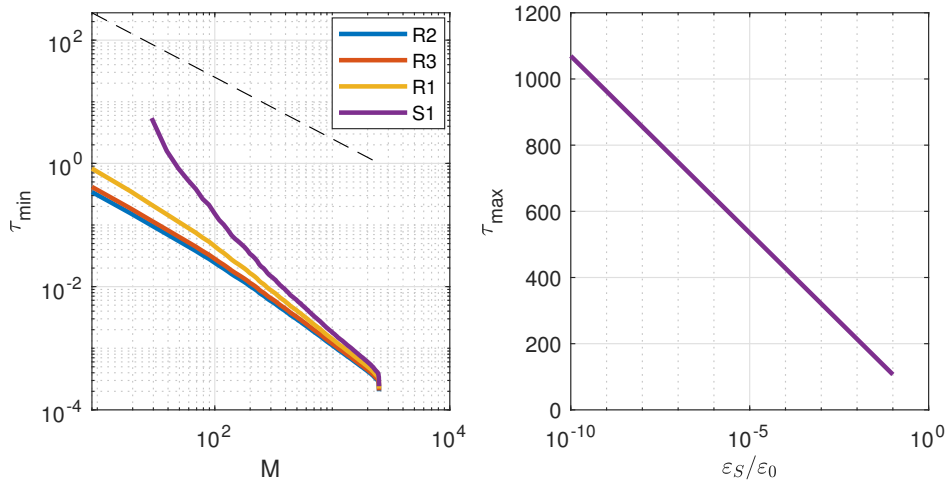


Figure 4.7 – (Left) Lower limit for τ according to equation 4.21. The dashed line represents the product $\tau M = 2500$, which was used in this work. (Right) Upper limit for τ according to equation 4.22.

As seen above, τ can affect the Krylov span approximation as well as the F and the Fréchet derivative approximations. In this section we address only the effect of τ on the F and the Fréchet derivative approximations and therefore we ensured that M was so large as not to affect the results. The effects of M and τ on the Krylov span approximation are discussed in the next section.

Figure 4.8 shows the real part of the R2 eigenvalue for various combinations of τ and ε, with both first and second-order accurate Fréchet derivatives. It also shows the error relative to the reference case. Figure 4.9 shows the same data, but for mode S1. A rapid increase in error is observed on the right-hand side of these figures. This is associated with nonlinear effects in the flow solution as we will discuss. Note, the effective upper boundaries of τ are much more restrictive than those of equation 4.22 even for the stable modes. The error increase for lower τ cannot be linked to the effect described by equation 4.21, as we have chosen a value of M large enough so that it no longer influences the results. This error has a different origin which will also be addressed.

To explain the nonlinear effect, we use figure 4.10. On the left, the figure shows results of the time evolution of the base flow with no disturbances other than the noise floor, which is at the level 10^{-13}. The figure displays the contribution of each mode to the flow as it evolves. These curves were obtained by reconstructing the output from the flow solver from linear combination of all 2500 modes retrieved by the global stability analysis. It is impossible to fully reconstruct the signal unless all modes are available, so we have used a least squares approach to obtain an optimal representation in this limited set. At $\tau = 20$, mode R2 already dominates the flow. However, as early as $\tau = 10$, modes R2 and R3 are present and growing exponentially. Figure 4.10 (Right) shows snapshots of

DISTRIBUTION A: Distribution approved for public release. Distribution unlimited

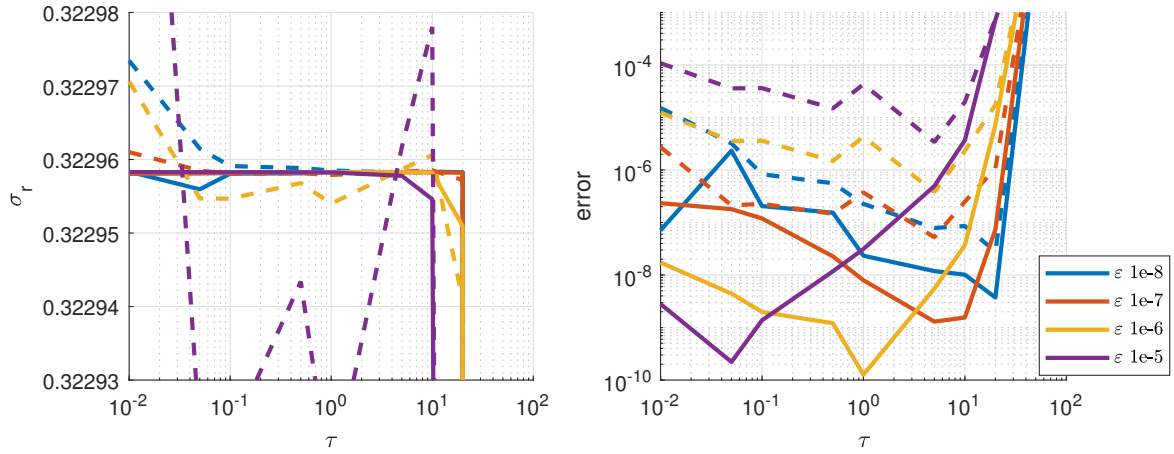


Figure 4.8 – Real part of the R2 eigenvalue as a function of τ for selected values of ε. Dashed lines represent the first-order accurate Fréchet derivative, while full lines represent the second-order accurate derivative. (Left) Absolute value. (Right) Difference to the reference case.

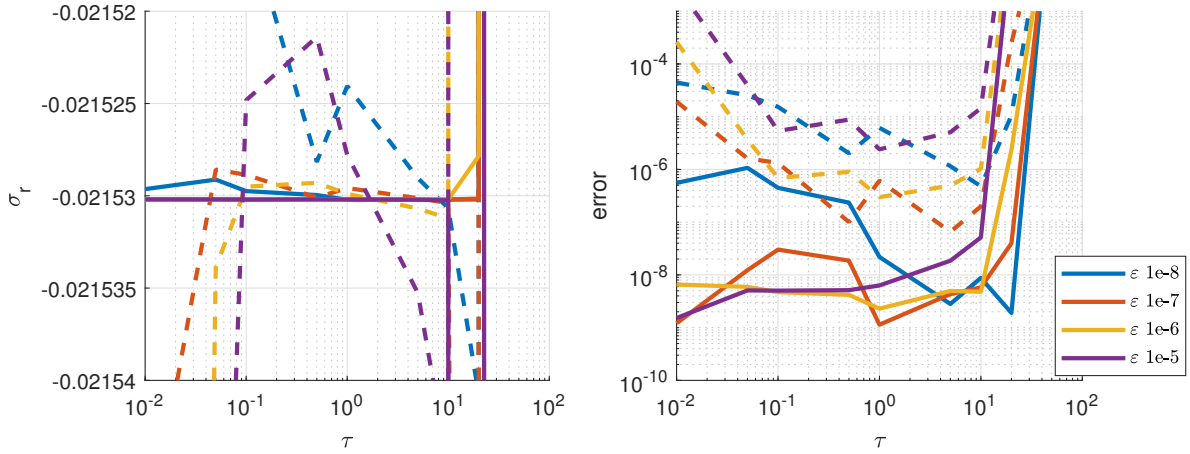


Figure 4.9 – Real part of the S1 eigenvalue as a function of τ for selected values of ε. Dashed lines represent the first-order accurate Fréchet derivative, while full lines represent the second-order accurate derivative. (Left) Absolute value. (Right) Difference to the reference case.

the flow fluctuations along the time evolution, illustrating the emergence of the R2 mode. At $\tau = 50$, the gray lines that depict stable modes start growing as well, until reaching saturation at $\tau = 90$; yet those modes did not become unstable. This is an artifact of the dominant mode's nonlinearity.

An estimate of the magnitude of the nonlinear terms of the disturbance Navier-Stokes equations is the square of the leading mode, formally $\varepsilon^2 e^{2\sigma_1^R \tau}$, which matches the growth rate observed in the figure. As this nonlinear content grows, it contaminates the evolution of the sought modes because the Arnoldi algorithm projects this nonlinear

DISTRIBUTION A: Distribution approved for public release. Distribution unlimited

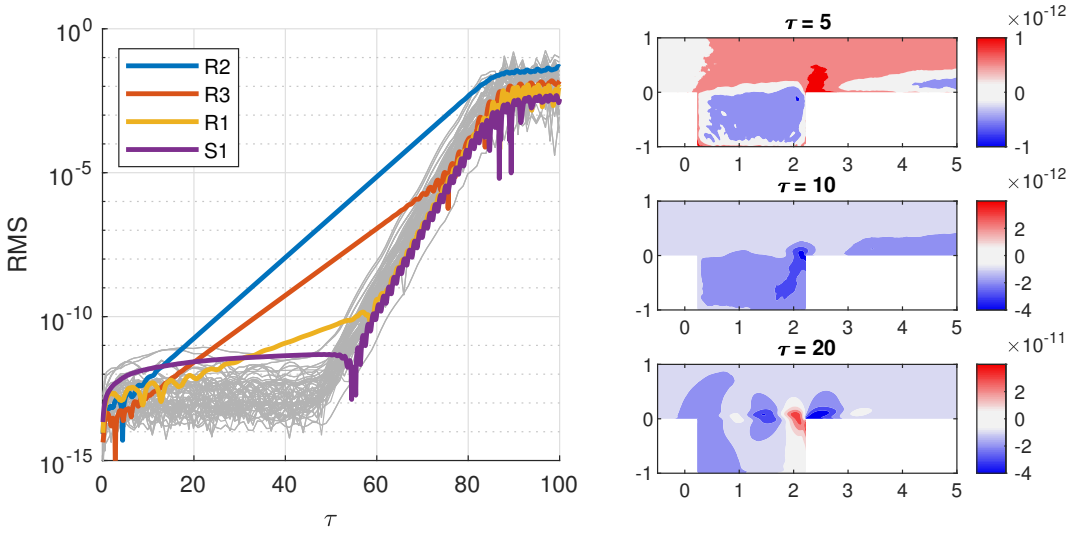


Figure 4.10 – (Left) Evolution of each mode in the flow as it is simulated starting from the base flow without the introduction of any disturbance other than the discretization error. Modes R1 to R3 and S1 are highlighted. Solution projections on the 100$^{\text{th}}$ least stable are shown as thin gray lines. (Right) Snapshots of the density fluctuation at $\tau = 5$, 10, and 20.

content onto the linear modes. Even the leading mode R2 is affected, as reflected in the irregular oscillations shortly after the limit cycle is reached. The nonlinear error is, naturally, only present if a nonlinear solver is used. It is relevant only for unstable flows and more critical for large values of τ, when the most unstable modes have enough time to grow and become nonlinear.

Figure 4.11 shows the same analysis as figure 4.10, but for different starting conditions. In the upper row, we added the initial disturbance of the Arnoldi procedure, ζ_1, to the base flow with magnitudes $\varepsilon = 10^{-5}$, 10^{-7} and 10^{-9}. The bottom row uses disturbance ζ_{100}, corresponding to the 100$^{\text{th}}$ Arnoldi iteration. Similar results would be obtained if other iterations were chosen. This illustrates the mode evolution within each Arnoldi iteration. In these cases, the nonlinearities surfaced much earlier in the simulation, especially for larger values of ε.

This phenomenon defines an upper bound of τ, which can be estimated as follows. It is required that the mode amplitude be substantially larger than the nonlinear error contamination,

$$\varepsilon e^{\sigma_i^R \tau} \gg \varepsilon^2 e^{2\sigma_1^R \tau} \ , \tag{4.23}$$

leading to

$$\tau \ll \frac{\ln(\varepsilon)}{\sigma_i^R - 2\sigma_1^R} \ . \tag{4.24}$$

DISTRIBUTION A: Distribution approved for public release. Distribution unlimited

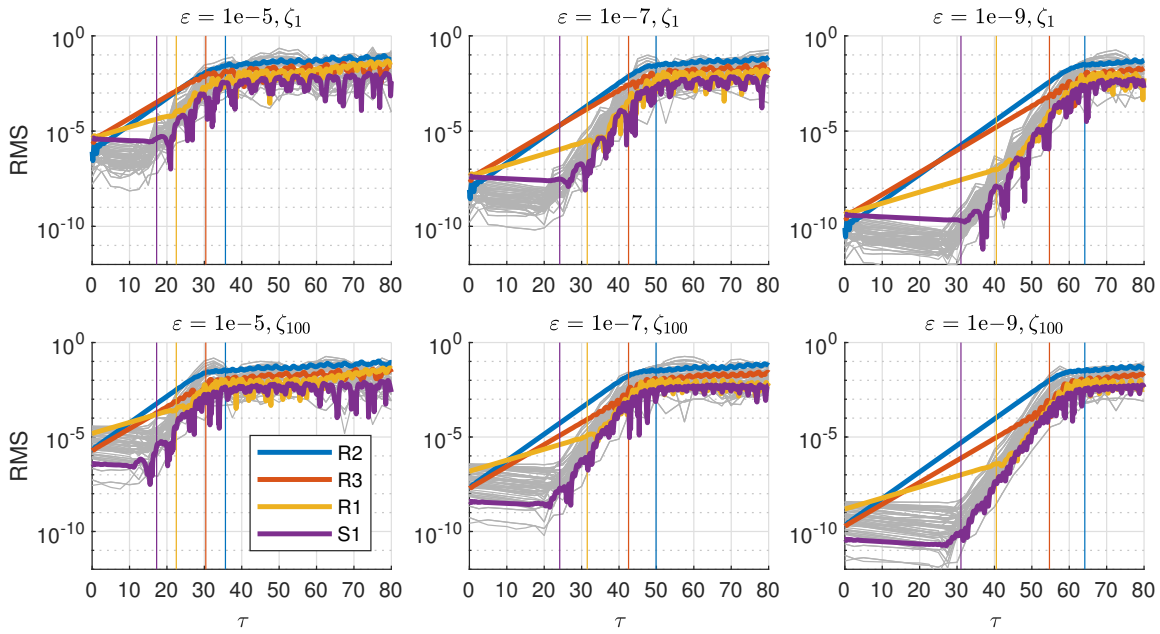


Figure 4.11 – Evolution of each mode in the flow as it is simulated from different starting conditions. Modes R1 to R3 and S1 are highlighted. Modes up to the 100$^{\text{th}}$ least stable are shown as thin gray lines. Vertical lines depict the upper limits of τ, as given by equation 4.24.

Using equation 4.24, we computed the τ bounds associated with each mode, represented by the vertical lines in figure 4.11. They offer good estimates of the values of τ from which the linear projection of each mode shows nonlinear effects. This is also the time from which there is a massive error increment in figures 4.8 and 4.9. As seen in these figures, the bounds slightly decrease for more stable and are not affected by the order of accuracy of the Fréchet derivative. The estimates captured consistently the effect of ε and apply for any Krylov iteration. It is important to note that, if there are no unstable modes, these nonlinear effects should reduce with time and the upper bound given by equation 4.22 is likely to be the only constraint for large τ.

As for the lower values of τ, Figures 4.8 and 4.9 show a slow increase in error as τ is reduced. This is associated with the discretization error of the Fréchet derivative approximations, which in turn affects σ_A. If there is not enough time of flow evolution, the finite differences in the Fréchet derivative, become vulnerable to numerical errors of the flow solver.

We developed estimates for an optimal τ as follows. We can include in equation 4.19 the nonlinear error neglected in the previous section, which becomes

$$E_B = \mathcal{O}((\varepsilon\sqrt{N})^n) + \mathcal{O}(\varepsilon_S/\varepsilon) + \mathcal{O}(\varepsilon e^{2\sigma_1^R \tau}) \ . \tag{4.25}$$

DISTRIBUTION A: Distribution approved for public release. Distribution unlimited

From equation 4.6, we have

$$dA = \frac{1}{\tau} e^{-A\tau} dB \ . \tag{4.26}$$

Substituting E_B from equation 4.25 into dB, the norm of the error in A is

$$E_A \approx \frac{(\varepsilon\sqrt{N})^n + \varepsilon_S/\varepsilon + \varepsilon e^{2\sigma_1^R \tau}}{\|\tau e^{A\tau}\|} \ . \tag{4.27}$$

For small τ, the denominator of equation 4.27 can be written as

$$E_A \approx \frac{(\varepsilon\sqrt{N})^n + \varepsilon_S/\varepsilon + \varepsilon e^{2\sigma_1^R \tau}}{\tau} \ , \tag{4.28}$$

which predicts a slow accuracy degradation as τ reduces. The behavior is consistent with the results shown in figures 4.8 and 4.9. As explained above, the error arises in the Fréchet derivative approximations, but is governed by the accuracy of the flow solver and hence we assign it to errors in the F approximations. The rate of increase of error as τ reduces is not dependent on either the Fréchet derivative accuracy order or on ε, as suggested by figures 9 and 10 .

If τ is so large that the leading mode becomes dominant, we approximate$\|e^{A\tau}\|$ by $e^{\sigma_1^R \tau}$, the leading eigenmode, which yields

$$E_A \approx \frac{(\varepsilon\sqrt{N})^n + \varepsilon_S/\varepsilon + \varepsilon e^{2\sigma_1^R \tau}}{\tau e^{\sigma_1^R \tau}} \ . \tag{4.29}$$

This equation is plotted in Figure 4.12 (Left) for various combinations of ε and Fréchet derivative order of accuracy approximations. Figures 4.8 and 4.9 show the error in the eigenvalues σ, while equation 4.29 and figure 4.12 relate to the error in $A\zeta$, which is of the same order of the errors in A itself, as ζ has a unitary norm. However, according to Davis and Moler (1978), when a small disturbance is added to an invertible matrix, its eigenvalues will be changed by an amount whose upper bound is proportional to the norm of said disturbance. Since matrix A is invertible (as it has no null eigenvalue), this explains why E_A and E_σ behave similarly. This also justifies the estimates of optimal ε.

Equation 4.29 can provide estimates of the optimal τ for the dominant mode. However, for less unstable (or more stable) modes, the upper boundary of τ reduces (see figure 4.11) and so would optimal τ. Figures 4.10 and 4.11 indicate that each mode behaves independently from the others regarding nonlinear errors. This observation led us

DISTRIBUTION A: Distribution approved for public release. Distribution unlimited

to an ad-hoc equation that offers good estimates of optimal τ for any given eigenvalue. We simply replace $e^{A\tau}$ by $e^{\sigma_i^R \tau}$ in equation 4.27 for each mode i, yielding

$$E_{A_i} \approx \frac{(\varepsilon\sqrt{N})^n + \varepsilon_S/\varepsilon + \varepsilon e^{2\sigma_1^R \tau}}{\tau e^{\sigma_i^R \tau}} , \tag{4.30}$$

where E_{A_i} is meant to indicate the error in matrix A which would affect accuracy of eigenvalue i. For small τ, it reduces to equation 4.28. Also note that, for large τ and stable flows, the equation leads to the upper bound expressed by equation 4.24, as presented by Gómez, Gómez and Theofilis (2014). Figure 4.12 (Right) shows the value of E_{A_i} for Mode S1, while figure 4.12 (Left) can be interpreted as the equivalent for Mode R2. By comparing figure 4.12 with figures 4.8 and 4.9, we observe that equation 4.30 adequately accounts for the reduction of the optimum τ for less unstable modes, see figure 4.11.

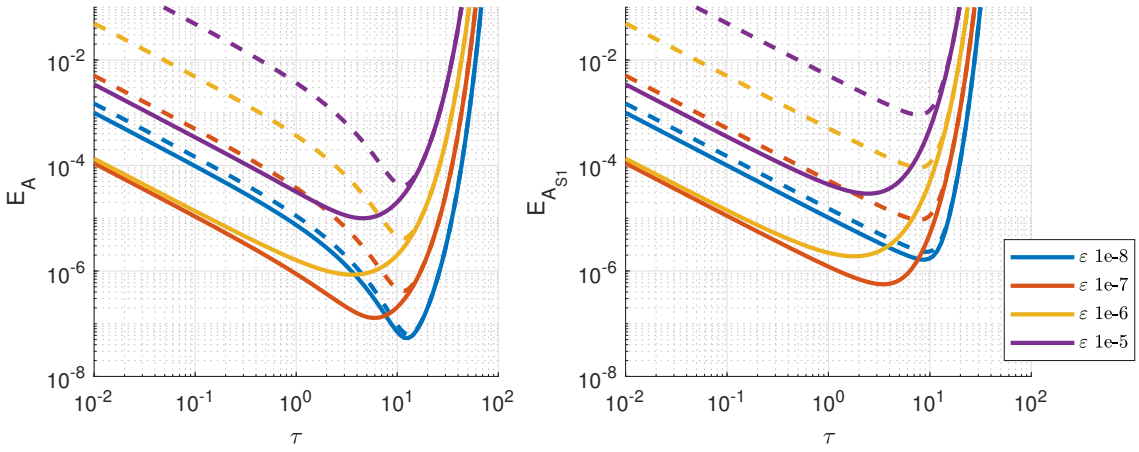


Figure 4.12 – Estimate of the error in $A\zeta$ as a function of τ for select values of ε, (Left) using equation 4.29 and (Right) using equation 4.30 with values corresponding to mode S1. The solid lines represent second order accurate Fréchet derivative approximation and the dashed lines, first order approximation.

An estimate of the eigenvalues is needed as input for equations 4.27 to 4.30, which may not be known a priori. Therefore, it is important to quantify the sensitivity of optimal τ to the eigenvalues. Figure 4.13 (Left) shows the value of E_A for mode R2 for a range of hypothetical values of σ_{R2}^R and τ, as computed by equation 4.30. The actual value, $\sigma_{R2}^R = 0.3230$, is indicated by the black line. Each color represents a different value of Δ_σ, which was added to σ_{R2}. ε was fixed at 10^{-6} and the second order accurate Fréchet derivative was used. The figure shows that the error is much more sensitive to changes in σ when τ is large. Figure 4.13 (Center) shows error estimates for mode S1 as σ_{R2} is changed, while Figure 4.13 (Right) shows error estimates for mode S1 as its own eigenvalue changes.

The figure shows that the value of optimal τ for both the leading mode and the other modes are not very sensitive to the values of neither the leading eigenvalue nor

DISTRIBUTION A: Distribution approved for public release. Distribution unlimited

the sought eigenvalue. Moreover, it shows that choosing a τ smaller than τ_{opt} does not degrade the accuracy substantially and prevents the risk of the very dangerous nonlinear contamination. Therefore, a safe approach is to use a value of τ somewhat smaller than the optimum dictated by equation 4.29; in our study, very good results were produced for τ about 5 times smaller than the upper limit given by equation 4.24.

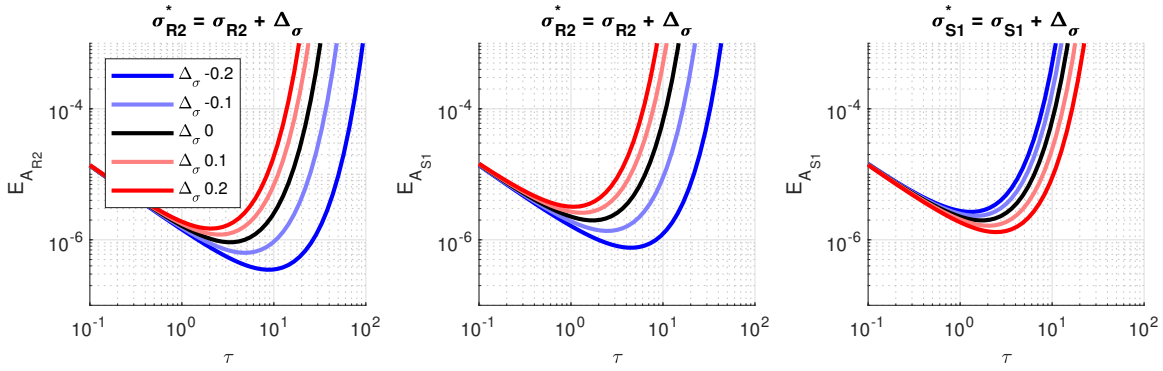


Figure 4.13 – (Left) Values of E_A for mode R2 when the real part of its eigenvalue is changed. (Center) Values of E_A for mode S1 when the real part of the leading eigenvalue is changed. (Right) Values of E_A for mode S1 when the real part of its eigenvalue is changed.

Equations 4.29 and 4.30 comprise not only the effects of τ, but also that of ε and of the order of accuracy of the Fréchet derivative approximation investigated in the previous section. It can be used as follows. Following the guidelines above, it is anticipated that, the error associated with the nonlinear term will be negligible to be on the safe side. Hence, differentiation of either of these equations leads to equation 4.20. With ε_{opt} defined, it is possible to obtain the optimal value of τ from equation 4.30 with a rough estimate of the leading eigenvalue and the most stable eigenvalues sought. Analytically differentiating this equation with respect to τ does not lead to simple expressions, hence we refrain from presenting it. The equation also allows the evaluation of the effect of increasing the order of accuracy of the Fréchet approximations, of reducing the flow solver noise floor and of increasing the computational grid.

It is possible to introduce a renormalization step in the algorithm to increase the maximum value of τ, while keeping the disturbance norm within an acceptable range, away from both nonlinear effects and rounding errors. However, the renormalization of the disturbance would affect all modes equally; for example, reducing the norm of stable modes to keep an unstable mode from becoming nonlinear. In practice, the effect of the renormalization on the error could be estimated by subtracting the real part of σ_1 from all eigenvalues, which can be thought of as forcing the first mode to have neutral stability and adjusting the amplitude of all other modes accordingly. Figure 4.14 shows the predicted error according to equation 4.30 with and without renormalization. In both

DISTRIBUTION A: Distribution approved for public release. Distribution unlimited

cases, the second order accurate Fréchet derivative is used. By using the renormalization, equation 4.30 predicts virtually unlimited accuracy for the first mode for very large values of τ. Naturally, this would not be possible due to rounding errors during the renormalization subroutine, which, however, were not accounted for by the equation.

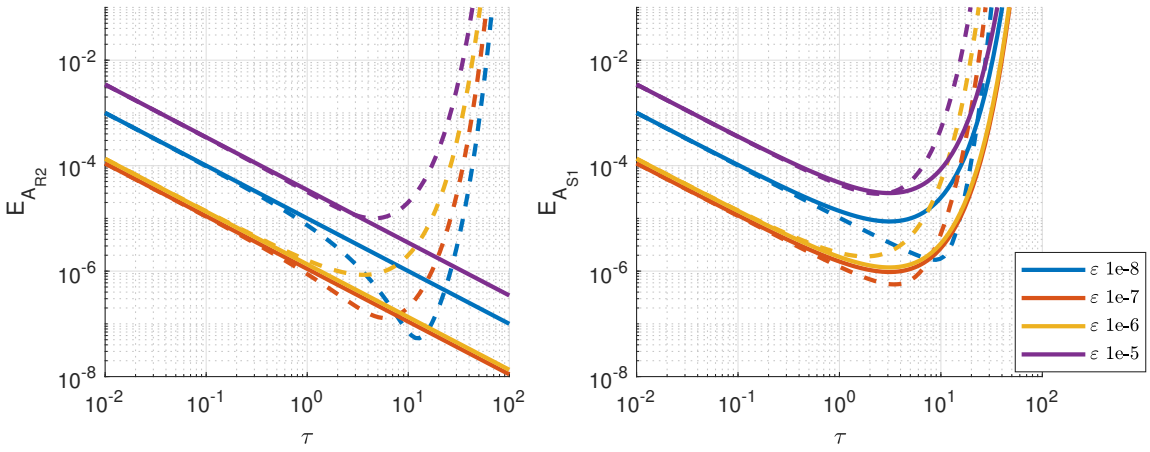


Figure 4.14 – Estimate of the error in $A\zeta$ as a function of τ for select values of ε, using equation 4.30 for modes R2 (Left) and S1 (Right). The solid lines represent the case with renormalization and dashed lines, without.

Figure 4.15 shows the measured error for modes R2 and S1 for various values of τ, with $\varepsilon = 10^{-7}$ and second order accurate Fréchet derivative and compares the regular case to cases that were renormalized at different intervals T_R. This result closely matches figure 4.14, in which there was in increased accuracy in the leading mode at the cost of reduced accuracies for other modes.

In sum, renormalization techniques might mitigate the non-linear effects; however, they carry the added cost of causing non-leading modes to decay into background noise more quickly. In fact, if τ is large enough so that all non-leading modes become negligible in comparison to the leading mode each time the flow solver is called, this method becomes very similar to the Residual Algorithm, presented by Theofilis and Colonius (2003), which is only able to capture the leading mode of a flow.

Nonetheless, for stable flows, i.e., $\sigma_1^R < 0$, renormalization might increase the accuracy of the least stable eigenvalues by keeping them at larger amplitudes. For instance, in a hypothetical flow where the least stable eigenvalues are given by $\sigma_1 = -0.1$, $\sigma_2 = -0.12$, $\sigma_3 = -0.2$, equation 4.30 predicts the values shown in figure 4.16. In this scenario, eigenvalues that are very close to the least stable mode, such as σ_2, have a slightly increased accuracy. However, the benefits of renormalization only appear at very high values of τ, which might hinder the ability to accurately retrieve the imaginary part of the eigenvalues, due to the multivalence of the complex logarithm function, which adds an undetermined contribution of $2\pi n/\tau$, with n integer, to the imaginary part. As τ grows

DISTRIBUTION A: Distribution approved for public release. Distribution unlimited

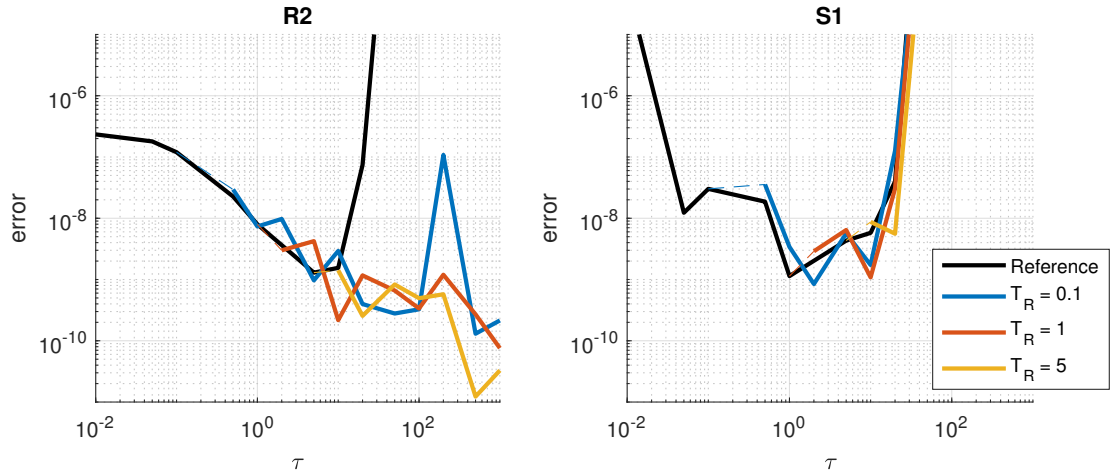


Figure 4.15 – Difference in the real part of the eigenvalue corresponding to modes R2 (Left) and S1 (Right) as a function of τ for $\varepsilon = 10^{-7}$ and second order accurate Fréchet derivative. The black line is the reference case, with no renormalization and the colored lines represent different intervals of renormalization.

larger, the distance between consecutive candidates for the imaginary part reduces, making it difficult the compute the value of n.

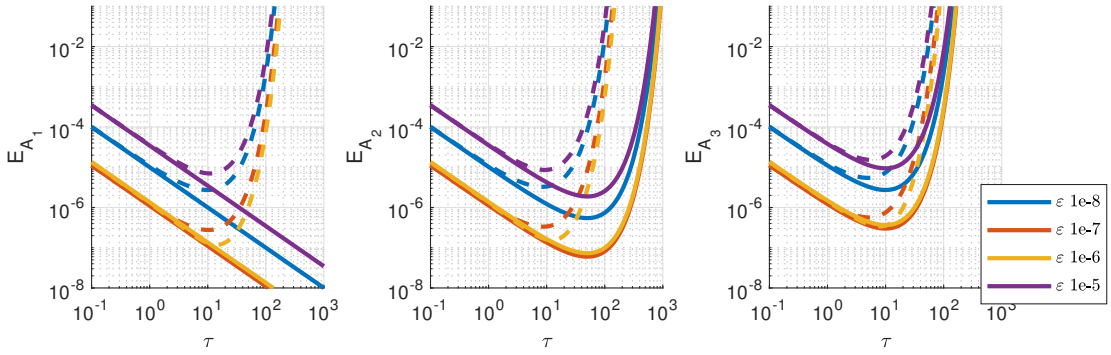


Figure 4.16 – Estimate of the error in $A\zeta$ as a function of τ for select values of ε, using equation 4.30 for a hypothetical flow with the least stable eigenvalues given by $\sigma_1 = -0.1$, $\sigma_2 = -0.12$, $\sigma_1 = -0.2$. The solid lines represent the case with renormalization and dashed lines, without.

4.6 Krylov span dimension and optimization of the total computational time

Following Goldhirsch, Orszag and Maulik (1987), the origin of the lower boundary for τM (equation 4.21) is the error caused by truncating the eigenspectrum to the first M

DISTRIBUTION A: Distribution approved for public release. Distribution unlimited

modes, which is

$$Error \propto \left| e^{(\sigma_{M+1}-\sigma_1)\tau M} \right| \ . \tag{4.31}$$

This reflects the observation that, in case the growth rates are too close to each other, the total integration time (τM) must be long enough for a mode to be properly identified, hence the boundary. At a glance, it may seem that any combination of τ and M that gives the same total filtering time (as they refer to τM) would produce the same level of accuracy. Nevertheless, increasing M has the additional benefit of moving σ_{M+1} further to the left of the spectrum, hence further reducing this type of error. This suggests that increasing M instead of τ is more cost effective. However, as discussed in section 4.2.3, for large values of M the cost tends to increase nonlinearly with M.

Hence there remains the question of the optimal balance between τ and M that allows the required modes to be retrieved with the desired accuracy and lowest C. With this goal, we mapped the error for various combinations of τ and M, for $\varepsilon = 10^{-6}$ and for first and second-order accurate Fréchet derivatives. Figures 4.17 and 4.18 give the results for modes R2 and S1, respectively. The colored contours indicate iso-levels of error relative to the reference case. The white area for large τ and M was not covered in the study, while in the white areas for small M, the algorithm did not find the sought mode. The solid light gray lines are isocontours of computational cost, as computed by equation 4.15 with the coefficients from table 4.1. From left to right, they represent 5 minutes, 10 minutes, 30 minutes and 1 hour of wall-time, excluding start-up time which is independent of τ and M. The dashed gray lines indicate constant values of $t = \tau M$. Note that, contrary to the previous two sections, this section also addresses the issue of computational time required for a given accuracy and as such the numerical results are dependent on the speed of the flow solver, the efficiency of the eigenvalue problem solver and the computational resources. Nevertheless, the conclusions still serve as general guidelines for improving solution efficiency.

Consistent with Goldhirsch, Orszag and Maulik (1987), in both figures 4.17 and 4.18, the error is larger if the product τM is small. The bounds for τ discussed in the previous section are also observable in the figures. At large τ there are the nonlinear effects which rapidly reduce accuracy. At small τ there is a gradual reduction in accuracy at large M.

Both figures illustrate interesting aspects of the trade-off between τ and M. For $M < 20$, iso-accuracy lines approach the vertical, indicating that, in this region, increasing M is more beneficial than increasing τ. This may be a manifestation of the extra benefit of increasing M discussed in connection with equation 4.31. However, at least for the unstable mode, figure 4.8 suggests this may also be a manifestation of errors associated with nonlinear effects caused by large τ. Away from this region, the extra benefit of

DISTRIBUTION A: Distribution approved for public release. Distribution unlimited

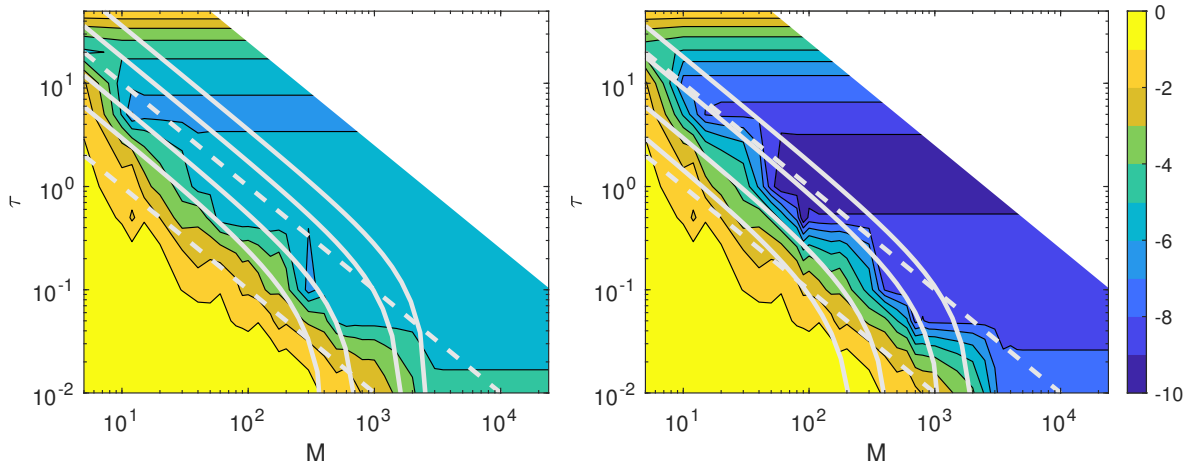


Figure 4.17 – Isocontours of $\log_{10}$(Error) of the real part of the R2 mode, using $\varepsilon = 10^{-6}$. The full gray lines represent a constant computational cost of 5 minutes, 10 minutes, 30 minutes and 1 hour from left to right. The dashed gray lines indicate constant $t = \tau M$. (Left) First order accurate Fréchet derivative. (Right) Second order accurate Fréchet derivative.

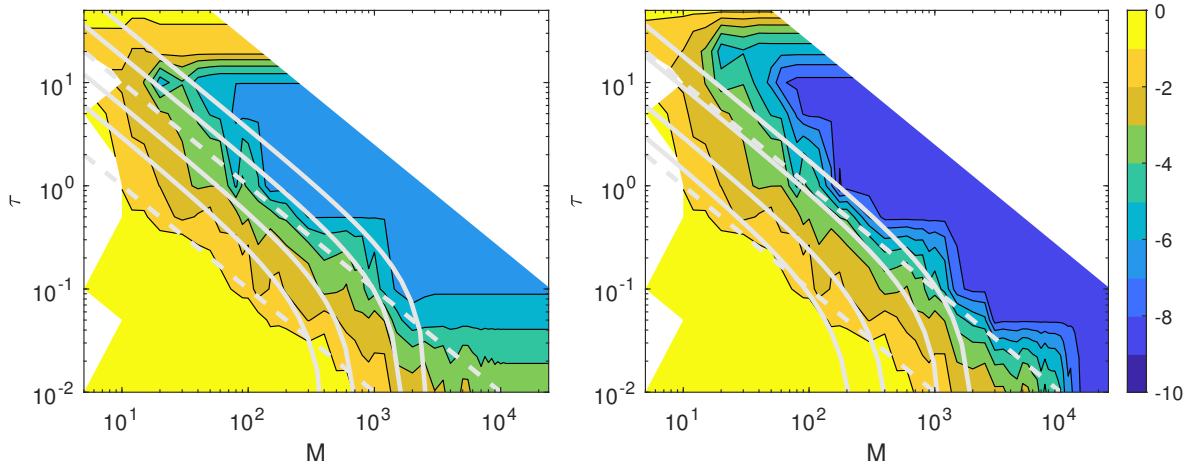


Figure 4.18 – Isocontours of $\log_{10}$(Error) of the real part of the S1 mode, using $\varepsilon = 10^{-6}$. The full gray lines represent a constant computational cost of 5 minutes, 10 minutes, 30 minutes and 1 hour from left to right. The dashed gray lines indicate constant $t = \tau M$. (Left) First order accurate Fréchet derivative. (Right) Second order accurate Fréchet derivative.

increasing M does not appear to be relevant.

In a large central portion of the figures, the curves of iso-cost are roughly parallel to the constant τM lines. This corresponds to the region were the cost of running the flow solver dominates the computations, see figure 4.1. At large M, the cost increases massively, becoming almost independent of τ. It must also be considered that this argument disregards the fact that increasing M has the added benefit of retrieving more modes; that is, we assumed a given set of eigenvalues is desired.

DISTRIBUTION A: Distribution approved for public release. Distribution unlimited

The results indicate that the most cost-effective approach is to use a total integration time τM with the largest τ possible that is still below the upper bounds established, which, from section 4.5, tends to provide better accuracy. Under these circumstances the cost is mostly that of running the flow solver. We recall that the cost was measured by wall-time, which, in our solver, is essentially proportional to CPU time; hence, similar conclusions would have been reached if either were the measure of cost. Therefore, optimal τ does not depend on M, which once more removes one dimension of the parametric search. After establishing ε and τ from the equations of the previous sections, we should run the Arnoldi algorithm and monitor the solution for increasing M until the desired accuracy or minimum error bound is reached. As opposed to τ and ε, M does not need to be decided in advance and its effect on the solution can monitored as the algorithm runs. Our study was restricted to 2D simulations. For 3D simulations, the wall-time or CPU-time associated with the flow integration would be substantially longer and the conclusion would still hold.

Restarted Arnoldi methods considerably reduce the cost associated with the Gram-Schmidt orthonormalization, but, as long as the cost is dominated by the flow solver, this strategy would not be beneficial. This is the situation in our test case, and reason restarted methods were not considered here as it would not affect the optimal parameters. For 3D simulations the CPU-time associated with the flow solver tends be even longer and even less likely to benefit from restarted algorithms. Overall, our results suggest that a wide range of applications would not benefit from restarted algorithms.

The similarity between both frames in each of the figures 4.17 and 4.18 for contour levels down to 10^{-5} is remarkable. This indicates that, for these error levels, the truncation order of the Fréchet derivative does not play a role, as discussed in section 4.4. There is an exception for very small τ, for which there is an effect of the truncation error on levels above 10^{-5}, which is consistent with section 4.5. Hence, under these circumstances, the first-order is the most efficient approach as it requires shorter computation times for the same accuracy. On the other hand, first-order accuracy could not reach an error level below 10^{-6}, while second-order accuracy consistently provides errors of 10^{-8}. This is more clearly illustrated and extended for other eigenvalues in Figure 4.19 which shows the eigenvalue convergence history for first and second-order accurate Fréchet approximations, and for different integration times.

Overall, the results show that, for this problem, if the target error level is about 10^{-5}, first-order is the better choice, whereas, if errors below 10^{-6} are required, at least second-order accurate Fréchet is needed. It should be added that $\varepsilon = 10^{-6}$ is optimal for second order accurate Fréchet derivative approximations, and suboptimal for first order; therefore, it is possible that slightly more accurate results would still be possible with first order. In the choice of the target accuracy, one must also consider that, for open flow

DISTRIBUTION A: Distribution approved for public release. Distribution unlimited

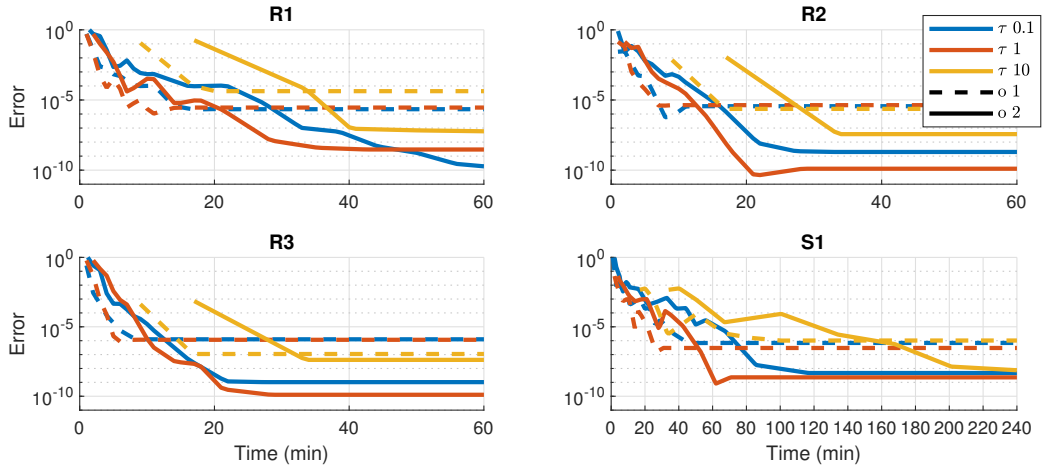


Figure 4.19 – Error of the first four eigenvalues as computational time is increased. $\tau = 0.1, 1, 10$, $\varepsilon = 10^{-6}$. Note that the time scale for mode S1 is different than that of modes R1 to R3.

applications, for example, details of the far field boundary conditions can easily affect the computation of leading eigenvalues in the range of 10^{-5} or above (OHMICHI; SUZUKI, 2016).

4.7 Rate of convergence of eigenfunctions and eigenvalues

In this section, we seek to evaluate how the accuracy of the eigenfunction estimates is affected by the parameters chosen, as well as how it affects the eigenvalue convergence rate. Figure 4.19 shows that the more unstable modes reach minimum error progressively faster. In fact, for mode S1, the error starts decreasing consistently only after all unstable modes have approached their minimum error values. This is associated with eigenfunction representation in the Krylov subspace, as we will discuss. Hence, it is important to investigate the accuracy of the eigenfunction estimates.

Figures 4.20 and 4.21 show the error of the eigenfunctions retrieved for modes R2 and S1, respectively. This error is computed as the mean absolute difference between an eigenfunction and its reference, both eigenfunctions have unitary norm ℓ_2. Using the absolute value of the eigenfunction, our results are unaffected by differences in the eigenfunction phase. The white areas close to the corners of the figures were not included in our parametric sweep.

Consistently, the parameters leading to most accurate eigenvalue results worked for the eigenfunctions as well. Looking at mode R2, the eigenfunction reaches an accuracy of up to 10^{-9} with a first-order accurate Fréchet derivative and up to 10^{-11} with a second-order one. Mode S1 reached an accuracy 10^{-7} with a first-order accurate derivative, while

DISTRIBUTION A: Distribution approved for public release. Distribution unlimited

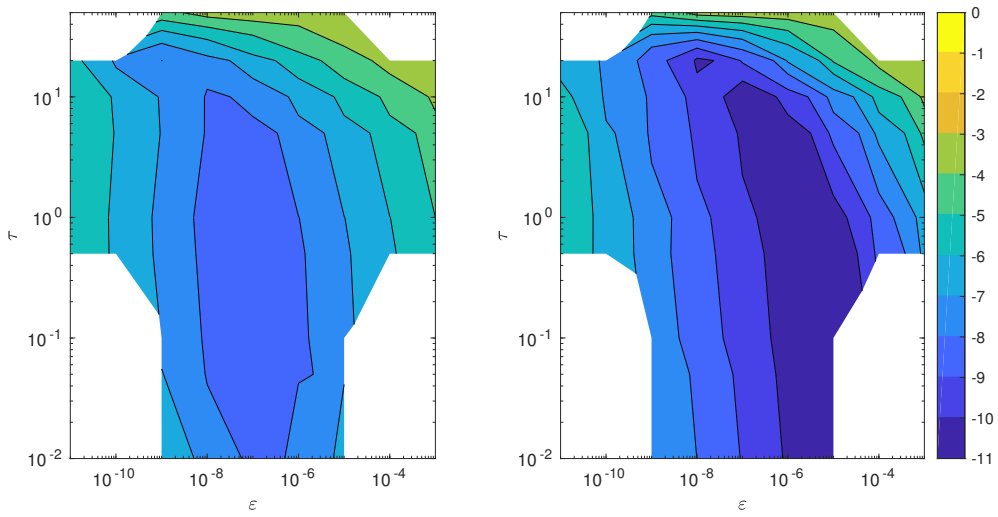


Figure 4.20 – Isocontours of $\log_{10}$(Error) of the eigenfunction of R2 for (Left) first-order accurate Fréchet derivative and (Right) second-order derivative.

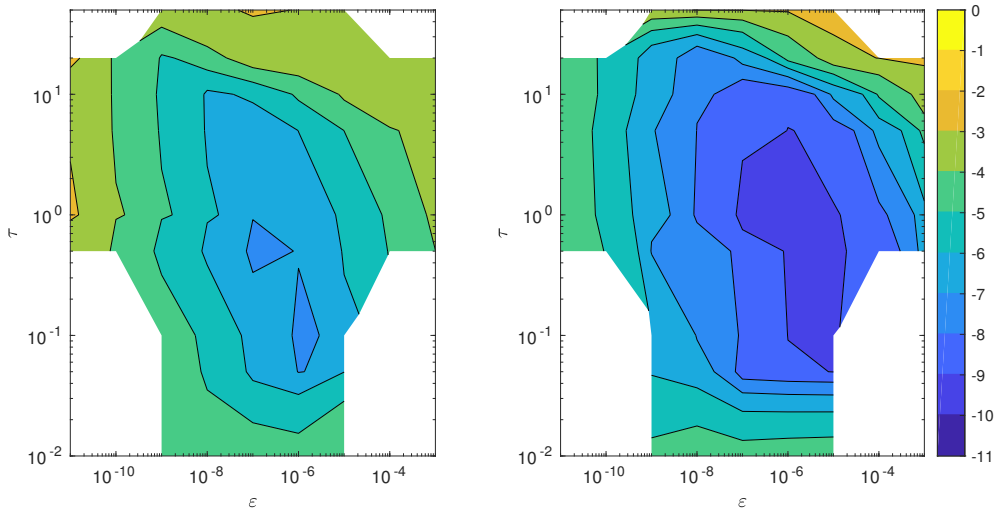


Figure 4.21 – Isocontours of $\log_{10}$(Error) of the eigenfunction of S1 for (Left) first-order accurate Fréchet derivative and (Right) second-order derivative.

the second-order one achieved 10^{-9}.

In some ways, these pictures summarize results obtained for the eigenvalues too. At large τ there are nonlinear effects that affect the accuracy. For small τ and small ε the computation of F becomes vulnerable to the discretization error. For large ε, there are both nonlinear and Fréchet derivative truncation errors, while, at low ε, there are discretization errors in F. Because of these effects, the region of maximum accuracy lies at the center. For second order accurate Fréchet derivatives, the truncation error reduces more rapidly, such that for this case the optimal region moves to the right as compared to the first order accurate one.

DISTRIBUTION A: Distribution approved for public release. Distribution unlimited

In the time-stepping method discussed, the eigenfunctions of each flow mode are retrieved as a linear combination of ζ_i, that are the initial disturbances in each iteration of the Arnoldi procedure. The weight of each ζ_i is given by the eigenvectors of matrix H, as per step 12 of Algorithm 1. By examining the eigenvectors ϕ_H, we can infer how much each iteration contributes to the convergence of a mode. Figure 4.22 shows $|\phi_H|$ as a function of M for R1, R2, R3 and S1 in our reference case. The most unstable modes converge faster. After a mode reaches convergence and therefore can be accurately filtered out of the flow by the Gram-Schmidt orthonormalization, the convergence rate of the next one is accelerated. This is because the converged mode can be accurately removed from the next disturbance by the Gram-Schmidt algorithm, which hence concentrates on filtering of the next dominant mode. It must also be added that modes which are almost orthogonal are expected to have smaller effects on each other. This is possibly an explanation for the faster convergence of mode R3 relative to R1. The convergence of the eigenfunction closely follows, and explains, the convergence of eigenvalues in figure 4.19.

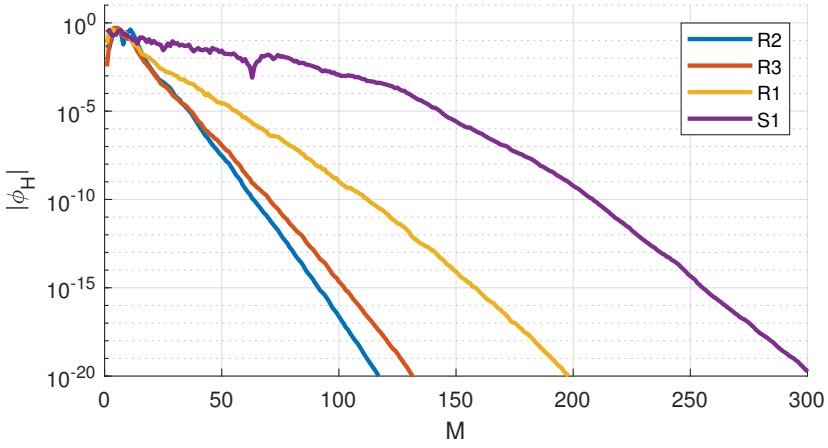


Figure 4.22 – Weight of each disturbance ζ_i in the eigenfunctions of modes R1, R2, R3 and S1.

4.8 Conclusion

We sought to establish guidelines for choosing computational parameters when performing a time-stepping, Jacobian-free global instability analysis of a flow. This procedure requires a solver that produces a flow solution, F. The computational parameters considered were disturbance magnitude (ε), order of accuracy of the Fréchet derivative approximation (n), integration time (τ) and dimension of the Krylov span (M). The analysis was carried out with codes developed in-house and used a two-dimensional compressible open cavity flow as an example; however, these guidelines should be valid for other types of flows and solvers, including three-dimensional scenarios. The following

DISTRIBUTION A: Distribution approved for public release. Distribution unlimited

sources of error may exist in this problem: (1) truncation error associated with the Fréchet derivative approximations; (2) discretization errors in the computation of F, which can be truncation or round-off; (3) errors associated with the nonlinear terms of the Navier-Stokes equations; and (4) errors associated with the Krylov subspace approximation. Parameter n affects the truncation error (1). Parameter ε affects the truncation (1), discretization (2) and the nonlinear (3) errors. Parameter M affects the Krylov subspace approximation (4) only, while parameter τ affects all errors.

In principle, the choice of ε, τ and M constitutes a search in a three-dimensional space. However, our analysis demonstrated that optimal τ must correspond to effectively negligible nonlinear terms. This led to the optimal ε being independent of τ and M, which reduces one dimension in the parametric search. The analysis also showed that optimal τ is independent on M and leads to the most cost-effective choice of τM, which reduces another dimension in the parametric search. Hence, as a guideline, one must first determine ε_{opt}, next τ_{opt} and finally M. M does not need to be known a priori and can be monitored along the Arnoldi iterations at no cost.

It was further found that optimal values of ε depend on a balance between truncation error (1) and discretization error (2) and can be estimated a priori by equation 4.20. Equation 4.19 can be used to evaluate the benefit of increasing the accuracy order of the Fréchet derivative approximations, the consequences of using less accurate flow solvers, and the care that must be taken when large grids are employed.

Our analysis shows that optimal values of τ can be established primarily based on its impact on the error associated with computing F and the Fréchet derivative, disregarding its impact on the Krylov span approximation. Under these circumstances, optimal τ depends on a complicated balance between the truncation error (1) and the discretization error (2), which both grow as τ reduces, and the nonlinear term error (3), which grows as τ increases. As such, optimal τ depends on ε, ε_S, n, on the mesh size, and on the growth rates of the modes involved. It is possible to estimate optimal τ by finding the minimum of equation 4.30. The magnitudes of the eigenvalues are required, but a guess would be enough. Figure 4.12 shows that the error increases massively for $\tau > \tau_{opt}$ and much less so for $\tau < \tau_{opt}$, hence, to be on the safe side, it is advisable to use values of τ somewhat smaller than τ_{opt}, perhaps a factor of 5. It is important to note that the discussion focused on a situation where a nonlinear solver is used for an unstable flow, which is common. If a linear solver is used, upper bounds for τ apply only for stable modes and can be obtained from equation 4.22 (GÓMEZ; GÓMEZ; THEOFILIS, 2014), which is also embedded in equation 4.30.

In our study, with optimal parameters, second order accurate Fréchet derivative approximations consistently provided eigenvalue computations within an accuracy of 10^{-8}. First order ones consistently offered eigenvalue accuracy of 10^{-5}, even with slightly

DISTRIBUTION A: Distribution approved for public release. Distribution unlimited

suboptimal parameters. If this reduced accuracy is sufficient, first order can deliver it at about half the cost of the second order one, as it needs only one call to the flow solver per Arnoldi iteration. For open flows, small variations in the numerical boundary conditions used to represent an infinite domain can easily affect the fourth or even the third decimal place of the eigenvalue computation (OHMICHI; SUZUKI, 2016). Hence, with the optimal values of ε and τ, it is likely that, in many applications, first order accurate Fréchet derivative approximations would be the most cost-effective choice.

Parameter M affects only the accuracy of the Krylov span approximations, in the form of its product with τ. In fact, our tests demonstrate that the accuracy increases with τM, as explained by Goldhirsch, Orszag and Maulik (1987). M, however, has a more complicated impact on computation time because the Gram-Schmidt procedure scales with M^2 and the eigenvalue problem with around M^3, thus it is interesting to reduce M. Hence using optimal τ also leads to the most cost-effective approach. Under these circumstances, the computational effort is used almost entirely in the flow solver, and scales linearly with M. Hence, optimizations in the orthogonalization or in the eigenvalue solver algorithm have almost no impact. In contrast to ε and τ, there is not an optimal M for maximum accuracy. As M increases, the error in the eigenvalues eventually reduces to a noise floor associated with the other errors. As the Arnoldi algorithm evolves, the accuracy of the eigenvalues can be monitored until the target level or the noise floor is achieved. Contrary to ε and τ, the desired M does not need to be known a priori. If three-dimensional flows are investigated, the cost associated with the flow solver would be even larger and the conclusions would still hold. In our analysis the wall-time was used as a measure of cost. In many applications, CPU-time could be a better measure; however, given that at optimal conditions the cost is dominated by the flow solver, using CPU-time as a measure of cost would lead to the same guidelines. It is important to mention that in situations such as our test 2D case where the computational cost is dominated by the flow solver, the used of restarted Arnold methods does not improve efficiency, and for that reason it was not studied here. In 3D global instability analysis, restarted methods are even less likely to be advantageous.

Beyond these guidelines, we investigated the rate of convergence of the eigenvalues and observed that an eigenvalue initiates a rapid convergence only after the eigenfunction of some previous eigenvalues have converged. This is associated with the level of orthogonality between these eigenfunctions. Hence, eigenvalue convergence requires eigenfunction convergence and the current guidelines work for both.

DISTRIBUTION A: Distribution approved for public release. Distribution unlimited

Chapter 5

Large Open Cavities

5.1 Introduction

Several features of vehicles, ranging from small ones, such as gaps at doors and windows, to large ones, such as the landing gear wells of airplanes and car sunroofs can be represented by the simple geometry of an open cavity. The flow recirculates inside the cavity and a mixing layer forms at its opening. Under certain circumstances, the flow in unstable and oscillations develop, and high levels of sound are emitted. In transonic and supersonic flows, such oscillations can greatly increase the aerodynamic drag of surfaces with cavities (MCGREGOR; WHITE, 1970). Owen (1958), Dix and Bauer (2000) indicate that pressure fluctuations in the cavities can affect the aircraft structure and cause structural fatigue.

In the next section, we discuss the two-dimensional linear stability of the open cavity flow, especially its sensitivity to the incoming boundary layer thickness and Mach number. In the following sections, we analyze how three-dimensionality affects Rossiter modes, in the form of span-wise modulation of such modes as well as their interaction with centrifugal modes (MATHIAS; MEDEIROS, 2019a; MATHIAS; MEDEIROS, 2020).

A 6^{th} order spectral-like spatial differentiation is chosen for these simulations, while the time integration is done by the classical 4^{th} order Runge-Kutta scheme. The anti-aliasing filter coefficient is set to $\alpha = 0.49$ and it is turned off close to the open boundaries, while reduced order schemes, with smaller stencils, are used close to the walls. Meshes are constructed following the guidelines presented in chapter 3.

DISTRIBUTION A: Distribution approved for public release. Distribution unlimited

5.2 Two-dimensional results

Initially, our study was inspired by that of Yamouni, Sipp and Jacquin (2013), but, as opposed to them, who looked at very high Reynolds numbers, we were interested on conditions close to critical. This led us to lower Re_D numbers, guided by ROWLEY, COLONIUS and BASU (2002), Brès and Colonius (2008), Sun et al. (2017). Since we focus on the Rossiter modes only, a short cavity was used with a fixed $L/D = 2$ to avoid wake modes. Two main aspects are studied: the effect of the thickness of the incoming boundary layer; and the effect of the free flow Mach number.

Figure 5.1 shows results for a typical scenario investigated in this section, corresponding to the following parameters: $L/D = 2$, $Re_D = 1000$, $D/\theta = 100$ and $Ma = 0.5$. The left-hand side gives the pressure fluctuation contours of Rossiter mode 2 at an arbitrary phase, the thick black lines represent fluctuation amplitude level zero. The right-hand side shows the wall-normal velocity contours for modes 1 to 5, which will be referred here as R1 through R5. The mode number refers to the number of vortices in the mixing layer.

The Rossiter modes are described as a feedback mechanism involving four steps, namely: (1) Kelvin-Helmholtz (KH) vortices grow in the mixing layer at the cavity opening, (2) these vortices reach the trailing edge and emit sound, (3) the acoustic waves travel upstream and (4) excite new KH instabilities at the cavity leading edge. However, it is not entirely clear how much a global stability analysis can explain and predict this complicated (and non-linear) behavior. Originally, the Rossiter modes referred to the limit cycle oscillations observed in experiments. In linear stability analysis we obtain an approximation of such modes and when necessary to avoid confusion we use the term Rossiter mode linear approximation.

Further details of the analysis can be found in (MATHIAS; MEDEIROS, 2021b).

5.2.1 Influence of the boundary layer thickness

The literature overlooks the influence of the boundary layer thickness on the Rossiter instability. Studies focus on very specific D/θ values and, for that reason, here we investigate it in detail. A sweep of D/θ was performed (figure 5.2), where the Mach number was fixed at $Ma = 0.5$ and D/θ ranged between 10 and 200. In all cases, $L/D = 2$ and $Re_D = 1000$. Higher values of D/θ enhanced the instability. For very small D/θ, only R1 is unstable and the higher the Rossiter mode the more stable it is. Rossiter modes R4 and R5 were still immersed in the mode cloud and not identifiable, hence, not shown. In the parameter range investigated, the growth rates increase with D/θ, as observed at higher Reynolds numbers by Yamouni, Sipp and Jacquin (2013), and reach a saturation for large D/θ. Higher Rossiter modes show stronger variation of growth rates with respect to

DISTRIBUTION A: Distribution approved for public release. Distribution unlimited

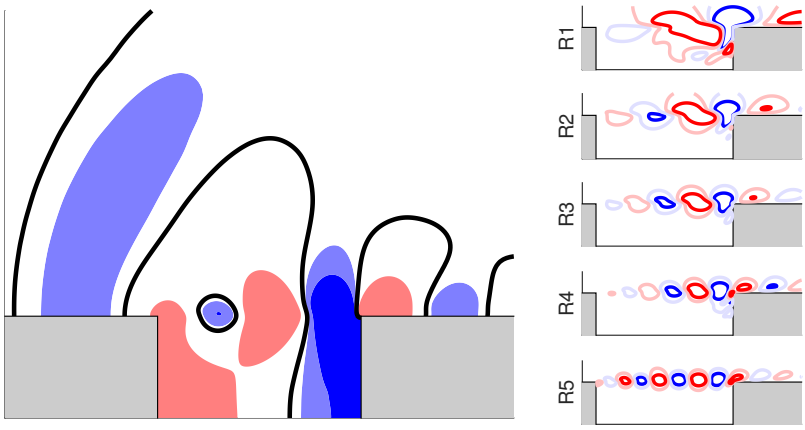


Figure 5.1 – Eigenfunctions of Rossiter mode linear approximations at $Re_D = 1000$, $D/\theta = 100$ and $Ma = 0.5$, at an arbitrary phase. (Left) Contours of pressure for mode 2. Black lines indicated level zero. (Right) Contours of wall-normal velocity for modes 1 to 5.

D/θ and saturate at higher values of D/θ. For these reasons, at higher D/θ, R2 overtakes mode R1 and becomes dominant. Afterwards, R3 also becomes more unstable than R1. The overall picture conveys the idea that, as D/θ increases, higher Rossiter modes become dominant if a saturation is not reached before. For the current parameter range only R1 and R2 dominate, but it seems that for higher Re or longer cavities, higher Rossiter modes could become dominant. At the same time, a slight increase in the mode frequency was observed. This is consistent with other studies which attribute the frequency increase to the higher convective velocity of the KH vortices in the mixing layer.

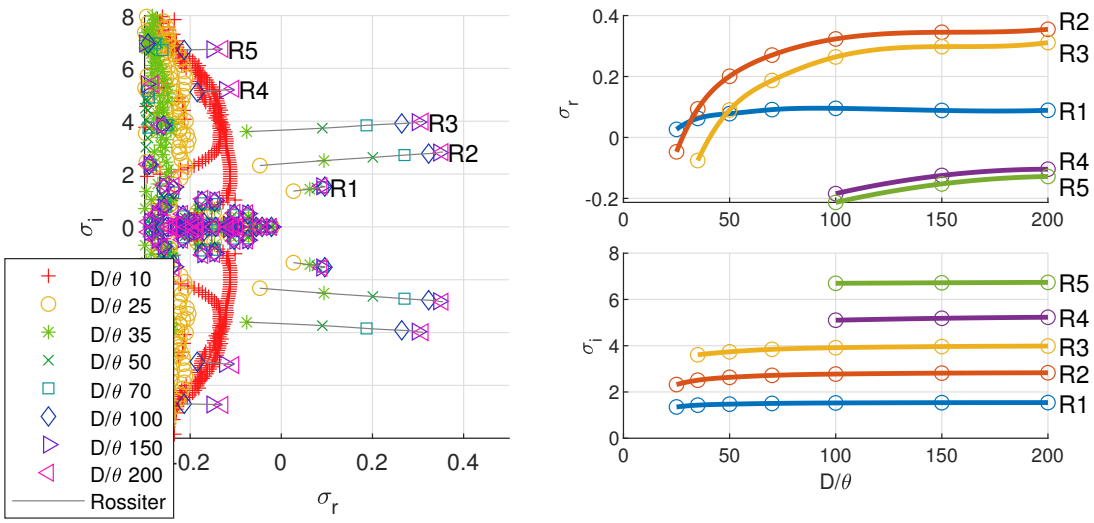


Figure 5.2 – Eigenvalues from the D/θ ratio sweep ($Re_D = 1000$, $Ma = 0.5$). (Left) Eigenspectrum. (Right) Real and imaginary parts of Rossiter mode eigenvalues.

DISTRIBUTION A: Distribution approved for public release. Distribution unlimited

In the current parameter space, the analysis indicates that, as D/θ increases, the flow moves from a regime where mode R1 dominates to one where modes R2 and R3 dominate. The increased instability for thinner boundary layers was attributed to the corresponding thinner mixing layers, which greatly enhanced the spatial amplification in the flow over the cavity, the unstable part of the cycle of the Rossiter modes. To substantiate the argument, the spatial growth of each mixing layer profile was obtained by solving the Orr-Sommerfeld equation. These amplification rates were integrated along the mixing layer to obtain the total spatial growth for each frequency ω, and are shown as the solid lines in figure 5.3 for different D/θ. In this analysis, the last 5% of the cavity length were disregarded, as the parallel-flow approximation was considered invalid there. The picture also includes bi-global stability growth rates of the Rossiter modes R1 to R5, which are referred to the vertical scale on the right-hand side of the frame. The figure shows that the global instability results are consistent with the mixing layer instability. Clearly, the dominant modes are selected by the mixing layer instability, confirming experimental observations by Sarohia (1977). The saturation at higher D/θ is also explained by this instability. This analysis considers incompressible flow, but at $Ma = 0.5$ the stability is not severely affected by compressibility, in particular the most unstable frequency.

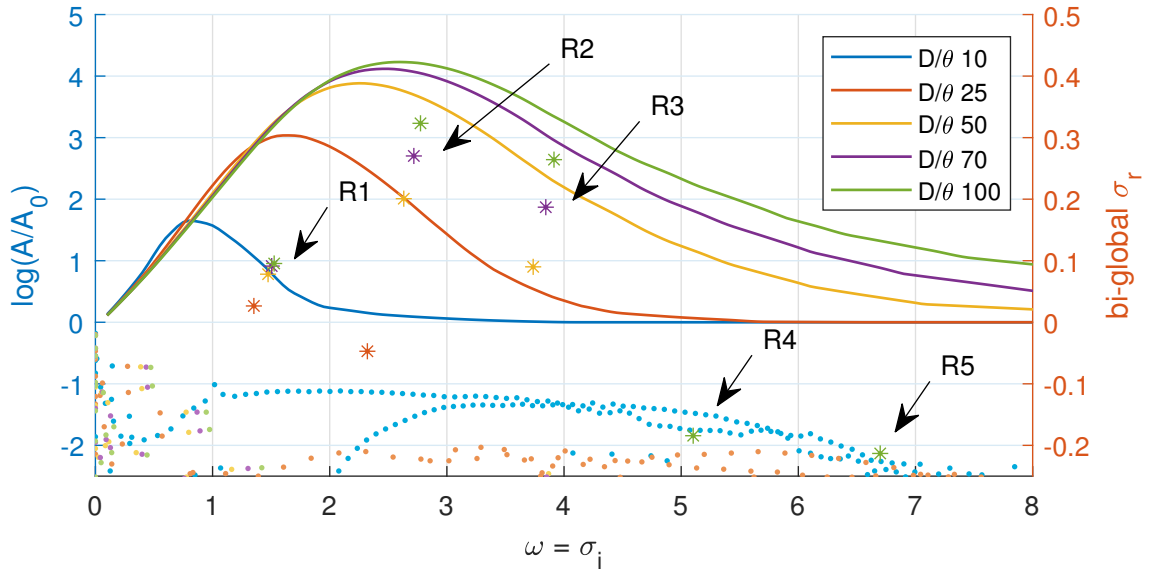


Figure 5.3 – Mixing layer integrated spatial amplification factor compared to the global instability results. The asterisks indicate the global modes eigenvalues of Rossiter modes and the dots are other eigenvalues, they refer to the scale on the right-hand side of the frame.

DISTRIBUTION A: Distribution approved for public release. Distribution unlimited

5.2.2 Influence of the Mach number

The previous section indicated that, in the current parameters, as D/θ increases, the flow moves from a regime where mode R1 dominates to one where modes R2 and R3 dominate. For the analysis of the compressibility effects, two representative Mach number sweeps were performed. As observed in figure 5.2, the thicker boundary layer at $D/\theta = 29.7$ represents a situation where only a pair of Rossiter modes is slightly unstable, while the thinner boundary layer at $D/\theta = 100$ is a more complex situation, with up to four unstable modes with higher temporal amplification levels. Figures 5.4 and 5.5 give, as a function of Mach number, the real and imaginary parts of the eigenvalues for both D/θ selected.

Within the parameter range covered, in general the sensitivity of the growth rates with respect to the Mach number was stronger for lower Mach numbers. For low D/θ (figure 5.4), at low Mach numbers, both R1 and R2 are stable and only these two modes become unstable as the Mach number increases. At low Mach numbers, R1 is the least stable. It becomes unstable at $Ma = 0.3$ and its growth rates saturates at about $Ma = 0.4$. R2 is more stable at low Mach numbers, but saturates only at higher Mach numbers, such that it becomes more unstable than R1 for $Ma > 0.5$.

For high D/θ (figure 5.5), four Rossiter mode linear approximations can be unstable in the Mach number range covered. Mode R2 is the most unstable for all Mach numbers and both R1 and R2 growth rates increase with the Mach number at the lower end but saturate at about $Ma = 0.3$. R3 and R4 are affected by compressibility in a more complex way. In all cases, the frequency reduces with the Mach number, a feature that is predicted by the Rossiter empirical equation and caused by the slower acoustic propagation upstream.

In summary, the most salient features of the Mach number effect are (1) the strong destabilizing effect of compressibility at low Mach number and (2), at high Mach numbers, either saturation or irregular behavior, depending on mode number and D/θ.

There is a strong destabilizing effect of Mach number at low number seen in figures 5.4 and 5.5, where compressibility has a small stabilizing effect on the mixing layer instability. Since Mach number did not considerably change the mixing layer profiles, the enhancement of the instability could not be associated directly with it. The receptivity of shear layer instability modes is not known to be very sensitive to the Mach number. On the other hand, the transfer of energy into acoustic waves grows very rapidly with the Mach number (GOLDSTEIN, 1976).

DISTRIBUTION A: Distribution approved for public release. Distribution unlimited

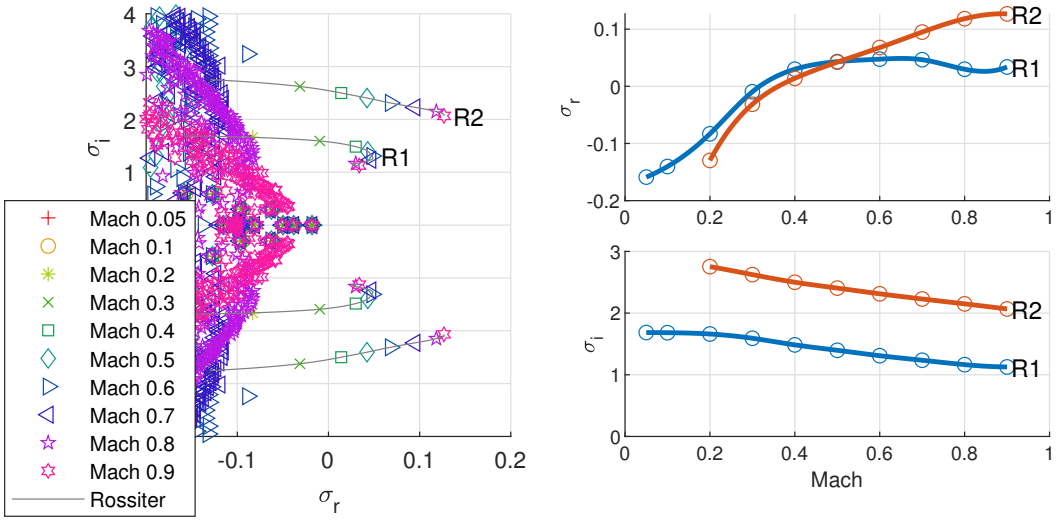


Figure 5.4 – Eigenvalues from the first Mach number sweep ($Re_D = 1149$, $D/\theta = 29.7$). (Left) Eigenspectrum. (Right) Real and imaginary parts of Rossiter mode eigenvalues.

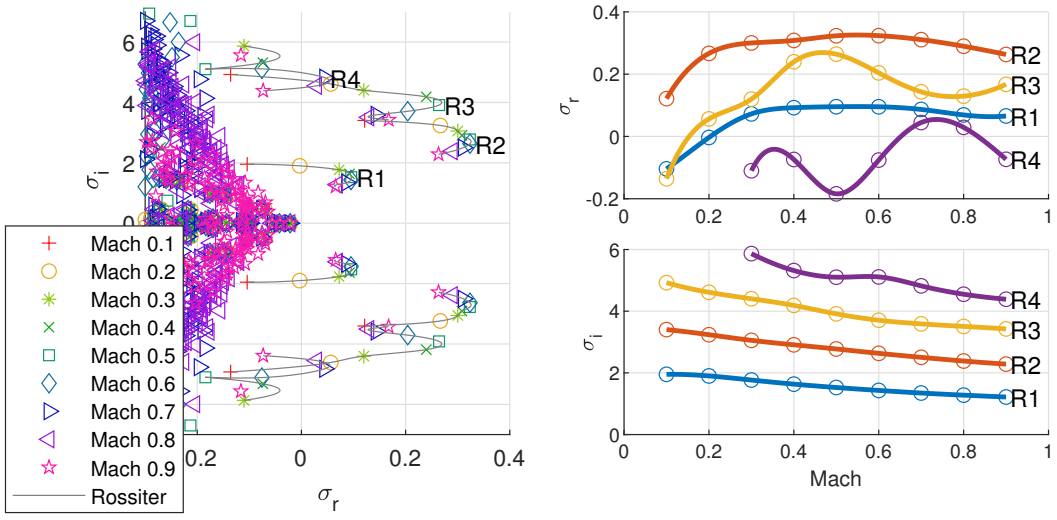


Figure 5.5 – Eigenvalues from the second Mach number sweep ($Re_D = 1000$, $D/\theta = 100$). (Left) Eigenspectrum. (Right) Real and imaginary parts of Rossiter mode eigenvalues.

Howe (2004) investigates the emission of sound by a cavity at low Mach numbers. In Howe's model, the acoustic energy transfer (ET_{Ac}) was computed as

$$ET_{Ac} = \frac{E_{Ac}}{E_{SL}} \ , \tag{5.1}$$

DISTRIBUTION A: Distribution approved for public release. Distribution unlimited

where

$$E_{Ac} = \int_{P_{Ac}} |p|^2 \, dx \ , \tag{5.2}$$

is the acoustic power in the far field and

$$E_{SL} = \int_{P_{SL}} |\nabla \cdot (\boldsymbol{\omega} \wedge \boldsymbol{v})| \, dx, \tag{5.3}$$

is the source term. In the equations, p, v and $\boldsymbol{\omega}$ are, respectively, pressure, velocity and vorticity, which can be obtained from the eigenfunctions of the Rossiter mode linear approximations. This was done as illustrated in figure 5.6. The source term was estimated by integrating across the shear layers, along the vertical black line shown in the figure. For the acoustic power, the integration was along a semi-circumference centered at the cavity trailing edge with radius equals to $2D$, starting at the cavity leading edge, but ending before the wake of Rossiter modes (the green line). It is not entirely clear whether this region corresponds to the near or the far field of the acoustic source, particularly in view that the extension of these fields is also affected by the Mach number. Regardless of that, we will refer to this region as acoustic field. Clearly, this position provides an estimate of the pressure fluctuations that trigger the Kelvin-Helmholtz vortices. In the picture, isocontours of the values of pressure and velocity eigenfunctions of the Rossiter mode 2 at $Ma = 0.6$ were overlaid to illustrate the flow at an arbitrary phase.

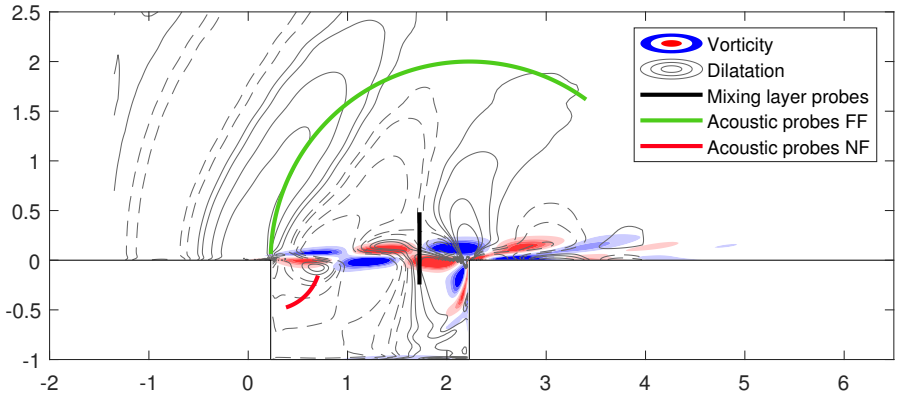


Figure 5.6 – Location of probes for the analysis of sound emission. Gray contours indicate dilatation fluctuations of the second Rossiter mode at $Ma = 0.6$, full line for positive contours and dashed line for negative ones. Colored contours indicate vorticity fluctuations. The black line indicates region of evaluation of sound source magnitude. Red and green lines indicate regions of evaluation of the magnitude of the pressure fluctuations.

In the analysis, the pressure and the velocities are normalized by their far-field values. Figure 5.7 shows the ET_{AC} as a function of Mach number, for modes 1 and 2 at

DISTRIBUTION A: Distribution approved for public release. Distribution unlimited

$D/\theta = 29.7$. The picture includes power functions of exponent 2 and 3 for reference. The acoustic energy transfer increases with the Mach number raised to a power between 2 and 3, depending on the Mach number and the mode.

The evaluation of the source term and acoustic power was also carried out with other integration regions around the green and black lines of figure 5.6. The near-field probes, shown in red, were used to test the sensitivity of results to the location of the probes and led to comparable, albeit noisier results.

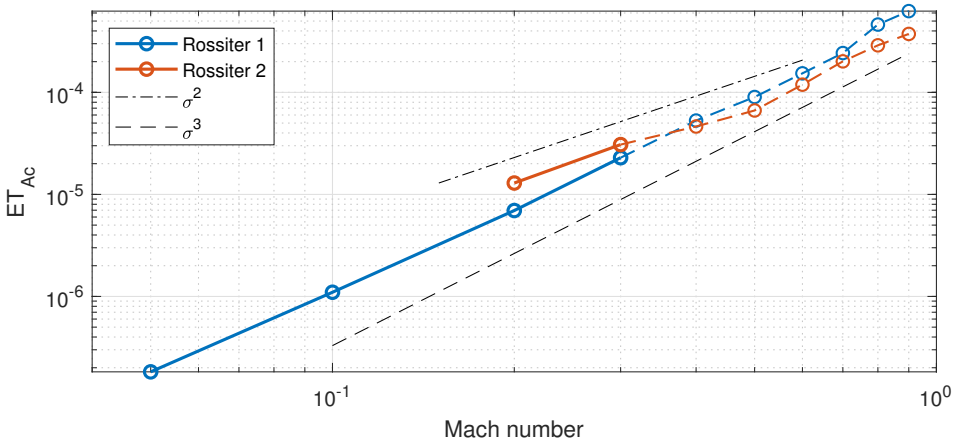


Figure 5.7 – Acoustic energy transfer (ET_{AC}) as a function of Mach number for the linear approximation of Rossiter modes 1 (blue) and 2 (red). The dashed and dashed-dotted lines represent Ma^3 and Ma^2 respectively.

The results are consistent with those by Howe (2004), which suggests that, at most frequencies, a dipole dominates the acoustic emission of the open cavity, which is proportional to $\rho_0 U^3 Ma^3$. However, it is unclear whether our so-called acoustic region corresponds to the near or the far field of the acoustic source. Moreover, Howe's theory is restricted to very low Mach numbers. Yamouni, Sipp and Jacquin (2013) also presents other arguments for a dipole source in connection with the acoustic cavity modes. In any case, more important for our analysis is the observation that indeed a consistent quantification of energy transfer could be extracted from the eigenfunctions and that the strong dependence on the Mach number offers an explanation for the large sensitivity of the amplification rates of the linear Rossiter mode at low Mach numbers.

Figure 5.5 also shows that, for high D/θ, modes 3 and 4 growth rates depend on Mach number in a very complex way, while modes 1 and 2 display a smooth dependence on Mach for both values of D/θ considered. Yamouni, Sipp and Jacquin (2013) observed a similar complex dependence and linked it to a resonance between Rossiter modes and standing acoustic waves in the cavity. These standing waves are described by Plumblee, Gibson and Lassiter (1962).

Figure 5.8 presents the frequency of Rossiter and standing waves modes as a

DISTRIBUTION A: Distribution approved for public release. Distribution unlimited

function of Mach number. The blue solid lines represent the Rossiter modes as predicted by

$$\omega = \frac{2\pi N_R}{\frac{1}{\kappa} + Ma\left(1 + \frac{0.514}{L/D}\right)}, \tag{5.4}$$

an equation proposed by Block (1976), which considers the cavity aspect ratio (L/D). In the equation, N_R is the Rossiter mode number and $\kappa = 1/1.75$ is an empirical constant. In the figure, the dashed orange lines represent the standing wave modes given by (PLUMBLEE; GIBSON; LASSITER, 1962)

$$\omega = \frac{\pi}{2Ma}\left[\left(\frac{M_p}{L}\right)^2 + \left(\frac{N_p}{D}\right)^2\right], \tag{5.5}$$

where M_P is the number of standing waves wavelengths in the stream-wise direction and N_P, in the wall-normal direction. The modes are identified by (M_P, N_P). In the case of a cavity with aspect ratio L/D=2, modes (2,0) and (0,1) coincide in frequency.

The figure also displays results from global instability analysis given by the circles. The circle radius is proportional to the distance from neutral stability conditions, the solid circles represent instability while hollow circles represent stability. Large, filled symbols indicate strong instability, large hollow symbols, the opposite.

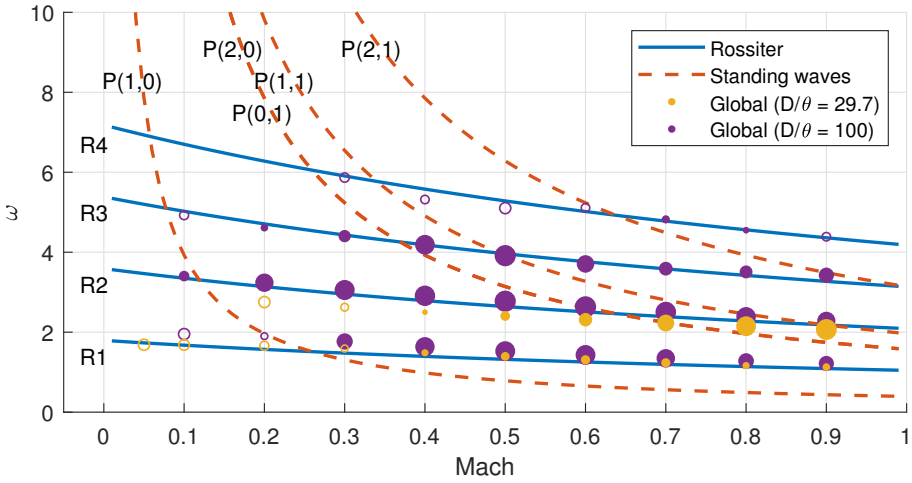


Figure 5.8 – Frequency predictions of Rossiter modes (blue) and standing wave modes (orange) compared to the global mode results (circles). The circle radius is proportional to the distance from neutral stability, the solid circles represent instability while hollow circles represent stability.

A correlation can be found between both types of modes and the global instability results. Rossiter mode 3 shows increased instability when the R3 curve approaches the $P(2,0)$ and $P(1,1)$ curves and, at a higher Mach numbers, the $P(2,1)$ curve. Mode R4 is

DISTRIBUTION A: Distribution approved for public release. Distribution unlimited

also affected by these interactions, not only on the growth rates but also in the frequency, the latter may be associated with the fact that this mode is only marginally unstable or stable. Albeit less pronounced, variations in frequency consistent with this argument are also observed for R3.

At lower frequencies, the $P(m,n)$ curves tend to become parallel to the R1 and R2 curves. This smooths out the dependence on Mach number but may be associated with a maximum instability for R1 at $Ma = 0.6$ and low D/θ (see figure 5.4), which has also been reported by Sun et al. (2017) at similar conditions. It may also explain why, contrary to all other modes that were observed to saturate at $Ma = 0.6$, mode 2 at low D/θ, seems to saturate only at $Ma = 0.9$.

5.3 Three-dimensional global stability

Apart from the two-dimensional modes that dominate in the form of Rossiter modes, in this parametric region, there are also three-dimensional unstable modes; namely centrifugal modes and span-wise modulated Rossiter modes. In this section, we investigate three-dimensional instability for an array of span-wise wave numbers (β), so that the periodicity in this direction has length $L_Z = 2\pi/\beta$. The LST routine was used in span-wise spectral mode, in which a single span-wise wave number is allowed each time. The 2D case is equivalent to $\beta = 0$, which considers the domain to be infinite and uniform in this direction.

Figure 5.9(Left) shows the eigenvalues as a function of β. Note that centrifugal modes have much lower amplification rates than Rossiter modes. Their frequency is lower by about one order of magnitude.

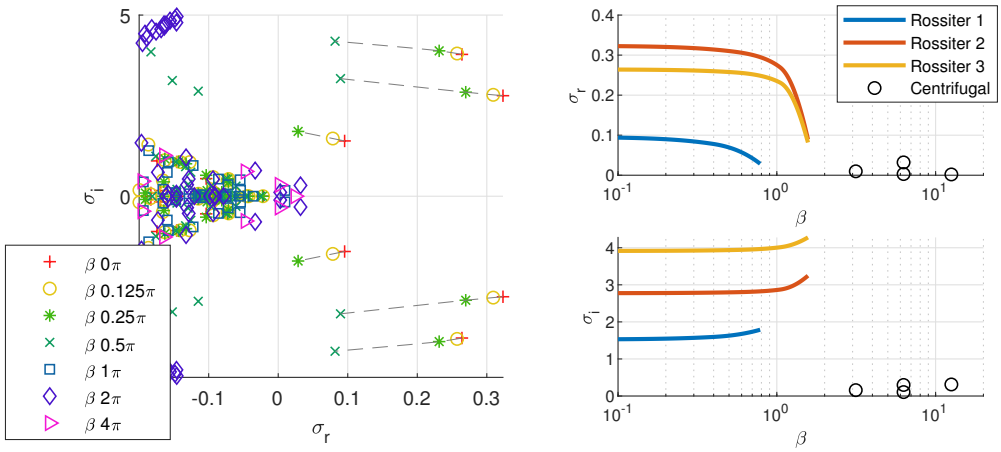


Figure 5.9 – Eigenvalues from the span-wise wave number sweep ($Re_D = 1000$, $D/\theta = 100$, $L/D = 2$, $Ma = 0.5$). (Left) Spectra in the complex plane. (Right) Real and imaginary parts of the eigenvalues of the Rossiter and centrifugal modes.

DISTRIBUTION A: Distribution approved for public release. Distribution unlimited

At lower β, Rossiter modes dominate. Slightly above $\beta = 1$, their growth rate reduces sharply. At the higher end of the spectrum, centrifugal modes appear. Under these conditions, there is no value of β for which both Rossiter and centrifugal modes are unstable. Figure 5.10 shows the most unstable modes for $\beta = \pi/4$ and $\beta = 2\pi$ at an arbitrary phase, they are Rossiter and centrifugal modes, respectively. In the next section, we further explore the instability analysis; however, the results shown here are representative of the parameter space investigated, in particular the fact that 2D Rossiter modes have much higher growth rates and frequencies in comparison with centrifugal modes.

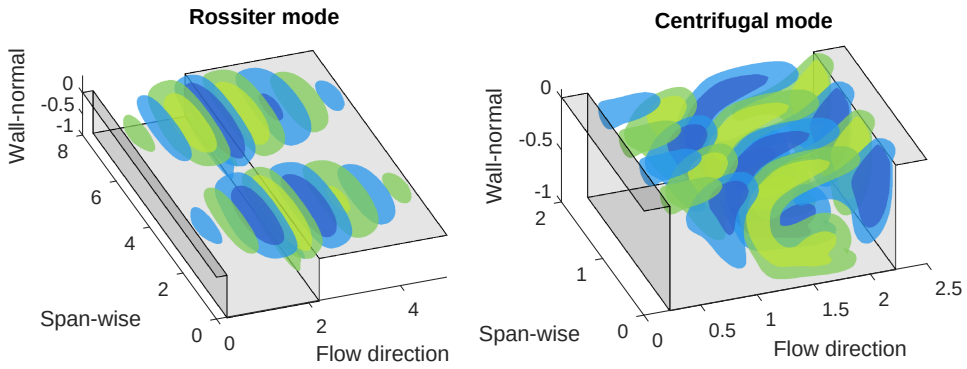


Figure 5.10 – Most unstable eigenmodes from the 3D LST analysis. (Left) $\beta = \pi/4$, isosurfaces of density. (Right) $\beta = 2\pi$, isosurfaces of span-wise velocity.

5.4 Non-linear effects

Next, we wanted to verify to which extent the global linear stability results could predict the nonlinear behavior of the flow. For this, DNS were performed. The study initiated with the $Re_D = 1000$, $D/\theta = 100$, $L/D = 2$, $Ma = 0.5$ case, the same presented in the previous section. Figure 5.11 presents results of 2D and 3D simulations. At the left-hand side of the figure, we show the time series of pressure at the cavity trailing edge at an arbitrary span-wise position for both 2D and 3D cases; at the right-hand side, we compare their spectra.

For the initial condition of the 2D case, no noise was added apart from the numerical background noise which stood at 10^{-13}. In the 3D simulation, a small span-wise disturbance was also added to trigger the three-dimensional effects. The flow was periodic in the span-wise direction and the span-wise domain was long enough that the flow became statistically independent on this direction, as is discussed later in this section.

DISTRIBUTION A: Distribution approved for public release. Distribution unlimited

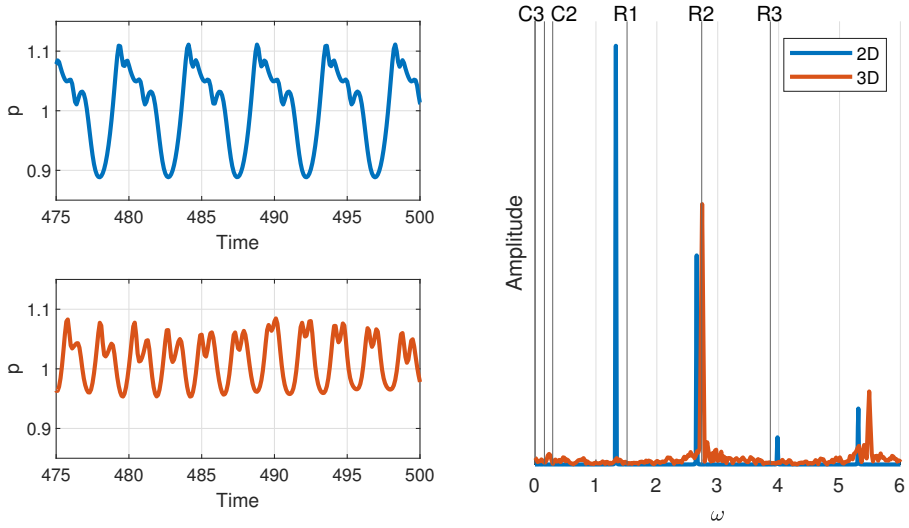


Figure 5.11 – Comparison between 2D and 3D simulations of the $Re_D = 1000$, $D/\theta = 100$, $L/D = 2$, $Ma = 0.5$ case. (Left) Time series of pressure at the trailing edge. (Right) Spectrum. The vertical lines mark angular velocities predicted by the linear stability analysis for each Rossiter mode (R1 through R3) and centrifugal mode (C2 and C3).

Previous section showed that the Rossiter mode was essentially 2D and much more unstable than the centrifugal modes. This suggests that 2D simulation should capture most features of the nonlinear regime of the cavity flow. However, while LST predicts the R2 mode as dominant, in the nonlinear simulation the R1 is the dominant. Perhaps even more surprising is that for the 3D simulation, the dominant mode is the R2 with a frequency very close to the LST predictions. In the 3D simulation, there is also a small peak in the spectrum between the frequencies predicted for centrifugal modes C2 and C3, at $\omega_{C2} = 0.29$ and $\omega_{C3} = 0.15$, respectively. In this section, we investigate why the 3D simulation results were closer to the 2D linear stability prediction than the 2D simulation.

Linear stability is expected to provide good predictions of the nonlinear behavior if the flow is close enough to the neutral conditions. However, it is difficult to predict a priori just how close it needs to be. We then tested conditions close to neutral and progressively more unstable to try and identify the mechanism that could explain the observation in figure 5.11. Three cases were chosen based on linear stability analysis. The first case (`R`) has no unstable centrifugal modes, only Rossiter modes are unstable. The second case (`C`) is the opposite, no unstable Rossiter modes, only centrifugal ones are unstable. The third case (`R+C 1`) is unstable for both types of modes, albeit at a much lower instability level when compared to the case from figure 5.11, which hereinafter will be referred to as case `R+C 2`. `R+C 3` is the most unstable of all cases. Table 5.1 summarizes the parameters for these cases. Note that Mach and Reynolds numbers were used to control the instability of each type of mode, considering that Rossiter is much more sensitive to Mach number than

DISTRIBUTION A: Distribution approved for public release. Distribution unlimited

the centrifugal mode, as was seen in the diagram by Brès and Colonius (2008), shown in figure 1.2. The table also shows which of the Rossiter and centrifugal modes were unstable in each scenario, sorted from the most to the least unstable.

Table 5.1 – Cases defined to investigate the interaction of Rossiter and centrifugal modes

Case	Re_D	Ma	D/θ	L/D	Rossiter	Centrifugal
`R`	1200	0.5	25	2	Unstable (R1)	Stable
`C`	1500	0.3	25	2	Stable	Unstable (C2)
`R+C 1`	1500	0.5	25	2	Unstable (R1)	Unstable (C2)
`R+C 2`	1000	0.5	100	2	Unstable (R2, R3, R1)	Unstable (C1, C2, C3)
`R+C 3`	1500	0.5	100	2	Unstable (R3, R2, R1)	Unstable (C1, C2, C3)

Figure 5.12 shows the growth rate of the most unstable mode as a function of β for each of the first three cases. The colored regions in the plot represent distinct types of modes. The centrifugal modes are subdivided into 3 groups of decreasing value of β (BRÈS; COLONIUS, 2008). Centrifugal mode I is stationary, i.e. $\omega = 0$, while mode II has the highest frequency of the three. In the first three cases considered, only mode II becomes unstable.

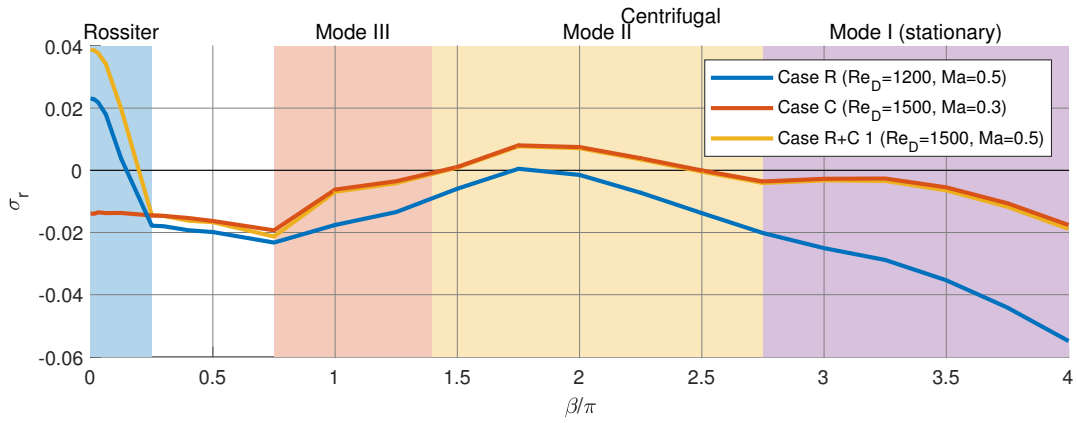


Figure 5.12 – Most unstable mode at each β for the first three cases defined in table 5.1. Each colored region represents a different type of mode.

The time series of pressure fluctuation from these cases are shown in figure 5.13, each color represents a probe in a different span-wise position. In agreement with the LST, case `R` becomes two-dimensional after fully developed, despite displaying some three-dimensionality between $t = 300$ and $t = 500$ shown by the different signals from each probe. Also in agreement with the LST, case `C` shows only three-dimensional oscillations. The span-wise distance between the probes is half a wavelength of the most unstable centrifugal mode, and the signals are perfectly consistent with this situation. The span-wise domain of case `C` corresponded two periods of the most unstable centrifugal mode; while, for case `R`, the domain was large enough for the span-wise modulated Rossiter modes of wave numbers as low as $\beta = \pi/16$. Case `R+C 1` presents a combination of both Rossiter and

DISTRIBUTION A: Distribution approved for public release. Distribution unlimited

centrifugal modes. Figure 5.14 shows that the nonlinear flow oscillates at the frequencies very close to those predicted by the LST. Hence, unlike the more unstable case `R+C 2`, these marginally unstable cases agreed with the global stability analysis.

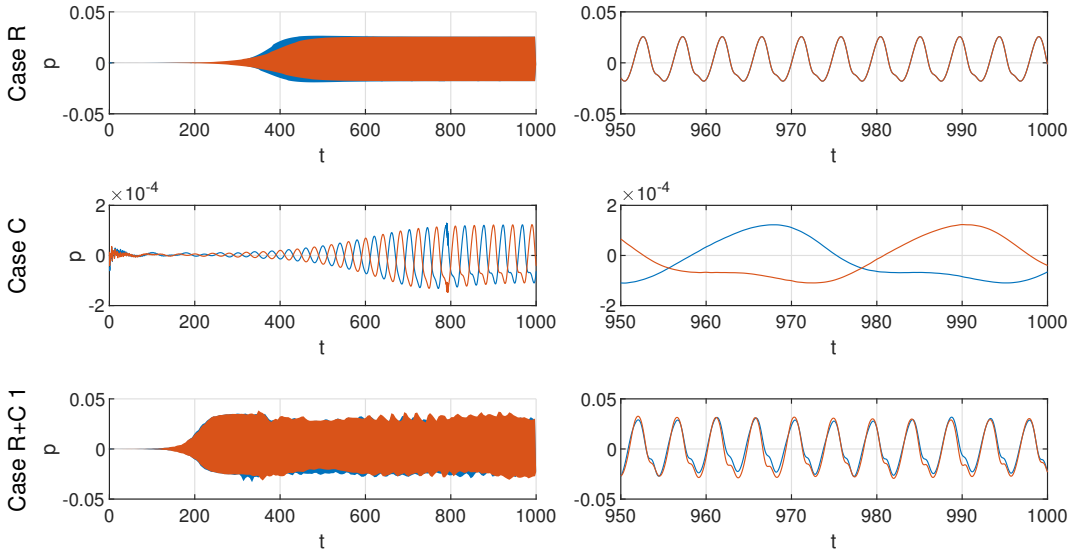


Figure 5.13 – Time series of pressure fluctuation for the cases defined in table 5.1. Blue and orange curves represent different span-wise positions.

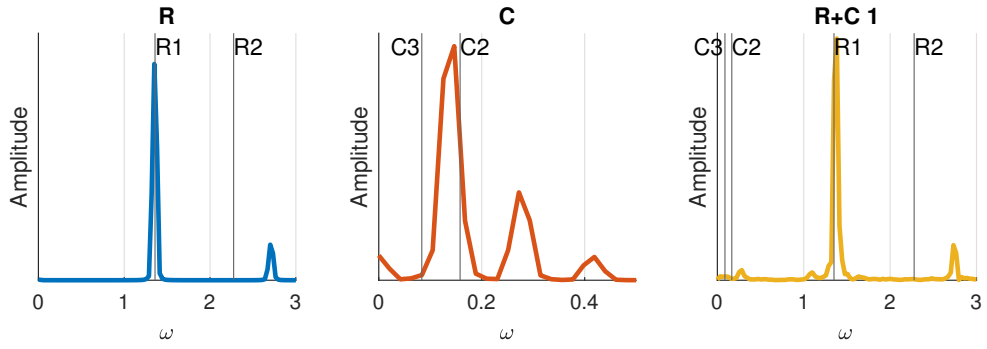


Figure 5.14 – Spectra of cases `R`, `C` and `R+C 1`. The linear predictions of angular velocities of each mode are also marked.

The last case is `R+C 3`, which is more unstable than `R+C 2` and much more unstable than `R+C 1`. It is defined by $L/D = 2$, $Re_D = 1500$, $D/\theta = 100$ and $Ma = 0.5$. Compared to case `R+C 2`, the Reynolds number based on cavity depth was increased from 1000 to 1500. The linear stability results of cases `R+C 1`, `R+C 2` and `R+C 3` are shown in figure 5.15. The time series of the simulations of case `R+C 3` are shown in figure 5.16.

Cases `R+C 2` and `R+C 3` reached comparable simulation results, in which the signals are much more irregular that of case `R+C 1`. The linear stability analysis of case `R+C 3` predicts Rossiter mode 3 to be the most unstable, at $\sigma_{R3} = 0.42 \pm 3.9i$, slightly ahead of

DISTRIBUTION A: Distribution approved for public release. Distribution unlimited

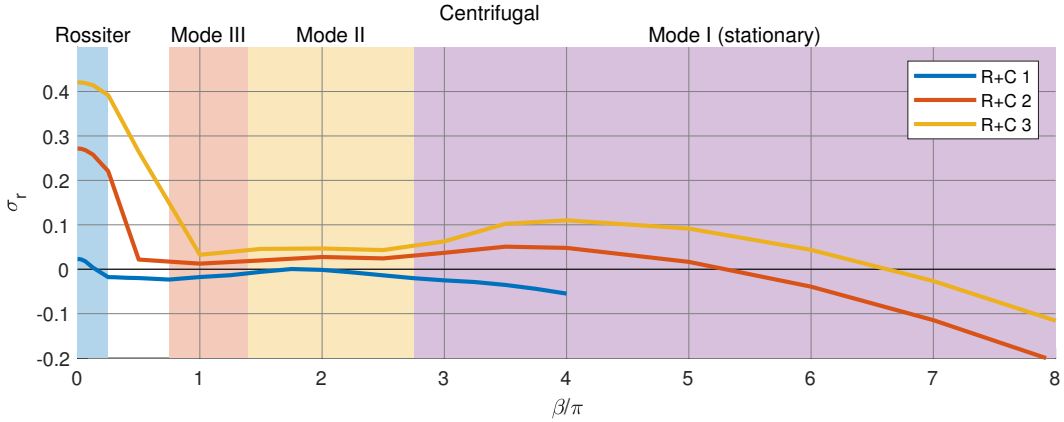


Figure 5.15 – Most unstable linear mode for cases `R+C 1`, `R+C 2` and `R+C 3` for various values of β.

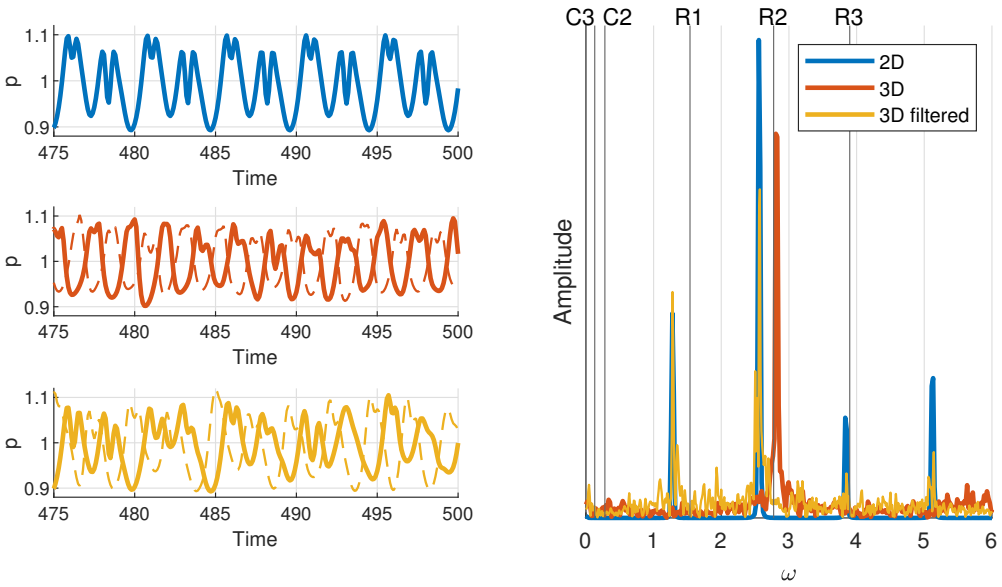


Figure 5.16 – Comparison between 2D and 3D simulations of case `R+C 3` ($Re_D = 1500$, $D/\theta = 100$, $L/D = 2$, $Ma = 0.5$). (Left) Time series of pressure at the trailing edge. The dashed lines were measured at another span-wise position. (Right) Spectrum. The vertical lines mark angular velocities predicted by the linear stability analysis for each Rossiter mode (R1 through R3).

mode 2, which is at $\sigma_{R2} = 0.41 \pm 2.8i$. Modes 1 and 4 are also unstable, but much less so, at $\sigma_{R1} = 0.12 \pm 1.5i$ and $\sigma_{R4} = 0.10 \pm 5.1i$, respectively. By looking at the spectrum of case `R+C 3` (figure 5.16), we observe that the flow is dominated by Rossiter mode 2, which is close to the prediction by the linear stability analysis. Unlike case `R+C 2`, the centrifugal modes were not visible in the spectrum. However, the 2D simulation of case `R+C 3` shows a different picture. Even though Rossiter mode 2 still dominates the flow, it is at a frequency different than that predicted by the linear stability analysis. Moreover, the spectrum shows a strong subharmonic, indicating that the flow is close to switching

DISTRIBUTION A: Distribution approved for public release. Distribution unlimited

to Rossiter mode 1. Figure 5.17 compares snapshots of wall-normal velocity for the 2D simulation of cases `R+C 2` and `R+C 3` and the 3D simulation of case `R+C 3`. Note that there is a single vortex in the cavity opening for the 2D simulation of case `R+C 2`, indicating that Rossiter mode 1 dominates the flow. Both 2D and 3D simulations of case `R+C 3` show two vortices in the cavity opening, indicating Rossiter mode 2 to be dominant.

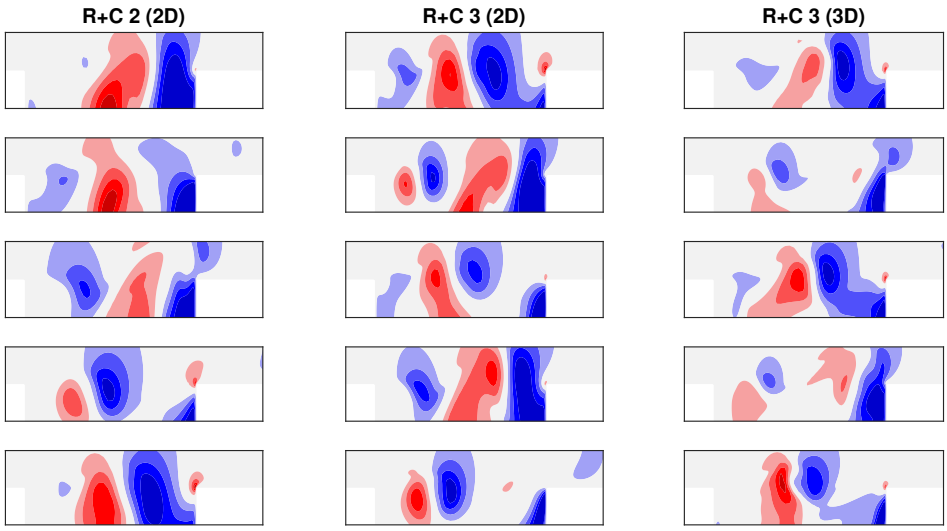


Figure 5.17 – Snapshots of wall-normal velocity for the 2D simulation of cases `R+C 2` and `R+C 3` and the 3D simulation of case `R+C 3`. The snapshots of the 3D simulation were taken at an arbitrary span-wise position.

For the `R+C 3` case, once more 3D simulations showed better agreement with LST than 2D simulations. To try and understand this observation, the following strategy was employed: There are two types of unstable three-dimensional modes in these flows: centrifugal modes and span-wise modulated Rossiter modes. We have artificially removed the centrifugal modes from the flow by using a span-wise mesh that is too course to resolve their high wave numbers. In this way, we can remove the effect of the centrifugal mode from the 3D simulation. Figure 5.16 also shows the resulting time series of this simulation as well as its spectrum. The dashed line in the left-hand side of the figure shows the pressure data for another span-wise position, which are different from the first probe, meaning that the flow still has three-dimensional effects. The spectrum of the 3D filtered case has peaks at the same frequencies as the 2D case.

From section 5.2.1, we know that one of the deciding factors for the selection of the Rossiter modes is the thickness of the mixing layer above the cavity. Thinner mixing layers are more unstable, relative to the cavity size, and favor Rossiter modes of higher order. Figure 5.18 (Middle) shows the thickness of the mixing layer for case `R+C 3` in four situations: the base flow, the mean flow of the 2D simulation, the mean flow of the 3D simulation and the mean flow of the filtered 3D simulation. The bottom part of this figure

DISTRIBUTION A: Distribution approved for public release. Distribution unlimited

shows the total spatial amplification for each case for a range of angular velocities ω, the angular velocities of Rossiter modes 1 through 3 are also marked in the figure.

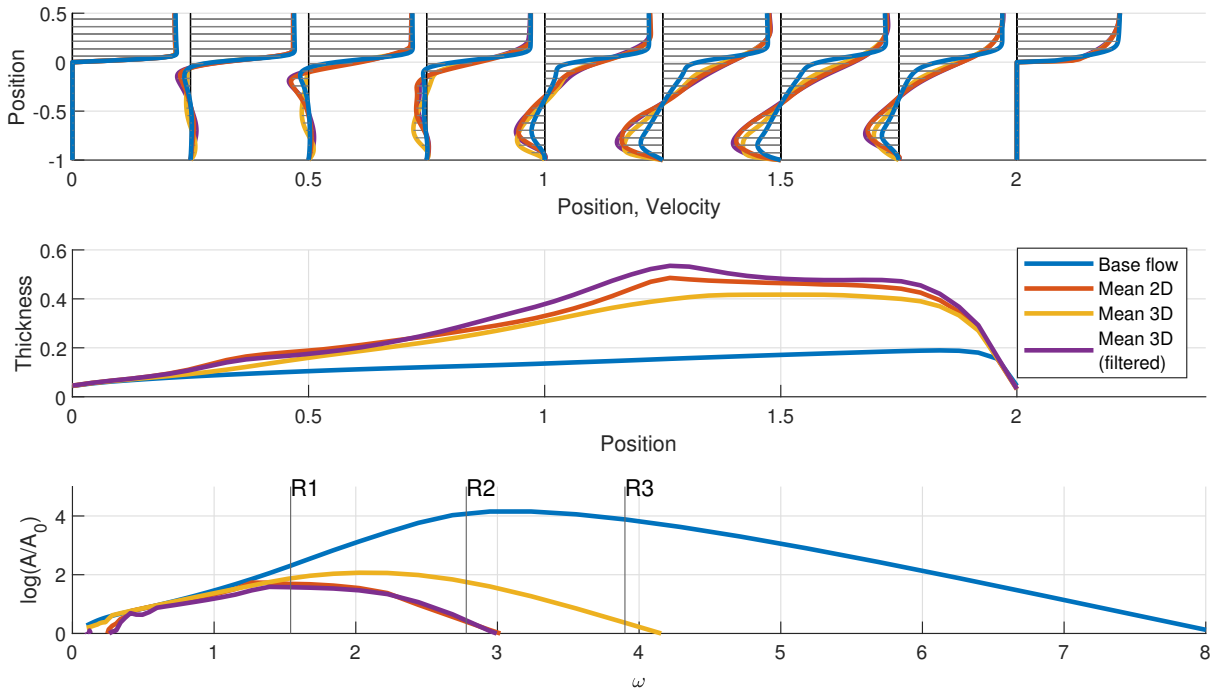


Figure 5.18 – (Top) Velocity profiles of the mean flow. (Middle) Mixing layer thickness for different situations of case `R+C 3` (Bottom) Total spatial amplification of each mixing layer as a function of ω.

For all mean flows, the mixing layer is considerably thicker than of the base flow. However, the 3D case has not thickened as much as the 2D case. Furthermore, the filtered 3D case is much closer to the 2D case than to the well-resolved 3D case. A similar conclusion can be reached by looking at the spatial amplification along the mixing layer for each scenario. The base flow clearly favors the frequencies of Rossiter modes 2 and 3, matching the global stability prediction. The 3D case has similar amplifications at the frequencies of Rossiter modes 1 and 2. The 2D and the 3D filtered cases clearly favor the first Rossiter mode, which explains the strong subharmonic of Rossiter mode 2 in the spectra, meaning that the flow is close to switching to Rossiter mode 1.

Further evidence of the effect of the centrifugal mode can be seen in figure 5.19, which shows the spectra of case `R+C 3` for the 2D, 3D and filtered 3D simulations as a function of time, which was obtained with the use of Hanning windows. The sampling frequency was set to 10 and each window was 1024 samples long, resulting in windows that are 102.4 time units long. The time series for this figure is the pressure at a probe at the cavity trailing edge at an arbitrary span-wise position. Once more, the strong subharmonic of the second Rossiter mode can be seen in the 2D and filtered 3D cases, albeit the latter does not have a spectrum as regular as the former. Figure 5.20 shows the same analysis, but this time the signal is from a probe of wall-normal velocity inside the cavity, at three

DISTRIBUTION A: Distribution approved for public release. Distribution unlimited

quarters of the length and half of the depth, which is much more suited for capturing centrifugal modes. This probe shows that the centrifugal modes are always present in the low end of the spectrum of the 3D case. In the filtered case, a signal appears sporadically, which may be an ill resolved version of the centrifugal mode. These centrifugal modes were not seen in the previous image because their eigenfunctions only have a very small projection of pressure at the trailing edge; most of these modes' fluctuation happen in the velocity field inside the cavity.

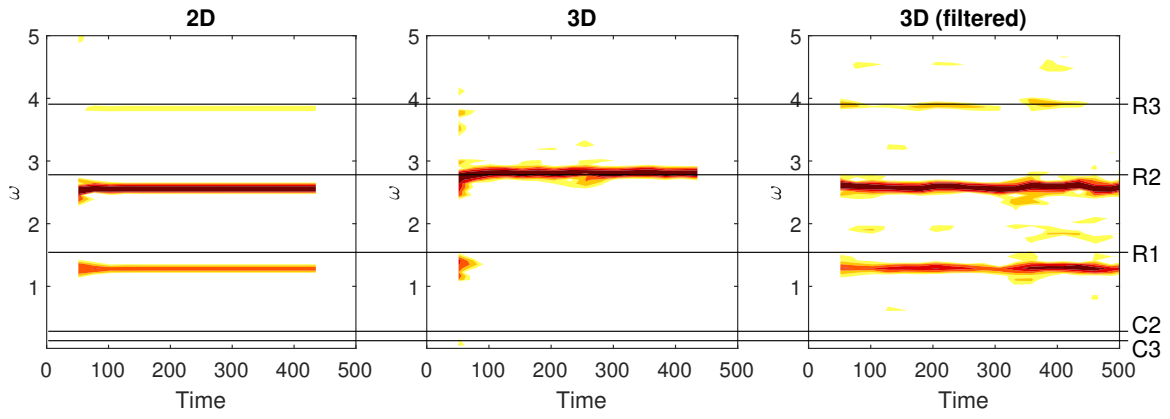


Figure 5.19 – Spectrum of pressure at the trailing edge as a function of time for case `R+C 3` ($Re_D = 1500$, $D/\theta = 100$, $L/D = 2$, $Ma = 0.5$) for (Left) the 2D simulation, (Center) the 3D simulation and (Right) the filtered 3D simulation. LST-predicted frequencies for Rossiter modes are also shown.

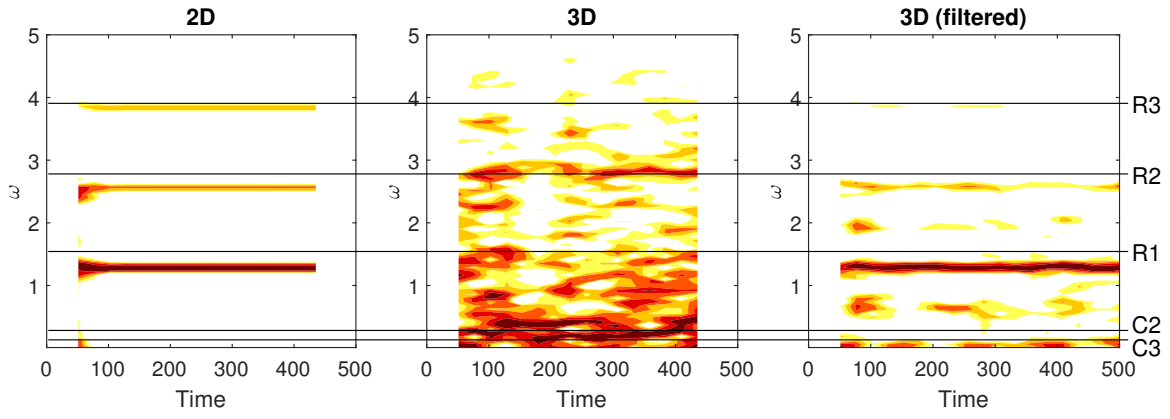


Figure 5.20 – Spectrum of wall-normal velocity inside the cavity as a function of time for case `R+C 3` ($Re_D = 1500$, $D/\theta = 100$, $L/D = 2$, $Ma = 0.5$) for (Left) the 2D simulation, (Center) the 3D simulation and (Right) the filtered 3D simulation. LST-predicted frequencies for Rossiter modes are also shown.

Figure 5.21 shows the time-series and spectra of case `R+C 3` for the 2D, 3D and filtered 3D simulations after the limit cycle was reached. This time, the wall-normal velocity inside the cavity was used for a better visualization of the centrifugal modes.

DISTRIBUTION A: Distribution approved for public release. Distribution unlimited

There is a small peak in the spectrum at $\omega = 0.21$, which is between the frequencies predicted for centrifugal modes II and III, at $\omega_{C2} = 0.28$ and $\omega_{C3} = 0.13$, respectively. Both these centrifugal modes were predicted as unstable by the linear stability analysis.

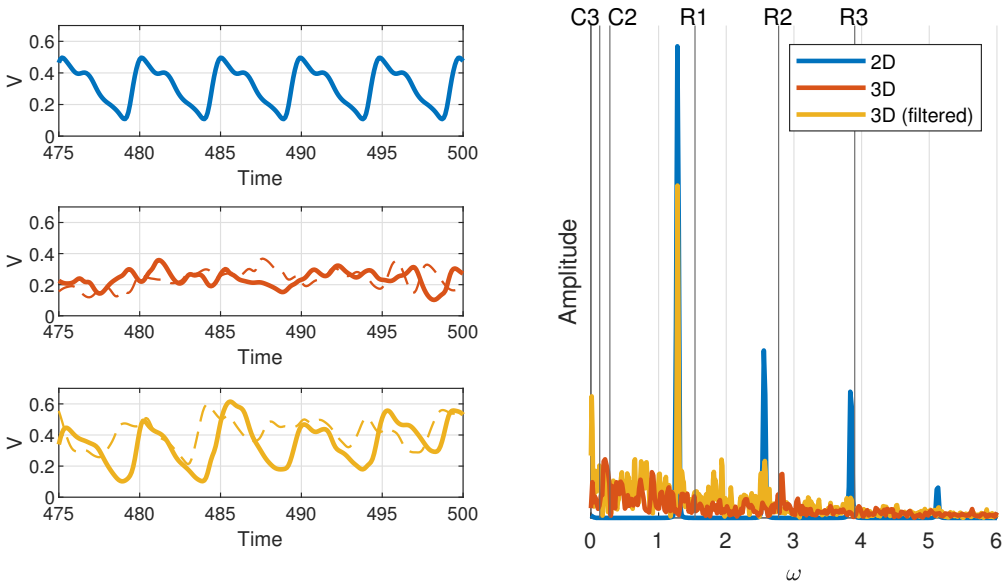


Figure 5.21 – Comparison between 2D and 3D simulations of case `R+C 3` ($Re_D = 1500$, $D/\theta = 100$, $L/D = 2$, $Ma = 0.5$). (Left) Time series of wall-normal velocity in the cavity. The dashed lines were measured at another span-wise position. (Right) Spectrum. The vertical lines mark angular velocities predicted by the linear stability analysis for each Rossiter mode (R1 through R3).

By taking the two-dimensional spectrum of the limit cycle of case `R+C 3`, in both time and span-wise direction, we can confirm the presence of centrifugal modes. Figure 5.22 shows the spectra of pressure at the cavity trailing edge and of wall-normal velocity inside the cavity. The pressure spectrum shows very little three-dimensional activity and has a very large peak, which corresponds to the second Rossiter mode. The velocity spectrum, on the other hand, is better suited to capture the centrifugal modes and shows no clear peak in the Rossiter mode frequency; however, there is energy at low frequency, especially between $\beta = 0.5\pi$ and $\beta = \pi$, including substantial energy at frequency $\omega = 0.21$, which corresponds to the LST prediction of centrifugal mode III.

To test the robustness of these results, we have taken a fully developed 2D simulation, converted it to 3D and added a small disturbance (white noise of RMS equals to 10^{-10}) to trigger the 3D instabilities. After some time, the dominant mode had switched from Rossiter mode 1 to mode 2. Later in this simulation (at $t = 250$), we have added a filter to damp out all three-dimensional oscillations, forcing the flow to become 2D again, which has caused Rossiter mode 1 to emerge once more. Figure 5.23 shows the spectrum of pressure (left) and velocity (right) for this case.

Finally, we wish to understand what the minimum span-wise domain length for an

DISTRIBUTION A: Distribution approved for public release. Distribution unlimited

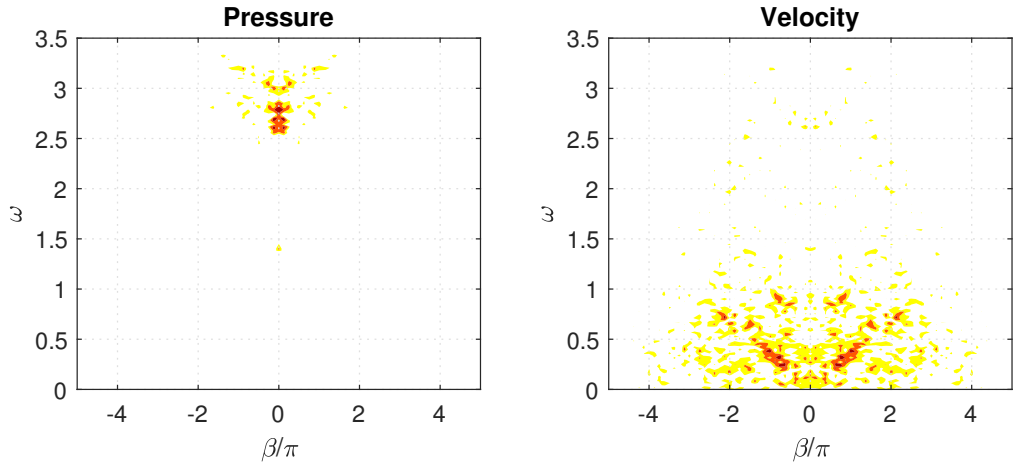


Figure 5.22 – Temporal and span-wise spectrum for the limit cycle of `R+C 3` ($Re_D = 1500$, $D/\theta = 100$, $L/D = 2$, $Ma = 0.5$). (Left) Pressure at the cavity trailing edge (Right) Wall-normal velocity inside the cavity.

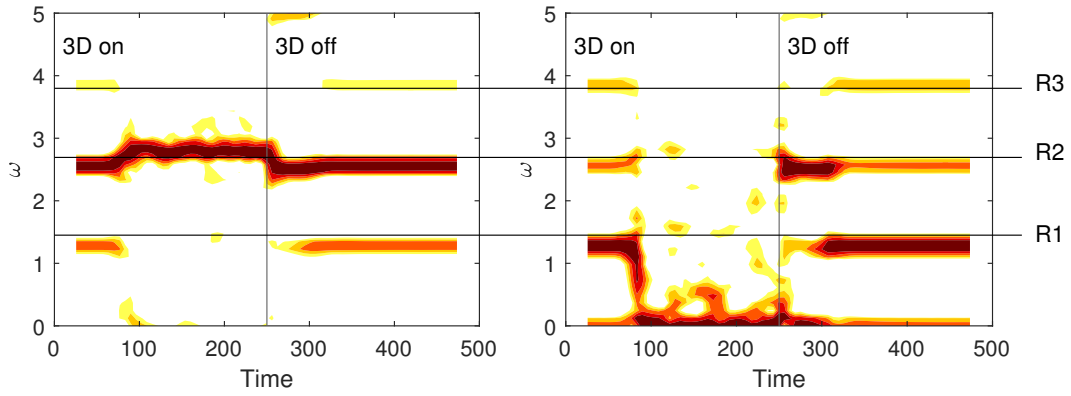


Figure 5.23 – Spectrum of (Left) pressure and (Right) velocity of case `R+C 3` ($Re_D = 1500$, $D/\theta = 100$, $L/D = 2$, $Ma = 0.5$), beginning with the 2D limit cycle, then with 3D effects turned on and off at $t = 0$ and $t = 250$, respectively. Expected frequencies for Rossiter modes are also shown.

accurate simulation is. According to figure 5.15, the maximum instability of a centrifugal mode happens at span-wise wave number $\beta = 4\pi$, which corresponds to a period length of half the cavity depth. Figure 5.24 shows the spectrum as a function of time for various span-wise wave numbers. In the figure, L_z corresponds to the period length of the most unstable centrifugal mode. The second frame, which corresponds to a domain that is too narrow for this mode, shows results very similar to those of the 2D case. The third frame, when the domain length is enough for just one period of this mode shows results that are already very similar to the larger domains, but still contains a considerable amplitude peak near the frequencies of the first Rossiter mode; furthermore, the peak corresponding to the second Rossiter mode is not fully formed in the velocity spectrum. The Rossiter 1 peak is only gone when the domain is large enough for four period lengths of this mode, when the

DISTRIBUTION A: Distribution approved for public release. Distribution unlimited

saturated flow state can be said to have become statistically independent on the span-wise domain. The last frame shows the spectrum for a domain that is 32 times the period size of the most unstable centrifugal mode, the reasoning behind such a large simulation is that we intended to use a domain that is large enough for the unstable 3D-modulated Rossiter modes to appear, so that we could check whether they would affect the flow in a significant manner; nonetheless, there are no considerable differences between this and the previous frame.

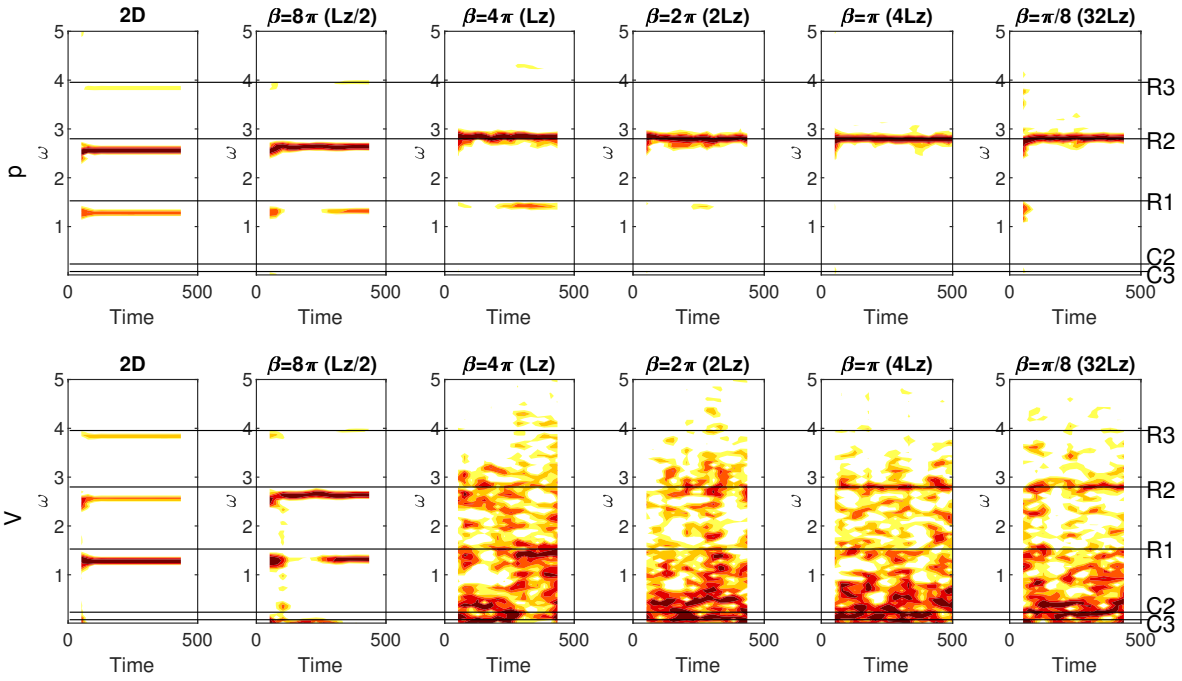


Figure 5.24 – Spectrum of (Top) pressure at the trailing edge and (Bottom) wall-normal velocity inside the cavity as a function of time for case `R+C 3` ($Re_D = 1500$, $D/\theta = 100$, $L/D = 2$, $Ma = 0.5$) for various span-wise domain lengths. Expected frequencies for Rossiter modes are also shown.

The same approach can help to further explore results from case `R+C 2`. Figure 5.25 shows a time series of wall-normal velocity inside the cavity, which is more adequate to capture centrifugal modes in the flow, as opposed to the time series of pressure shown in figure 5.11. There is a peak at $\omega = 0.25$, just below $\omega_{C2} = 0.29$, which was predicted by the linear analysis for centrifugal mode II. By looking at the spectrum as a function of time for this case, in figure 5.26, we can see that, when compared to case `R+C 3`, this time the centrifugal modes can be seen much more clearly.

The two-dimensional spectrum of case `R+C 2` is shown in figure 5.27. It is much clearer than that of case `R+C 3`. This time, the wall-normal velocity probes were able to capture both Rossiter and Centrifugal modes. The largest peak is at $\beta = 0$ and $\omega = 2.7$, corresponding to the second Rossiter mode. The lower frequency peaks, at $\beta = 2\pi$ correspond to centrifugal mode II.

DISTRIBUTION A: Distribution approved for public release. Distribution unlimited

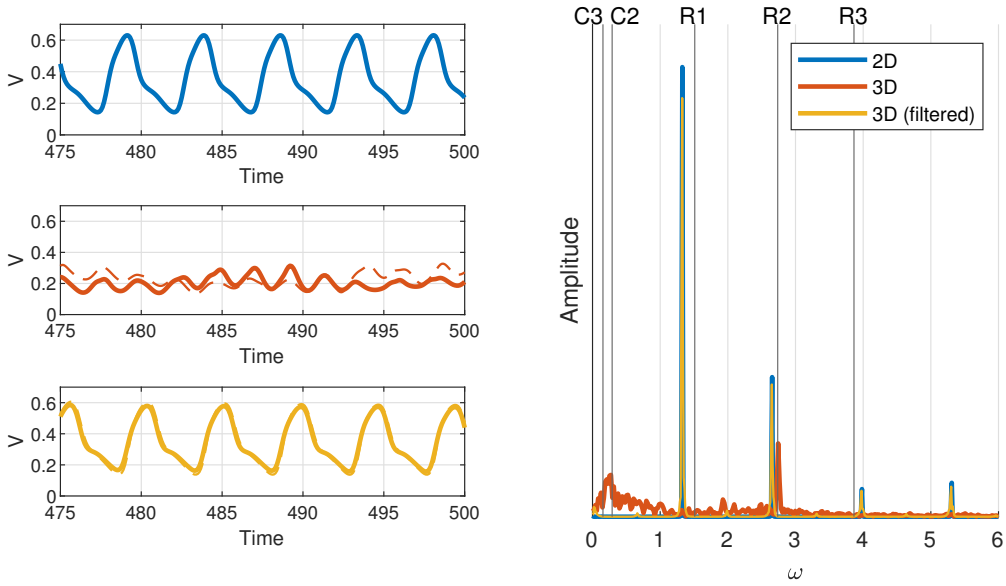


Figure 5.25 – Comparison between 2D and 3D simulations of case `R+C 2` ($Re_D = 1000$, $D/\theta = 100$, $L/D = 2$, $Ma = 0.5$). (Left) Time series of wall-normal velocity inside the cavity. The dashed lines were measured at another span-wise position. (Right) Spectrum. The vertical lines mark angular velocities predicted by the linear stability analysis for each Rossiter mode (R1 through R3) and centrifugal mode (C2 and C3).

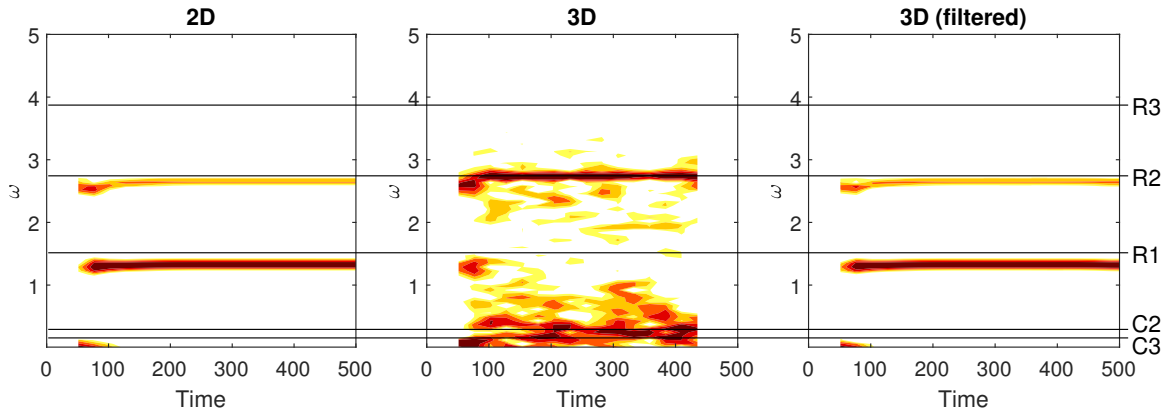


Figure 5.26 – Spectrum of wall-normal velocity inside the cavity as a function of time for case `R+C 2` ($Re_D = 1000$, $D/\theta = 100$, $L/D = 2$, $Ma = 0.5$) for (Left) the 2D simulation, (Center) the 3D simulation and (Right) the filtered 3D simulation. Expected frequencies for Rossiter modes are also shown.

DISTRIBUTION A: Distribution approved for public release. Distribution unlimited

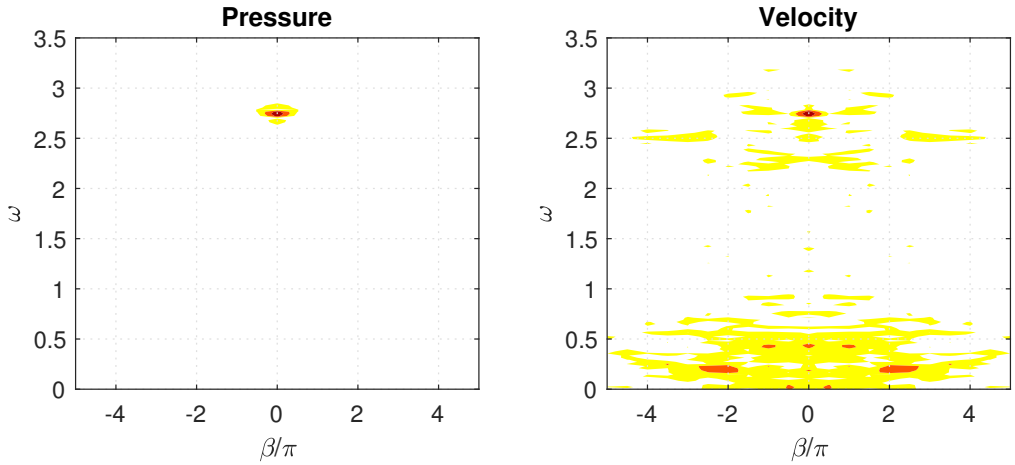


Figure 5.27 – Temporal and span-wise spectrum for the limit cycle of `R+C 2` ($Re_D = 1000$, $D/\theta = 100$, $L/D = 2$, $Ma = 0.5$). (Left) Pressure at the cavity trailing edge (Right) Wall-normal velocity inside the cavity.

DISTRIBUTION A: Distribution approved for public release. Distribution unlimited

5.5 Conclusion

Several parameters govern the flow in an open compressible cavity. Since we focused on Rossiter mode, we set the ratio L/D to 2 to avoid the wake modes that happen at large values of L/D. Our literature review shows that the incoming boundary layer thickness, defined here by D/θ, is often overlooked; only Yamouni, Sipp and Jacquin (2013) shows results for a sweep of this parameter, yet only briefly and used to select one D/θ to be used in their subsequent study. Here, we focus on near-critical conditions, where the global stability analysis is expected to be more meaningful, this also differs from Yamouni, Sipp and Jacquin (2013), who also used 2D LST but investigated very unstable conditions. Our analysis confirmed that the flow stabilizes as D/θ decreases, as expected from the instability of the mixing layer and noted by Yamouni, Sipp and Jacquin (2013). However, we went further to show that the Rossiter mode selection and its hierarchy are governed by the instability of the mixing layer. This was demonstrated by comparing the results of global instability with the results of linear spatial stability of the mixing layer. This explains why thicker mixing layers favor Rossiter modes of lower order, which display lower frequencies. Sarohia (1977) also investigated the possibility that the mixing layer controlled the frequency of the Rossiter mode. But their local analysis results were compared with nonlinear experiments. As will be seen here, this comparison can be misleading.

The analysis revealed that there were essentially two scenarios, one at low and another at high D/θ ratios. We chose a representative D/θ for each scenario and performed a Mach number sweep between 0.1 and 0.9. Yamouni, Sipp and Jacquin (2013) noticed an irregular effect of Mach and argued that this effect was due to the stabilizing effect of Mach number on the mixing layer competing with the destabilizing effect of resonances between Rossiter modes and standing acoustic wave modes. Their scenario corresponded more closely with that of large D/θ. In our work, we demonstrated another effect, which causes the Mach number to have a strong destabilizing effect at the low subsonic range: the increased acoustic emission at higher Mach numbers, which increase the efficiency of the feedback mechanism of Rossiter modes. In this study, we found that the energy transfer increases by about Ma^3 (see also (MATHIAS; MEDEIROS, 2021b)), consistent the cavity noise emission models that apply to this scenario (HOWE, 2004).

The three-dimensional linear stability results revealed two types of unstable three-dimensional modes: span-wise modulated Rossiter modes and centrifugal modes. Despite being essentially two-dimensional, Rossiter modes may also be unstable is slightly modulated in the span-wise direction. On the other hand, centrifugal modes reach their peak instability in smaller wave lengths.

Our non-linear simulations showed that both Rossiter and centrifugal modes may happen at the same time and interact, despite Rossiter modes being much more linearly

DISTRIBUTION A: Distribution approved for public release. Distribution unlimited

unstable and having much higher frequencies than centrifugal modes, under the flow conditions here studied. Under many circumstances, centrifugal modes are very small and difficult to identify but play a vital role in defining the resulting Rossiter modes and their frequencies. In both scenarios we tested in 2D and 3D (namely cases `R+C 2` and `R+C 3`), the 3D simulation remained closer to the predictions given by the linear stability analysis. By closer to the linear prediction, we mean that the dominant mode in the nonlinear simulation was the same as the linearly most unstable. It is interesting to observe that while the 2D mode is much more unstable, the 2D simulation fails to capture even the most elementary features of the flow, for example, the frequency of the oscillation.

A special 3D simulation was also prepared in which centrifugal modes were numerically filtered. This simulation resulted in a flow that is closer to the 2D simulations as opposed to the 3D ones; therefore, we could confirm that the centrifugal modes play an important role in selecting the dominant Rossiter mode. It was also shown that, in comparison with the 2D and the filtered case, the mean flow of the unfiltered 3D simulation was closer to the the base flow, which may partially explain the observation. Yet, LST predicts multiple unstable Rossiter modes (from R1 to R3) and with different dominant mode depending on the flow parameters. However, in the parameter space investigated, the 3D simulations always showed a dominant R2 mode.

DISTRIBUTION A: Distribution approved for public release. Distribution unlimited

DISTRIBUTION A: Distribution approved for public release. Distribution unlimited

Chapter 6

Effects of Gaps on Boundary Layer Transition

6.1 Introduction

We define a gap as a subset of open cavities in which its dimensions are of the same order of magnitude as the boundary layer thickness. In chapter 5, the open cavities were much larger than the boundary layer and ended up dominating the dynamics of the flow. In this chapter, cavities are much smaller and now represent small imperfections on a surface; therefore, we intend to understand the interaction between phenomena in the boundary layer with those of the gap (MATHIAS; MEDEIROS, 2019b; MATHIAS; MEDEIROS, 2021a). Moreover, due to the reduced D/θ ratio of gaps, we expect them to be more globally stable when compared to large cavities.

6.2 Mesh and domain independence

The mesh used in this chapter follows the guidelines presented in section 3.4. For $Re_{\delta_0^*} = 600$, $L = 10$, $D = 5$, $Ma = 0.5$, it contains 450 by 156 nodes in the stream-wise and wall-normal directions, respectively. The minimum spacing is $0.08\delta^*$ in both directions. The mesh is shown in figure 6.1. The top part shows the node spacing for stream-wise (left) and wall-normal (right) directions. The bottom part shows the relative spacing variation from one node to the next. The two valleys in X spacing at the top left figure correspond to the gap's leading and trailing edge.

Similarly to chapter 5, a 6^{th} order spectral-like spatial differentiation is chosen for these simulations, while the time integration is done by the classical 4^{th} order Runge-Kutta

DISTRIBUTION A: Distribution approved for public release. Distribution unlimited

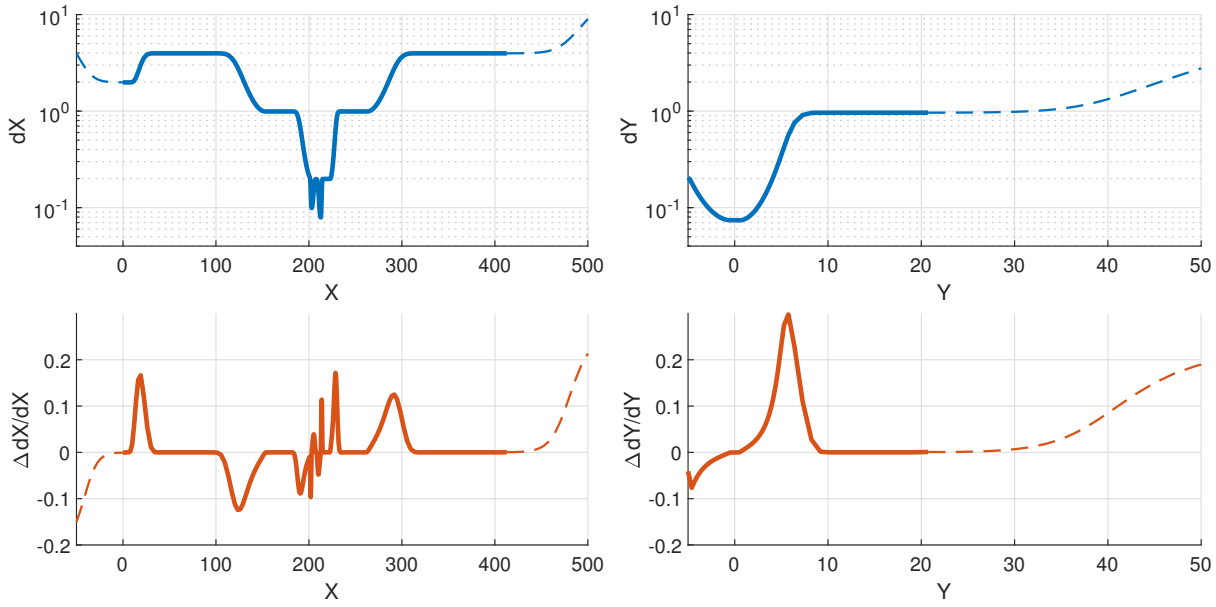


Figure 6.1 – Mesh for the gap simulation with $Re_{\delta_0^*} = 600$, $L/\delta_0^* = 10$, $D/\delta_0^* = 5$, $Ma = 0.5$.

scheme. The anti-aliasing filter coefficient is set to $\alpha = 0.49$ and it is turned off close to the open boundaries, while reduced order schemes, with smaller stencils, are used close to the walls.

All the base flows were obtained by using the techniques described in section 3.5. Figure 6.2 illustrates the base flow for the case mentioned above, while figure 6.3 shows the results of its global stability analysis. This is a stable case, with the first Rossiter mode close to critical stability, its eigenvalue is at $\sigma = -0.0066 \pm 0.02267$.

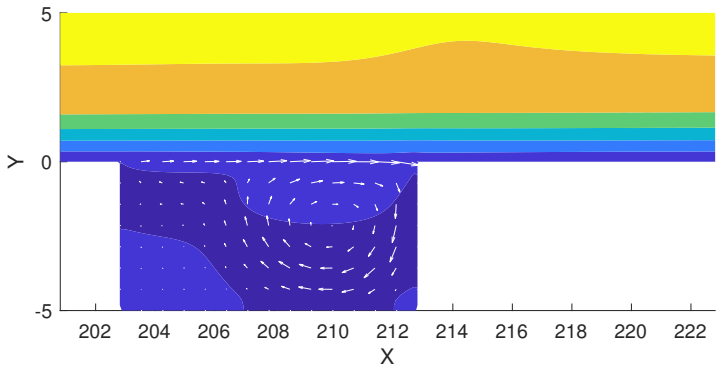


Figure 6.2 – Baseflow at the gap for $Re_{\delta_0^*} = 600$, $L/\delta_0^* = 10$, $D/\delta_0^* = 5$, $Ma = 0.5$. Each contour represents 20% of the free-flow velocity.

DISTRIBUTION A: Distribution approved for public release. Distribution unlimited

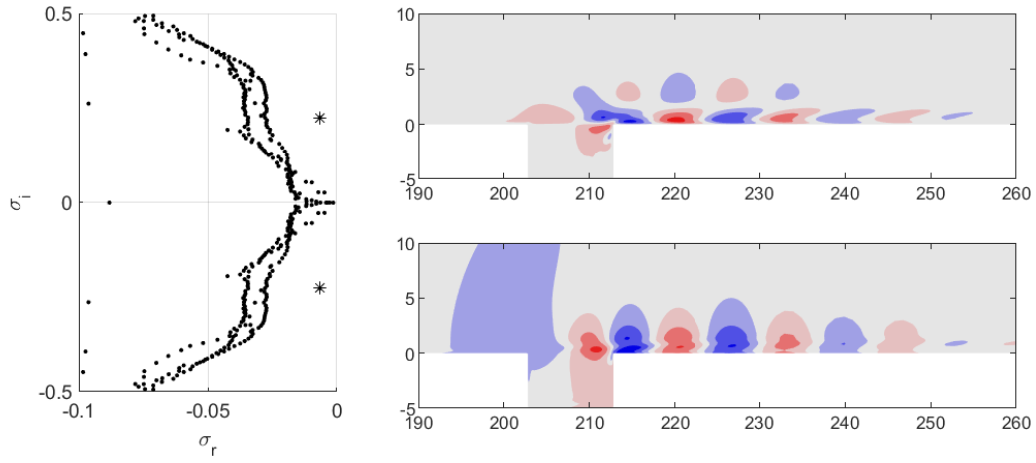


Figure 6.3 – Global stability results for $Re_{\delta_0^*} = 600$, $L/\delta_0^* = 10$, $D/\delta_0^* = 5$, $Ma = 0.5$. (Left) Eigenvalues map with the first Rossiter mode highlighted. (Right) Real part of the eigenfunctions of the first Rossiter mode: (Top) Stream-wise velocity and (Bottom) Density.

6.2.1 Mesh independence

A more refined mesh was constructed to test the solution's independence. The mesh was refined by a factor of two by adding an extra node between each pair of nodes in the original mesh, in both directions. The resulting mesh has roughly four times the number of nodes of the original, with 899×311 nodes. Figure 6.4 compares the eigenvalues of the original mesh to the refined mesh. The first Rossiter mode moves from $\sigma = -0.0066 \pm 0.02267$ to $\sigma = -0.0069 \pm 0.02269$. The difference in the real part was in the 4^{th} decimal place, while the imaginary part has changed in the 5^{th} decimal.

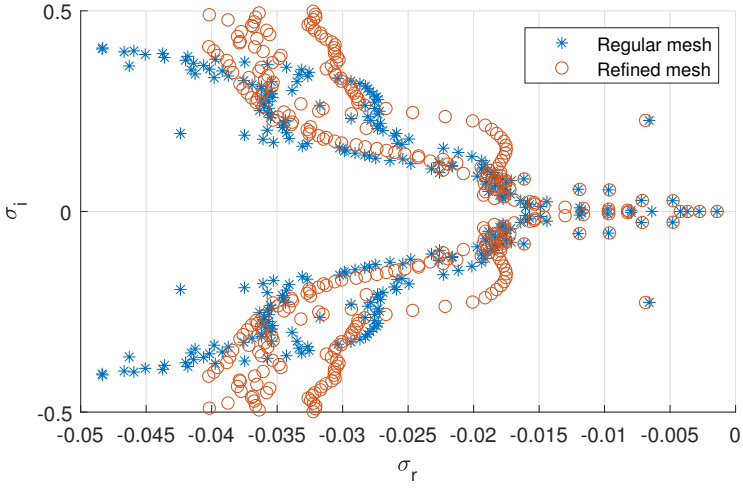


Figure 6.4 – Eigenvalues obtained with the regular mesh compared to those obtained with the refined mesh.

DISTRIBUTION A: Distribution approved for public release. Distribution unlimited

There is a branch of modes that appears in the results of the refined mesh in the region defined by $-0.02 \leq \sigma_r \leq -0.017$ and $0.1 \leq \sigma_i \leq 0.2$ but does not appear when the regular mesh was used. Upon closer inspection, these modes are related to the TS waves downstream from the gap. Capturing such modes is not relevant for this global instability analysis; therefore, this mesh was not required to accurately resolve them. Nonetheless, for the spatial stability analysis shown in this chapter, the mesh refinement in this area was increased according to the guidelines established in section 3.4 as these temporally stable modes may combine in such a way that forms a spatially unstable area (GASTER, 1965). Figure 6.5 exemplifies one of those modes, at $\sigma = -0.0175 \pm 0.155i$.

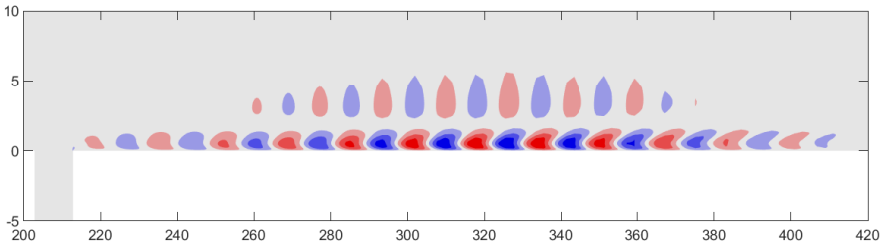


Figure 6.5 – Eigenfunction of stream-wise velocity of the mode at $\sigma = -0.0175 \pm 0.155i$.

6.2.2 Domain independence

Domain independence was tested by changing the SFD filter strength at the open boundaries. After a base flow is reached, this filter is turned on only at the buffer zones and Δ, the parameter which sets the period of the cut-off frequency, is set to infinity, with the intention of damping out all kinds of oscillations before they reach the open boundaries. χ, the parameter that sets the filter strength, must be chosen such that the filter is strong enough to damp incoming waves but not too strong as to reflect those waves. If the buffer zone is large enough, there is a range of χ that is between those two extremes that provides adequate damping for outgoing waves. Furthermore, if the physical domain is large enough, when χ is inside this adequate range, it should not affect the flow solution as well as its modes. Figure 6.6 shows the eigenvalues obtained with various values of χ.

In the range $0 \leq \chi \leq 10^{-3}$, non-physical unstable modes were retrieved by the global stability routine, they are seen in the figure at the $\sigma_r > 0$, $|\sigma_i| < 0.05$ region. The eigenfunction of those modes reveal that they are strongly related to reflections between the inlet and outlet boundaries. As χ increases, those non-physical modes are damped out and the cloud of non-physical modes moves to the left of the complex plane. At $\chi = 10^1$ and larger, the cloud of modes can be seen moving to the right of the complex plane again, indicating that the transition between physical domain and buffer zones became too sudden which causes reflections. It was not possible to run the routine with $\chi > 10^2$, as the buffer zone became too stiff and caused numerical instabilities.

DISTRIBUTION A: Distribution approved for public release. Distribution unlimited

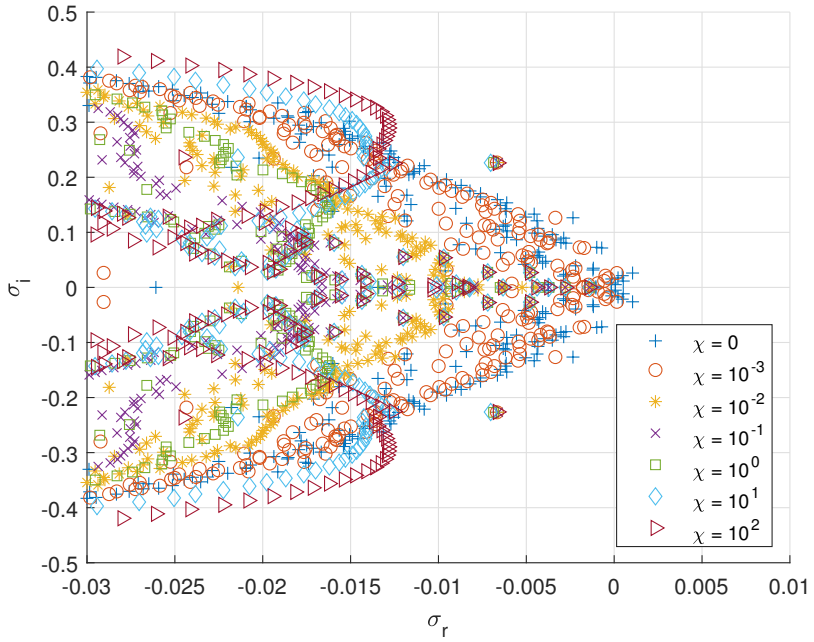


Figure 6.6 – Eigenvalues obtained with various values of χ in the SFD filter.

In the range $10^{-2} \leq \chi \leq 10^{0}$, the cloud of non-physical modes is well into the stable region, leaving only the physical modes, which are mostly unaffected by χ in this range. Therefore, we conclude that the result depends neither on the physical domain size nor on the filter strength used, as long as χ is in the range $10^{-2} \leq \chi \leq 10^{0}$. For the rest of this chapter, we use $\chi = 10^{-1}$.

6.3 Effects of the gap on the boundary layer momentum and displacement thicknesses and spatial stability

Figure 6.7 compares the boundary layer displacement (δ^*) and momentum (θ) thickness for the reference case with and without the gap, the flow parameters are $Re_{\delta_0^*} = 600$, $L = 10$, $D = 5$, $Ma = 0.5$, which correspond to $L/D = 2$, $D/\theta = 13$ and $Re_D = 3000$. The effect is mostly localized at the gap and immediately downstream, with a localized reduction of the displacement thickness and, consequently, the shape factor $H = \delta^*/\theta$. Further downstream, the effect on H is negligible and the only long-term effect of the gap is a slight downstream shift of $0.9\delta^*$ of both thickness profiles.

To measure the effect of the cavity on the spatial stability, we disturbed the flow with a wave packet, constructed in the same manner as done by Martinez and Medeiros (2016). 25 angular frequencies, linearly distributed in the range $0.02 \leq \omega \leq 0.5$ are used to build this wave packet, its amplitude being smaller than 10^{-6} to keep it in the linear

DISTRIBUTION A: Distribution approved for public release. Distribution unlimited

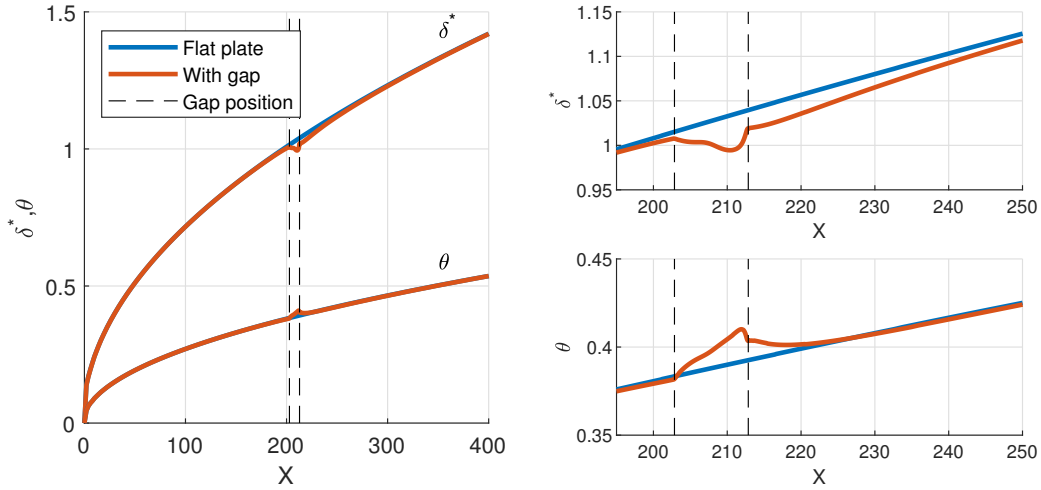


Figure 6.7 – Boundary layer displacement and momentum thickness with and without the gap for the following parameters: $Re_{\delta_0^*} = 600$, $L = 10$, $D = 5$, $Ma = 0.5$

regime.

Figure 6.8 (Left) shows the pressure at wall height at various points across the flat plate. x_c marks the gap leading edge and the distance from it is measured in terms of δ_0^*. It is possible to observe a very subtle increase in the amplitude downstream from the gap as well as a small change in phase.

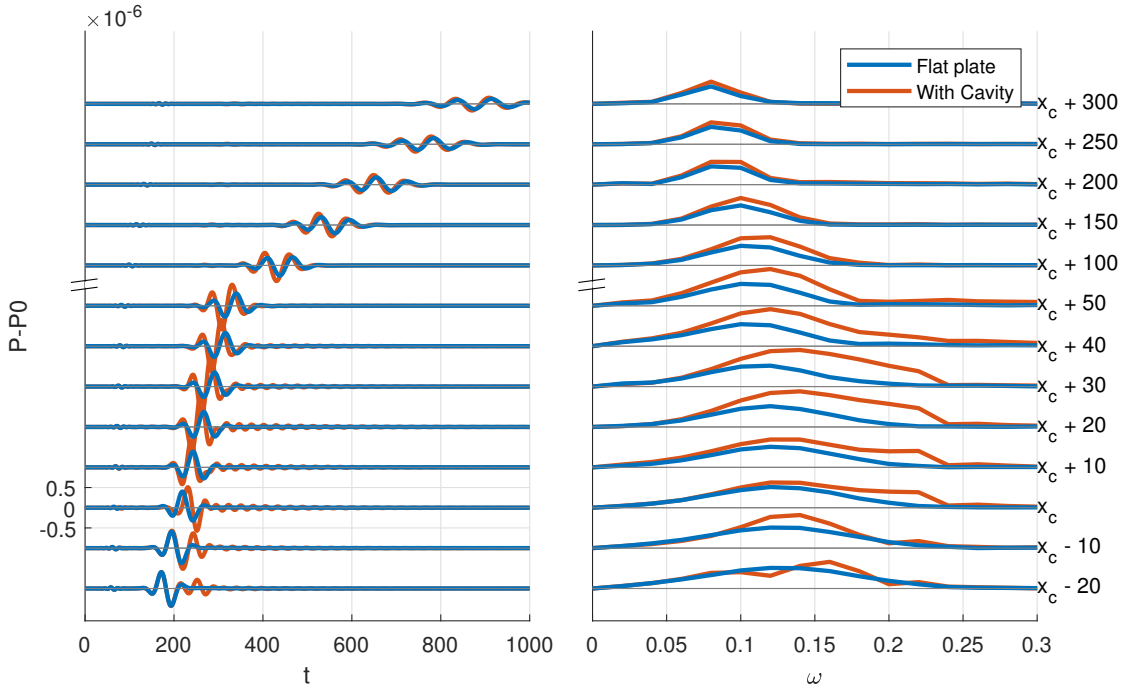


Figure 6.8 – (Left) Temporal evolution of the wave packet with and without the gap. (Right) Spectrum of the wave packet at each probe.

A spectral analysis of the wave packet at the various probes, shown in figure 6.8 (Right), revealed that, due to the spatial stability of the boundary layer, frequencies in the

DISTRIBUTION A: Distribution approved for public release. Distribution unlimited

range $0.05 \leq \omega \leq 0.2$ dominate the flow close to x_c, and that the gap has impacted mostly the higher end of this range. It is also possible to see that immediately downstream of the gap, there is a secondary peak at $\omega = 0.22$, which matches the least stable Rossiter mode revealed by the global stability analysis that will be shown in section 6.4. However, this secondary peak is quickly damped out due to being in the spatially stable range. Looking back at figure 6.8 (Left), the probes that are close to the gap keep showing high-frequency oscillations after the wave packet has passed. In the two probes that are placed upstream from the gap, we can also observe the wave packet was partially reflected by it, these probes also show the acoustic emission of the Rossiter modes, explaining the slight peak at $\omega = 0.22$ in their spectra. In the long-term, at $x_c + 300$, the dominant frequency was $\omega = 0.08$, at which the amplitude of the wave packet was 25% larger when the gap was present.

After the wave packet passed, the gap kept oscillating at the frequency of Rossiter mode 1, which was deemed the most unstable by the global stability analysis. Figure 6.9 shows filled contours of density (Top) and stream-wise velocity (Bottom) fluctuations at the gap. In the left-hand side, time $t = 250$ is shown, just when the wave packet is passing over the gap. In the right-hand side, $t = 500$ is shown, when the wave packet is well past the gap and the remaining oscillation can be seen. The black and white lines on the right-hand side images show positive and negative oscillations of both variables as predicted by the global stability analysis, which are remarkably similar to the oscillation that has remained in the gap after the wave packet has passed, including the acoustic emission. It is concluded that TS waves can excite modes in the gap.

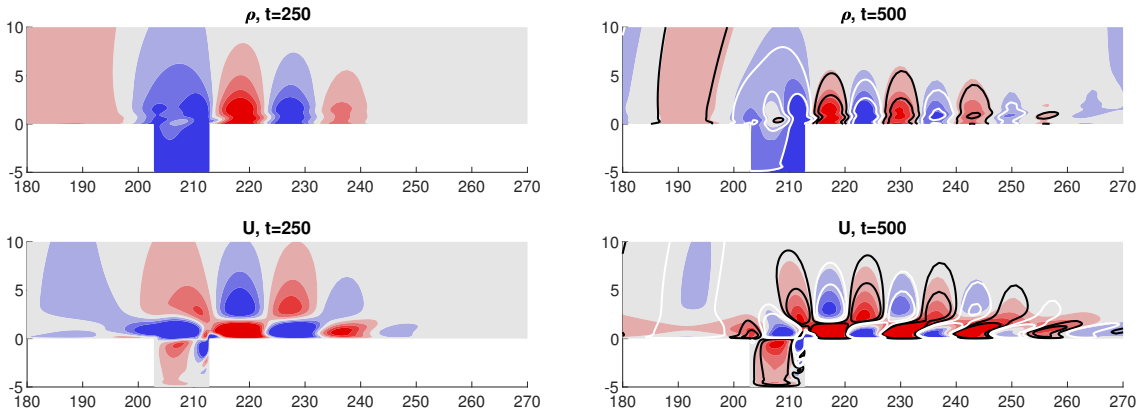


Figure 6.9 – Density (Top) and stream-wise velocity (Bottom) fluctuations at times $t = 250$ (Left) and $t = 500$ (Right). Red and blue areas represent positive and negative oscillations of the flow, respectively. Black and white lines represent the positive and negative oscillations predicted by the global stability analysis, note that the phase and levels were shifted to match the flow's.

DISTRIBUTION A: Distribution approved for public release. Distribution unlimited

6.4 Two-dimensional global stability

Considering the reference case above, we changed its parameters individually in order to observe the influence of each of them on the global stability. Special attention was given to the Mach number. Figure 6.10 (Left) shows the eigenvalues as the Mach number was increased from 0.3 up to 0.8 (Cases `Ma03` to `Ma08`). There is a peak in the stability at $Ma = 0.8$, similar to what was observed for larger cavities (MATHIAS; MEDEIROS, 2021b). Figure 6.10 (Right) shows the eigenvalues for variations in gap length, from 10 to 20 (Cases `L10` to `L20`). The flow becomes unstable for $L \geq 15$, when the second Rossiter mode has $\sigma_r > 0$. In chapter 5 and in (MATHIAS; MEDEIROS, 2021b), we have established that the mixing layer stability plays a very important role in selecting the most unstable Rossiter mode due to a preferred band of frequencies that has the greatest spatial amplification in the mixing layer. Another phenomenon that has a strong destabilizing effect on these modes is the resonance with standing wave modes in the gap (YAMOUNI; SIPP; JACQUIN, 2013; PLUMBLEE; GIBSON; LASSITER, 1962), also consistent with the results from large cavities.

The values of Re_{δ^*} just upstream of the gap indicate that the flow would remain laminar if not for the addition of the gap. In this scenario, increasing the values of Re_{δ^*}, which destabilizes the boundary layer, means that the ratio D/δ^* also increases, which stabilizes the global modes of the gap. A similar comparison can be made for the Mach number, which stabilizes the boundary layer (in the subsonic range used in this study) but destabilizes the flow in the gap.

In all scenarios presented in this chapter, it is possible to observe a trend that the most unstable Rossiter modes are always in the $0.2 \leq \sigma_i \leq 0.3$ range. These angular velocities are higher than the unstable range for TS waves.

Two other scenarios were tested for their global stability. When the Reynolds number, based on δ_0^* was increased from 600 to 1000, the flow has remained stable, but by a smaller margin, as the real part of the Rossiter mode eigenvalue changed from $\sigma_r = -0.0066$ to $\sigma_r = -0.0021$. On the other hand, increasing the gap depth from 5 to 10 δ_0^* has caused this mode to become slightly unstable ($\sigma_r = 0.0017$).

DISTRIBUTION A: Distribution approved for public release. Distribution unlimited

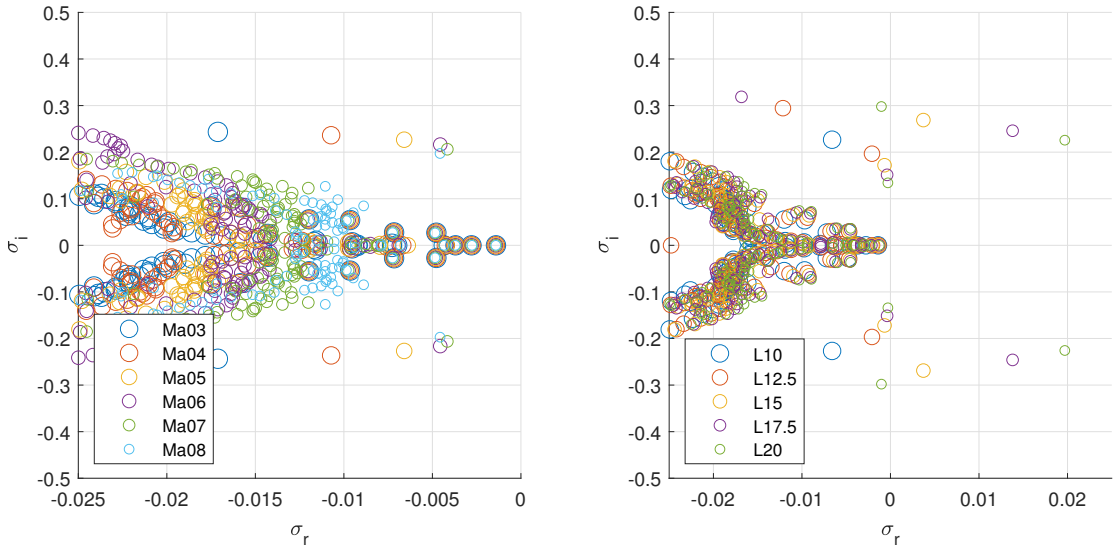


Figure 6.10 – (Left) Effect of the Mach number on the eigenmodes. (Right) Effect of gap length on the eigenmodes.

6.5 Three-dimensional global stability

Three-dimensional modes are also of concern in gaps, as they may cause oscillations that might eventually evolve into turbulence. We have used our LST routine to compute the global modes at various span-wise wave numbers ($\beta = 2\pi/L_Z$). The amplification rate of the most unstable mode at each value of β for three different Reynolds numbers is shown in figure 6.11. At $Re_{\delta^*} = 400$, the flow is stable. At $Re_{\delta^*} = 600$, the centrifugal mode II became unstable, at $\beta = 0.4\pi$. At $Re_{\delta^*} = 1000$, centrifugal mode I is also unstable. In all three cases, two-dimensional modes have remained stable.

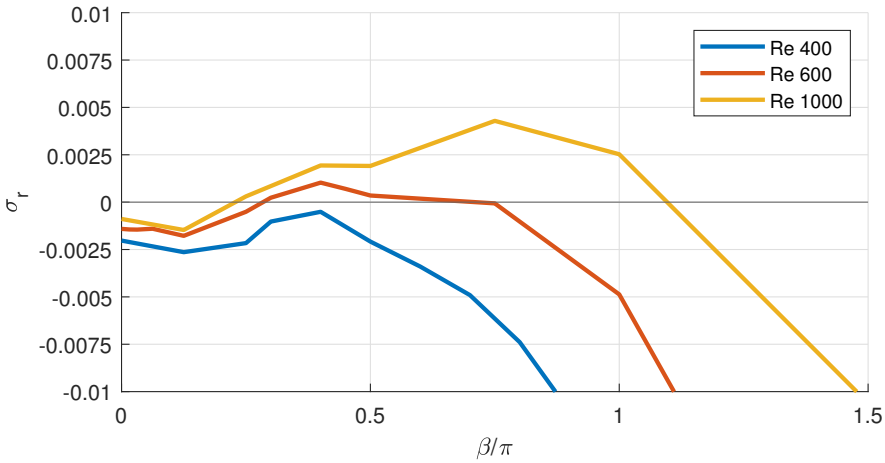


Figure 6.11 – Amplification rate of the leading mode for the parameters $L = 10$, $D = 5$, $Ma = 0.5$ and $Re_{\delta_0^*} = 400$, 600, 1000 at various span-wise wave numbers

The three types of centrifugal modes shown by Brès and Colonius (2008) can be

DISTRIBUTION A: Distribution approved for public release. Distribution unlimited

found in our results. At $Re_{\delta_0^*} = 1000$, $L = 10$, $D = 5$ and $Ma = 0.5$, for example, Mode I is the leading mode at $\beta = 3\pi/4$; its eigenvalue is $\sigma = -6 \times 10^{-5} \pm 0i$, which puts it very close to critical stability. At $\beta = \pi/2$, mode II leads the flow with $\sigma = 4 \times 10^{-4} \pm 0.016i$, making it slightly unstable. Mode III is leading at $\beta = \pi/4$, with $\sigma = -5 \times 10^{-4} \pm 0.007i$. The eigenfunctions of these modes are shown in figure 6.12.

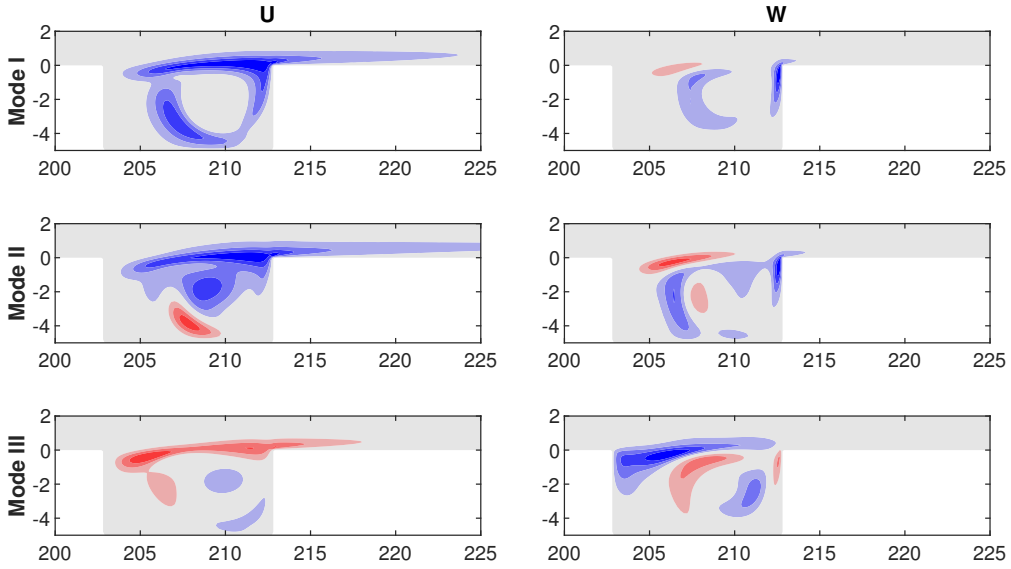


Figure 6.12 – Centrifugal modes I, II and III for $Re_{\delta_0^*} = 1000$, $L = 10$, $D = 5$ and $Ma = 0.5$. $\beta = 3/4\pi$, $\pi/2$ and $\pi/4$, respectively. (Left) Stream-wise velocity. (Right) Span-wise velocity.

We performed a sweep of gap sizes to access its impact on 2D and 3D instabilities. Reynolds number is fixed at $Re_{\delta_0^*} = 600$ and Mach number, at $Ma = 0.5$. Figure 6.13 shows the type of linear instabilities that appear for each combination of L and D. As Reynolds number based on boundary layer thickness is fixed, by increasing the ratios L/δ_0^* or D/δ_0^*, we also increase the Reynolds number based on gap length or depth, respectively. Generally, the flow becomes unstable for either $L/\delta_0^* \geq 7.5$ or $D/\delta_0^* \geq 3$. In the figure, each symbol represents that either 2D or 3D modes were found to be unstable at each point of the parametric space. The number besides the marker indicates which unstable centrifugal or Rossiter modes were found, in decreasing order of amplification rate.

Sarohia (1977) presents a similar diagram with experimental results of L and D that caused oscillations in the gap. He found that the cavity oscillates for $L\sqrt{Re_{\delta_0^*}}/\delta_0^* > 300$. In our analysis, at $Re_{\delta_0^*} = 600$, this limit corresponds to $L/\delta_0^* > 12.2$, which is approximately where both Rossiter and centrifugal modes become unstable. These results can also be compared to those of Beguet et al. (2017) and Crouch, Kosorygin and Sutanto (2020), shown in figure 2.7, in which they have found that bypass transition occurs for either $L/\delta_0^* > 18$ or $D/\delta_0^* > 2$. These figures are not directly comparable, due to different Reynolds and,

DISTRIBUTION A: Distribution approved for public release. Distribution unlimited

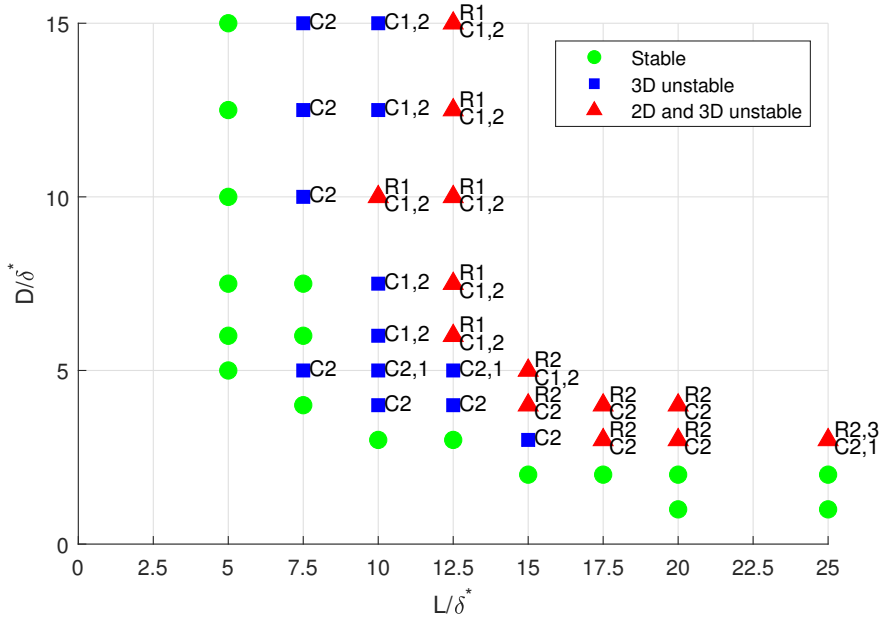


Figure 6.13 – Types of instabilities found for various combinations of gap length and depth, at $Re_{\delta_0^*} = 600$ and $Ma = 0.5$. The numbers beside the markers indicate which types of unstable centrifugal modes were found, in decreasing order of amplification rate.

especially, Mach numbers, which were much lower than 0.5 in their experiments.

By approaching the unstable region of the figure at a fixed value of D/δ_0^*, say 10, and increasing the value of L/δ_0^*, the first unstable mode that is encountered is C2. As L/δ_0^* is increased further, C1 then becomes unstable and may reach growth rates larger than those of C2. Finally, R1 becomes unstable. At much larger values of L/δ_0^*, R2 becomes the leading mode of the flow. This switch from R1 to R2 happens for the same reason we have noted in figure 6.10: The mixing layer selects modes with angular velocities in the range $0.2 \leq \omega \leq 0.3$, which corresponds to different Rossiter modes as L changes. This is due to this range of ω corresponding to vortices of a certain range of sizes, therefore, depending on the length of the cavity, different amounts of vortices will fit between the leading and the trailing edge.

On the other hand, if we fix the value of L/δ_0^*, say 20, and increase D/δ_0^*, both Rossiter and centrifugal modes become unstable at about the same value of D. The dominant Rossiter mode is dependent on the value of L, while centrifugal mode 2 was always dominant for the range of parameters we have used.

Larger gaps are usually more unstable, as can be expected by the greater Reynolds number with respect to either the gap's length or depth. One exception to this rule is the point at $L/\delta_0^* = 7.5$ and $D/\delta_0^* = 7.5$, which is stable, despite the unstable centrifugal mode found in point $L/\delta_0^* = 7.5$ and $D/\delta_0^* = 5$. The reason for this is still unclear but suggests that the ratio L/D also plays a role in this situation; nonetheless, both cases are very

DISTRIBUTION A: Distribution approved for public release. Distribution unlimited

close to the neutral stability. In our parametric space, no combinations of L and D were found to produce unstable 2D and stable 3D modes. However, this may not always be the case as, by increasing the Mach number, Rossiter modes destabilize, while centrifugal modes are mostly unaffected.

6.6 Direct Numerical Simulation of three-dimensional modes

As an example, we simulated the $Re_{\delta_0^*}$, $L = 10$, $D = 5$ and $Ma = 0.5$ case until the limit cycle was reached. This case has two types of unstable centrifugal mode. C2 has its peak instability at $\beta = 0.4\pi$, when $\sigma = 0.001 \pm 0.017i$; and C1 is most unstable at $\beta = 0.6$, with $\sigma = 6 \times 10^{-4} \pm 0i$. The simulation was done with a span-wise period of $L_Z = 20$, which is equivalent to $\beta = 0.1\pi$, therefore it is enough for four periods of C2 and six of C1. Figure 6.14 shows isosurfaces of stream-wise and span-wise velocity fluctuations in this case. Note that, for clarity, only a quarter of the span-wise domain is shown here. The angular velocity and span-wise wave numbers indicate that C2 was dominant in this case. The same conclusion can be reached by comparing the snapshots to the eigenmodes (see figures 6.11 and 6.12). The maximum velocity fluctuation in these snapshots was 3% of the free-stream velocity.

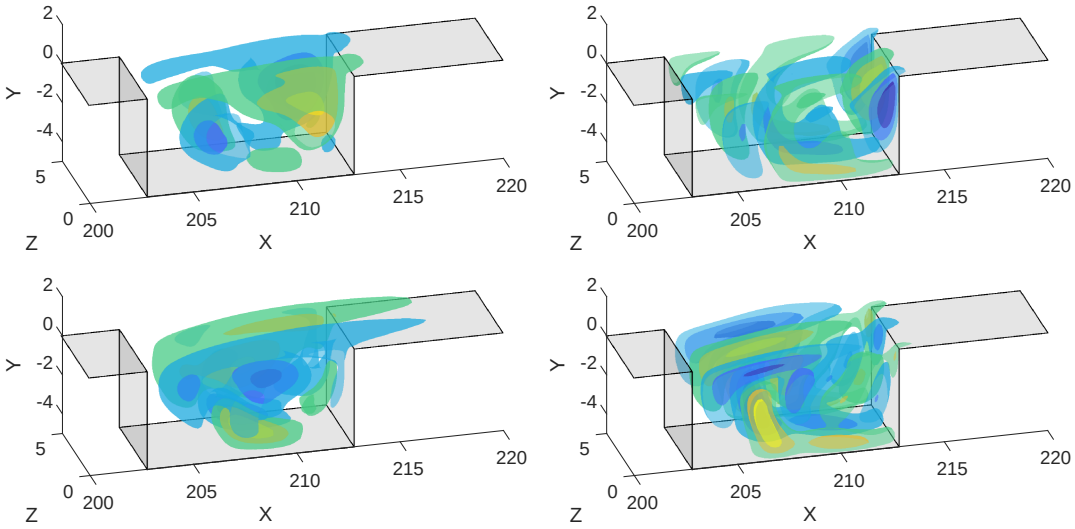


Figure 6.14 – Isosurfaces of (Left) stream-wise and (Right) span-wise velocity fluctuations at two different times (Top and Bottom) for the $Re_{\delta_0^*}$, $L = 10$, $D = 5$ and $Ma = 0.5$ case. Only a quarter of the span-wise domain is shown for clarity.

Figure 6.15 shows the time series of pressure at the trailing edge of the cavity at two different span-wise positions and the corresponding spectrum. The peak is at $\omega = 0.015$, slightly below the linearly predicted value of $\omega = 0.017$ for C2. The 2D spectrum can be seen in figure 6.16, it shows a very clear peak at $\omega = 0.015$, $\beta = 0.4\pi$, which corresponds

DISTRIBUTION A: Distribution approved for public release. Distribution unlimited

to C2, confirming the observations from figure 6.14. The other peaks in the spectrum are harmonics of the first peak.

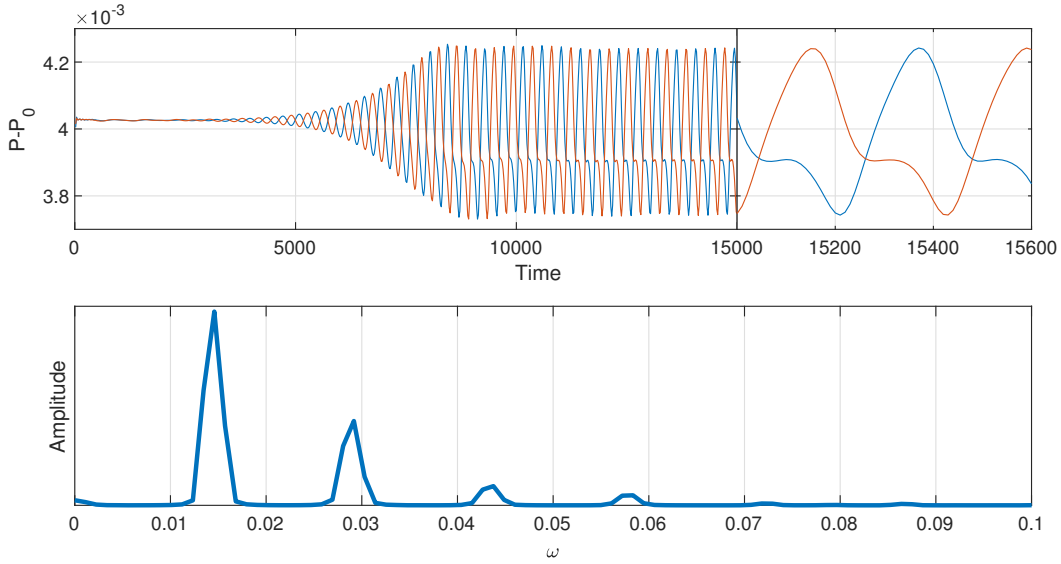


Figure 6.15 – (Top) Temporal series of pressure at the trailing edge of the gap at two different span-wise positions, at opposite phases for the $Re_{\delta_0^*}$, $L = 10$, $D = 5$ and $Ma = 0.5$ case. (Bottom) Spectrum of the limit cycle.

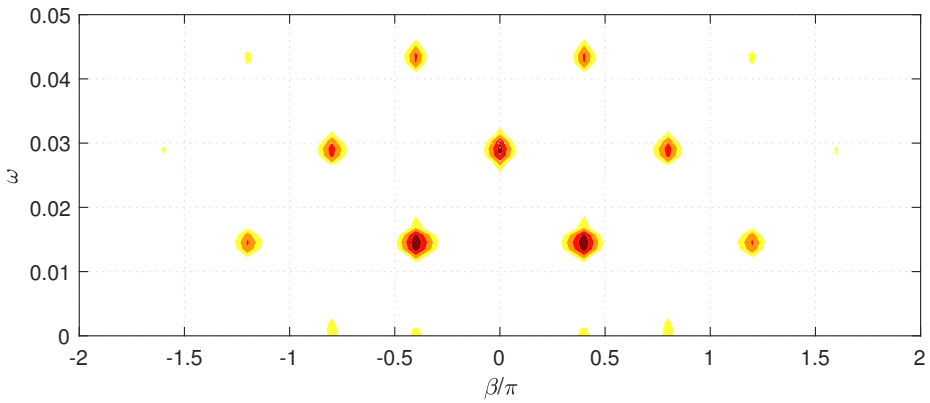


Figure 6.16 – Temporal and span-wise spectrum for the limit cycle of the $Re_{\delta_0^*}$, $L = 10$, $D = 5$ and $Ma = 0.5$ case.

In figure 6.17, we compare the boundary layer thickness of the base flow against the values obtained in the limit cycle. The yellow region represents the range of thickness values from both snapshots at all span-wise positions. The centrifugal modes had a greater effect on the displacement thickness, which, nonetheless, varied by less than 1% downstream of the gap. The mean flow, not shown in the figure, differs from the base flow by less than 0.1% after the gap.

DISTRIBUTION A: Distribution approved for public release. Distribution unlimited

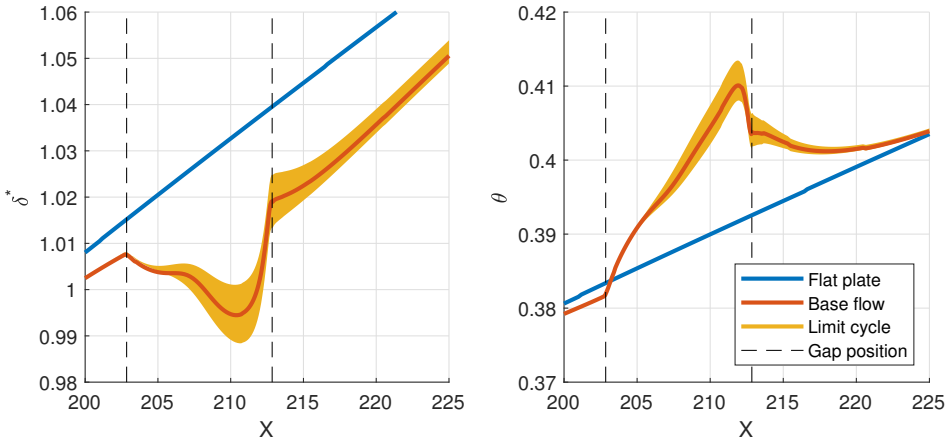


Figure 6.17 – Boundary layer displacement and momentum thickness of the base flow and of the limit cycle $Re_{\delta_0^*} = 600$, $L = 10$, $D = 5$, $Ma = 0.5$

6.7 Conclusion

We simulated gaps with various combinations of Reynolds and Mach numbers and different L/δ_0^* and D/δ_0^* ratios. If Reynolds and Mach numbers are sufficiently high, the flow becomes globally unstable and oscillates even when external disturbances cease.

In the stable cases, i.e., when no globally unstable modes are present, a static base flow was obtained, and the wave packets we have introduced in the simulation indicated that the boundary layer instability interacts with shallow cavities in a way that favors some frequencies. It is expected that the localized change in the boundary layer, shown by Worner, Rist and Wagner (2003) for small bumps, also plays a role for gaps. Another effect is the interaction with Rossiter modes, that can be excited by the passing wave packet and remain oscillating; however, if these modes are stable, they will eventually decay.

Globally unstable gaps can happen at values of Re_δ^* below critical stability for the TS waves. By moving the gap downstream, while keeping its dimensions constant, the value of Re_δ^* would increase, due to the growth of the boundary layer; however, the gap's global modes would also become more stable, due to the the stabilizing effect of decreasing L/δ_0^* and D/δ_0^* ratios. In a similar manner, decreasing the Mach number, which destabilizes the boundary layer, has the opposite effect on the gap, and causes it to become more stable.

When the flow is non-dimensionalized by the free-stream velocity and by δ_0^*, the most unstable Rossiter modes happen in the $0.2 \leq \omega \leq 0.3$ angular velocity range, which does not match the spatially unstable range of TS waves in our parametric space. Nevertheless, there may exist a flow that makes both frequency ranges overlap, increasing the potential interaction of the modes, perhaps by adding a pressure gradient or at a specific combination of Mach number and gap length. We leave this as a suggestion for

DISTRIBUTION A: Distribution approved for public release. Distribution unlimited

future works.

We performed a sweep of L/δ_0^* and D/δ_0^*, which indicate that there are maximum values of either parameter that keep the flow stable. Similarly, Beguet et al. (2017), Crouch, Kosorygin and Sutanto (2020) have found that there are thresholds of both L and D that when either one is crossed, the gap causes a bypass transition in the boundary layer. Further investigation is needed to determine the combination and the amplitude of modes that cause this bypass transition.

DISTRIBUTION A: Distribution approved for public release. Distribution unlimited

DISTRIBUTION A: Distribution approved for public release. Distribution unlimited

Chapter 7

Discussion and Final Remarks

In this thesis, we have implemented and used computational tools to analyze the stability characteristics of open cavities in a subsonic, compressible flow. Such geometry can be used as a simple representation of multiple types of real-world scenarios. Understanding the stability characteristics of a flow in such geometries is of fundamental importance to improve the aerodynamic performance of new aircraft or other vehicles.

7.1 Direct Numerical Simulation

Two main computational routines are used in this work: a Direct Numerical Solver (DNS) and a Linear Stability Theory routine (LST). In chapter 3, our Direct Numerical Simulation code was presented. It was based on the previous code used by the research group, but completely rewritten. Matlab® and Fortran were used to combine the strengths of each language. The preprocessing is completely done in Matlab®, which allows for great flexibility when setting up each case for simulation. The flow simulation is done by the Fortran part of the code, which is parallelized by MPI. Its modularity was always kept in mind, which allowed the code to be adapted and used by the rest of the research group in their own simulations. Compared to the previous code, the computational cost was reduced in half.

7.2 Linear Stability Analysis

In chapter 4, we show the implementation of our Linear Stability Theory routine, which is of the time-stepping type. This routine is able of computing the global stability modes of a flow without directly using its Jacobian matrix. Instead, the algorithm uses

DISTRIBUTION A: Distribution approved for public release. Distribution unlimited

the flow solver itself to build a reduced order approximation of the Jacobian matrix. In our literature review, there was very little in terms of guidelines for the parameters that must be chosen when setting up the method.

We developed equations to predict the effect of grid dimension, DNS noise floor, order of the Fréchet derivative approximation, disturbance magnitude, and integration time on the error. This includes the following sources of error: discretization of the solver, truncation of the Fréchet derivative approximation, and nonlinearities. We developed equations and guidelines for optimal selection of parameters and showed that they change substantially with grid size and solver accuracy. We concluded that, under optimal conditions, first order accurate Fréchet derivative approximation may be all that is needed for reasonable precision. This is particular true with open flow instability studies because the effect of different implementation of equally sound representations of a boundary condition at infinity may easily lead to variations of 10^{-3} in eigenvalue estimates (OHMICHI; SUZUKI, 2016). Moreover, optimal parameters for accuracy also lead to lowest cost for a given accuracy. Under optimal conditions, the total computational cost scales linearly with the Krylov span dimension, M; super-linear costs are negligible and progressively smaller as the grid increases, such as for three-dimensional cases. Optimal parameters for most accurate eigenvalues also lead to most accurate eigenfunctions.

7.3 Cavities

We have used our global stability code to access the instability of both Rossiter and centrifugal modes at different combinations of parameters such as incoming boundary layer thickness, free-flow Mach number and domain span-wise length. Then, we used our DNS to simulate these flows in 2 and 3 dimensions to compare the nonlinear results to linear predictions.

For 2D cavities, close to the critical conditions, increasing the ratio D/θ destabilizes the flow. We observed two scenarios, one with low and another with high D/θ ratios, which result in different Rossiter modes dominating the flow. The dominating Rossiter mode is selected by the mixing layer.

The Mach number has a, predominantly, destabilizing effect on both D/θ scenarios, which is associated to an increased acoustic emission. This destabilizing effect is more pronounced at lower Mach numbers and the amplification rates have saturated around $Ma = 0.5$ in our parametric space. Some higher-order Rossiter modes have an irregular relation with the Mach number, which is due to interaction with standing acoustic waves in the cavity.

Rossiter modes are essentially 2D and have amplification rates much higher than

DISTRIBUTION A: Distribution approved for public release. Distribution unlimited

centrifugal modes, which are 3D. Therefore, it would be reasonable to assume that a 2D simulation might be adequate in this scenario. Nevertheless, in general, 3D simulations may differ considerably from 2D ones. In 3D simulations, the frequency and the dominant modes tend agree better with the LST. We observed that the 2D and 3D simulations modify the base flow in different ways, resulting in distinct mixing layers, which ultimately may select different dominant modes. Still, not all modes predicted by the LST were seen, as all our simulations were dominated by a single Rossiter mode at a time.

7.4 Gaps

For gaps dimensions that can be observed on a wing, there are Rossiter and centrifugal modes that become unstable at Re_θ values that are remarkably low and still well into the laminar region of the boundary layer. They possibly cause bypass transition (there is evidence from experiments by Crouch, Kosorygin and Sutanto (2020) and simulations in the group), but the transition itself was not the scope of this study. The destabilizing effect of Mach number is also observed in gaps, with important implications, as airplanes fly at higher Mach numbers, and the current approach in industry apparently does not take that into account.

LST reveals that both Rossiter and centrifugal can be unstable in gaps. By sweeping L and D, a boundary of instability appeared and was consistent with experimental observations of transition in low-speed wind tunnels ($Ma < 0.1$). A sharp boundary of instability at $L/\delta_0^* = 7.5$ and $D/\delta_0^* = 3$ was observed in close correspondence with low-speed experiments. (SAROHIA, 1977; BEGUET et al., 2017; CROUCH; KOSORYGIN; SUTANTO, 2020)

The study showed different hierarchies of instability with different Rossiter and centrifugal modes becoming dominant. The hierarchy was very sensitive to the L/D ratio. By reaching the L/δ_0^* threshold, centrifugal modes became unstable before Rossiter modes, while at the D/δ_0^* threshold, both modes became unstable at the same time.

7.5 Suggestion for future works

Regarding the interaction of Rossiter and centrifugal modes, it is possible that the instability of the mean flow in time and span is not enough to capture all the physics, therefore analyzing the stability of Rossiter modes at different phases of the centrifugal mode cycle may improve our understanding of this phenomenon.

For more unstable flows, it is progressively more difficult to identify the centrifugal mode, but within our parameter space they play a very important role even if they are

DISTRIBUTION A: Distribution approved for public release. Distribution unlimited

only marginally unstable. Analysis such as a Spectral Proper Orthogonal Decomposition (SPOD) might shed a light on which modes are present when the flow is fully developed. (SCHMIDT; COLONIUS, 2020)

There are many geometric aspects of gaps that can be further explored, such as asymmetry in the leading and trailing edge heights. Moreover, by further increasing the gap length, its behavior may change, as wake modes should start to dominate the flow instead of Rossiter modes.

Finally, we also suggest that the simulation domain could be increased as to also contain the transition. This way, it would be possible to measure how much the existence of unstable Rossiter or centrifugal modes could impact the actual transition to turbulence.

DISTRIBUTION A: Distribution approved for public release. Distribution unlimited

Bibliography

ÅKERVIK, E. et al. Steady solutions of the Navier-Stokes equations by selective frequency damping. **Physics of Fluids**, v. 18, n. 6, p. 68–102, 2006. ISSN 10706631. Available from Internet: <http://scitation.aip.org/content/aip/journal/pof2/18/6/10.1063/1.2211705>.

ARNOLDI, W. E. The principle of minimized iterations in the solution of the matrix eigenvalue problem. **Quarterly of Applied Mathematics**, v. 9, n. 1, p. 17–29, 1951.

BAGHERI, S.; ÅKERVIK, E.; BRANDT, L.; HENNINGSON, D. S. Matrix-Free Methods for the Stability and Control of Boundary Layers. **AIAA Journal**, v. 47, n. 5, p. 1057–1068, may 2009. ISSN 0001-1452. Available from Internet: <https://arc.aiaa.org/doi/10.2514/1.41365>.

BARKLEY, D.; BLACKBURN, H. M.; SHERWIN, S. J. Direct optimal growth analysis for timesteppers. **International Journal for Numerical Methods in Fluids**, v. 57, n. 9, p. 1435–1458, jul 2008. ISSN 02712091. Available from Internet: <http://doi.wiley.com/10.1002/fld.1824>.

BEGUET, S.; PERRAUD, J.; FORTE, M.; BRAZIER, J.-P. Modeling of Transverse Gaps Effects on Boundary-Layer Transition. **Journal of Aircraft**, v. 54, n. 2, p. 794–801, 2017. ISSN 0021-8669. Available from Internet: <https://arc.aiaa.org/doi/10.2514/1.C033647>.

BERGAMO, L. F.; GENNARO, E. M.; THEOFILIS, V.; MEDEIROS, M. A. Compressible modes in a square lid-driven cavity. **Aerospace Science and Technology**, Elsevier Masson SAS, v. 44, p. 125–134, jul 2015. ISSN 12709638. Available from Internet: <https://linkinghub.elsevier.com/retrieve/pii/S1270963815001030>.

BLOCK, P. J. W. **Noise response of cavities of varying dimensions at subsonic speeds**. [S.l.], 1976. 1–36 p.

BRÈS, G. A.; COLONIUS, T. Three-dimensional instabilities in compressible flow over open cavities. **Journal of Fluid Mechanics**, v. 599, p. 309–339, mar 2008. ISSN 0022-1120. Available from Internet: <http://www.journals.cambridge.org/abstract_S0022112007009925>.

BRYNJELL-RAHKOLA, M.; SHAHRIARI, N.; SCHLATTER, P.; HANIFI, A.; HENNINGSON, D. S. Stability and sensitivity of a cross-flow-dominated Falkner–Skan–Cooke boundary layer with discrete surface roughness. **Journal of Fluid Mechanics**, v. 826, p. 830–850, sep 2017. ISSN 0022-1120. Available from Internet: <https://www.cambridge.org/core/product/identifier/S0022112017004669/type/journal_article>.

DISTRIBUTION A: Distribution approved for public release. Distribution unlimited

CARVALHO, A. E. B. de; MATHIAS, M. S.; MEDEIROS, M. A. F. A study on three-dimensional and isolated roughness induced transition. In: **Proceedings of the 12th ABCM Spring School on Transition and Turbulence**. Blumenau, Brazil: ABCM, 2020.

CATTAFESTA, L. N.; WILLIAMS, D. R.; ROWLEY, C. W.; ALVI, F. S. Review of Active Control of Flow-Induced Cavity Resonance. **33rd AIAA Fluid Dynamics Conference**, p. 1–20, 2003.

CHIBA, S. Global Stability Analysis of Incompressible Viscous Flow. **Journal of Japan Society of Computational Fluid Dynamics**, v. 7, n. 1, p. 20–48, 1998.

COLONIUS, T. An overview of simulation, modeling, and active control of flow/acoustic resonance in open cavities. In: **39th Aerospace Sciences Meeting and Exhibit**. Reno, NV, USA: [s.n.], 2001. p. 1 – 12. Available from Internet: <http://arc.aiaa.org/doi/abs/10.2514/6.2001-76>.

CROUCH, J.; KOSORYGIN, V.; NG, L. Modelling the Effects of Steps on Boundary-Layer Transition. In: **IUTAM Symposium on Laminar-Turbulent Transition**. Dordrecht: Kluwer Academic Publishers, 2006. p. 37–44. ISBN 978-1-4020-4159-4. Available from Internet: <http://link.springer.com/10.1007/1-4020-4159-4_4>.

CROUCH, J. D.; KOSORYGIN, V. S.; SUTANTO, M. I. Modeling Gap Effects on Transition Dominated by Tollmien-Schlichting Instability. In: **AIAA AVIATION 2020 FORUM**. Reston, Virginia: American Institute of Aeronautics and Astronautics, 2020. p. 1–8. ISBN 978-1-62410-598-2. Available from Internet: <https://arc.aiaa.org/doi/10.2514/6.2020-3075>.

CROUCH, J. D.; NG, L. L. Variable N-Factor Method for Transition Prediction in Three-Dimensional Boundary Layers. **AIAA Journal**, v. 38, n. 2, p. 211–216, feb 2000. ISSN 0001-1452. Available from Internet: <https://arc.aiaa.org/doi/10.2514/2.973>.

DAVIS, G. J.; MOLER, C. B. Sensitivity Of matrix eigenvalues. **International Journal for Numerical Methods in Engineering**, v. 12, n. 9, p. 1367–1373, 1978. ISSN 0029-5981. Available from Internet: <https://onlinelibrary.wiley.com/doi/10.1002/nme.1620120905>.

DIX, R. E.; BAUER, R. C. **Experimental and Theoretical Study of Cavity Acoustics**. [S.l.], 2000.

EAST, L. Aerodynamically induced resonance in rectangular cavities. **Journal of Sound and Vibration**, v. 3, n. 3, p. 277–287, may 1966. ISSN 0022460X. Available from Internet: <https://linkinghub.elsevier.com/retrieve/pii/0022460X66900964>.

EDWARDS, W.; TUCKERMAN, L.; FRIESNER, R.; SORENSEN, D. Krylov Methods for the Incompressible Navier-Stokes Equations. **Journal of Computational Physics**, v. 110, n. 1, p. 82–102, jan 1994. ISSN 00219991. Available from Internet: <https://linkinghub.elsevier.com/retrieve/pii/S0021999184710072>.

ERIKSSON, L. E.; RIZZI, A. Computer-aided analysis of the convergence to steady state of discrete approximations to the euler equations. **Journal of Computational Physics**, v. 57, n. 1, p. 90–128, jan 1985. ISSN 00219991. Available from Internet: <https://linkinghub.elsevier.com/retrieve/pii/0021999185900543>.

DISTRIBUTION A: Distribution approved for public release. Distribution unlimited

GAITONDE, D. V.; VISBAL, M. R. **High-Order Schemes for Navier-Stokes Equations: Algorithm and Implementation Into FDL3DI**. [S.l.], 1998.

GASTER, M. A note on the relation between temporally-increasing and spatially-increasing disturbances in hydrodynamic stability. **Journal of Fluid Mechanics**, v. 14, n. 2, p. 222–224, oct 1962. ISSN 0022-1120. Available from Internet: <http://www.journals.cambridge.org/abstract_S0022112062001184https://www.cambridge.org/core/product/identifier/S0022112062001184/type/journal_article>.

_____. On the generation of spatially growing waves in a boundary layer. **Journal of Fluid Mechanics**, v. 22, n. 3, p. 433–441, jul 1965. ISSN 0022-1120. Available from Internet: <https://www.cambridge.org/core/product/identifier/S0022112065000873/type/journal_article>.

_____. Understanding the Effects of Surface Roughness on the Growth of Disturbances. In: **46th AIAA Fluid Dynamics Conference**. Reston, Virginia: American Institute of Aeronautics and Astronautics, 2016. p. 3–11. ISBN 978-1-62410-436-7. Available from Internet: <http://arc.aiaa.org/doi/10.2514/6.2016-4384>.

GENNARO, E. M.; RODRÍGUEZ, D.; MEDEIROS, M. A. F.; THEOFILIS, V. Sparse Techniques in Global Flow Instability with Application to Compressible Leading-Edge Flow. **AIAA Journal**, v. 51, n. 9, p. 2295–2303, sep 2013. ISSN 0001-1452. Available from Internet: <https://arc.aiaa.org/doi/10.2514/1.J051816>.

GLOERFELT, X. **Cavity noise**. Paris: Citeseer, 2009. v. 3. 1–169 p. ISBN 9780511546143.

GOLDHIRSCH, L.; ORSZAG, S. A.; MAULIK, B. K. An efficient method for computing leading eigenvalues and eigenvectors of large asymmetric matrices. **Journal of Scientific Computing**, v. 2, n. 1, p. 33–58, mar 1987. ISSN 0885-7474. Available from Internet: <http://link.springer.com/10.1007/BF01061511>.

GOLDSTEIN, M. E. **Aeroacoustics**. [S.l.]: McGraw-Hill International Book Company, 1976. ISBN 9780070236851.

GÓMEZ, F.; GÓMEZ, R.; THEOFILIS, V. On three-dimensional global linear instability analysis of flows with standard aerodynamics codes. **Aerospace Science and Technology**, Elsevier Masson SAS, v. 32, n. 1, p. 223–234, jan 2014. ISSN 12709638. Available from Internet: <http://linkinghub.elsevier.com/retrieve/pii/S1270963813001879>.

GÓMEZ, F.; PÉREZ, J. M.; BLACKBURN, H. M.; THEOFILIS, V. On the use of matrix-free shift-invert strategies for global flow instability analysis. **Aerospace Science and Technology**, v. 44, p. 69–76, jul 2015. ISSN 12709638. Available from Internet: <http://linkinghub.elsevier.com/retrieve/pii/S1270963814002284>.

HELLER, H. H.; HOLMES, D. G.; COVERT, E. E. Flow-induced pressure oscillations in shallow cavities. **Journal of Sound and Vibration**, v. 18, n. 4, p. 545–553, 1971. ISSN 10958568.

HIMENO, F. H. T.; MATHIAS, M. S.; MEDEIROS, M. A. F. DNS of a small roughness immersed in a boundary layer: body-fitted and approximated methods comparison. In: **Proceedings of the Ibero-Latin-American Congress on Computational Methods in Engineering**. Foz do Iguaçu, Brazil: [s.n.], 2020. Available from Internet: <https://www.cilamce.com.br/arearestrita/apresentacoes/196/7756.pdf>.

DISTRIBUTION A: Distribution approved for public release. Distribution unlimited

HIMENO, F. H. T.; MATHIAS, M. S.; MEDEIROS, M. A. F. de. Direct Numerical Simulation of Wave Packets Over a Rough Flat Plate. In: **Proceedings of the 25th International Congress of Mechanical Engineering**. ABCM, 2019. Available from Internet: <http://abcm.org.br/anais-de-eventos/COB2019/1154>.

HOUGHTON, E. L.; CARPENTER, P. W.; COLLICOTT, S.; VALENTINE, D. **Aerodynamics for Engineering Students**. Elsevier Science, 2012. ISBN 9780080966335. Available from Internet: <https://books.google.com.br/books?id=rA6mIXaF69kC>.

HOWE, M. Mechanism of sound generation by low Mach number flow over a wall cavity. **Journal of Sound and Vibration**, v. 273, n. 1-2, p. 103–123, may 2004. ISSN 0022460X. Available from Internet: <http://linkinghub.elsevier.com/retrieve/pii/S0022460X03006448>.

HOWE, M. S. Edge, cavity and aperture tones at very low Mach numbers. **Journal of Fluid Mechanics**, v. 330, p. 61–84, jan 1997. ISSN 0022-1120. Available from Internet: <https://www.cambridge.org/core/product/identifier/S0022112096003606/type/journal_article>.

INGEN, J. L. van. A suggested semi-empirical method for the calculation of the boundary layer transition region. In: TECHNISCHE HOGESCHOOL. **Second European Aeronautical Congress, Scheveningen, Netherlands**. Delft, Nederlands, 1956.

JUNIPER, M. P.; HANIFI, A.; THEOFILIS, V. Modal Stability Theory. **Applied Mechanics Reviews**, v. 66, n. 2, p. 021004, mar 2014. ISSN 0003-6900. Available from Internet: <https://asmedigitalcollection.asme.org/appliedmechanicsreviews/article/doi/10.1115/1.4026604/395150/Modal-Stability-TheoryLecture-notes-from-the>.

KLEBANOFF, P. S.; TIDSTROM, K. D. Mechanism by Which a Two-Dimensional Roughness Element Induces Boundary-Layer Transition. **Physics of Fluids**, v. 15, n. 7, p. 1173–1188, 1972. ISSN 00319171. Available from Internet: <http://scitation.aip.org/content/aip/journal/pof1/15/7/10.1063/1.1694065>.

KNOLL, D.; KEYES, D. Jacobian-free Newton–Krylov methods: a survey of approaches and applications. **Journal of Computational Physics**, v. 193, n. 2, p. 357–397, jan 2004. ISSN 00219991. Available from Internet: <https://linkinghub.elsevier.com/retrieve/pii/S0021999103004340>.

KOLMOGOROV, A. N. **The Local Structure of Turbulence in Incompressible Viscous Fluid for Very Large Reynolds Numbers**. 1991. 9–13 p.

KOOK, H.; MONGEAU, L. Analysis of the periodic pressure fluctuations induced by flow over a cavity. **Journal of Sound and Vibration**, v. 251, n. 5, p. 823–846, apr 2002. ISSN 0022460X. Available from Internet: <http://linkinghub.elsevier.com/retrieve/pii/S0022460X01940131>.

KRISHNAMURTY, K. **Acoustic Radiation from Two-dimensional Rectangular Cutouts in Aerodynamic Surfaces**. Washington, 1956. 1 – 36 p.

LEHOUCQ, R. B.; SORENSEN, D. C. Deflation Techniques for an Implicitly Restarted Arnoldi Iteration. **SIAM Journal on Matrix Analysis and Applications**, v. 17, n. 4, p. 789–821, 1996. ISSN 0895-4798.

DISTRIBUTION A: Distribution approved for public release. Distribution unlimited

LELE, S. K. Compact finite difference schemes with spectral-like resolution. **Journal of Computational Physics**, v. 103, n. 1, p. 16–42, nov 1992. ISSN 00219991. Available from Internet: <https://linkinghub.elsevier.com/retrieve/pii/002199919290324R>.

LI, N.; LAIZET, S. 2DECOMP and FFT-A Highly Scalable 2D Decomposition Library and FFT Interface. **Cray User Group 2010 conference**, p. 1–13, 2010.

LIEPMANN, H. W. Investigations on Laminar Boundary-Layer Stability and Transition on Curved Boundaries. **NACA Wartime Report W107 (ACR3H30)**, n. Naca Wartime Report - W109, p. 68, 1943. Available from Internet: <http://hdl.handle.net/2060/19930093709>.

LIU, Q.; GÓMEZ, F.; THEOFILIS, V. Linear instability analysis of low- incompressible flow over a long rectangular finite-span open cavity. **Journal of Fluid Mechanics**, v. 799, p. R2, jul 2016. ISSN 0022-1120. Available from Internet: <https://www.cambridge.org/core/product/identifier/S0022112016003918/type/journal_article>.

LOISEAU, J.-C.; BUCCI, M. A.; CHERUBINI, S.; ROBINET, J.-C. **Computational Modelling of Bifurcations and Instabilities in Fluid Dynamics**. Cham: Springer International Publishing, 2019. v. 50. 33–73 p. (Computational Methods in Applied Sciences, v. 50). ISBN 978-3-319-91493-0. Available from Internet: <http://link.springer.com/10.1007/978-3-319-91494-7>.

LOISEAU, J.-C.; ROBINET, J.-C.; CHERUBINI, S.; LERICHE, E. Investigation of the roughness-induced transition: global stability analyses and direct numerical simulations. **Journal of Fluid Mechanics**, v. 760, p. 175–211, dec 2014. ISSN 0022-1120. Available from Internet: <https://www.cambridge.org/core/product/identifier/S0022112014005898/type/journal_article>.

MACK, C. J.; SCHMID, P. J. A preconditioned Krylov technique for global hydrodynamic stability analysis of large-scale compressible flows. **Journal of Computational Physics**, v. 229, n. 3, p. 541–560, feb 2010. ISSN 00219991. Available from Internet: <https://linkinghub.elsevier.com/retrieve/pii/S0021999109005117>.

MAREC, J. P. Drag Reduction: a Major Task for Research. In: THIEDE, P. (Ed.). **Aerodynamic Drag Reduction Technologies Proceedings of the CEAS/DragNet European Drag Reduction Conference**. Potsdam, Germany: Springer, 2001. p. 17–27. ISBN 354041911X. Available from Internet: <http://www.springer.com/de/book/9783540419112>.

MARTINEZ, A. **Towards natural transition in compressible boundary layers**. 2016. Tese (PhD. thesis) — University of São Paulo, 2016.

MARTINEZ, A.; MEDEIROS, M. F. Direct numerical simulation of a wavepacket in a boundary layer at Mach 0.9. In: **46th AIAA Fluid Dynamics Conference**. Reston, Virginia: American Institute of Aeronautics and Astronautics, 2016. v. 414, p. 1–33. ISBN 978-1-62410-436-7. ISSN 00221120. Available from Internet: <http://arc.aiaa.org/doi/10.2514/6.2016-3195>.

MATHIAS, M. S.; MEDEIROS, M. A. F. Direct Numerical Simulation of a Compressible Flow and Matrix-Free Analysis of its Instabilities over an Open Cavity. **Journal of Aerospace Technology and Management**, v. 10, p. 1–13, jul 2018. ISSN 2175-9146.

DISTRIBUTION A: Distribution approved for public release. Distribution unlimited

Available from Internet: <http://www.jatm.com.br/ojs/index.php/jatm/article/view/949>.

_____. Comparison Between Two and Three-Dimensional Direct Numerical Simulations of Rossiter Modes in Open Cavity Flow. In: **Proceedings of the 25th International Congress of Mechanical Engineering**. ABCM, 2019. Available from Internet: <http://abcm.org.br/anais-de-eventos/COB2019/0712>.

_____. Global instability analysis of a boundary layer flow over a small cavity. In: **AIAA Aviation 2019 Forum**. Reston, Virginia: American Institute of Aeronautics and Astronautics, 2019. p. 1–13. ISBN 978-1-62410-589-0. Available from Internet: <https://arc.aiaa.org/doi/10.2514/6.2019-3535>.

_____. Interaction between Rossiter and Görtler modes in the compressible flow in an open cavity. In: **AIAA AVIATION 2020 FORUM**. Reston, Virginia: American Institute of Aeronautics and Astronautics, 2020. v. 1 PartF, p. 1–6. ISBN 978-1-62410-598-2. Available from Internet: <https://arc.aiaa.org/doi/10.2514/6.2020-3074>.

_____. Spatial instability of boundary layers over small cavities and comparison to global modes. In: **AIAA AVIATION 2021 FORUM**. Reston, Virginia: American Institute of Aeronautics and Astronautics, 2021. ISBN 978-1-62410-610-1. Available from Internet: <https://arc.aiaa.org/doi/10.2514/6.2021-2931>.

_____. The effect of incoming boundary layer thickness and Mach number on linear and nonlinear Rossiter modes in open cavity flows. **Theoretical and Computational Fluid Dynamics**, may 2021. ISSN 0935-4964. Available from Internet: <https://link.springer.com/10.1007/s00162-021-00570-2>.

MCGREGOR, O. W.; WHITE, R. A. Drag of rectangular cavities in supersonic and transonic flow including the effects of cavity resonance. **AIAA Journal**, v. 8, n. 11, p. 1959–1964, nov 1970. ISSN 0001-1452. Available from Internet: <https://arc.aiaa.org/doi/10.2514/3.6032>.

MESEGUER-GARRIDO, F.; VICENTE, J. de; VALERO, E.; THEOFILIS, V. On linear instability mechanisms in incompressible open cavity flow. **Journal of Fluid Mechanics**, v. 752, p. 219–236, aug 2014. ISSN 0022-1120. Available from Internet: <https://www.cambridge.org/core/product/identifier/S0022112014002535/type/journal_article>.

MORKOVIN, M. V.; RESHOTKO, E.; HERBERT, T. Transition in open flow systems - a reassessment. **Bulletin of the American Physical Society**, v. 39:1882, 1994.

NEGI, P. S.; HANIFI, A.; HENNINGSON, D. S. On the linear global stability analysis of rigid-body motion fluid–structure-interaction problems. **Journal of Fluid Mechanics**, v. 903, p. A35, nov 2020. ISSN 0022-1120. Available from Internet: <https://www.cambridge.org/core/product/identifier/S0022112020006850/type/journal_article>.

OHMICHI, Y.; SUZUKI, K. Assessment of global linear stability analysis using a time-stepping approach for compressible flows. **International Journal for Numerical Methods in Fluids**, v. 80, n. 10, p. 614–627, apr 2016. ISSN 02712091. Available from Internet: <https://onlinelibrary.wiley.com/doi/10.1002/fld.4166>.

DISTRIBUTION A: Distribution approved for public release. Distribution unlimited

ORR, W. M. F. The Stability or Instability of the Steady Motions of a Perfect Liquid and of a Viscous Liquid. Part II: A Viscous Liquid. **Proceedings of the Royal Irish Academy. Section A: Mathematical and Physical Sciences**, v. 27, p. 69–138, 1909.

OWEN, T. B. **Techniques of pressure fluctuation measurements**. [S.l.], 1958. 1 – 75 p.

PAULA, I. B. de; WÜRZ, W.; MENDONÇA, M. T.; MEDEIROS, M. A. F. Interaction of instability waves and a three-dimensional roughness element in a boundary layer. **Journal of Fluid Mechanics**, v. 824, p. 624–660, aug 2017. ISSN 0022-1120. Available from Internet: <https://www.cambridge.org/core/product/identifier/S0022112017003627/type/journal_article>.

PLOGMANN, B.; WÜRZ, W.; KRÄMER, E. On the disturbance evolution downstream of a cylindrical roughness element. **Journal of Fluid Mechanics**, v. 758, p. 238–286, nov 2014. ISSN 0022-1120. Available from Internet: <https://www.cambridge.org/core/product/identifier/S0022112014004996/type/journal_article>.

PLUMBLEE, H. E.; GIBSON, J. S.; LASSITER, L. W. **Theoretical and Experimental Investigation of The Acoustic Response of Cavities In An Aerodynamic Flow**. [S.l.], 1962. 1–167 p.

PRANDTL, L. Motion of Fluids with Very Little Viscosity. In: **Internationalen Mathematiker-Kongresses**. Heidelberg: [s.n.], 1904. p. 1–8.

QADRI, U. A.; SCHMID, P. J. Frequency selection mechanisms in the flow of a laminar boundary layer over a shallow cavity. **Physical Review Fluids**, v. 2, n. 1, p. 013902, jan 2017. ISSN 2469-990X. Available from Internet: <https://link.aps.org/doi/10.1103/PhysRevFluids.2.013902>.

RAYLEIGH, J. W. S. On the stability, or instability, of certain fluid motions. **Proceedings of the London Mathematical Society**, x, p. 57–72, 1879. ISSN 0024-6115. Available from Internet: <http://onlinelibrary.wiley.com/doi/10.1112/plms/s1-11.1.57/epdf>.

RENEAUX, J. Overview on drag reduction technologies for civil transport aircraft. In: **European Congress on Computational Methods in Applied Sciences and Engineering (ECCOMAS)**. Jyväskylä: [s.n.], 2004. p. 1–18. Available from Internet: <http://echo.onera.fr/daap/reduction-trainee-civil/drag-reduction-technologies-for-civil-transport-aircraft-reneaux.pdf>.

REYNOLDS, O. An Experimental Investigation of the Circunstances Which Determine Whether the Motion of Water Shall Be Direct or Sinuous, and of the Law of Resistance in Parallel Channels. **Proceedings of the Royal Society of London**, v. 35, p. 84–99, 1883.

_____. On the Dynamical Theory of Incompressible Viscous Fluids and the Determination of the Criterion. **Proceedings of the Royal Society of London**, 1894.

ROCKWELL, D.; NAUDASHER, E. Self Sustained Oscillations of Impinging Free Shear Layers. **Ann. Rev. Fluid Mech.**, v. 11, p. 67–94, 1979.

RODRIGUES, S. B. Improving the IMEX method with a residual balanced decomposition. **eprint arXiv**, p. 1–19, may 2017. Available from Internet: <http://arxiv.org/abs/1705.04870v3>.

DISTRIBUTION A: Distribution approved for public release. Distribution unlimited

ROSHKO, A. **Some Measurements of Flow in a Rectangular Cavity**. [S.l.], 1955. 1 – 22 p.

ROSSITER, J. E. **Wind-tunnel experiments on the flow over rectangular cavities at subsonic and transonic speeds**. London, 1964. 1 – 36 p. Available from Internet: <http://repository.tudelft.nl/view/aereports/uuid:a38f3704-18d9-4ac8-a204-14ae03d84d8c/>.

ROWLEY, C. W.; COLONIUS, T.; BASU, A. J. On self-sustained oscillations in two-dimensional compressible flow over rectangular cavities. **Journal of Fluid Mechanics**, v. 455, p. 315–346, mar 2002. ISSN 0022-1120. Available from Internet: <https://www.cambridge.org/core/product/identifier/S0022112001007534/type/journal_article>.

ROWLEY, C. W.; WILLIAMS, D. R. Dynamics and Control of High-Reynolds-Number Flow Over Open Cavities. **Annual Review of Fluid Mechanics**, v. 38, n. 1, p. 251–276, jan 2006. ISSN 0066-4189. Available from Internet: <https://www.annualreviews.org/doi/10.1146/annurev.fluid.38.050304.092057>.

SAAD, Y. **Iterative Methods for Sparse Linear Systems**. Society for Industrial and Applied Mathematics, 2003. ISBN 978-0-89871-534-7. Available from Internet: <http://epubs.siam.org/doi/book/10.1137/1.9780898718003>.

SANTOS, P. H. R.; MATHIAS, M. S.; HIMENO, F. H. T.; MEDEIROS, M. A. F. On the receptivity of acoustic waves over localized roughness in compressible boundary layers. In: **Proceedings of the 18th Brazilian Congress of Thermal Sciences and Engineering**. [S.l.]: ABCM, 2020.

SAROHIA, V. Experimental Investigation of Oscillations in Flows Over Shallow Cavities. **AIAA Journal**, v. 15, n. 7, p. 984–991, jul 1977. ISSN 0001-1452. Available from Internet: <http://arc.aiaa.org/doi/10.2514/3.60739>.

SCHLICHTING, H. Laminare Strahlausbreitung. **Z. angew. Math. Mech.**, v. 13, p. 260–263, 1933.

SCHLICHTING, H.; GERSTEN, K. **Boundary Layer Theory**. 8th. ed. [S.l.]: Springer-Verlag Berlin Heidelberg, 2000.

SCHMIDT, O. T.; COLONIUS, T. Guide to Spectral Proper Orthogonal Decomposition. **AIAA Journal**, v. 58, n. 3, p. 1023–1033, mar 2020. ISSN 0001-1452. Available from Internet: <https://arc.aiaa.org/doi/10.2514/1.J058809>.

SCHUBAUER, G.; SKRAMSTAD, H. Laminar boundary-layer oscillations and transition on a flat plate. **Journal of Research of the National Bureau of Standards**, v. 38, n. 2, p. 251, feb 1947. ISSN 0091-0635. Available from Internet: <https://nvlpubs.nist.gov/nistpubs/jres/38/jresv38n2p251_A1b.pdf>.

SILVA, H. G.; SOUZA, L. F.; MEDEIROS, M. A. F. Verification of a mixed high-order accurate DNS code for laminar turbulent transition by the method of manufactured solutions. **International Journal for Numerical Methods in Fluids**, v. 64, n. 3, p. 336–354, sep 2010. ISSN 02712091. Available from Internet: <https://onlinelibrary.wiley.com/doi/10.1002/fld.2156>.

DISTRIBUTION A: Distribution approved for public release. Distribution unlimited

SIPP, D.; LEBEDEV, A. Global stability of base and mean flows: a general approach and its applications to cylinder and open cavity flows. **Journal of Fluid Mechanics**, v. 593, p. 333–358, dec 2007. ISSN 0022-1120. Available from Internet: <https://www.cambridge.org/core/product/identifier/S0022112007008907/type/journal_article>.

SOMMERFELD, A. Ein Beitrag zur hydrodynamischen Erklaerung der turbulenten Fluessigkeitsbewegungen. In: **Proceedings of the 4th International Congress of Mathematicians**. [S.l.: s.n.], 1908. p. 116–124.

SOUZA, L. F.; MENDONÇA, M. T.; MEDEIROS, M. A. F. The advantages of using high-order finite differences schemes in laminar-turbulent transition studies. **International Journal for Numerical Methods in Fluids**, v. 48, n. 5, p. 565–582, 2005. ISSN 02712091.

SUN, Y.; TAIRA, K.; CATTAFESTA, L. N.; UKEILEY, L. S. Spanwise effects on instabilities of compressible flow over a long rectangular cavity. **Theoretical and Computational Fluid Dynamics**, p. 1–11, nov 2016. ISSN 0935-4964. Available from Internet: <http://link.springer.com/10.1007/s00162-016-0412-y>.

_____. Biglobal instabilities of compressible open-cavity flows. **Journal of Fluid Mechanics**, v. 826, p. 270–301, sep 2017. ISSN 0022-1120. Available from Internet: <https://www.cambridge.org/core/product/identifier/S0022112017004165/type/journal_article>.

TAIRA, K. et al. Modal Analysis of Fluid Flows: An Overview. **AIAA Journal**, v. 55, n. 12, p. 4013–4041, dec 2017. ISSN 0001-1452. Available from Internet: <https://arc.aiaa.org/doi/10.2514/1.J056060>.

TAM, C. The acoustic modes of a two-dimensional rectangular cavity. **Journal of Sound and Vibration**, v. 49, n. 3, p. 353–364, dec 1976. ISSN 0022460X. Available from Internet: <https://linkinghub.elsevier.com/retrieve/pii/0022460X76904260>.

TEMPERTON, C. Algorithms for the solution of cyclic tridiagonal systems. **Journal of Computational Physics**, v. 19, n. 3, p. 317–323, nov 1975. ISSN 00219991. Available from Internet: <https://linkinghub.elsevier.com/retrieve/pii/0021999175900819>.

TEZUKA, A.; SUZUKI, K. Three-Dimensional Global Linear Stability Analysis of Flow Around a Spheroid. **AIAA Journal**, v. 44, n. 8, p. 1697–1708, aug 2006. ISSN 0001-1452. Available from Internet: <https://arc.aiaa.org/doi/10.2514/1.16632>.

THEOFILIS, V. Advances in global linear instability analysis of nonparallel and three-dimensional flows. **Progress in Aerospace Sciences**, v. 39, n. 4, p. 249–315, may 2003. ISSN 03760421. Available from Internet: <https://linkinghub.elsevier.com/retrieve/pii/S0376042102000301>.

_____. Global Linear Instability. **Annual Review of Fluid Mechanics**, v. 43, n. 1, p. 319–352, jan 2011. ISSN 0066-4189. Available from Internet: <https://www.annualreviews.org/doi/10.1146/annurev-fluid-122109-160705>.

THEOFILIS, V.; COLONIUS, T. An Algorithm for the Recovery of 2- and 3D BiGlobal Instabilities of Compressible Flow Over 2D Open Cavities. In: **33rd AIAA Fluid Dynamics Conference and Exhibit**. Reston, Virigina: American Institute of Aeronautics and Astronautics, 2003. ISBN 978-1-62410-095-6. Available from Internet: <https://arc.aiaa.org/doi/10.2514/6.2003-4143>.

DISTRIBUTION A: Distribution approved for public release. Distribution unlimited

TIETJENS, O. Beiträge zur Entstehung der Turbulenz. **Z. angew. Math. Mech.**, v. 5, p. 200–217, 1925.

TINOCO, E. N. et al. Summary Data from the Sixth AIAA CFD Drag Prediction Workshop: CRM Cases. **Journal of Aircraft**, v. 55, n. 4, p. 1352–1379, jul 2018. ISSN 0021-8669. Available from Internet: <https://arc.aiaa.org/doi/10.2514/1.C034409>.

TOLLMIEN, W. Über die Entstehung der Turbulenz. In: **Nachrichten der Gesellschaft der Wissenschaften zu Göttingen**. Göttingen: [s.n.], 1929. p. 21–44.

_____. **The production of turbulence**. Washington, 1932. v. 609.

VICENTE, J. de; BASLEY, J.; MESEGUER-GARRIDO, F.; SORIA, J.; THEOFILIS, V. Three-dimensional instabilities over a rectangular open cavity: from linear stability analysis to experimentation. **Journal of Fluid Mechanics**, v. 748, p. 189–220, 2014. ISSN 0022-1120. Available from Internet: <http://www.journals.cambridge.org/abstract_S0022112014001268>.

WANG, Y. X.; GASTER, M. Effect of surface steps on boundary layer transition. **Experiments in Fluids**, v. 39, n. 4, p. 679–686, oct 2005. ISSN 0723-4864. Available from Internet: <http://link.springer.com/10.1007/s00348-005-1011-7>.

WILLIAMS, D.; ROWLEY, C. Recent Progress in Closed-Loop Control of Cavity Tones. In: **44th AIAA Aerospace Sciences Meeting and Exhibit**. Reston, Virigina: American Institute of Aeronautics and Astronautics, 2006. ISBN 978-1-62410-039-0. Available from Internet: <https://arc.aiaa.org/doi/10.2514/6.2006-712>.

WORNER, A.; RIST, U.; WAGNER, S. Humps/Steps Influence on Stability Characteristics of Two-Dimensional Laminar Boundary Layer. **AIAA Journal**, v. 41, n. 2, p. 192–197, feb 2003. ISSN 0001-1452. Available from Internet: <https://arc.aiaa.org/doi/10.2514/2.1960>.

YAMOUNI, S.; SIPP, D.; JACQUIN, L. Interaction between feedback aeroacoustic and acoustic resonance mechanisms in a cavity flow: a global stability analysis. **Journal of Fluid Mechanics**, v. 717, p. 134–165, feb 2013. ISSN 0022-1120. Available from Internet: <https://www.cambridge.org/core/product/identifier/S0022112012005630/type/journal_article>.

DISTRIBUTION A: Distribution approved for public release. Distribution unlimited

Appendix 2

DISTRIBUTION A: Distribution approved for public release. Distribution unlimited

University of São Paulo
São Carlos School of Engineering

Marcello Augusto Faraco de Medeiros

AFOSR Report
Study on the impact of gaps in the boundary layer stability

São Carlos

2022

DISTRIBUTION A: Distribution approved for public release. Distribution unlimited

DISTRIBUTION A: Distribution approved for public release. Distribution unlimited

LIST OF FIGURES

Figure 1 – Examples of gaps between wing panels, main element and flap/aileron/slat in (a); junction of the nose with the fuselage and the landing gear doors gaps in (b); panel junctions present on the engine nacelle in (c). 14
Figure 2 – Schematic representation showing the profile view of the flat plate containing the gap immersed inside a laminar boundary layer. 15
Figure 3 – Comparison of parameter space envelope defined for the experiments and data extracted from Crouch, Kosorygin and Sutanto (2020). 16
Figure 4 – Boundary layer neutral stability curve. 20
Figure 5 – Experimental evidence of the boundary layer instability predicted by the LST. 21
Figure 6 – Tollmien-Schlichting wave amplitude profile. 21
Figure 7 – Schematic representation of the K-type transition proposed by Klebanoff and Tidstrom (1956)., extracted from Kachanov (1994). 22
Figure 8 – Smoke visualization of the staggered Λ-vortices in (a) and a schematic representation Λ-vortices breakdown in (b). 23
Figure 9 – Characteristics of a turbulent spot artificially generated. from Klebanoff and Schubauer (1955). 24
Figure 10 – Stages of the boundary layer transition. 25
Figure 11 – Envelope of T-S growth ratio indicating the transition. 25
Figure 12 – Qualitative flowchart showing the routes of boundary layer breakdown to turbulence. 26
Figure 13 – Flow visualization of the acoustic radiation emanating due to cavity instability. 28
Figure 14 – Classification of the flow regimes (permanent or oscillatory) as a function of a novel dimensionless parameter, $(L/\delta)Re_\delta{}^{1/2}$. 29
Figure 15 – Contours of instantaneous iso-vorticity for arbitrary distinct times exhibiting different modes of cavity instability. 30
Figure 16 – Amplification factor and non-dimensional frequency of the leading 3D eigenvalues. 33
Figure 17 – Most unstable centrifugal stream-wise velocity amplitude function $(\lambda/D = 0.5)$ for a cavity with $L/D = 6$. 34
Figure 18 – Representation of the T-S amplification affected by the presence of a gap. 35
Figure 19 – Root-mean-square of streamwise unsteady velocity along the chord for different experiment runs. 35
Figure 20 – Correlation scheme of the ΔN as a function of the gap geometry in (a) and the bypass locus diagram given by the red filled circles in (b). . . . 37

DISTRIBUTION A: Distribution approved for public release. Distribution unlimited

Figure 21 – Mesh spacing for x axis in (a) and y in (b). 42
Figure 22 – Plot of a typical computational mesh grid for the current work. Only every tenth consecutive node and the domain boundaries exhibited. An auxiliary plot on top right zooms in the gap region. Solid lines represent the wall (magenta is free-slip, and green is no-slip). Blue dashed lines indicate the domain-interior/buffer zone interface. 43
Figure 23 – Comparison of the dispersive error of the numerical schemes. In blue, the SL6 scheme, and in orange, the SL6O3, after the optimization according to Gaitonde and Shang (1996). 45
Figure 24 – Spectral function of the numerical filter proposed by Gaitonde and Visbal (1998). 47
Figure 25 – Scheme representing the parallel processing and the flowchart for derivatives evaluation. 50
Figure 26 – Flowchart of the algorithm utilized for the global instability analysis proposed by Tezuka and Suzuki (2006) and implemented by Mathias (2017). 53
Figure 27 – Effect of increasing the filtering time τM on convergence of the 2D (a) and 3D (b) eigenvalues from the linear stability analysis of a representative run. 55
Figure 28 – Diagram exhibiting the gap geometries covered in the current work and the impact on the transition measured by Crouch, Kosorygin and Sutanto (2020). 57
Figure 29 – Mesh spacing between two consecutive grid nodes in streamwise (a) and wall-normal (b) axis for the meshes employed for the grid dependence test. Only the domain of interest is exhibited. Gap's corners locations are displayed by black dashed lines in (a). 58
Figure 30 – Comparison of the frequency spectra from the wall-normal velocity signal, v/U_∞, measured inside the boundary layer just downstream of the gap. 59
Figure 31 – Time history of the maximum absolute residual from the streamwise velocity for the runs L17D3 and L20D4. 60
Figure 32 – Streamwise unsteady velocity signals measured by probes located inside the gap in (a) and (b), just downstream of the gap in (c) and (d), and far downstream in (d) and (e). Time series of (a), (c), and (e) were taken from run L17D3, whereas the others from run L20D4. 62
Figure 33 – Frequency spectrum comparing the signal exhibited in Figure 32d with results from Crouch, Kosorygin and Sutanto (2020) and the frequency prediction by Block (1976). 63

DISTRIBUTION A: Distribution approved for public release. Distribution unlimited

Figure 34 – Instantaneous crossflow and streamwise velocity contours for runs L17D3 and L20D4 in equivalent phases. We employed 256 equally spaced levels between the minimum and the maximum of each run with the color bar scale kept constant for each variable. 63
Figure 35 – Time series of the maximum absolute residual of the all dependent variables from the run L20D4 with aid from the SFD technique. 64
Figure 36 – Comparison with various DNS velocity profiles and Blasius' right upstream of the gap. 65
Figure 37 – Iso-contours of the non-dimensional spanwise vorticity and stream-lines overlaid from the steady solutions for the runs: (a) L17D3, (b) L20D4, (c) L24D2, and (d) L27D2. 66
Figure 38 – Comparison of the boundary layer displacement thickness evolution with the Blasius. The x axis is normalized by the length of the gap. . . 67
Figure 39 – Comparison of the boundary layer shape factor with the Blasius. The x axis is normalized by the length of the gap. 67
Figure 40 – Gap shear layer spreading rate of both aspect ratios $L/D = 5$ in (a) and $L/D = 10$ in (b). The vorticity thickness distribution over the stream-wise axis is normalized by its respective value at the gap leading edge. A linear fitting is also exhibited. 68
Figure 41 – Eigenvalues spectra from the runs with aspect ratio $L/D = 5$ (a) and $L/D = 10$ (b) in the complex plane. The imaginary axis indicates the circular frequency, whereas the real corresponds to amplification or damping rate. 69
Figure 42 – Eigenfunctions of the the most unstable Rossiter mode (R_2) from the run L20D4. 71
Figure 43 – $\hat{v}$ eigenfunctions of the different Rossiter modes from run L27D2. . . . 71
Figure 44 – Several phases comprising one oscillation period of the Rossiter (R_2) streamwise velocity eigenfunction from run L20D4. 72
Figure 45 – Amplification and Strouhal number based on displacement thickness *versus* spanwise wavelength of the dominant centrifugal modes for $L/D = 5$ in (a) and (b), and for $L/D = 10$ in (c) and (d). 73
Figure 46 – Spectra of eigenvalues for the centrifugal modes with several spanwise wavenumbers for L/D=5 in (a) and $L/D = 10$ in (b). 74
Figure 47 – $\hat{u}$ eigenfunctions of the centrifugal modes from L20D4. 75
Figure 48 – Iso-surface of the leading streamwise velocity eigenfunctions, $\hat{u}$, of the centrifugal *modes i*, *ii*, and *iii*, from the runs L20D4 (left) and L27D2 (right). Spanwise wavelenghts indicated in sub-figures and contour levels in the ticks of the color bar. 77

DISTRIBUTION A: Distribution approved for public release. Distribution unlimited

Figure 49 – Hydrodynamic instability analysis, using Linear Stability Theory (LST), for the four representative cases of the transition process. Both figures show the most unstable modes for each frequency along with Z. The figure on the right refers to amplification, while the one on the left refers to frequency. 79

Figure 50 – The image shows the colormap of the U component of the velocity at the center of the Z domain. 79

Figure 51 – In the left figure is represented the comparative C_f along with the plate. The figure on the right shows a comparison of the law of the wall. . . . 80

Figure 52 – In the pictures we have the FFT along Z for the values of X inside the cavity, using the W component of the velocity. In the right image, we have 100 dimensionless moments after the left image. 81

Figure 53 – In the pictures, we have the λ_2 method to representing the beginning of the emission of the spot in the left picture. In the right picture, we have a few dimensionless instants after the left picture, the representation of a cut of the domain in the XZ plane, with Y of $0.5\delta^*$. 81

Figure 54 – In the figure, we have the colormap of the boundary layer at the center of the domain in Z, after the convection of the turbulence spot. 82

Figure 55 – In the left picture, we have the comparative C_f after the cavity. In the right picture, we have the wall law for the end of the domain. 82

Figure 56 – In the pictures we have the FFT along Z for the values of X inside the cavity, using the W component of the velocity. In the right image, we have 100 dimensionless instants after the left image. 83

Figure 57 – In the figures, we have the λ_2 method, where the structures are being convected from the cavity, at two different instants. The figure on the left represents the domain of the emission process of three-dimensional structures, and in the figure on the right, 100 dimensionless instants, we can see more three-dimensional structures within the two-dimensional structures. 84

Figure 58 – In the figures, we have on the left the friction coefficient for the entire useful domain downstream to the cavity. The figure on the right, shows us the wall law, near the end of the domain, where it already presents a good agreement with the law of the wall. 85

Figure 59 – In the figure, we have a boundary layer with a wall law near a fully developed boundary layer, indicating that we have a possible fully developed region after this point. 85

DISTRIBUTION A: Distribution approved for public release. Distribution unlimited

Figure 60 – In the figures, we have the Fourier transforms along Z, for all X of the domain, using the W component of the velocity. The left figure represents the beginning of the initial spot propagation. The figure on the right represents the developed flow. 86

Figure 61 – In the figures, we have the slices of the velocity component U at the center of the Z-domain. In the left figure, we have the initial spot that was convected from the cavity during its propagation over the plate. In the figure on the right, we have about 50 dimensionless instants, after the image on the right. In this image, we can observe the development of the flow, after the spot leaves the plate. 87

Figure 62 – In the figures, we have the two-dimensional Fourier transforms (2D FFT), for two different positions in the flow. The 2D FFT was performed using a fixed value of X and Y, and doing the transform using the variables Z and T (time). In the figure at left, we have the 2D FFT, for the position $X = 265$ and $Y = 0$, of the density in the plate, we can see in it the presence of a well defined Rossiter mode in the region of $\beta = 0$ and $\omega \approx 0.19$, close to those expected by LST. In the left figure, we have the 2D FFT, for the position $X = 300$ and $Y = 0.2$, of the density in the boundary layer, we can still see the Rossiter modes present. 88

Figure 63 – The image shows the λ_2 method present downstream to the cavity, for the entire useful domain. The image was taken for the fully developed flow. 89

Figure 64 – In the figures, we have the U-component slices of the velocity, for two different time instants. The image on the right shows the flow with an increment of 50 dimensionless instants after the image on the left. . . . 89

Figure 65 – In the left figure, we have the comparison of C_f, where it is possible to see a smaller transition region, as well as a transition in a smaller domain. In the right figure, we have the law of the wall before the end of the domain, confirming the transition. 90

Figure 66 – In the figure, we have the λ_2 method showing the structures convected out of the cavity. 91

Figure 67 – In the figure, we have the λ_2 method showing the downstream convected structures of the cavity. 92

Figure 68 – In the figure, we have the FFT along Z for all values of X inside the cavity, using the W component of the velocity, located 1 δ^* from the bottom of the cavity at two different time instants. The figure on the right represents 50 dimensionless instants after the image on the left. . 93

DISTRIBUTION A: Distribution approved for public release. Distribution unlimited

Figure 69 – In the figure, we have the FFT along Z for all values of X downstream of the cavity, using the W component of the velocity, located 0.5 δ^* from the plate at two different time instants. The figure on the right represents 50 dimensionless instants after the image on the left. 94
Figure 70 – In the figure, we have the 2D FFT for two different points on the plate. The 2D FFT has been computed using the density along Z and T for two different points on the plate. The left picture represents the 2D FFT over the plate at X = 265 and Y = 0, while the right picture represents the 2D FFT at X = 300 and Y = 0. 95
Figure 71 – In the figure, we have the 2D FFT for two different points on the plate. The 2D FFT was computed using the W component of the velocity along Z and T for two different points on the plate. The left picture represents the 2D FFT over the plate at X = 300 and Y = 0.8, while the right picture represents the 2D FFT at X = 400 and Y = 0.8. . . . 96
Figure 72 – Mapping using LST of the modes present for different depths and cavity lengths. Mapping using $Ma = 0.5$ and $Re_{\delta^*} = 600$. 97
Figure 73 – Analysis of the most unstable modes obtained by LST, for the cases with depth $D = 3$. The left figure shows the amplification, while the right figure shows the frequencies. 98
Figure 74 – Analysis of the most unstable modes obtained by LST, for the cases with length $L = 12.5$. The left figure shows the amplifications, while the right figure shows the frequencies. 99
Figure 75 – Correlation of the impact on the boundary layer transition as a function of the gap geometry, according to Crouch, Kosorygin and Sutanto (2020), and the modes from the linear stability analysis (bar plot). Open markers indicate transition by T-S waves, whereas filled markers, bypass transition. 101

DISTRIBUTION A: Distribution approved for public release. Distribution unlimited

LIST OF TABLES

Table 1 – Flow parameters for the different simulation runs covered in the present work. 57
Table 2 – Meshes for grid dependence test. 59
Table 3 – Frequency spectra peak comparison of the solution for different meshes. 60
Table 4 – Eigenvalues associated with the Rossiter mode. 70
Table 5 – Leading eigenvalues associated with the centrifugal mode. 76
Table 6 – Summary of linear stability analysis eigenvalues and transition mechanism according to experimental results from Crouch2020. 102

DISTRIBUTION A: Distribution approved for public release. Distribution unlimited

DISTRIBUTION A: Distribution approved for public release. Distribution unlimited

CONTENTS

1 INTRODUCTION . . . 13
1.1 Motivation . . . 13
1.2 Problem description . . . 15
1.3 Objective . . . 17
1.4 Report organization . . . 17

2 LITERATURE REVIEW . . . 19
2.1 Boundary layer transition . . . 19
2.2 Cavity instability . . . 27
2.2.1 Rossiter instability . . . 27
2.2.2 Centrifugal instability . . . 32
2.3 Effect of gaps in boundary layer transition . . . 34

3 METHODOLOGY . . . 39
3.1 Direct Numeric Simulation . . . 39
3.1.1 Governing equations . . . 39
3.1.2 Computational domain . . . 41
3.1.3 Boundary and initial condition . . . 42
3.1.4 Spatial derivatives method . . . 43
3.1.5 Anti-aliasing filter . . . 46
3.1.6 Linear system solver . . . 46
3.1.7 Time integration . . . 48
3.1.8 Selective frequency damping . . . 49
3.1.9 Parallel execution . . . 50
3.2 Instability Analysis . . . 50
3.2.1 Arnoldi-based time-stepping method . . . 51
3.2.2 Algorithm optimal parameters . . . 54

4 RESULTS . . . 57
4.1 Grid dependence test . . . 58
4.2 Unsteady solution . . . 60
4.3 Steady solution . . . 63
4.4 Rossiter instability . . . 68
4.5 Centrifugal instability . . . 72
4.6 Transition induced by the gap . . . 78
4.6.1 Case A: $Re_{\delta^*} = 734$ and $Ma = 0.2$ . . . 78

DISTRIBUTION A: Distribution approved for public release. Distribution unlimited

4.6.1.1 Case B: $Re_{\delta^*} = 693$ and $Ma = 0.5$ 80
4.6.1.2 Case C: $Re_{\delta^*} = 734$ and $Ma = 0.9$ 83
4.6.1.3 Case D: $Re_{\delta^*} = 734$ and $Ma = 0.5$ 88
4.7 Possible Scenarios for transition induced by a gap 97
4.7.1 Large L 98
4.7.2 Large D 99
4.8 Discussion 100

5 CONCLUSION 103

REFERENCES 105

DISTRIBUTION A: Distribution approved for public release. Distribution unlimited

1 INTRODUCTION

1.1 Motivation

Examinations made by Prandtl (1905) (also available in Tollmien, Schlichting and Görtler (1961) and Prandtl (1928)) led to the identification of a peculiar fluid behavior on solid surfaces. The fluid viscosity is responsible for promoting fluid adherence with the solid surface. As a result, one velocity profile develops, in which a certain distance the profile reaches the free-stream velocity. This particular region of the flow was named the boundary layer. Typically the velocity gradient is severe. Hence, shear forces in the boundary layer have significant importance, even in fluids with low viscosity. At the time, this finding represented a remarkable advance because several theories neglected the viscous terms of the Navier-Stokes Equations, and many events observed in practice could not be well represented mathematically, e. g. flow separation. Afterward, Blasius (1908) – English version available in Blasius (1950) – introduced the analytical solution for the incompressible flow parallel to a semi-infinite flat plate with zero pressure gradient.

Much study has focused on the boundary layer because it is extensively present in the aeronautical field. There are shear forces in the boundary layer that have dissipative nature as a characteristic. Specifically, in an aircraft, these forces contribute to drag in the form of viscous skin friction. Drag implies penalizing part of the thrust produced by an aircraft engine and, therefore, engineering has an economic interest in its reduction. In addition to this aspect, aircraft certification entities impose increasingly challenging targets regarding the harmful gases for the environment emission level. The International Civil Aviation Organization (ICAO) determines in its resolution A40-18 a 2050 target of 50% reduction in CO_2 emissions compared to 2005 levels. The report Flightpath (2011), which deals with strategic guidelines aimed at the European aeronautics industry, defines a goal for 2050, a reduction of 75% in CO_2 emissions per passenger-kilometer and 90% decrease in NO_x emission.

To illustrate the impact on economic and environmental aspects caused by drag, Schneider (2001) quantifies in its analysis that a hypothetical reduction of 1% in the total aerodynamic drag of a large commercial aircraft operating over long distances would result in savings of 400,000 liters of fuel and reduction of 5,000 kg of harmful gases emitted per year. The author further estimates that 15% in fuel-related operating cost savings can double the company's profit over one year. Marec (2001) states that about 50% of the total drag of a typical civil transport aircraft resides in viscous drag. Regarding aircraft operation, drag reduction directly affects its autonomy, as suggested by Paula (2007), and influences the take-off payload as well. Reneaux (2004) cites an increase of 1.6 ton in aircraft payload, equivalent to about 10 passengers, caused by a hypothetical reduction of

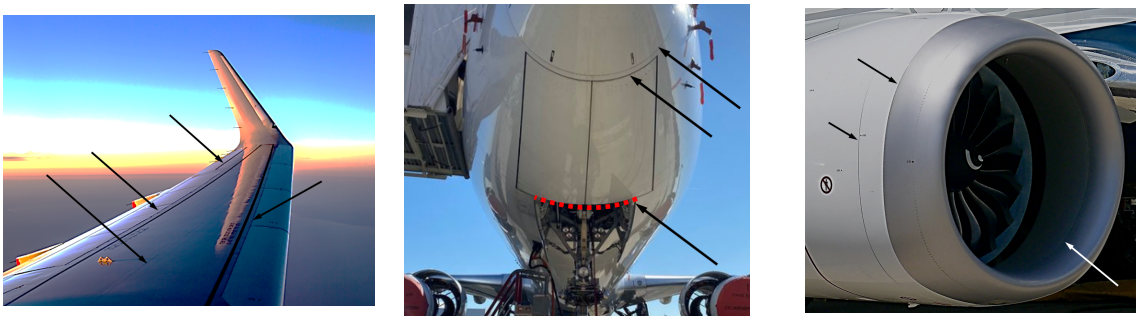
DISTRIBUTION A: Distribution approved for public release. Distribution unlimited

1% in the drag of a typical aircraft.

A turbulent boundary layer has higher levels of skin friction drag than a laminar one. Commonly, a boundary layer becomes turbulent through a transition process. Concisely, this process typically involves the receptivity of the boundary layer to natural disturbances present in the flow, followed by an oscillatory movement that amplifies and evolves until the rupture into the turbulent regime. In 2D boundary layers, the dominant oscillation mode is called the Tollmien-Schlichting (T-S) wave. With a better understanding of the turbulence transition physics phenomena, it is possible to implement more effective techniques to push the transition location downstream and, thus, obtain a smaller portion of the turbulent boundary layer. Furthermore, the prediction and identification of the transition location are highly substantial for performance evaluation during the design stage in the aerospace industry.

According to Medeiros (2017), determining the laminar-turbulent transition location in boundary layers is a challenge even on surfaces that can be considered perfectly smooth. Most surfaces are also not smooth in their manufacture, and depending on the operation, incrustation of dirt, insect fouling, and detrition contribute to include minor defects in the surface of an aircraft, Krishnan *et al.* (2016). In addition, it is necessary to establish the level of tolerance to consider an effectively smooth surface and consider the cost of reaching and maintaining this surface within the levels advised as advantageous, or determine the amount of laminar flow that would be profitable.

Figure 1 – Examples of gaps between wing panels, main element and flap/aileron/slat in (a); junction of the nose with the fuselage and the landing gear doors gaps in (b); panel junctions present on the engine nacelle in (c).



(a) (b) (c)

Source: Images from the internet.

Several transition prediction techniques support the aerodynamic design of an aircraft, for instance, the semi-empirical method e^N developed by Ingen (1956) and Smith and Gamberoni (1956). However, such methods consider the surface to be perfectly smooth, and in practice, a series of irregularities are existent on the surface of an aircraft. According to Crouch, Kosorygin and Sutanto (2020), the literature presents many studies that

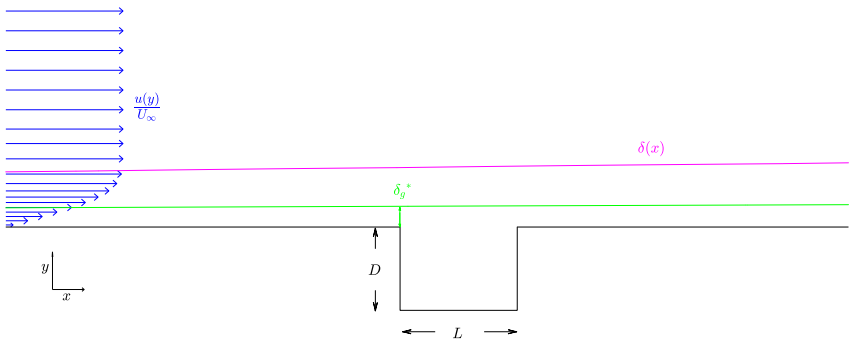
DISTRIBUTION A: Distribution approved for public release. Distribution unlimited

investigate the influence of steps, humps, and roughness on the boundary layer transition, but cavities receive less attention, although they are present on several occasions. One can easily find fabrication gaps or spacing formed between two surfaces in an aircraft wing, fuselage, or nacelle, as shown in Figure 1. Such irregularities introduce significant effects on the boundary layer stability. Therefore, a deeper investigation is necessary.

1.2 Problem description

The purpose of this work is to investigate the influence of small two-dimensional cavities, from now on referred to as two-dimensional gaps, on the two-dimensional boundary layer stability. The term "gap" is relevant, as many works in the literature deal with flow over cavities whose reference lengths are much greater than the thickness of the boundary layer (two or more orders of magnitude), according to Mathias and Medeiros (2019). Therefore, the simulations focus on small gaps, less explored in the literature, particularly in the parametric region inside the envelope specified for the setup designed for experiments in a near future.

Figure 2 – Schematic representation showing the profile view of the flat plate containing the gap immersed inside a laminar boundary layer.



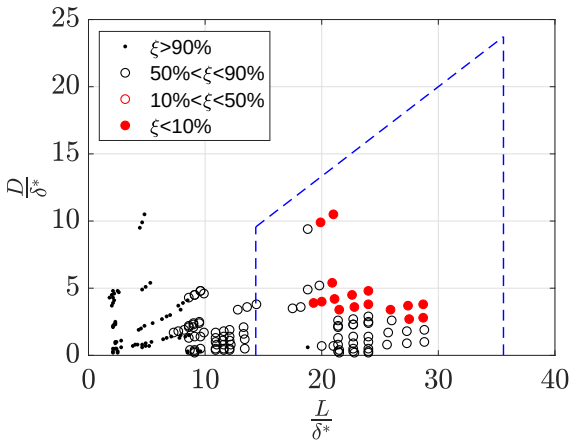
Source: Author (2021).

Figure 2 presents schematically the main parameters involved in the problem. The laminar boundary layer forms over the leading edge of the flat plate and develops until it passes over the gap. The gap has the characteristic dimensions: length, L, and depth, D. Usually, these geometric parameters are dimensionless by the boundary layer displacement thickness over the gap's upstream corner, δ_g^*. The ratio L/D is the cavity aspect ratio. Such parameter classifies the gaps as shallow or deep. Results obtained in the literature indicate that the different flow regimes vary accordingly with the cavity aspect ratio changing. Chapter 2 presents aspects concerning these flow regimes. The Reynolds and

DISTRIBUTION A: Distribution approved for public release. Distribution unlimited

Mach number complete the main parameters from this flow. The first usually employs the cavity length, (Re_L), the depth, (Re_D), the displacement thickness, ($Re_{\delta_g^*}$), or the momentum thickness, (Re_{θ_g}), as the reference length. For the current work, the second only reach the incompressible and subsonic flows regime ($M_\infty < 0.1$).

Figure 3 – Comparison of parameter space envelope defined for the experiments and data extracted from Crouch, Kosorygin and Sutanto (2020).



Source: Author (2021).

We discussed the parametric space envelope for the current study in collaboration with Dr. Jeffrey D. Crouch from Boeing, and the actual research group sought to reproduce the parametric space previously investigated by him and his collaborators, as in Crouch, Kosorygin and Sutanto (2020) and Crouch and Kosorygin (2020). The work carried out by Crouch, Kosorygin and Sutanto (2020) investigated the impact of gaps on the boundary layer transition. Part of their analysis quantified the transition location with the presence of the gap, normalized by the base case (absent gap), through the ξ parameter. Their results, which were extracted and shown in Figure 3, helped to define the parametric space specified for the experimental setup, which corresponds to the region delimited by the dashed lines in blue. The criterion adopted to classify the bypass transition is $\xi < 10\%$. It is possible to identify a threshold region between the two forms of transition, bypass or dominated by the T-S mode. This specific region where bypass transition occurs is the main concerning of the current report.

DISTRIBUTION A: Distribution approved for public release. Distribution unlimited

1.3 Objective

The present report investigates the linear stability of the 2D flow past a gap located over a flat plate, in the parameter space covered by Crouch, Kosorygin and Sutanto (2020) and Beguet *et al.* (2017), and try to correlate these results with the experimental results from the literature. Furthermore, this report covers a numerical study of the transition induced by a gap.

1.4 Report organization

Based on the presented, this report is structured as follows:

- Chapter 2 presents the literature review. Firstly, a contextualization of the boundary layer stability and the transition will be displayed. Afterward, the section explores the literature concerning the flow over cavities, and finally, the impact of gaps in boundary layer transition.
- Chapter 3 describes the methodology for the computational study.
- Chapter 4 exhibits the results obtained for the cases covered and the discussion.
- Chapter 5 expresses the concluding remarks and suggestions.

DISTRIBUTION A: Distribution approved for public release. Distribution unlimited

DISTRIBUTION A: Distribution approved for public release. Distribution unlimited

2 LITERATURE REVIEW

2.1 Boundary layer transition

A few years before the boundary layer formulation, Reynolds (1883) carried out a series of experiments to study the law of resistance to the motion of water in pipes. The author identified two flow patterns through dye injection: direct and sinuous. The fluid flowed in an orderly manner at sufficiently low speeds, however above a critical value of velocity was noted the presence of eddies and higher levels of mixture between the emission line of the dye and the surrounding fluid. These results exposed evidence of turbulent flow, and these findings suggested that the transition between regimes occurred because the flow became unstable.

The concept of stability had already been introduced previously by Stokes (1843), although little explored by him. About thirty years after Stokes' work, Lord Rayleigh began several theoretical studies in an attempt to improve the concept of stability of governing physical equations, as in Rayleigh (1879), Rayleigh (1887) and Rayleigh (1895). The viscous terms, neglected in his analysis, precluded determining a critical Reynolds value. These studies were precursors for the analysis of flow stability.

In the early 20th century, Orr (1907) and Sommerfeld (1908) deduced, independently, the equation which allowed the stability analysis of the boundary layer. The Equation 2.1, later called the Orr-Sommerfeld Equation (OSE), was obtained through manipulating the Linearized Navier-Stokes Equations (LNSE) for viscous parallel flow. The LNSE possesses three main characteristics: (i) a steady parcel, related to the base flow, and an unsteady component, a superimposed harmonic disturbance with relatively small amplitude, composes the flow variables; (ii) the base flow is considered parallel, that is, its profile does not change along the streamwise coordinate; (iii) the omission of non-linear terms. Note that the Equation 2.1 displays the Orr-Sommerfeld Equation in the 2D form.

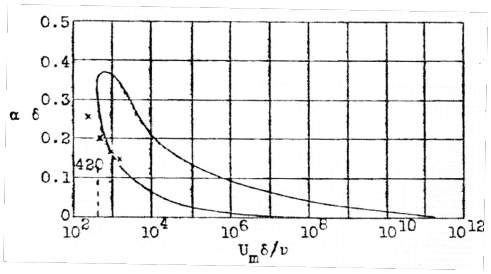
$$(\alpha U - \omega)(v'' - \alpha^2 v) - \alpha v U'' = -\frac{i}{Re_{\delta^*}}(v'''' - 2\alpha^2 v'' + \alpha^4 v) \tag{2.1}$$

The unsteady harmonic disturbance terms are represented in form of normal modes, as an amplitude coefficient, a function of the wall-normal coordinate y, multiplied by a harmonic term, with a spatial wavelength, α, and a temporal frequency, ω, both dimensionless by its respective scales. At the time, the problem consisted of a temporal problem. Thus, the temporal frequency is a complex number in which its real part indicates the phase frequency, while its imaginary part determines the amplification factor, in the case of an unstable state, or the damping factor, otherwise. If its imaginary part equals zero, a neutral state occurs, where nor amplification or damping occurs.

DISTRIBUTION A: Distribution approved for public release. Distribution unlimited

Just after a few decades, Tollmien (1931) and Schlichting (1933) presented significant advances regarding the referred equation, which marked the beginning of the Linear Stability Theory (LST). Through the solution of the temporal problem, the authors presented the numerical calculation of the indifference Reynolds number in their results, which is the maximum value for the stability condition, the neutral stability curves, and the constant amplification rate curves. Figure 4 displays the neutral stability curve calculated by Tollmien (1931).

Figure 4 – Boundary layer neutral stability curve.



Source: Tollmien (1931).

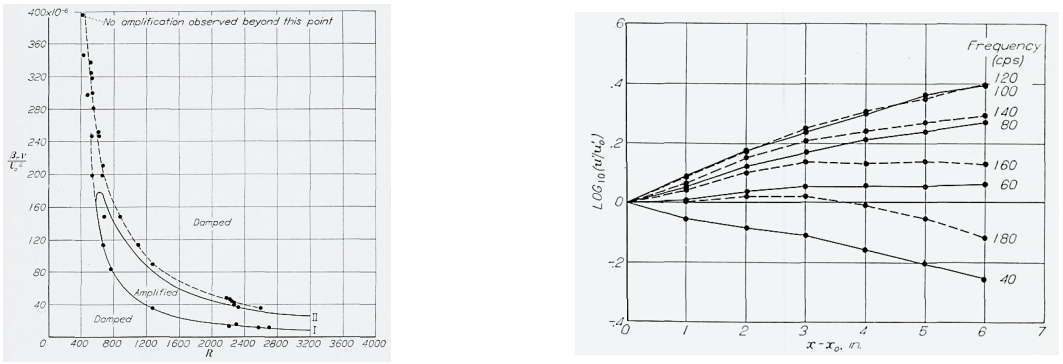
The Linear Stability Theory was only confirmed through the experiments by Schubauer and Skramstad (1948). The authors employed tests on a flat plate positioned inside a wind tunnel. They measured oscillations inside the boundary layer in natural transition experiments. However, they found it more advantageous to reduce the free stream turbulence level and then impose a monochromatic excitation in the boundary layer through a vibrating ribbon parallel to the plate inside the boundary layer. The results showed good agreement with the LST. Figure 5 exhibits the comparison between the theory and their experiments. The authors found good accordance with the theoretical neutral stability curve (Figure 5a), the spatial function of the oscillating wave, and the exponential behavior for amplification of unstable frequencies, as well as for the decaying of stable frequencies (Figure 5b).

Although the LST treats the problem as temporal, in practical terms, the boundary layer stability consists of a spatial stability problem. Later, Gaster (1962) demonstrated, through the Cauchy-Riemann relations, that in regions close to the neutral curve, spatial growth is related to temporal growth through the group velocity, given by the relation $c_g = \partial\omega/\partial\alpha$.

As summarized in Mack (1984), the boundary conditions for the disturbance equation are homogeneous, as the amplitude decays in a sufficiently large distance and at the walls. Thus, the solution is obtained through an eigenvalue problem (EVP). It is necessary to specify some parameters to obtain the dispersion relation. The natural unstable mode present in the boundary layer receives the name of Tollmien-Schlichting (T-S) mode, or T-S wave. Figure 6 depicts the T-S eigenfunction profile. In Figure 6a,

DISTRIBUTION A: Distribution approved for public release. Distribution unlimited

Figure 5 – Experimental evidence of the boundary layer instability predicted by the LST.

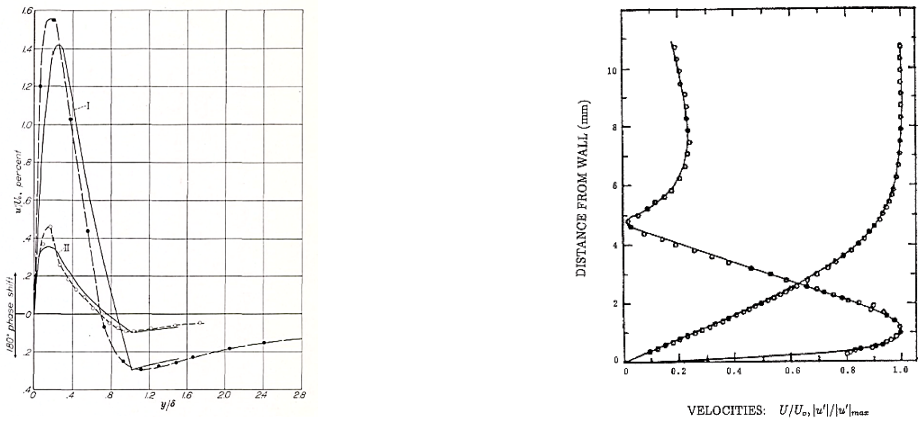


(a) (b)

Source: Schubauer and Skramstad (1948).

the comparison between the measurements made by Schubauer and Skramstad (1948) and the theoretical profile according to H. Schlichting, and likewise, in Figure 6b, the theoretical-experiment comparison by Saric (1990).

Figure 6 – Tollmien-Schlichting wave amplitude profile.



(a) (b)

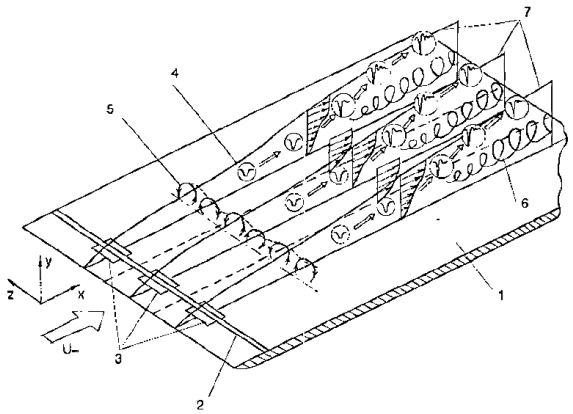
Source: Schubauer and Skramstad (1948) in (a) and Saric (1990) in (b).

Klebanoff and Tidstrom (1959) and Klebanoff, Tidstrom and Sargent (1962) also employed the vibrating ribbon technique as an artificial source of disturbances. Their investigations showed that the presence of three-dimensional instabilities due to non-linear effects dominate in the late stages of transition through an energy concentration mechanism that is distributed alternately in the direction of the span. A theoretical approach of the secondary motion had been developed already by Benney and Lin (1960). Figure 7 displays a schematic picture of such dynamics. These regions with energy concentration are related to the presence of longitudinal vortices and are the places where the laminar regime breaks down. Furthermore, the authors identified a hairpin-shaped eddy structure in the final

DISTRIBUTION A: Distribution approved for public release. Distribution unlimited

process of breakdown into turbulence. Later, this type of laminar-turbulent transition was called K-type transition.

Figure 7 – Schematic representation of the K-type transition proposed by Klebanoff and Tidstrom (1956)., extracted from Kachanov (1994).



Source: Kachanov (1994).

The analytical study of Craik (1971) revealed the existence of non-linear resonance of waves in the boundary layer. The study investigated a triad of Tollmien-Schlichting waves, where one of them was two-dimensional, and the other two were oblique waves propagating at equal and opposite angles to the flow direction. The author demonstrated that it is possible to occur a resonance among a 2D wave with temporal frequency twice times the temporal frequency of the oblique modes since its phase velocity is equal. For some flow conditions from Klebanoff, Tidstrom and Sargent (1962), there was agreement among the frequencies and the spanwise wavenumber predicted by this novel concept. However, some other flow conditions did not agree.

Herbert (1984) numerically studied the case of primary resonance in the Floquet system of stability equations of a spanwise modulated flow. The work demonstrated that his theory was able to numerically model the early stages of the K-breakdown and quantitatively understand why the sub-harmonic instability was not observed experimentally by Klebanoff, Tidstrom and Sargent (1962).

The results from Kachanov, Kozlov and Levchenko (1977) exhibited a different path of the turbulence transition, relative to the K-type from Klebanoff, Tidstrom and Sargent (1962). In this type of transition, no turbulent spikes of unsteady velocity records were observed, as opposite to Schubauer and Skramstad (1948). The spectral analysis of this transition process leads to a four stages subdivision. Initially, a weakly linear development occurred as the growth of fundamental frequency harmonics of the imposed perturbation. Growth attenuation of these components marks the second stage, while low frequency and sub-harmonic content appear in the spectrum. Subsequently, three-dimensional effects interaction occurs among the low-frequency pulsation, the fundamental mode, and its

DISTRIBUTION A: Distribution approved for public release. Distribution unlimited

harmonics. Lastly, the process presents harmonics attenuation and laminar breakdown. This kind of transition driven by three-dimensional sub-harmonic resonance interactions was called N-type transition.

The investigation of Kachanov and Levchenko (1984) studied this second breakdown regime. The appearance of the low-frequency content in the spectrum occurred due to a pair of oblique sub-harmonic waves, agreeing with the theoretical model from Craik (1971). The authors attributed the different regimes to two interaction processes that take place at the same time. However, the distinct excitation conditions may favor only one of these, which will prevail and dominate the transition regime.

The experimental research of Knapp and Roache (1968) combined the smoke visualization and hot-wire anemometry to investigate the transition in axisymmetric ogive nose cylinder aligned with the flow. The author classified the regions of the turbulence transition and, and it was one of the first works to exhibit the N-type laminar breakdown, characterized by the Λ-vortices displayed in the staggered layout. Figure 8 exhibit a photograph of the Λ-vortices in the staggered arrangement, in Figure 8a, and a schematic representation of the Λ-vortices and the hairpin vortices just before the turbulent breakdown, in Figure 8b.

Figure 8 – Smoke visualization of the staggered Λ-vortices in (a) and a schematic representation Λ-vortices breakdown in (b).



(a) (b)

Source: Knapp and Roache (1968).

The experiments by Gaster (1990) led to the conclusion that large-amplitude T-S waves were unstable to weak excitations at their subharmonic frequencies. Furthermore, the rate of amplification of the sub-harmonic content was proportional to the square of the fundamental, in accordance with the weakly non-linear theory.

As the natural transition exhibits a spectral content of a range of frequencies rather than a monochromatic, Gaster (1968) presented a theoretical study of three-dimensional wave packets. Next, Gaster (1975) presented the experimental implementation of 3D wave-packets. An acoustic impulsive point-like disturbance created wave packets that spread out as it convects downstream. The wave packet exhibited a bowed shape at a sufficient distance from the source. Far downstream, it exhibited a distortion in the time

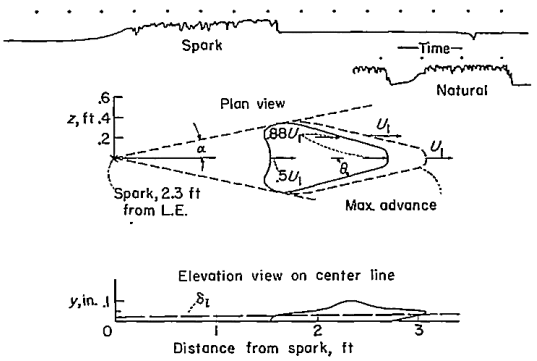
DISTRIBUTION A: Distribution approved for public release. Distribution unlimited

domain, where its peak, initially at the centerline, split and moved to a spanwise distance from the centerline, indicating an oblique wave. The spectral results showed a presence of non-linear effects further downstream by the presence of very low-frequency and harmonic content.

The work of Medeiros and Gaster (1999a) and Medeiros and Gaster (1999b) also experimentally investigated the evolution of wavepackets. The results showed the influence of the phase of the packet relative to the envelope in the non-linear evolution. The presence of oblique modes with a temporal frequency close to the sub-harmonic of the most unstable frequency of the wave packet occurred as well.

The evolution of a point-like monochromatic wave train disturbance was also experimentally investigated by Medeiros (2004). The author found mean flow distortion originated from non-linear interaction. The phenomenon happened in two different stages. In the first, the mean flow distortion is negative in the centerline of the wave train, with two symmetrical positive streaks on both sides of the centerline. In the second stage, the central negative streak split into two, and new streaks formed along the spanwise axis, associated with the peak-valley structure from Klebanoff, Tidstrom and Sargent (1962). A theoretical approach from the parabolized stability equation (PSE) exhibited agreement between the most unstable modes and the experimentally observed.

Figure 9 – Characteristics of a turbulent spot artificially generated. from Klebanoff and Schubauer (1955).



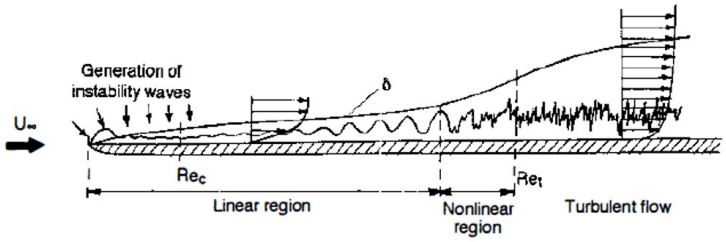
Source: Klebanoff and Schubauer (1955).

After the establishment of the boundary layer stability concept, Klebanoff and Schubauer (1955) expanded the research to investigate the transition process. Through the analysis of the hot-wire output signal, the authors identified, in the transition region, bursts with significantly higher amplitude and frequency in the streamwise velocity. Such structures, named turbulent spots, consist of a portion concentrated with turbulent eddies immersed in the laminar/transitional boundary layer, as exhibited in Figure 9. The authors conclude that an artificial turbulent spot, generated by the electric discharge from a spark inside the boundary layer, possesses characteristics similar to the observed in the natural

DISTRIBUTION A: Distribution approved for public release. Distribution unlimited

transition.

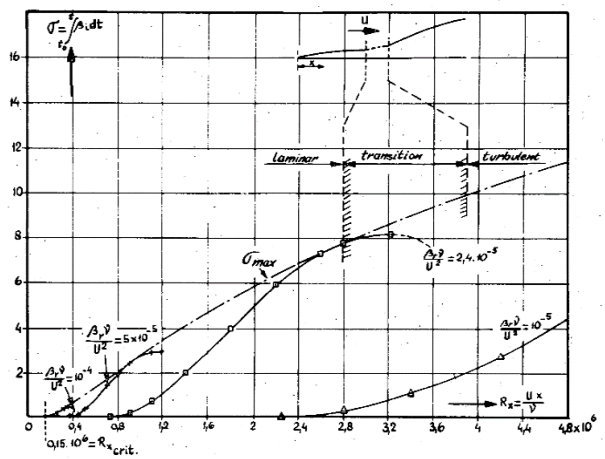
Figure 10 – Stages of the boundary layer transition.



Source: Kachanov (1994).

In summary, the laminar-turbulent transition of a two-dimensional boundary layer is represented by the scheme in Figure 10, taken from Kachanov (1994). The boundary layer is sensitive to disturbances of different natures, and the process of incorporating such disturbances is called receptivity. Up to the critical value of the Reynolds number Re_{δ^*}, the perturbations attenuate. Typically, once the flow reaches the critical Reynolds, instability arises. Thus, a certain frequency range amplifies. While the T-S wave has a small amplitude, the LST can model the amplification of the oscillation. Such a region is called the linear region. However, secondary instabilities and the considerable increase in perturbation amplitude lead to the non-linear region in the final stage of the transition. Consequently, the laminar regime breaks and the turbulent boundary layer occurs.

Figure 11 – Envelope of T-S growth ratio indicating the transition.



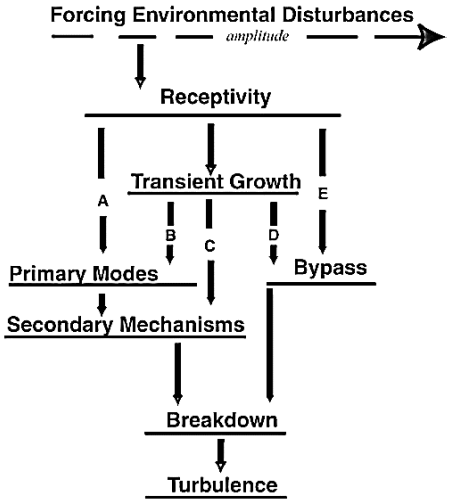
Source: Ingen (1956).

Concerning the transition location detection, Ingen (1956) and Smith and Gamberoni (1956) suggested, independently, a semi-empirical method, based on the linear stability theory, for incompressible two-dimensional flow. The method, named as e^N, correlates the transition region to the locus where the T-S wave growth ratio reach a certain threshold determined experimentally. The authors determined the envelope of

DISTRIBUTION A: Distribution approved for public release. Distribution unlimited

amplification as a function of the Re_x, which is the Reynolds number with the streamwise axis as reference length. The envelope corresponds to the maximum integral growth for each unstable frequency, within the range of the critical Re_x up to the transition. His study indicated that when the T-S amplification reach the value $A/A_0 = e^{7.8}$, the 2D Blasius boundary layer attains the transition. Smith and Gamberoni (1956) found a different value for N based on their experiments, $N = 9$. Such transition prediction method have been extensively employed in the aeronautic field, being present in low-fidelity airfoil design and analysis codes, for instance, the MSES and XFOIL, developed by Drela and Giles (1987).

Figure 12 – Qualitative flowchart showing the routes of boundary layer breakdown to turbulence.



Source: Saric, Reed and Kerschen (2002).

Still, other dynamics may arise in the transition process. The flowchart from Saric, Reed and Kerschen (2002) in Figure 12 depicts the commonly observed routes of transition in laminar boundary layers. From the figure, all possible scenarios pass through the receptivity stage, which establishes the character of the initial disturbances. The previous review regarding boundary layer transition consists of the route A. The transient growth, which is a possible starting point for routes B, C, and D, is a different perspective regarding the stability analysis. It considers the short-term stability analysis through the non-modal theory. According to Schmid (2007), two non-normal stable modes can interact with each other and result in a net amplification. The route E refers to a transition process that deviates from the dynamics predicted by the LST. Thus, it is commonly referred to as bypass transition.

DISTRIBUTION A: Distribution approved for public release. Distribution unlimited

2.2 Cavity instability

2.2.1 Rossiter instability

Investigations of the flow over cavities revealed the oscillatory nature of pressure. The initial motivation of the studies, e.g. Norton (1952), Fail, Owen and Eyre (1954), aimed at understanding these pressure fluctuations as it excites harmful vibrations from the structural point of view (buffeting) for aircraft parts such as the housing of the landing gear or bomb bay in military aircraft.

Later, effects related to aeroacoustics, e.g. Plumblee, Gibson and Lassiter (1962), Rossiter (1964), flow instability, e.g. Colonius, Basu and Rowley (1999), Brés and Colonius (2008), Meseguer-Garrido *et al.* (2014), Liu, Gomez and Theofilis (2016), and transition, e.g. Perraud *et al.* (2004), Zahn and Rist (2016), Beguet *et al.* (2017), and Crouch, Kosorygin and Sutanto (2020), were better understood as a consequence.

Roshko (1955) was one of the first works on the experimental study of the flow inside a two-dimensional cavity. The motivation was to investigate the stability of the vortex system present inside the cavity and its contribution to the drag force. The author concluded that the contribution to drag is mainly due to pressure forces. Although one can neglect the frictional forces for the drag calculation, it is determinant for the stability of the vortex system inside the cavity. Furthermore, the author observed a regime dominated by pressure fluctuations of great magnitude for two ranges of aspect ratio values ($L/D < 0.5$ and $1.15 < L/D < 2$). The oscillation arose due to an exchange between two states of stability. Finally, he found that sound production is associated with stagnation pressure at the rear edge of the cavity.

Krishnamurty (1955) discovered acoustic radiation in the flow over small rectangular cavities. The author employed the schlieren technique for flow visualization and HWA for acoustic field frequency measurements. The intensity of acoustic radiation, when the incident boundary layer was laminar, was greater rather than a turbulent boundary layer. Besides, the character of the acoustic field depends on the cavity dimensions and free-stream velocity or Mach number. Figure 13 displays the images obtained by the schlieren technique, showing the acoustic waves generated at the cavity trailing edge and their dependence on the cavity aspect ratio. Finally, the author concluded that cavities with a lower aspect ratio ($L/D < 2$) emitted high-frequency, high-intensity, and directional acoustic radiation in the laminar regime for a range of Mach values. The frequency was inversely proportional to the cavity length. At the time, he had already highlighted the possibility of these disturbances exerting influence on the boundary layer stability.

Plumblee, Gibson and Lassiter (1962) developed a theoretical model for the characteristic resonant response of a cavity. Experiments allowed comparison and validation of the analytical results. The investigation indicated that the acoustic response of the cavity

DISTRIBUTION A: Distribution approved for public release. Distribution unlimited

Figure 13 – Flow visualization of the acoustic radiation emanating due to cavity instability.



Source: Krishnamurty (1955).

subject to flow in both regimes (subsonic/supersonic) includes the involvement of two phenomena: random frequency response and discrete resonant frequency response. The latter occurs primarily in deep cavities ($L/D \leq 1$), in which the depth mode is dominant.

Rossiter (1964) experimentally identified two distinct regimes influenced by the cavity aspect ratio (L/D). The first pattern occurs for deep cavities, $L/D \leq 4$, with the frequency spectrum marked by a distinct tonal frequency. However, for larger aspect ratios ($L/D > 4$), the author noticed random fluctuations. Their results revealed a coupling between acoustic radiation and the emission of eddies on the upstream edge of the cavity. The vortices convect and impinge with the rear edge of the cavity. Consequently, the collision causes an acoustic emission that propagates upstream and feeds back the vortices formation by destabilizing the cavity shear layer. The author proposed a semi-empirical model, given by Equation 2.2 for the frequency prediction. A considerable attenuation in the amplitude of the unsteady pressure occurred after adding a spoiler in the cavity leading edge.

$$f = \frac{U}{L}\frac{(m-\gamma)}{\left(\frac{1}{K}+M\right)} \tag{2.2}$$

Where:

U: Freestream velocity.
L: Cavity length.
m = 1,2,3... : Modes.
M: Mach number.
γ: Empirical constant related to the phase between the vortex emission and acoustic radiation.
K: Empirical constant related to the vortex convective velocity.

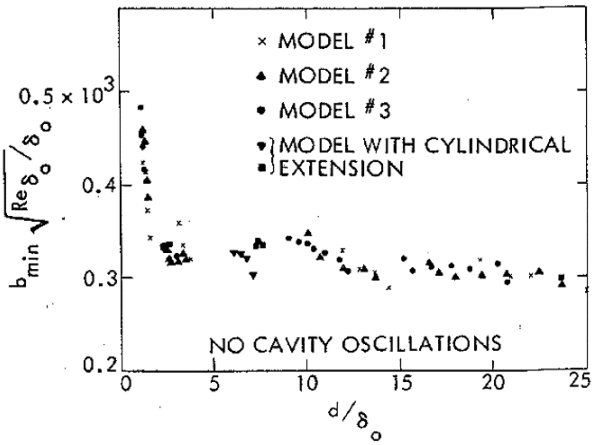
East (1966) carried out experimental experiments similar to Rossiter (1964), seeking to investigate the validity of the models proposed by him, and also by Plumblee, Gibson

DISTRIBUTION A: Distribution approved for public release. Distribution unlimited

and Lassiter (1962). Assuming that the Equation 2.2 was correct and establishing a criterion to determine the resonance condition, the author was able to evaluate the values of K, through the frequency and velocity measured, for different flow regimes and cavity aspect ratio. The author concluded that the formula postulated by Rossiter is consistent. Furthermore, he proved that the theoretical model of Plumblee, Gibson and Lassiter (1962) is also valid. The acoustic coupling between pressure fluctuations of the shear layer and the cavity acoustic modes produced the discrete frequency in the spectrum.

The work carried out by Tam and Block (1978) aimed to develop a mathematical model which includes the parameter θ/D in formulation, as well as the aspect ratio L/D. Experiments also were performed for validation. The results showed good agreement with Rossiter's results and, as predicted by Krishnamurty (1955), confirmed that the momentum thickness of the incident boundary layer exerts a significant influence on the flow. Two distinct tonal production mechanisms occurred, and the transition between these regimes was smooth. The first happened in the range of $M < 0.15$, with its principal cause attributed to the resonance of normal (depth) modes, forced by the energy of the cavity shear layer oscillation. The second involves the feedback between reflections of compression waves generated at the cavity's trailing edge with the oscillations of the shear layer.

Figure 14 – Classification of the flow regimes (permanent or oscillatory) as a function of a novel dimensionless parameter, $(L/\delta)Re_\delta{}^{1/2}$.



Source: Sarohia (1977).

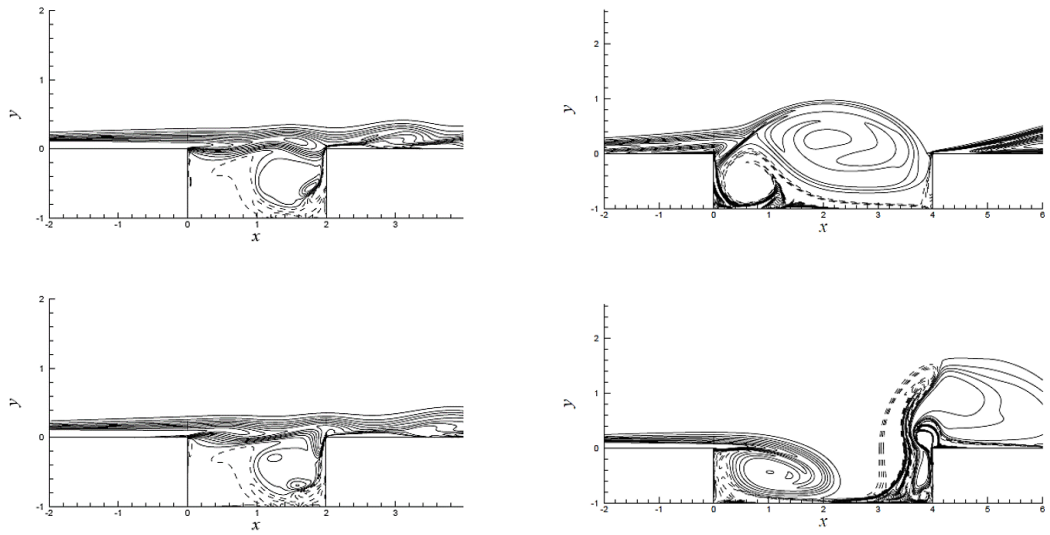
Sarohia (1977) carried out an extensive series of experiments to further investigate the role of the cavity shear layer and the pressure oscillation. The author employed an axisymmetric model containing a cavity with changeable geometry. Its depth and length could vary independently. A laminar incoming boundary layer and subsonic values of free-stream Mach number covered his investigation. Through dimension analysis, the author proposed a threshold to determine whether the flow inside the cavity oscillates or is steady, as shown in Figure 14. The dimensionless parameter is given by $(L/\delta)Re_\delta{}^{1/2}$. Furthermore, two distinct regimes were observed and later documented by Gharib and

DISTRIBUTION A: Distribution approved for public release. Distribution unlimited

Roshko (1987) and Colonius, Basu and Rowley (1999), marked by a jump in the value of the Strouhal number fL/U. The spreading rate of the shear layer momentum thickness in the second regime exhibited a considerable increase compared to the first regime. The author concluded that the oscillation phenomenon in subsonic flows is not an acoustic mechanism in the direction of the flow. These oscillations result from disturbances that propagate and amplify in the shear layer along the cavity.

Gharib and Roshko (1987) studied the effect of the cavity unsteady flow on drag. The author identified four different flow regimes. A stationary regime followed by oscillation in the other three regimes. Two of them had a distinct frequency, one with a lower frequency and a wavelength of one-half of the cavity's length, whereas the other with a higher frequency and a wavelength of one-third of the cavity's length. The author classified these two regimes as self-sustained oscillation mode. In the last regime observed, which occurred for a cavity with great stream-wise length, the flow field resembled a three-dimensional bluff-body wake. The reason why it was named wake mode. This particular flow regime exhibited an asymmetrical behavior and a considerable increase in drag.

Figure 15 – Contours of instantaneous iso-vorticity for arbitrary distinct times exhibiting different modes of cavity instability.



(a) Shear layer mode. (b) Wake mode.

Source: Colonius, Basu and Rowley (1999).

Colonius, Basu and Rowley (1999) performed direct numerical simulation (DNS) of the compressible Navier-Stokes Equations, to investigate resonant instabilities of the flow over cavities. Their results confirmed the presence of the modes identified by Sarohia (1977) and Gharib and Roshko (1987). The authors observed an intermittent transition between the different regimes without overlapping at the same instant. The frequencies for this regime agreed with the semi-empirical model of Rossiter (1964). The emission of large eddies from the cavity characterized the wake mode. Such vortices had dimensions close

DISTRIBUTION A: Distribution approved for public release. Distribution unlimited

to the cavity's size. The cycle involved two distinct events: the vortex formation and its abrupt expulsion. The phenomenon of transient laminar separation was a decisive factor for this regime. Figure 15 displays the flow-field from both modes.

Cattafesta, Garg and Jones (1998) carried out experiments on compressible flow-induced cavity oscillations. The work aimed to understand whether multiple Rossiter modes coexist simultaneously or they switch back and forth. The data analysis with the aid of the Short-Time Fourier Transform (STFT) and the Morlet Wavelet techniques revealed that when the flow conditions favor more than one Rossiter mode, the dominant mode alternatively switches among them. Also, depending on the frequency of the modes the non-linear coupling can occur. Such behavior produced a low-frequency content in the spectrum.

Rowley, Colonius and Basu (2000) numerically investigated the compressible flow over cavities, using DNS to simulate the flow and Proper Orthogonal Decomposition (POD) technique for analysis of coherent structures and oscillation modes. His study focused on small cavities ($D/\delta^* \approx 10$) with aspect ratio, $L/D = 2$, and $L/D = 4$, and Mach number, $M = 0.6$. The Reynolds values employed are of the order of $Re_{\delta^*} \approx 20$. The modes were compared with the linear theory for the Kelvin-Helmholtz instability and showed good agreement, even in regions close to the trailing edge. However, the model used was not well suited to capturing low-frequency modes.

Yamouni, Sipp and Jacquin (2013) performed global stability analysis of the open cavity flow. Their Mach ranged from the incompressible ($M = 0$) up to the subsonic compressible regime ($M \leq 0.9$). The study revealed the acoustic feedback mechanism from Rossiter (1964) and the acoustic resonance within the cavity from Plumblee, Gibson and Lassiter (1962). Their results suggested that the Rossiter mechanism of instability predominates in low Mach, and as the Mach number increases, the authors observed an overshoot in amplification of unstable Rossiter modes when occurred coupling with the acoustic modes from Plumblee, Gibson and Lassiter (1962). This could explain the reason why the Mach number exerts a destabilizing role when increased.

Mathias and Medeiros (2018) performed a parametric sweep to study the Rossiter dependency on the Mach number and the displacement thickness over the gap through DNS and instability analysis. The author concluded that the incoming boundary layer plays a role in selecting which Rossiter mode will occur, whereas the Mach increases the acoustic energy transfer and, consequently, the temporal growth of the mode. Their results also indicated that the coupling between Rossiter modes and the acoustic resonance from Plumblee, Gibson and Lassiter (1962) is related to the peak in the amplification rate.

Sun *et al.* (2017) investigated the stability of compressible flows over open cavities. The authors carried out 2D and 3D DNS, as well as the global stability analysis to 2D and 3D disturbances. The parametric space covered the free stream Mach number within the

DISTRIBUTION A: Distribution approved for public release. Distribution unlimited

range $0.3 \leq M_\infty \leq 1.4$. Their results exhibited agreement between the 2D DNS and the 2D instability analysis. They noticed that the dominant Rossiter mode switched when the Mach number surpassed certain value. In the subsonic regime, $M_\infty < 0.6$, an increase in Mach resulted in increase of the instability. However, in the transonic regime, the Rossiter mode stabilized as the Mach number was increased, mainly for the cavity with aspect ratio $L/D = 6$.

2.2.2 Centrifugal instability

Bayly (1988) performed an analytical approach to extend Rayleigh's centrifugal instability theory for inviscid two-dimensional flows. The author carried out the instability analysis through the Floquet analysis on the flow streamlines. The instability condition happened when closed convex streamlines had a decreasing circulation in the outward direction.

The work carried out by Theofilis (2000) employed the three-dimensional instability analysis on the permanent incompressible two-dimensional laminar flow over an open cavity. The objective was to determine three-dimensional modes distinct from the two-dimensional Rossiter instabilities. The author found the best numerical strategy to model the cavity as a lid-driven cavity and concluded that the open cavity base flow has much more stringent spatial resolution requirements when compared to other flows for the accurate calculation of amplification/damping rates. However, the mode frequencies converged more easily.

Albensoeder, Kuhlmann and Rath (2001) numerically investigated for both finite and infinite lid-driven cavity flow modes. For shallow cavities, the most unstable fluctuations were a pair of oscillatory modes with a short wavelength. The amplitude function presented relevant intensity near the downstream edge of the gap. Two distinct modes could occur for aspect ratio close to the unit. A stationary or a pair of oscillatory modes, depending on flow conditions and the geometry. In deep cavities, the dominant mode was steady with a long wavelength.

Non, Pierre and Gervais (2006) performed an analytical study on the stability of a spanwise infinitely long lid-driven cavity. The authors built the neutral curves for different Reynolds and wavenumbers. They identified that the first mode to become unstable was stationary, which bifurcates at a local minimum in the $\beta \times Re$ chart. The absolute minimum occurred for a longer spanwise wavelength, and the dominant mode is the stationary one, anew.

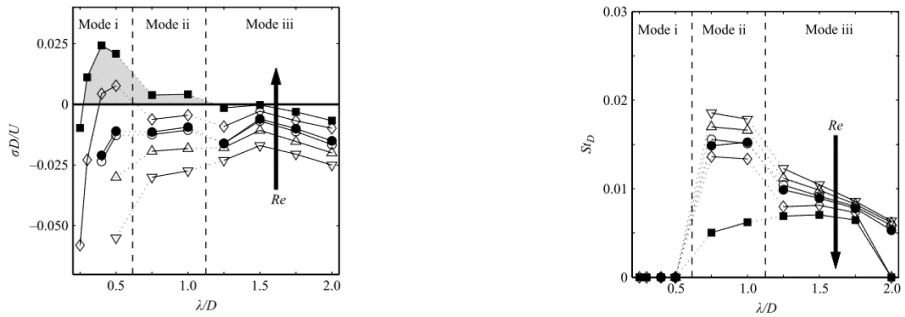
Faure *et al.* (2007) performed a series of experiments of flow visualizations to comprehend better the 2-D and 3-D topology of the flow past open cavities. They reported the presence of 3D structures for a range of Reynolds number and aspect ratio.

Brés and Colonius (2008) carried out numerical studies via DNS to investigate

DISTRIBUTION A: Distribution approved for public release. Distribution unlimited

the stability of three-dimensional perturbations in two-dimensional compressible subsonic flows over open cavities, with an aspect ratio in the range of $2 \leq L/D \leq 4$. Their results indicated the presence of an oscillatory mode in the spanwise direction, with a wavelength of the order of the cavity depth, as indicated in Figure 16. According to them, this instability arose due to a non-acoustic nature, attributed to a mechanism of centrifugal instability. The Rossiter modes subject to this 3D oscillation undergo low-frequency spanwise modulation due to non-linear interactions.

Figure 16 – Amplification factor and non-dimensional frequency of the leading 3D eigenvalues.



(a) Amplification *versus* spanwise wavelength.

(b) Strouhal *versus* spanwise wavelength.

Source: Brés and Colonius (2008).

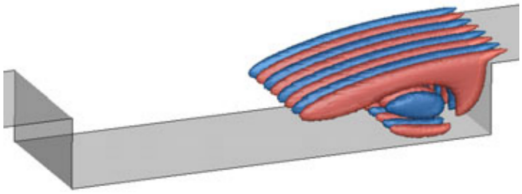
De Vicente *et al.* (2014) numerically and experimentally investigated the centrifugal instability in flow regimes in which the Rossiter mode is not present for gaps with aspect ratio $L/D = 2$. The authors constructed the neutral stability diagram for different spanwise wavenumbers and Reynolds and reported a rich experimental characterization of the flow's oscillation structures.

The work from Meseguer-Garrido *et al.* (2014) numerically scanned an extensive parametric space to survey the neutral and amplification curves for different gap geometry and flow conditions. The authors noted the presence of two three-dimensional modes, a bifurcated one (with oscillatory and stationary components depending on the flow conditions) and a purely traveling mode. The stability dependence of these modes was studied by sweeping mainly the following parameters: the characteristic Strouhal number, the Reynolds number, and the aspect ratio.

Sun *et al.* (2017) examined the stability characteristics of the compressible open-cavity flow via DNS and Bi-Global method. The authors simulated 2D and 3D flows. Their stability analysis presented results similar to Brés and Colonius (2008). The author advised that cavities with larger aspect ratios had relevant non-linear interactions between the 2D and 3D modes, diverging from the linear assumptions of stability analysis. Figure 17 exhibits an example of an eigenfunction of one of the centrifugal modes from his work.

DISTRIBUTION A: Distribution approved for public release. Distribution unlimited

Figure 17 – Most unstable centrifugal stream-wise velocity amplitude function ($\lambda/D = 0.5$) for a cavity with $L/D = 6$.



Source: Sun *et al.* (2017).

Mathias and Medeiros (2020) numerically investigated the interaction between Rossiter and centrifugal modes in sub-sonic flow over open cavities. After the linear stability analysis, the authors identified the preferred 3D spanwise wavelength to determine the spanwise domain in the 3D DNS. They also noted that in the 3D runs, the spectrum peaks associated with the Rossiter were less sharp than in the 2D runs. They attributed this to a spanwise modulation of the Rossiter due to the centrifugal modes. According to them, such motion could potentially alter the base flow and consequently its stability.

2.3 Effect of gaps in boundary layer transition

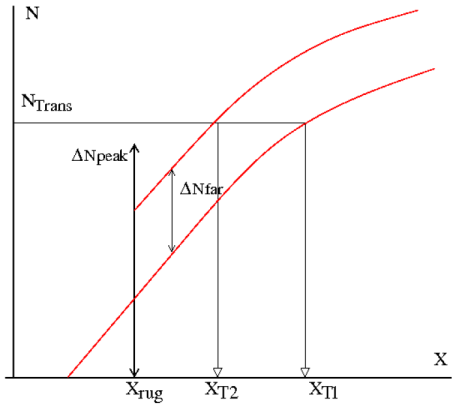
Perraud, Arnal and Kuehn (2014) performed numerical studies to develop a model capable of obtaining the variation of the factor-N, ΔN, given the presence of a gap, in comparison with the case without it. The authors noted that the impact on the-N factor was independent of the cavity depth when $L/D < 3.33$. The frequency spectrum presented low-frequency and high-frequency components. They also reported the presence of the bypass transition in runs with higher gaps length. The developed model separated the ΔN parameter into two parts. One corresponds to the variation located over the cavity, called ΔN_{peak}, and the other represents the displacement of the curve, called ΔN_{far}. Figure 18 displays a schematic representation of the behavior of the amplification curve caused by the presence of a cavity.

The numerical and experimental work developed by Forte *et al.* (2015) investigated the impact caused by gaps in the transition of the boundary layer over an airfoil. The main goal was to validate the numerical model developed by Perraud, Arnal and Kuehn (2014). The authors concluded that the cavity length is a relevant parameter to estimate the critical condition where the bypass transition occurs. Figure 19 displays the root-mean-square unsteady velocity along the airfoil chord for a constant free-stream velocity for different gap geometries.

The work of Beguet *et al.* (2017) brings together results of several experimental, numerical, and theoretical researches on the effect of gaps on the boundary layer transition.

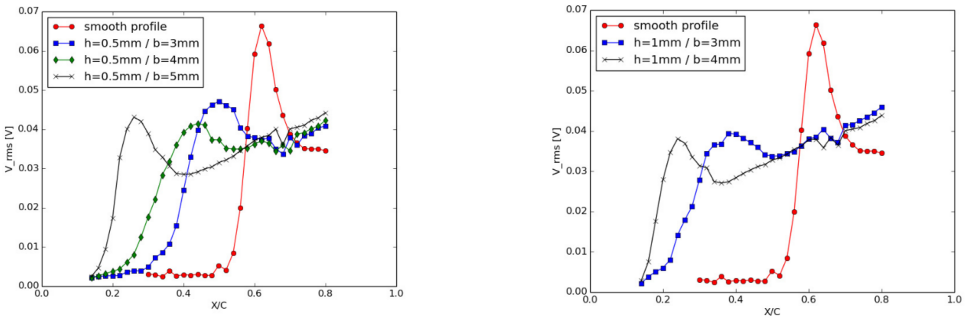
DISTRIBUTION A: Distribution approved for public release. Distribution unlimited

Figure 18 – Representation of the T-S amplification affected by the presence of a gap.



Source: Perraud, Arnal and Kuehn (2014).

Figure 19 – Root-mean-square of streamwise unsteady velocity along the chord for different experiment runs.



(a) Evolution of perturbation velocity along the chord for a cavity with depth $D = 0.5$ mm and different lengths.

(b) Evolution of the perturbation velocity along the chord for a cavity with depth $D = 1.0$ mm and different lengths.

Source: Forte *et al.* (2015).

They initially investigated gaps as an alternative to forcing a turbulent boundary layer without changing its thickness, in contrast with an excrescence or roughness. For 2D flows, the investigated parametric space presented as limits for the forced transition, the values of $L/\delta^* \geq 18$ and $D/\delta^* \geq 2$. The theoretical approach of the LST for the local profiles obtained for their numeric computed steady base flow exhibited two behaviors for a lower and a higher frequency range. The first manifested a slightly pronounced growth of the T-S unstable frequencies range locally over the gap and further downstream. The oscillation components with a higher range of frequency were highly amplified just over the gap. The authors also reported a great local change in the shape factor, $H = \delta * /\theta$, over the gap, from the common value 2.59 to near 7.00.

Crouch and Kosorygin (2020) performed experimental correlations, investigating

DISTRIBUTION A: Distribution approved for public release. Distribution unlimited

step, regular protrusion, and gap effects on the boundary layer transition with a slight non-zero imposed pressure gradient. The author sought to correlate the variation of the N-factor, ΔN, as a function of the parameter h/δ^*, and also D/δ^*. The h parameter represents the height of the protrusion or forward-facing step, whereas D represents the depth for the cavity or the backward-facing step. The linear combination of the results of the forward-facing and backward-facing step modeled well the ΔN, according to the results for the rectangular protrusion. However, for shallow gaps, the model was best represented only by a backward-facing step correlation.

Crouch, Kosorygin and Sutanto (2020) also experimentally performed correlations for the ΔN, for gaps with different aspect ratios and sizes. The authors found a range of values where there is a change in T-S growth and a range of parameters where bypass transition occurred. Figure 20b depicts the diagram that delimits the bypass transition locus, built by the authors. They observed that in a particular run where bypass transition occurred, the oscillation frequency was about 5 times greater than the frequency content expected for the most magnified T-S for this flow conditions. They also proposed a model to estimate the variation ΔN according to the gap geometry, as shown in Equation 2.3. For shallow gaps, with $L/D > 35$, the ΔN depends only on the depth and is well modeled by the backward-facing step correlations, while for deep gaps, $L/D < 35$, the ΔN depends only on the length. Below is the correlation equation proposed by Crouch, Kosorygin and Sutanto (2020). Figure 20a, from Crouch, Kosorygin and Sutanto (2020), schematically describes the correlation of the ΔN factor as a function of the geometric characteristics of the cavity.

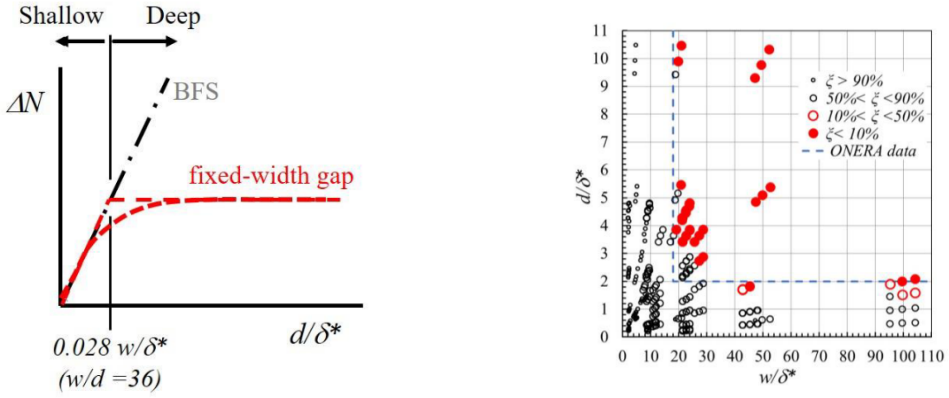
$$\Delta N = 0{,}122\frac{L}{\delta^*}\tanh\left(36\frac{D}{L}\right) \tag{2.3}$$

Mishriky and Walsh (2018) performed a simpler numerical approach, through the Unsteady Reynolds-Averaged Navier-Stokes equations (URANS) method, to study the influence that deep gaps had on the transition of a laminar boundary layer over a flat plate and an airfoil as well. Based on the analysis of several cases, the author defined a dimensionless parameter capable of predicting the presence of bypass transition. The critical value occurred in the range $L/\theta\sqrt{Re_\theta} > \ 600$.

Zahn and Rist (2016) numerically investigated through DNS the impact of deep gaps on the laminar-turbulent transition of a Blasius boundary layer at Mach $M = 0.6$. His study compared the growth of T-S waves (ΔN) artificially introduced in the flow for the runs with and without the gap. The authors concluded that the acoustic feedback mechanism in the cavity formed a stationary acoustic wave that had a substantial impact on ΔN. The author compared the T-S growths for an asymmetric cavity and a forward-facing step with the same height as the difference of the front and rear lip of the asymmetric

DISTRIBUTION A: Distribution approved for public release. Distribution unlimited

Figure 20 – Correlation scheme of the ΔN as a function of the gap geometry in (a) and the bypass locus diagram given by the red filled circles in (b).



Source: Crouch, Kosorygin and Sutanto (2020).

gap. For a given gap geometry, the author found a reduction in ΔN for the run with the asymmetric cavity.

Mathias and Medeiros (2019) performed DNS and global instability analysis of the flow over gaps with aspect ratio $L/D = 2$ and 5. Furthermore, the author inserted T-S wavepackets upstream of the small cavity to check the interaction between them. The authors also compared the results with a wave packet over a flat plate in the same flow conditions. The wave packets presented a local change over the gap. Further downstream such distortion was attenuated, except for a phase shift. The wave packet exhibited a considerable spatial distortion locally over the cavity, and a pronounced spike occurred at the trailing edge of the gap. The frequency content revealed a change in amplitude for higher frequencies, whereas negligible effect in the lower range of frequencies. The temporal instability analysis of a run with stable condition revealed that the less stable mode had an eigenfunction very similar to the flow field of the base flow plus a monochromatic disturbance with the same frequency.

DISTRIBUTION A: Distribution approved for public release. Distribution unlimited

DISTRIBUTION A: Distribution approved for public release. Distribution unlimited

3 METHODOLOGY

The present section describes the numerical approach, consisting of two stages: the direct numerical simulation (DNS), covered in section 3.1 and the linear stability analysis, in section 3.2.

The DNS approximates an unsteady solution of the Navier-Stokes Equations without turbulence modeling. If the flow is globally stable, the long-term solution will reach a steady-state, also known as the base flow. In contrast, in the case of a globally unstable flow, it is possible to dampen the oscillations through the selective frequency damping (SFD) technique to reach the base flow.

The linear stability analysis assesses the stability, neutrality, or instability of a given base flow to 2D and 3D disturbances. The method, implemented by Mathias (2017), attains the oscillation modes of the base flow through the evaluation of the eigenvalues and eigenfunctions of the flow Jacobian matrix, which is approximated by an Arnoldi-based time-stepping method.

3.1 Direct Numeric Simulation

The DNS solver is an in-house code developed by the own research group. Details of the implementation of the code are provided in the current section, albeit a supplementary reading is available in Bergamo (2014), Martinez (2016), and Mathias (2017). To enhance the computational efficiency, the solver runs in Fortran 90, and the 2DECOMP&FFT library performs the processing parallelization. The scientific computational software Matlab employs pre and post-processing.

3.1.1 Governing equations

The compressible Navier-Stokes Equations (NSE) are used to model the flow. As acoustic resonance within the gap can cause the Rossiter instability, the solver must assess compressibility effects. The Navier-Stokes Equations refers to the set of equations obtained by deriving the physical laws of conservation of mass, momentum, and energy in a fluid. State equations for ideal gas supplement the NSE.

The flow is defined by five variables: density (ρ), internal energy (e) and the three components of velocity in the Cartesian system, $\vec{V} = [u \;\; v \;\; w]^T$, all of them functions of space and time. The code employs the equations in the non-conservative formulation.

DISTRIBUTION A: Distribution approved for public release. Distribution unlimited

Below, the equations used by the numeric solver.

$$\frac{\partial \rho}{\partial t} = -\rho \frac{\partial u_i}{\partial x_i} - u_i \frac{\partial \rho}{\partial x_i} \tag{3.1}$$

$$\frac{\partial u_j}{\partial t} = -u_i \frac{\partial u_j}{\partial x_i} - \frac{1}{\rho}\frac{\partial p}{\partial x_j} + \frac{1}{\rho}\frac{\partial \tau_{ij}}{\partial x_i} \tag{3.2}$$

$$\frac{\partial e}{\partial t} = u_i \frac{\partial e}{\partial x_i} - \frac{p}{\rho}\frac{\partial u_i}{\partial x_i} + \frac{\tau_{ij}}{\rho}\frac{\partial u_j}{\partial x_i} - \frac{1}{\rho}\frac{\partial q_i}{\partial x_i} \tag{3.3}$$

Where the viscous stress tensor and heat flux are given by:

$$\tau_{ij} = \frac{\mu}{Re}\left(\frac{\partial u_i}{\partial x_j} + \frac{\partial u_j}{\partial x_i} - \frac{2}{3}\delta_{ij}\frac{\partial u_k}{\partial x_k}\right) \tag{3.4}$$

$$q_i = -\frac{\mu}{(\gamma - 1)\ Re\ Pr\ M_\infty^2}\frac{\partial T}{\partial x_i} \tag{3.5}$$

According to the ideal gas law, one has:

$$T = e\gamma(\gamma - 1){M_\infty}^2 \tag{3.6}$$

$$p = (\gamma - 1)\rho\ e \tag{3.7}$$

Dynamic viscosity is modeled by the Sutherland Equation:

$$\mu = \frac{1.367}{T + 0.367}T^{\frac{3}{2}} \tag{3.8}$$

Reynolds, Prandtl, and Mach numbers are given, respectively, by:

$$Re = \frac{\tilde{\rho}\ \tilde{U}_\infty\ L_0}{\tilde{\mu}} \tag{3.9}$$

$$Pr = \frac{\tilde{\mu}\ \tilde{c}_p}{\tilde{k}} \tag{3.10}$$

$$M_\infty = \frac{\tilde{U}_\infty}{\sqrt{\gamma\ \tilde{R}\ \tilde{T}_\infty}} \tag{3.11}$$

The sub-index, $_\infty$, represents free-stream, and superscript, $\tilde{}$, indicate quantities in dimensional form. The appropriate scales are shown below:

$$\rho = \frac{\tilde{\rho}}{\tilde{\rho}_\infty},\ p = \frac{\tilde{p}}{\tilde{\rho}_\infty \tilde{U}_\infty^2},\ x_i = \frac{\tilde{x}_i}{L_0},\ T = \frac{\tilde{T}}{\tilde{T}_\infty},\ u_i = \frac{\tilde{u}_i}{\tilde{U}_\infty},\ t = \frac{\tilde{t}\,\tilde{U}_\infty}{L_0},\ e = \frac{\tilde{e}}{\tilde{U}_\infty^2} \tag{3.12}$$

DISTRIBUTION A: Distribution approved for public release. Distribution unlimited

Because cavity shear layer instability is essentially a two-dimensional phenomenon, it was employed a 2D DNS for practical reasons. Thus, a null spanwise velocity and null derivatives for all flow variables in such direction.

3.1.2 Computational domain

The DNS code uses structured Cartesian mesh for domain discretization. The mesh has a standard uniform spacing. However, one can employ grid refinement in particular regions where is expected higher derivative values. The refinement technique concentrates nodes in pre-defined regions, through the allocation of attractors. The parameters used to define the attractor are region, size, and strength. Each spatial direction can be refined independently.

The attractor is defined by the following transformation of the spatial domain:

$$\eta = \int 1 \; + \; \sum \left(R_i \; e^{\frac{x - L_i}{S_i}} \right) dx \tag{3.13}$$

Where R_i, L_i, and S_i are, respectively, the strength of the attractor, the location, and its size. Part of the routine ensures that specified nodes remain fixed, for instance, the leading edge of the flat plate, or the corners of the gap, slightly distorting the spacing of the surrounding nodes.

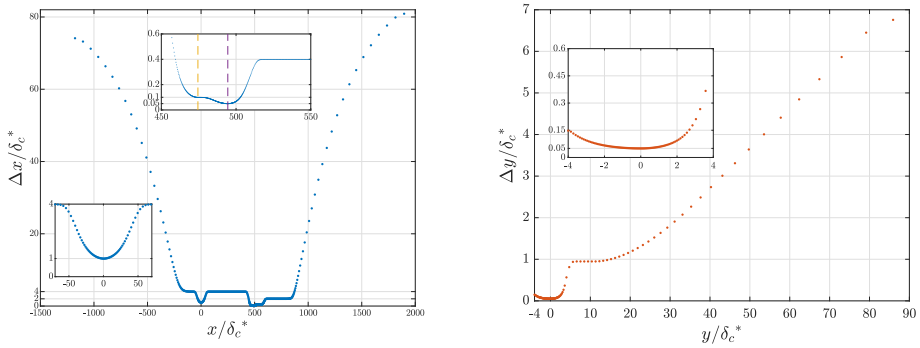
The domain presents buffer zones at the open boundaries to avoid the reflection of oscillations, thus providing suitable far-field conditions. Two factors inherent to buffer zones contribute to this: (i) gradually increase the spacing between the nodes and (ii) reduce the accuracy order of the method used for the spatial derivatives. A smooth transition between the spatial derivative methods occurs due to the linear combination of both methods. Therefore, the closer to the domain-useful/buffer zone interface, the greater the influence of the higher-order method. The length for this transition region, in the current simulations, had a value of 20% of the buffer zone span for each direction. Two different analytical functions were employed for the buffer zone spacing enhance, the sigmoid function in the x-axis, and the exponential function, in the y-axis.

Figure 21 exhibits the typical mesh spacing for the current DNS. The Figure 21a displays the stream-wise axis, x, spacing, while Figure 21b shows the wall-normal axis, y.

Different levels of refinement are applied. It is possible to note grid refinement around the zero in Figure 21a, which is the flat plate's leading edge. Stagnation occurs in this location, and as a result, a pressure gradient develops. Ergo, adequated mesh refinement is necessary to ensure a good Blasius profile. The zone with massive refinement is the gap, as it is the region of the simulation with great values of derivatives. The minimum spacing of the nodes occurs in its trailing corner. Following the flow trajectory,

DISTRIBUTION A: Distribution approved for public release. Distribution unlimited

Figure 21 – Mesh spacing for x axis in (a) and y in (b).



(a) (b)

Source: Author (2021).

the nodes in the x axis stretch out after the gap until the outflow buffer zone. Once is expected oscillation inside the boundary layer downstream of the cavity, a constant level with refinement occurs closer to it, followed by the second level of spacing, which is slightly higher than the previous. In the y axis, exhibited in Figure 21b, the minimum spacing occurs at the zero, which is the coordinate of the flat plate.

3.1.3 Boundary and initial condition

Figure 22 depicts the typical computational domain employed. The left edge, usually referred to as the inflow boundary, corresponds to the domain's upstream. Alternatively, the right edge corresponds to the outflow. The Dirichlet condition is set for the variables velocity and temperature, at the inflow, through the imposition of constant and uniform values along the y axis. The Neumann condition is defined for the pressure, therefore, with the first derivative null. At the outflow, the pressure has Dirichlet's condition, whereas the other variables have Neumann's condition.

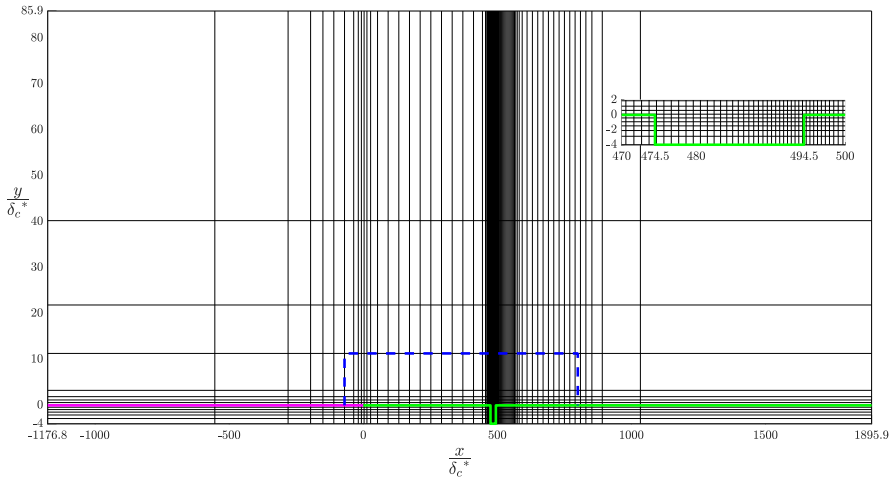
The top edge of the domain corresponds to the open boundary. There, all variables have a null second derivative. The walls of the flat plate and gap are represented in Figure 22 by the solid lines, being the magenta, free-slip wall, and the green, no-slip wall. The first represents the incoming free stream, while the second the flat plate itself.

The free-slip wall has a null derivative of the stream-wise component relative to the y. The no-slip wall possesses a null stream-wise and wall-normal velocity component. Furthermore, an imposed value of the internal energy, $e_0 = 1/((\gamma^2 - \gamma)M^2{}_\infty)$, and a null derivative for the pressure relative to its normal direction, i.e. relative to y axis in the horizontal walls or relative to x axis in the vertical walls of the gap.

The pressure and temperature are not computed directly by the governing equations but through the internal energy and density equations, Equation 3.1 and Equation 3.3,

DISTRIBUTION A: Distribution approved for public release. Distribution unlimited

Figure 22 – Plot of a typical computational mesh grid for the current work. Only every tenth consecutive node and the domain boundaries exhibited. An auxiliary plot on top right zooms in the gap region. Solid lines represent the wall (magenta is free-slip, and green is no-slip). Blue dashed lines indicate the domain-interior/buffer zone interface.



Source: Author (2021).

respectively. Thus, the routine responsible to apply the boundary conditions first changes the energy to respect the temperature conditions and posteriorly computes the density to respect the continuity.

The boundary conditions in the corners of the gap have a particular treatment. Because the corner has two directions, the boundary condition in one direction may violate the condition in the other direction. Therefore, at the gap corners, the pressure is calculated as the average of the pressures that satisfy the boundary condition in each direction.

The initial condition may be the Blasius boundary layer with null pressure/temperature gradient, computed numerically through the solution of the Blasius equation, a uniform flow, or finally, a previous solution from another simulation. For the last, it is necessary to perform a linear interpolation to adequate the available values of the variables for the actual mesh.

3.1.4 Spatial derivatives method

The spatial derivative terms are approximated by finite differences schemes with spectral-like resolution according to Lele (1992). Consider a uniformly spaced grid, $x_i = h(i-1)$ for $1 \leq i \leq N$, representing the independent variable, and the dependent variable at the nodes, $f_i = f(x_i)$. The finite difference approximation, f'_i, to the first derivative can

DISTRIBUTION A: Distribution approved for public release. Distribution unlimited

be written in the following form.

$$\beta f'_{i-2} + \alpha f'_{i-1} + f'_i + \alpha f'_{i+1} + \beta f'_{i+2} = a\frac{f_{i+1} - f_{i-1}}{2h} + b\frac{f_{i+2} - f_{i-2}}{4h} + c\frac{f_{i+3} - f_{i-3}}{6h} \quad (3.14)$$

Where α, β, a, b, and c are adjustable coefficients, and h is the uniform distance between the nodes. Applying the Taylor series and matching the coefficients of same order, one obtains the linear system that relates the coefficients. Below are the equations that govern the coefficients for each order. The formal truncation error is given by the order of the first unmatched term.

$$a + b + c = 1 + 2\alpha + 2\beta \qquad O(h^2) \quad (3.15)$$

$$a + 2^2 b + 3^2 c = 2\frac{3!}{2!}(\alpha + 2^2\beta) \qquad O(h^4) \quad (3.16)$$

$$a + 2^4 b + 3^4 c = 2\frac{5!}{4!}(\alpha + 2^4\beta) \qquad O(h^6) \quad (3.17)$$

For both α and β equal to zero, the method is defined explicitly. If the coefficient $a = 1$ and $b = c = 0$, the Equation 3.14 degenerates into the second-order explicit finite difference method. This particular scheme was chosen to approximate the spatial derivatives in the buffer zones. In contrast, we selected the sixth-order implicit scheme for the interior domain spatial derivatives. For this, $\alpha \neq 0$ and $\beta = 0$. The ill-posed system is avoided through the imposition of a fourth equation.

To evaluate the errors associated with the approximation, Lele (1992) compares the Fourier coefficients of the derivative obtained from the diffentiation scheme with the exact Fourier schemes. Thus, assuming a periodic domain [0,L], where $f_1 = f_{N+1}$, and $h = L/N$, one can decompose into a discrete Fourier transform.

$$f(x) = \sum_{k=-N/2}^{k=N/2} \hat{f}_k \, \exp\left(\frac{i2\pi kx}{L}\right) \quad (3.18)$$

It is convenient to define the scaled wavenumber, $\omega = 2\pi k/N$, and the scaled coordinate, $s = x/h$, with the Fourier modes simplified by $\exp(i\omega s)$. The i corresponds to $i = \sqrt{-1}$. The Fourier analysis of errors performed by Lele (1992) yields in the following relation.

$$\omega'(\omega) = \frac{a\sin(\omega) + (b/2)\sin(2\omega) + (c/3)\sin(3\omega)}{1 + 2\alpha\cos(\omega) + 2\beta\cos(2\omega)} \quad (3.19)$$

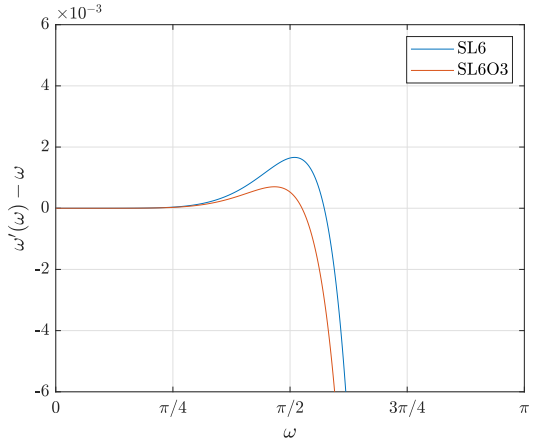
DISTRIBUTION A: Distribution approved for public release. Distribution unlimited

The parameter ω' represents the modified wavenumber. Therefore, within a defined range of wavenumber, it is possible to consider the method spectral-like, as one can ensure that the modified wavenumber is the same as the wavenumber itself, or present a neglegible error. The DNS uses the parameter $\omega'(\omega_f) = \omega_f = 1.8$ as criteria. Thereby, it is possible to determine the coefficients from the numerical scheme.

Recently, another form to determine the coefficients was implemented according to Gaitonde and Shang (1996). The procedure is to first determine the optimal value of α, which is obtained through the value that minimize the accumulated dispersion error along the interval $\omega \in [0,\omega_f]$ according to Equation 3.20. Such optimization produces less overshoot in the dispersion error for wavenumbers below ω_f. The trade-off of is the increasing in error for wavenumbers above this limit. However, the anti-aliasing filter is more restrictive in this region. Figure 23 exhibits the comparison of the dispersive error as a function of the wavenumber for the previous scheme (SL6) and the actual (SL6O3).

$$\min\{\varepsilon_{disp}(\alpha,\omega_f)\} = \min \int_0^{\omega_f} |\omega'(\omega;\alpha) - \omega| d\omega \tag{3.20}$$

Figure 23 – Comparison of the dispersive error of the numerical schemes. In blue, the SL6 scheme, and in orange, the SL6O3, after the optimization according to Gaitonde and Shang (1996).



Source: Author (2021).

Close to the boundaries, there is two possible ways to avoid that the stencil requires a node that are nonexistent: keep the order and use an asymetric scheme or reduce the order and keep a centered scheme. The latter is more appropriate to the current study, because test runs showed that, despite the loss in accuracy, it not jeopardizes the numerical stability. Therefore, for the spatial derivative approximation of a point two grid nodes distant from the boundary, for simplicity $i = 2$, the scheme reduces the order from the sixth-order implicit to the fourth-order implicit. Following, the imediate point ($i = 1$)

DISTRIBUTION A: Distribution approved for public release. Distribution unlimited

employs a fourth-order compact scheme, similar to the Padè scheme, and finally a asymetric third-order compact scheme at the boundary ($i = 0$).

The chain rule is applied to adequate the derivatives, as the numerical schemes are tailored for a uniformly spaced mesh, which is not the type of mesh utilized by the actual simulations.

3.1.5 Anti-aliasing filter

The motion in the shortest wavelength resolved by the mesh is numerically transferred to long wavelengths, thus causing the solution to diverge, according to Eriksson and Rizzi (1985). A method should attenuate aliasing effects from high-frequency numerical noise. Otherwise, the solution may diverge. Consequently, not being a trustworthy model for physical representation.

The solution implemented is a numerical low-pass filter, as proposed by Gaitonde and Visbal (1998). This technique aids to dissipate the motion in wavelengths shorter than the Nyquist frequency, an intrinsic characteristic from the conversion of a continuous function to a discrete sequence. The Nyquist limit is given by one-half the spatial sample rate, i.e. one-half the mesh resolution.

The authors propose a filter more consistent with tridiagonal-based schemes of up to 10th order. A single parameter controls the degree of filtering, defined as α_f. In summary, the procedure is to replace the values of the computed derivatives, f', for $\bar{f}'$, according to the following equation.

$$\alpha_f \bar{f}'_{i-1} + \bar{f}'_i + \alpha_f \bar{f}'_{i+1} = \sum_{n=0}^{N} \frac{a_n}{2}(f_{i+n} - f_{i-n}) \tag{3.21}$$

For 10th-order accuracy, the coefficients are: $a_0 = (193 + 126\alpha_f)/256$, $a_1 = (105 + 302\alpha_f)/256$, $a_2 = [15(2\alpha_f - 1)]/64$, $a_3 = [45(1 - 2\alpha_f)]/512$, $a_4 = [5(2\alpha_f - 1)]/256$, and $a_5 = (1 - 2\alpha_f)/512$.

The frequency response of the Equation 3.21 is real-valued and only modifies the amplitude of each wave component. The Equation 3.22 below formulates the spectral function operator. Figure 24 depicts the frequency response for $\alpha_f = 0.49$, same selected value for the current simulations.

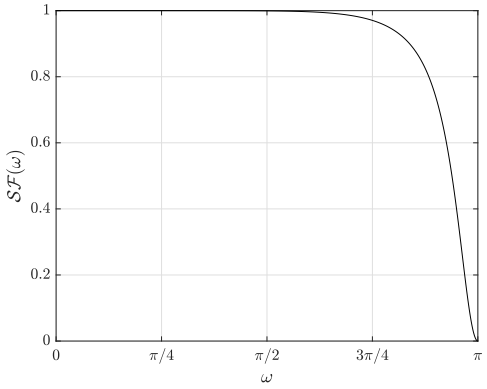
$$\mathcal{SF}(w) = \frac{\sum_{n=0}^{N} a_n cos(nw)}{1 + 2\alpha_f cos(w)} \tag{3.22}$$

3.1.6 Linear system solver

The Thomas algorithm solves the linear system that arises due to implicit nature of the method from the spatial derivatives and the anti-aliasing filter computing.

DISTRIBUTION A: Distribution approved for public release. Distribution unlimited

Figure 24 – Spectral function of the numerical filter proposed by Gaitonde and Visbal (1998).



Source: Author (2021).

A non-cyclical ($a_1 = c_n = 0$) tridiagonal system for n unknowns may be written as below.

$$\begin{bmatrix} b_1 & c_1 & & & a_1 \\ a_2 & b_2 & c_2 & & \\ & a_3 & b_3 & \ddots & \\ & & \ddots & \ddots & c_{n-1} \\ c_n & & & a_n & b_n \end{bmatrix} \begin{bmatrix} x_1 \\ x_2 \\ x_3 \\ \vdots \\ x_n \end{bmatrix} = \begin{bmatrix} d_1 \\ d_2 \\ d_3 \\ \vdots \\ d_n \end{bmatrix}$$

Next, the Thomas algorithm to obtain the unkwnown matrix, $[x_1,x_2,\ldots,x_n]^T$, is presented.

Algorithm 1 Thomas algorithm

for $i = 2,\ldots,n$ **do**
  $a_i = a_i/b_{i-1}$
  $b_i = b_i - a_i c_{i-1}$
  $d_i = d_i - a_i d_{i-1}$
end for
$x_n = d_n/b_n$
for $i = n-1, n-2,\ldots,1$ **do**
  $x_i = (d_i - c_i x_{i+1})/b_i$
end for

If the system is cyclical, one should use the algorithm proposed by Temperton (1975) to adapt the original linear system. Therefore, making it possible to run the Thomas algorithm. Thus, yielding in the following.

DISTRIBUTION A: Distribution approved for public release. Distribution unlimited

$$\begin{bmatrix} b_2 & c_2 & & & 0 \\ a_3 & b_3 & c_3 & & \\ & a_4 & b_4 & \ddots & \\ & & \ddots & \ddots & c_{n-1} \\ 0 & & & a_n & b_n \end{bmatrix} \begin{bmatrix} x_2 \\ x_3 \\ x_4 \\ \vdots \\ x_n \end{bmatrix} = \begin{bmatrix} d_2 - a_1 x_1 \\ d_3 \\ d_4 \\ \vdots \\ d_n - c_n x_1 \end{bmatrix}$$

3.1.7 Time integration

Similar to the separation of variables method, the right-hand side of the governing equations contains all the spatial terms, and posteriorly, the solver performs a time integration. The method employed for time marching is the fourth-order Runge-Kutta method. The equations below exhibit the numerical method. The solver also can perform the time integration by the Euler method, however only the previous was employed in the current.

$$U^{n+1} = U^n + \frac{\Delta t}{6}(K_1 + 2K_2 + 2K_3 + K_4) \tag{3.23}$$

$$K_1 = f(U^n) \tag{3.24}$$

$$K_2 = f(U^n + \frac{\Delta t}{2} K_1) \tag{3.25}$$

$$K_3 = f(U^n + \frac{\Delta t}{2} K_2) \tag{3.26}$$

$$K_4 = f(U^n + \Delta t K_3) \tag{3.27}$$

The DNS code allows it to operate in two ways: constant time step or maximum time step for numerical stability. The convergence condition given by the Courant-Friedrichs-Lewy (CFL) parameter evaluates the numerical stability. The diffusive and convective stability equations, Equation 3.28 and Equation 3.29, respectively, provide the quantitative value for the time step for the fourth-order Runge-Kutta method. It is advisable not to employ values higher than 1.3 for the CFL.

$$\Delta t \leq \frac{Re}{\left(\frac{1}{{\Delta x_{min}}^2} + \frac{1}{{\Delta y_{min}}^2} + \frac{1}{{\Delta z_{min}}^2}\right)} \tag{3.28}$$

$$\Delta t \leq \frac{CFL_{max}}{\left(\frac{1/M_\infty + u_{max}}{\Delta x_{min}} + \frac{1/M_\infty + v_{max}}{\Delta y_{min}} + \frac{1/M_\infty + w_{max}}{\Delta z_{min}}\right)} \tag{3.29}$$

DISTRIBUTION A: Distribution approved for public release. Distribution unlimited

According to the convective stability condition, Equation 3.29, we can note that a low value of free stream Mach number causes a severe reduction of the maximum step for time integration.

3.1.8 Selective frequency damping

In some cases, the respective flow is globally unstable, thus it is impossible to numerically compute the steady-state solution of the Navier-Stokes Equations by time-marching methods. However, the base-flow is essential for the instability analysis. Åkervik *et al.* (2006) proposes an artifice, adapted from large-eddy simulation (LES) methods, to surpass such disadvantage, the selective frequency damping (SFD).

The SFD works as a low pass filter in the time domain, which helps to dampen unstable modes present in the flow. It comes from proportional feedback control techniques. The SFD method adds a dissipative relaxation term proportional to the high-frequency content of the velocity fluctuations in the governing equations. This term, exhibited in Equation 3.30, has as its coefficient the difference between the variables in adjacent time steps, so, as the SFD action damps the modes, the lower is the value of that forcing term, and the flow asymptotically approaches the steady-state.

$$\frac{\partial \mathbf{U}}{\partial t} = f(\mathbf{U}) - \chi(\mathbf{U} - \mathbf{w}) \tag{3.30}$$

The variable $\mathbf{w}$ represents the steady-state target flow. As this value is not available *a priori*, it is substituted by a previous flow with reduced temporal fluctuations. For this, one can define a convolution of the flow with the temporal filter kernel, T, as the target, according to the equations below.

$$T(\tau - t,\Delta) = \frac{1}{\Delta} \exp\left(\frac{\tau - t}{\Delta}\right) \tag{3.31}$$

$$\mathbf{w} = \bar{\mathbf{U}}(t) = \int_{-\infty}^{t} T(\tau - t,\Delta)\mathbf{U}(\tau)d\tau \tag{3.32}$$

The DNS adopts the filter in the differential form, and it is advanced in time using the integration scheme, otherwise, it would be infeasible. The differential form is represented by the following equation.

$$\frac{\partial \bar{\mathbf{U}}}{\partial t} = \frac{\mathbf{U} - \bar{\mathbf{U}}}{\Delta} \tag{3.33}$$

The Δ parameter controls the cutoff frequency, $\omega_c = 1/\Delta$. The frequency should be smaller than the frequency expected by the unstable mode. As a guideline, Åkervik *et al.* (2006) states that the cutoff frequency has to be placed well within the damped region, e.g. $\omega_c \approx (1/2)\omega_{unst}$. The χ parameter is related to the gain, and it compensates for the

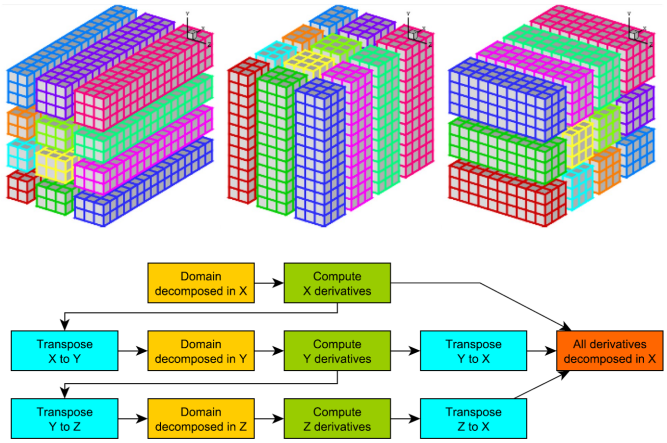
DISTRIBUTION A: Distribution approved for public release. Distribution unlimited

growth rates of the mode. It is advisable a value of twice the estimated growth rate for the gain parameter, χ. Both parameters are controlled by the user in the pre-processing procedure.

3.1.9 Parallel execution

The 2DECOMP&FFT library, Li and Laizet (2010), performs the parallel processing of the solver through the MPI protocol. Figure 25 schematically represents the domain decomposition, according to this library. Each MPI process holds all values of the discrete domain in one direction exclusively, most often, the x direction. Therefore, the routine permutes the computational domain for the derivatives and filters calculation in the other axes.

Figure 25 – Scheme representing the parallel processing and the flowchart for derivatives evaluation.



Source: Li and Laizet (2010) and Mathias (2017).

There is a bottleneck regarding the number of MPI processes, limited by the mesh geometry. The solver calls the subroutine for the boundary conditions when the domain is decomposed in the stream-wise x direction. For computing the wall-normal Neumann boundary condition, the solver must access the information of some points in the y direction, according to the numerical stencil specified by the method. If the numbers required for the boundary condition calculation are eventually stored in another processor, it is impossible to perform the evaluation. To avoid this, a check routine during the pre-compilation procedure suggests changing the number of processors specified when the aforementioned occurs.

3.2 Instability Analysis

According to Juniper, Hanifi and Theofilis (2014), the modal approach is the fundamental mathematical tool for analysis of the flow instability subject to small-amplitude

DISTRIBUTION A: Distribution approved for public release. Distribution unlimited

perturbations. However, complex flows like the actual open cavity problem do not allow the assumption of parallel flow, as seen previously in Chapter 2. So, as in Theofilis (2011), the global instability analysis is the proposed method to evaluate the flow's eigenspectrum.

There are two distinct forms to calculate the flow's eigenspectrum, the matrix-forming or the time-stepping method. For the actual flow, the latter is advantageous because not requires the cumbersome task of computing an expensive matrix. Thus, is the method employed. More about the implementation and validation of the method is available in Mathias (2017).

3.2.1 Arnoldi-based time-stepping method

According to Theofilis (2011), the time-stepping method departs from the equations of motion treated as an initial value problem (IVP), as follows.

$$\frac{\partial \mathbf{q}}{\partial t} = \mathbf{F}(\mathbf{q}) \tag{3.34}$$

In the Equation 3.34 above, $\mathbf{F}$ describes the spatial operator pertinent to the complete discrete field vector, $\mathbf{q} = [u \;\; v \;\; w \;\; \rho \;\; e]^T$. If $\mathbf{F}$ is perturbed by an arbitrary vector, $\mathbf{q}_0$, and the existence of the limit given by the Equation 3.35 with $\epsilon \in \mathbb{R}$, one can define the Fréchet derivative linear operator $\mathbf{A}(\mathbf{q})$, which is the Jacobian $\mathbf{A}(\mathbf{q}) = \partial\mathbf{F}/\partial\mathbf{q}$.

$$\lim_{|\epsilon|\to 0} \frac{\|\mathbf{F}(\mathbf{q} + \epsilon\mathbf{q}_0) - [\mathbf{F}(\mathbf{q}) + \epsilon\mathbf{A}(\mathbf{q})\mathbf{q}_0]\|}{|\epsilon|} = 0 \tag{3.35}$$

Furthermore, Tezuka and Suzuki (2006) and Mathias (2017) correlates this definition to the linearized Taylor series expansion around the base solution plus a small amplitude disturbance, $\mathbf{U} = \mathbf{U}_0 + \mathbf{u}$, yielding in Equation 3.37.

$$F(\mathbf{U}_0 + \mathbf{u}) = F(\mathbf{U}_0) + \frac{\partial F(\mathbf{U}_0)}{\partial \mathbf{U}}\mathbf{u} + O(\mathbf{u}^2) \tag{3.36}$$

$$\frac{\partial \mathbf{u}}{\partial t} = \mathbf{A}\mathbf{u} \tag{3.37}$$

Integrating the Equation 3.37 with respect to time from 0 to τ, one obtain.

$$\mathbf{u}(\tau) = \exp(\mathbf{A}\tau)\,\mathbf{u}_0 = \mathbf{B}\,\mathbf{u}_0 \tag{3.38}$$

In the actual time-step method, the matrix $\mathbf{B}$ is numerically approximated by Arnoldi's method, as in Arnoldi (1951), ergo the Jacobian matrix, $\mathbf{A}$, can be easily computed. In summary, this method recursively multiplies the matrix $\mathbf{B}$ by a vector

DISTRIBUTION A: Distribution approved for public release. Distribution unlimited

that is in the Krylov subspace, $K_M = \text{span}\{\zeta_1, \mathbf{B}\zeta_1, \ldots, \mathbf{B}^{M-1}\zeta_1\}$, and the eigenvector corresponding to the eigenvalue with the greatest absolute value is then filtered.

The initial disturbance, ζ_1, can be modeled as several functions. The current method uses a Gaussian distribution because it excites a pre-selected range of modes, moreover is a deterministic function. The following equation reveals the mathematical model of the initial disturbance.

$$\zeta_1 = [u_1 \;\; v_1 \;\; w_1 \;\; \rho_1 \;\; e_1]^T \tag{3.39}$$

$$u_1,\, v_1,\, \rho_1,\, e_1 = \exp\Big(-\alpha_x(x - x_0)^2 - \alpha_y(y - y_0)^2 \Big)\, \cos(\beta z) \tag{3.40}$$

$$w_1 = \exp\Big(-\alpha_x(x - x_0)^2 - \alpha_y(y - y_0)^2 \Big)\, \sin(\beta z) \tag{3.41}$$

The left-hand size term of Equation 3.38 corresponds to $\mathbf{B}\zeta$. Below, the description for a first-order approximation.

$$\mathbf{B}\zeta = \frac{1}{\epsilon_0}[\mathbf{F}(\mathbf{U}_0 + \epsilon_0\zeta) - \mathbf{F}(\mathbf{U}_0)] + O(\epsilon_0) \tag{3.42}$$

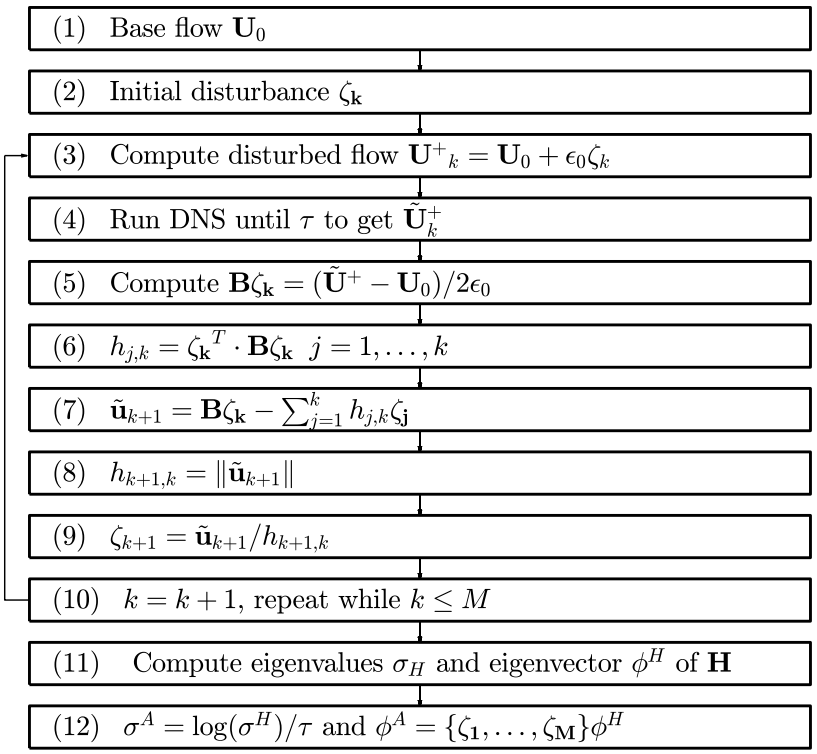
The scalar ϵ_0 represents the amplitude of the disturbance. The parcel $\mathbf{F}(\mathbf{U}_0 + \epsilon_0\zeta)$ is the DNS result after adding the disturbance and integrating through the time τ. To compensate for an eventual drift, the term $\mathbf{F}(\mathbf{U}_0)$ is the time integration of the base flow $\mathbf{U}_0$ without adding the disturbance term.

Figure 26 displays a flowchart to aid the understanding of the algorithm implemented. The base flow obtained from a previous run from the DNS is necessary. The initial disturbance computing occurs as aforementioned. Next, the solver adds the disturbance to the base flow, and in step 4, the routine calls the DNS, which performs the time integration until the final time, τ, specified by the user. The next step computes the Frechét derivative as in Equation 3.42.

The Gram-Schmidt orthogonalization computes the disturbance for the next iteration. This method comprises steps 6 to 9. In step 6 occurs the storage of the column k in the Hessemberg matrix $\mathbf{H}$ according to $h_{j,k} = {\zeta_\mathbf{k}}^T \cdot \mathbf{B}\zeta_\mathbf{k}, \;\; j = 1, \ldots, k$. The term $\mathbf{B}\zeta$ is subtracted by the projection of the current disturbance in step 7 to establish an orthogonal basis. After computing the new disturbance ζ_{k+1}, then a new iteration occurs until it reaches the number of Krylov subspaces also predefined by the user.

DISTRIBUTION A: Distribution approved for public release. Distribution unlimited

Figure 26 – Flowchart of the algorithm utilized for the global instability analysis proposed by Tezuka and Suzuki (2006) and implemented by Mathias (2017).



Source: Adapted from Mathias (2017).

Finally, the Equation 3.43 and Equation 3.44 compute the eigenspectrum and its associated eigenfunctions.

$$\sigma^A = \log(\sigma^H)/\tau \tag{3.43}$$

$$\phi^A = \{\zeta_\mathbf{1}, \ldots, \zeta_\mathbf{M}\}\phi^H \tag{3.44}$$

Some important notes have to be pointed out:

- Arnoldi's method converges readily for the less damped modes. Therefore is a good option to evaluate the unstable modes present in the flow.
- The real part of the flow's eigenvalues, $\Re\{\sigma^A\} = \sigma^A{}_r$, is associated with the growth/damp rate, whereas the imaginary part, $\Im\{\sigma^A\} = \sigma^A{}_i$, corresponds to the circular frequency of the mode. As the imaginary part of the flow's eigenvalues

DISTRIBUTION A: Distribution approved for public release. Distribution unlimited

corresponds to the amplification factor in the foremost temporal approaches, this is a piece of relevant information.

- Because the complex natural logarithm function is multivalued, for great values of the temporal integration, τ, one has to check if the frequency corresponds to the first branch, i.e. $n = 0$ in the term $2\pi n/\tau$. Such is an easy task since one can measure the time series of the flow oscillation caused by the instability during the previous DNS stage.

3.2.2 Algorithm optimal parameters

The user has to specify four numerical parameters before running the linear stability analysis method: the order of the Fréchet derivative approximation (n), the amplitude of the initial disturbance (ϵ_0), the integration time (τ), and the dimension of the Krylov span (M).

Concerning the Fréchet derivative approximation, the second-order approximation produces more accurate results compared to the first order, however with an increased computational cost as a trade-off. We decided to prioritize the agility, therefore we chose the first approximation of the Fréchet derivative. As a quantitative analysis, the study performed by Mathias (2021) measured the accuracy levels for both orders of approximation. The author noted that the accuracy of the eigenvalue changed from 10^{-5} to 10^{-8} by changing the Fréchet derivative approximation from the first to second order, respectively. Assuming that the conditions for the current work are similar, the accuracy of 10^{-5} is sufficient.

The choice for the remaining three parameters was also supported by the study of Mathias (2021). The parameter ϵ_0 exhibited an independence of the two remaining parameters. Thus, it was the first to be specified. According to the author, the optimal value of initial disturbance is related to the number of flow variables, size of the discretized domain, and the order of the Fréchet derivative approximation. The Equation 3.45 exhibits the model proposed to estimate the order of magnitude of the optimal initial disturbance, ϵ_{opt}. The value N corresponds to the product of the number of grid nodes by the number of flow variables (5 for 3D or 4 in case of a 2D flow) and n corresponds to the order of the Fréchet derivative approximation. The term ϵ_{base} stands for the magnitude of the base flow noise floor.

$$\epsilon_{opt} = \mathcal{O}\left(\left(\frac{\epsilon_{base}}{\sqrt{N}}\right)^{\frac{1}{n+1}}\right) \tag{3.45}$$

His results exhibited that the parameter τ influences the method as follows. To approximate the response of the base flow oscillation after an initial disturbance, the

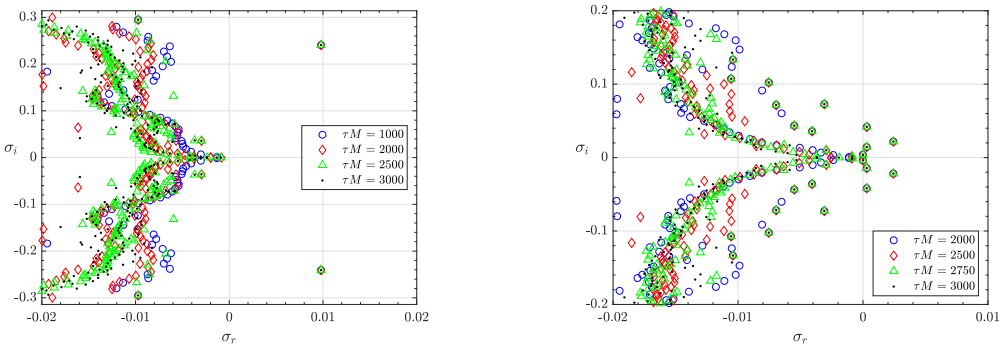
DISTRIBUTION A: Distribution approved for public release. Distribution unlimited

DNS solver is called. If the time integration is such, $\tau \to 0$, non-linear effects from the DNS are negligible. However, the flow's modes take less time to evolve, and depending on its amplification rate, it could require a larger number of Krylov span M. Otherwise, if $\tau \to \infty$, the method requires fewer iterations M, but non-linear effects can compromise the approximation. Therefore, the optimal parameter, τ_{opt}, has to reach a balance between these two phenomena. Equation 3.46 approximates the error of the eigenvalue i in the flow's Jacobian matrix A. The parameter σ_1^R and σ_i^R indicate the real parcel of the leading and desired eigenvalues, respectively. To achieve τ_{opt} it is advisable to minimize Equation 3.46. If one opts for safety, the time integration value should be lesser than τ_{opt}, because Equation 3.46 tends to infinity as $\tau \to \infty$. In the current work, we have opted for a conservative value of τ.

$$E_{A_i} \approx \frac{(\epsilon_0\sqrt{N})^n + \epsilon_{base}/\epsilon_0 + \epsilon_0 \exp(2\sigma_1^R\tau))}{\tau \exp(\sigma_i^R\tau))} \tag{3.46}$$

Finally, Mathias (2021) suggests the procedure to achieve the suitable Krylov span M. His survey indicated that the filtering time, τM should be long enough for the modes to discern from each other. However, it is more advantageous to use τ as large as possible within the limits established by Equation 3.46. Because, his results demonstrated that the computational costs increased non-linearly with M, whereas increased linearly with τ. Hence, after determining the order of the Fréchet derivative approximation and the optimal values of ϵ_0 and τ, the Krylov span M can be monitored, ergo one may stop the method when the desired eigenvalue reach the convergence criteria adopted. Figure 27 depicts the effect of increasing the value of M for fixed values of n, ϵ_0, and τ, for a run from the present work.

Figure 27 – Effect of increasing the filtering time τM on convergence of the 2D (a) and 3D (b) eigenvalues from the linear stability analysis of a representative run.



(a) L20D4 $\beta = 0$ (b) L20D4 $\beta = \pi/3$

Source: Author (2021).

DISTRIBUTION A: Distribution approved for public release. Distribution unlimited

DISTRIBUTION A: Distribution approved for public release. Distribution unlimited

4 RESULTS

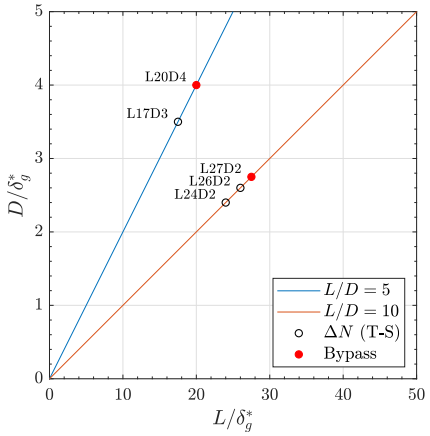
This chapter gathers the results obtained. The first section presents the assessment regarding the validity of the solutions. Next, the flow characteristics from the 2D DNS and the modes computed through the 2D and 3D instability analysis are presented, for a gap with aspect ratio $L/D = 5$ and $L/D = 10$. Table 1 displays the cases covered.

Table 1 – Flow parameters for the different simulation runs covered in the present work.

Run	L/δ^*	D/δ^*	L/D	Re_{δ^*}	Re_D	Re_L	M_∞
L17D3	17.50	3.50	5.00	1312	4591	22956	0.053
L20D4	20.00	4.00	5.00	1405	5621	28106	0.065
L24D2	24.00	2.40	10.00	1470	3528	35280	0.065
L26D2	26.00	2.60	10.00	1297	3372	33715	0.053
L27D2	27.50	2.75	10.00	1370	3764	37640	0.060

Source: Elaborated by the author.

Figure 28 – Diagram exhibiting the gap geometries covered in the current work and the impact on the transition measured by Crouch, Kosorygin and Sutanto (2020).



Source: Author (2021).

Such parameters were obtained thanks to a private contact with Dr. Crouch, that gently provided the experimental data from the work Crouch, Kosorygin and Sutanto (2020) necessary to establish the flow conditions for the simulations. We sought to reproduce two different aspect ratios, because the possible unstable modes are highly dependent on the geometry. However, we focused on the aspect ratio $L/D = 5$, once Dr. Crouch found a particular tonal frequency, out of the unstable frequencies range for the T-S mode,

DISTRIBUTION A: Distribution approved for public release. Distribution unlimited

which led to the transition. This mode had a dimensional frequency about 5× greater than expected for the T-S in such flow conditions.

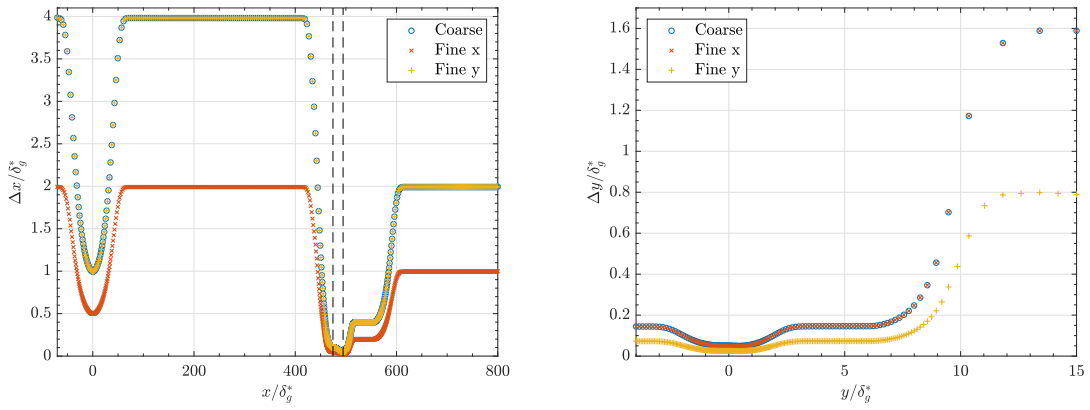
Figure 28 exhibits the gap geometries and the impact on boundary layer transition according to Crouch, Kosorygin and Sutanto (2020). Open markers in black correspond to gap geometry which altered the transition location to relatively upstream of the smooth flat plate reference run, whereas closed red markers represent geometries that promoted transition practically over the gap.

4.1 Grid dependence test

This section presents the grid dependence test, a key aspect to assure the physics of the solution, besides establishing the accuracy level of the numeric results. We have chosen the run L20D4 for the grid dependence test because it is the crucial run among the flow conditions covered in the present work.

The method adopted to generate different meshes with equivalent characteristics was rescaling the spacing distribution of the mesh. A finer grid was formed by repeatedly halving the intervals k_{ref} times between the grid nodes in each direction, only in the domain of interest. For the current work, $k_{ref} = 1$ was sufficient. To speed up the process, we refined the two spatial directions independently. Figure 29 exhibits the comparison of the mesh spacing as a function of each axis of the three different meshes. Table 2 displays the main features of each mesh.

Figure 29 – Mesh spacing between two consecutive grid nodes in streamwise (a) and wall-normal (b) axis for the meshes employed for the grid dependence test. Only the domain of interest is exhibited. Gap's corners locations are displayed by black dashed lines in (a).



(a) (b)

Source: Author (2021).

Figure 30 show the non-dimensional frequency spectrum of the wall-normal velocity measured just downstream of the gap, at $(x/\delta_g^*; y/\delta_g^*) = (500; 2)$. We can see a small

DISTRIBUTION A: Distribution approved for public release. Distribution unlimited

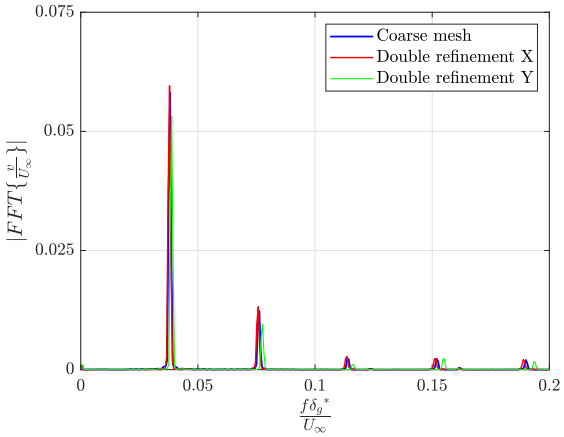
Table 2 – Meshes for grid dependence test.

Mesh	Nodes (x)	Nodes (y)	Nodes (useful domain)	Δx_{min}	Δx_{max}	Δy_{min}	Δy_{max}
Coarse	1106	153	1026×129	0.050	4.000	0.050	1.600
Refined (x)	2131	153	2091×129	0.025	2.000	0.050	1.600
Refined (y)	1106	208	1026×190	0.050	4.000	0.025	0.800

Source: Elaborated by the author.

deviation in the frequency peak for the three meshes. Table 3 exhibits the values of the peak frequency and amplitude for the three meshes and their error relative to the coarse mesh. We were more concerned about the frequency accuracy, which we considered to be grid-independent. Nonetheless, we could employ a mesh more refined in the wall-normal direction. The amplitude revealed this with more clarity. Although, a finer mesh implies a significantly higher computational cost. The minimum spacing causes a substantial decrease in the time-step to reach the same CFL, according to Equation 3.29, besides the greater quantity of grid nodes. The grid dependence study revealed that all three meshes had proven their capability to capture the instability phenomenon. Furthermore, we reached a satisfactory balance between computational costs and numerical accuracy. To put in quantitative perspective, the mesh with double refinement in y direction takes 1.88 core-hour to reach the same convective time that the coarsest mesh takes 1.00 core-hour. In total, about 250,000 core-hours, including DNS and linear stability analysis, had been employed.

Figure 30 – Comparison of the frequency spectra from the wall-normal velocity signal, v/U_∞, measured inside the boundary layer just downstream of the gap.



Source: Author (2021).

DISTRIBUTION A: Distribution approved for public release. Distribution unlimited

Table 3 – Frequency spectra peak comparison of the solution for different meshes.

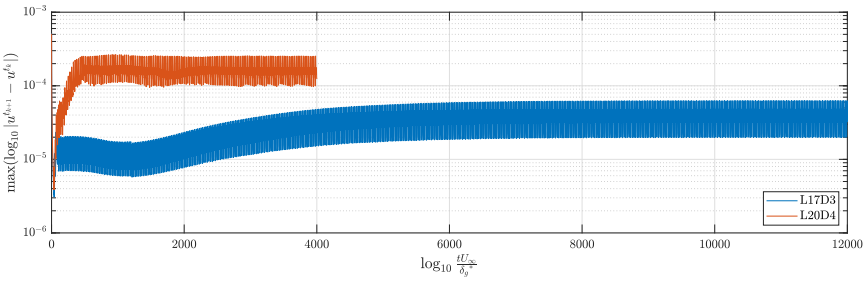
Mesh	Amplitude	Relative error (amplitude) [%]	Frequency	Relative error (frequency) [%]
Coarse	0.058231	0	0.038112	0
Refined (x)	0.059570	2.299332	0.037896	0.565227
Refined (y)	0.053192	8.653615	0.038793	1.787706

Source: Elaborated by the author.

4.2 Unsteady solution

For all the runs except the L24D2, the 2D DNS exhibited self-sustained oscillations. Such motion occurred because of a temporal instability due to the gap present in the boundary layer. In other words, except for the run L24D2, the flow was globally unstable. The flow oscillations develop, and after a sufficient time, they saturate and consequently reach the limit cycle. The time each flow took to attain the limit cycle gives a clue about the magnitude of the temporal amplification rate. Figure 31 shows an example of this behavior for the gap with aspect ratio $L/D = 5$. We can see that the less unstable run (L17D3) takes a meaningful time to settle in the limit cycle compared to the run L20D4.

Figure 31 – Time history of the maximum absolute residual from the streamwise velocity for the runs L17D3 and L20D4.



Source: Author (2021).

Figure 32 displays the unsteady streamwise velocity measured by probes located around the gap after the oscillation settled for runs L17D3 and L20D4. The probes' coordinates are exhibited in the top left of each subplot. The analysis of the signals revealed that the flow oscillation magnitudes from run L17D3 were significantly lesser than from the run L20D4, despite both flows being unstable. Furthermore, both runs exhibited harmonics in the signal, possibly indicating non-linear interaction. However, the harmonics from run L17D3 were almost imperceptible, except in regions where the amplitude was relatively strong. We expect that the 3D DNS with the same flow conditions will present

DISTRIBUTION A: Distribution approved for public release. Distribution unlimited

lower amplitudes, based on the literature.

We computed the non-dimensional frequency spectrum by taking the absolute values from the signals Fast Fourier Transform (FFT). We also applied the Hanning window function after clipping out the initial transient of the time series. According to Bendat and Piersol (2010), it is advisable to correct the amplitude after windowing the signal. For the Hanning window, the scale factor for the amplitude is $\sqrt{8/3}$. Figure 33 exhibits the spectrum corresponding to the signal from Figure 32d. Also, in Figure 33 one can see the displacement thickness based Strouhal number, $St_{\delta_g^*} = f\delta_g^*/U_\infty$, measured by Crouch, Kosorygin and Sutanto (2020) in the correspondent flow condition and the prediction by Block (1976), according to the Equation 4.1 below. This equation is a modified version of Rossiter's semi-empirical formula. We chose it because there was no need to determine the phase lag between the acoustic emission and vortex formation.

$$St_{R_m} = \frac{\delta_g^*}{L} \frac{m}{\frac{1}{K_v} + M_\infty\left(1 + \frac{0.514D}{L}\right)} \tag{4.1}$$

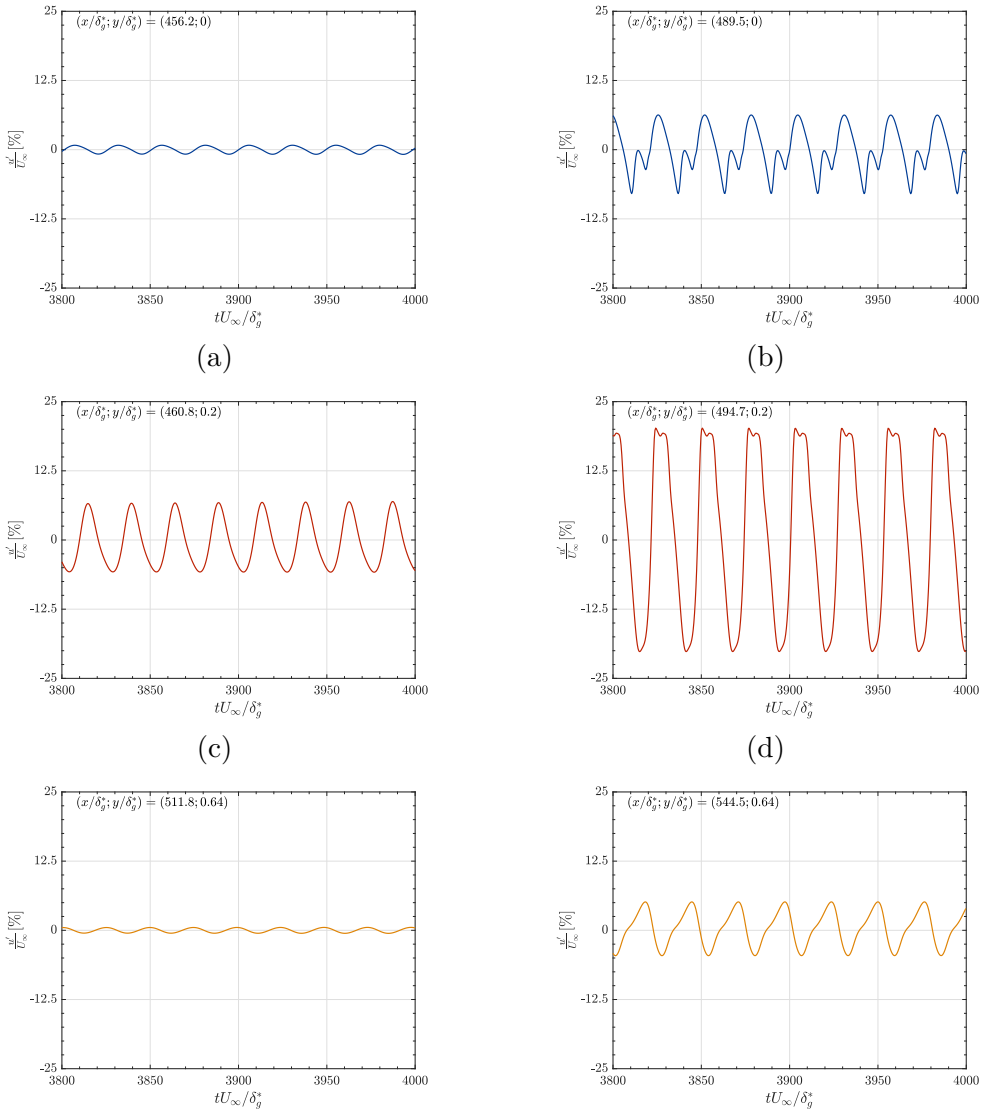
Here, $m = 1,2,\ldots$ represent which Rossiter mode in the case. For the aspect ratio $L/D = 5$, we found the Rossiter second mode, marked by the presence of two pairs of vortices inside the gap. The parameter K_v represents the non-dimensional streamwise wavenumber of the cavity shear layer oscillation. We determined such value through the snapshots from the 2D DNS, just downstream the gap in a wall-normal distance correspondent to the outer maxima. For the run L20D4, the second Rossiter streamwise wavenumber was $K_v = 0.4028$.

A normalized deviation of about 3% occurred between the St_{R_2} from Block (1976) prediction and the actual frequency. Also, a satisfactory agreement with the Strouhal from Crouch, Kosorygin and Sutanto (2020), within a 4% percent of relative deviation. The authors of the referred work imposed a pressure distribution with a slight pressure gradient over the model. It can potentially alter the frequency. Furthermore, the inaccuracies from their experimental measurements and the current work may cause a deviation in the frequency. The 2D flowfield are most likely to differ from the 3D, another probable cause that may cause the results to diverge. Nonetheless, it is plausible to affirm that the current oscillation frequency matched the experimentally experienced by Crouch, Kosorygin and Sutanto (2020), suggesting that possibly the Rossiter mode occurred in the bypass transition run, namely the *Case C*. However, it is not clear whether the Rossiter mode caused the transition to bypass the usual T-S mode.

Figure 34 depicts iso-contours of the crossflow and streamwise velocity. We were able to compute the latter after the base flow solution, once one must subtract the instantaneous total velocity field by the time-invariant solution. An interesting fact was the profile of the streamwise disturbance velocity, Figure 34b and Figure 34d, quite similar

DISTRIBUTION A: Distribution approved for public release. Distribution unlimited

Figure 32 – Streamwise unsteady velocity signals measured by probes located inside the gap in (a) and (b), just downstream of the gap in (c) and (d), and far downstream in (d) and (e). Time series of (a), (c), and (e) were taken from run L17D3, whereas the others from run L20D4.

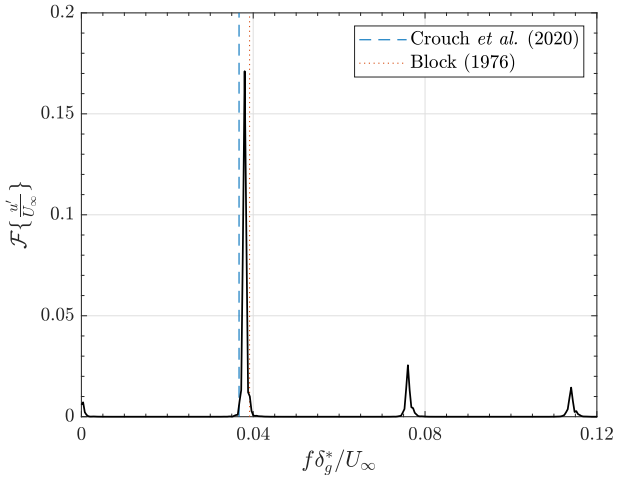


Source: Author (2021).

to the Tollmien-Schlichting eigenfunction. However, the temporal frequency was greater than the T-S unstable range of frequencies for the present runs. The temporal frequency measured for runs L17D3 and L20D4 were $St_{\delta_g^*} = f\delta_g^*/U_\infty = 0.040$ and 0.038, respectively. According to the Block (1976) expression, the frequency of the Rossiter mode decays as we increase the gap length, which we observed in the current simulation. In addition, the Rossiter mode's wavelength and phase velocity differed from the T-S mode. The only similarity remained in the spatial amplitude distribution (eigenfunction). These wave characteristics will be treated in detail next.

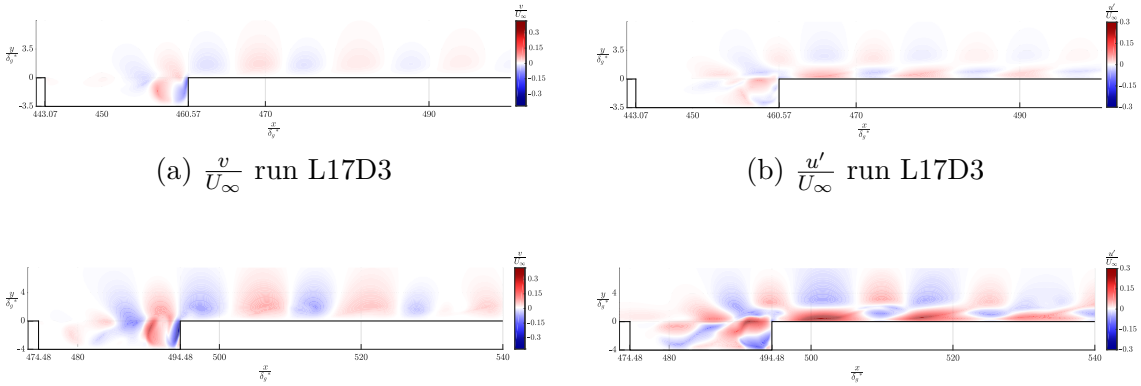
DISTRIBUTION A: Distribution approved for public release. Distribution unlimited

Figure 33 – Frequency spectrum comparing the signal exhibited in Figure 32d with results from Crouch, Kosorygin and Sutanto (2020) and the frequency prediction by Block (1976).



Source: Author (2021).

Figure 34 – Instantaneous crossflow and streamwise velocity contours for runs L17D3 and L20D4 in equivalent phases. We employed 256 equally spaced levels between the minimum and the maximum of each run with the color bar scale kept constant for each variable.



(a) $\frac{v}{U_\infty}$ run L17D3 (b) $\frac{u'}{U_\infty}$ run L17D3

(c) $\frac{v}{U_\infty}$ run L20D4 (d) $\frac{u'}{U_\infty}$ run L20D4

Source: Author (2021).

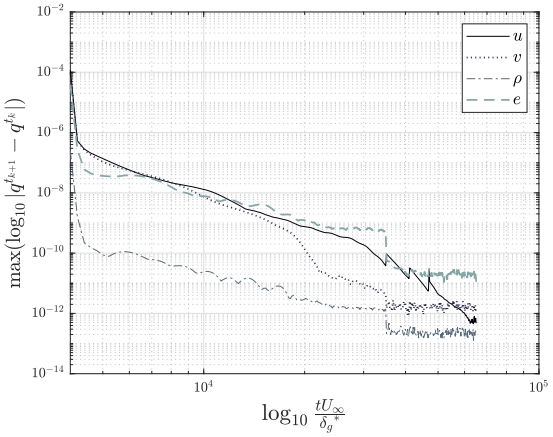
4.3 Steady solution

We prompt the SFD to dampen flow oscillations after the unsteady 2D DNS reaches the limit cycle in the unstable flows. The Fast Fourier Transform of the time series acquired during the DNS supports in determining the cut-off frequency. As suggested by Åkervik *et al.* (2006), we set the cut-off frequency around one-half lesser than the dominant disturbance frequency. We changed the gain parameter gradually according to the output from the convergence time series. The value defined as a sound gain for all simulations

DISTRIBUTION A: Distribution approved for public release. Distribution unlimited

was $\chi = 0.05$.

Figure 35 – Time series of the maximum absolute residual of the all dependent variables from the run L20D4 with aid from the SFD technique.



Source: Author (2021).

The instability analysis requires a very tight accuracy. Because the method runs the DNS to filter the less stable modes, persistent small oscillation in the flow can contaminate the actual flow's modes or cause the emergence of spurious modes. Consequently, one advises time variations of about the order of magnitude of the machine epsilon to consider a proper steady solution. Figure 35 displays the maximum absolute iteration residuals for all the flows' variables for the run L20D4. In the late stages, we employed a technique to perform a time average from several results before running the solver. This maneuver aided the dispersion of slower oscillations that were still eventually present in the flow.

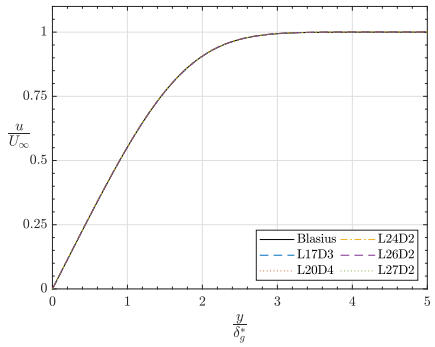
The length scale used as the basis for all spatial variables was the displacement thickness over the upstream corner of the gap, δ_g^*. The pre-processing routine had to specify the coordinates of the gap position before starting the unsteady simulation. Thus, for a given Reynolds number, the stream-wise position of the gap was defined through the laminar Blasius boundary layer. In non-dimensional form, the stream-wise location of the upstream corner of the gap for a Blasius boundary layer is $x_g/\delta_g^* = Re_{\delta_g^*}/1.7208^2$. The first procedure was checking the boundary layer profile of the base flows at the gap's leading edge.

Figure 36 exhibits the comparison of the profiles computed by the DNS for all runs with the Blasius theoretical profile at the upstream corner of the gap. The DNS profiles are plotted in colored dashed lines, whereas the Blasius is in solid black. The latter was also obtained numerically through the Blasius equation solution. The maximum relative error, computed as the absolute difference divided by the local theoretical value, was 0.73% at $y/\delta_g^* = 0.45$. Despite the presence of a weak stream-wise velocity gradient in the flat plate's leading-edge, which usually leads to a slight deviation in the profile, we found that

DISTRIBUTION A: Distribution approved for public release. Distribution unlimited

variation surprisingly low.

Figure 36 – Comparison with various DNS velocity profiles and Blasius' right upstream of the gap.



Source: Author (2021).

Figure 37 exhibits the steady solution (base flow) obtained. The contours show the non-dimensional spanwise vorticity, whereas the solid lines indicate the streamlines of the flowfield. The black streamlines exhibit clockwise streamlines. The streamlines inside the gap were computed by numerically solving the Poisson's Equation using Liebmann's iterative method from Biringen and Chow (2011). According to White (2006), for a steady viscous 2D flow, the stream function can be obtained by the stream function-vorticity formulation given by the Equation 4.2. The boundary conditions employed to compute the streamlines in the domain interior of the gap was $\psi = 0$ at the solid walls, whereas in the top boundary, $\psi(x) = -\int v\, dx$, for each interval between two consecutive grid node along x. To validate the approximate ψ solution, we retrieved the streamwise and crossflow velocity field, $\partial\psi/\partial x = -v$ and $\partial\psi/\partial y = u$, and compared to the actual DNS solution. We reached a reasonable agreement.

$$\nabla^2\psi = -\omega_z \tag{4.2}$$

In Figure 37a and Figure 37c we show the base flow for the runs with aspect ratio $L/D = 5$, and in Figure 37b and Figure 37d, $L/D = 10$. The differences between the runs with the same aspect ratio are nearly imperceptible. However, the flow topology reveals a notable change from $L/D = 5$ to $L/D = 10$.

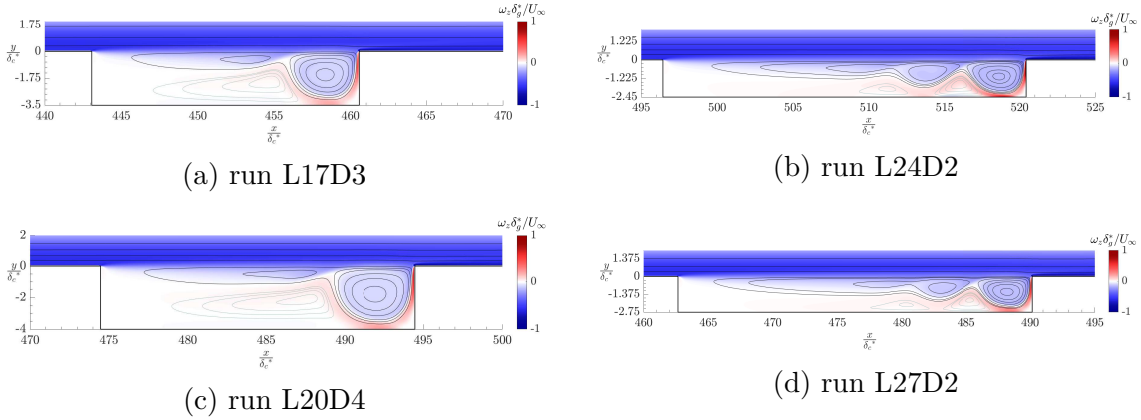
For the first aspect ratio, a small, however more intense vortex occurs with approximately a size of a quarter of the gap's length, next to the downstream corner. A pair of elongated counterrotating eddies occupy the remaining gap's space and has a width of about one-half cavity's depth.

For a shallower gap, we notice the presence of an extra pair of vortices compared to the previous geometry. Close to the downstream end, a vortex, with a size close to

DISTRIBUTION A: Distribution approved for public release. Distribution unlimited

the gap's depth, also occurs. However, the superior elongated vortex appears to be two vortices merged. The central vortex has a size slightly smaller than the most downstream vortex. Near to the bottom of the gap, two weak counterrotating vortices appear in the interstices of the three superior vortices.

Figure 37 – Iso-contours of the non-dimensional spanwise vorticity and stream-lines overlaid from the steady solutions for the runs: (a) L17D3, (b) L20D4, (c) L24D2, and (d) L27D2.



(a) run L17D3

(b) run L24D2

(c) run L20D4

(d) run L27D2

Source: Author (2021).

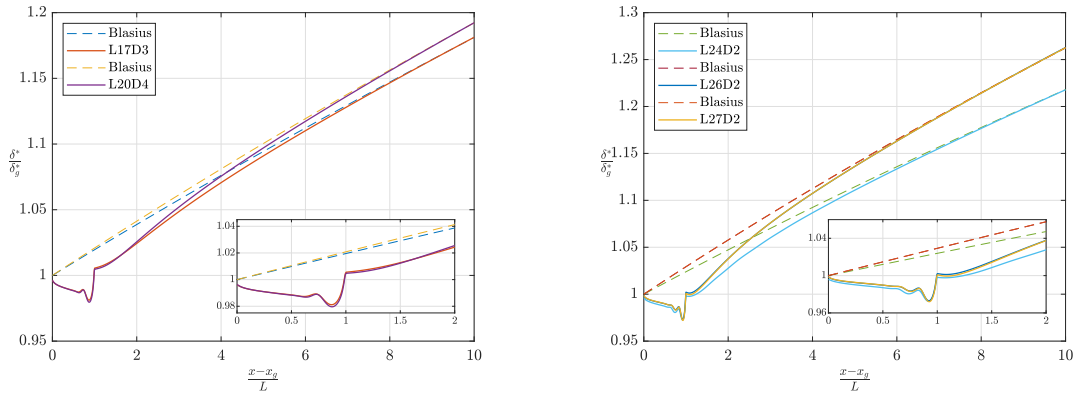
The presence of the gap causes the shrinkage of the boundary layer displacement thickness, as exhibited in Figure 38. A practically constant reduction occurs for a distance of about two-thirds of the gap length for both aspect ratios, followed by a rough decrease and increase in the remaining region. The minimum displacement thickness possesses a value of about 95% of the local theoretical's and occurs at roughly 90% of gap length. This behavior most likely happens due to the vortices inside the gap. We attribute the first reduction to the flow rate towards the cavity, caused by the elongated pair of vortices, whereas the sharper is to the most intense vortex near the cavity's downstream end. Between each pair of consecutive vortices, one can note a slight leap, as well as an abrupt increase in the boundary layer over the gap's trailing edge. Because presumably, the flow stagnation by the recirculating flow and the cavity wall, respectively. The boundary layer shrinkage is sensed downstream for approximately 9× the gap length until the growth of the displacement thickness returns to the same rate as the Blasius boundary layer with no hysteresis.

Figure 39 exhibits the ratio of the boundary layer displacement thickness by the momentum thickness, or shape factor, $H = \delta^*/\theta$. We can see a reduction of the shape factor, with the minimum occurring at the gap's trailing edge for all runs. Although the displacement thickness decreases over the gap, we observed an increase in the momentum thickness relative to the Blasius boundary layer.

Figure 40 shows the gap shear layer spreading rate. We used the vorticity thickness,

DISTRIBUTION A: Distribution approved for public release. Distribution unlimited

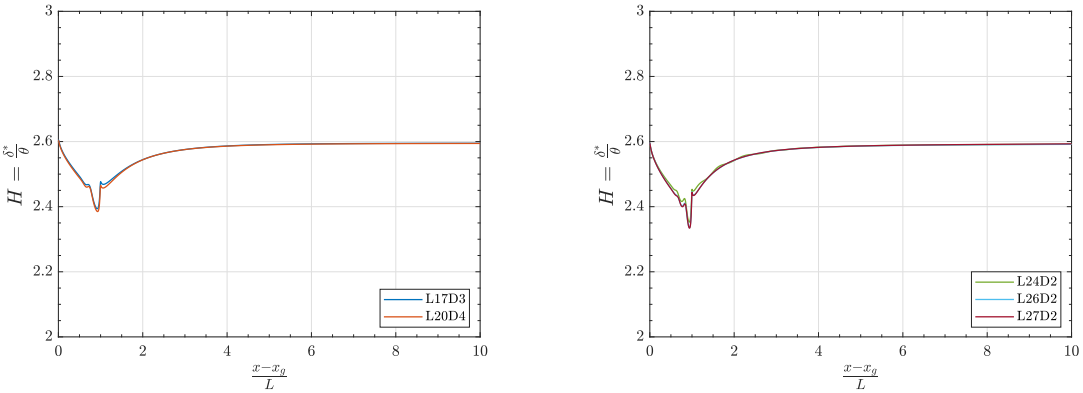
Figure 38 – Comparison of the boundary layer displacement thickness evolution with the Blasius. The x axis is normalized by the length of the gap.



(a) $L/D = 5$ (b) $L/D = 10$

Source: Author (2021).

Figure 39 – Comparison of the boundary layer shape factor with the Blasius. The x axis is normalized by the length of the gap.



(a) $L/D = 5$ (b) $L/D = 10$

Source: Author (2021).

defined by Equation 4.3 to perform such analysis. Here, the denominator is the maximum numerical value of the wall-normal derivative of the streamwise steady velocity, $\bar{U}$.

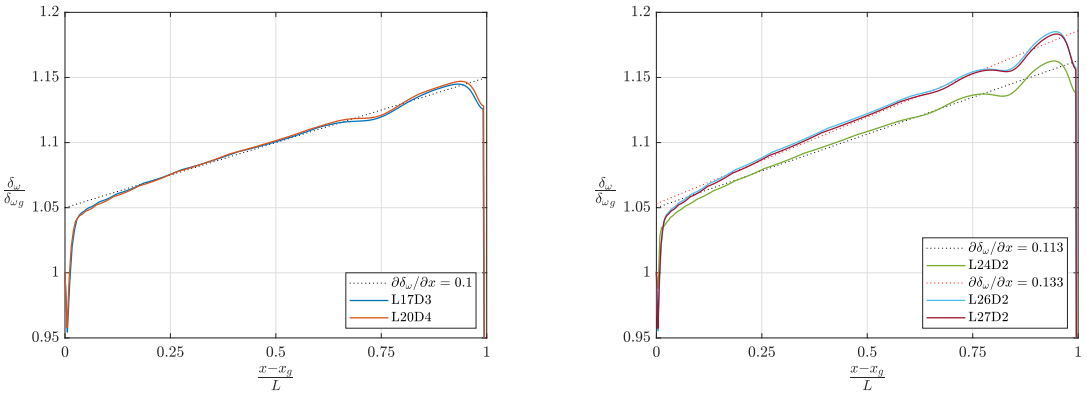
$$\delta_\omega = \frac{U_\infty}{\max[\partial \bar{U}(y)/\partial y]} \tag{4.3}$$

The ordinate axis from Figure 40 was normalized by the vorticity thickness at the upstream corner of the gap, $\delta_{\omega g}$. In Figure 40a we can see the vorticity thickness distribution for the aspect ratio $L/D = 5$, whereas Figure 40b exhibits for the $L/D = 10$ aspect. Both figures display a dotted line exhibiting a linear fit to the numerical data. We can see a practically linear growth for all runs. For the first aspect ratio, both runs L17D3

DISTRIBUTION A: Distribution approved for public release. Distribution unlimited

and L20D4 had a spreading rate of $\partial\delta_\omega/\partial x = 0.100$. The second aspect ratio presented two different values. For the stable run, L24D2, a milder vorticity growth, $\partial\delta_\omega/\partial x = 0.113$, yet greater than the value of the previous geometry. The unstable runs, L26D2 and L27D2, presented the highest spreading rate, $\partial\delta_\omega/\partial x = 0.133$. The present results confirm the trend observed by Sarohia (1977) that the vorticity thickness streamwise growth rate increases with L/δ_g^*. The numerical values of the derivatives $\partial\delta_w/\partial x$ were slightly greater than the numerically obtained by Rowley (2002) for a run with a similar aspect ratio. Still, its Reynolds number employed was significantly lower, almost 20× smaller than the current.

Figure 40 – Gap shear layer spreading rate of both aspect ratios $L/D = 5$ in (a) and $L/D = 10$ in (b). The vorticity thickness distribution over the stream-wise axis is normalized by its respective value at the gap leading edge. A linear fitting is also exhibited.



(a) $L/D = 5$ (b) $L/D = 10$

Source: Author (2021).

4.4 Rossiter instability

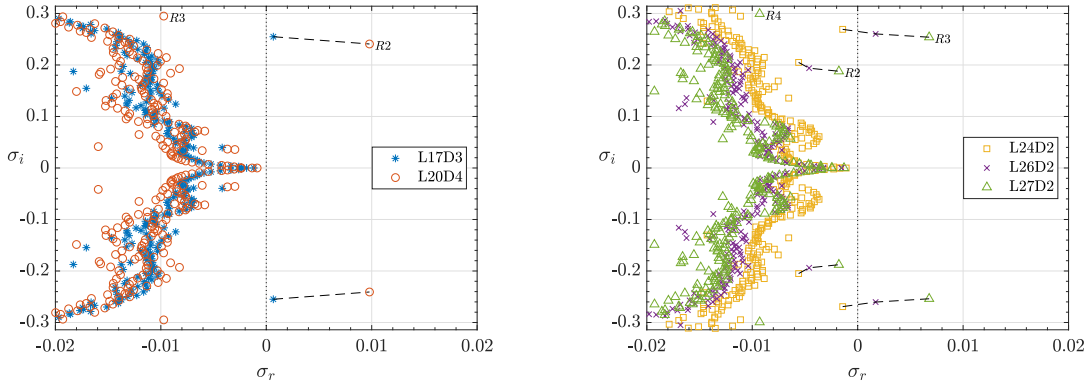
Once the base flow was available, we evaluated the flow's eigenvalues in search of unstable modes. Firstly, we performed the 2D instability analysis to verify the presence of the Rossiter mode, in other words, with a spanwise wavenumber $\beta = 0$, or a spanwise wavelength $\lambda_z = \infty$. The next session will describe the 3D instability analysis.

We expected to find the Rossiter instability in the runs that the 2D DNS exhibited self-sustained oscillations, for instance, all the runs except the L24D2. Figure 41 displays the flow's eigenvalues spectrum for both gap's aspect ratio, $L/D = 5$ in Figure 41a and $L/D = 10$ in Figure 41b.

The run L17D3 presented a marginally unstable state with a small amplification factor. Moreover, the run L20D4 exhibited an amplification rate one order of magnitude greater. The imaginary part of the eigenvalues tells us the circular frequency of the mode.

DISTRIBUTION A: Distribution approved for public release. Distribution unlimited

Figure 41 – Eigenvalues spectra from the runs with aspect ratio $L/D = 5$ (a) and $L/D = 10$ (b) in the complex plane. The imaginary axis indicates the circular frequency, whereas the real corresponds to amplification or damping rate.



(a) $L/D = 5$ (b) $L/D = 10$

Source: Author (2021).

Again, we observed that the frequency tends to decrease as increasing the gap length, as the expression given by the Equation 4.1. The frequency of the most unstable mode of L20D4 matched the peak in the spectrum exhibited previously in Figure 33.

Similar behavior happened with the second aspect ratio. The runs that anticipated the transition location by altering the T-S growth presented a stable Rossiter mode in L24D2 and a marginally unstable in L26D2. Again, the case which promoted bypass transition, according to Crouch, Kosorygin and Sutanto (2020), presented a Rossiter mode with a considerably greater amplification rate compared to the other runs. The amplification of the run L27D2 was about 4× greater than the run L26D2. The Table 4 summarizes the eigenvalues from the instability analysis regarding the Rossiter layer mode.

Figure 42 reveals the iso-contours of the eigenfunctions' real part amplitude from the flow variables $\hat{u}$, $\hat{v}$, and $\hat{\rho}$, respectively, of the run L20D4 in an arbitrary phase. The eigenfunctions were quite similar to the snapshots of the 2D DNS results exhibited in Figure 34. It resembled some other Rossiter shape modes from the literature, for instance from Rowley (2002), Theofilis and Colonius (2004), Sun *et al.* (2017), and Mathias and Medeiros (2018).

We can see the presence of two vortices inside the gap, leading to the conclusion that such oscillation mode was the Rossiter second mode (R_2). It was possible to verify the presence of the Rossiter third mode (R_3) in the eigenvalue spectrum from the run L20D4. It was unfeasible to identify the third Rossiter (R_3) from the run L17D3 and the first Rossiter (R_1) from L17D3 and L20D4 because they were mixed among other stable oscillations modes, and the instability analysis routine saves only a few unstable modes to prevent excessive storage. The same happened to the aspect ratio $L/D = 10$.

DISTRIBUTION A: Distribution approved for public release. Distribution unlimited

One difference between the two aspect ratios was which Rossiter mode was dominant. The gaps with $L/D = 5$ presented the second Rossiter mode, while the Rossiter third mode appeared in the cavities with $L/D = 10$. Another aspect that occurred for the latter was the presence of the second Rossiter mode moving towards instability. Possibly, a slightly wider gap or the same geometry with greater Reynolds or Mach number will present multiple Rossiter modes simultaneously. As mentioned in the literature, wider gaps are more susceptible to present multiple Rossiter modes. Finally, we noticed that the range of circular frequency of the dominant Rossiter modes does not vary, even with a drastic change in the aspect ratio, remaining around 0.25 rad/s.

Figure 43 displays the difference among the different Rossiter modes' eigenfunctions for the same run, L27D2 more specifically. The flow variable presented in Figure 43 is the wall-normal velocity, $\hat{v}$. As commented previously, the amount of vortices inside the gap indicates which Rossiter is the mode in question. We can see that there are two, three,

Table 4 – Eigenvalues associated with the Rossiter mode.

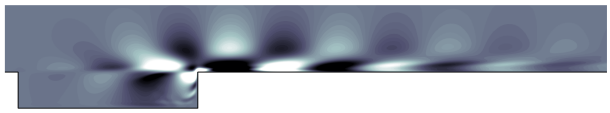
L/D	Run	State	Modes		Transition
5	L17D3	U	R_2	$0.0007 + i0.2549$	T-S
			R_3	-	
			R_4	-	
	L20D4	U	R_2	$0.0098 + i0.2407$	B
			R_3	$-0.0097 + i0.2649$	
			R_4	-	
10	L24D2	S	R_2	$-0.0043 + i0.2071$	T-S
			R_3	$-0.0010 + i0.2707$	
			R_4	-	
	L26D2	U	R_2	$-0.0046 + i0.1938$	T-S
			R_3	$0.0017 + i0.2603$	
			R_4	-	
	L27D2	U	R_2	$-0.0017 + i0.1878$	B
			R_3	$0.0068 + i0.2539$	
			R_4	$-0.0093 + i0.2994$	

Source: Elaborated by the author.

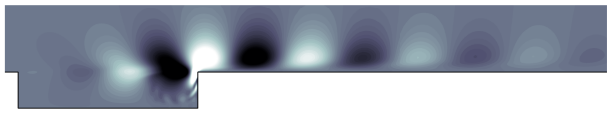
Note: (U) Unstable; (S) Stable; (T-S) Transition dominated by Tollmien-Schlichting; (B) Bypass transition. Latter characteristics according to Crouch, Kosorygin and Sutanto (2020). Red colored font indicate the dominant unstable mode.

DISTRIBUTION A: Distribution approved for public release. Distribution unlimited

Figure 42 – Eigenfunctions of the the most unstable Rossiter mode (R_2) from the run L20D4.



(a) $\hat{u}$



(b) $\hat{v}$

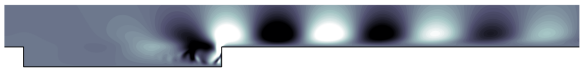


(c) $\hat{\rho}$

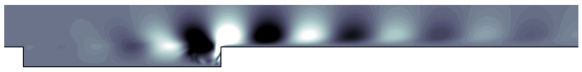
Source: Author (2021).

and four vortices inside the gap in Figure 43a, Figure 43b, and Figure 43c, respectively.

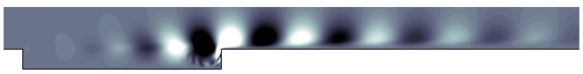
Figure 43 – $\hat{v}$ eigenfunctions of the different Rossiter modes from run L27D2.



(a) Rossiter R_2



(b) Rossiter R_3



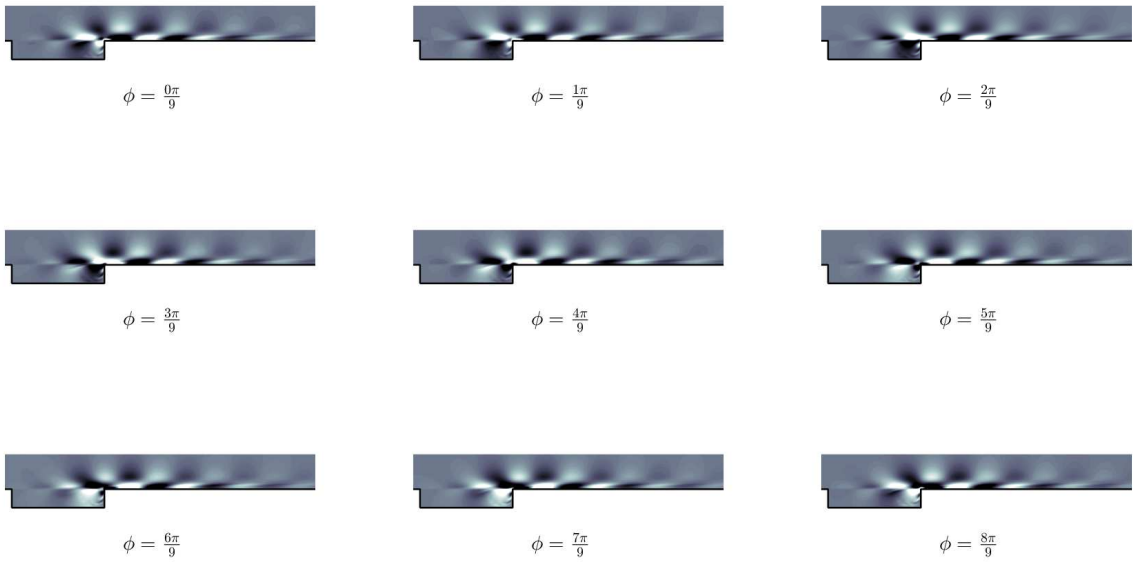
(c) Rossiter R_4

Source: Author (2021).

Figure 44 exhibits distinct phases of the streamwise velocity eigenfunction, $\hat{u}$, spaced by 1/9 of the temporal oscillation period. It is possible to see a phase difference between the regions outside and inside the gap. However, it looks like the downstream corner of the gap influences the shape of the mode, modifying the phase velocity locally. As a result, the spatial amplitude distribution far downstream presents a phase shift of π, at $y/\delta_g^* \approx 1$, between the inner and the outer peaks, similarly to the T-S mode.

DISTRIBUTION A: Distribution approved for public release. Distribution unlimited

Figure 44 – Several phases comprising one oscillation period of the Rossiter (R_2) streamwise velocity eigenfunction from run L20D4.



Source: Author (2021).

4.5 Centrifugal instability

We performed the 3D linear stability analysis to investigate the presence of the centrifugal mode. The solver assumes periodicity in the spanwise axis when called by the time-stepping method. We must specify a spanwise wavenumber as input for so. The cumbersome task is performing a parametric sweep for several spanwise wavelengths, $\lambda_z = 2\pi/\beta$. Just the runs that are the threshold for bypass transition according to Crouch, Kosorygin and Sutanto (2020) were analyzed. Ergo, we did not perform a spanwise wavelength sweep for the 3D instability analysis in the run L24D2.

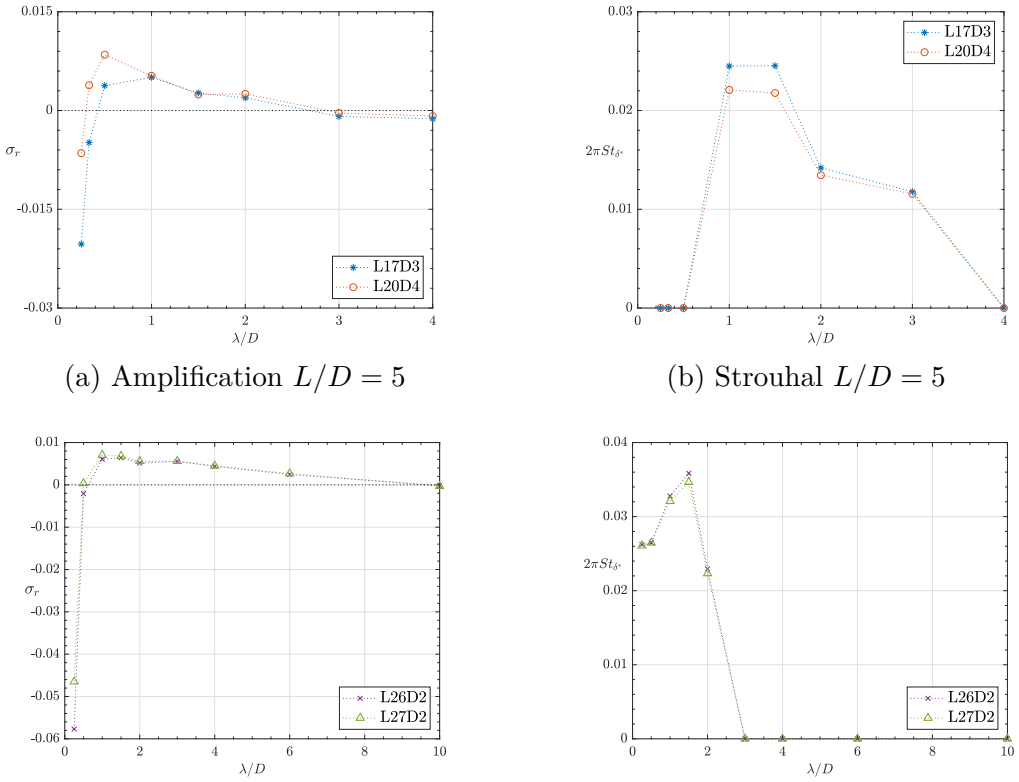
According to Brés and Colonius (2008) and Meseguer-Garrido *et al.* (2014), the centrifugal modes tend to be related to the gap depth. Also, the dominant 3D modes usually have wavelengths around one-half or one depth of cavity. This information helped to define the range of spanwise wavelength to cover. The procedure was to find the lower instability limit and gradually change the λ_z/D parameter up to the upper limit. The spanwise wavelengths range found was $0.25 \leq \lambda_z/D \leq 4$ for the aspect ratio $L/D = 5$, and $0.25 \leq \lambda_z/D \leq 10$ for $L/D = 10$.

Figure 45 depicts the range of unstable centrifugal modes and their respective temporal frequencies. It exhibits only the dominant mode for each spanwise wavelength. We can see a resemblance of the amplification curves for both aspect ratios, as shown in Figure 45a and Figure 45c, despite the range of λ_z/D with unstable centrifugal modes being considerably greater for $L/D = 10$. The most unstable mode for $L/D = 5$ had a

DISTRIBUTION A: Distribution approved for public release. Distribution unlimited

spanwise wavelength $\lambda_z/D = 0.5$, while for $L/D = 10$ was $\lambda_z/D = 1.0$. However, the spanwise wavelength non-dimensional by the gap displacement thickness were closer for both aspect ratios, and refining the spacing $\Delta\lambda_z/D$ of the parametric sweep could reveal the most unstable spanwise wavelength more accurately.

Figure 45 – Amplification and Strouhal number based on displacement thickness *versus* spanwise wavelength of the dominant centrifugal modes for $L/D = 5$ in (a) and (b), and for $L/D = 10$ in (c) and (d).



(a) Amplification $L/D = 5$

(b) Strouhal $L/D = 5$

(c) Amplification $L/D = 10$

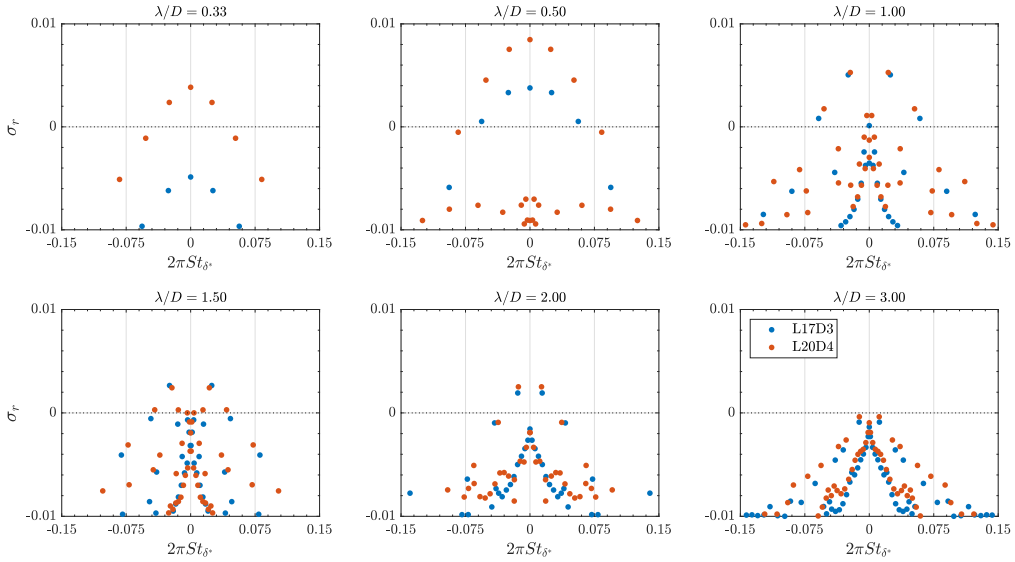
(d) Strouhal $L/D = 10$

Source: Author (2021).

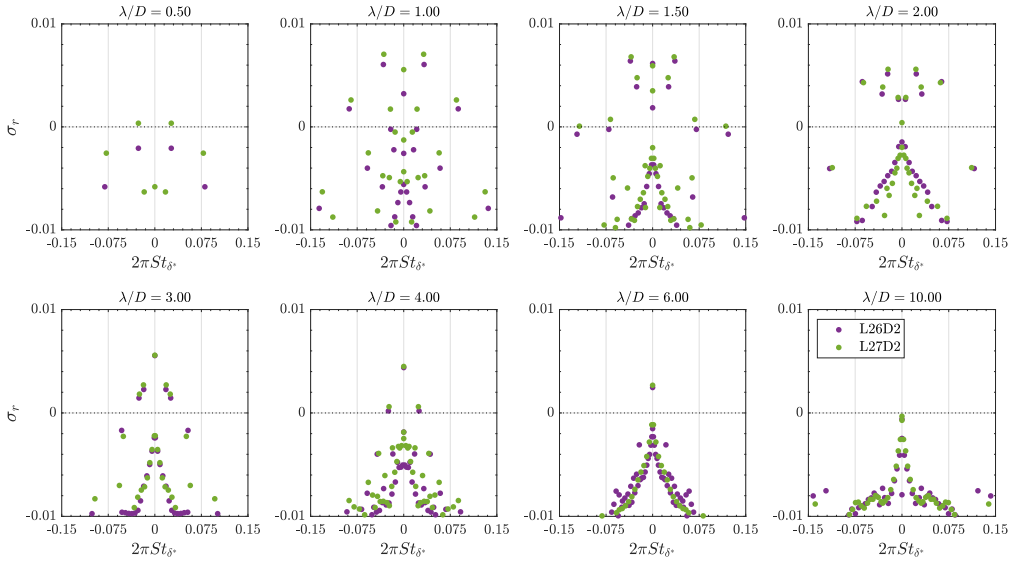
One crucial difference among the runs was the behavior of the most unstable centrifugal mode. In the runs L17D3, L26D2, and L27D2, the dominant 3D eigenvalue was an oscillatory mode, whereas, in the run L20D4, the most unstable was a standing mode. Figure 45b and Figure 45b reveals such demeanor. Another difference in trend between the two aspect ratios was the circular frequency of the modes for greater values of β, being stationary for $L/D = 5$ and oscillatory for $L/D = 10$. The curves exhibited in Figure 45a and Figure 45b were very similar to the results by Brés and Colonius (2008). However, the same does not happen for a very shallow gap, $L/D = 10$. Also, there is a lack of literature results regarding gaps with larger aspect ratios. We believe that the drastic change in the baseflow alters the 3D instability nature.

DISTRIBUTION A: Distribution approved for public release. Distribution unlimited

Figure 46 – Spectra of eigenvalues for the centrifugal modes with several spanwise wavenumbers for L/D=5 in (a) and $L/D = 10$ in (b).



(a) $L/D = 5$



(b) $L/D = 10$

Source: Author (2021).

Figure 46 presents the complex eigenvalue spectra for both aspect ratios, for the unstable range of spanwise wavelengths. It is possible to observe several kinds of unstable modes. An increase in Reynolds number slightly increased the instability and decreased the temporal frequency in unsteady modes, as anticipated by Brés and Colonius (2008).

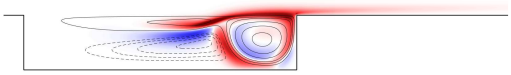
Moreover, the results presented a good comparison with the lid-driven cavity

DISTRIBUTION A: Distribution approved for public release. Distribution unlimited

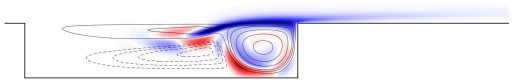
instability analysis from Albensoeder, Kuhlmann and Rath (2001) regarding the neutral Reynolds. For this comparison, we followed the recommendations by Brés and Colonius (2008) to compute the equivalent lid-driven velocity, as the streamwise average velocity at the mouth of the gap, $y/\delta_g^* = 0$. The value for the run L17D3 was $U_{lid} = 0.0761$, and 0.0781 for L20D4, within the typical range of $5\% - 15\%$, provided by Brés and Colonius (2008). Applying the scale parameters transformation, the neutral Reynolds number based on displacement thickness according to Albensoeder, Kuhlmann and Rath (2001) was $Re_n = 1126$, and 960, for the runs L17D3 and L20D4, respectively. Both runs had a higher value of Reynolds and presented unstable 3D modes.

For gaps with $L/D = 5$, for greater values of β, which is equivalent to lower values of the spanwise wavelength, a family of modes emerges, led by a stationary eigenvalue. We believe that this standing mode found is equivalent with the reported by Brés and Colonius (2008), referred to as *mode i*. It is the most unstable among all 3D modes for the run L20D4, as shown in Figure 46a for $\lambda_z/D = 0.50$. Also, we can see the presence of two unstable traveling modes, which we believe belong to the same class of modes. The second most unstable is equivalent to the *mode ii*, following the nomenclature from Brés and Colonius (2008). Seemingly, the literature lacks reports regarding the third from this family. Figure 47 displays the streamwise velocity eigenfunction in a phase where its real part maximum matches the absolute maximum for the three aforementioned. Furthermore, the figure exhibits the streamlines from the base flow, with clockwise streamlines represented by solid lines.

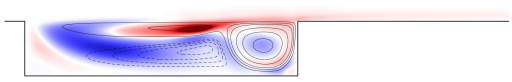
Figure 47 – $\hat{u}$ eigenfunctions of the centrifugal modes from L20D4.



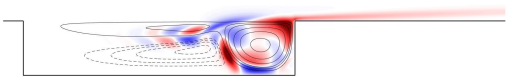
(a) Mode i (stationary) $\lambda_z/D = 0.50; 2\pi St_{\delta_g^*} = 0$



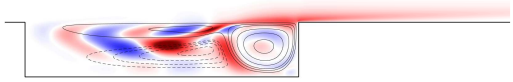
(b) Mode iia (traveling) $\lambda_z/D = 0.50; 2\pi St_{\delta_g^*} = 0.024$



(c) Mode iiia (traveling) $\lambda_z/D = 1.50; 2\pi St_{\delta_g^*} = 0.0039$



(d) Mode iib (traveling) $\lambda_z/D = 0.50; 2\pi St_{\delta_g^*} = 0.051$



(e) Mode iiib (traveling) $\lambda_z/D = 1.50; 2\pi St_{\delta_g^*} = 0.0143$

Source: Author (2021).

DISTRIBUTION A: Distribution approved for public release. Distribution unlimited

It is possible to observe a resemblance regarding its spatial structures. The stationary mode from Figure 47a exhibits a positive streamwise velocity along the peripherical region of the primary vortex. The positive streak occurs at $z/\delta_g^* = 0 + \lambda_z n$, with $n = 0,1,2,\ldots,$ whereas a negative streak occurs at $z/\delta_g^* = \pi + \lambda_z n$. There are negative and positive velocities around the elongated secondary vortex upstream. Additionally, the positive streak covers a great portion of the downstream top half of the gap up to the flat plate. The structure essentially remains the same for the modes represented in Figure 47b and Figure 47d. However, the difference appeared in the quantity and length of the azimuthal structures of the velocity streaks. The *mode ii* presented two structures instead of one, as from *mode i*, and so on. Consequently, the azimuthal length was reduced by a factor of two and four, respectively. Besides, the number of structures in the upstream eddy also increases from one pair in Figure 47a to two pairs in Figure 47b, and finally four pairs in Figure 47d. The frequency seems to duplicate from the *mode iia* for *mode iib* too.

Likewise, runs L17D3 and L20D4 presented another 3D mode family, which occurred for wider spanwise wavelengths. Figure 47c and Figure 47e depict its eigenfunctions. These modes had spatial structures more intense near the upstream region of the gap, opposite to the previous family of modes with more intense activity close to the primary vortex of the gap. Also, one can note an abrupt decrease in its temporal frequency compared to the previous group. Brés and Colonius (2008) refer to this eigenvalue as *mode iii*. Likewise, as the number of spatial structures around the secondary vortex increases from Figure 47c to Figure 47e also occurs a similar increase in the frequency.

Table 5 – Leading eigenvalues associated with the centrifugal mode.

	L17D3				L26D2			
	λ/D	β	σ_r	$i\sigma_i$	λ/D	β	σ_r	$i\sigma_i$
mode i	0.50	π	0.0037	0	1.50	$16\pi/33$	0.0061	0
mode ii	1.00	$\pi/2$	0.0050	0.0245	1.50	$16\pi/33$	0.0064	0.0358
mode iii	2.00	$\pi/4$	0.0019	0.0142	2.00	$4\pi/11$	0.0051	0.0229
	L20D4				L27D2			
	λ/D	β	σ_r	$i\sigma_i$	λ/D	β	σ_r	$i\sigma_i$
mode i	0.50	π	0.0084	0	1.50	$16\pi/33$	0.0059	0
mode ii	0.50	π	0.0075	0.0241	1.00	$8\pi/11$	0.0070	0.0321
mode iii	2.00	$\pi/4$	0.0025	0.0135	2.00	$4\pi/11$	0.0056	0.0223

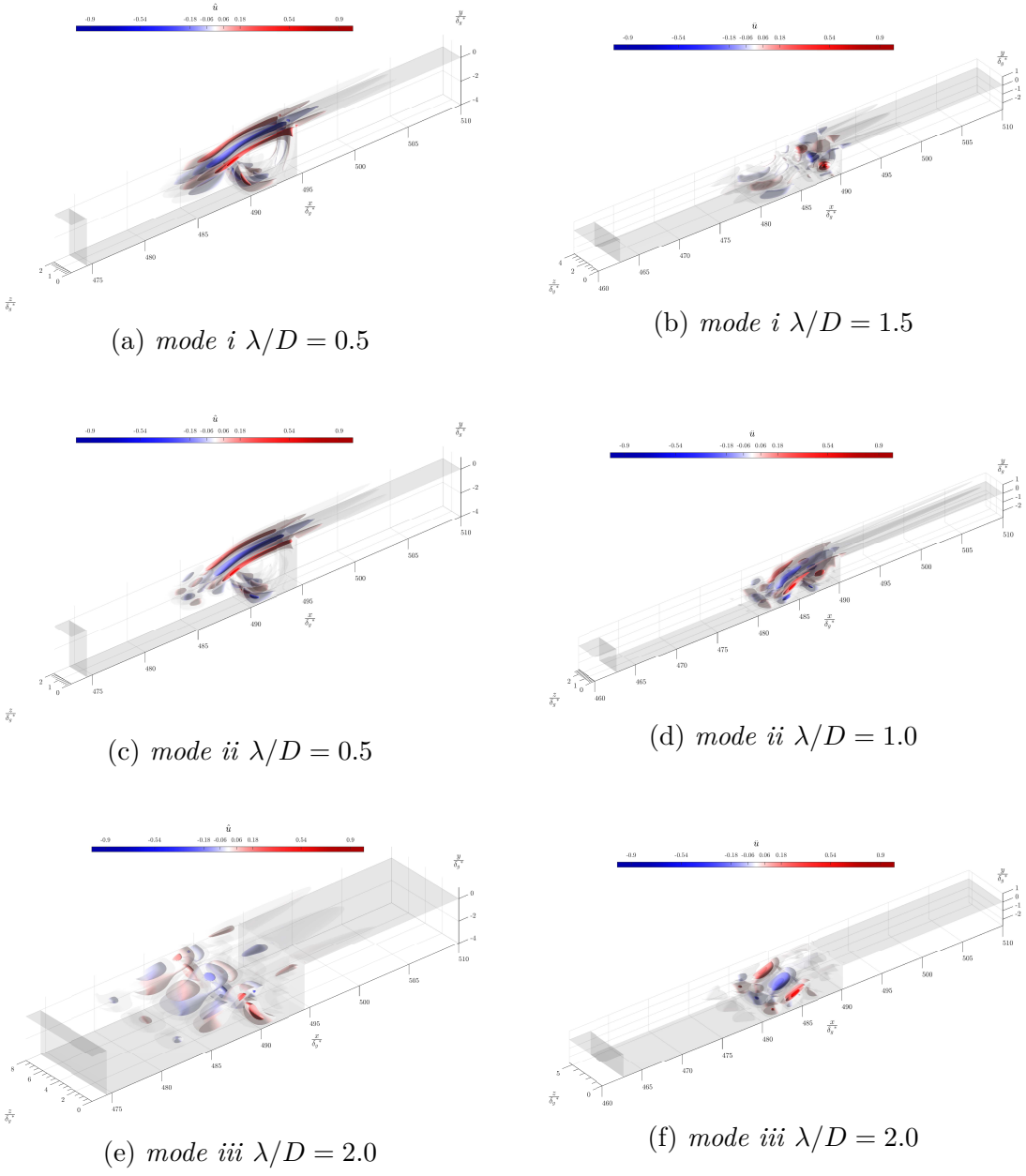
Source: Elaborated by the author.

Note: Red colored font indicates dominant mode.

For gaps with $L/D = 10$, starting from the lower values of the spanwise wavelength

DISTRIBUTION A: Distribution approved for public release. Distribution unlimited

Figure 48 – Iso-surface of the leading streamwise velocity eigenfunctions, $\hat{u}$, of the centrifugal *modes i*, *ii*, and *iii*, from the runs L20D4 (left) and L27D2 (right). Spanwise wavelenghts indicated in sub-figures and contour levels in the ticks of the color bar.



(a) *mode i* $\lambda/D = 0.5$

(b) *mode i* $\lambda/D = 1.5$

(c) *mode ii* $\lambda/D = 0.5$

(d) *mode ii* $\lambda/D = 1.0$

(e) *mode iii* $\lambda/D = 2.0$

(f) *mode iii* $\lambda/D = 2.0$

Source: Author (2021).

forward, the first mode to become unstable was a traveling mode. After visually inspecting its eigenfunction, we believe that it is the *mode ii*. One can see from Figure 46 that for a range of $1 \leq \lambda_z/D \leq 4$ there was a presence of simultaneous multiple centrifugal modes. Although, the *mode ii* was the dominant mode, with the greatest amplification rate and persisting for a greater band of spanwise wavelengths. The *mode iii* became the dominant only in $\lambda_z/D = 2$. For lower values of β, a stationary mode prevailed among the

DISTRIBUTION A: Distribution approved for public release. Distribution unlimited

other centrifugal modes and endured up to $\lambda_z/D \approx 10$, which was the upper limit for the unstable range of spanwise wavelength.

Even though the gap geometries presented several unstable centrifugal modes, only the dominant ones will dictate the preferred spanwise wavelengths in an infinitely long gap. Table 5 gathers the leading eigenvalues from the three families of the centrifugal modes for each run, using the nomenclature by Brés and Colonius (2008). The red-colored font indicates the dominant from each run. Figure 48 exhibits the three dimensional plot of the streamwise velocity eigenfunctions, $\hat{u}$, from the leading centrifugal modes. Plots on the left correspond to the run L20D4, whereas plots on the right to L27D2.

4.6 Transition induced by the gap

The elements involved in the transition process will be demonstrated using four different case studies, dimensionless by the displacement thickness at the leading edge of the cavity. The four cases have aspect ratio given by $L/D = 2$. Cases A, C and D, have Depth $D/\delta^* = 6.11$. Case B, on the other hand, has $D/\delta^* = 5.77$. All the cases, are presented in the table Table **??**.

Case	Re_{δ^*}	Ma	3D modes (Centrifugal)	2D modes (Rossiter)	Turbulence
A	734	0.2	Unstable	Stable	No
B	693	0.5	Unstable	Unstable	Only one spot
C	734	0.9	Unstable	Unstable	Yes
D	734	0.5	Unstable	Unstable	Yes

All are present in Figure 49, and the Amplifications and Frequencies for different β are shown. For all cases, hydrodynamic instability analysis was performed for β from 0.1 to 1, for centrifugal (three-dimensional) modes, and for β equal to 0, for Rossiter (two-dimensional) modes.

4.6.1 Case A: $Re_{\delta^*} = 734$ and $Ma = 0.2$

This case was chosen so that the presence of unstable centrifugal modes but stable Rossiter modes occurred, which can be visualized in Figure 49. For this case, no signs of a possible boundary layer transition along the useful domain were observed, therefore, is considered a stable case, as can be seen in the image of Figure 50, which represents the cut of the flow at the center of the domain in the Z direction, where it is possible to observe a boundary layer similar to the Blasius boundary layer profile.

We can observe in the left-hand side of Figure 51 that the friction coefficient was lower than that of a laminar boundary layer. This decrease may indicate a thickening in the boundary layer, caused by the presence of the cavity, as well as seen in the image on the right, where we have the law of the wall calculated for the experiment, whose result is consistent with that of a laminar boundary layer.

DISTRIBUTION A: Distribution approved for public release. Distribution unlimited

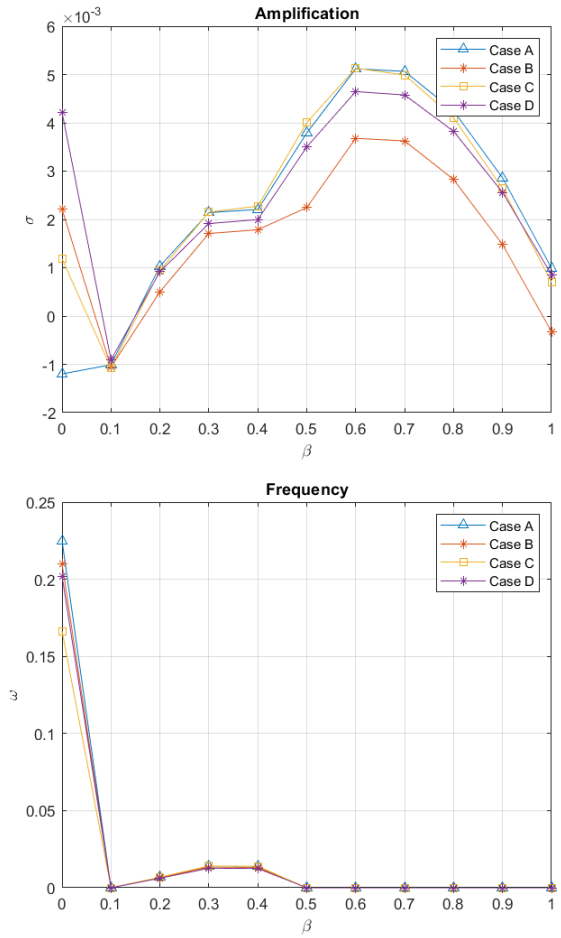


Figure 49 – Hydrodynamic instability analysis, using Linear Stability Theory (LST), for the four representative cases of the transition process. Both figures show the most unstable modes for each frequency along with Z. The figure on the right refers to amplification, while the one on the left refers to frequency.

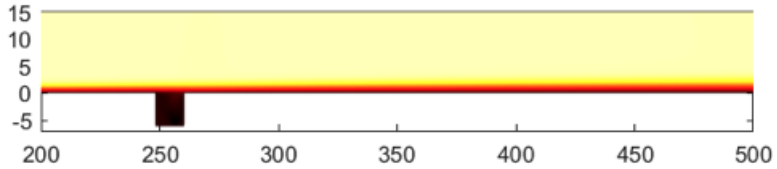


Figure 50 – The image shows the colormap of the U component of the velocity at the center of the Z domain.

Regarding the analysis of the modes inside the cavity, it was expected that the modes would be consistent with those observed in the LST. For this, a Fourier transform along Z was performed for all X inside the cavity, done at 2 different times to represent the convection of these modes inside the cavity. These results are present in Figure 52, as the purpose was to show the centrifugal modes, a fixed position at the bottom of the cavity was chosen, as well as the W component of the velocity.

To aid the visualization of the modes of interest (those previously obtained in the

DISTRIBUTION A: Distribution approved for public release. Distribution unlimited

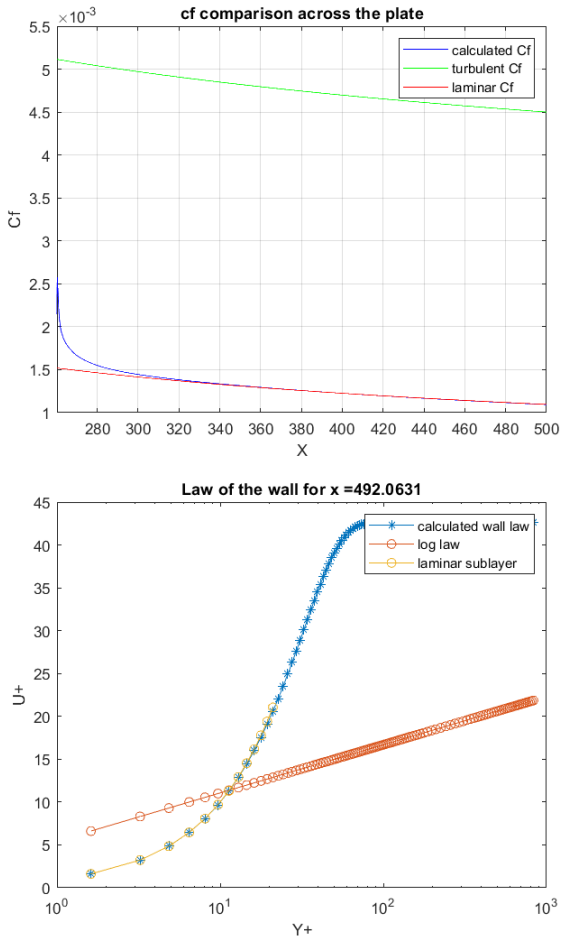


Figure 51 – In the left figure is represented the comparative C_f along with the plate. The figure on the right shows a comparison of the law of the wall.

LST Figure 49), two dashed lines were drawn, representing the upper and lower limits of the β tested in the LST. The continuous line was drawn so that it would be more convenient to visualize the most unstable centrifugal modes, that is, the modes with β between $0.5 \leq \beta \leq 1$. Hereby, it is possible to see that the most unstable modes inside the cavity are in the region predicted by the LST.

4.6.1.1 Case B: $Re_{\delta*} = 693$ and $Ma = 0.5$

This second case was chosen in a manner that there would be an unstable Rossiter mode, as well as centrifugal modes, with a lesser degree of instability than Case A. The differnece of this case to the previous one is the presence of a single convected turbulence spot from the cavity. This spot can be observed in two different ways in **??**, being seen at the moment of its propagation to the end of the plate, as well as instants after its emission while still in the domain.

After spot convection, the flow stabilizes again, and a Blasius-like boundary layer can be seen in Figure 54.

DISTRIBUTION A: Distribution approved for public release. Distribution unlimited

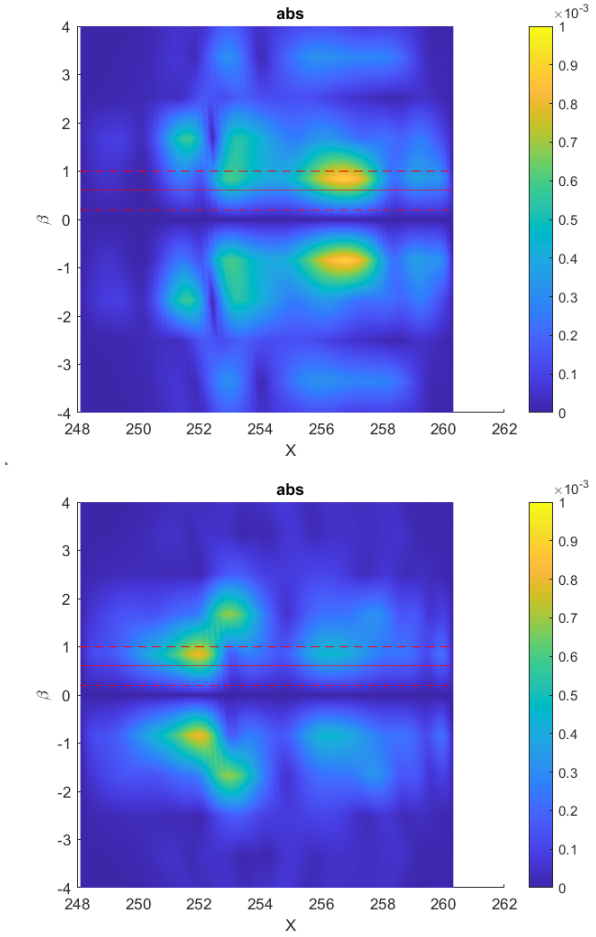


Figure 52 – In the pictures we have the FFT along Z for the values of X inside the cavity, using the W component of the velocity. In the right image, we have 100 dimensionless moments after the left image.

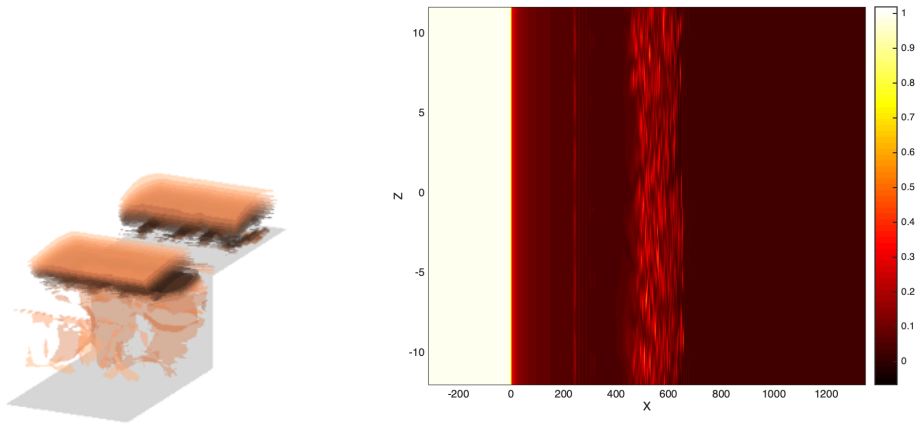


Figure 53 – In the pictures, we have the λ_2 method to representing the beginning of the emission of the spot in the left picture. In the right picture, we have a few dimensionless instants after the left picture, the representation of a cut of the domain in the XZ plane, with Y of $0.5\delta^*$.

DISTRIBUTION A: Distribution approved for public release. Distribution unlimited

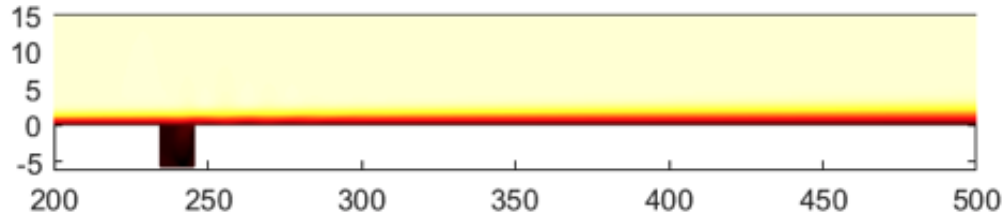


Figure 54 – In the figure, we have the colormap of the boundary layer at the center of the domain in Z, after the convection of the turbulence spot.

We can notice that after the leave of the spot the boundary layer stabilized again, returning to have similar characteristics to those present in Case A. In **??**, we can see the C_f along with the plate, as well as the wall law, which indicates that we have a laminar boundary layer again, but it gets thicker after the spot passes.

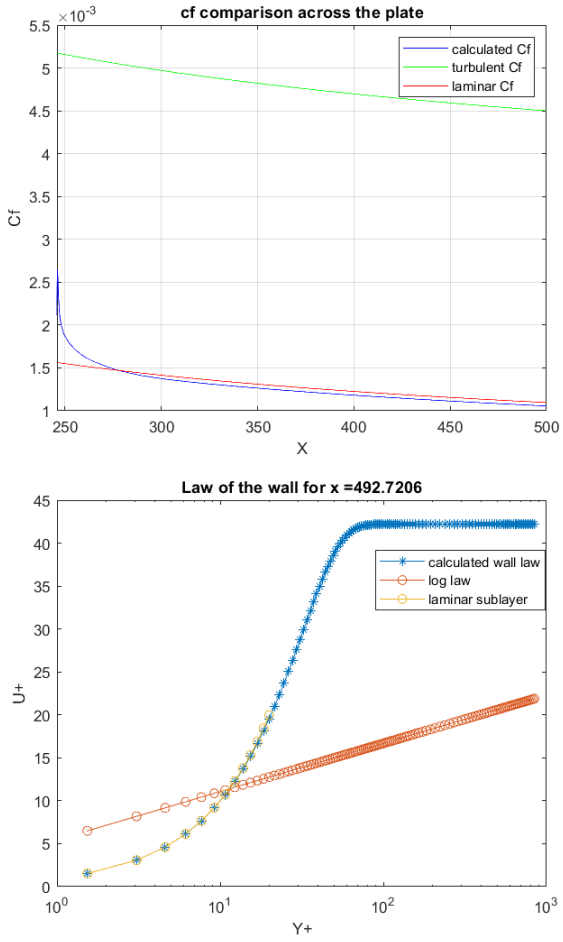


Figure 55 – In the left picture, we have the comparative C_f after the cavity. In the right picture, we have the wall law for the end of the domain.

As we can see in **??**, after the cavity, the boundary layer has a lower coefficient of friction than a laminar boundary layer, indicating again a thicker layer. This thicker layer could explain the stabilization of the flow, making it more difficult to destabilize the

DISTRIBUTION A: Distribution approved for public release. Distribution unlimited

cavity again, and in turn, cause a definite transition.

Here, the analysis of the modes present inside the cavity, in the same way as for the previous case, straight lines were drawn along β equal to 1,0.1 and 0.5, to delimit the same regions of interest. In Figure 56, we can observe that again, the amplitude peek inside the cavity, is in the region found in the LST in Figure 49. For this the Fourier transform along Z is illustrated, for different values of X inside the cavity, at two different time instants, to show the movement of these modes along the cavity.

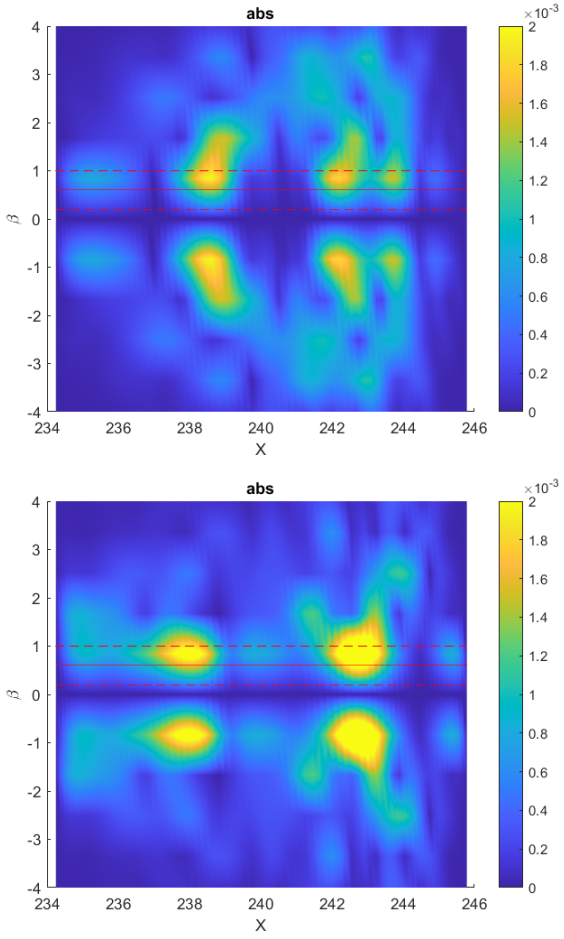


Figure 56 – In the pictures we have the FFT along Z for the values of X inside the cavity, using the W component of the velocity. In the right image, we have 100 dimensionless instants after the left image.

We can notice that, after the evolution of time, there is a change in intensity and the modes become more concentrated in the expected region.

4.6.1.2 Case C: $Re_{\delta^*} = 734$ and $Ma = 0.9$

The third case was chosen so that the presence of even more unstable centrifugal modes than Case B occurred, as well as the presence of unstable Rossiter modes. Increasing the three-dimensional instability levels, as well as increasing the Re_{δ^*}, leaving the flow even

DISTRIBUTION A: Distribution approved for public release. Distribution unlimited

more unstable. For this scenario, a higher Mach (0.9 in the case) was chosen to maintain an unstable Rossiter mode, but with an instability level below that of case D.

By increasing the levels of three-dimensional instabilities, i.e., increasing the amplification of the centrifugal modes, as well as, making the boundary layer more unstable by increasing Re_{δ^*}, it was possible to generate a transition, however outside the useful domain used in the previous cases. Therefore, in this case, the useful domain was extended by twenty-five downstream cavity lengths.

As we can see in Figure 57, the structures leaving from within the cavity, at two different instantiations, we can see the presence of two-dimensional vortices, along with three-dimensional vortices.

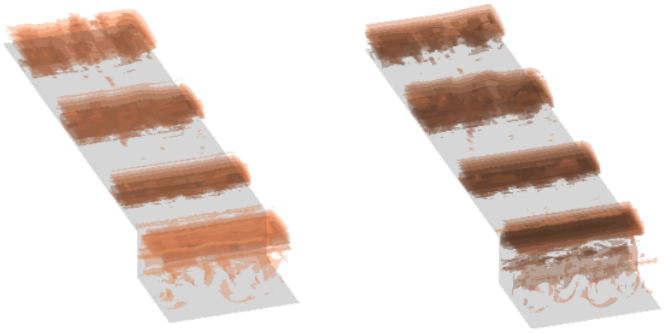


Figure 57 – In the figures, we have the λ_2 method, where the structures are being convected from the cavity, at two different instants. The figure on the left represents the domain of the emission process of three-dimensional structures, and in the figure on the right, 100 dimensionless instants, we can see more three-dimensional structures within the two-dimensional structures.

In Figure 58, we can see that the part near the end of the domain starts to have more structure, becoming more similar to the friction coefficient of a turbulent case. In the same figure, we can notice that the behavior of the wall law, gets closer to the log law, indicating the presence of a turbulent boundary layer. It is possible to notice clearly, in Figure 58 a region with friction coefficient above a turbulent case, indicating a possible boundary layer with less thickness. This region could indicate a transition region, where the turbulent boundary layer, is not yet fully developed. The turbulent boundary layer, starts to look like a fully developed layer around X approximately 492, as can be seen in Figure 59.

Turning now to the analysis of the spectra present downstream the cavity, we can see that at the beginning of the transition process, we have convection from a spot, which can be visualized in Figure 60. We have in this figure the beginning of the transition process, as well as when the flow stabilizes, showing that there is a wide spectrum of unsteady modes as the turbulent boundary layer develops. The red dotted lines in the images define the boundaries of the unsteady modes found by the LST. The centerline

DISTRIBUTION A: Distribution approved for public release. Distribution unlimited

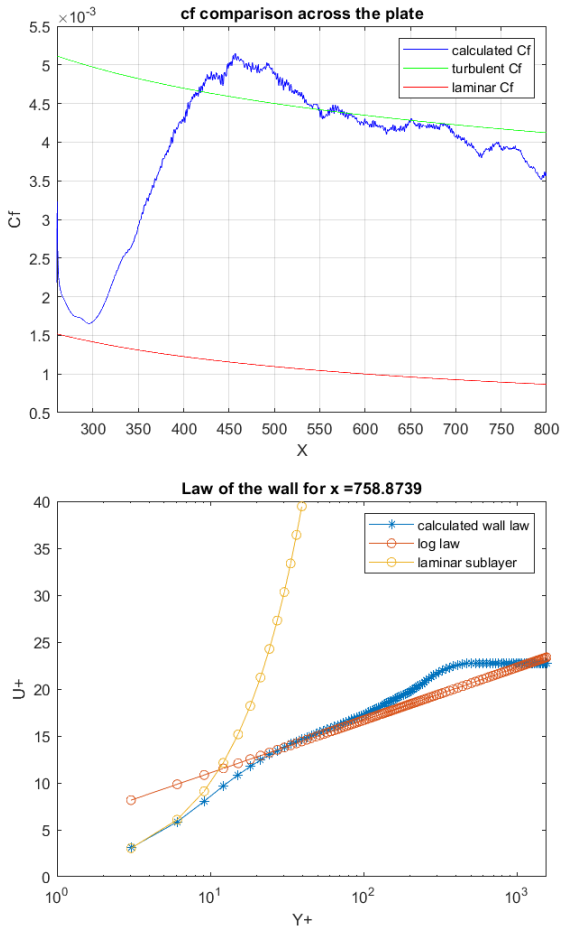


Figure 58 – In the figures, we have on the left the friction coefficient for the entire useful domain downstream to the cavity. The figure on the right, shows us the wall law, near the end of the domain, where it already presents a good agreement with the law of the wall.

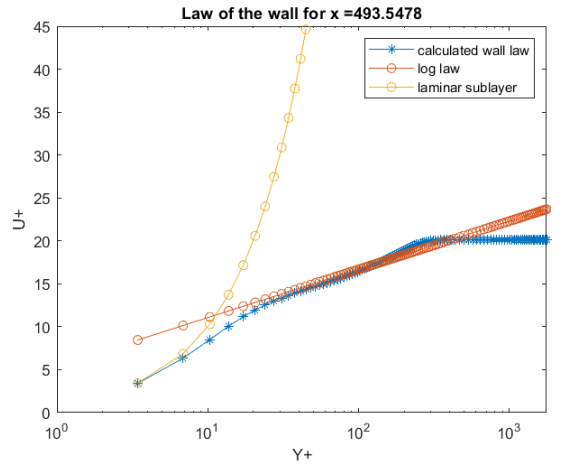


Figure 59 – In the figure, we have a boundary layer with a wall law near a fully developed boundary layer, indicating that we have a possible fully developed region after this point.

DISTRIBUTION A: Distribution approved for public release. Distribution unlimited

separates the region into two subregions again, from $\beta = 0.1$ to 0.5, an unstable region, which however has the lowest amplitude values than the $\beta = 0.5$ to 1 region. We can notice that parts of the regions with higher amplitude are present in this region, although they become more diffuse as they go downstream in the cavity.

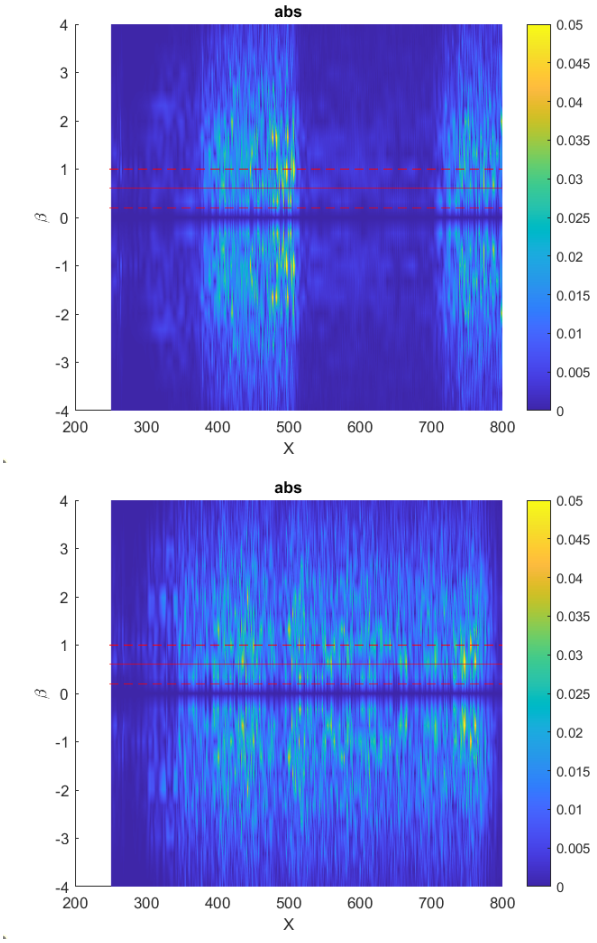


Figure 60 – In the figures, we have the Fourier transforms along Z, for all X of the domain, using the W component of the velocity. The left figure represents the beginning of the initial spot propagation. The figure on the right represents the developed flow.

In addition, we can also see this development in sections of the boundary layer, present in **??**. In this figure, we can see the initial spot being convected, in the left image, as well as the flow developing in the right image.

In case C, we can notice a clear difference from the behavior present in case B, where after the initial spot emission, the flow stabilizes and returns to a laminar flow. In this case, after the emission of the spot, we have higher levels of three-dimensional instabilities. Suggesting that the levels of centrifugal instabilities may be linked with the boundary layer transition.

Having already commented on the importance of centrifugal modes, we need to comment on what happens with the two-dimensional modes (Rossiter modes). These modes,

DISTRIBUTION A: Distribution approved for public release. Distribution unlimited

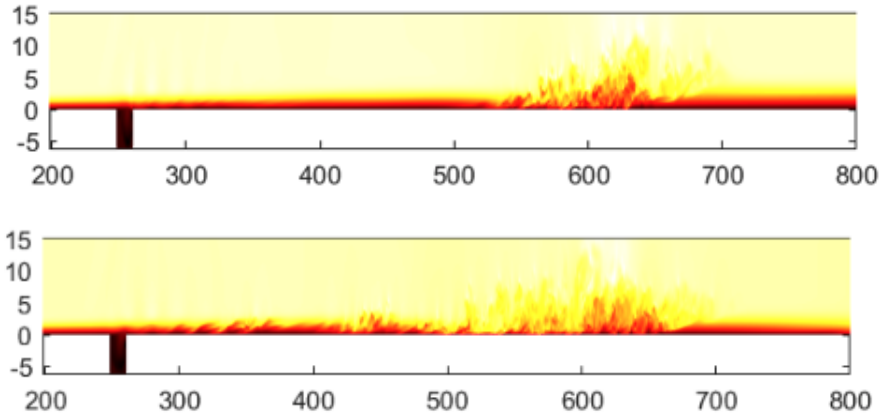


Figure 61 – In the figures, we have the slices of the velocity component U at the center of the Z-domain. In the left figure, we have the initial spot that was convected from the cavity during its propagation over the plate. In the figure on the right, we have about 50 dimensionless instants, after the image on the right. In this image, we can observe the development of the flow, after the spot leaves the plate.

as observed in LST, have well-defined frequencies, and can be identified more efficiently and cleanly using variables such as pressure (or density) on the wall. To understand how it behaves, two-dimensional Fourier transforms were performed, along the Z-axis and over time. The two-dimensional Fourier transforms are shown in Fig.

In Figure 62, we can see how the two-dimensional modes leave the cavity in the left image, as well as, we can see how these modes are behaving in the transition region. More details of the behavior of these modes will be discussed in case D. It can be seen that just after the cavity (which is situated in the region of X approximately 245 and X approximately 260), at the X position equal to 265, we have a mode with much higher amplitude than the others, with frequency ω and $\beta = 0$, in the region expected for Rossiter modes. As we progress downstream the cavity, and leave the plate, going to position $X = 300$ and $Y = 0.2\delta^*$, we have that the Rossiter modes are still present, as well as we can visualize the presence of stationary centrifugal modes, with zero frequency, image present in Figure 62, right.

To finish case C, we have Figure 63, where the entire downstream domain is present, showing the λ_2 method, when the flow is fully developed.

DISTRIBUTION A: Distribution approved for public release. Distribution unlimited

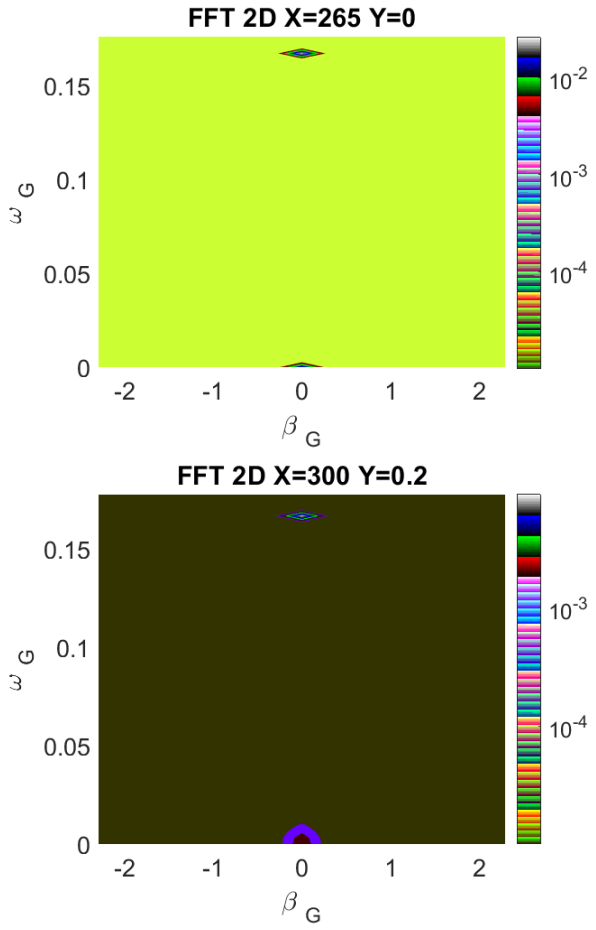


Figure 62 – In the figures, we have the two-dimensional Fourier transforms (2D FFT), for two different positions in the flow. The 2D FFT was performed using a fixed value of X and Y, and doing the transform using the variables Z and T (time). In the figure at left, we have the 2D FFT, for the position $X = 265$ and $Y = 0$, of the density in the plate, we can see in it the presence of a well defined Rossiter mode in the region of $\beta = 0$ and $\omega \approx 0.19$, close to those expected by LST. In the left figure, we have the 2D FFT, for the position $X = 300$ and $Y = 0.2$, of the density in the boundary layer, we can still see the Rossiter modes present.

4.6.1.3 Case D: $Re_{\delta^*} = 734$ and $Ma = 0.5$

Having obtained the transition with Case C, the next logical step would be to further increase the two-dimensional instability. For this, the Mach chosen was 0.5, where we have a region whose Rossiter mode becomes even more unstable. With this increase in instability, it was again possible to reduce the domain, since as can be seen in Figure 64, the boundary layer develops at a smaller distance in X.

As can be seen in Figure 64, the flow has anticipation at the transition point compared to case C. Looking at C_f and the wall law in Figure 65, we can notice that the flow is already turbulent in the useful domain, having a good agreement with the log law in the wall law comparison.

DISTRIBUTION A: Distribution approved for public release. Distribution unlimited

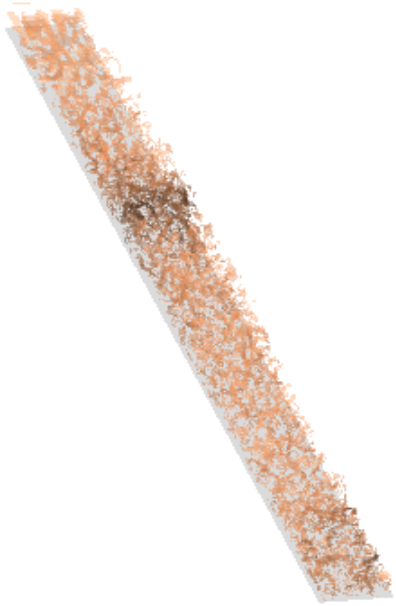


Figure 63 – The image shows the λ_2 method present downstream to the cavity, for the entire useful domain. The image was taken for the fully developed flow.

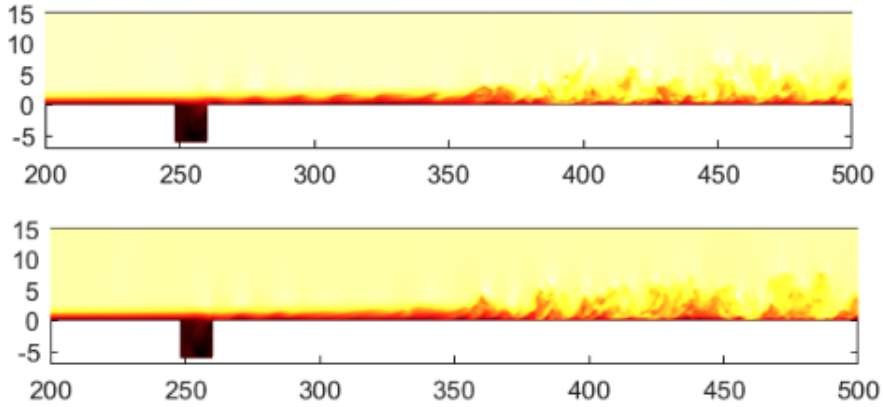


Figure 64 – In the figures, we have the U-component slices of the velocity, for two different time instants. The image on the right shows the flow with an increment of 50 dimensionless instants after the image on the left.

Using the Lambda 2 method, to visualize the structures being convected from the cavity, we can see in Figure 66, better defined three-dimensional structures compared to those in case C. One can notice that two-dimensional modes are convected along with

DISTRIBUTION A: Distribution approved for public release. Distribution unlimited

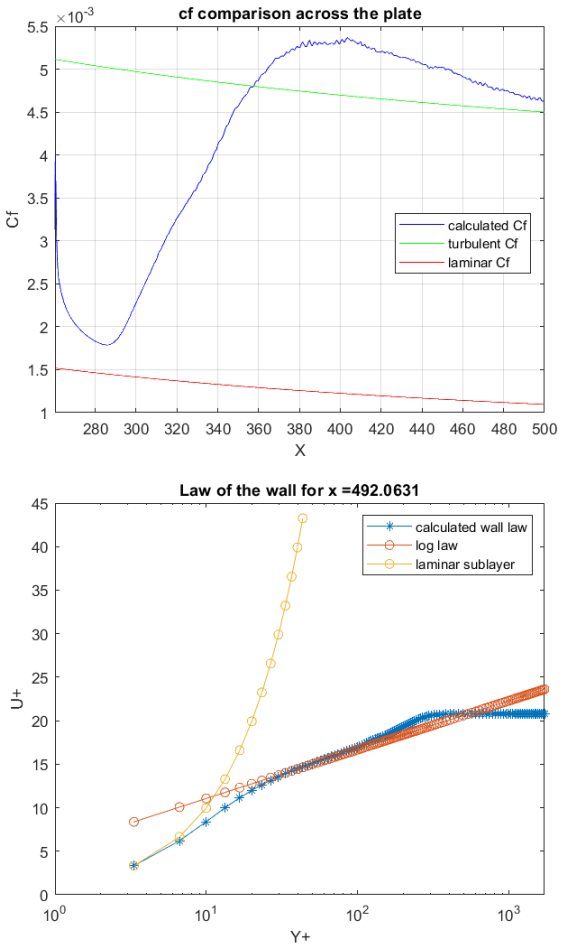


Figure 65 – In the left figure, we have the comparison of C_f, where it is possible to see a smaller transition region, as well as a transition in a smaller domain. In the right figure, we have the law of the wall before the end of the domain, confirming the transition.

three-dimensional modes. As the vortices are convected off the plate, they lose their two-dimensional structures, with the flow becoming turbulent.

We can also notice in Figure 67 that after this transition region, we have a rapid three-dimensionalization of the structures, reinforcing the characteristics of a turbulent flow. These structures start to grow as they propagate along X until they reach the end of the domain. We can note, that the region immediately after the cavity, still presents relatively two-dimensional structures, which become increasingly three-dimensional with the spatial evolution.

Unlike case C, where the 2D structures remain for larger values of X, in case D, the structures appear only in a small region after the cavity, quickly losing their two-dimensionality. With this, we have indications that the Rossiter and centrifugal modes should be directly related to the boundary layer transition. Furthermore, there are indications that the levels of instabilities required, may come to depend on other variables, such as Re_{δ^*}, cavity depth, as well as cavity length, may come to interfere with

DISTRIBUTION A: Distribution approved for public release. Distribution unlimited

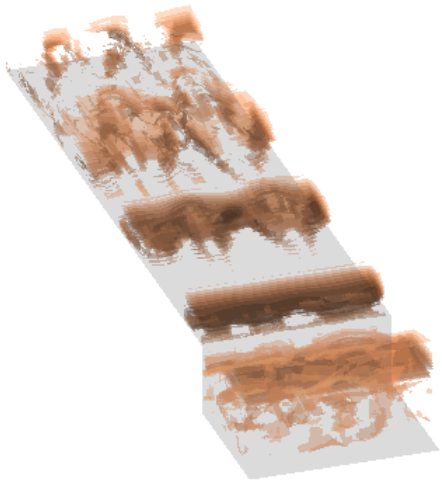


Figure 66 – In the figure, we have the λ_2 method showing the structures convected out of the cavity.

the transition.

Figure 68 exhibits the analysis of the spectra present in the flow inside the cavity. Using the FFT along Z, for all X inside the cavity, we can see that just as in case B, the modes with higher amplitude are again in the region predicted by LST, mainly in the region between the dotted lines and in the upper band, as predicted earlier.

It is possible to notice that the structures are not only very close to the expected region, but they move through the cavity. With this, it is possible to note that there is an internal dynamic in the cavity, linked to the centrifugal modes. Concerning the analysis outside the cavity, using the FFT along Z for all X of the domain downstream the cavity, for the W component of the velocity, we can note that there is a scattering of the spectrum, as in case C. This behavior can be observed in Figure 69.

We can observe that there is a large dispersion of modes, something that does not occur inside the cavity. This dispersion can be explained by the fact that we are working with a turbulent boundary layer, however, it is still possible to see memories of the cavity modes, even in the turbulent region.

Finally, 2D FFTs were used, with the objective of trying to map the behavior of the modes as they move through the domain. In Figure 70, we have the 2D FFT for a point on the plate near the trailing edge of the cavity, calculated using the density on the plate, as well as the 2D FFT calculated for about four cavity lengths, downstream the

DISTRIBUTION A: Distribution approved for public release. Distribution unlimited

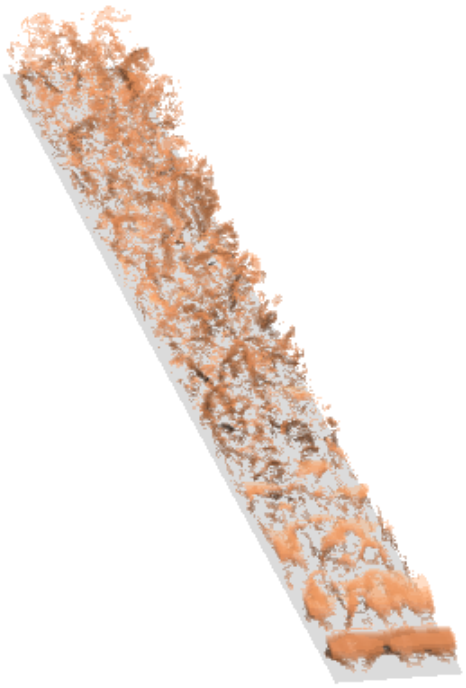


Figure 67 – In the figure, we have the λ_2 method showing the downstream convected structures of the cavity.

cavity, using the density on the plate.

We can see in the image, that even at X = 300, we can still see a memory of the Rossiter mode in the plate. However, as we move away from the trailing edge of the cavity, the intensity of the Rossiter mode decreases. Also, by switching the variable to the W component of the velocity, and scaling the boundary layer, we can see a presence of the centrifugal modes, as well as scattering in the frequency where the Rossiter mode used to be, especially in the β region where the centrifugal modes are, in Figure 71. Further downstream, in the same figure, the Rossiter mode ceases to have a relevant amplitude. The modes with lower frequency presented more relevance and memory in the turbulent region.

These lower-frequency modes, located in the β region near the Rossiter modes, may indicate some mixing between 2D and 3D modes, especially considering that the modes become low-frequency, similar to the centrifugal modes found in the LST.

DISTRIBUTION A: Distribution approved for public release. Distribution unlimited

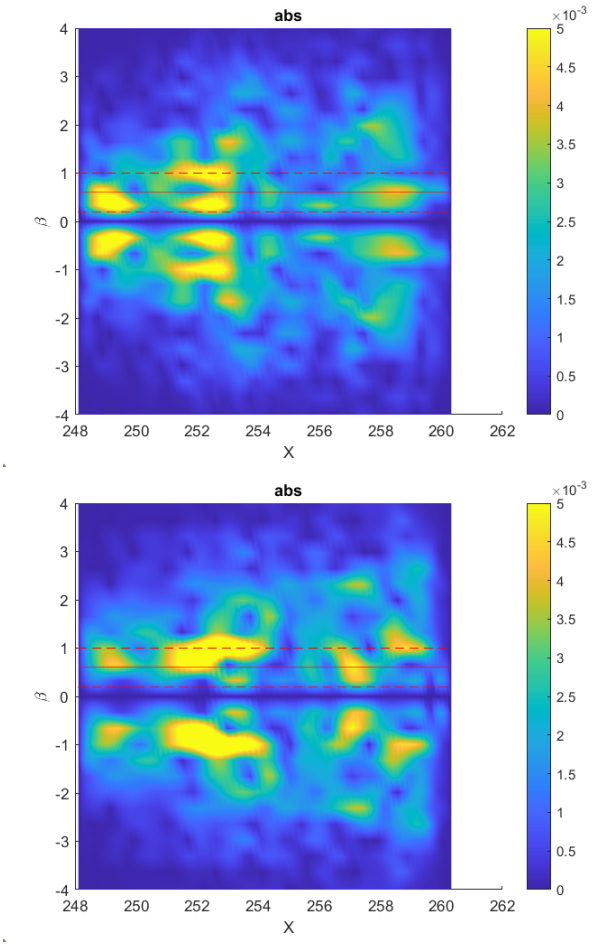


Figure 68 – In the figure, we have the FFT along Z for all values of X inside the cavity, using the W component of the velocity, located 1 δ^* from the bottom of the cavity at two different time instants. The figure on the right represents 50 dimensionless instants after the image on the left.

DISTRIBUTION A: Distribution approved for public release. Distribution unlimited

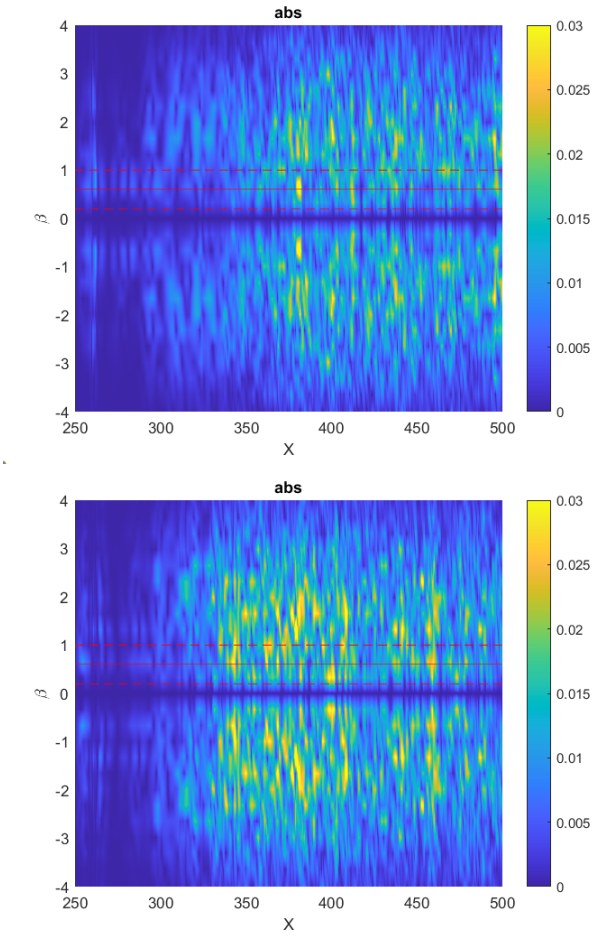


Figure 69 – In the figure, we have the FFT along Z for all values of X downstream of the cavity, using the W component of the velocity, located 0.5 δ^* from the plate at two different time instants. The figure on the right represents 50 dimensionless instants after the image on the left.

DISTRIBUTION A: Distribution approved for public release. Distribution unlimited

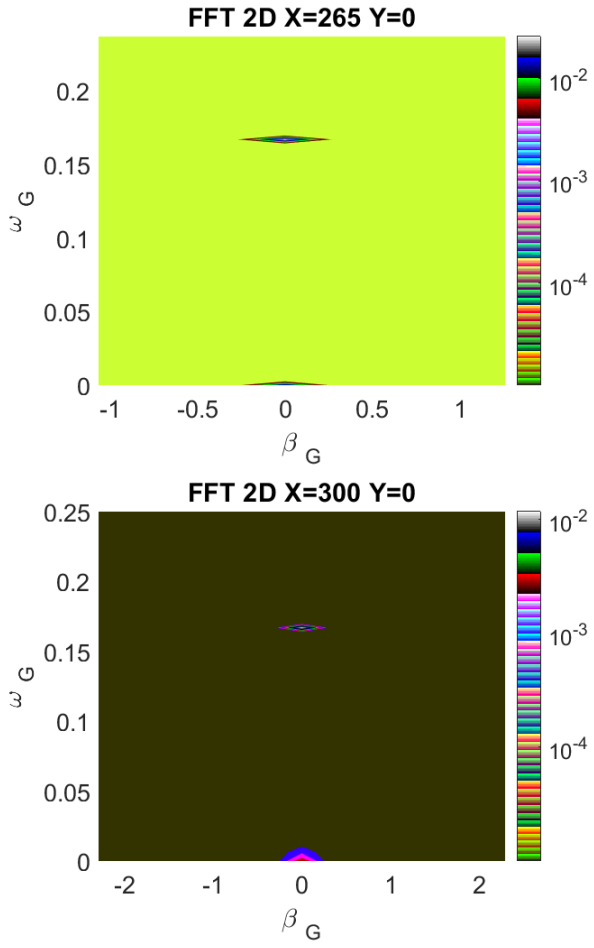


Figure 70 – In the figure, we have the 2D FFT for two different points on the plate. The 2D FFT has been computed using the density along Z and T for two different points on the plate. The left picture represents the 2D FFT over the plate at X = 265 and Y = 0, while the right picture represents the 2D FFT at X = 300 and Y = 0.

DISTRIBUTION A: Distribution approved for public release. Distribution unlimited

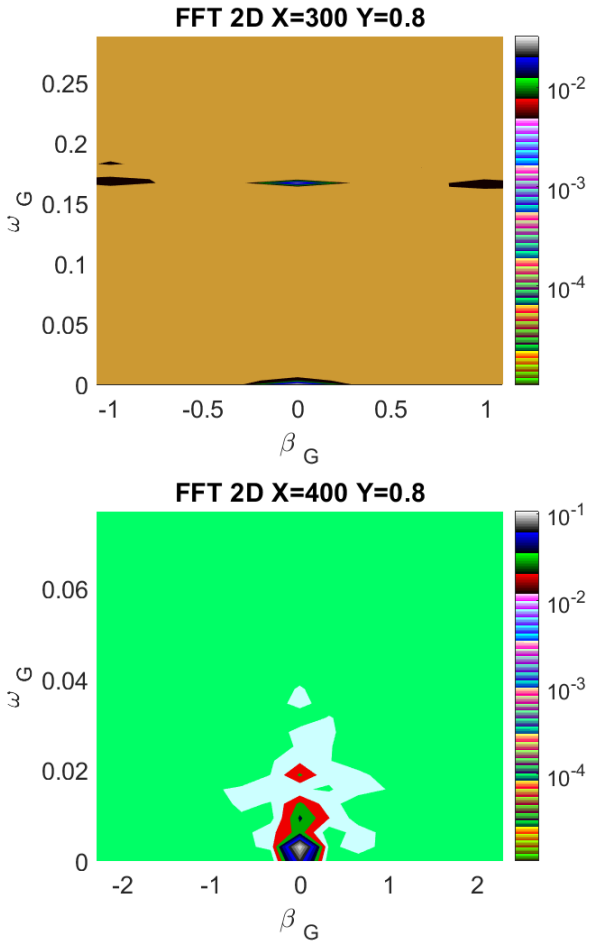


Figure 71 – In the figure, we have the 2D FFT for two different points on the plate. The 2D FFT was computed using the W component of the velocity along Z and T for two different points on the plate. The left picture represents the 2D FFT over the plate at X = 300 and Y = 0.8, while the right picture represents the 2D FFT at X = 400 and Y = 0.8.

DISTRIBUTION A: Distribution approved for public release. Distribution unlimited

4.7 Possible Scenarios for transition induced by a gap

As showed previously, we have different unsteady modes involved, however, only variables such as Mach number and Reynolds number were analyzed. Despite the change in depths and lengths as a consequence, all the tested cavities have identical aspect ratios ($L/D = 2$), as well as similar cavity depths and lengths showing a difference of less than 10% in the variation of these variables. Therefore, it is necessary, to study the behaviors for changes in these variables. Using results obtained in the Mathias (2021) group, LST and mapping were processed. This mapping can be seen in Figure 72.

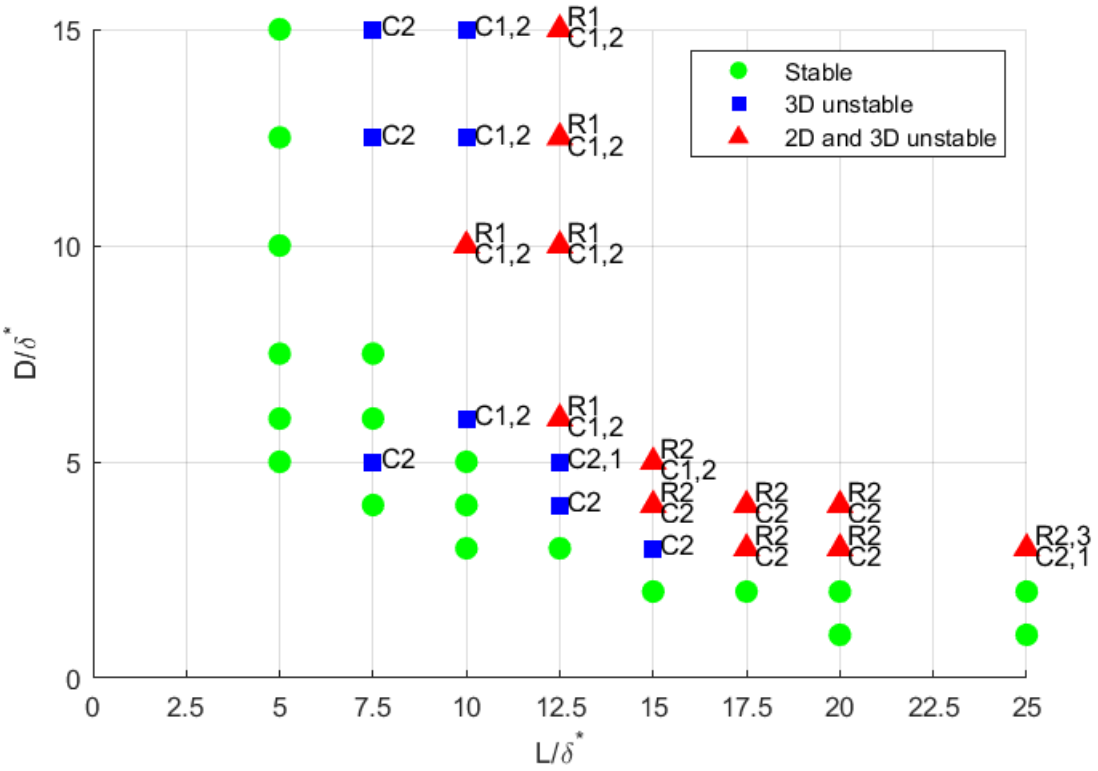


Figure 72 – Mapping using LST of the modes present for different depths and cavity lengths. Mapping using $Ma = 0.5$ and $Re_{\delta^*} = 600$.

In Figure 72, we can draw two straight lines, one horizontal using a depth D/δ^* fixed at 3, where varying the length of the cavity, we have changes in the stability of the flow. In addition to this first straight line, we can draw a second straight line, now vertically, for a value of L/δ^* fixed at 12.5, where varying this time, the depth of the cavity, we also have a change in the stability of the flow.

We can notice that the unsteady modes in each line are distinct. For cavities with greater depths, we have centrifugal modes 1 and 2 as the main three-dimensional unsteady modes, while the main two-dimensional mode is Rossiter 1. However, for cavities with greater length, we have that the unstable 2D mode, is Rossiter 2 (as the length increases, Rossiters 3 and 4 should eventually appear), and the main 3D modes, is centrifugal mode

DISTRIBUTION A: Distribution approved for public release. Distribution unlimited

2.

4.7.1 Large L

In Figure 73, we have two images. The image on the right contains the amplifications of the unsteady modes for each of the cases, while the one on the left shows the frequencies for the cases. The amplification and frequency were dimensionless by the depth of the cavity.

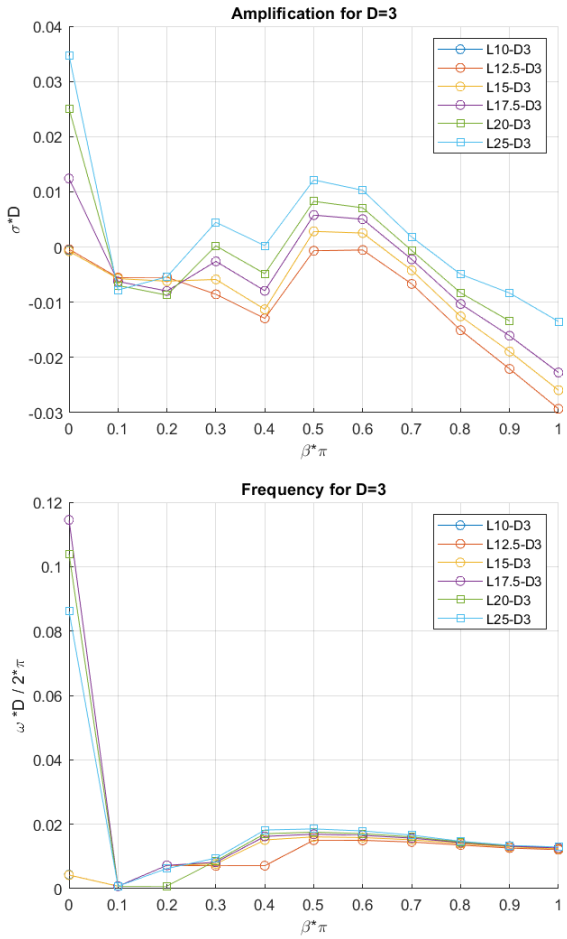


Figure 73 – Analysis of the most unstable modes obtained by LST, for the cases with depth $D = 3$. The left figure shows the amplification, while the right figure shows the frequencies.

Two typical behaviors can be noted, the first, for amplification, where, as the length increases, the Rossiter modes become increasingly unstable, as do the centrifugal modes. The second behavior is with respect to the frequencies of each mode. As the length increases, centrifugal mode 1 also becomes unstable, however, mode 2 remains more unstable for the values tested.

DISTRIBUTION A: Distribution approved for public release. Distribution unlimited

4.7.2 Large D

As in the case of fulfilled cavities, in Figure 74, we have two images. The right-hand side image contains the amplification of the unsteady modes for each of the cases, while the left-hand side presents the frequencies for the cases. The amplification and frequency were dimensionless by the depth of the cavity again, in this case, this dimensionless is even more important since we are working with different cavity depths.

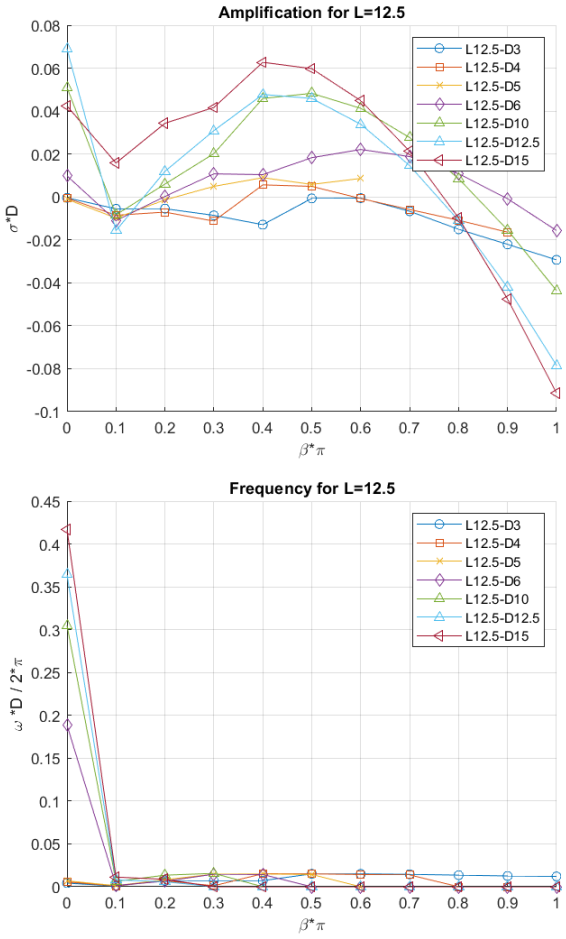


Figure 74 – Analysis of the most unstable modes obtained by LST, for the cases with length $L = 12.5$. The left figure shows the amplifications, while the right figure shows the frequencies.

The amplification for these cases has similar behavior to that found previously, that is, as the depth increases, the Rossiter modes tend to destabilize, but unlike the previous case, the most unstable Rossiter mode remains mode 1. In addition, deeper cavities, exhibit greater three-dimensional instability. However, the most interesting effect is linked to the frequencies. As the cavity gets deeper, the amount of unstable centrifugal 1 modes increases, that is, the oscillating centrifugal modes tend to be contained in regions with smaller β. Another effect that can be observed in frequency, is that for deeper cavities, we have higher frequencies for the Rossiter modes.

DISTRIBUTION A: Distribution approved for public release. Distribution unlimited

4.8 Discussion

The results from the 2D linear stability analysis revealed the presence of the Rossiter mode in the parametric space close to the bypass transition threshold in the diagram from Crouch, Kosorygin and Sutanto (2020). These cases also presented several 3D centrifugal modes within a range of spanwise wavenumbers as shown in Figure 45 and Figure 46 (see also Table 5), including the presence of stationary and traveling centrifugal modes. Furthermore, we presented the shape of the eigenfunctions from the leading unstable modes, as shown in Figure 48. The results indicated that the centrifugal instability neutral region was lesser than the neutrality for the Rossiter mode. The centrifugal instability neutral condition of the lid-driven cavity from Albensoeder, Kuhlmann and Rath (2001) was adapted to the current problem, following the method from Brés and Colonius (2008), and it was verified that the Reynolds number covered was unstable to centrifugal modes indeed.

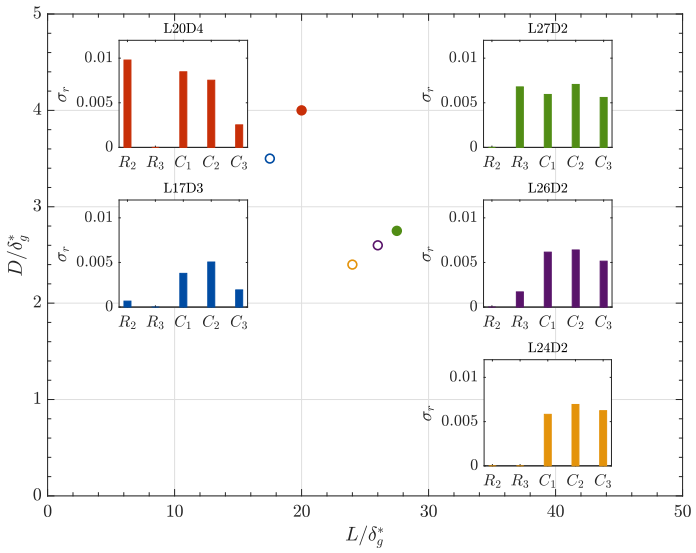
For both aspect ratios, we have found a Rossiter mode with a low amplification rate in the flow condition that anticipates the bypass transition whereas, a strong amplification rate occurred in the run corresponding to the bypass transition. Although, this correlation was stronger for $L/D = 5$. Figure 41 and the Table 4 supports this analysis. We also found that the dominant Rossiter mode changed from the aspect ratio of 5 to 10, from the Rossiter second mode (R_2) to the third mode (R_3). The appearance of an extra vortex in the base flow could be decisive for this. However, the circular temporal frequency of the different Rossiter modes remained close to range around 0.25 rad/s. Such frequency is about 2× the frequency of branch II of the T-S unstable frequency range for the Reynolds number around $Re_{\delta^*} = 1400$. Therefore, in these flow conditions, it is most likely that the Rossiter mode has a minor impact on the T-S wave. However, the results revealed centrifugal modes with a temporal frequency close to the T-S unstable range of frequencies for the local Reynolds number. The centrifugal instability could interact with the T-S wave, altering its growth (ΔN) in cases where the gap caused the transition to move upstream.

Figure 75 summarizes the results. We only carried out one 3D stability run for L24D2, *a posteriori*, employing the dominant spanwise wavelength revealed from the other runs with the same aspect ratio to verify the occurrence of centrifugal instability, amplification rate, and what mode occurred. One can see a stronger correlation concerning the Rossiter instability rather than the centrifugal. The numerical results support the idea that the centrifugal mode occurrence allows the flow to become 3D, and the Rossiter mode triggers the transition. Other works from the literature reported the non-linear interaction between the Rossiter and Centrifugal modes, for instance, Sun *et al.* (2017) (§4.3), Mathias and Medeiros (2020) (Fig. 5) and Mathias (2021) (Fig. 5.20).

After the linear stability analysis, a 3D DNS was carried out, in four different

DISTRIBUTION A: Distribution approved for public release. Distribution unlimited

Figure 75 – Correlation of the impact on the boundary layer transition as a function of the gap geometry, according to Crouch, Kosorygin and Sutanto (2020), and the modes from the linear stability analysis (bar plot). Open markers indicate transition by T-S waves, whereas filled markers, bypass transition.



Source: Author (2021).

scenarios, to better investigate the impact of the Rossiter and centrifugal modes on the boundary layer transition induced by the gap. The condition where a stable Rossiter together with unstable centrifugal modes did not produced turbulent flow. The two intermediate cases presented turbulent spots. From these two cases, the one with a greater centrifugal amplification indicated transition. Finally, the fourth case had the greatest value of Rossiter amplification rate and also presented transition. These results confirm the linear stability analysis, where the presence of unstable Rossiter and centrifugal modes after reached a threshold of amplification rate, promote a condition for transition.

DISTRIBUTION A: Distribution approved for public release. Distribution unlimited

Table 6 – Summary of linear stability analysis eigenvalues and transition mechanism according to experimental results from Crouch2020.

	$L/D = 5$					$L/D = 10$				
	L17D3					L26D2				
	Mode	λ/D	β	$\sigma_r(10^{-3})$	$2\pi St_{\delta_g^*}$	Mode	λ/D	β	$\sigma_r(10^{-3})$	$2\pi St_{\delta_g^*}$
T-S*	R_2	∞	0	0.7	0.2549	R_2	∞	0	-4.6	0.1938
	R_3	∞	0	-	-	R_3	∞	0	1.7	0.2603
	C_1	0.50	π	3.7	0	C_1	1.50	$16\pi/33$	6.1	0
	C_2	1.00	$\pi/2$	5.0	0.0245	C_2	1.50	$16\pi/33$	6.4	0.0358
	C_3	2.00	$\pi/4$	1.9	0.0142	C_3	2.00	$4\pi/11$	5.1	0.0229
	L20D4					L27D2				
	Mode	λ/D	β	$\sigma_r(10^{-3})$	$2\pi St_{\delta_g^*}$	Mode	λ/D	β	$\sigma_r(10^{-3})$	$2\pi St_{\delta_g^*}$
Bypass*	R_2	∞	0	9.8	0.2407	R_2	∞	0	-1.7	0.1878
	R_3	∞	0	-9.7	0.2649	R_3	∞	0	6.8	0.2539
	C_1	0.50	π	8.4	0	C_1	1.50	$16\pi/33$	5.9	0
	C_2	0.50	π	7.5	0.0241	C_2	1.00	$8\pi/11$	7.0	0.0321
	C_3	2.00	$\pi/4$	2.5	0.0135	C_3	2.00	$4\pi/11$	5.6	0.0223

Source: Elaborated by the author.

Note: * The form of transition ("T-S" or "Bypass") indicated in first column refers to results from Crouch, Kosorygin and Sutanto (2020).

DISTRIBUTION A: Distribution approved for public release. Distribution unlimited

5 CONCLUSION

The current work addresses the numerical investigation via direct numerical simulation and linear stability of the Blasius boundary layer with a gap, nothing else than a small cavity with its references length of the order of magnitude of the boundary layer thickness.

The work from the literature, Crouch, Kosorygin and Sutanto (2020), supported the choice for the flow conditions employed in the simulations. The parametric region aimed at gaps with the aspect ratio (L/D) of 5 and 10, as exhibited in Figure 28 and in Table 1. In a particular locus of the diagram proposed by Crouch, Kosorygin and Sutanto (2020), we can see a threshold for two different impacts on the transition. On the one hand, we have the boundary layer transition dominated by T-S waves, with the gap anticipating the transition location. On the other hand, occurs a leap in the transition location to a region practically over the small cavity. Also, the frequencies associated with transition differ from the T-S usual frequencies in the latter. Such behavior characterizes a bypass transition mechanism.

Based on this, we sought to perform a series of two-dimensional direct numerical simulations as a precursor stage of the linear stability analysis. Therefore, the flows from the 2D DNS that revealed the presence of self-sustained oscillations indicated flow instability. The run L20D4 presented a strong oscillatory motion with the temporal frequency close to the measured by Crouch, Kosorygin and Sutanto (2020) in the correspondent flow conditions, within a 4% of relative error. Such unsteady motion visually resembled the Rossiter mode reported in the literature. Additionally, according to the frequency prediction expression Equation 4.1 from Block (1976), it was caused by the Rossiter second mode.

In case of an unstable flow, we prompted the selective frequency damping according to Åkervik *et al.* (2006) to reach the steady solution of the Navier-Stokes Equation. The characterization of the base flows exhibited the presence of vortices inside the gap, which were crucial to instability, as exhibited in Figure 37. For both aspect ratios, a primary vortex occurred in the downstream portion of the cavity whereas, a secondary elongated vortex at the upstream region. The main difference from the aspect ratio of 5 to 10 was an extra vortex between the primary and secondary vortex. Other features were surveyed and compared to the literature, for instance, the cavity shear layer spreading rate.

We performed the linear stability analysis of the base flow. The linear stability analysis method was an Arnoldi-based time-stepping algorithm, which uses the flow solver to approximate the eigenvalues and eigenfunctions of the flow's Jacobian matrix. We performed the instability study of the 2D base flow and the 3D analysis, assuming

DISTRIBUTION A: Distribution approved for public release. Distribution unlimited

periodicity in the spanwise direction. For the latter, we carried out a parametric sweep of several spanwise wavenumbers to build the range of unstable β.

Finally, a 3D DNS was performed to promote a deep investigation of the Rossiter and centrifugal modes on the process of the boundary layer transition. The non-linear 3D DNS confirmed that these modes contribute for the bypass transition.

DISTRIBUTION A: Distribution approved for public release. Distribution unlimited

REFERENCES

ÅKERVIK, E. *et al.* Steady solutions of the navier-stokes equations by selective frequency damping. **Physics of Fluids**, AIP Publishing, v. 18, n. 6, p. 068102, 2006.

ALBENSOEDER, S.; KUHLMANN, H. C.; RATH, H. J. Three-dimensional centrifugal-flow instabilities in the lid-driven-cavity problem. **Physics of Fluids**, v. 13, n. 1, p. 121–135, 2001. ISSN 10706631.

ARNOLDI, W. E. The principle of minimized iterations in the solution of the matrix eigenvalue problem. **Quarterly of Applied Mathematics**, v. 9, p. 17–29, 1951.

BAYLY, B. J. ThreeâĂŘdimensional centrifugalâĂŘtype instabilities in inviscid twoâĂŘdimensional flows. **Physics of Fluids**, v. 31, n. 1, p. 56–64, 1988. ISSN 0031-9171.

BEGUET, S. *et al.* Modeling of transverse gaps effects on boundary-layer transition. **Journal of Aircraft**, v. 54, n. 2, p. 794–801, 2017. ISSN 00218669.

BENDAT, J. S.; PIERSOL, A. G. **Random data: analysis and measurement procedures**. 4. ed. [*S.l.: s.n.*]: John Wiley & Sons, 2010. ISBN 0470248777.

BENNEY, D. J.; LIN, C. C. On the secondary motion induced by oscillations in a shear flow. **Physics of Fluids**, v. 3, n. 4, p. 656–657, 1960. ISSN 10706631.

BERGAMO, L. F. **Instabilidade hidrodinâmica linear do escoamento compressível em uma cavidade**. 2014. Dissertação (Mestrado) — Escola de Engenharia de SÃčo Carlos, 2014. Available at: http://www.teses.usp.br/teses/disponiveis/18/18148/tde-28052014-164324/.

BIRINGEN, S.; CHOW, C.-Y. **An Introduction to Computational Fluid Mechanics by Example**. [*S.l.: s.n.*]: John Wiley & Sons, Inc., 2011. ISBN 9780470549162.

BLASIUS, H. Grenrschichten in flussgkeiten mit kleiner reibung. **Zeitschrift fÃijr Angewandte Mathematik und Physik**, v. 56, p. 1–37, 1908.

BLASIUS, H. The boundary layers in fluids with little friction. **Technical Memorandum 1256, National Advisory Committee for Aeronautics**, 1950.

BLOCK, P. J. W. **Noise response of cavities of varying dimensions at subsonic speeds**. [*S.l.*], 1976. 0–35 p. Available at: https://ntrs.nasa.gov/citations/19770007874.

BRÉS, G. A.; COLONIUS, T. Three-dimensional instabilities in compressible flow over open cavities. **Journal of Fluid Mechanics**, v. 599, p. 309–339, 2008. ISSN 00221120.

CATTAFESTA, L. N.; GARG, S. K.; JONES, G. S. M. S. Experiments on compressible flow-induced cavity oscillations. *In*: **29th AIAA Fluid Dynamics Conference**. [*S.l.: s.n.*], 1998.

COLONIUS, T.; BASU, A. J.; ROWLEY, C. W. Numerical investigation of the flow past a cavity. *In*: **5th AIAA/CEAS Aeroacoustics Conference and Exhibit**. [*S.l.: s.n.*], 1999.

DISTRIBUTION A: Distribution approved for public release. Distribution unlimited

CRAIK, A. D. Non-linear resonant instability in boundary layers. **Journal of Fluid Mechanics**, v. 50, n. 2, p. 393–413, 1971. ISSN 14697645.

CROUCH, J. D.; KOSORYGIN, V. S. Surface step effects on boundary-layer transition dominated by tollmien–schlichting instability. **AIAA Journal**, American Institute of Aeronautics and Astronautics (AIAA), v. 58, n. 7, p. 2943–2950, jul 2020.

CROUCH, J. D.; KOSORYGIN, V. S.; SUTANTO, M. I. Modeling Gap Effects on Transition Dominated by Tollmien-Schlichting Instability. **AIAA AVIATION Forum June 15-19**, 2020. Available at: http://dx.doi.org/10.2514/6.2020-3075.

De Vicente, J. *et al.* Three-dimensional instabilities over a rectangular open cavity: From linear stability analysis to experimentation. **Journal of Fluid Mechanics**, v. 748, p. 189–220, 2014. ISSN 14697645.

DRELA, M.; GILES, M. B. Viscous-inviscid analysis of transonic and low reynolds number airfoils. **AIAA Journal**, v. 25, n. 10, p. 1347–1355, 1987.

EAST, L. F. Aerodynamically induced resonance in rectangular cavities. **Journal of Sound and Vibration**, v. 3, n. 3, p. 277–287, 1966. ISSN 10958568.

FAIL, R.; OWEN, T.; EYRE, R. C. W. **Low speed tunnel tests on the flow in bomb bays and its effect on drag and vibration**. [*S.l.*], 1954.

FAURE, T. M. *et al.* Visualizations of the flow inside an open cavity at medium range Reynolds numbers. **Experiments in Fluids**, v. 42, n. 2, p. 169–184, 2007. ISSN 07234864.

FLIGHTPATH. **Flightpath 2050 - Europes Vision for Aviation Maintaining Global Leadership & Serving Societys Needs**. [*S.l.*], 2011. ISBN 978-92-79-19724-6. Available at: https://ec.europa.eu/transport/sites/transport/files/modes/air/doc/flightpath2050.pdf.

FORTE, M. *et al.* Experimental and Numerical Study of the Effect of Gaps on Laminar Turbulent Transition of Incompressible Boundary Layers. **Procedia IUTAM**, Elsevier B.V., v. 14, n. 0, p. 448–458, 2015. ISSN 22109838. Available at: http://dx.doi.org/10.1016/j.piutam.2015.03.073.

GAITONDE, D.; SHANG, J. S. High-order finite-volume schemes in wave propagation phenomena. **27th Plasma Dynamics and Lasers Conference**, n. June, 1996.

GAITONDE, D. V.; VISBAL, M. R. **High-Order Schemes for Navier-Stokes Equations: Algorithm and Implementation Into FDL3DI**. [*S.l.*], 1998. Available at: https://apps.dtic.mil/sti/citations/ADA364301.

GASTER, M. A note on the relation between temporally-increasing and spatially-increasing disturbances in hydrodynamic stability. **Journal of Fluid Mechanics**, v. 14, n. 2, p. 222–224, 1962.

GASTER, M. The development of three-dimensional wave packets in a boundary layer. **Journal of Fluid Mechanics**, v. 32, n. 1, p. 173–184, 1968. ISSN 14697645.

DISTRIBUTION A: Distribution approved for public release. Distribution unlimited

GASTER, M. An experimental investigation of the formation and development of a wave packet in a laminar boundary layer. **Proceedings of the Royal Society of London. A. Mathematical and Physical Sciences**, v. 347, n. 1649, p. 253–269, 1975. ISSN 0080-4630.

GASTER, M. The nonlinear phase of wave growth leading to chaos and breakdown to turbulence in a boundary layer as an example of an open system. **Proceedings of the Royal Society of London. Series A: Mathematical and Physical Sciences**, v. 430, n. 1878, p. 3–24, 1990. ISSN 0962-8444.

GHARIB, M.; ROSHKO, A. The effect of flow oscillations on cavity drag. **Journal of Fluid Mechanics**, v. 177, n. 11, p. 501–530, 1987. ISSN 14697645.

HERBERT, T. Three-dimensional phenomena in the transitional flat-plate boundary layer. 1984.

INGEN, J. L. van. A suggested semi-empirical method for calculation of the boundary layer transition region. **Technische Hogeschool Vliegtuigbouwkunde - Report V.T.H.-74**, 1956.

JUNIPER, M. P.; HANIFI, A.; THEOFILIS, V. Modal stability theory. **Applied Mechanics Reviews**, v. 66, n. 2, 2014. ISSN 00036900.

KACHANOV, Y. S. Physical mechanisms of laminar-boundary-layer transition. **Annual Review of Fluid Mechanics**, v. 26, p. 411–482, 1994.

KACHANOV, Y. S.; KOZLOV, V. V.; LEVCHENKO, V. Y. Nonlinear development of a wave in a boundary layer. **Fluid Dynamics**, v. 12, n. 3, p. 383–390, 1977. ISSN 15738507.

KACHANOV, Y. S.; LEVCHENKO, V. Y. The resonant interaction of disturbances at laminar-turbulent transition in a boundary layer. **Journal of Fluid Mechanics**, v. 138, n. 1984, p. 209–247, 1984. ISSN 14697645.

KLEBANOFF, P. S.; SCHUBAUER, G. **Contributions on the mechanic of boundary-layer transition**. Washington, 1955. 12 p. Available at: https://ntrs.nasa.gov/archive/nasa/casi.ntrs.nasa.gov/19930092285.pdf.

KLEBANOFF, P. S.; TIDSTROM, K. D. Contributions on the mechanics of boundary-layer transition. **NACA Technical Report 1289**, 1956. Available at: https://ntrs.nasa.gov/archive/nasa/casi.ntrs.nasa.gov/19930092285.pdf.

KLEBANOFF, P. S.; TIDSTROM, K. D. **EVOLUTION OF AMPLIFIED WAVES LEADING TO A TRANSITION IN A BOUNDARY LAYER WITH ZERO PRESSURE GRADIENT**. [*S.l.*], 1959. 74 p. Available at: https://archive.org/details/nasa_techdoc_19890068568/page/n3/mode/2up.

KLEBANOFF, P. S.; TIDSTROM, K. D.; SARGENT, L. M. The three-dimensional nature of boundary-layer instability. **Journal of Fluid Mechanics**, v. 12, n. 1, p. 1–34, 1962. ISSN 14697645.

KNAPP, C. F.; ROACHE, P. J. A combined visual and hot-wire anemometer investigation of boundary-layer transition. **AIAA Journal**, v. 6, n. 1, p. 29–36, 1968. ISSN 00011452.

DISTRIBUTION A: Distribution approved for public release. Distribution unlimited

KRISHNAMURTY, K. **Acoustic radiation from two-dimensional rectangular cutouts in aerodynamic surfaces**. Washington, US, 1955. Available at: https://digital.library.unt.edu/ark:/67531/metadc57843/.

KRISHNAN, K. *et al.* Characterization of insect residue on an aerodynamic leading edge. **8th AIAA Atmospheric and Space Environments Conference**, n. June, 2016.

LELE, S. K. Compact finite and difference schemes and with spectral-like and resolution. **Journal of Computational physics**, v. 103, p. 16–42, 1992.

LI, N.; LAIZET, S. **2DECOMP&FFT - A Highly Scalable 2D Decomposition Library and FFT Interface**. [*S.l.*], 2010.

LIU, Q.; GOMEZ, F.; THEOFILIS, V. Linear instability analysis of low-Re incompressible flow over a long rectangular finite-span open cavity. **Journal of Fluid Mechanics**, v. 799, n. 2016, p. R2, 2016. ISSN 14697645.

MACK, L. M. Boundary Layer Linear Stability Theory. **Agard**, v. 709, n. 3, p. 1–150, 1984.

MAREC, J.-P. Drag reduction: a major task for research. *In*: **Aerodynamic Drag reduction technologies: proceedings of the CEAS, DragNet European Drag Reduction Conference 19 - 21 June 2000, Potsdam, Germany**. [*S.l.: s.n.*], 2001. p. 17 – 28. ISSN 0179-9614.

MARTINEZ, A. **Towards natural transition in compressible boundary layers**. 2016. Tese (Doutorado) — Escola de Engenharia de SÃčo Carlos, 2016.

MATHIAS, M. S. **Análise de instabilidade de escoamentos compressíveis sobre uma cavidade aberta por um método numérico sem formação de Jacobiano**. 2017. Dissertação (Mestrado) — Escola de Engenharia de São Carlos, Universidade de São Paulo, 2017.

MATHIAS, M. S. **Computational study of the hydrodynamic stability of gaps and cavities in a subsonic compressible boundary layer**. 2021. Tese (Doutorado) — São Carlos School of Engineering, University of São Paulo, 2021.

MATHIAS, M. S.; MEDEIROS, M. A. F. Global instability analysis of a boundary layer flow over a small cavity. **AIAA Aviation 2019 Forum 17-21 June 2019, Dallas, Texas**, 2019.

MATHIAS, M. S.; MEDEIROS, M. A. F. de. The influence of the boundary layer thickness on the stability of the rossiter modes of a compressible rectangular cavity. **2018 Fluid Dynamics Conference**, 2018.

MATHIAS, M. S.; MEDEIROS, M. A. F. de. Interaction between rossiter and görtler modes in the compressible flow in an open cavity. **Aiaa Aviation 2020 Forum**, v. 1 PartF, p. 1–6, 2020.

MEDEIROS, M. A. F. The nonlinear evolution of a wavetrain emanating from a point source in a boundary layer. **Journal of Fluid Mechanics**, v. 508, p. 287–317, 2004.

MEDEIROS, M. A. F. **Effect of a gap on natural transition to turbulence in a boundary layer**. [*S.l.*], 2017.

DISTRIBUTION A: Distribution approved for public release. Distribution unlimited

MEDEIROS, M. A. F.; GASTER, M. The influence of phase on the nonlinear and evolution of wavepackets in boundary layers. **Journal of Fluid Mechanics**, v. 397, p. 259–283, 1999.

MEDEIROS, M. A. F.; GASTER, M. The production of subharmonic waves in the nonlinear evolution of wavepackets in boundary layers. **Journal of Fluid Mechanics**, v. 399, p. 301–318, 1999.

MESEGUER-GARRIDO, F. *et al.* On linear instability mechanisms in incompressible open cavity flow. **Journal of Fluid Mechanics**, v. 752, p. 219–236, 2014. ISSN 14697645.

MISHRIKY, F.; WALSH, P. C. Boundary-layer transition prediction over cavities and its morphing skin design application. **AIAA Journal**, v. 56, n. 12, p. 4685–4696, 2018. ISSN 00011452.

NON, E.; PIERRE, R.; GERVAIS, J. J. Linear stability of the three-dimensional lid-driven cavity. **Physics of Fluids**, v. 18, n. 8, 2006. ISSN 10706631.

NORTON, D. A. **Investigation of B47 bomb bay buffet**. [*S.l.*], 1952.

ORR, W. M. The stability or instability of the steady motions of a perfect liquid and of a viscous liquid. part ii. *In*: **Proceedings of the Royal Irish Academy. Section A: Mathematical and PhysicalSciences**. [*S.l.: s.n.*], 1907. v. 27, p. 69–138. Available at: http://www.jstor.org/stable/20490591.

PAULA, I. B. de. **Influência de uma rugosidade tridimensional isolada na transição de uma camada limite sem gradiente de pressão**. 2007. Tese (Doutorado) — Escola de Engenharia de São Carlos, Universidade de São Paulo, 2007.

PERRAUD, J.; ARNAL, D.; KUEHN, W. Laminar-turbulent transition prediction in the presence of surface imperfections. **International Journal of Engineering Systems Modelling and Simulation**, Inderscience Publishers, v. 6, n. 3-4, p. 162–170, 2014. ISSN 17559766.

PERRAUD, J. *et al.* Laminar-Turbulent Transition on Aerodynamic Surfaces with Imperfections. **RTO-AVT-111 Symposium**, n. October 2004, p. 4–7, 2004.

PLUMBLEE, H. E.; GIBSON, J. S.; LASSITER, L. W. Theoretical and Experimental Investigation of The Acoustic Response of Cavities In An Aerodynamic Flow. **Technical Report**, n. USAF Report WADD-TR-61-75, p. 1–167, 1962.

PRANDTL, L. Über Flüssigkeitsbewegung bei sehr kleiner Reibung. **Verhandlungen des III. Internationalen Mathematiker-Kongresses**, p. 484–491, 1905.

PRANDTL, L. Motion of fluids with very little viscosity. **Technical Memorandum 452, National Advisory Committee for Aeronautics**, 1928.

RAYLEIGH, L. On the stability, or instability, of certain fluid motions. *In*: **Proceedings of the London Mathematical Society**. [*S.l.: s.n.*], 1879. (1, v. 11), p. 57–72.

RAYLEIGH, L. On the stability, or instability, of certain fluid motions ii. *In*: **Proceedings of the London Mathematical Society**. [*S.l.: s.n.*], 1887. (1, v. 19), p. 67–75.

DISTRIBUTION A: Distribution approved for public release. Distribution unlimited

RAYLEIGH, L. On the stability, or instability, of certain fluid motions iii. *In*: **Proceedings of the London Mathematical Society**. [*S.l.: s.n.*], 1895. (1, v. 27), p. 5–12.

RENEAUX, J. Overview on drag reduction technologies for civil transport aircraft. **European Congress on Computational Methods in Applied Sciences and Engineering ECCOMAS 2004**, 2004.

REYNOLDS, O. An experimental investigation of the circumstances which determine whether the motion of water shall be direct or sinuous, and of the law of resistance in parallel channels. **Philosophical Transactions of the Royal Society of London**, v. 35, p. 84–99, 1883. ISSN 0261-0523.

ROSHKO, A. **Some measurements of flow in a rectangular cutout**. [*S.l.*], 1955. Available at: https://authors.library.caltech.edu/51772/1/ROSnacatn3488.pdf.

ROSSITER, J. E. Wind-tunnel experiments on the flow over rectangular cavities at subsonic and transonic speeds. **Reports and Memoranda No. 3438 - Aeronautical Research Council - Ministry of Aviation**, 1964.

ROWLEY, C. W. **Modeling, Simulation, and Control of Cavity Flow Oscillations**. 2002. 144 p. Tese (Ph.D.) — California Institute of Technology, 2002.

ROWLEY, C. W.; COLONIUS, T.; BASU, A. J. POD based models of self-sustained oscillations in the flow past an open cavity. *In*: **6th Aeroacoustics Conference and Exhibit**. [*S.l.: s.n.*], 2000.

SARIC, W. S. Low-speed experiments: Requirements for stability measurements. *In*: **Instability and Transition**. New York: Springer-Verlag, 1990, (ICASE/NASA LaRC, v. 1). p. 162–174. ISBN 978-1-4612-8008-8.

SARIC, W. S.; REED, H. L.; KERSCHEN, E. J. Boundary-layer receptivity to freestream disturbances. **Annual Review of Fluid Mechanics**, v. 34, n. 1, p. 291–319, 2002. Available at: https://doi.org/10.1146/annurev.fluid.34.082701.161921.

SAROHIA, V. Experimental investigation of oscillations in flows over shallow cavities. **AIAA Journal**, v. 15, n. 7, p. 984–991, 1977. ISSN 00011452.

SCHLICHTING, H. Laminare strahlausbreitung. **ZAMM - Journal of Applied Mathematics and Mechanics / Zeitschrift für Angewandte Mathematik und Mechanik**, v. 13, n. 4, p. 260–263, 1933.

SCHMID, P. J. Nonmodal stability theory. **Annual Review of Fluid Mechanics**, v. 39, p. 129–162, 2007. ISSN 00664189.

SCHNEIDER, W. The importance of aerodynamics in the development of commercially successful transport aircraft. *In*: **Aerodynamic Drag reduction technologies: proceedings of the CEAS, DragNet European Drag Reduction Conference 19 - 21 June 2000, Potsdam, Germany**. [*S.l.: s.n.*], 2001. p. 9–16.

SCHUBAUER, G. B.; SKRAMSTAD, H. K. Laminar boundary-layer oscillations and transition on a flat plate. **National Advisory Committee for Aeronautics - Report No. 909**, 1948.

DISTRIBUTION A: Distribution approved for public release. Distribution unlimited

SMITH, A. M. O.; GAMBERONI, N. **Transition, Pressure Gradient, and Stability Theory**. [*S.l.*], 1956. 59 p. Available at: https://engineering.purdue.edu/~aae519/BAM6QT-Mach-6-tunnel/otherpapers/smith-amo-eN-douglas-es26388-1956.pdf.

SOMMERFELD, A. Ein beitrag zur hydrodynamischen der turbulenten fluessigkeits-bewegüngen. *In*: **Proceedings of the 4th International Mathematical Congress**. Rome: [*S.l.: s.n.*], 1908. v. 3, p. 116–124.

STOKES, G. G. On some cases of fluid motion. **Transactions of the Cambridge Philosophical Society**, v. 3, p. 105, 1843.

SUN, Y. *et al.* Biglobal instabilities of compressible open-cavity flows. **Journal of Fluid Mechanics**, v. 826, p. 270–301, 2017. ISSN 14697645.

TAM, C. K.; BLOCK, P. J. On the tones and pressure oscillations induced by flow over rectangular cavities. **Journal of Fluid Mechanics**, v. 89, n. 2, p. 373–399, nov 1978. ISSN 14697645. Available at: https://www.cambridge.org/core/product/identifier/S0022112078002657/type/journal{_}arti.

TEZUKA, A.; SUZUKI, K. Three-dimensional global linear stability analysis of flow around a spheroid. **AIAA Journal**, v. 44, n. 8, p. 1697–1708, 2006. ISSN 00011452.

THEOFILIS, V. Globally unstable basic flows in open cavities. *In*: **AIAA/CEAS Aeroacoustics Conference**. Lahaina: [*S.l.: s.n.*], 2000. p. 12.

THEOFILIS, V. Global linear instability. **Annual Review of Fluid Mechanics**, v. 43, n. 1, p. 319–352, 2011. Available at: https://doi.org/10.1146/annurev-fluid-122109-160705.

THEOFILIS, V.; COLONIUS, T. Three-dimensional instabilities of compressible flow over open cavities: Direct solution of the BiGlobal eivenvalue problem. **34th AIAA Fluid Dynamics Conference and Exhibit**, n. June, 2004.

TOLLMIEN, W. The production of turbulence. **National Advisory Committee for Aeronautics - Technical Memorandum no. 609**, 1931.

TOLLMIEN, W.; SCHLICHTING, H.; GöRTLER, H. Über Flüssigkeitsbewegung bei sehr kleiner Reibung. In: Riegels F.W. (eds) Ludwig Prandtl Gesammelte Abhandlungen. *In*: _____. Springer, Berlin, Heidelberg, 1961. cap. 4, p. 575–584. ISBN 978-3-662-11837-5. Available at: https://link.springer.com/chapter/10.1007/978-3-662-11836-8_43.

WHITE, F. M. **Viscous fluid flow**. 3. ed. [*S.l.: s.n.*]: McGraw-Hill Companies, 2006. ISBN 978-0072402315.

YAMOUNI, S.; SIPP, D.; JACQUIN, L. Interaction between feedback aeroacoustic and acoustic resonance mechanisms in a cavity flow: A global stability analysis. **Journal of Fluid Mechanics**, v. 717, p. 134–165, 2013. ISSN 00221120.

ZAHN, J.; RIST, U. Impact of deep gaps on laminar - Turbulent transition in compressible boundary-layer flow. **AIAA Journal**, v. 54, n. 1, p. 66–76, 2016. ISSN 00011452.

DISTRIBUTION A: Distribution approved for public release. Distribution unlimited

Appendix 3

DISTRIBUTION A: Distribution approved for public release. Distribution unlimited

Effect of Bumps and Isolated Roughness on Evolution of Tollmien-Schlichting Waves

AFOSR Report #0000/00000

Carvalho, Ana E. B.

Himeno, Fernando H. T.

Medeiros, Marcello A. F. Medeiros

Sao Carlos, Sao Paulo - Brazil, 26 de março de 2022

DISTRIBUTION A: Distribution approved for public release. Distribution unlimited

Summary

1 Introduction **1**

2 DNS Code **7**
2.1 Governing equations . . . 7
2.2 Numerical methods . . . 8
2.2.1 Mesh and domain . . . 8
2.2.2 Boundary conditions . . . 8
2.2.3 Spatial derivatives . . . 9
2.2.4 Time integration . . . 14
2.2.5 Aliasing filter . . . 15
2.2.6 Buffer-zones . . . 16
2.2.7 Domain decomposition, parallelization . . . 16
2.3 Parametric space and excitation description . . . 17
2.3.1 Monochromatic . . . 18
2.3.2 Wavepacket . . . 18

3 Preliminary Tests **21**
3.1 Spatial derivative optimization test . . . 21
3.2 Mesh independence . . . 21
3.3 Comparison with literature . . . 26

4 Results **28**
4.1 Linear/non-linear maximum bump height . . . 28
4.2 Base flow distortion caused by bumps . . . 29
4.3 TS waves interacting with bumps . . . 34
4.3.1 The effect of the bump height . . . 34
4.3.2 The effect of Mach . . . 35
4.3.3 The effect of TS frequency . . . 37
4.3.4 Region of influence of bumps and base flow . . . 39
4.4 Taylor-Stokes approximation . . . 41

5 Conclusions **45**

Events and Publications **49**

References **50**

DISTRIBUTION A: Distribution approved for public release. Distribution unlimited

1 Introduction

The motivation for the flow transition study focused on aeronautical applications, arises from the interest of reducing friction drag which means delaying the laminar to turbulent transition as much as possible. Estimates show that about 50% of the total drag of a commercial aircraft is due to friction drag where 25% is caused by wings citeMarec2001. It impacts on the aircraft fuel consumption but also in the total amount of pollutants that are emitted into the atmosphere.

Although in a restricted way, the laminar technology was used in development of nacelles and empennages of the *Boeing 787* [1] and also to the *Honda Jet*, along the region of the aircraft's nose and wings [2]. Other examples of the possible application of this technology are in the aerospace industry in the design of reentry surfaces, in the design of blade profiles for turbines, wind blades, etc.

The development of the laminar technology is possible by a good representation of the boundary layer in several operating regime. This represents a great difficulty for the industry in which the most used methods can present errors in the drag estimates in the order of 10% whilst the desired precision would be around 2.5 to 5% [3, 4]. The reason for not enough precision is due to the complexity of the phenomena involved in the transition of open flows, considerably different from free shear layers and contained flows [5]. In open flows a large parametric range of conditions affects the transition, such as the free flow turbulence level, surface irregularities, etc. [6].

A simplified schematic of boundary layer transition routes is presented in figure 1.1 [7, 6, 8]. This scheme illustrates how small perturbations, in the form of acoustic waves or external turbulence, etc., that are already present in the free flow penetrate the boundary layer as stable and/or unstable fluctuations of the base flow in a process called receptivity [5]. At this stage, depending on the amplitude, frequency and phase of the initial fluctuations these waves can increase in magnitude up to lead to turbulence [9]. When the amplitudes of the initial fluctuations are considerably large, the transition follows the most abrupt route, **E**, rapidly evolving into turbulence following a nonlinear evolution.

For low amplitude fluctuations, **A**, the amplification rate is smooth and the evolution follows a linear regime and are well represented by the Linear Stability Theory (LST). The most simplified approach to this analysis considers local instability considering parallel mean flow and neglecting nonlinear terms, giving rise to a fourth-order partial

DISTRIBUTION A: Distribution approved for public release. Distribution unlimited

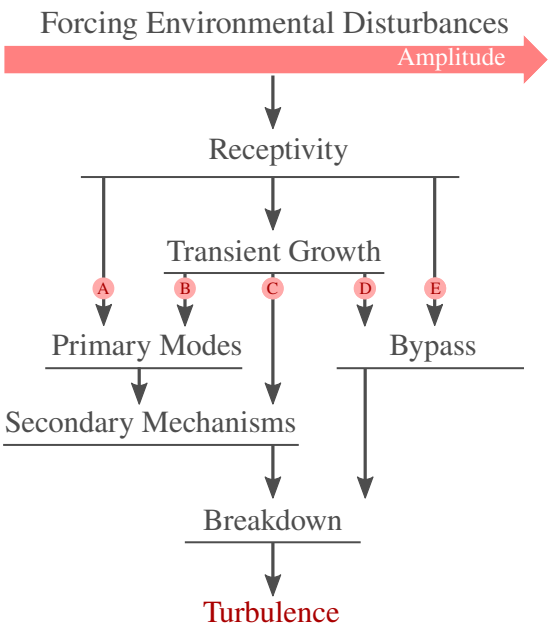


Figura 1.1: Boundary layer transition routes [7, 6, 8].

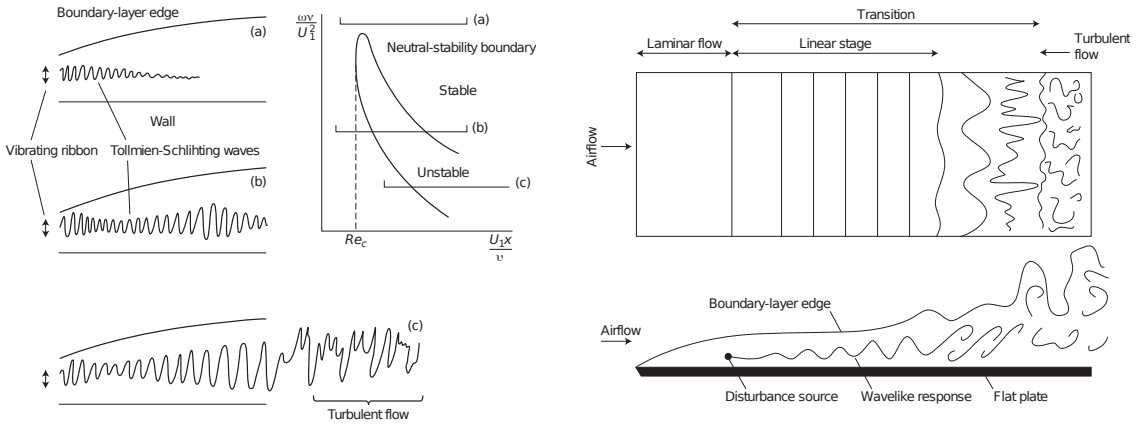
ordinary equation, known as the Orr-Sommerfeld Equation (OSE) [10, 11]. The solution of this eigenvalue problem was later presented through the efforts of Tollmien [12] and Schlichting [13], being therefore called Tollmien-Schlichting (TS) waves. This model was experimentally credited by the experiments of Schubauer and Skramstadt [14] using a low-turbulence wind tunnel.

The results of the OSE solution can be summarized through the instability diagram, figure 1.2.a, in which a neutral curve is identified relating the frequency of a monochromatic perturbation and the Reynolds number. Within the region delimited by the neutral curve, the TS waves are amplified and outside the waves rapidly decays.

The process in which this primary unstable wave leads to the boundary layer transition involves a threshold amplitude in which three-dimensional and non-linear phenomena arise generating secondary instabilities. From this stage, the flow fluctuations grow rapidly when compared to the linear evolution until finally leading to the [6] transition. Among the secondary mechanisms identified and well accepted so far are the fundamental, the subharmonic and the oblique resonance, also known as K, H and O-types, respectively. Figure 1.3 presents the evolution of the structures observed in these secondary mechanisms. These results were obtained by our group through simulations using a DNS code [16].

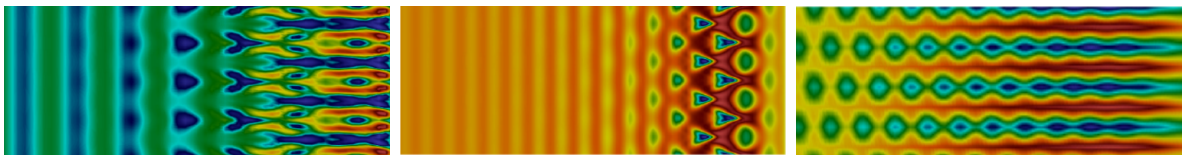
The fundamental mechanism was initially identified through the experiments of Kle-

DISTRIBUTION A: Distribution approved for public release. Distribution unlimited



(a) (b)

Figura 1.2: Schematic of the evolution of a TS wave along the boundary layer for different initial conditions and a representation of transition stages from laminar to turbulent [15].



(a) Tipo-K (b) Tipo-H (c) Tipo-O

Figura 1.3: Flow pattern observed in K-, H- and O-type secundary instabilities [16].

banoff et al. [17] in which spaced vibrating tapes were used to disturb the flow. This type of instability is associated with the formation of longitudinally aligned vortices [18]. Models were developed to explain the formation of these vortices [19, 20, 21]. Craik's resonant triad model [22], involving the interaction of a two-dimensional mode and a pair of oblique subharmonic modes, showed the possibility of subharmonic interactions although not fully explaining the fundamental mechanism.

Another sequence of experiments, performed by Kachanov et al. [23] investigated the formation of longitudinal vortices. In these experiments it was verified the existence of the subharmonic mechanism that, unlike the fundamental one, showed a staggered vortex pattern, as observed in experiments and visualizations of later flows [24, 25].

A model for the secondary mechanisms is then proposed by Herbert [26] considering spatial periodicity in the flow direction given by a finite amplitude TS. With this theory it is possible to show that the subharmonic resonance occurs in a band of unstable oblique waves that widens as the amplitude of the primary wave increases. From a threshold amplitude, the amplification of the oblique modes of the same frequency of the primary

DISTRIBUTION A: Distribution approved for public release. Distribution unlimited

wave occurs, explaining the first stages of Klebanoff's experiment [27].

The oblique transition mechanism was discovered numerically initially in the compressible regime at Mach 1.6 [28] and later in the incompressible regime [29]. In this mechanism, a threshold amplitude is not identified and the modes grow linearly transferring energy to oblique modes with twice the frequency while harmonics are generated in this way. Its linear and nonlinear effects are difficult to separate in addition to requiring less energy in the oblique modes to initiate when compared to the fundamental and subharmonic resonances [30]. Some authors suggest this instability explain the transition route for supersonic regime [31, 32].

Although the study of secondary instabilities represents a major evolution within the topic of transition, these studies consider the evolution of very controlled perturbations with limited frequencies and amplitudes but in a real scenario, ideal situations rarely occur. The term natural transition is used to refer to the real mechanism that occurs in nature. Under these conditions, the initial perturbations are random, that is, they are composed of fluctuations with different frequencies and amplitudes.

One technique that has been used to reproduce the natural transition is to excite the flow with perturbations that resemble those present in free flow turbulence, called white noise sequences. Shaikh and Gaster [33, 34] observed that white noise drives the flow to transition by generating turbulent spots in a similar way to that from uncontrolled experiments. The results obtained show that the first non-linear stages of white noise evolution involve the appearance of waves with a frequency lower than that of the TS waveband, similar to the results obtained with wavepackets. These and other works suggest that wave packets may represent a part of the natural transition process [35, 16].

Gaster and Grant [36] and Gaster [37] present an experimental study involving wavepackets. The disturbance is introduced into the boundary layer through a point acoustic source and is composed by a band of Fourier modes. As different amplification rates are present in the excitation, only a narrow range of frequencies is observed in the flow and waves combine to form a wavepacket. Theoretically, it was proposed that each mode would evolve independently and results obtained experimentally and theoretically reached good agreement. The packet scattering in both the flow direction and the span could be well verified by the theory. A result also found was the presence of nonlinear effects with amplitude much lower than those observed in two-dimensional plane waves [38].

Other experimental works around the investigation of wavepackets analyzed the evolution from the amplification up to the turbulent spots generation [39], followed by the

DISTRIBUTION A: Distribution approved for public release. Distribution unlimited

individual analysis of the paths to study nonlinear evolution [40]. It was also found the pressure gradient represents an important role in the evolution of a wavepacket [41]. Medeiros and Gaster [42, 43] present studies involving wavepackets with moderate amplitude and phase influence to study the effects of moderately nonlinear evolution. Subsequently, Medeiros [44] presents results involving modulation aspects of wavepackets.

The consideration of surface irregularities is of great importance in the study of the natural transition of boundary layers. On real surfaces, is inevitable the presence of joints, gaps, rivets, deformities caused by manufacturing and painting methods or even dirt accumulated in operation.

The influence of isolated roughness on the position of the transition point has been studied experimentally since the 40's [45, 46]. After that, Klebanoff and Tidstrom [17] show that two-dimensional roughness distorts the mean flow, affecting the flow stability. More recent computational works [47], study the effect of bumps with different formats, heights and lengths. Bumps can advance the transition process considerably depending on their shape. The far most critical is that where the bump has sharp corners [48, 49, 47].

For small or intermediate roughness (below 40% of the boundary layer displacement thickness), these irregularities affect the boundary layer characteristics and the behavior of the disturbances present in the flow by basically three paths. First, because they can represent a source of receptivity, that is, their dimensions can provide a means of converting large-scale perturbations into smaller-scale perturbations that may be selected by the boundary layer [50, 51, 52]. Second, because these irregularities affect the local characteristics of the boundary layer itself, which can make it more or less stable [48], including generating instabilities different from the TS wave. Third, they can directly affect the TS [53]. Within the context of the instability route, some authors suggest the roughness is related to the fundamental, K-type, instability [54, 55, 53].

Numerical modeling the geometry of bumps can be a very difficult task, especially when dealing with a very small one, as proposed in the present study. Common methodologies used for simulating these cases consider the immersed boundary technique but it is also possible to approximate the bump effect by non-zero boundary conditions.

In the immersed boundary methods, the surfaces are defined directly in the computational domain, providing a more faithful representation of the phenomena that occur in the bump region with some implementation cost. To get around this problem, Peskin [56] proposed a method where a force field actuates in the flow in such a way that it provides the immersed boundary conditions. Subsequently, a similar methodology is developed Goldstein et al. [57] and applied in the context of open flow. Other works

DISTRIBUTION A: Distribution approved for public release. Distribution unlimited

have used this procedure successfully [58, 48]. Although efficient, this method adds a high computational cost since at each time step the force field need to be calculated.

The approximation modeling is obtained from the velocity profile without roughness. With the profile derivatives and by Taylor expansion, it is possible to define a non-zero boundary condition on the wall that mimics the flow distortion caused by the immersed boundary. This method has been widely used in the study of receptivity [59, 58, 60, 61]. The great advantage of this method is the simple implementation, especially in an already consolidated code, in which the inclusion of immersed walls would require major changes. Limitations of this method, arises from the fact that its use is limited by the bump height since the expansion accuracy degrades with the bump height.

Most studies involving bumps focus on the receptivity that occurs in this irregularity [46, 52, 51, 62]. In the present work, however, we investigate the interaction between the bump with an wavepacket disturbance excited upstream to the bump or in other words, how an existing TS wave is affected by the bump.

The bump has sharp corner edges which means that it is the most critical scenario compared to other shape. The element is meshed (body-fitted) but results considering the approximation method is also presented. For the approximated one, we further improved the traditional method considering the Stokes layer effect. The agreement with the body-fitted bump is remarkable with lower mesh cost.

We show the influence of the bump height from 5% up to 40% the displacement thickness in flows where the Mach number varies from $M = 0.1$ up to $M = 0.9$. Furthermore, the wavepacket disturbance allows the analysis to be extended for a band of modes not only a monochromatic TS wave.

DISTRIBUTION A: Distribution approved for public release. Distribution unlimited

2 DNS Code

2.1 Governing equations

The present Direct Numerical Simulation (DNS) code solves the complete set of conservation equations (mass, momentum and energy) that describes the fluid motion in three-dimensional and compressible flows. These equations can be written, in non-conservative form and non-dimensional variables, as follows,

$$\frac{\partial \varrho}{\partial t} = -\varrho \frac{\partial u_i}{\partial x_i} - \frac{\partial \varrho}{\partial x_i} u_i, \qquad \text{(conserv. mass)} \tag{2.1}$$

$$\frac{\partial u_j}{\partial t} = -\frac{\partial u_j}{\partial x_i} u_i - \frac{1}{\varrho}\frac{\partial p}{\partial x_j} + \frac{1}{\varrho}\frac{\partial \tau_{ij}}{\partial x_i}, \qquad \text{(conserv. momentum)} \tag{2.2}$$

$$\frac{\partial e}{\partial t} = -\frac{\partial e}{\partial x_i} u_i - \frac{p}{\varrho}\frac{\partial u_i}{\partial x_i} + \frac{1}{\varrho}\tau_{ij}\frac{\partial u_i}{\partial x_i} - \frac{1}{\varrho}\frac{\partial q_i}{\partial x_i}, \qquad \text{(conserv. energy)} \tag{2.3}$$

where u_i denotes the velocity components along the three cartesian directions (x, y, z), ϱ, density, e, internal energy and p, pressure. The viscous tensor, τ, and the heat flux, q, are defined as,

$$\tau_{ij} = \frac{\mu}{Re}\left(\frac{\partial u_i}{\partial x_j} + \frac{\partial u_j}{\partial x_i} - \frac{2}{3}\delta_{ij}\frac{\partial u_k}{\partial x_k}\right), \qquad q_i = -\frac{\mu}{(\gamma - 1) Re\ Pr\ M_\infty^2}\frac{\partial T}{\partial x_i},$$

where Re, M and Pr denote the non-dimensional numbers: Reynolds, Mach and Prandtl, respectively, $\delta_{i,j}$ denotes the Kronecker delta function (0, if $i \neq j$; 1 if $i = j$), γ, the fluid heat capacity ratio and μ, the dynamic viscosity which is modeled following the Sutherland's Law,

$$\mu = \frac{1 + C}{T + C} T^{\frac{3}{2}},$$

where C is a constant parameter and T denotes temperature.

DISTRIBUTION A: Distribution approved for public release. Distribution unlimited

The unknown variables pressure, density and energy (or temperature) are related by assuming the ideal gas hypothesis which provides the equation of state as follows,

$$p = (\gamma - 1)\rho e = \frac{\rho T}{\gamma M_\infty^2}. \tag{2.4}$$

Then, the DNS code solves the set of equations composed by the five unknown variables: u, v, w, ϱ and e, each one dependent on position (x, y, z) and time, t.

Dimensional and non-dimensional values are related as follows,

$$\varrho = \frac{\varrho^*}{\varrho_\infty^*}, \quad p = \frac{p^*}{p_\infty^* {U_\infty^*}^2}, \quad x_i = \frac{x_i^*}{\delta_{1,R}^*}, \quad T = \frac{T^*}{T_\infty^*}, \quad u_i = \frac{u_i^*}{U_\infty^*}, \quad t = \frac{t^* U_\infty^*}{\delta_{1,R}^*}, \quad e = \frac{e^*}{{U_\infty^*}^2}, \tag{2.5}$$

where subscript '$_\infty$' and superscript '*' denote, respectively, free flow and dimensional values. The free flow velocity, U_∞^*, is considered as the velocity reference. The length reference, $\delta_{1,R}^*$, is the dimensional displacement thickness at a reference station. The input non-dimensional numbers are defined as,

$$Re = \frac{\varrho_\infty^* U_\infty^* \delta_{1,R}^*}{\mu_\infty^*}, \qquad Pr = \frac{\mu_\infty^* {c_p}^*}{k^*}, \qquad M_\infty = \frac{U_\infty^*}{c_\infty^*}, \tag{2.6}$$

where c_p^* is the fluid specific heat, k^* is fluid thermal conductivity and $c_\infty^* = \sqrt{\gamma p_\infty^* / \rho_\infty^*}$ the speed of sound. For all simulations presented here, $Pr = 0.71$, $\gamma = 1.4$, $T_\infty^* = 300\ [K]$, $C = 110\ [K]/T_\infty^*$.

2.2 Numerical methods

2.2.1 Mesh and domain

Mesh is composed by an orthogonal-cartesian grid and code allows the inclusion of different stretching along the domain. Figure 2.1 presents a scheme of the simulated domain containing a rectangular meshed element.

2.2.2 Boundary conditions

For all cases the boundary conditions are summarized as follows:

DISTRIBUTION A: Distribution approved for public release. Distribution unlimited

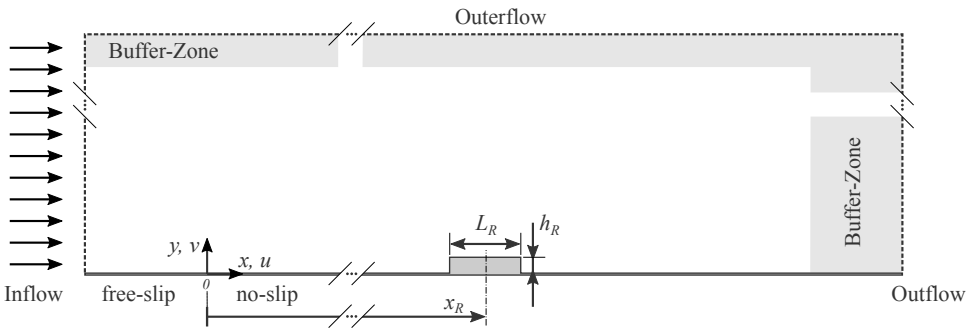


Figura 2.1: Scheme of the simulation domain of a generic plate with a bump element with sharp edges corner.

- Inflow: uniform flow, constant temperature and null gradient of pressure along the streamwise direction;
- Outflow: pressure is constant and second derivative is null for the other variables;
- Outerflow: second derivative is set to zero for all variables;
- Walls: no-slip and no-penetration conditions for velocity, the temperature is fixed and pressure gradient null in the normal direction;

There is also a region at the wall between the inflow and plate leading edge with free-slip condition necessary to accommodate the flow before the boundary layer.

Pressure and temperature are variables computed from density and energy values. Temperature depends solely on energy, pressure depends on both energy and density. The code first change the energy to observe the temperature condition and later the density is calculated to keep the pressure condition.

The points corresponding to the bump corners observes the Neumann condition for pressure from distinct walls. Then, the density calculated in some direction might violate the boundary condition from another one. To circumvent this problem the pressure at the corner nodes are set to be the mean value that meet the boundary condition for each direction.

2.2.3 Spatial derivatives

Spatial derivatives calculation considers 6th order finite difference spectral-like scheme [63]. For some generic variable ϕ, the spatial derivative at some node denoted as i far from the boundaries can be expressed as,

DISTRIBUTION A: Distribution approved for public release. Distribution unlimited

$$\alpha\phi'_{i-1} + \phi'_i + \alpha\phi'_{i+1} = c\frac{\phi_{i+3} - \phi_{i-3}}{6h} + b\frac{\phi_{i+2} - \phi_{i-2}}{4h} + a\frac{\phi_{i+1} - \phi_{i-1}}{2h}, \tag{2.7}$$

where h is the mesh spacing and α, a, b e c are parameters of the derivative scheme. The system is tridiagonal to reduce the computational cost. For the 6th order of accuracy, these parameters must be a solution of the following set of equations,

$$\begin{aligned} a + b + c &= 1 + 2\alpha \quad (\mathcal{O}(h^2)), \\ a + 2^2 b + 3^2 c &= 2\frac{3!}{2!}\alpha \quad (\mathcal{O}(h^4)), \\ a + 2^4 b + 3^4 c &= 2\frac{5!}{4!}\alpha \quad (\mathcal{O}(h^6)). \end{aligned} \tag{2.8}$$

One additional constraint must be provided to solve the system and can also be used for the scheme optimization by Fourier analysis of equation 2.7 [63, 64],

$$\hat{\mathcal{A}}(\mathrm{w}) = i\frac{a\sin(\mathrm{w}) + (b/2)\sin(2\mathrm{w}) + (c/3)\sin(3\mathrm{w})}{1 + 2\alpha\cos(\mathrm{w})}, \tag{2.9}$$

where $\mathrm{w} = 2\pi kh/L = 2\pi k/N$ denotes a scaled wavenumber for a domain $[0, L]$ discretized by N points. Note that $\hat{\mathcal{A}}(\mathrm{w})$ is purely imaginary since equation 2.7 is symmetric so the associated error has only a dispersive character, $E_{disp}(\mathrm{w}) = \Im(\hat{\mathcal{A}}(\mathrm{w})) - \mathrm{w}$.

Following the procedure described by Gaitonde et al. [64], the criteria used for optimization is based on the integral of the dispersive error,

$$\mathcal{E}_{disp}(\alpha, \mathrm{w}_f) = \int_0^{\mathrm{w}_f} |\mathrm{E}_{disp}(\mathrm{w})|\, d\mathrm{w}, \tag{2.10}$$

Figure 2.2 shows contours of $\mathcal{E}_{disp}$ for a range of parameters α and w. The curve indicates the minimum error when a parameter is fixed. For comparison, circles correspond to the error of schemes that is optimized by the integral of dispersive error ($SL6O$) and

DISTRIBUTION A: Distribution approved for public release. Distribution unlimited

another one previously implemented in the code ($SL6$) in which the constraint imposed was $E_{disp}(\mathrm{w}_f) = 0$ for $\mathrm{w}_f = 1.8$.

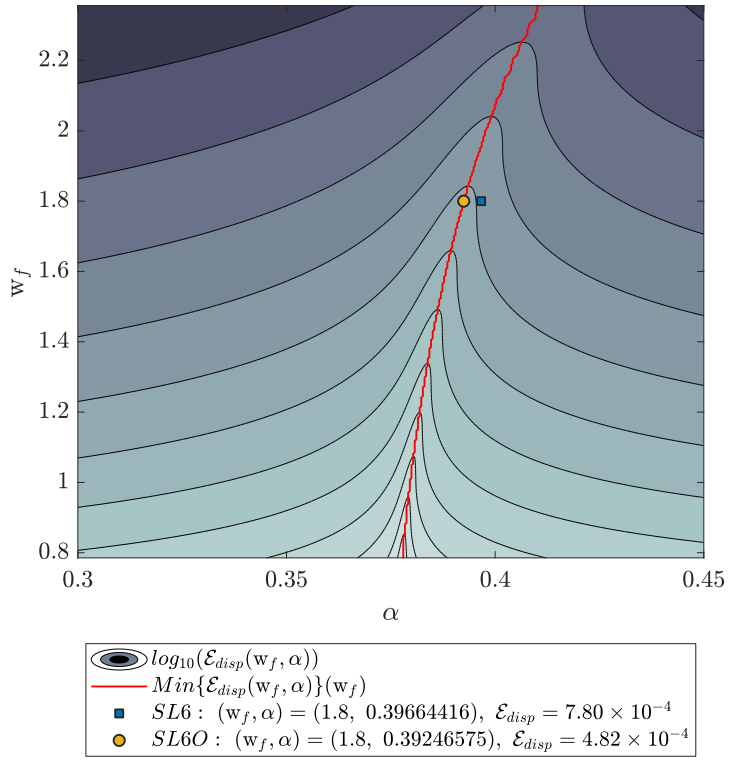


Figura 2.2: Contours of $\mathcal{E}_{disp}(\alpha, \mathrm{w}_f)$ for the 6th order derivative scheme.

For nodes near the wall the derivative scheme must be changed because of the stencil size available. Compared to the inner one, these schemes might be asymmetric to maintain the inner order or symmetric with a lower order. Asymmetric schemes introduces not only a dispersive but also a dissipative error, so we keep schemes symmetric up to the point next to boundary. For the boundary node it is inevitably asymmetric. Tables 2.1 and 2.2 summarize the parameters of all schemes and related nodes.

Scheme	Point	α	a	b	c
$SL6O$	inner	0.392465753	1.565410959	0.237260274	-0.017739726
$SL4O$	$i = 2$	0.350978474	1.567318982	0.134637965	0
$C4$	$i = 1$	$1/4$	$3/2$	0	0

Tabela 2.1: Parameters of symmetric derivative schemes: inner and near to boundary nodes.

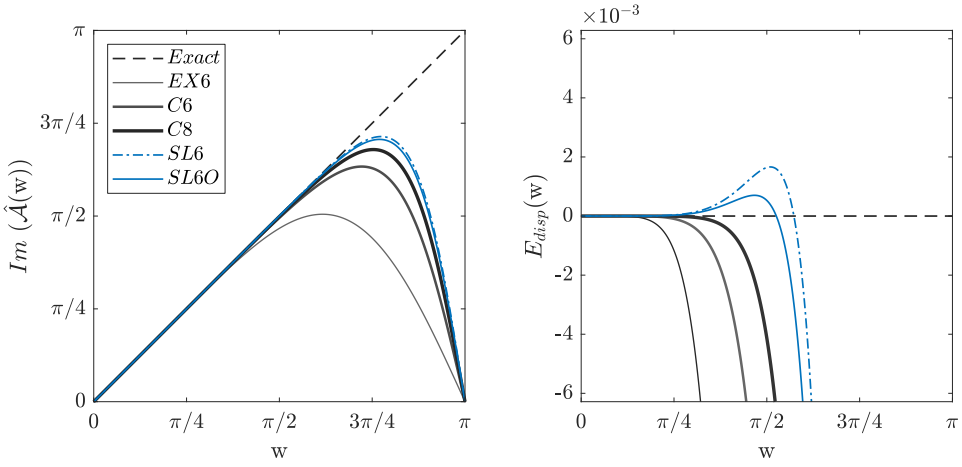
DISTRIBUTION A: Distribution approved for public release. Distribution unlimited

Scheme	α_0	a_0	b_0	c_0	d_0
$C3O - Asym.$	2.836465	-2.778822	1.581767	1.336465	-0.139411

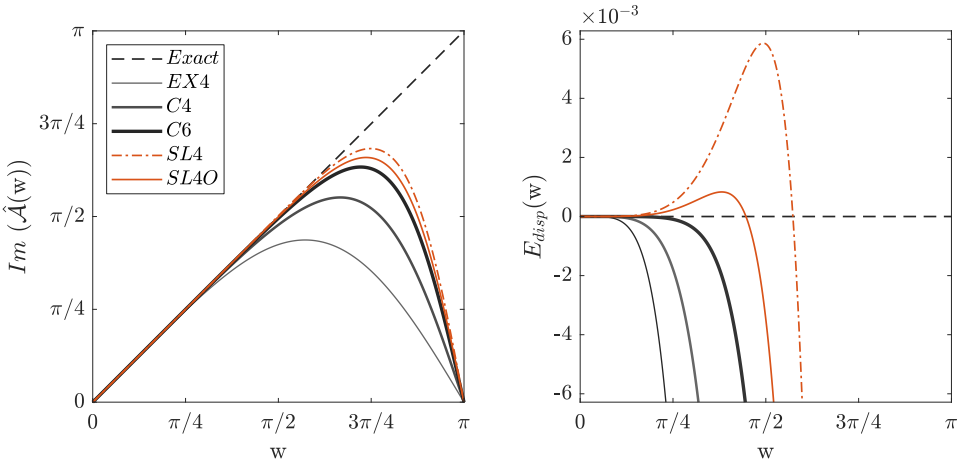
Tabela 2.2: Parameters of asymmetric derivative scheme for the boundary node.

Figure 2.3 compares the error response of the schemes presented in tables 2.1 and 2.2. Compared to $SL6$, $SL6O$ presents reduced error and lower overshooting response for higher wavenumbers. The same is observed comparing $SL4$ and $SL4O$. For the boundary node the lower order $C3O - Asym.$ was chosen because it is more numerically stable than the previous scheme, $C6 - Asym.$.

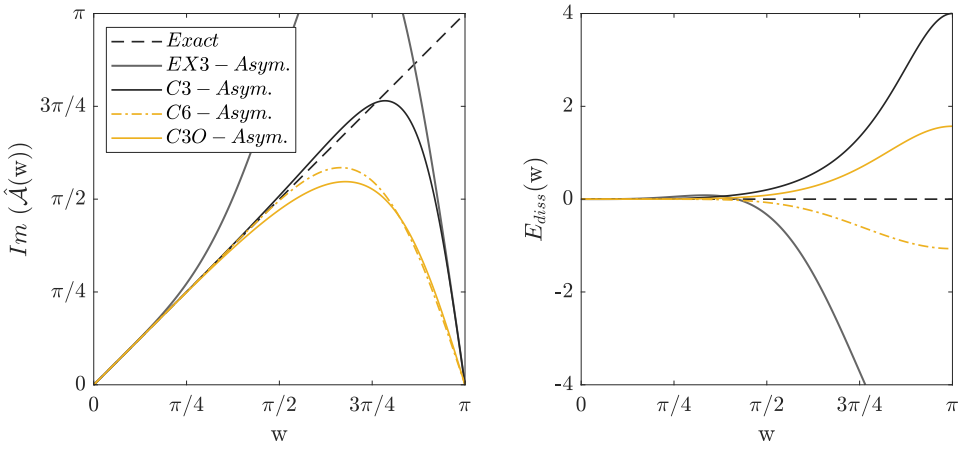
DISTRIBUTION A: Distribution approved for public release. Distribution unlimited



(a) Inner



(b) $i = 1$ and $i = 2$



(c) $i = 0$

Figura 2.3: Comparison of error response of some derivative schemes. Numbers indicate the order of each method and 'EX': explicit; 'C': Compact; 'SL': Spectral-like.

DISTRIBUTION A: Distribution approved for public release. Distribution unlimited

2.2.4 Time integration

Time integration is made by the classic 4th order Runge-Kutta (RK4) method. Let $\mathbf{U}^n$ be the flow state at some step n and $\mathbf{f}$ the time derivative of the flow. Then, the next step is given by,

$$\mathbf{U}^{n+1} = \mathbf{U}^n + \frac{\Delta t}{6}(\mathbf{K}_1 + 2\mathbf{K}_2 + 2\mathbf{K}_3 + \mathbf{K}_4), \tag{2.11}$$

with,

$$\begin{aligned}
\mathbf{K}_1 &= \mathbf{f}(\mathbf{U}^n), \\
\mathbf{K}_2 &= \mathbf{f}(\mathbf{U}^n + \frac{\Delta t}{2}\mathbf{K}_1), \\
\mathbf{K}_3 &= \mathbf{f}(\mathbf{U}^n + \frac{\Delta t}{2}\mathbf{K}_2), \\
\mathbf{K}_4 &= \mathbf{f}(\mathbf{U}^n + \Delta t\mathbf{K}_3).
\end{aligned} \tag{2.12}$$

For numerical stability the largest time step is defined following the Courant-Friedrichs-Lewy (CFL) condition,

$$\Delta t \leq \frac{Re}{\frac{1}{{\Delta x_{min}}^2} + \frac{1}{{\Delta y_{min}}^2} + \frac{1}{{\Delta z_{min}}^2}}, \tag{2.13}$$

$$\Delta t \leq \frac{CFL_{max}}{\frac{\left(\frac{1}{M} + u_{max}\right)}{\Delta x_{min}} + \frac{\left(\frac{1}{M} + v_{max}\right)}{\Delta y_{min}} + \frac{\left(\frac{1}{M} + w_{max}\right)}{\Delta z_{min}}}. \tag{2.14}$$

DISTRIBUTION A: Distribution approved for public release. Distribution unlimited

First condition observes the flow diffusive characteristics and is calculated once since it is only dependent on the mesh parameters. Second condition depends on the mesh, simulation Mach and flow state, so it computed every step based on a CFL_{max} defined. The value of $CFL_{max} = 1.3$ is used for all presented cases.

2.2.5 Aliasing filter

Code has implemented a spatial low-pass filter which attenuates the aliasing effects due to the mesh discretization. Similar to spatial derivatives method it is tridiagonal based scheme but based on only one free-parameter, α_f, proposed by Gaitonde et al. [65]. The order of accuracy is 10 which demands an stencil of 11 points. For some generic variable ϕ at some point i, filter updates the values of ϕ by the filtered variable, $\bar{\phi}$, so the inner formula and related coefficients (table 2.3) are as follows,

$$\alpha_f \bar{\phi}_{i-1} + \bar{\phi}_i + \alpha_f \bar{\phi}_{i+1} = \sum_{k=0}^{5} \frac{a_k}{2} (\phi_{i-k} + \phi_{i+k}). \tag{2.15}$$

a_0	a_1	a_2	a_3	a_4	a_5
$\frac{193 + 126\alpha_f}{256}$	$\frac{105 + 302\alpha_f}{256}$	$\frac{-15 + 30\alpha_f}{64}$	$\frac{45 - 90\alpha_f}{512}$	$\frac{-5 + 10\alpha_f}{256}$	$\frac{1 - 2\alpha_f}{512}$

Tabela 2.3: Coefficients of the 10th order spatial filter with one free-parameter, α_f.

In our simulations we set $\alpha_f = 0.49$ which almost represents the case without filter in which $\alpha_f = 0.5$.

For points near to boundaries it is not possible to use the $F10$ filter. The boundary layer is very sensitive to the solution near the wall so careful attention must be given to the filter ing process in this region. The options would be keep the inner order and apply asymmetric filters, lower the order up to boundaries considering available stencil and/or smoothly decrease the filter strength. Considering the higher refinement mesh level near the wall and that the inner scheme has almost no filter actuating our treatment is to not apply filter near the wall.

DISTRIBUTION A: Distribution approved for public release. Distribution unlimited

2.2.6 Buffer-zones

Buffer-zones are placed between the physical domain and outflow/outerflow boundaries. In these non-physical regions, a Selective Frequency Damping (SFD) filter [66] is used to avoid reflections at the open boundaries where the boundary conditions are applied. The SFD actuates damping the waves coming from the physical domain which is done solving the system,

$$\mathbf{U}_t = \mathbf{f}(\mathbf{U}) - \chi(\mathbf{U} - \bar{\mathbf{U}}), \tag{2.16}$$

$$\bar{\mathbf{U}}_t = \frac{\mathbf{U} - \bar{\mathbf{U}}}{\Delta}, \tag{2.17}$$

where χ controls the filter strength, Δ is related to a cutoff frequency ($\omega_c = 1/\Delta$) and bar denotes the steady state. The first equation simply replaces equation 2.11,

$$\mathbf{U}^{n+1} = \mathbf{U}^n + \frac{\Delta t}{6}(\mathbf{K}_1 + 2\mathbf{K}_2 + 2\mathbf{K}_3 + \mathbf{K}_4) - \Delta t\chi(\mathbf{U} - \bar{\mathbf{U}}), \tag{2.18}$$

while the second one is solved as,

$$\bar{\mathbf{U}}^{n+1} = \bar{\mathbf{U}}^n + \Delta t\frac{\mathbf{U}^n - \bar{\mathbf{U}}^n}{\Delta}. \tag{2.19}$$

Along the buffer-zones the χ parameter changes smoothly to avoid some possible abrupt change in solution.

2.2.7 Domain decomposition, parallelization

The DNS code is implemented in *Fortran 90* language and parallelization is made by *MPI* (*Message Passage Interface*). 2DECOMP&FFT library [67] is then used to domain decomposition.

Further details of the code are provided in some of the previous publications of this group [68, 69, 70, 16, 71, 72].

DISTRIBUTION A: Distribution approved for public release. Distribution unlimited

2.3 Parametric space and excitation description

The results presented in this report consider the bidimensional analysis of TS waves interacting with bumps with different heights at different Mach numbers. The simulation Reynolds is based on the displacement thickness so $Re = Re_{\delta_{1,R}} = U_\infty \delta_{1,R}/\nu$ in which $\delta_{1,R}$, corresponds to the displacement thickness at the bump center. Table 2.4 summarizes the parametric space covered.

Tabela 2.4: Simulated cases.

$Re = Re_{\delta_{1,R}}$	$Re_{\delta_{1,E}}$	M	x_E	x_R	L_R	h_R
950	700	0.1	174.2	321.8	18.2	0
		0.3				0.05
		0.6				0.10
		0.9				0.20
						0.40
1088	907	0.1	254.8	367.4	20	0
						0.06
						0.12
						0.23
						0.47

Cases in which $Re = 1088$ with heights of $h_R = [0.23,\ 0.47]$ correspond to the parametric conditions simulated by Wörner et al. [48] and are used for comparison reason. For these cases, the excitation is monochromatic with frequency of $F = 49.34 \times 10^{-6}$. Results for lower heights, $h_R = [0.06,\ 0.12]$, are shown to update the authors' conclusions about the linear/non-linear limit of TS amplification versus bump height.

Cases in which $Re = 950$ have parametric space inspired by experiments of de Paula et al. [53] which investigated the effects of monochromatic waves interacting with isolated bumps. Here the bumps are assumed bidimensional as it represents a prior step to simulate the tridimensional case. For the current 2d simulations, monochromatic and wavepackets are used as excitation disturbances and compressible effects are investigated.

The TS waves are introduced as a non homogeneous condition at the wall upstream to the bump. For preliminary tests it is done by considering a monochromatic signal. The same is done for the Taylor-Stokes approximation method analysis. For other results, the disturbance is composed by several modes, i.e., a wavepacket.

The range of frequencies are selected based on modes instability. Figure 2.4 shows the growth rate for a wide range of frequencies obtained by an incompressible PSE code [73]

DISTRIBUTION A: Distribution approved for public release. Distribution unlimited

providing a preliminary estimate of the most unstable band. F is the non-dimensional or reduced frequency defined as $F = 2\pi f^* \nu^* / {U_\infty^*}^2$ in dimensional variables or considering the non-dimensional parameters $F = \omega / Re$.

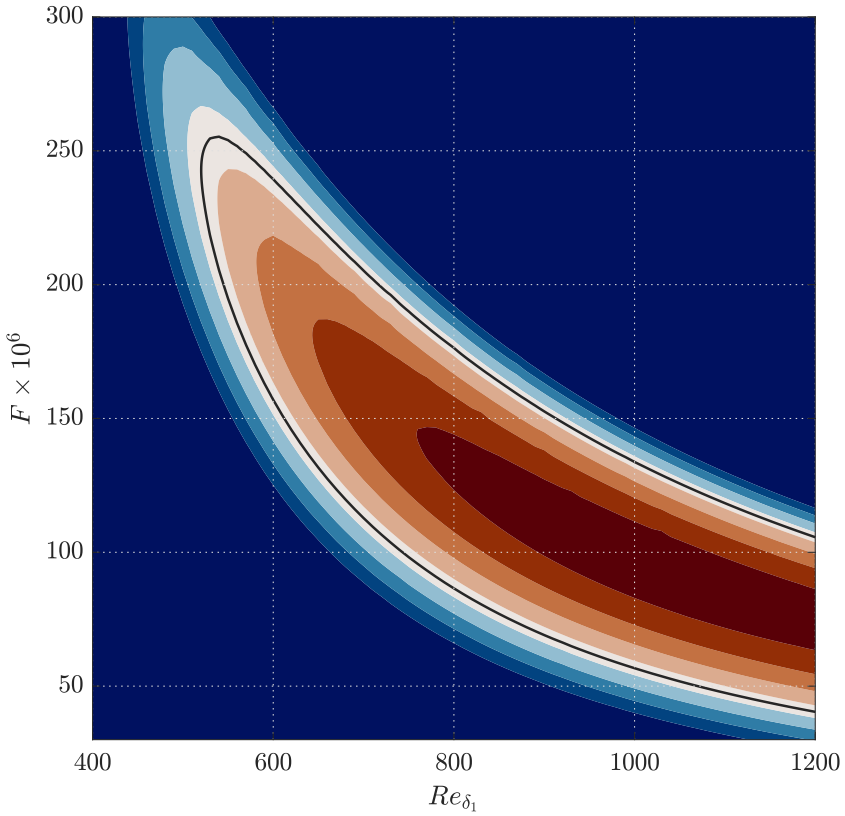


Figura 2.4: Growth rate based on evolution of u_{max}.

2.3.1 Monochromatic

Figure 2.5 shows the physical space of wall velocity to produce a monochromatic excitation disturbance. It is composed by a periodic function both in x and time. As shown in figure 2.4, the selected frequency of $F = 90 \times 10^{-6}$ is inside the unstable band along the domain showed.

2.3.2 Wavepacket

A gaussian shaped function is used to introduce the wavepacket excitation disturbance along the x direction. Along time, a sum of periodic functions compose the signal. The frequency bandwidth of this signal controls the simulation time needed to introduce the

DISTRIBUTION A: Distribution approved for public release. Distribution unlimited

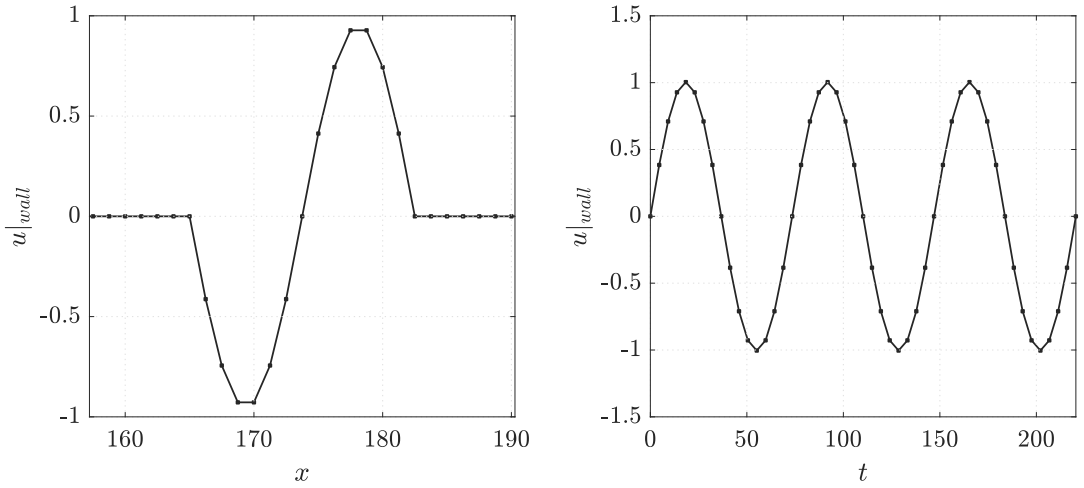


Figura 2.5: Excitation disturbance at wall for a monochromatic signal, $F = 90 \times 10^{-6}$. $Re = 950$.

complete disturbance. The lower the fundamental mode, the higher the simulation time required to introduce the full signal. In order to shorten this time, after the summation a gaussian function is applied establishing a smooth threshold. The physical and spectral space of such function are shown in figures 2.6 and 2.7, respectively.

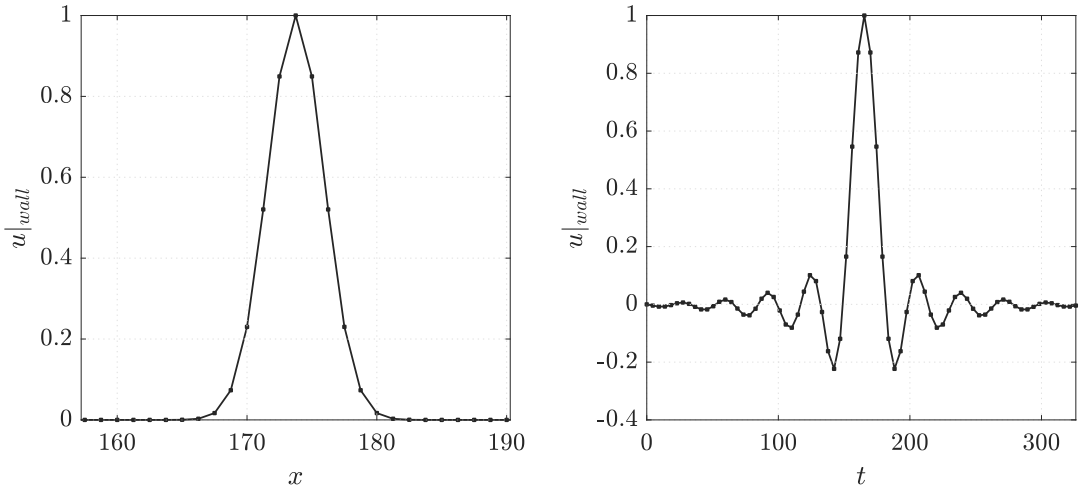


Figura 2.6: Excitation disturbance at wall for a wave packet signal. $Re = 950$.

Comparing the spectrum of figure 2.7 and the growth rate from figure 2.4, the excitation signal covers the most unstable band.

It is also necessary to ensure that the distance between excitation and bump is sufficient to the wavepacket development. Figure 2.8 shows the wavepacket evolution along a smooth plate at a fixed position relative to the local displacement thickness (δ_1).

DISTRIBUTION A: Distribution approved for public release. Distribution unlimited

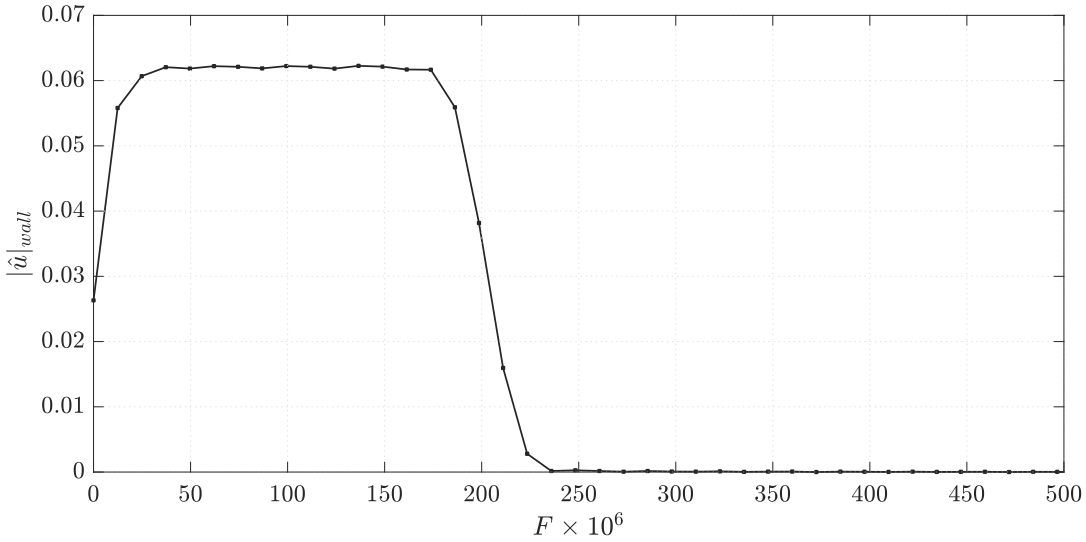


Figura 2.7: Spectrum of the excitation disturbance at wall for a wave packet signal.

The chosen stations correspond to intermediate positions between an excitation, x_E, and the reference position which corresponds to the bump center location, x_R where $Re = Re_{\delta_{1,R}} = 950$. The intervals correspond to integer numbers of the bump length of this case, .

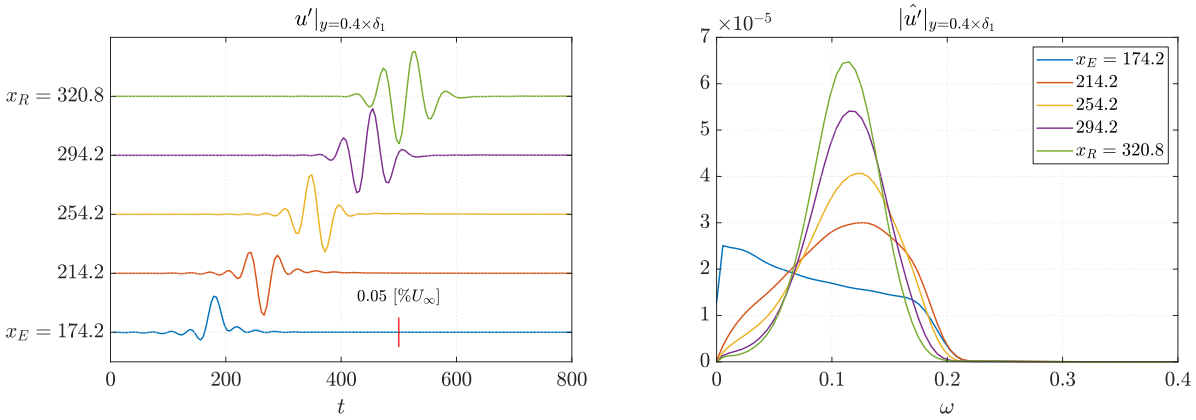


Figura 2.8: Wavepacket evolution along the plate from excitation to the reference locations, x_E and x_R respectively. L_R denotes the bump length ($L_R \approx 18.18 \times \delta_{1,R}$). Signals extracted at $y = 0.75 \times \delta_1$ for each station.

DISTRIBUTION A: Distribution approved for public release. Distribution unlimited

3 Preliminary Tests

3.1 Spatial derivative optimization test

The optimized derivative scheme denoted as $SL6O3$ as described in section 2.2.3 is compared to an other prior implemented scheme, $SL6$. Figure 3.1 shows the convergence of the base flow considering the same mesh e initial initial conditions. The improvement of $SL6O3$ compared to $SL6$ is clear since the last one does not converge to a steady state. This caused mainly by high wavenumber fluctuations that are amplified at the bump corner edges for $SL6$.

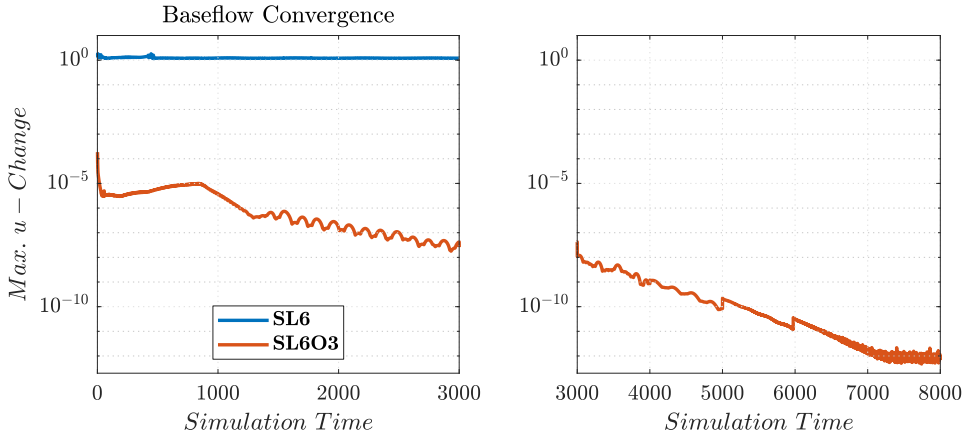


Figura 3.1: Base flow convergence for derivatives scheme $SL6$ and $SL6O3$ with the same mesh and initial condition.

3.2 Mesh independence

In simulating the interaction between the TS waves and roughness the employed mesh must be capable to reproduce both the wave propagation and local effects that occurs at the roughness neighborhood, whether they are caused in the base flow or by the TS wave.

The solution accuracy must be such that it is sufficient to capture the effect of a bump with height of at least 5% which presents an amplitude increase around 2.5% relative to

DISTRIBUTION A: Distribution approved for public release. Distribution unlimited

the smooth case. In our simulations we assume that solution is independent of mesh if the relative error is lower than 1%.

The accuracy of a propagating wave solution is affected by the the minimum spacement normal to plate, Δy_{min}, and also by the spacement along the propagation direction related to its wavelength here defined as typical spacement, Δx_{typ}. Prior simulations showed the accuracy required is obtained with parameters of Δx_{typ} around 13 points per TS wavelength. At the sharp edges corners the local refinement of $\Delta x_{min} = \Delta y_{min}$ around 0.01 is needed to solve a bump of 5% height, i.e., five points up to bump top. Despite being a very small $\Delta(x, y)_{min}$ the refinement can be rapidly increased up to the typical parameter along both directions [74].

Figure 3.2 shows three meshes used to simulate the smooth plate boundary layer. The amplitude of TS waves with frequencies of $F = 90 \times 10^{-6}$ and $F = 120 \times 10^{-6}$ along the meshes of figure 3.2 are shown in figure 3.3. Results indicate the *mesh* 0 is independent of mesh for the TS propagation considering the established criteria of 1%.

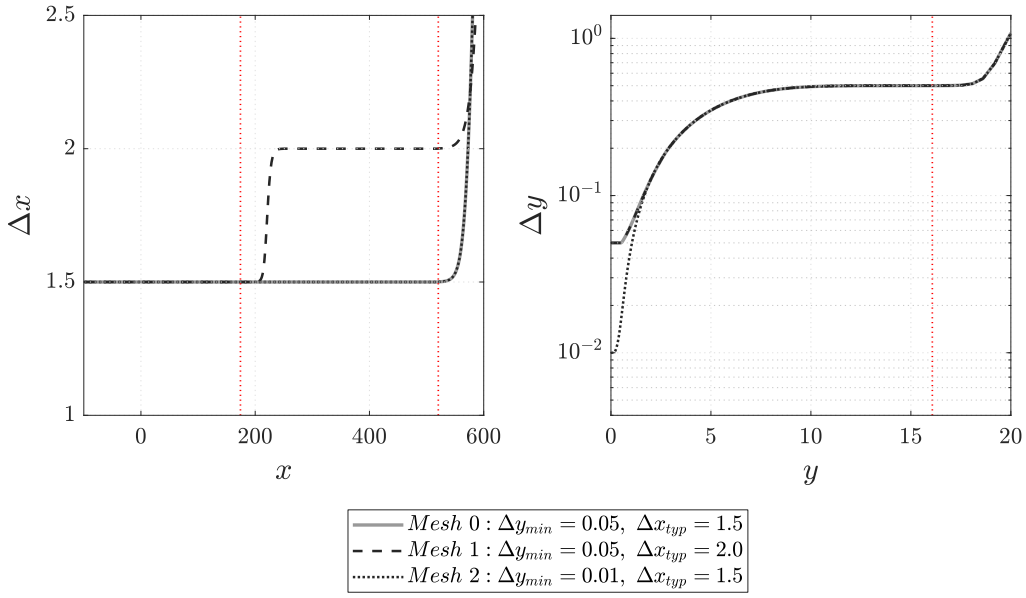


Figura 3.2: Meshes used to evaluate the impact of typical and minimum refinement in the propagation of a TS wave.

Figure 3.4 shows a mesh with $\Delta x_{min} = \Delta y_{min} = 0.01$ and another one with halved spacement. The smooth "mesh 0"is shown for visual reference and a detailed view close to the bump trailing edge is also provided. The relative error between these meshes are presented in figure 3.5 showing mesh independence for "mesh R0".

DISTRIBUTION A: Distribution approved for public release. Distribution unlimited

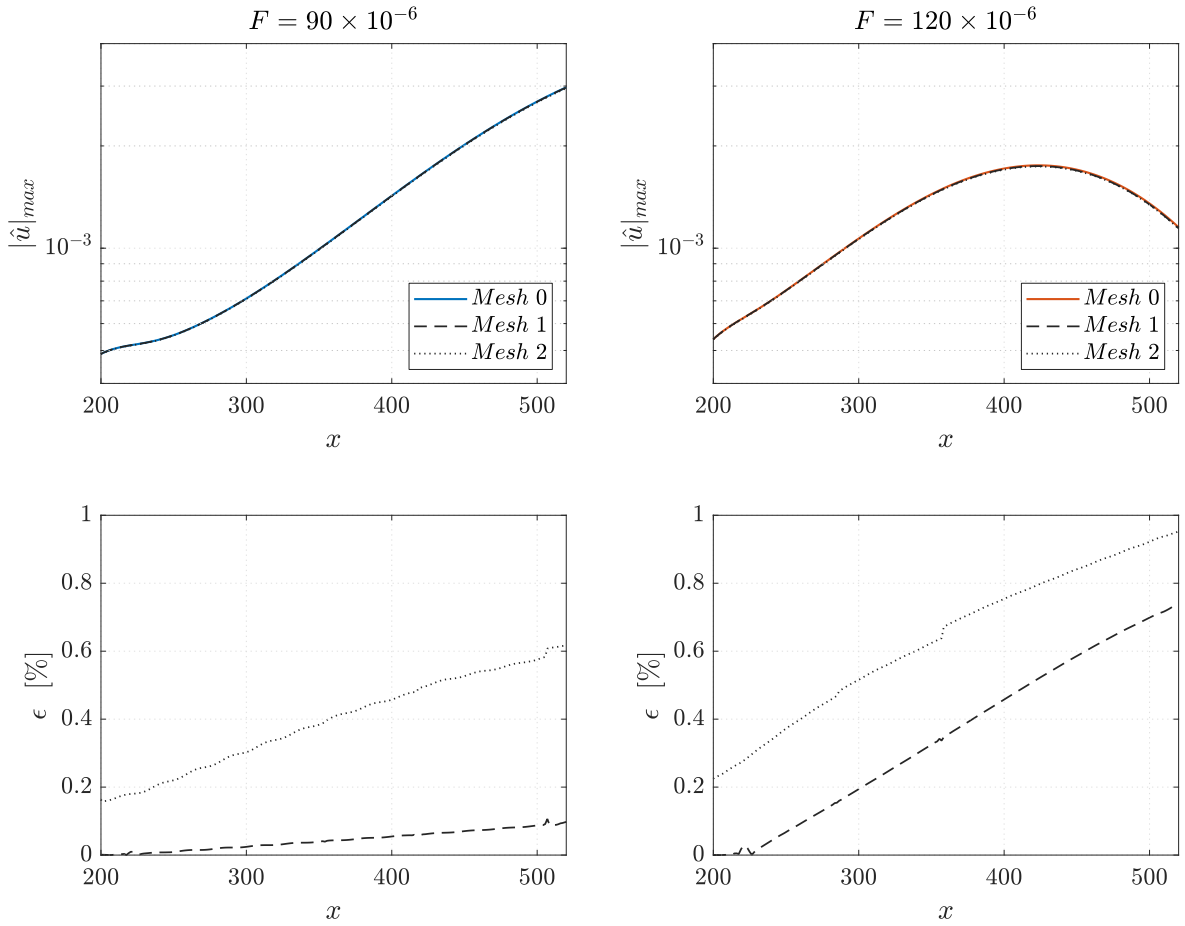


Figura 3.3: Maximum TS amplitude and absolute relative error for meshes shown in fig. 3.2.

DISTRIBUTION A: Distribution approved for public release. Distribution unlimited

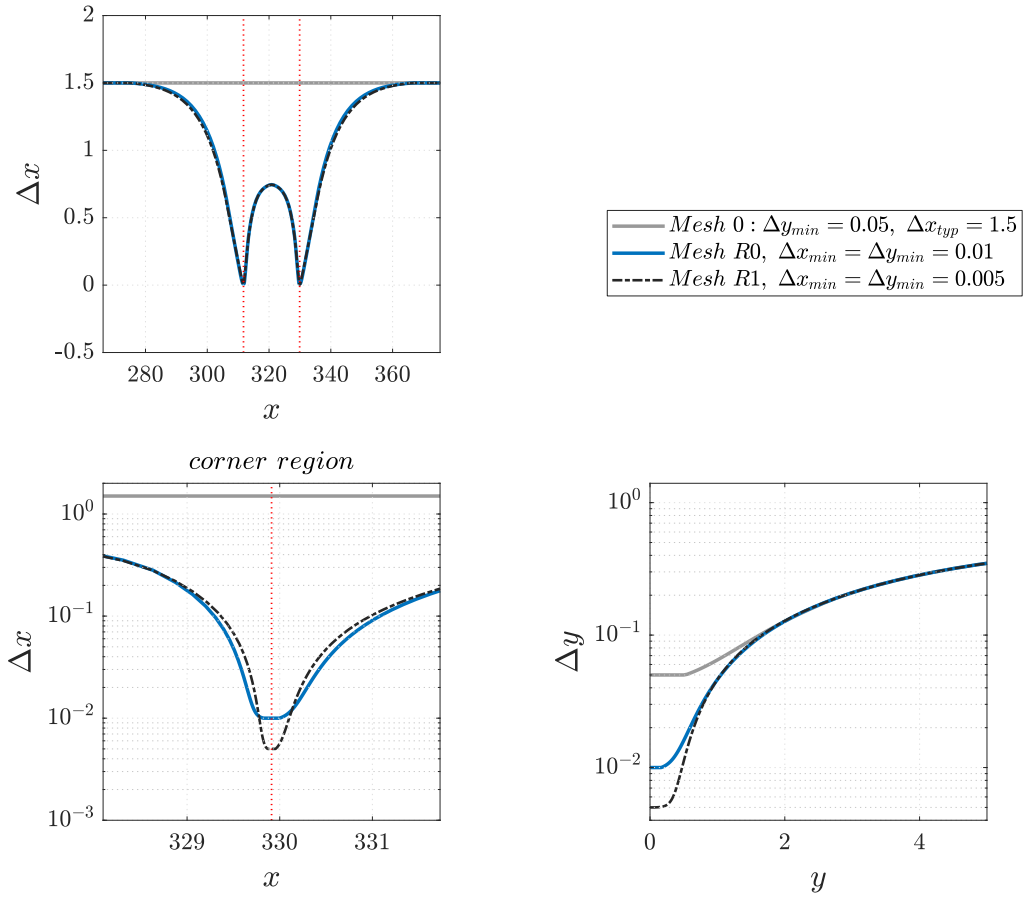


Figura 3.4: Meshes used to evaluate the impact of mesh refinement at the sharp corners region.

DISTRIBUTION A: Distribution approved for public release. Distribution unlimited

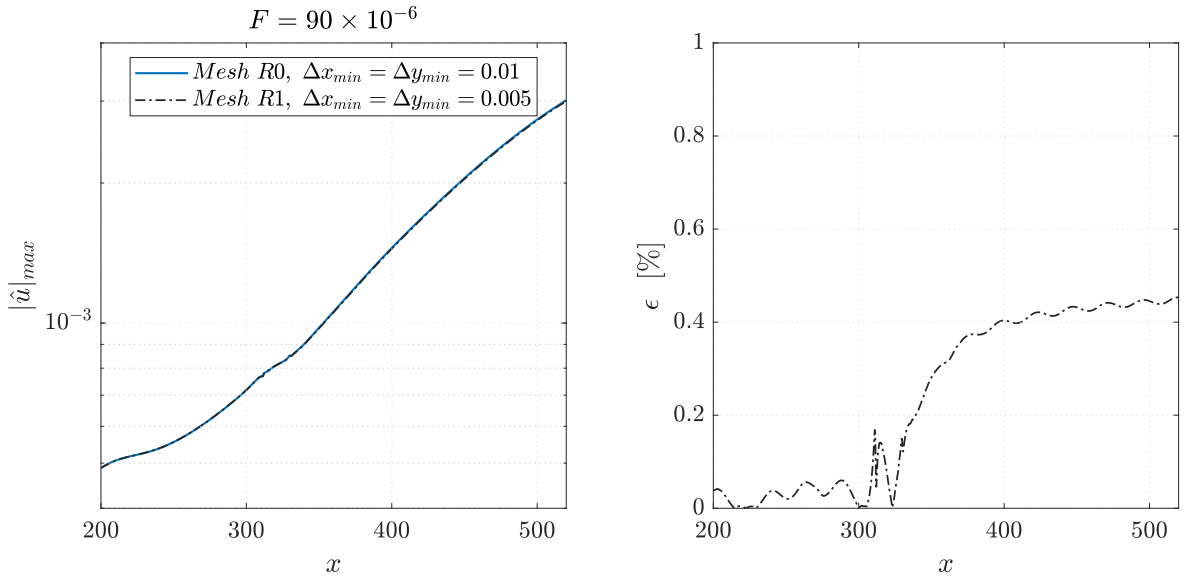


Figura 3.5: Maximum TS amplitude and absolute relative error for meshes shown in fig. 3.4 for a roughness with height of $h_R = 0.05$ placed at $Re_{\delta_1} = 950$.

DISTRIBUTION A: Distribution approved for public release. Distribution unlimited

3.3 Comparison with literature

Figure 3.6 shows a comparison between the amplitude solution provided by the DNS and that obtained by a PSE [75]. The comparison is remarkable for both frequencies.

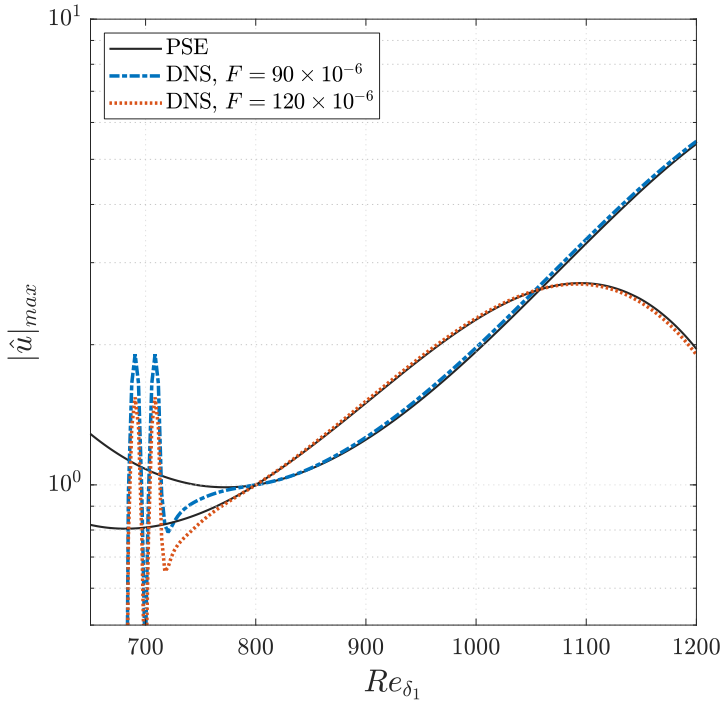


Figura 3.6: DNS and PSE results comparing the maximum TS amplitude for reduced frequencies of $F = [90,\ 120] \times 10^{-6}$. $Re = 950$ and amplitude normalized at $Re_{\delta_1} = 800$.

The DNS is also compared with the simulations results from [48]. Figure 3.7 shows the evolution of the TS wave along the plate for different bump heights. The agreement is better seen by comparing the amplitude factor relative to the smooth plate given by the authors. Figure 3.8 compares our results and that reported by authors for heights of $h_R = 0.23$ and $h_R = 0.47$. Literature results are also plotted with a correction of 7% in amplitude over response that authors reported to observe when comparing their results with an experiment. Our results show very good agreement.

DISTRIBUTION A: Distribution approved for public release. Distribution unlimited

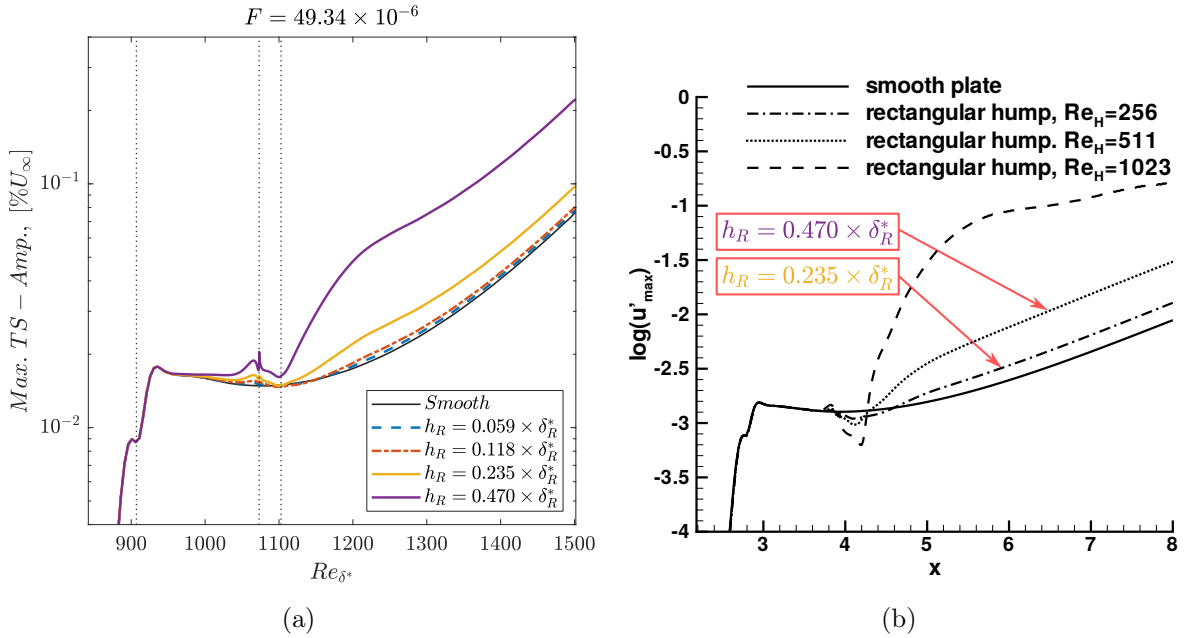


Figura 3.7: Amplitude of TS wave with $F = 49.34 \times 10^{-6}$ for different bump heights comparing our results and that from Wörner et al. [48].

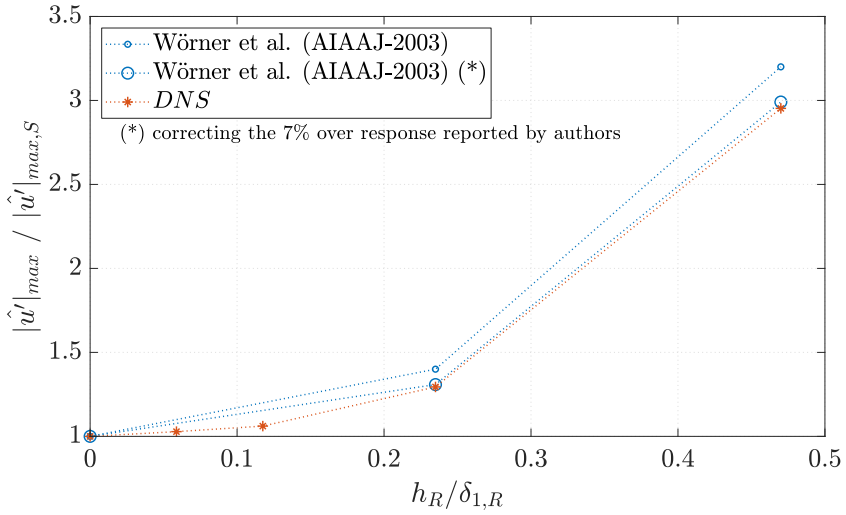


Figura 3.8: Bump height effect on TS amplitude relative the smooth plate for DNS and Wörner et al. [48].

DISTRIBUTION A: Distribution approved for public release. Distribution unlimited

4 Results

4.1 Linear/non-linear maximum bump height

Results from comparison with Wörner et al. [48] also show that the maximum height in which the amplitude increase still scales linearly is not $h_R = 0.47$ as the authors argue but lower. Linear/non-linear threshold is better suited for a height between $h_R = 0.10$ and $h_R = 0.20$ as shown by figure 4.1.

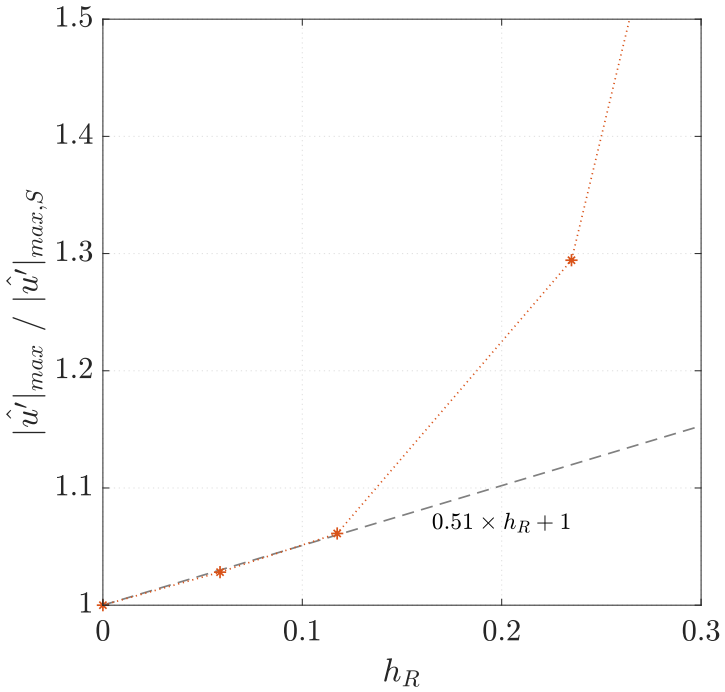


Figura 4.1: .

This result agrees with that expected considering the asymptotic theory for very small heights. The amplification factor for heights lower than $h_R = 0.10$ are lower than 5% relative the smooth plate. Then, the fact that our code is capable to capture this very small linear change is one that most validate the results found.

DISTRIBUTION A: Distribution approved for public release. Distribution unlimited

4.2 Base flow distortion caused by bumps

This section provides some highlights of the bump height effect on base flow for cases with $Re = 950$ and $M = 0.1$ (2.4). Figure 4.2 shows how bumps of different heights affects the boundary layer. The magnitude of distortion differs considerably as the heights increases. The streamlines in figure 4.2 also show the boundary layer tends to return to smooth one. Far downstream it takes a longer distance but it still show an asymptotic behavior.

The velocity profiles for positions far upstream, bump center and far downstream are showed in figure 4.2. Results show that major distortion is constrained in the bump region. The magnitude of change depends on the bump height but it decrease rapidly along the normal direction. Far downstream, at $x = 400$, the boundary layer of the most critical bump height has a maximum difference less than 1% of U_∞ compared to the smooth one.

Figure 4.5 shows the displacement thickness, momentum thickness and shape factor for different heights of bump. Local effect are noted again but with integrated variables some trends for magnitude values versus bump height can be seen more clearly. These variables also provide a better definition on the region of influence of these bumps, a topic that will be addressed in other sections.

DISTRIBUTION A: Distribution approved for public release. Distribution unlimited

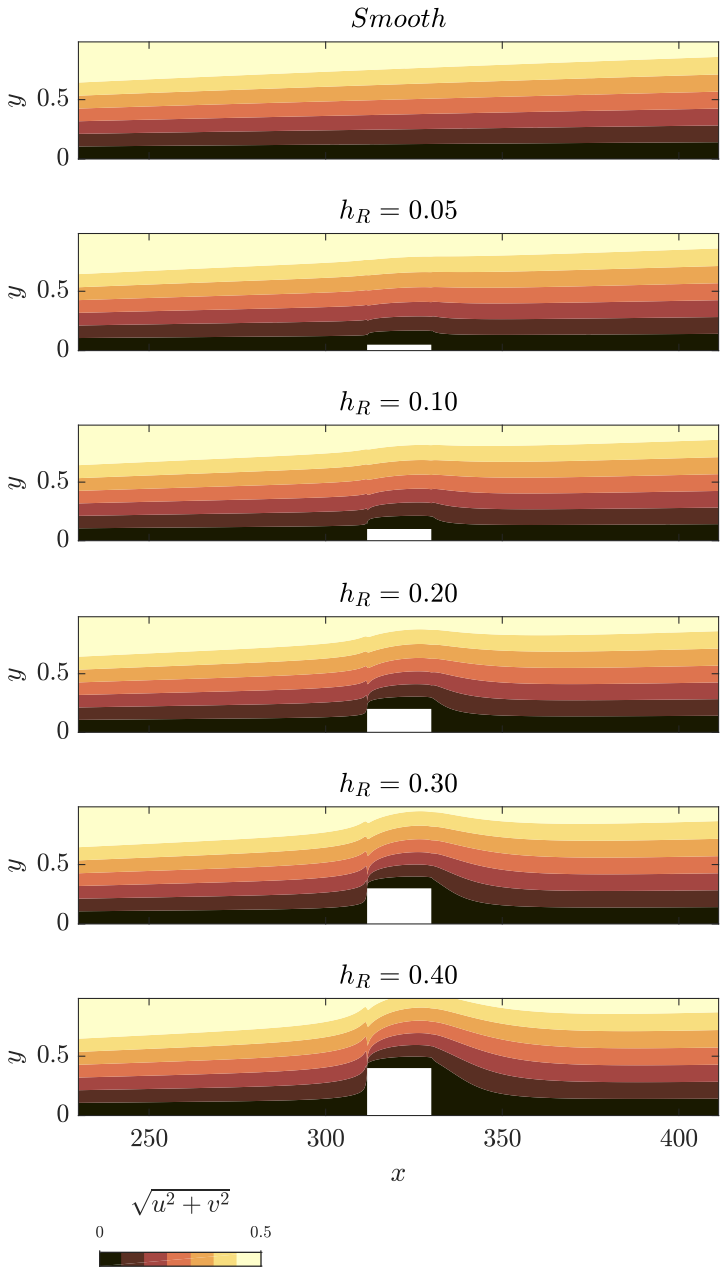


Figura 4.2: Velocity magnitude for different heights of bumps.

DISTRIBUTION A: Distribution approved for public release. Distribution unlimited

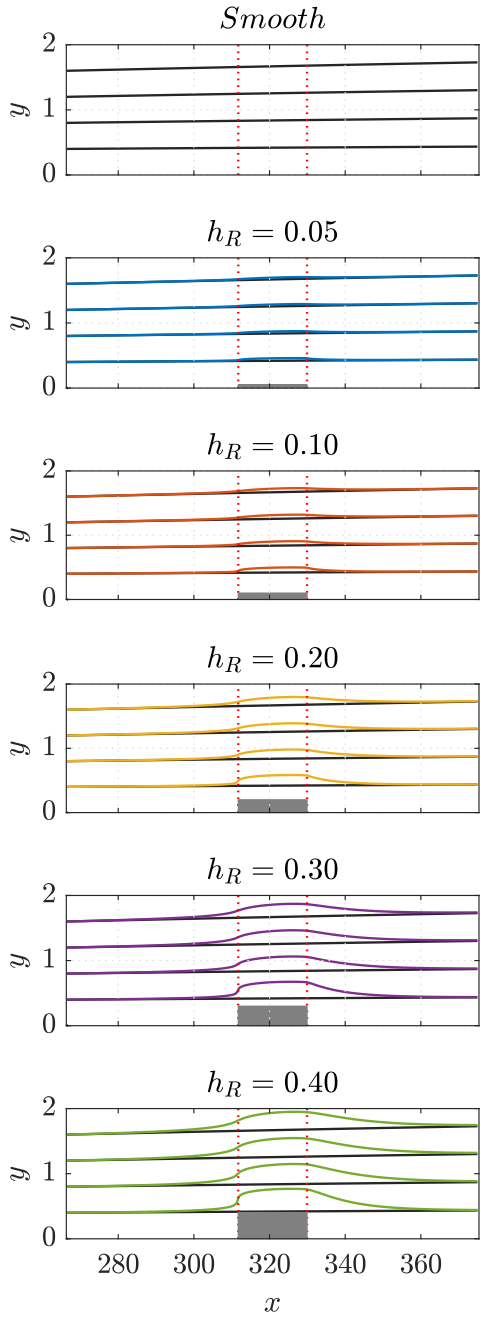


Figura 4.3: Streamlines for different heights of bumps. The smooth plate streamline is shown in all plots for reference.

DISTRIBUTION A: Distribution approved for public release. Distribution unlimited

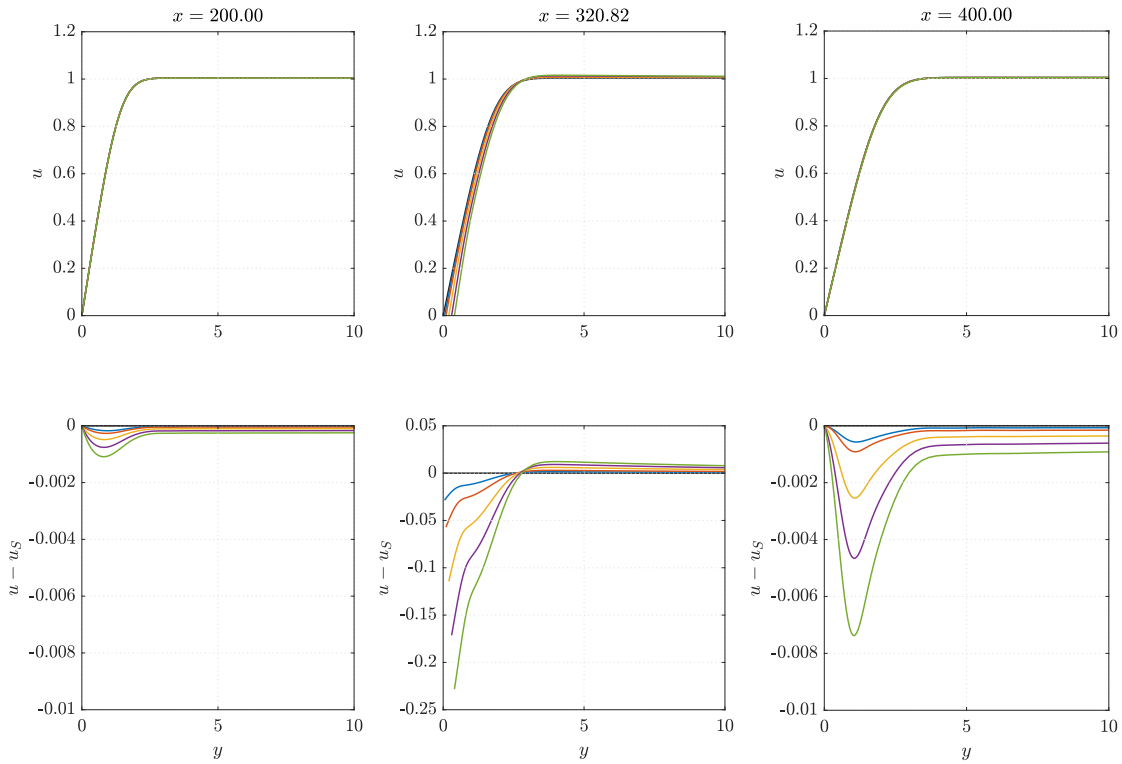


Figura 4.4: Velocity profile of base flow showing the local distortion caused by bumps of different heights.

DISTRIBUTION A: Distribution approved for public release. Distribution unlimited

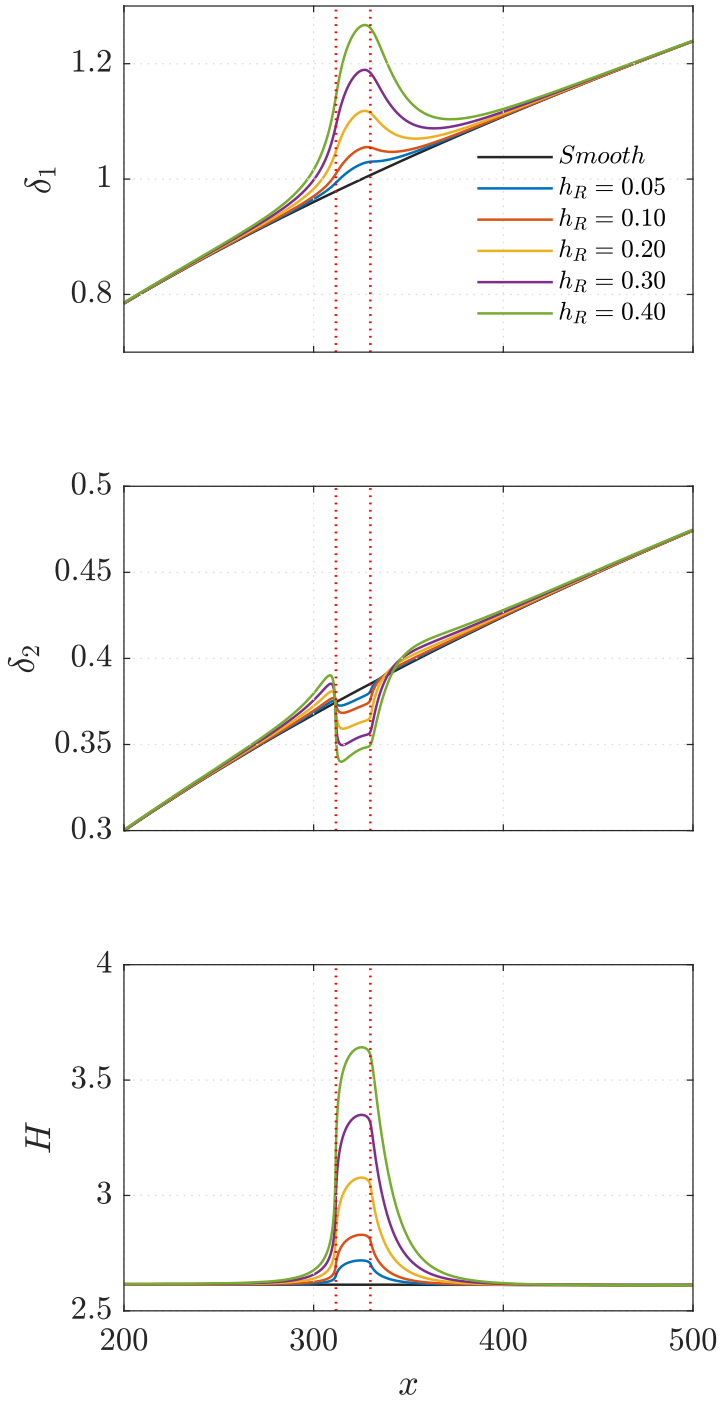


Figura 4.5: Displacement thickness (δ_1), momentum thickness (δ_2) and shape factor (H) for different bump heights.

DISTRIBUTION A: Distribution approved for public release. Distribution unlimited

4.3 TS waves interacting with bumps

In the previous sections we showed the developments in numerical tools provided very accurate simulations, with which, it was possible to study various aspects of the effect of bumps on the TS wave evolution.

Here we investigate the effect of bumps of different heights and the influence of Mach number for $Re = 950$ cases (table 2.4). The excitation disturbance is the wavepacket described in 2.3.2 so analysis is also extended to consider these effects with varying TS frequency.

4.3.1 The effect of the bump height

Figure 4.6 shows the amplitude change caused by bumps of different heights. The amplification factor relative smooth surface is also shown for better visualization. The Mach number is $M = 0.1$ and the TS frequency is $F = 90 \times 10^{-6}$.

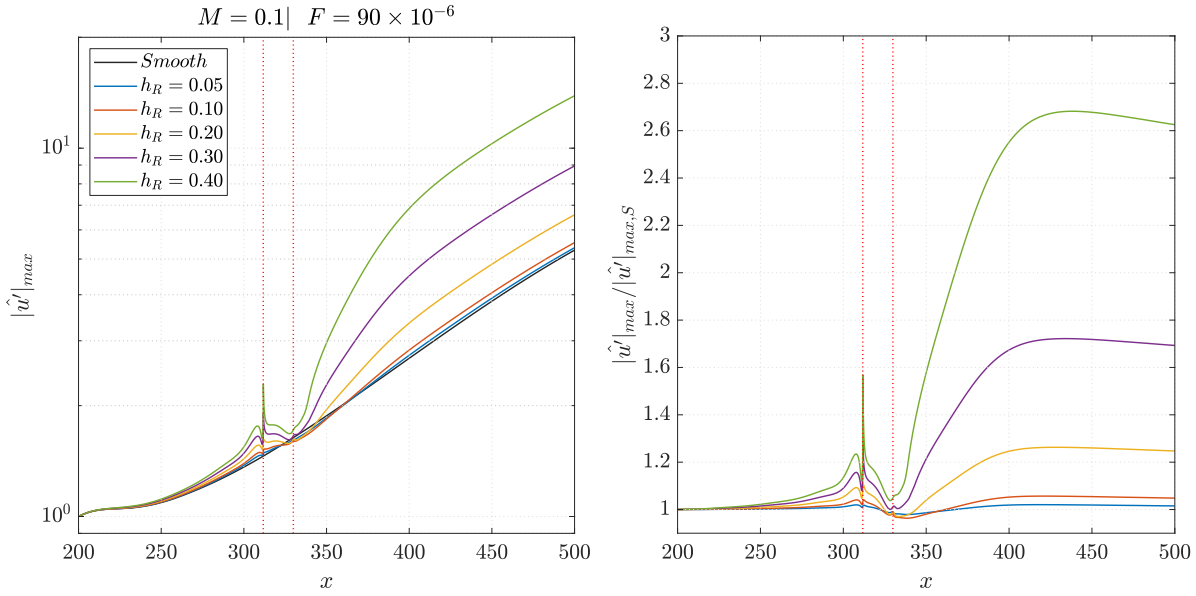


Figura 4.6: Amplitude evolution of the TS mode of $F = 90 \times 10^{-6}$ for different bump heights at $M = 0.1$.

The TS amplitude increases as the bump height increases as already shown by [48] which was reproduced in preliminary tests figure 3.7.

As the amplitude change varies considerably with height it would be better to understand the problem with another approach rather than comparing the amplitude. Our

DISTRIBUTION A: Distribution approved for public release. Distribution unlimited

analysis includes the investigation based on growth rate which are shown in figure 4.7 for the cases presented before.

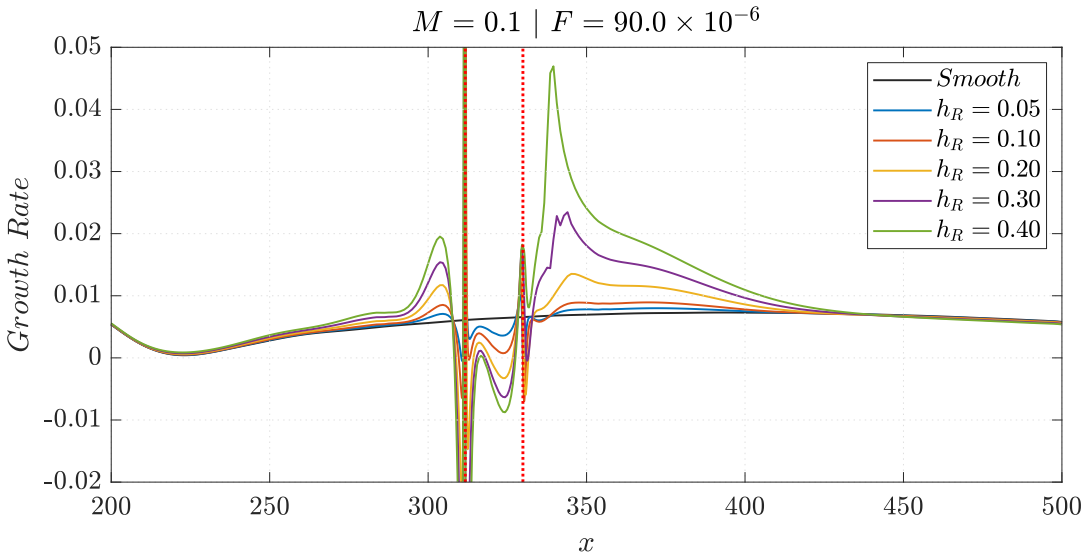


Figura 4.7: Growth rate change caused by bumps with different heights compared to the smooth plate.

The growth rate reaches a maximum over the plate if no bump is present and then decay. The bump inclusion affects the growth rate locally and maximum magnitude depends on height but downstream, the growth rate returns back to that observed in the smooth plate. Moreover, the plate location where it occurs seems to be the same regardless of height. Then, the region where growth rate differs from that of smooth plate can be associated as the region of influence of a bump itself.

4.3.2 The effect of Mach

The same analysis from previous section is now extended by comparing the results of low Mach regime, $M = 0.1$, to that obtained for $M = 0.3$, $M = 0.6$ and $M = 0.9$. The effect of bump height change at these Mach numbers are shown in figure 4.8 comparing the smooth case to each bump height for a selected TS frequency of $F = 90 \times 10^{-6}$.

For heights up to $h_R = 0.10$ the amplitude change is small with evolution mainly following that of smooth. In this scenario as Mach increases the selected mode became more stable. For higher heights the amplitude change is quite different from the smooth one. The height itself is responsible for considerable part of this change. However, it can be noted that for higher bumps the amplitude evolution also changes compared to that

DISTRIBUTION A: Distribution approved for public release. Distribution unlimited

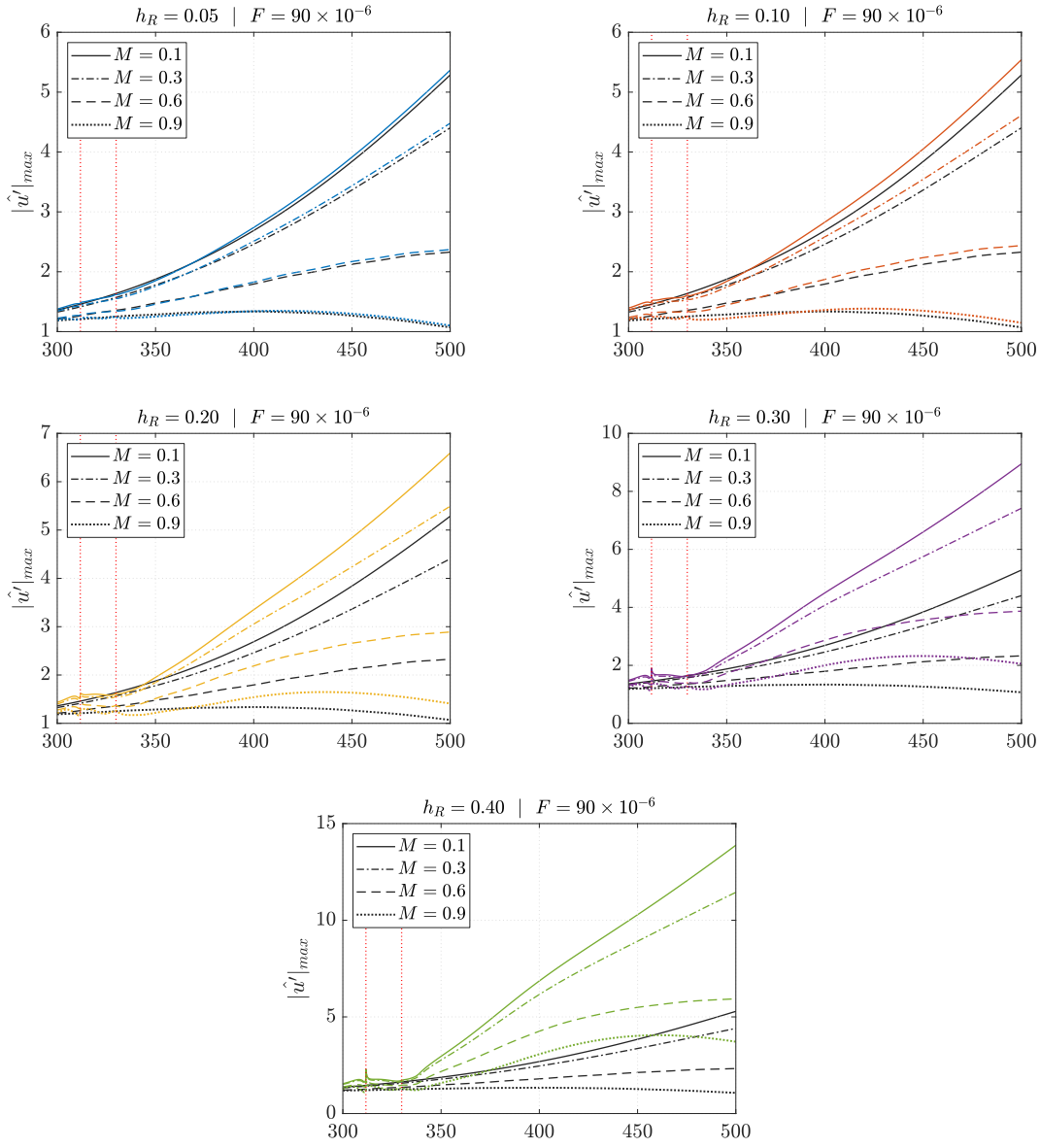


Figura 4.8: Amplitude evolution of the TS mode of $F = 90 \times 10^{-6}$ for different bump heights with varying Mach.

from smooth.

In figure 4.9 the amplitude factor relative the smooth is plotted grouping all bump heights. At subsonic regime the amplitude has small changes in amplitude factors which decreases with increasing Mach. But at transonic speeds the opposite effect seems to occur and amplitude factor is dramatically increased.

As done for previous section the growth rate is also investigated and results are pre-

DISTRIBUTION A: Distribution approved for public release. Distribution unlimited

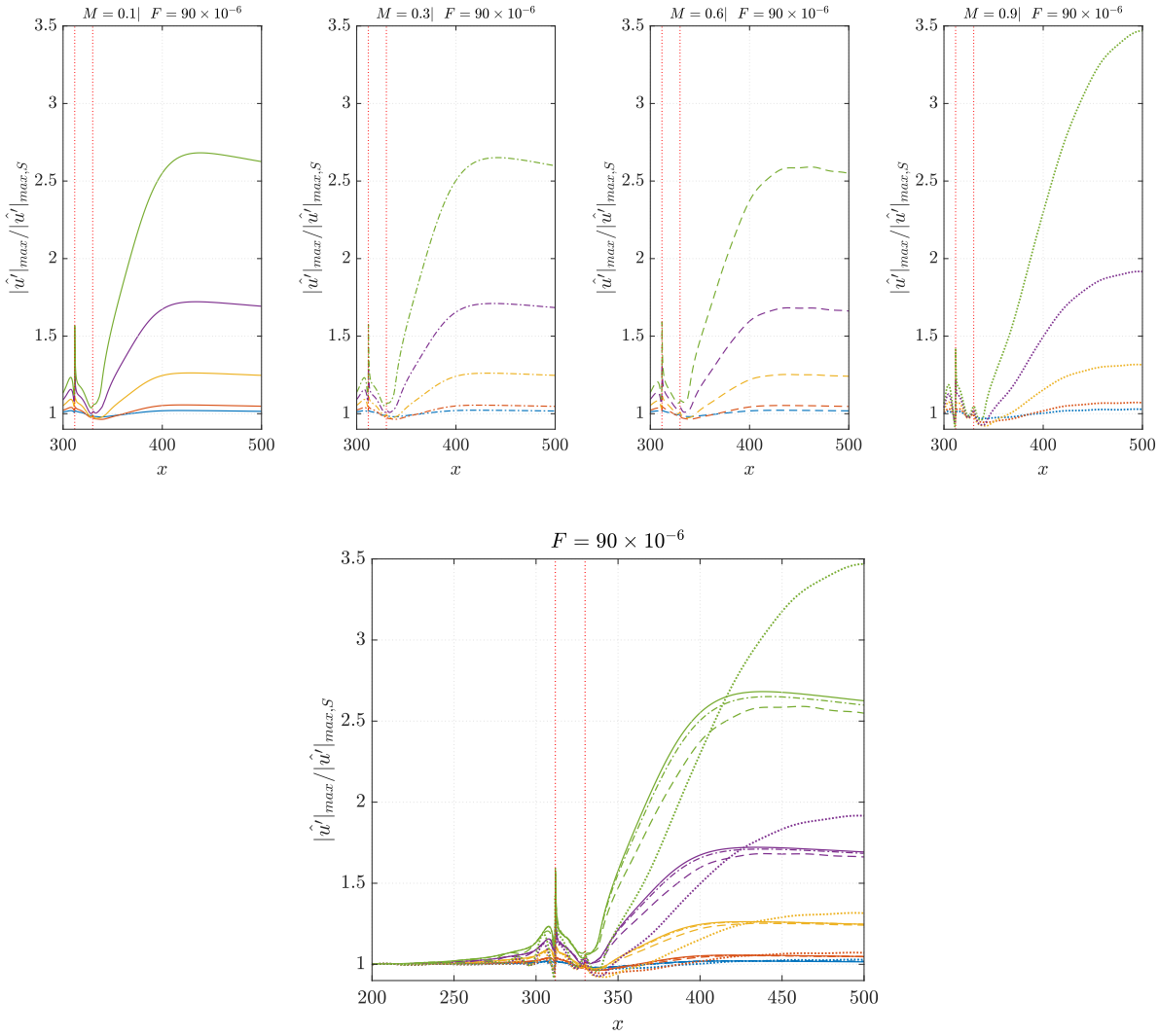


Figura 4.9: Amplitude evolution of the TS mode of $F = 90 \times 10^{-6}$ for different bump heights with varying Mach.

sented in figure 4.10. It shows the region of bump influence has only small changes caused by compressible effects for subsonic regime. For transonic the bump influence region becomes longer.

4.3.3 The effect of TS frequency

Figure 4.11 shows the effect of bumps of different heights for some TS frequencies and $M = 0.1$. As the frequency increases the relation of growth rate for bump and smooth cases becomes higher which means that the TS amplification is higher for high frequencies.

DISTRIBUTION A: Distribution approved for public release. Distribution unlimited

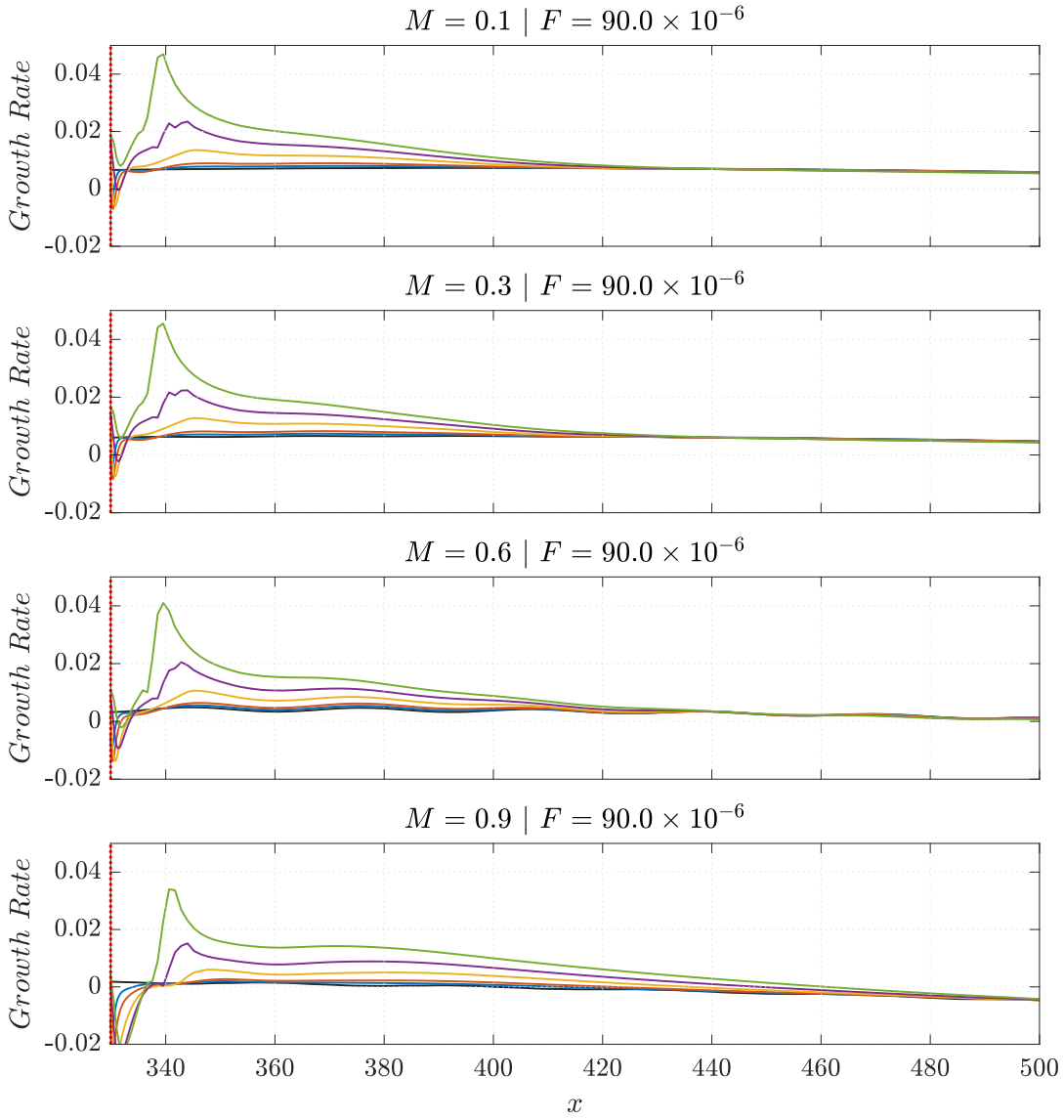


Figura 4.10: Mach effect on the T-S growth rate compared to the smooth plate.

Despite of that, the region of influence of bumps seems to be not affected with frequency change.

Figure 4.12 shows the combined effect of frequency and Mach change at a station far downstream ($x = 500$). The left column shows the spectral content of fluctuation for all simulated Mach numbers versus frequency. Right column shows the amplification of bump cases relative to smooth.

The higher the Mach number the lower is frequency of maximum amplification so the unstable band shifts to lower frequencies. Results also show the amplification of the unstable band becomes wider with bumps of heights over and equal to $h_R = 0.10$.

DISTRIBUTION A: Distribution approved for public release. Distribution unlimited

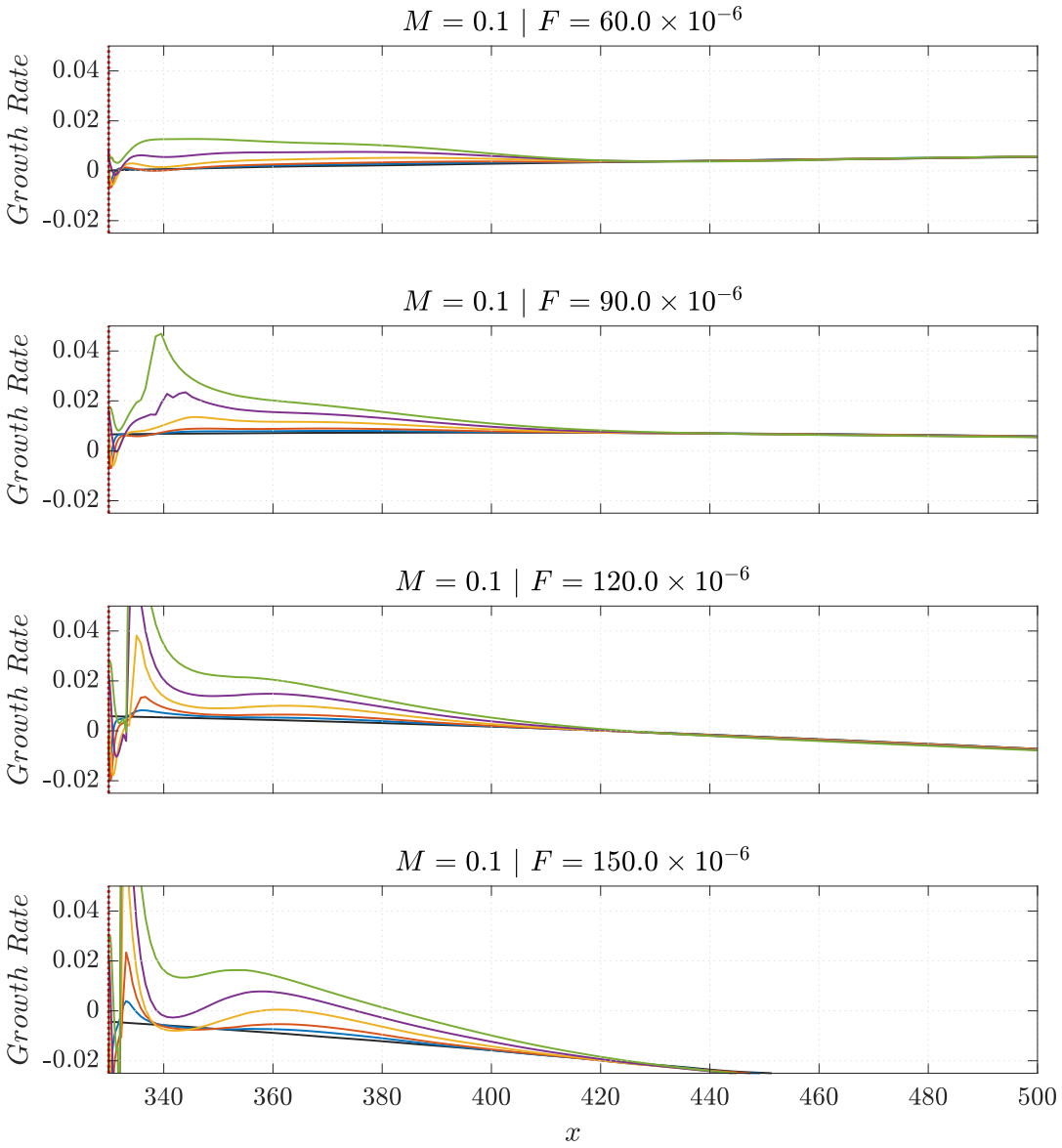


Figura 4.11: Effect of bumps on growth rate for different frequencies compared to the smooth plate.

It is noted that transonic regime presents the lowest amplification compared to lower Mach numbers but in other hand, this is also the condition in which the bumps most increase the relative amplification.

4.3.4 Region of influence of bumps and base flow

The growth rates showed in previous sections suggested that the effect of bumps on TS growth is constrained in some region. It would be interesting if the location where this

DISTRIBUTION A: Distribution approved for public release. Distribution unlimited

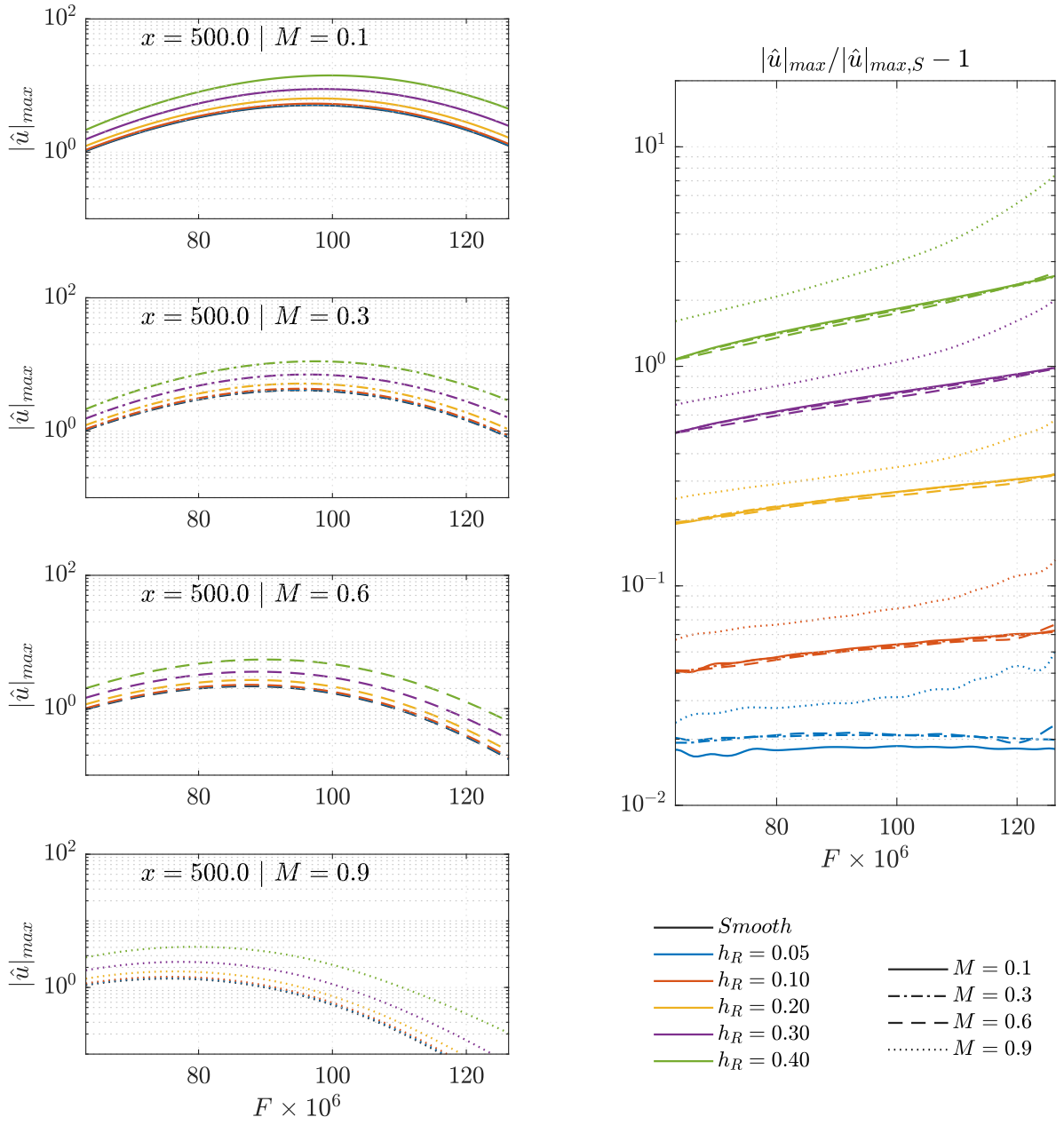


Figura 4.12: TS amplitude far downstream comparing the effect of the bump height with varying Mach number. Left plot values are normalized by amplitude at $x = 200$

effect vanishes can be tracked by just inspecting the base flow.

Candidates for this tracer are presented in figure 4.13 in which variables are plotted by considering the relative change caused by bumps. The shape factor seems to be a good option but this topic is still under investigation.

DISTRIBUTION A: Distribution approved for public release. Distribution unlimited

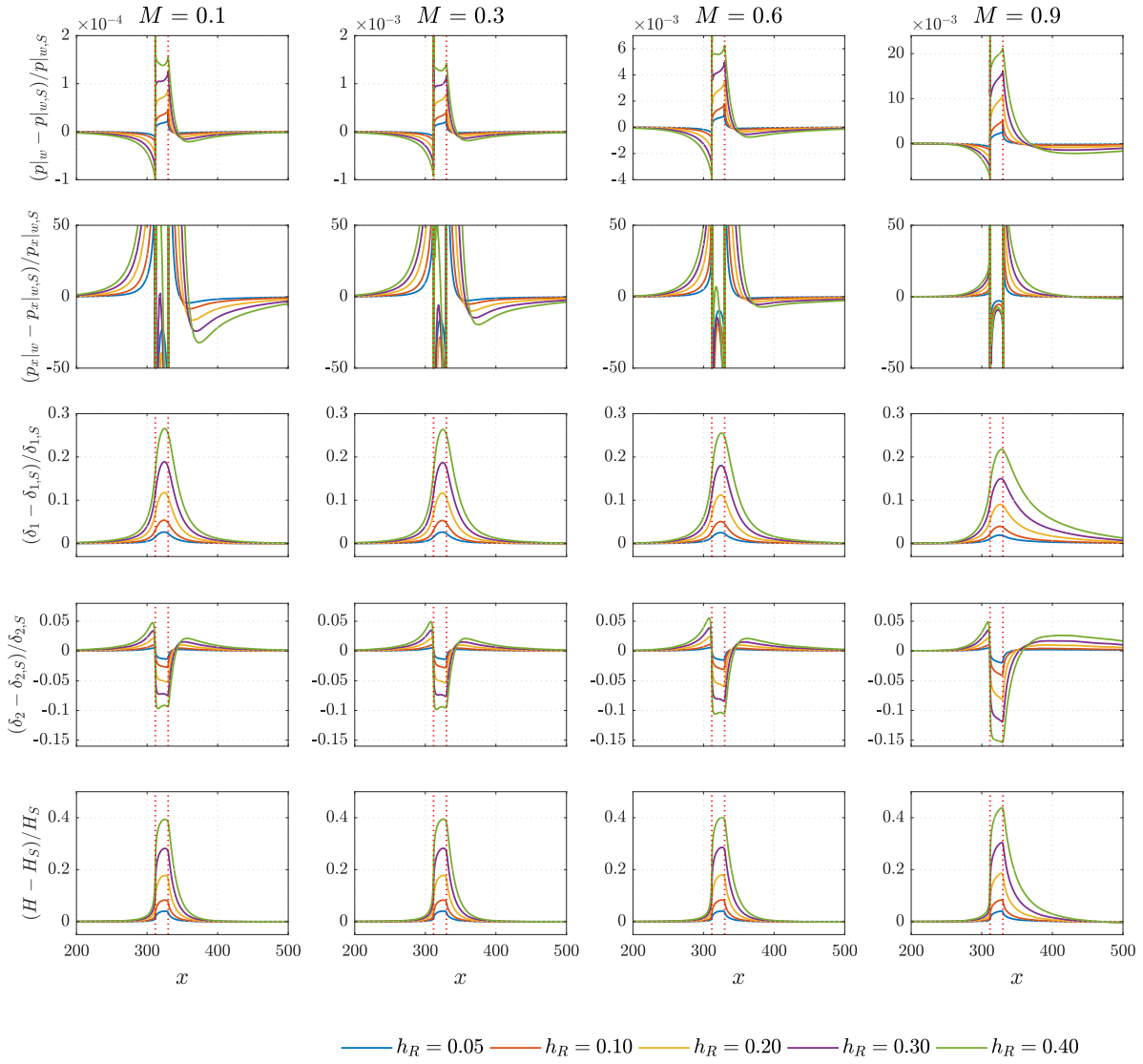


Figura 4.13: Base flow variables for different bump heights and Mach numbers relative to smooth.

4.4 Taylor-Stokes approximation

Since the grid refinement in the wall normal direction as well as the streamwise direction had to be very strong, we found this would lead to very large computational demands in 3D case of a TS wave interaction with an isolated roughness. To circumvent this difficulty we developed an approximate but very accurate methods to represent a small roughness in a numerical simulation.

For small enough bumps, the approximation method assumes the distortion caused by this element is localized and the velocity profile changes linearly compared to the smooth

DISTRIBUTION A: Distribution approved for public release. Distribution unlimited

case. Then, such an excrescence could be mimicked by applying a non-homogeneous boundary condition along the smooth plate wall. These conditions are simply obtained by a Taylor expansion of the velocity profiles provided either by a previous simulation or assuming the Blasius boundary layer:

$$u|_{wall} = -h_R \left.\frac{\partial u}{\partial y}\right|_{wall}, \qquad v|_{wall} = -h_R \left.\frac{\partial v}{\partial y}\right|_{wall}. \tag{4.1}$$

We further considered a transient correction to account to the local change caused by the TS on top of the bump. This done similarly to the done to base flow but the transient data is used instead. Another correction is made for the Stokes layer which is used to correct the excitation phase. It is needed to compensate the time that the transient condition introduced on the wall takes to reach the top of the mimicked bump.

Then, once the base flow is converged by using just the steady condition from 4.1, the TS excitation is introduced upstream and the transient correction is added to the steady wall conditions,

$$u(t)|_{wall} = u_0|_{wall} + \Re(f_{TS,Amp}\ f_{TS,\phi}) \tag{4.2}$$

with,

$$f_{TS,Amp} = |\hat{u'}|\ exp(i\omega t), \tag{4.3}$$

$$f_{TS,\phi} = exp(\ i(\ \phi\{\hat{u'}\} - \Delta_{stokes}\ h_R) - \Delta_{stokes}\ h_R), \tag{4.4}$$

$$\Delta_{stokes} = -\sqrt{\omega Re/2}, \tag{4.5}$$

where the amplitude and phase of fluctuation velocity are given by a previous TS run. If only the smooth plate is available there is no information of any bump but a second iteration with the first as input can provide a better approximation.

The first and second iteration are compared in figure 4.14 with the body-fitted bump and smooth as visual reference. The first approximation corrects some of the local effects but downstream, the amplitude is affected by wall conditions which decreases the TS amplitude downstream. The agreement with body-fitted is achieved in a second iteration for both local and downstream amplitude.

DISTRIBUTION A: Distribution approved for public release. Distribution unlimited

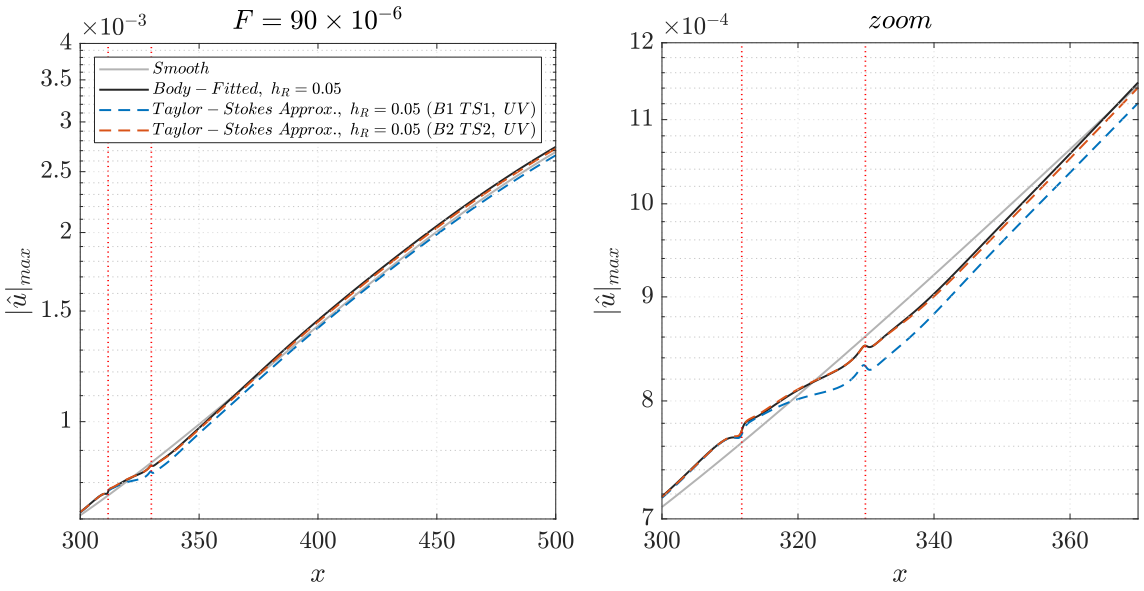


Figura 4.14: First and second iteration of Taylor-Stokes approximation compared to the body-fitted bump.

This result is consistent because by considering the smooth case as input, the flow information is mainly given by u velocity gradient as v component is negligible. The velocity gradients that occurs in the bump region is only provided after a first iteration.

The transient correction as it is proposed here is not considered in others studies. In figure 4.15 we compare the solutions obtained by considering just the steady state approximation and that in which the transient correction is accounted. Despite presenting a good estimate for the amplitude downstream, the case without correction is not capable to reproduce the local changes.

The main interest on the development of the Taylor-Stokes approximation relies in the fact that the simulation cost for simulating body-fitted bumps increases drastically due to Δy_{min} required. For an efficient approximation method same accuracy order must be provided by a coarser mesh. This analysis is presented by figure 4.16 which shows that error is lower than 1% for a mesh with $\Delta y_{min} = 0.05$ while the body-fitted requires $\Delta y_{min} = 0.01$.

DISTRIBUTION A: Distribution approved for public release. Distribution unlimited

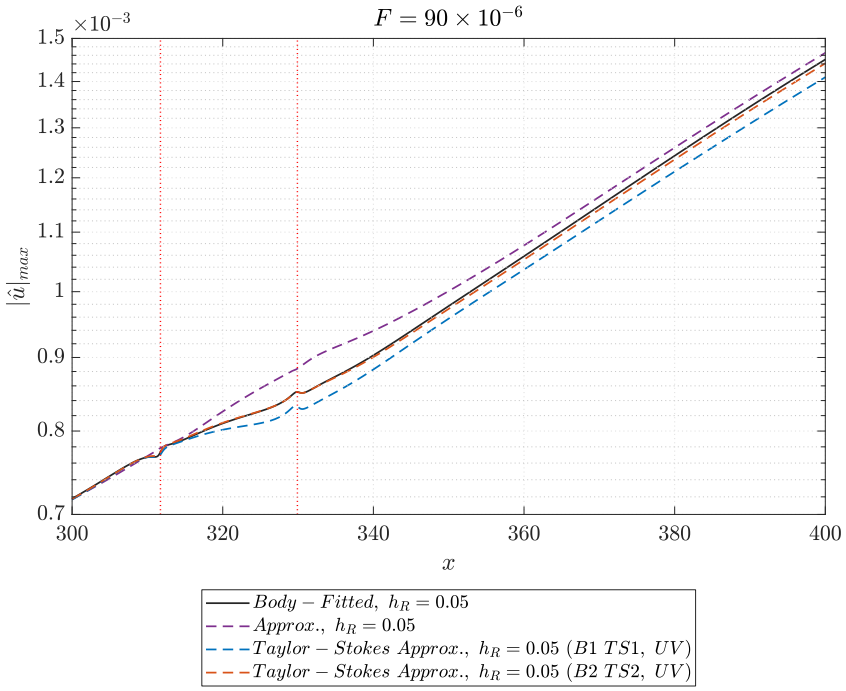


Figura 4.15: Effect of TS transient correction on local and downstream solution.

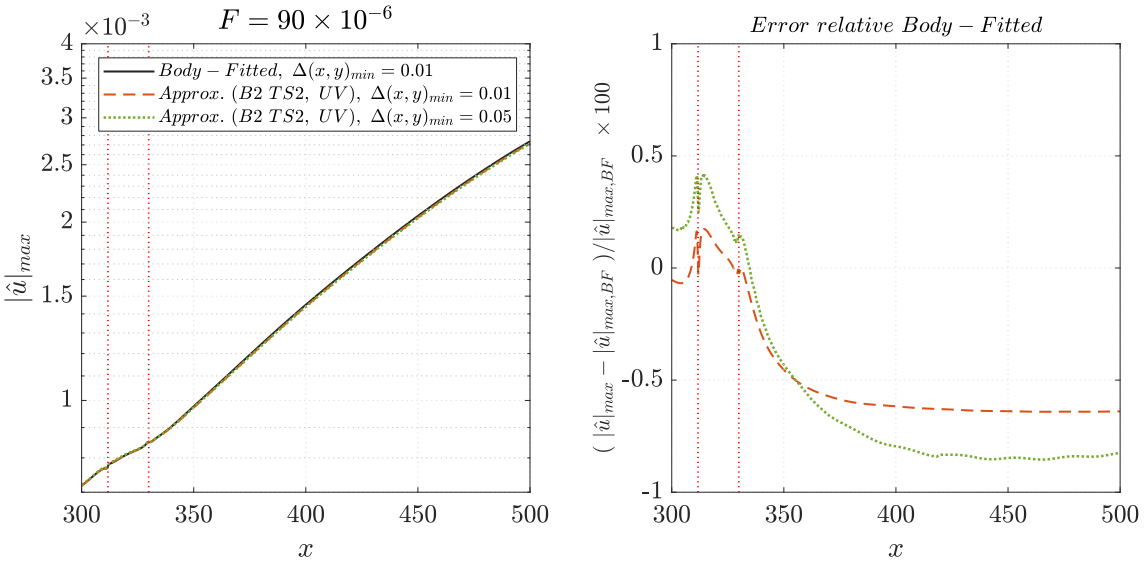


Figura 4.16: Mesh convergence analysis for approximation method. The most refined mesh case is the same as shown in figure 4.14.

DISTRIBUTION A: Distribution approved for public release. Distribution unlimited

5 Conclusions

The initial focus here was on the interaction of TS waves with a two dimensional bump. In this work-package this was intended both as a model for the effect of steps on transition and as a way towards the isolated roughness. Previous experiments developed in the group on the interaction between isolated roughness and TS waves showed that under some circumstances even the nominally smooth surface case (meaning the roughness completely retracted, height less than 1% the displacement thickness, δ_1), the roughness had a strong effect [53]. In that work this was associated with a critical amplitude of TS waves which triggered secondary instability at the roughness. It was further observed that the effect on the TS wave scaled linearly with the isolated roughness height only up to heights of 5%. Hence on the two dimensional scenario we also focused on small roughness. The small two dimensional bump has an also small effect on the evolution of a TS wave. A 5% high bump increases the amplitude of the TS wave by only 2.5%, which would be negligible for practical purposes. However, this is also a primary model for distributed roughness, which can have a large integrated effect. Hence, understanding this scenario is relevant.

- Accuracy requirements: The simulation of the interaction between a small bump and a TS wave has proven to be more difficult and more computational demanding than anticipated. Accurately capturing the 2.5% increase in amplitude of a TS wave caused by a roughness required a 10 fold increase in resolution in the wall normal direction and 100 fold in the streamwise direction, in comparison to smooth surfaces. These results improved upon previous less accurate numerical results of bump effect on TS wave and provided almost perfect agreement with carefully controlled experiments;

- Linear regime: The more accurate results indicated that the regime within which the bump height has a linear effect on the TS wave evolution in limited to about 10% (δ_1), whereas previous works suggested 40%. Above 10% the effect of the bump increases massively and at 40% it causes an increase of 170% in the TS wave amplitude;

- The two effects of the bump on the TS evolution. First there is an effect at the roughness, but there is also an effect at the bump wake. To establish the downs-

DISTRIBUTION A: Distribution approved for public release. Distribution unlimited

tream region over which the roughness had a effect, the growth rates were extracted from the DNS results with and without a bump, and compared. It was found that the waves require a substantial extent to return to what would be effectively its growth on a smooth surface. Somewhat unexpected, it was found that, within the roughness height range covered, the region affected by the roughness was almost independent on the bump height. Nevertheless, the effect within that region was very dependent on the bump height. The good accuracy of the simulations was fundamental for these conclusions;

- Downstream region of influence of the bump: It would be interesting to establish a region of influence based on the baseflow parameters and hence avoid the need to simulate the TS waves. Several parameters were considered, such as, the pressure gradient, the displacement and momentum thicknesses, the shape factor and the Falkner-Skan parameter. None of them offered a good indication of the region of influence and this topic is still under investigation;

- Compressibility effects: The influence of Mach number on the effect of a bump on the TS wave evolution has not been addressed systematically. Here it was found that Mach increases the effect of the bump. For example, for a bump height 40% at Mach $M = 0.1$, the TS wave amplitude increases by 160% whereas at $M = 0.9$, it increases by 250%. However the effect at the roughness is relatively small. The Mach effect is mostly a consequence of the downstream region affected by the bump, which increases substantially, in particular when approaching the transonic speeds. For example, from $M = 0.1$ to $M = 0.9$ the extent of this region increases two-fold;

- Influence of frequency: The influence of frequency on the effect of a bump on the TS wave evolution has been overlooked in the literature. We are left with the impression that it is assumed that this effect is negligible. We addressed this issue by investigating the interaction of pulse generated wavepackets with a bump. Theoretically, the pulse contains all frequencies. In practice it contains a large number of frequencies which in the linear regime behave independently. The packet can be made very small so as to behave linearly and, if the code is sufficiently accurate, the modes can be extracted from the packet to provide the influence of frequency. It was found that for bump heights below 10%, the effect was independent on frequency. Above it, the effect of the bump increased with the frequency. The frequency influence is larger at higher Mach numbers and higher bump heights. The difference within the range of unstable TS waves can amount to 100% increase in bump effect;

DISTRIBUTION A: Distribution approved for public release. Distribution unlimited

- Underlying physics: It is conjectured that the underlying physics is as follows. The effect of the bump has two origins, one at the bump itself, here referred to as bump effect, and the other associated with the wake, the wake effect. The bump effect is linear with respect to bump height, independent on the frequency and dominates at small heights. The roughness wake is thought to have an effect of the same nature as that of an adverse pressure gradient, albeit smaller. Indeed the profile in the wake leans towards that of an adverse pressure gradient. As the bump height increases the region affected by the roughness does not extend, but within this region the profile is substantially more distorted and produce much larger effects on the TS waves. As Mach increases, the wake region extends, intensifying the bump effect. The adverse pressure gradient has a small effect on the first branch of the boundary layer instability loop, but substantially increases the frequencies at the second branch. One effect of the adverse pressure gradient is then to increase the frequency of the dominant modes. The argument is consistent with a negligible influence of frequency for small bump heights and enhancement of higher frequencies in the nonlinear regime of the high bumps;

- New method for the simulation of small surface imperfections. The high demand on computational grid for the correct simulation of the effect of bump on the TS waves would pose even higher demands for the isolated roughness case, not only because a third dimension would be added, but also because strong refinement would also be needed in this direction. However, it should be possible to develop less demanding but sufficiently accurate methods to represent a 5% high roughness. The idea was to apply a condition at the wall that would enforce a no-slip and no penetration condition at the roughness top. This can be done using a Taylor expansion, and has been applied in some analytical approaches in fluid mechanics, among them, receptivity to acoustic waves. The approach can be viewed as an application of perturbation methods. The problem here was that in 2D the effect was very small and so required very high accuracy. This situation demanded several improvements on this technique. For instances the time lag (and amplitude decay) between the application of boundary condition at the wall and its effect at the roughness top position was important. To compensate for it a Stokes layer flow correction was implemented which precisely time advanced (and magnified) the boundary condition. These however was not sufficient and a second order approximation had to be used, in an approach that can be viewed as an application of iterative perturbation methods. For the 5%, the target for the 3D simulations, the approach was

DISTRIBUTION A: Distribution approved for public release. Distribution unlimited

very accurate, but degraded rapidly above it and was inadequate for 10%. It must also be considered that the isolated 3D case will be less demanding in accuracy for the reason that follows. For the 2D case the effect is an increase of about 2% in TS wave amplitude. Hence 2% error in amplitude may lead to 100% error in the estimation of this effect. The isolated roughness problem is one of receptivity of 3D waves from the 2D ones. Just in any receptivity problem, the aim is to estimate accurately the amplitude of the resulting initial wave, here the oblique TS wave. In this problem, a 2% error in TS wave amplitude imparts a similar level of inaccuracy to the problem;

- Isolated roughness problem. With the difficulties faced we were not yet able to simulate the interaction between a TS wave and an isolated roughness. We have support from another agency for the PhD student that was responsible for this workpackage. The simulations are under way and we intend to report to AFOSR within a year.

DISTRIBUTION A: Distribution approved for public release. Distribution unlimited

Events and Publications

- **AIAA AVIATION Forum**: *American Institute of Aeronautics and Astronautics, Aviation Forum and Exposition, 2021*, EUA. Title: *DNS of a Tollmien-Schlichting Wave Interacting with a Roughness Modeled via Body-fitted and Approximation Methods*;

- **XXV ICTAM**: *XLI Ibero-Latin-American Congress on Computational Methods in Engineering*, Milan, Italy. Title: *On the simulation of TS waves over very small isolated roughness and its results*;

- **COBEM 2021**: *26th International Congress of Mechanical Engineering*, Brazil. Title: *Receptivity of acoustic waves on localized roughness in compressible laminar boundary layer*;

- **COBEM 2021**: *26th International Congress of Mechanical Engineering*, Brazil. Title: *Compressible Direct Numerical Simulation of Tollmien-Schlichting waves interacting with a two-dimensional isolated roughness*;

- **CILAMCE 2020**: *XLI Ibero-Latin-American Congress on Computational Methods in Engineering*, Foz do Iguaçu, PR, Brazil. Title: *DNS of a small roughness immersed in a boundary layer: body-fitted and approximated methods comparison*. Proceedings of the Ibero-Latin-American Congress on Computational Methods in Engineering, ISSN 2675-6269;

- **ENCIT 2020**: *18th Brazilian Congress of Thermal Sciences and Engineering*, Brazil. Title: *Numerical simulation of Tollmien-Schlichting waves interacting with a three-dimensional and isolated roughness*;

- **EPTT 2020**: *XII Spring School on Transition ans Turbulence, 2020*, Brazil. Title: *A study on three-dimensional and isolated roughness induced transition*;

- **EPTT 2020**: *XII Spring School on Transition ans Turbulence, 2020*, Brazil. Title: *On the receptivity of acoustic waves over localized roughness in compressible boundary layer*;

DISTRIBUTION A: Distribution approved for public release. Distribution unlimited

- **COBEM 2019**: *25th International Congress of Mechanical Engineering*, Uberlandia, Parana, Brazil. Título: *Direct Numerical Simulation of Wave Packets over a Rough Flat Plate*. DOI: 10.26678/ABCM.COBEM2019.COB2019-1154;
- ***IUTAM 2019***: *International Union of Theoretical and Applied Mechanics - Symposium on Laminar-Turbulent Transition 2019*, London, UK. Title: *On Subharmonic Resonance and other Nonlinear Mechanisms in Wavepackets in Boundary Layers*;

DISTRIBUTION A: Distribution approved for public release. Distribution unlimited

References

[1] BOEING: 787 By Design: Superior Technology. 2020. https://www.boeing.com/commercial/787/by-design/#/superior-tech. Accessed: 2020-06.

[2] HONDA Global | Design Innovation. 2020. https://global.honda/products/HondaJet/innovation.html. Accessed: 2020-06.

[3] THIBERT, J.; ARNAL, D. A review of ONERA aerodynamic research in support of a future supersonic transport aircraft. *Progress in Aerospace Sciences*, v. 36, n. 8, p. 581–627, nov 2000. ISSN 03760421. Disponível em: <http://linkinghub.elsevier.com/retrieve/pii/S0376042100000105>.

[4] KAYNAK, Ü.; GÜRDAMAR, E. Boundary-Layer Transition Under the Effect of Compressibility for the Correlation Based Transition Model. In: *46th AIAA Aerospace Sciences Meeting and Exhibit*. Reston, Virigina: American Institute of Aeronautics and Astronautics, 2008. p. 1–9. ISBN 978-1-62410-128-1. Disponível em: <http://arc.aiaa.org/doi/10.2514/6.2008-774>.

[5] MORKOVIN, M. V. On the many faces of transition. In: *Viscous drag reduction*. [S.l.]: Springer, 1969. p. 1–31.

[6] SARIC, W. S.; REED, H. L.; KERSCHEN, E. J. Boundary-Layer Receptivity to Freestream Disturbances. *Annual Review of Fluid Mechanics*, v. 34, n. 1, p. 291–319, jan 2002. ISSN 0066-4189. Disponível em: <http://www.annualreviews.org/doi/10.1146/annurev.fluid.34.082701.161921>.

[7] MORKOVIN, M. Transition in open flow systems: a reassessment. *Bull. Am. Phys. Soc.*, v. 39, p. 1882, 1994.

[8] FEDOROV, A. Transition and stability of high-speed boundary layers. *Annual review of fluid mechanics*, Annual Reviews, v. 43, p. 79–95, 2011.

[9] KACHANOV, Y. S. Physical mechanisms of laminar-boundary-layer transition. *Annual review of fluid mechanics*, Annual Reviews 4139 El Camino Way, PO Box 10139, Palo Alto, CA 94303-0139, USA, v. 26, n. 1, p. 411–482, 1994.

DISTRIBUTION A: Distribution approved for public release. Distribution unlimited

[10] ORR, W. M. The stability or instability of the steady motions of a perfect liquid and a viscous liquid. part i: A perfect liquid; part ii: A viscous liquid. In: *Proceedings of the Royal Irish Academy*. [S.l.: s.n.], 1907.

[11] SOMMERFELD, A. Ein Beitrag zur hydrodynamischen Erklaerung der turbulenten Fluessigkeitsbewegungen. In: *Proceedings of the 4th International Congress of Mathematicians*. [S.l.: s.n.], 1908. p. 116–124.

[12] TOLLMIEN, W. Über die entstehung der turbulenz. 1. mitteilung. *Nachrichten von der Gesellschaft der Wissenschaften zu Göttingen, Mathematisch-Physikalische Klasse*, v. 1929, p. 21–44, 1928.

[13] SCHLICHTING, H. Zur enstehung der turbulenz bei der plattenströmung. *Nachrichten von der Gesellschaft der Wissenschaften zu Göttingen, Mathematisch-Physikalische Klasse*, v. 1933, p. 181–208, 1933.

[14] SCHUBAUER, G. B.; SKRAMSTAD, H. K. *Laminar Boundary Layer Oscillations and Stability of Laminar Flow*. [S.l.], 1943.

[15] HOUGHTON, E. L. et al. *Aerodynamics for Engineering Students*. Elsevier Science, 2012. ISBN 9780080966335. Disponível em: <https://books.google.com.br/books?id=rA6mIXaF69kC>.

[16] MARTINEZ, A. *Towards natural transition in compressible boundary layers*. Tese (PhD. thesis) — University of São Paulo, 2016.

[17] KLEBANOFF, P.; TIDSTROM, K. Mechanism by which a two-dimensional roughness element induces boundary-layer transition. *The Physics of Fluids*, American Institute of Physics, v. 15, n. 7, p. 1173–1188, 1972.

[18] HAMA, F. R.; LONG, J. D.; HEGARTY, J. C. On transition from laminar to turbulent flow. *Journal of Applied Physics*, American Institute of Physics, v. 28, n. 4, p. 388–394, 1957.

[19] BENNEY, D. J.; LIN, C. C. On the secondary motion induced by oscillations in a shear flow. *Physics of Fluids*, v. 3, n. 4, p. 656–657, 1960. Disponível em: <http://pof.aip.org/resource/1/pfldas/v3/i4/p656_s1>.

[20] BENNEY, D. A non-linear theory for oscillations in a parallel flow. *Journal of Fluid Mechanics*, Cambridge University Press, v. 10, n. 2, p. 209–236, 1961.

DISTRIBUTION A: Distribution approved for public release. Distribution unlimited

[21] STUART, J. On the non-linear mechanics of wave disturbances in stable and unstable parallel flows part 1. the basic behaviour in plane poiseuille flow. *Journal of Fluid Mechanics*, Cambridge Univ Press, v. 9, n. 03, p. 353–370, 1960.

[22] CRAIK, A. D. D. *Non-linear resonant instability in boundary layers*. 1971. 393 p.

[23] KACHANOV, Y. S.; KOZLOV, V.; LEVCHENKO, V. Y. Nonlinear development of a wave in a boundary layer. *Fluid dynamics*, Springer, v. 12, n. 3, p. 383–390, 1977.

[24] KACHANOV, Y. S.; LEVCHENKO, V. Y. The resonant interaction of disturbances at laminar-turbulent transition in a boundary layer. *Journal of Fluid Mechanics*, Cambridge University Press, v. 138, p. 209–247, 1984.

[25] SARIC, W.; THOMAS, A. Experiments on the subharmonic route to turbulence in boundary layers. *tcpf*, p. 117–122, 1984.

[26] HERBERT, T. Secondary instability of boundary layers. *Annual Review of Fluid Mechanics*, Annual Reviews 4139 El Camino Way, PO Box 10139, Palo Alto, CA 94303-0139, USA, v. 20, n. 1, p. 487–526, 1988.

[27] KLEBANOFF, P.; TIDSTROM, K.; SARGENT, L. The three-dimensional nature of boundary-layer instability. *Journal of Fluid Mechanics*, Cambridge Univ Press, v. 12, n. 01, p. 1–34, 1962.

[28] BESTEK, H.; THUMM, A.; FASEL, H. Direct numerical simulation of the three-dimensional breakdown to turbulence in compressible boundary layers. In: SPRINGER. *Thirteenth International Conference on Numerical Methods in Fluid Dynamics*. [S.l.], 1993. p. 145–149.

[29] SCHMID, P.; HENNINGSON, D. A new mechanism for rapid transition involving a pair of oblique waves. *Physics of Fluids A: Fluid Dynamics*, American Institute of Physics, v. 4, n. 9, p. 1986–1989, 1992.

[30] SCHMID, P.; REDDY, S.; HENNINGSON, D. Transition thresholds in boundary layer and channel flows. In: *Advances in turbulence VI*. [S.l.]: Springer, 1996. p. 381–384.

[31] MAYER, C. S. J.; TERZI, D. A. V.; FASEL, H. F. Direct numerical simulation of complete transition to turbulence via oblique breakdown at mach 3. *Journal of Fluid Mechanics*, Cambridge University Press, v. 674, p. 5–42, 2011.

DISTRIBUTION A: Distribution approved for public release. Distribution unlimited

[32] MAYER, C. S.; WERNZ, S.; FASEL, H. F. Numerical investigation of the nonlinear transition regime in a mach 2 boundary layer. *Journal of fluid mechanics*, Cambridge University Press, v. 668, p. 113, 2011.

[33] SHAIKH, F. *Turbulent spots in a transitional boundary layer.* Tese (Doutorado) — University of Cambridge, 1993.

[34] SHAIKH, F. N.; GASTER, M. The non-linear evolution of modulated waves in a boundary layer. *Journal of Engineering Mathematics*, v. 28, n. 1, p. 55–71, 1994. ISSN 0022-0833.

[35] GOSTELOW, J.; THOMAS, R. Effects of strong adverse pressure gradients and incident wakes on transition and calming. In: SPRINGER. *IUTAM Symposium on Laminar-Turbulent Transition*. [S.l.], 2006. p. 133–138.

[36] GASTER, M.; GRANT, I. *An Experimental Investigation of the Formation and Development of a Wave Packet in a Laminar Boundary Layer*. 1975. 253–269 p.

[37] GASTER, M. A theoretical model of a wave packet in the boundary layer on a flat plate. *Proceedings of the Royal Society of London. A. Mathematical and Physical Sciences*, The Royal Society London, v. 347, n. 1649, p. 271–289, 1975.

[38] GASTER, M. The physical processes causing breakdown to turbulence. In: *12th Naval Hydrodynamics Symposium, Washington*. [S.l.: s.n.], 1978.

[39] COHEN, J.; BREUER, K. S.; HARITONIDIS, J. H. On the evolution of a wave packet in a laminar boundary layer. *Journal of fluid mechanics*, Cambridge University Press, v. 225, p. 575–606, 1991.

[40] COHEN, J. The initial evolution of a wave packet in a laminar boundary layer. *Physics of Fluids*, American Institute of Physics, v. 6, n. 3, p. 1133–1143, 1994.

[41] BECH, K. H.; HENNINGSON, D. S.; HENKES, R. A. Linear and nonlinear development of localized disturbances in zero and adverse pressure gradient boundary-layers. *Physics of Fluids*, American Institute of Physics, v. 10, n. 6, p. 1405–1418, 1998.

[42] MEDEIROS, M. A.; GASTER, M. The production of subharmonic waves in the nonlinear evolution of wavepackets in boundary layers. *Journal of Fluid Mechanics*, Cambridge University Press, v. 399, p. 301–318, 1999.

DISTRIBUTION A: Distribution approved for public release. Distribution unlimited

[43] MEDEIROS, M. A.; GASTER, M. The influence of phase on the nonlinear evolution of wavepackets in boundary layers. *Journal of Fluid Mechanics*, Cambridge University Press, v. 397, p. 259–283, 1999.

[44] MEDEIROS, M. A. The nonlinear evolution of a wavetrain emanating from a point source in a boundary layer. *Journal of Fluid Mechanics*, Cambridge University Press, v. 508, p. 287–317, 2004.

[45] TANI, I.; HAMA, R.; MITUISI, S. On the permissible roughness in the laminar boundary layer. *title Report of Aeronautical Research Institute, Tokyo Imperial University*, v. 15, n. 199, p. 417, 1940.

[46] TANI, I. Effect of two-dimensional and isolated roughness on laminar flow. In: *Boundary layer and flow control*. [S.l.]: Elsevier, 1961. p. 637–656.

[47] SUMARIVA, J. A. F.; HEIN, S.; VALERO, E. On the influence of two-dimensional hump roughness on laminar-turbulent transition. *Physics of Fluids*, AIP Publishing LLC, v. 32, n. 3, p. 034102, 2020.

[48] WORNER, A.; RIST, U.; WAGNER, S. Humps/steps influence on stability characteristics of two-dimensional laminar boundary layer. *Aiaa J.*, v. 41, n. 2, p. 192–197, 2003. ISSN 0001-1452.

[49] WANG, Y.; GASTER, M. Effect of surface steps on boundary layer transition. *Experiments in Fluids*, Springer, v. 39, n. 4, p. 679–686, 2005.

[50] CHOUDHARI, M.; STREETT, C. L. A finite reynolds-number approach for the prediction of boundary-layer receptivity in localized regions. *Physics of Fluids A: Fluid Dynamics*, American Institute of Physics, v. 4, n. 11, p. 2495–2514, 1992.

[51] CROUCH, J. Localized receptivity of boundary layers. *Physics of Fluids A: Fluid Dynamics*, American Institute of Physics, v. 4, n. 7, p. 1408–1414, 1992.

[52] GOLDSTEIN, M. E. Scattering of acoustic waves into tollmien-schlichting waves by small streamwise variations in surface geometry. *Journal of Fluid Mechanics*, Cambridge University Press, v. 154, p. 509–529, 1985.

[53] PAULA, I. de et al. Interaction of instability waves and a three-dimensional roughness element in a boundary layer. *Journal of Fluid Mechanics*, Cambridge University Press, v. 824, p. 624, 2017.

DISTRIBUTION A: Distribution approved for public release. Distribution unlimited

[54] BREUER, K. S. et al. Linear and nonlinear evolution of boundary layer instabilities generated by acoustic-receptivity mechanisms. *Physics of Fluids*, American Institute of Physics, v. 8, n. 6, p. 1415–1423, 1996.

[55] PAULA, I. D.; WURZ, W.; MEDEIROS, M. Experimental study of a tollmien–schlichting wave interacting with a shallow 3d roughness element. *Journal of Turbulence*, Taylor & Francis, n. 9, p. N7, 2008.

[56] PESKIN, C. S. Numerical analysis of blood flow in the heart. *Journal of computational physics*, Elsevier, v. 25, n. 3, p. 220–252, 1977.

[57] GOLDSTEIN, D.; HANDLER, R.; SIROVICH, L. Modeling a no-slip flow boundary with an external force field. *Journal of computational physics*, Elsevier, v. 105, n. 2, p. 354–366, 1993.

[58] TERZI, D. V. et al. Immersed boundary techniques for high-order finite-difference methods. In: *15th AIAA Computational Fluid Dynamics Conference*. [S.l.: s.n.], 2001. p. 2918.

[59] COLLIS, S. S.; LELE, S. K. Receptivity to surface roughness near a swept leading edge. *Journal of Fluid Mechanics*, Citeseer, v. 380, p. 141–168, 1999.

[60] SCHRADER, L.-U.; BRANDT, L.; HENNINGSON, D. S. Receptivity mechanisms in three-dimensional boundary-layer flows. *Journal of Fluid Mechanics*, v. 618, n. 1, p. 209–241, 2009.

[61] SCHRADER, L.-U.; AMIN, S.; BRANDT, L. Transition to turbulence in the boundary layer over a smooth and rough swept plate exposed to free-stream turbulence. *Journal of fluid mechanics*, Cambridge University Press, v. 646, p. 297, 2010.

[62] RIZZETTA, D. P. et al. Direct numerical simulation of discrete roughness on a swept-wing leading edge. *AIAA journal*, v. 48, n. 11, p. 2660–2673, 2010.

[63] LELE, S. K. Compact finite difference schemes with spectral-like resolution. *Journal of computational physics*, Elsevier, v. 103, n. 1, p. 16–42, 1992.

[64] GAITONDE, D.; SHANG, J. High-order finite-volume schemes in wave propagation phenomena. In: *27th Plasma Dynamics and Lasers Conference*. [S.l.: s.n.], 1996. p. 2335.

DISTRIBUTION A: Distribution approved for public release. Distribution unlimited

[65] GAITONDE, D. V.; VISBAL, M. R. *High-Order Schemes for Navier-Stokes Equations: Algorithm and Implementation Into FDL3DI*. [S.l.], 1998.

[66] ÅKERVIK, E. et al. Steady solutions of the Navier-Stokes equations by selective frequency damping. *Physics of Fluids*, v. 18, n. 6, p. 068102, 2006. ISSN 10706631. Disponível em: <http://scitation.aip.org/content/aip/journal/pof2/18/6/10.1063/1.2211705>.

[67] LI, N.; LAIZET, S. 2DECOMP & FFT-A Highly Scalable 2D Decomposition Library and FFT Interface. *Cray User Group 2010 conference*, p. 1–13, 2010.

[68] BERGAMO, L. F. et al. Compressible modes in a square lid-driven cavity. *Aerospace Science and Technology*, Elsevier, v. 44, p. 125–134, 2015.

[69] MARTÍNEZ, A. G.; GENNARO, E. M.; MEDEIROS, M. A. Wavepackets in boundary layers close to transonic speeds. *Procedia IUTAM*, Elsevier, v. 14, p. 374–380, 2015.

[70] MARTINEZ, A. G.; MEDEIROS, M. A. Direct numerical simulation of a wavepacket in a boundary layer at mach 0.9. In: *46th AIAA Fluid Dynamics Conference*. [S.l.: s.n.], 2016. p. 3195.

[71] MATHIAS, M. S. *Instability analysis of compressible flows over open cavities by a Jacobian-free numerical method*. Tese (Master Thesis) — Universidade de São Paulo, São Carlos, 2017.

[72] MATHIAS, M. S.; MEDEIROS, M. Direct numerical simulation of a compressible flow and matrix-free analysis of its instabilities over an open cavity. *Journal of Aerospace Technology and Management*, SciELO Brasil, v. 10, 2018.

[73] JUNIPER, M. P.; HANIFI, A.; THEOFILIS, V. Modal Stability Theory Lecture notes from the FLOW-NORDITA Summer School on Advanced Instability Methods for Complex Flows, Stockholm, Sweden, 2013 1. *Applied Mechanics Reviews*, v. 66, n. 2, p. 021004, mar 2014. ISSN 0003-6900. Disponível em: <http://appliedmechanicsreviews.asmedigitalcollection.asme.org/article.aspx?doi=10.1115/1.402660

[74] HIMENO, F. H.; MATHIAS, M.; MEDEIROS, M. Dns of a tollmien-schlichting wave interacting with a roughness modeled via body-fitted and approximation methods. In: _____. *AIAA AVIATION 2021 FORUM*. [s.n.], 2021. Disponível em: <https://arc.aiaa.org/doi/abs/10.2514/6.2021-2500>.

DISTRIBUTION A: Distribution approved for public release. Distribution unlimited

[75] JUNIPER, M. P.; HANIFI, A.; THEOFILIS, V. Modal Stability Theory. *Applied Mechanics Reviews*, v. 66, n. 2, p. 021004, 2014. ISSN 0003-6900. Disponível em: <http://appliedmechanicsreviews.asmedigitalcollection.asme.org/article.aspx?doi=10.1115/1.402660

DISTRIBUTION A: Distribution approved for public release. Distribution unlimited

Appendix 4

DISTRIBUTION A: Distribution approved for public release. Distribution unlimited

AFOSR Research Report: Experimental activities

University of São Paulo

São Carlos School of Engineering

Post-Graduate Program of Mechanical Engineering

Supervisor: Prof. Dr. Marcello Augusto Faraco de Medeiros

São Carlos, SP

2022

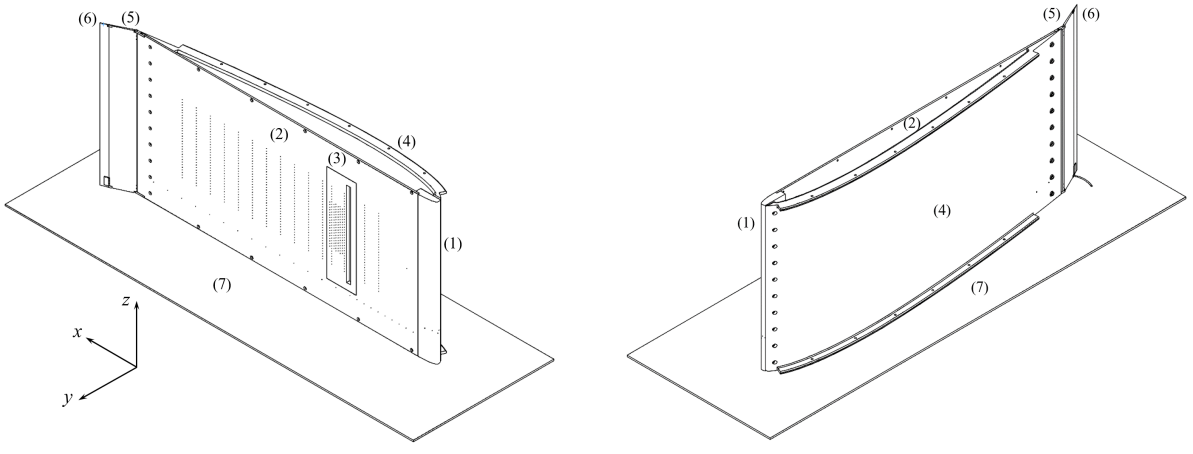
DISTRIBUTION A: Distribution approved for public release. Distribution unlimited

1 Experimental setup

As shown in Figura 1, the model designed for future experiments is composed of a series of components. Each component has a specific purpose to the flow requirements of the study of the boundary layer transition induced by a small gap with interchangeable geometry. The complete assembly of the model forms an aerodynamic profile inspired by the 4-digit NACA airfoil. The high-pressure side of the airfoil is the surface of interest and consequently where the experiments will occur.

The leading edge, item (1) of Figura 1, is the region of stagnation due to the deceleration of the incident flow. It is where the boundary layer emerges. The flat plate, item (2), comprises the entire extent of the model, where the boundary layer, the object of study, will evolve. The interchangeable cavity system, item (3), coupled to the flat plate, houses the mechanisms needed to alter the geometry. Its lid is installed flush with the flat plate surface. As the system has a considerable volume attached to the plate, we designed a smooth aerodynamic fairing, item (4), to prevent flow incidence directly over the cavity system. Finally, two control surfaces attached to the model's trailing edge allow the fine-tuning of the pressure distribution, the flap, and tab, item (5) and (6), respectively. The following sub-sections reveal the details of each element.

Figure 1 – Isometric view of the experimental rig. (1) Leading-edge; (2) Flat plate; (3) Cavity system; (4)Fairing; (5) Flap; (6) Tab; (7) Wind tunnel's test section floor.



(a) Top-side.

(b) Opposite-side.

1.1 Flat plate

The experimental setup is centered on the flat plate. The plate has dimensions of 2000 mm x 999 mm x 10 mm and is positioned vertically in the test section. The width of

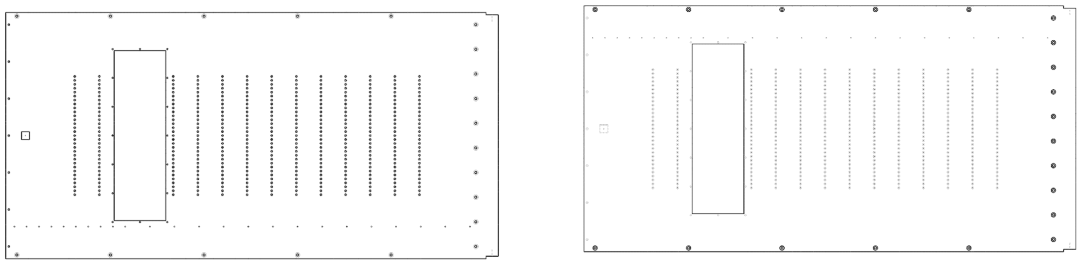
DISTRIBUTION A: Distribution approved for public release. Distribution unlimited

the plate was selected based on the height of the test chamber, being slightly smaller to allow fitting without deforming it. The plate's length is important for studying the final stages of the transition. According to **??**), the natural transition occurs at values close to $Re_x = 2.5 \cdot 10^6$, so it is important to have a plate with a length capable of reaching this value.

After careful analysis, the material chosen for the manufacture of the plate was aluminum. This material has good mechanical resistance, is considerably light in weight, important for handling the part during installation, and allows for a surface finish that maintains surface roughness within acceptable values. The selected material, together with the surface finishing process, is capable of producing a surface roughness around 3.2 μm, a value considered adequate for the experiments in question.

Figura 2 displays the drawings of the top view sides of the flat plate. In Figura 2a, the opposite face, where the boundary layer develops, whereas in Figura 2b, the representative side.

Figure 2 – Mechanical drawings exhibiting the top-view of the flat plate.



(a) Opposite side.

(b) Representative side.

The plate has a rectangular slot where the cavity system is fixed. At 200 mm from the front edge, there is a square hollow. Such a niche is a loudspeaker compartment containing 7 through holes arranged in a hexagonal shape with a central hole. These perforations have a diameter of 0.3 mm and their function is to transmit to the boundary layer an acoustic pressure induced by the loudspeaker membrane. This technique is used to introduce perturbations in the boundary layer, as **??**), Medeiros e Gaster (1999), Medeiros e Gaster (1999) and Medeiros (2004). The diameter of these holes was selected to cause minimal deformity on the boundary layer.

A line of static pressure taps parallel to the centerline, consisting of 24mm holes with 0.5mm diameter on the representative side, allows the static pressure measurements over the model, to adjust the pressure distribution. On the trailing edge, a system with a flap and tab is present. Note 2 undercuts on the rear corners, on both sides, for coupling this system. Such aerodynamic control surfaces allow adjustment of the pressure distribution over the plate. The actuation of these surfaces is carried out outside the tunnel, through a mechanism. Thus, the pressure distribution can be easily adjusted without the need to

DISTRIBUTION A: Distribution approved for public release. Distribution unlimited

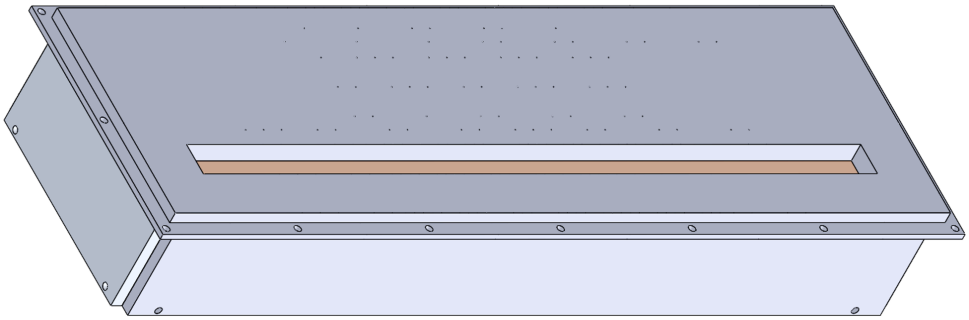
interrupt the wind tunnel operation.

The plate has 403 holes, which are housings for microphones. These niches are arranged in a matrix of 31×13, with a distance between holes of 16mm and 100mm between columns. The housings consist of two concentric holes with different diameters. The smaller diameter is 0.3mm in diameter and 1mm deep. This opening is intended to capture the pressure on the model. The largest has a diameter of 7 mm and allows coupling the microphones directly in the model. Such arrangement was conceived to capture, through pressure fluctuations, how the disturbances are distributed in the span-wise direction and stream-wise as well. According to Tsuji et al. (2007), this variation in diameters causes acoustic resonance, which introduces measurement errors in the reading of the microphones. However, the choice of dimensions followed its recommendations to attenuate such measurement error and shift the Helmholtz resonant frequency in the high-frequency range, that is, far from the unstable frequency band of the boundary layer.

1.2 Gap system

The cavity is a piece from a system composed of several components. This system, shown in Figura 3, has a box, a lid, the cavity bottom, mechanical stops, linear rail, and two stepper motors.

Figure 3 – Isometric view of cavity system.

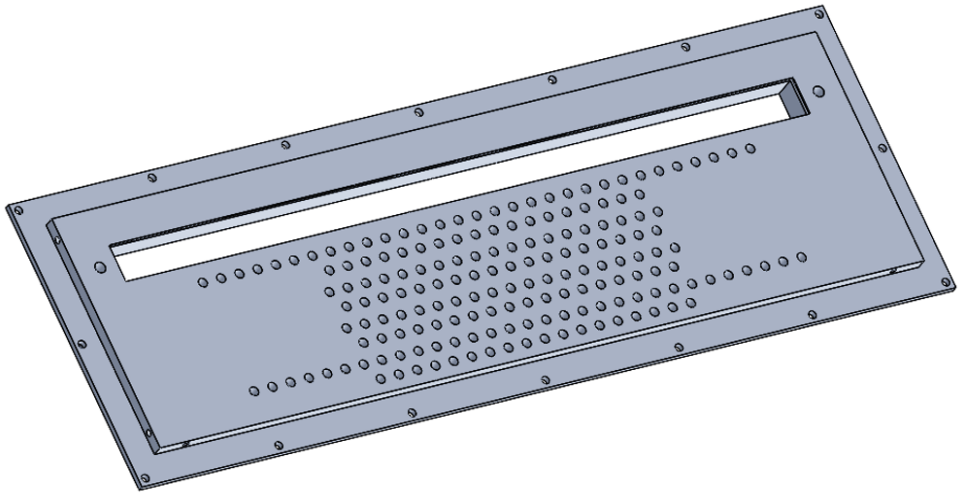


The box is only responsible for housing the system components. The lid is installed on the opposite side, with a flush attachment, thus avoiding unwanted protrusions on the surface of the model. Figura 4 displays the isometric view of the lid. The dimensions of the lid core are nominally equal to the dimensions of the flat plate slot and are 25mm thick. In the core, another cut, this being the sidewalls of the cavity. This slot has dimensions of 600 mm $\times$ 30 mm, which correspond to the cavity width (b) and the cavity length in the flow direction (L). Width has a value much greater than length, to avoid three-dimensional effects in the cavity flow, particularly in its central region. The sidewalls of this slot have a small gap to include a gasket, sealing the cavity. Furthermore, there are two blind holes, responsible for housing the linear rails.

DISTRIBUTION A: Distribution approved for public release. Distribution unlimited

The lid has 172 holes, with equivalent dimensions and functions as the flat plate microphone niches. However, two different arrangements are present on the lid. The first complete the arrangement of the flat plate with the cover installed on it. The second arrangement comprises rows with 18 and 19 staggered holes. This microphone array placed just downstream of the cavity is strategically positioned to capture flow structures convected from the cavity.

Figure 4 – Isometric view of cavity system lid.



The cavity floor fits into the slot in the lid. Such a component is a fabricated solid piece of aluminum. It has side skirts that have through holes, which contain *teflon* bushing as guides to the linear rails. The linear rails, made of stainless steel, are used to ensure that the lifting movement of the part is aligned.

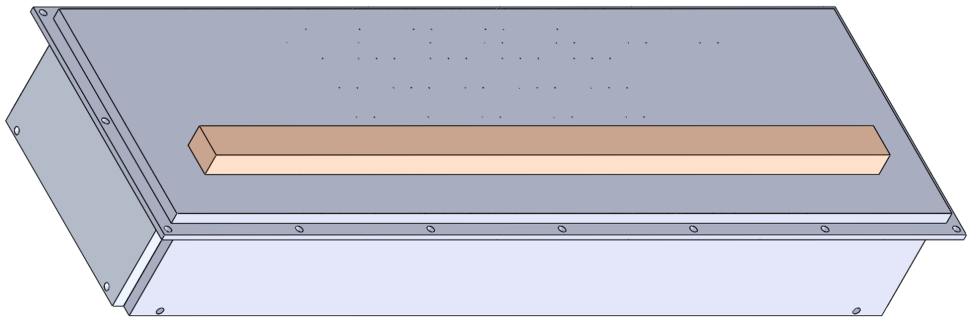
The bottom of the cavity may rise, changing the L/D aspect ratio. The drive takes place through two sets of threaded rod/stepper motors. Therefore, with the step retracted in its minimum stoke, the set forms a cavity with an aspect ratio $L/D = 1.5$. Oppositely, it becomes an isolated two-dimensional roughness with the same aspect ratio. The stroke of the bottom of the cavity is $\pm$20mm, with zero corresponding to the flat plate level. Figura 5 demonstrates this characteristic of the system. A computer drives the stepper motors, allowing for agile changing the cavity geometry without interrupting the wind tunnel's operation. Blind holes in the cavity floor house each stepper motor threaded rod as the cavity retracts. Mechanical stops installed in the case prevent impacts between the threaded rod and the end of these holes. The stepper motors are fitted externally to the bottom of the whole mechanism.

1.3 Fairing

The cavity system coupled on the opposite side of the plate with microphones together will form undesirable protrusions from an aerodynamic point of view. This

DISTRIBUTION A: Distribution approved for public release. Distribution unlimited

Figure 5 – Cavity bottom at its maximum stroke forms a 2D roughness.

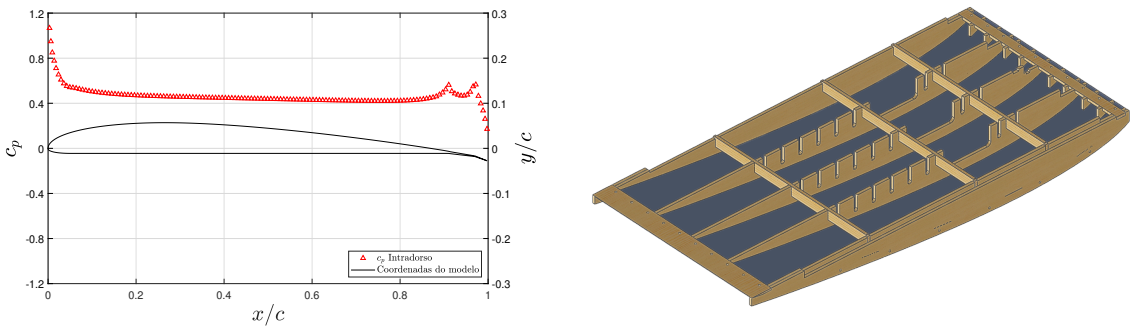


causes several aerodynamic effects, such as boundary layer separation, increased turbulent intensity, and pressure drop due to drag. The solution was to develop a fairing. Therefore, forming an aerodynamic profile when attached to the flat plate.

The strategy was to adapt the coordinates of the aerodynamic profiles to the geometric characteristics of the plate and the cavity system and, later, carry out an analysis of the flow using the software MSES and XFOIL Drela e Giles (1987).

The constant pressure distribution over the flat plate within a certain tolerance was the main criterion for the profile design. Other characteristics such as interference of the tunnel walls in the pressure distribution, as in **??**), and boundary layer separation was also analyzed. Figura 6a displays the model profile as well as the calculated pressure distribution on the flat plate, corresponding to the high-pressure side. The airfoil profile of the model has a maximum thickness of 6.8%, and maximum camber of 2.8%, both in 27% of the chord, which is 2.32 m with the leading edge, flap, and tab installed.

Figure 6 – Pressure distribution over the flat plate computed by the MSES in left vertical axis and profile coordinates in the right vertical axis in (a); isometric view of the fairing design in (b).



(a) (b)

Source: Author (2021).

Once defined the aerodynamic profile, we implemented its mechanical design. Figure Figura 6 displays the isometric view of the fairing computer-aided design. The fairing has

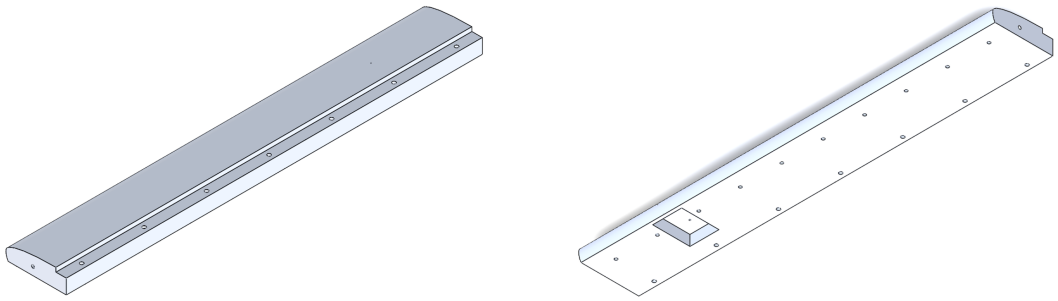
DISTRIBUTION A: Distribution approved for public release. Distribution unlimited

components similar to those of a typical aircraft wing, consisting of a structural frame with ribs, spars, and stringers covered with the skin. The frame was fabricated from naval plywood plates 10 mm thick, and the skin from a 0.5 mm thick aluminum sheet.

1.4 Leading edge

The leading edge is the component where the boundary layer emerges. It is made up of a solid piece made of aluminum. Its shape was carefully planned to respect the airfoil profile. This component couples to the flat plate, at the end that contains the fillister. The opposite face is where occurs the fairing fastening. Figura 7b displays the isometric views of the part. Figura 7a highlights the aerodynamic profile of the piece. As the cavity system's lid, the current part couples to the flat plate from the opposite side to minimize the presence of protrusions that can contaminate the boundary layer. One can observe from Figura 7b, a rectangular-shaped niche. This hollow allows one to access the pressure taps of the component and. The piece contains 5 pressure taps at different points to aid in determining the deflection angle of the flap and tab. To guarantee the part is securely fastened in the wind tunnel test chamber, two blind holes threaded into the side faces of the leading edge allow an extra point for fastening.

Figure 7 – Isometric view of the leading edge drawing.



(a) Top-side. (b) Bottom-side.

Source: Author (2021).

DISTRIBUTION A: Distribution approved for public release. Distribution unlimited

2 Experimental Methodology

The experimental procedure will be the disturbance of the boundary layer by means of a wave-packet generated by a loudspeaker. In this experimental technique, the loudspeaker generates, through an acoustic excitation, a pulse in the boundary layer. This, in turn, excites a band of TS modes, which, due to different amplification rates, only a few frequencies are observed in the signal spectrum in measurements downstream of the disturbance source. Therefore, in this experiment, the wave-packet is formed by the combination of several waves in the temporal domain. An advantage of this experimental technique is that it approximates the real situation, in which TS waves are excited by a range of frequencies.

Utilizing hot wire anemometry (HWA), boundary layer perturbations responses will be measured at selected positions in the streamwise and spanwise directions. The position selected relative to the boundary layer is $0.6\delta^*$, which is where the TS wave has the highest amplitude.

The experimental measurement region will contain 310 stations, which will be for each depth of cavity D. These measurement points will be distributed as:

1. 10 positions in the streamwise direction, starting from 300 mm downstream from the leading edge up to 1300 mm,
2. 31 positions in the spanwise direction, centered on the model centerline and far away 10mm of each other, covering a wingspan of 300mm.

In this experimental arrangement, pulses will be generated continuously at regular intervals and the probe will be held in each position for a time interval, not yet determined, to measure a set of wave-packets. This set of packets then will be ensemble-averaged to improve the signal-to-noise ratio. The execution of the experimental work is planned to be carried out in four phases:

1st - Measurement of the boundary layer profile;

2nd - Reproduction of **??**) wave-packet experiment to validate the structure;

3rd - Determination of the boundary layer transition point caused by the gap;

4th - Measurement of the effect of small gaps on TS waves.

The first planned stage of experiments has the objective of verifying the two-dimensionality of the boundary layer; without it, it is not possible to guarantee that the experiment is occurring as expected. The second stage, on the other hand, aims to test

DISTRIBUTION A: Distribution approved for public release. Distribution unlimited

the technique using a reference experiment and develop a base case, whereby the influence of the cavity will be evaluated. The third step aims to establish the limiting cases for performing this work. This group of experiments will only use the stations in the direction of the flow to determine the transition point. Finally, the fourth stage is the core of the work, in which different combinations of cavity depth D and of δ^*, and the effects on the TS waves will be measured.

2.1 Parametric space

For gap experiments, the parameters that control the parametric space are:

- Re_{δ^*} - Reynolds number based on displacement thickness δ^*;
- Re_D - Reynolds number based on cavity depth D;
- L/D - cavity aspect ratio;
- D/δ^*; - the ratio between depth D and displacement thickness δ^*.
- L/δ^*; - the ratio between width L and displacement thickness δ^*.

Of the four parameters, only one depends exclusively on the geometry of the gap (L/D). The others depend on the geometry of the gap and the wind tunnel freestream speed. The work carried out sought to adjust the values of L, D, and the initial position of the cavity in a way to fill the gap in the literature. There is a shortage of works for shallow cavities (depth ratio D/$\delta^* < 10$) in the literature, as cited by Mathias e Medeiros (2019) and Crouch, Kosorygin e Sutanto (2020). Experiments will be carried out exploring the following parameter variations:

1. The values of Re_{δ^*} at the leading edge of the gap will be varied between 850 and 1850.
2. The D/δ^* ratio can be varied between 0 and 21, thus ranging from cases of long and shallow cavities to deep cavities.
3. The ratio of gap width to boundary layer displacement thickness (L/δ^*) will cover the range between 14 and 31.2.

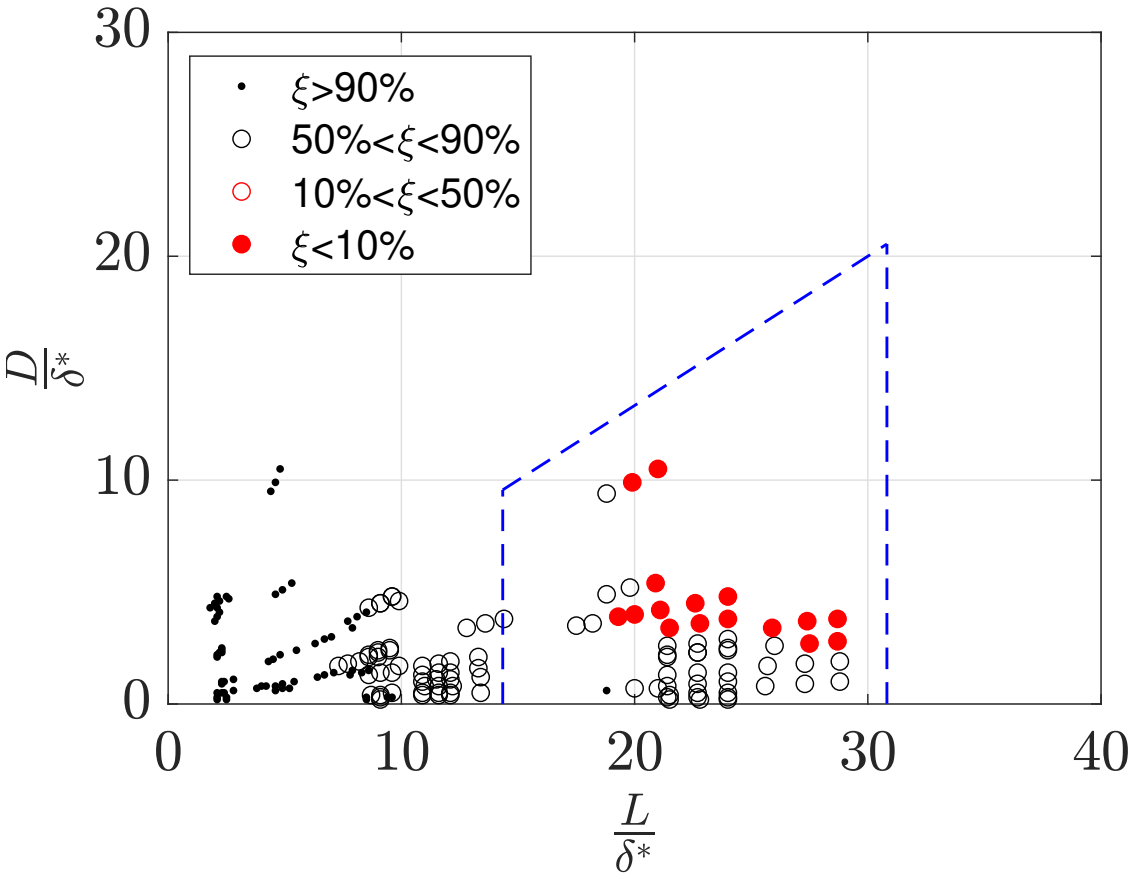
The parametric space encompasses the zone in which numerical and theoretical studies have identified a Rossiter-type instability, characterized by relatively deep and narrow gaps. This space also encompasses the scenario of shallow and long gaps, in which studies carried out by Boeing suggest that such gaps are stable but influence the evolution

DISTRIBUTION A: Distribution approved for public release. Distribution unlimited

of TS waves. Note that when we refer to deep or long gaps, we have the boundary layer thickness as a characteristic dimension. Therefore, in all cases, these are very small gaps, which are still very little explored in the literature.

Figure 8 shows a plot of L/δ^* x D/δ^*. The region inside the blue dashed lines represents the parametric space that will be achieved in the experiments. Data were taken from Crouch, Kosorygin e Sutanto (2020), ξ is the transition movement normalized by the transition length without the gap, this means that a lower ξ indicates a greater impact on the boundary layer transition due the presence of the gap.

Figure 8 – Comparison of the experiments parametric space with data from Crouch, Kosorygin e Sutanto (2020)



DISTRIBUTION A: Distribution approved for public release. Distribution unlimited

Bibliography

CROUCH, J. D.; KOSORYGIN, V. S.; SUTANTO, M. I. Modeling gap effects on transition dominated by tollmien-schlichting instability. In: *AIAA AVIATION 2020 FORUM*. American Institute of Aeronautics and Astronautics Inc, AIAA, 2020. v. 1 PartF, p. 1–8. ISBN 9781624105982. Disponível em: <https://arc.aiaa.org/doi/abs/10.2514/6.2020-3075>. Citado 2 vezes nas páginas 9 and 10.

DRELA, M.; GILES, M. B. Viscous-inviscid analysis of transonic and low Reynolds number airfoils. *AIAA Journal*, v. 25, n. 10, p. 1347–1355, 1987. ISSN 0001-1452. Citado na página 6.

MATHIAS, M. S.; MEDEIROS, M. A. Global instability analysis of a boundary layer flow over a small cavity. In: *AIAA Aviation 2019 Forum*. American Institute of Aeronautics and Astronautics Inc, AIAA, 2019. p. 1–13. ISBN 9781624105890. Disponível em: <https://arc.aiaa.org/doi/abs/10.2514/6.2019-3535>. Citado na página 9.

MEDEIROS, M. A.; GASTER, M. The production of subharmonic waves in the nonlinear evolution of wavepackets in boundary layers. *Journal of Fluid Mechanics*, Cambridge University Press, v. 399, p. 301–318, nov 1999. ISSN 00221120. Disponível em: <http://www.journals.cambridge.org/abstract_S0022112099006424>. Citado na página 3.

MEDEIROS, M. A. F. The nonlinear evolution of a wavetrain emanating from a point source in a boundary layer. *Journal of Fluid Mechanics*, Cambridge University Press, v. 508, p. 287–317, jun 2004. ISSN 0022-1120. Disponível em: <http://www.journals.cambridge.org/abstract_S0022112004009188>. Citado na página 3.

MEDEIROS, M. A. F.; GASTER, M. The influence of phase on the nonlinear evolution of wavepackets in boundary layers. *Journal of Fluid Mechanics*, Cambridge University Press, v. 397, p. S0022112099006175, oct 1999. ISSN 00221120. Disponível em: <http://www.journals.cambridge.org/abstract_S0022112099006175>. Citado na página 3.

TSUJI, Y. et al. Pressure statistics and their scaling in high-Reynolds-number turbulent boundary layers. *Journal of Fluid Mechanics*, Cambridge University Press, v. 585, p. 1–40, aug 2007. ISSN 00221120. Disponível em: <http://www.journals.cambridge.org/abstract_S0022112007006076>. Citado na página 4.

DISTRIBUTION A: Distribution approved for public release. Distribution unlimited